buildings

Special Issue Reprint

Buildings

10th Anniversary
Volume I

Edited by
David Arditi

MDPI

Buildings: 10th Anniversary-Volume I

Buildings: 10th Anniversary-Volume I

Editor

David Arditi

Editor
David Arditi
Illinois Institute of Technology
Chicago
USA

This is a reprint of articles from the Special Issue published online in the open access journal *Buildings* (ISSN 2075-5309) (available at: https://www.mdpi.com/journal/buildings/special_issues/Buildings_10th_Anniversary).

For citation purposes, cite each article independently as indicated on the article page online and as indicated below:

Lastname, A.A.; Lastname, B.B. Article Title. *Journal Name* **Year**, *Volume Number*, Page Range.

Cover image courtesy of S. R. Crown Hall, Illinois Institute of Technology, Chicago IL 60616

Contents

About the Editor

David Arditi

Dr. David Arditi is currently Professor Emeritus of Civil and Architectural Engineering at Illinois Institute of Technology. He is the founder and former Director of the Construction Engineering and Management Program. He established the Burton and Erma Lewis Construction Engineering and Management Laboratory in 1995 and the Trimble Technology Laboratory in 2022. Moreover, the sum of the funds that he raised in his academic career for research and lab development amounts to around USD 20 million. During his 50-year academic career, Professor Arditi conducted several funded research projects sponsored by federal and state agencies. He supervised the research of many PhD and MS students with diverse nationalities who occupy respectable academic and industry positions in over 20 countries. Dr. Arditi and his research associates have published close to 400 research papers in refereed national and international journals, edited books, and peer-reviewed conference proceedings. According to Google Scholar, by March 2024, Dr. Arditi's research papers received 15,814 citations and had an h-index of 73. He is currently serving as the Editor-in-Chief of *Buildings* (MDPI) and is Associate Editor of the *International Journal of Project Organization and Management*, in addition to serving on the editorial board of 12 journals in the field of construction project management. He regularly reviews research proposals, research papers, and textbooks for several research agencies and publishers located in the U.S., Canada, Saudi Arabia, Hong Kong, Israel, and Georgia. Dr. Arditi is an active member of several professional societies including CMAA, ASCE, AACE, and PMI. Furthermore, he is the recipient of multiple awards: he was elected to the College of Fellows of CMAA in 2013, named Professor of the Year by CAEE students in 2016, and elected a member of the National Academy of Construction (NAC) in 2022.

Preface

The scope of *Buildings* includes subjects related to building science, building engineering, building construction, and architecture. *Buildings* is organized into five sections: (1) Building Structures; (2) Building Materials and Repair and Renovation; (3) Building Energy, Physics, Environment, and Systems; (4) Architectural Design, Urban Science, and Real Estate; and (5) Construction Management, Computers, and Digitization. The "10th Anniversary" Special Issue comprises 39 research papers covering historical trends, the state of the art, current challenges, creative and innovative solutions, and future developments in each of these five sections (with 8 papers in Section 1, 6 in Section 2, 7 in Section 3, 6 in Section 4, and 12 in Section 5). Twenty-one papers focusing on the first three sections are in Book 1, whereas the remaining eighteen papers are in Book 2. I would like to thank the researchers who contributed to these two books of the Special Issue, as well as the reviewers, editors, and managerial staff (especially our Managing Editor at the time, Ms. May Zheng) who were involved in the production of this Special Issue. The multi-disciplinary nature of the 39 high-quality papers included in the "10th Anniversary" Special Issue reflects the high level of maturity that has been reached by *Buildings* over the last 10 years, as well as the wider impact of *Buildings* on building-related research and practices.

David Arditi
Editor

Article

The Journal *Buildings*: A Bibliometric Analysis (2011–2021)

Zhiwen Xiao [1], Yong Qin [1], Zeshui Xu [1,*], Jurgita Antucheviciene [2] and Edmundas Kazimieras Zavadskas [3]

1. Business School, Sichuan University, Chengdu 610064, China; farrah_x@163.com (Z.X.); yongqin_ahsc@163.com (Y.Q.)
2. Department of Construction Management and Real Estate, Vilnius Gediminas Technical University, Sauletekio al. 11, LT-10223 Vilnius, Lithuania; jurgita.antucheviciene@vilniustech.lt
3. Institute of Sustainable Construction, Vilnius Gediminas Technical University, Sauletekio al. 11, LT-10223 Vilnius, Lithuania; edmundas.zavadskas@vilniustech.lt
* Correspondence: xuzeshui@263.net

Abstract: The journal *Buildings* was launched in 2011 and is dedicated to promoting advancements in building science, building engineering and architecture. Motivated by its 10th anniversary in 2021, this study aims to develop a bibliometric analysis of the publications of the journal between April 2011 and October 2021. This work analyzes bibliometric performance indicators, such as publication and citation structures, the most cited articles and the leading authors, institutions and countries/regions. Science mappings based on indicators such as the most commonly used keywords, citation and co-citation, and collaboration are also developed for further analysis. In doing so, the work uses the Scopus database to collect data and Bibliometrix to conduct the research. The results show the strong growth of *Buildings* over time and that researchers from all over the world are attracted by the journal.

Keywords: bibliometrics; science mapping; Scopus; Bibliometrix

1. Introduction

Buildings is an international journal in the fields of building science, building engineering and architecture. Prof. Chimay J. Anumba, the founding editor, created the journal in 2011 [1]. Between 2011 and 2018, *Buildings* was published as a quarterly journal. In 2017, Prof. David Arditi became the editor-in-chief and in the next year, the journal increased the number of issues and began to publish every month. Today, the journal is well recognized in the scientific community. It is indexed in Scopus (Elsevier) and the Science Citation Index Expanded (SCIE) of Web of Science (Clarivate Analytics). According to the Journal Citation Reports (JCR) of the Web of Science, the journal's 2020 impact factor was 2.648, ranking 32nd of 66 journals in the category of Construction & Building Technology and 61st of 136 in Engineering, Civil. This was the first time that *Buildings* received an impact factor.

Recently, *Buildings* is celebrating its 10th anniversary. Inspired by this event, the main aim of this paper is to provide a thorough bibliometric analysis of the journal from the last ten years. A bibliometric performance analysis of *Buildings* is carried out based on key factors, such as the publication and citation structures, the most cited papers, and the leading authors, institutions and countries/regions. To map the bibliographic data graphically, this work uses a wide range of indicators including bibliographic coupling [2], co-citation [3], co-occurrence of keywords and collaboration. To this end, this work uses the Scopus database and Bibliometrix [4] to collect and analyze the bibliographic material.

Note that in the literature, it has become the norm to develop bibliometric research since it provides scholars with realistic and objective statistics and analysis, enabling researchers to build a comprehensive knowledge and understanding of the research field. The different application fields of bibliometric analysis include civil engineering and management [5], automation in construction [6], energy [7], road and bridge engineering [8],

transport [9], etc. Particularly, it is interesting to publish special issues or papers to celebrate the significant anniversary of a journal. A key example is that in 2015, *Knowledge-Based Systems* published a bibliometric analysis of its scientific content to celebrate its 25th birthday [10]. Many other journals have published special issues or papers to celebrate their anniversaries, such as *International Journal of Systems Science* [11] and *Information Sciences* [12].

This paper is organized as follows: Section 2 presents the bibliometric methods used in this paper. Section 3 provides the bibliometric performance analysis. The science mapping analysis of *Buildings* is carried out in Section 4. Finally, Section 5 gives a short description of the main findings and conclusions of the paper.

2. Bibliometric Methods

The term bibliometrics was first created by Paul Otlet [13] in 1934 and further defined by Broadus [14] as "the quantitative study of physical published units, or of bibliographic units, or of the surrogates for either". Bibliometrics is valued as an important and useful approach to analyze academic research outputs and deal with overwhelming volumes of information [15]. Several decades ago, it was difficult for researchers to collect and classify complex bibliometric data due to the lack of efficient technology or software. However, thanks to the rapid development of science and technology, different bibliometric tools and software are available now to assist scholars in conducting their research [16].

In this paper, the bibliometric data come from Scopus, one of the world's leading academic databases. Scopus covers more than 80 million documents and 17 million author profiles. The search covered the period from April 2011 to October 2021 using "Buildings" as the source title. Note that there was another journal with the same name between 1996 and 2002 and it is not included within the scope of this research. A total of 1466 articles shown as the results were considered (1542 articles have been published in *Buildings* so far, but the other 76 documents were omitted since they were not directly available in Scopus).

The authors used Bibliometrix to collect and analyze the dataset and develop the graphical visualization. This unique tool was developed in R language by Aria and Cuccurullo [4] in 2017. To conduct this study using a bibliometric method, several bibliometric indicators from different perspectives were considered. As for bibliometric performance analysis, we analyzed the journal's annual publications, citation structure and the most cited papers, as well as the leading authors, institutions and countries/regions. As for science mapping analysis in Section 4, we analyzed the keywords of the articles published in *Buildings* and describe studies based on citations, co-citations and collaborations. The whole process of bibliometric analysis of the journal is illustrated in Figure 1.
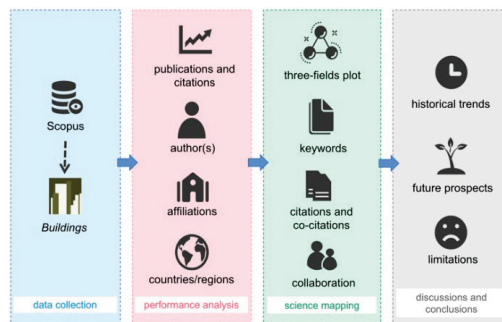
Figure 1. The process of bibliometric analysis.

3. Bibliometric Performance Analysis of *Buildings*

In this section, several performance indicators including the publication and citation structure, the most cited papers and the leading authors, institutions and countries/regions are used.

3.1. Structure of Publications and Citations

Buildings published its first volume with one issue in 2011 and expanded to contain four issues in the next year. In 2018, the journal adopted a monthly publication schedule and since then it has published 12 issues per year. The distribution of publications and citations up to October 2021 is shown in Table 1. Additionally, several citation thresholds are included to provide a better overview.

Table 1. Annual publication and citation structure.

Year	TP	TC	≥50	≥20	≥10	≥5	≥1
2011	2	13	0	0	1	1	1
2012	27	764	4	12	15	21	27
2013	39	407	1	6	14	26	38
2014	47	551	1	9	18	28	43
2015	75	1124	3	20	38	55	72
2016	51	500	0	5	22	39	49
2017	121	1695	4	31	64	96	121
2018	187	1638	2	18	61	110	177
2019	237	1684	1	14	66	121	224
2020	246	731	0	0	14	55	205
2021	434	307	0	0	2	6	154
Total	1466	9414	16	115	315	558	1111
%	100.00%		1.09%	7.84%	21.49%	38.06%	75.78%

Abbreviations: TP and TC = Total papers and citations; ≥50, ≥20, ≥10, ≥5, ≥1 = Number of papers with equal or more than 50, 20, 10, 5 and 1 citation(s).

Until 2016, the journal published a small number of papers per year. In 2017, more than twice as many articles as the previous year were published. This change reflects the growing popularity of *Buildings* in the scientific community. In 2020, the journal published its 1000th paper, which marked a new milestone. Between 2011 and 2016, the pattern of citations received per year was variable, reaching peaks of 1124 citations in 2015. Then, the number of citations remained around 1600 from 2017 to 2019 and decreased significantly after 2019. This phenomenon in the two last years (2020 and 2021) may be caused by the citation time-window [11], so citations may pick up in the following years. Note that 1.09% of papers receive more than 50 citations and 7.84% more than 20. A proportion of 38.06% of documents have more than five citations and 75.78% get at least one citation. It can be observed that once articles are a few years old, there are very few uncited articles in *Buildings*. This result shows that *Buildings* is a high-quality and widely recognized journal. Next, let us consider the most cited papers published in the journal. Note that research articles and review articles are divided and the results are summarized in Tables 2 and 3, respectively.

Table 2. Most cited papers (research articles).

R	TC	Title	Author/s	Year	C/Y
1	181	Design of A Sustainable Building: A Conceptual Framework for Implementing Sustainability in the Building Sector	Akadiri, P.O.; Chinyio, E.A.; Olomolaiye, P.O.	2012	18.10
2	94	A Comparative Cradle-to-Gate Life Cycle Assessment of Mid-Rise Office Building Construction Alternatives: Laminated Timber or Reinforced Concrete	Robertson, A.B.; Lam, F.C.F.; Cole, R.J.	2012	9.40
3	65	Fatigue-Prone Details in Steel Bridges	Haghani, R.; Al-Emrani, M.; Heshmati, M.	2012	6.50
4	63	Rethinking Design and Urban Planning for the Cities of the Future	Saaty, T.L.; De Paola, P.	2017	12.60
5	60	A Thermal Simulation Tool for Building and Its Interoperability through the Building Information Modeling (BIM) Platform	Bahar, Y.N.; Pere, C.; Landrieu, J.; Nicolle, C.	2013	6.67

Table 2. *Cont.*

R	TC	Title	Author/s	Year	C/Y
6	55	Rocking and Kinematic Approaches for Rigid Block Analysis of Masonry Walls: State of the Art and Recent Developments	Casapulla, C.; Giresini, L.; Lourenço, P.B.	2017	11.00
7	54	Adaptive Thermal Comfort in Japanese Houses during the Summer Season: Behavioral Adaptation and the Effect of Humidity	Rijal, H.B.; Humphreys, M.; Nicol, F.	2015	7.71
8	52	A Production Model for Construction: A Theoretical Framework	Antunes, R.; Gonzalez, V.	2015	7.43
9	50	Strategies for Applying the Circular Economy to Prefabricated Buildings	Minunno, R.; O'Grady, T.; Morrison, G.M.; Gruner, R.L.	2018	12.50
10	49	Seismic Analysis of Historic Masonry Buildings: The Vicarious Palace in Pescia (Italy)	Betti, M.; Galano, L.	2012	4.90
11	48	Daylight Design of Office Buildings: Optimisation of External Solar Shadings by Using Combined Simulation Methods	González, J.; Fiorito, F.	2015	6.86
12	48	Building Information Modelling for Smart Built Environments	Zhang, J.; Seet, B.-C.; Lie, T.T.	2015	6.86
13	47	Life Cycle Assessment (LCA) of Different Kinds of Concrete Containing Waste for Sustainable Construction	Colangelo, F.; Forcina, A.; Farina, I.; Petrillo, A.	2018	11.75
14	46	Material Efficiency of Building Construction	Ruuska, A.; Häkkinen, T.	2014	5.75
15	43	Economic-Environmental Indicators to Support Investment Decisions: A Focus on the Buildings' End-of-Life Stage	Fregonara, E.; Giordano, R.; Ferrando, D.G.; Pattono, S.	2017	8.60
16	43	BIM Guidelines Inform Facilities Management Databases: A Case Study over Time	Kensek, K.	2015	6.14
17	42	Integrating Simplified and Full Life Cycle Approaches in Decision Making for Building Energy Refurbishment: Benefits and Barriers	Oregi, X.; Hernandez, P.; Gazulla, C.; Isasa, M.	2015	6.00
18	41	Rooftop PV Potential in the Residential Sector of the Kingdom of Saudi Arabia	Khan, M.M.A.; Asif, M.; Stach, E.	2017	8.20
19	41	Using Genetic Algorithms for Real Estate Appraisals	Del Giudice, V.; De Paola, P.; Forte, F.	2017	8.20
20	39	Energy and Economic Evaluation of Green Roofs for Residential Buildings in Hot-Humid Climates	Mahmoud, A.S.; Asif, M.; Hassanain, M.A.; Babsail, M.O.; Sanni-Anibire, M.O.	2017	7.80

Table 3. Most cited papers (review articles).

R	TC	Title	Author/s	Year	C/Y
1	98	A Review of Seismic Isolation for Buildings: Historical Development and Research Needs	Warn, G.P.; Ryan, K.L.	2012	9.80
2	89	Self-Centering Seismic Lateral Force Resisting Systems: High Performance Structures for the City of Tomorrow	Chancellor, N.B.; Eatherton, M.R.; Roke, D.A.; Akbaş, T.	2014	11.16
3	83	The Vertical Farm: A Review of Developments and Implications for the Vertical City	Al-Kodmany, K.	2018	20.75
4	65	A Review of Psychological Literature on the Health and Wellbeing Benefits of Biophilic Design	Gillis, K.; Gatersleben, B.	2015	9.29
5	60	Performance Review of Prefabricated Building Systems and Future Research in Australia	Navaratnam, S.; Ngo, T.; Gunawardena, T.; Henderson, D.	2019	20.00
6	58	Estimation and Minimization of Embodied Carbon of Buildings: A Review	Akbarnezhad, A.; Xiao, J.	2017	11.60
7	51	PCMs for Residential Building Applications: A Short Review Focused on Disadvantages and Proposals for Future Development	Bland, A.; Khzouz, M.; Statheros, T.; Gkanas, E.I.	2017	10.20
8	49	Recent Progress in Daytime Radiative Cooling: Is It the Air Conditioner of the Future?	Santamouris, M.; Feng, J.	2018	12.25
9	32	A Scientometric Review and Metasynthesis of Building Information Modelling (BIM) Research in Africa	Saka, A.B.; Chan, D.W.M.	2019	10.67
10	32	Blockchain and Building Information Modeling (BIM): Review and Applications in Post-Disaster Recovery	Nawari, N.O.; Ravindran, S.	2019	10.67

Note that in the case of a tie in the number of citations, the youngest paper appears first. The most cited research article was published by Akadiri, P.O., Chinyio, E.A. and Olomolaiye, P.O. in 2012, with 181 citations. This paper proposed a framework based on the sustainable triple bottom line principle, including resource conservation, cost efficiency and design for human adaptation [17]. This paper is the only one that has received more than one hundred citations. Considering the indicator of citations per year, it can be found that Al-Kodmany, K. comes first. Prof. Al-Kodmany delivered a review on a vertical farm and analyzed its developments and implications for a vertical city [18]. Although this research was published only three years ago, it has received more than 70 citations, indicating the widespread interest in vertical farms.

3.2. Leading Authors, Institutions and Countries/Regions

This section reviews the most contributing authors, originating institutions and countries/regions based on published papers in *Buildings*.

First, the 20 most productive authors are shown in Table 4. To provide a better overview, several other bibliometric indicators including author Scopus ID, countries/regions, the number of citations and the cites per paper ratio are also considered. The table ranks the data based on the number of publications and, in the case of a tie, according to the number of citations. We can highlight that Dr. Sepasgozar, Prof. Al-Kodmany, Prof. Bedon and Dr. Zhang are the most productive authors in the journal. Dr. Sepasgozar published 14 scholarly papers in *Buildings* concerning digital technology applications, such as three-dimensional printing [19], digital twin [20] and additive manufacturing applications [21]. Prof. Al-Kodmany conducted research mainly on the sustainability of tall buildings [22–24], vertical farms [18] and vertical cities [25]. Note that Prof. Al-Kodmany and Bedon were the winners of the "*Buildings* 2018 Best Paper Awards" and "*Buildings* 2020 Young Investigator Awards", respectively. As Prof. Bedon and Dr. Zhang have only started publishing papers in *Buildings* in recent years, their citations are relatively low compared to other leading authors.

Table 4. Most productive authors.

R	Author	Scopus ID	Country/Region	TP	TC	TC/TP
1	Sepasgozar, S.M.E.	55924332100	Australia	14	224	16.00
2	Al-Kodmany, K.	6603005886	USA	9	191	21.22
3	Bedon, C.	57217221032	Italy	9	54	6.00
4	Zhang, X.	57209625490	Sweden	9	24	2.67
5	Iannace, G.	6506458238	Italy	8	93	11.63
6	Kvande, T.	6504559094	Norway	8	63	7.88
7	Lafhaj, Z.	6508004741	France	8	31	3.88
8	de Brito, J.	7003285554	Portugal	8	21	2.63
9	Blanchet, P.	7102260600	Canada	8	20	2.50
10	Trematerra, A.	56016998400	Italy	7	58	8.29
11	Wang, C.C.	57194027095	Australia	7	24	3.43
12	Silva, A.	25959361900	Portugal	7	11	1.57
13	de Paola, P.	56433637200	Italy	6	162	27.00
14	Lourenço, P.B.	7004615647	Portugal	6	101	16.83
15	Shirowzhan, S.	55923557900	Australia	6	66	11.00
16	Mojtahedi, M.	57211244906	Australia	6	59	9.83
17	Sassu, M.	6508376589	Italy	6	56	9.33
18	Ciaburro, G.	55459296100	Italy	6	47	7.83
19	Edwards, D.J.	7404086765	United Kingdom	6	27	4.50
20	Hammad, A.W.A.	56430620200	Australia	6	15	2.50

Another interesting issue to analyze is the most productive affiliations of the journal. For this purpose, Table 5 presents the 20 most productive affiliations. As in the previous table, other indicators are also included to provide a better overview. The University of New South Wales clearly obtains the first position with 46 articles, followed by the

University of Naples Federico II and the Norwegian University of Science and Technology. It is interesting to note that even though the University of Naples Federico II has published only about half as many articles as the University of New South Wales, it has a higher citation rate. Furthermore, the University of Naples Federico II and Norwegian University of Science and Technology have published almost the same number of papers, but the former has the leading number of citations.

Table 5. Most productive affiliations.

R	Affiliations	Country/Region	TP	TC	TC/TP
1	University of New South Wales	Australia	46	345	7.50
2	University of Naples Federico II	Italy	24	364	15.17
3	Norwegian University of Science and Technology	Norway	23	142	6.17
4	University of Minho	Portugal	20	175	8.75
5	Sapienza University of Rome	Italy	17	138	8.12
6	Curtin University	Australia	15	137	9.13
7	University of Pisa	Italy	14	185	13.21
8	Tongji University	China	13	124	9.54
9	The University of Melbourne	Australia	13	113	8.69
10	The University of Sydney	Australia	13	107	8.23
11	Ryerson University	Canada	13	98	7.54
12	The Hong Kong Polytechnic University	China	13	75	5.77
13	Rzeszow University of Technology	Poland	13	55	4.23
14	Deakin University	Australia	13	27	2.08
15	Lund University	Sweden	12	87	7.25
16	Aalto University	Finland	12	69	5.75
17	Delft University of Technology	The Netherlands	12	46	3.83
18	University of Florida	USA	11	102	9.27
19	University of Trieste	Italy	11	68	6.18
20	Polytechnic University of Bari	Italy	11	61	5.55

Finally, the most productive countries/regions are shown as follows in Table 6 and Figure 2. Globally, Italy dominates the list with nearly twice the number of papers than the USA, which is in second place. Australia comes in third, with 105 total papers. Note that in Tables 2 and 3, the majority of productive authors and institutions are from Italy and Australia, so there is no doubt that these countries rank high. Furthermore, Italy is the only country that has published more than 200 papers and has more than 2000 citations. From the indicator of MCP/MRP, we can conclude that countries such as Italy, Australia and United Kingdom have a strong willingness to cooperate with other countries/regions.

Table 6. Most productive countries/regions.

R	Country/Region	TP	SCP/SRP	MCP/MRP	TC	TC/TP
1	Italy	209	172	37	2085	9.98
2	USA	114	89	25	1118	9.81
3	Australia	105	71	34	741	7.06
4	United Kingdom	98	70	28	907	9.26
5	Poland	79	72	7	252	3.19
6	China	73	48	25	153	2.10
7	Portugal	53	45	8	287	5.42
8	Sweden	50	40	10	316	6.32
9	Canada	48	37	11	351	7.31
10	Spain	42	33	9	191	4.55

Table 6. *Cont*.

R	Country/Region	TP	SCP/SRP	MCP/MRP	TC	TC/TP
11	New Zealand	29	25	4	249	8.59
12	Finland	28	19	9	166	5.93
13	Germany	27	16	11	166	6.15
14	Japan	24	17	7	138	5.75
15	France	22	13	9	204	9.27
16	Korea	22	20	2	24	1.09
17	Norway	22	19	3	108	4.91
18	Saudi Arabia	21	16	5	154	7.33
19	Greece	18	16	2	63	3.50
20	Indonesia	17	13	4	138	8.12

Abbreviations: SCP/SRP = Single Country Production/Single Region Production; MCP/MRP = Multiple Country Production/Multiple Region Production.
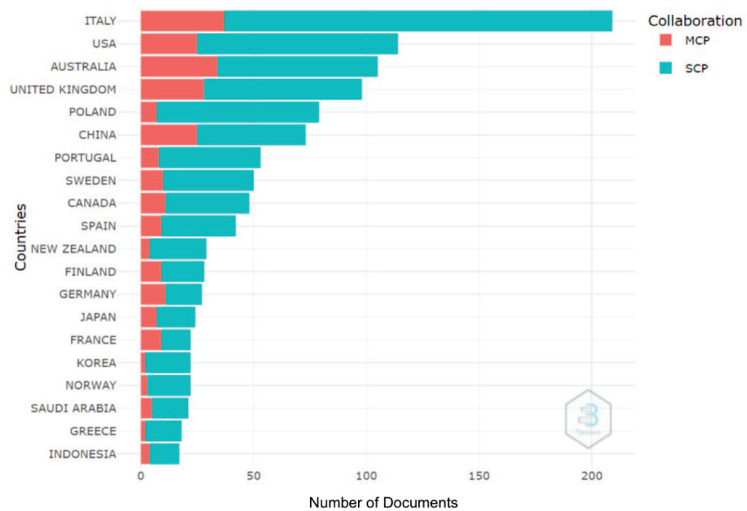
Figure 2. Most productive countries/regions.

4. Science Mapping Analysis of *Buildings*

This section developed a science mapping based on key factors including keywords, citation/co-citation and collaboration.

4.1. Analysis of Keywords

To begin with, we analyzed the author keywords occurring in the journal and their frequency, thematic map, growths, trends, and thematic evolution. Note that author keywords sum up the issues involved in an article and author preferences [26].

Figure 3 depicts a word cloud to show the 50 most frequent author keywords in papers in *Buildings*. The size of words demonstrates the word's frequency of occurrence. It is not surprising to find that the keyword "sustainability" is in the center of the graph, followed by "energy efficiency" and "thermal comfort". "Buildings", "bim" (Building Information Modeling) and "construction" also show their importance. "Climate change" has been a hot topic in recent years, especially in fields such as architecture and the environment. Other building performance parameters, such as "durability" and "natural ventilation", are also commonly utilized.

Figure 3. Word cloud of keywords.

Then, to get further understanding, Figure 4 depicts a thematic map of author keywords. A thematic map allows the visualization of four different typologies of themes based on two dimensions, i.e., density and centrality. Density is the strength of internal ties among all the keywords that are used to describe the research theme, while centrality is the strength of external ties to other themes by exploiting the authors' keyword field [27]. The upper-right quadrant called motor themes has clusters that are vital and well-developed in *Buildings*. In this quadrant, Cluster 1 includes "lean construction", "refurbishment", "embodied energy", "project management" and "case study". The position of Cluster 1 indicates its highest density among these keywords and its above-average importance. The upper-left quadrant called niche themes has clusters that are well-developed but not vital for the domain. From this quadrant, Cluster 1 includes "reinforced concrete", "cultural heritage", "pushover analysis", "seismic assessment" and "masonry", while Cluster 2 includes "durability", "concrete", "building envelope", "compressive strength" and "fly ash", and the third one includes "facility management" and "machine learning". Due to the close position of Cluster 1 and Cluster 2, we can argue that both of them are well developed but not the most vital for the domain. It is evident that Cluster 3 indicates its lowest importance in this map. The lower-left quadrant called emerging or declining themes has clusters with lower centrality as well as density in *Buildings*. The only cluster in this quadrant includes "optimization", "residential buildings", "energy performance" and "genetic algorithm". Finally, the lower-right quadrant called basic themes has clusters that are crucial for the domain but not well-developed or clusters that are cornerstones of the domain. In this quadrant, Cluster 1 includes "buildings", "climate change", "energy", "comfort" and "energy saving" and the second one includes "building information modeling", "construction", "productivity" and "retrofitting". It is obvious that some of them are basic concepts, such as "buildings", "construction" and so on. Some others, such as "climate change" and "energy saving", are important and need more attention.

Another interesting issue to consider is the annual growth of the top 10 keywords. Figure 5 demonstrates the evolution clearly from 2011 to 2021. On the whole, every keyword increased yearly, and this phenomenon also shows the sustained and steady development of *Buildings*. From the details, it is striking that "energy efficiency", "thermal comfort" and "sustainability" have remained the top three occurrences in the past decade. "Buildings", with a sharp increase in the curve, has emerged as the fourth most common occurrence since 2016. "BIM" has maintained a high growth rate since 2018; it emerged as the sixth most common keyword in 2021 while its occurrence was very low before 2018. Although "durability" consistently had the fewest occurrences, it has seen a significant increase after 2019, and we can assume that it will continue to grow in the future.
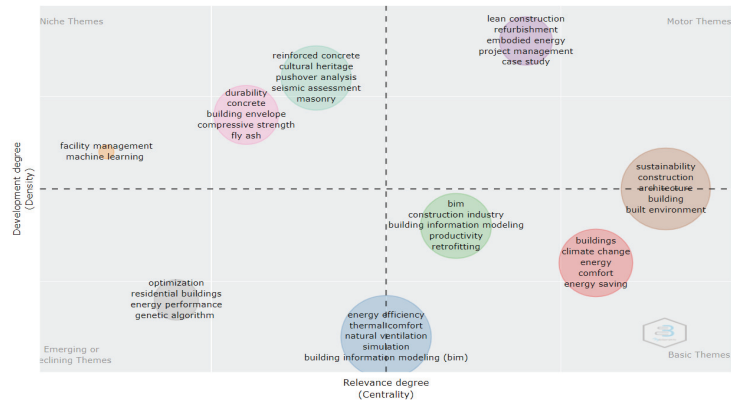
Figure 4. Thematic map of keywords.
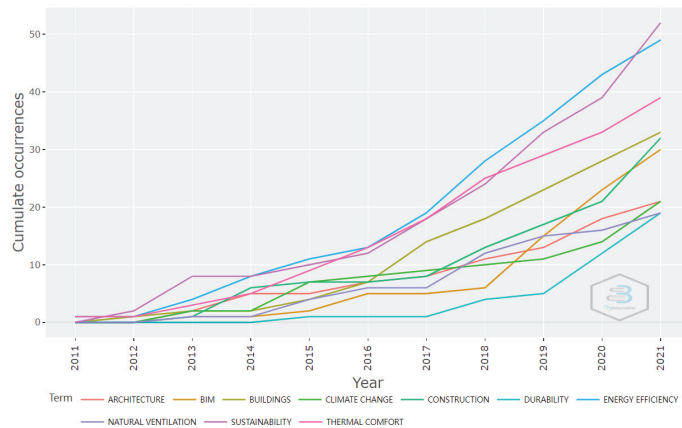
Figure 5. Growth of the top 10 keywords.

A further interesting issue is to analyze the trending topics in *Buildings*. Figure 6 depicts the top topics based on the keyword occurrences that have been continuously studied since 2011. As noted, on the right side of the figure, the topic frequency from 10 to 50 is demonstrated by the blue-filled circle, and the larger the circle, the higher the frequency. The topic "energy" was the only popular topic in the early years of *Buildings*. Then, in 2016 and 2017, some other topics such as "climate change", "simulation" and "energy efficiency" began to receive scholars' attention in *Buildings*. In 2016, "simulation" attracted more attention than "energy". Next, in 2017, "optimization", "sustainability" and "buildings" appeared in the trending topics list and continued to maintain scholars' attention. It is noticeable that "sustainability" and "construction" became the most two significant topics in 2019 and surpassed "energy efficiency" and "thermal comfort", which were most popular in 2018. However, from 2020 to 2021, "concrete", "cultural heritage", "durability" and "construction industry" have been focal points. Moreover, we can predict that these newly popular topics will continue to receive more attention in *Buildings*.
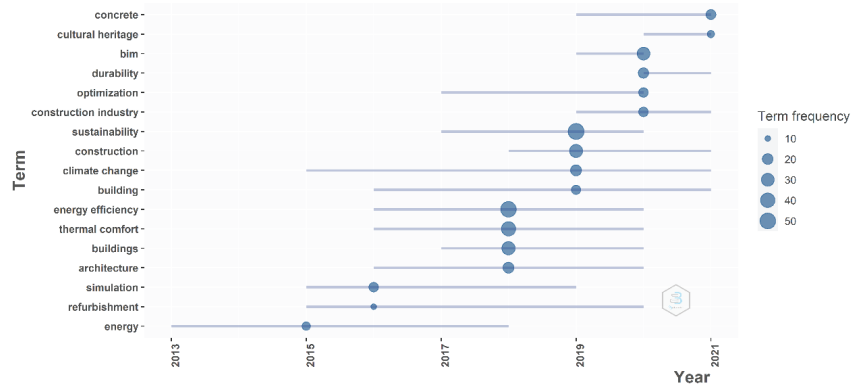
Figure 6. Trending topics.

Last but not least, in order to analyze the thematic evolution of the journal, we developed a Sankey diagram, shown in Figure 7. A Sankey diagram is used to show how different themes are connected and have developed in the past [28]. Each box in the map denotes a theme, and the size of boxes is proportional to the frequency of the theme's occurrences [29]. The flows connect each box showing the evolution traces of the theme, and the thicker the connecting line, the higher the linkage of the two themes.
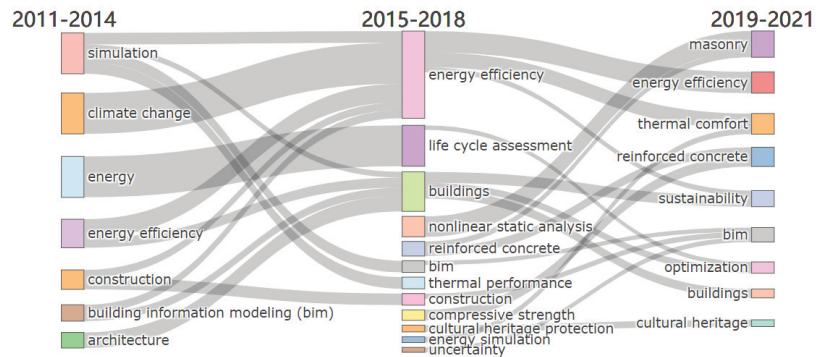
Figure 7. Thematic evolution.

From an overall perspective, it can be found that as time goes by, themes in *Buildings* are becoming increasingly diverse, probably because more and more scholars from different fields are attracted to the journal. It is noticeable that "energy efficiency" first appeared in 2011–2014, was further developed in the following four years, and continued to draw attention in the final time zone 2019–2021. Furthermore, this topic was the most popular one between 2015 and 2018. Some objective indicators, such as "optimization", "sustainability" and "thermal comfort", have only started to flourish in recent years. This result reflects the state-of-the-art of the journal.

4.2. Analysis of Three-Fields Plot

The three-fields plot embedded in the Bibliometrix tool allows us to understand the complete bibliometric research in one figure and exhibit proportionality among the content [27]. Figure 8 shows the most active 15 countries/regions in *Buildings* in the left field, keywords that these countries/regions are using in the middle field, and the main journal sources in the right field. From the middle field, we find that the scholars in *Buildings* focus more on "energy efficiency", "thermal comfort", "sustainability", "buildings" and

"construction". This field reveals hot topics that scholars should pay closer attention to. These results are the same as in Figure 3. Note that "energy efficiency" and "thermal comfort" are prevalent in *Energy and Buildings*, whereas "thermal comfort" is more prevalent in *Build and Environment*. Furthermore, it is obvious from the right field that *Energy and Buildings* and *Building and Environment* are playing the most significant roles as major sources in *Buildings*. From the left field, it is noticed that the United Kingdom, Italy, the USA and Australia have the largest number of publications in *Buildings* and cover most research areas, and this result is consistent with our previous analyses.
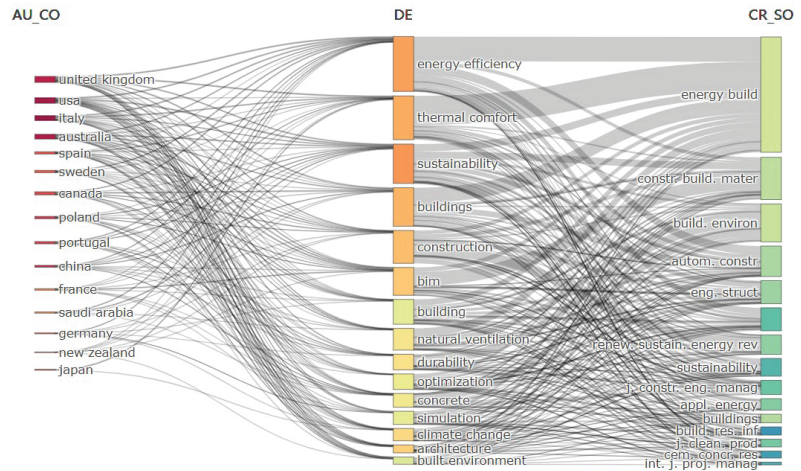
Figure 8. Three-fields plot.

4.3. Analysis of Citations and Co-Citations

We next created a historiograph of *Buildings*. Figure 9 shows the chronological map based on the most relevant citations. Each flow in the same color identifies a direct citation and signifies a concept and its historical development. The nodes in the flows are core documents with high citations (both local citations and global citations are taken into account). The largest citation stream is in blue, starting with the research of Vinokurov, M. in 2018 [30] and 2019 [31]. This path provides several new insights on the efficiency, economy and climate implications of the energy solutions. Note that as the most cited author in this figure, Fargnoli, M. is also marked in blue. He proposed two novel methods based on Preliminary Human Safety Assessment (PHSA) [32] and BIM [33] in order to enhance occupational safety in the construction industry. The second largest citation stream is in red, starting in 2019 and further developing in 2021. These papers in red provide insights into and analysis of seismic vulnerability [34], seismic assessment [35] and nonlinear static procedures [36]. Other citation streams all contain only a few nodes. From the diversity of colors in this map, we can conclude that *Buildings* covers a wide range of research topics and applications.

Then, we looked into the co-citations of journals regarding documents published in *Buildings*. A co-citation of journals occurs when two documents from different journals receive a citation from the same third document [3]. Fifty journals are shown in Figure 10. The colored circles and lines represent the journals and their co-linkages with other journals, respectively. At the same time, the size of the circle represents the citation weight [37]. We can intuitively see that this map is divided into three clusters with different colors. It is obvious that the three biggest circles in this colorful map are *Energy and Buildings* in green, *Building and Environment* in green and *Buildings* in blue. Therefore, these three journals have the largest number of citations and the broadest network. The blue *Buildings* circle links with journals such as *Sustainability* and *Automation in Construction*, and they form a

blue cluster together. As for the green cluster, *Energy and Buildings* has co-citations with *Automation in Construction, Energies* and other green circles. Similarly, the formation of the red cluster is based on the same theory. However, the red cluster has fewer citations and linkages than the other two clusters.
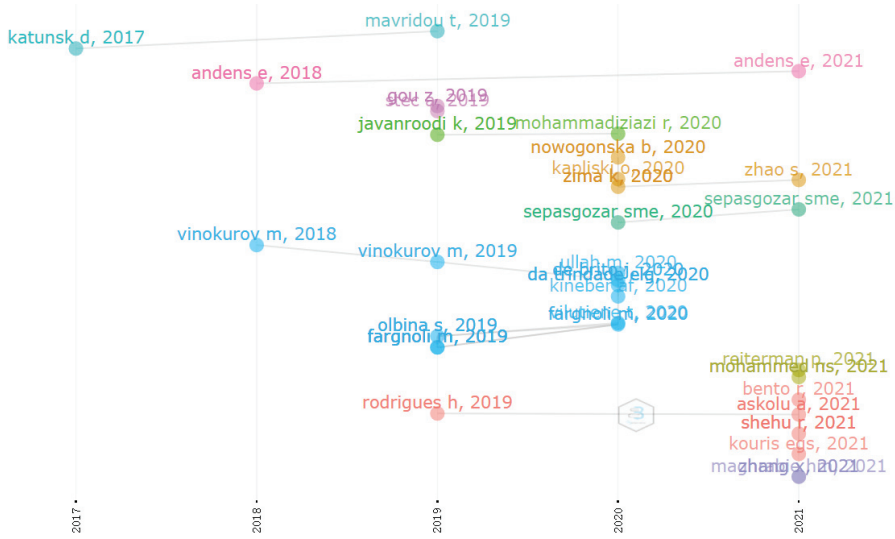
Figure 9. Historical direct citation network.
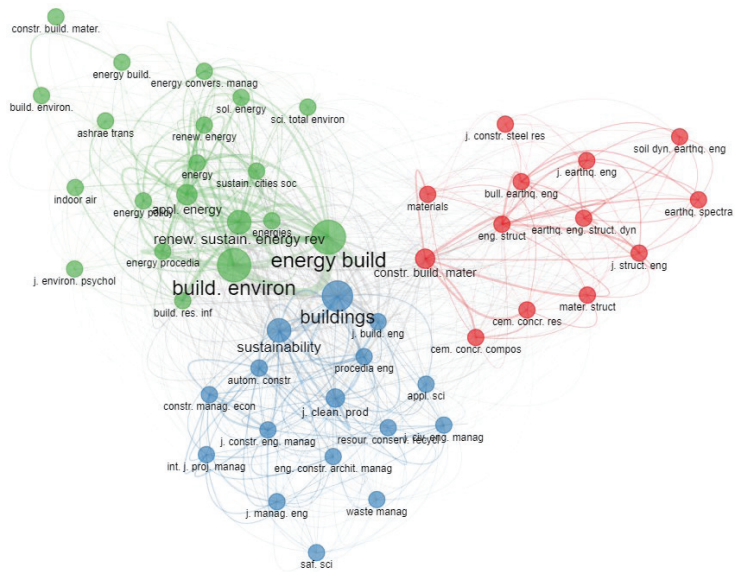
Figure 10. Co-citation network of journals.

4.4. Analysis of Collaboration

Figure 11 depicts the collaboration network of institutions in *Buildings*. The colored circles and lines represent the institutions and their collaborations with other institutions, respectively. This map is divided into seven clusters with different colors. By querying the

countries or regions where these institutions belong, it is not difficult to find that almost all the institutions in the same cluster come from the same country or region. For instance, Moscow Automobile and Road Construction University, Far Eastern Federal University, Belgorod State Technological University and Peter the Great Saint-Petersburg Polytechnic University are all located in Russia. Similarly, the institutions in the red cluster come from Australia, the pink from France, the yellow from Canada and the blue from Italy. However, the green cluster contains the University of New South Wales from Australia and Universidade Federal do Rio de Janeiro from Brazil, and the brown cluster contains the Central University of Technology from South Africa and Leeds Beckett University from the United Kingdom.
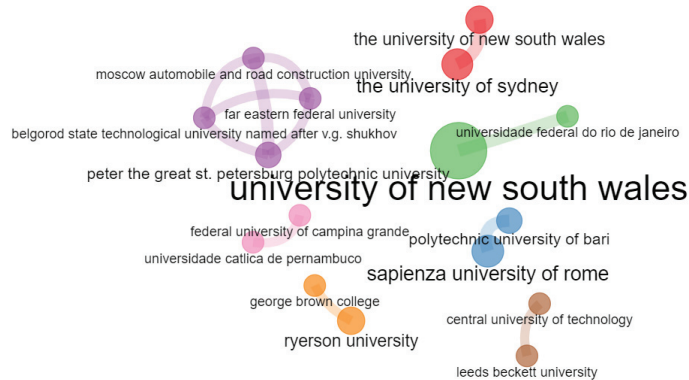
Figure 11. Collaboration network of institutions.

Buildings has a massive international collaboration, which contributes to the global academic exchange. The international collaboration network identifies how countries and regions are related in the journal. Figure 12 shows results at the geographic level, and Figure 13 shows these in detail. In Figure 12, the shade of countries/regions and the thickness of lines represents the number and the proportion of their collaborations, respectively. Not surprisingly, the most active area is the European sector. We can observe that China and Australia demonstrate the strongest cooperative tie with each other. In Figure 13, the size of countries/regions represents the number of their collaborations, and the larger the circle, the more cooperative partners they have. The thickness of lines indicates the closeness of the collaboration of countries/regions. Italy has the widest range of cooperative partners, followed by the United Kingdom, Australia, the USA and China. These five countries are high-yield countries. Furthermore, it can be observed that China, the USA and Australia have a strong connection with each other, and their willingness to cooperate with each other is evident.
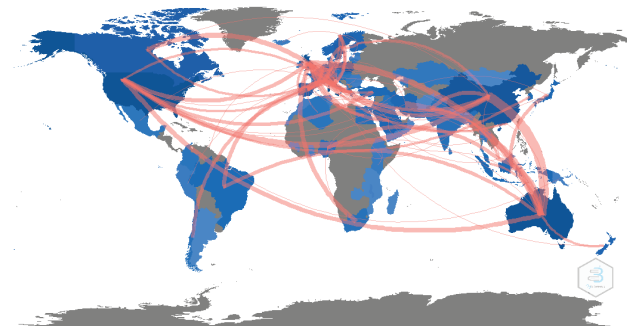
Figure 12. An overview of cooperation between countries/regions.
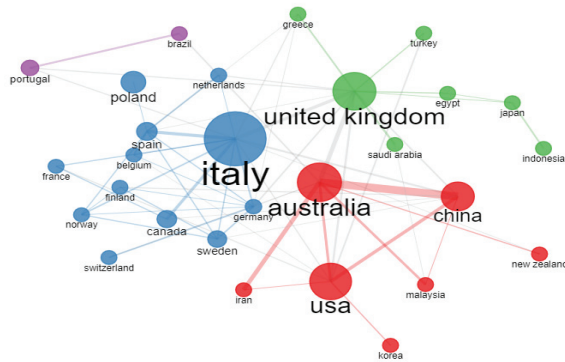
Figure 13. Collaboration network of countries/regions.

5. Discussions and Conclusions

Buildings was first published 10 years ago in 2011. Motivated by its 10th anniversary, this study presents a bibliometric analysis of publications in the journal between 2011 and 2021. This work adopts two bibliometric methods: performance analysis and science mapping [38].

Regarding performance analysis, the research first identified the publication and citation structure of the journal. The results show the strong growth of *Buildings* throughout time. Up to now, the journal has published more than one thousand documents and is widely acknowledged by scholars all over the world. The most cited paper, entitled "*Design of A Sustainable Building: A Conceptual Framework for Implementing Sustainability in the Building Sector*", was written by Akadiri, P.O., Chinyio, E.A. and Olomolaiye, P.O. in 2012. Then, this work reviewed the leading authors, institutions and countries/regions. The results indicate that Italy is the most productive country in *Buildings*, well above the results of the USA, which appears at the second position. The University of New South Wales, located in Australia, has been the most productive affiliation over the past 10 years with 46 publications and 345 citations in total. Looking at the most cited authors, we recognize the contributions of Sepasgozar, S.M.E. from Australia, Al-Kodmany, K. from the USA, Bedon, C. from Italy and Zhang, X. from Sweden. In this sense, it is clear that the journal is becoming very popular worldwide.

In order to delve deeper into the results, this work used science mapping in Section 4. This approach provides a more comprehensive visualization of the results. We considered author keywords, three-fields plot of institutions, keywords and main journal sources, citations, co-citations and collaboration. From the analysis of author keywords, we can conclude that the journal published more on the topics of "sustainability", "energy efficiency" and "thermal comfort". Between 2011 and 2014, scholars in *Buildings* published papers mainly about simulation, climate change and energy. However, in the following four years, "energy efficiency" became the most popular topic, followed by "life cycle assessment" and "buildings". In the last three years, "masonry", "energy efficiency" and "reinforced concrete" have attracted more attention from researchers. This result provides us with the developing trends of topics of the journal.

This journal is closely connected to other leading journals in the field, such as *Energy and Buildings* and *Building and Environment.* As for the collaboration network in *Buildings*, this study provides a knowledge domain map that identifies collaborative networks of researchers between journals and countries/regions. The results show that institutions from the same country or region work more closely together. Italy has the widest range of cooperative partners, followed by the United Kingdom, Australia, the USA and China. These five countries are high-yield countries.

This study is useful to scholars, publishers or others interested in building science, building engineering and architecture. It provides people with a comprehensive overview

of *Buildings* from the past ten years using a bibliometric method and also forms a base for initiating further study in this area. For example, it is worth noting that hot topics such as energy efficiency, cultural heritage and climate change may continue to attract attention. Furthermore, through the previous analysis, we can predict that the journal will be acknowledged by more and more people over the world in the future. The number of publications and citations will likely continue to increase, and the research topics in the journal may become increasingly various and in-depth. There is no doubt that *Buildings* will continue to provide a platform for the expression and dissemination of ideas and strengthen cooperation among authors, institutions and countries/regions, as well as build a bridge between academia and industry.

Furthermore, there are some gaps the journal should pay attention to. For example, with the increase in publications, the diversity of research directions and fields has increased, too. The journal should maintain a quality/quantity balance and also emphasize on the depth and contribution of articles. Furthermore, *Buildings* runs special issues to create collections of papers on specific topics, but the classification of special issues can be further refined and become more innovative. It is also advisable for the journal to take some measures, such as organizing academic events, to encourage scholars and promote the development of academia.

This study provides a full description of *Buildings* but also presents some limitations. Since the data were collected from the Scopus database, the limitations of this database may also apply to this study. For instance, 76 documents are omitted since they are not directly available in Scopus, so some results may not be completely correct. Another limitation is that although the work uses a wide range of indicators in order to provide a comprehensive overview from different perspectives, we have to acknowledge that the work is not perfect and there are some missing perspectives we did not take into consideration. Future research should make improvements in these two directions to provide better research.

Author Contributions: Conceptualization, Z.X. (Zhiwen Xiao) and Y.Q.; methodology, Z.X. (Zhiwen Xiao); software, Z.X. (Zhiwen Xiao) and Y.Q.; validation, Z.X. (Zeshui Xu), J.A. and E.K.Z.; resources, Z.X. (Zeshui Xu); data curation, Z.X. (Zeshui Xu); writing—original draft preparation, Z.X. (Zhiwen Xiao) and Y.Q.; writing—review and editing, Z.X. (Zeshui Xu), J.A. and E.K.Z.; visualization, Z.X. (Zhiwen Xiao) and Y.Q.; supervision, Z.X. (Zeshui Xu), J.A. and E.K.Z.; project administration, Z.X. (Zeshui Xu), J.A. and E.K.Z.; funding acquisition, Z.X. (Zeshui Xu). All authors have read and agreed to the published version of the manuscript.

Data Availability Statement: The data presented in this study are available on request from the corresponding author.

Conflicts of Interest: The authors declare no conflict of interest.

References

1. Anumba, C.J. Buildings: An open access journal for the built environment. *Buildings* **2011**, *1*, 1–3. [CrossRef]
2. Kessler, M.M. Bibliographic coupling between scientific papers. *Am. Doc.* **1963**, *14*, 10–25. [CrossRef]
3. Small, H. Co-citation in the scientific literature: A new measure of the relationship between two documents. *J. Am. Soc. Inf. Sci.* **1973**, *24*, 265–269. [CrossRef]
4. Aria, M.; Cuccurullo, C. Bibliometrix: An R-tool for comprehensive science mapping analysis. *J. Informetr.* **2017**, *11*, 959–975. [CrossRef]
5. Yu, D.J.; Xu, Z.S.; Antuchevičienė, J. Bibliometric analysis of the Journal of Civil Engineering and Management between 2008 and 2018. *J. Civ. Eng. Manag.* **2019**, *25*, 402–410. [CrossRef]
6. Tang, M.; Liao, H.; Yepes, V.; Laurinavičius, A.; Tupėnaitė, L. Quantifying and mapping the evolution of a leader journal in the field of civil engineering. *J. Civ. Eng. Manag.* **2021**, *27*, 100–116. [CrossRef]
7. Novas, N.; Alcayde, A.; Robalo, I.; Manzano-Agugliaro, F.; Montoya, F.G. Energies and Its Worldwide Research. *Energies* **2020**, *13*, 6700. [CrossRef]
8. Zhou, W.; Xu, Z.S.; Zavadskas, E.K.; Laurinavicius, A. The knowledge domain of the Baltic Journal of Road and Bridge Engineering between 2006 and 2019. *Baltic J. Road Bridge Eng.* **2020**, *15*, 1–30. [CrossRef]

9. Wang, X.X.; Xu, Z.S.; Ge, Z.J.; Zavadskas, E.K.; Skačkauskas, P. An overview of a leader journal in the field of transport: A bibliometric analysis of "Computer-aided civil and infrastructure engineering" from 2000 to2019. *Transport* **2021**, *35*, 557–575. [CrossRef]

10. Cobo, M.J.; Martínez, M.A.; Gutiérrez-Salcedo, M.; Fujita, H.; Herrera-Viedma, E. 25 years at Knowledge-Based Systems: A bibliometric analysis. *Knowl. -Based Syst.* **2015**, *80*, 3–13. [CrossRef]

11. Wang, X.X.; Chang, Y.; Xu, Z.S.; Wang, Z.D.; Kadirkamanathan, V. 50 years of international journal of systems science: A review of the past and trends for the future. *Int. J. Syst. Sci.* **2021**, *52*, 1515–1538. [CrossRef]

12. Yu, D.; Xu, Z.S.; Pedrycz, W.; Wang, W. Information sciences 1968–2016: A retrospective analysis with text mining and bibliometric. *Inf. Sci.* **2017**, *418–419*, 619–634. [CrossRef]

13. Rousseau, R. Forgotten founder of bibliometrics. *Nature* **2014**, *510*, 218. [CrossRef] [PubMed]

14. Broadus, R.N. Toward a definition of "bibliometrics". *Scientometrics* **1987**, *12*, 373–379. [CrossRef]

15. Merigó, J.M.; Cobo, M.J.; Laengle, S.; Rivas, D.; Herrera-Viedma, E. Twenty years of Soft Computing: A bibliometric overview. *Soft Comput.* **2019**, *23*, 1477–1497. [CrossRef]

16. Cancino, C.; Merigó, J.M.; Coronado, F.; Dessouky, Y.; Dessouky, M. Forty years of Computers & Industrial Engineering: A bibliometric analysis. *Comput. Ind. Eng.* **2017**, *113*, 614–629. [CrossRef]

17. Akadiri, P.O.; Chinyio, E.A.; Olomolaiye, P.O. Design of a sustainable building: A conceptual framework for implementing sustainability in the building sector. *Buildings* **2012**, *2*, 126–152. [CrossRef]

18. Al-Kodmany, K. The Vertical Farm: A review of developments and implications for the vertical city. *Buildings* **2018**, *8*, 24. [CrossRef]

19. Tahmasebinia, F.; Niemelä, M.; Ebrahimzadeh Sepasgozar, S.M.; Lai, T.Y.; Su, W.; Reddy, K.R.; Shirowzhan, S.; Sepasgozar, S.; Marroquin, F.A. Three-Dimensional printing using recycled high-density polyethylene: Technological challenges and future directions for construction. *Buildings* **2018**, *8*, 165. [CrossRef]

20. Tahmasebinia, F.; Fogerty, D.; Wu, L.O.; Li, Z.; Sepasgozar, S.M.E.; Zhang, K.; Sepasgozar, S.; Marroquin, F.A. Numerical analysis of the creep and shrinkage experienced in the Sydney Opera House and the rise of digital twin as future monitoring technology. *Buildings* **2019**, *9*, 137. [CrossRef]

21. Sepasgozar, S.M.E.; Shi, A.; Yang, L.; Shirowzhan, S.; Edwards, D.J. Additive manufacturing applications for Industry 4.0: A systematic critical review. *Buildings* **2020**, *10*, 231. [CrossRef]

22. Al-Kodmany, K. Green retrofitting skyscrapers: A review. *Buildings* **2014**, *4*, 683–710. [CrossRef]

23. Al-Kodmany, K. The sustainability of tall building developments: A conceptual framework. *Buildings* **2018**, *8*, 7. [CrossRef]

24. Al-Kodmany, K. New Suburbanism: Sustainable spatial patterns of tall buildings. *Buildings* **2018**, *8*, 127. [CrossRef]

25. Al-Kodmany, K. Sustainability and the 21st century vertical city: A review of design approaches of tall buildings. *Buildings* **2018**, *8*, 102. [CrossRef]

26. Wang, L.; Wei, Y.M.; Brown, M.A. Global transition to low-carbon electricity: A bibliometric analysis. *Appl. Energy* **2017**, *205*, 57–68. [CrossRef]

27. Mumu, J.R.; Tahmid, T.; Azad, M.d.A.K. Job satisfaction and intention to quit: A bibliometric review of work-family conflict and research agenda. *Appl. Nurs. Res.* **2021**, *59*, 151334. [CrossRef]

28. Aria, M.; Misuraca, M.; Spano, M. Mapping the evolution of social research and data science on 30 years of Social Indicators Research. *Soc. Indic. Res.* **2020**, *149*, 803–831. [CrossRef]

29. Srivastava, M. Mapping the influence of influencer marketing: A bibliometric analysis. *Mark. Intell. Plan.* **2021**, *39*, 979–1003. [CrossRef]

30. Vinokurov, M.; Grönman, K.; Kosonen, A.; Luoranen, M.; Soukka, R. Updating the path to a carbon-neutral built environment—What should a single builder do. *Buildings* **2018**, *8*, 112. [CrossRef]

31. Vinokurov, M.; Grönman, K.; Hammo, S.; Soukka, R.; Luoranen, M. Integrating energy efficiency into the municipal procurement process of buildings—Whose responsibility? *Buildings* **2019**, *9*, 45. [CrossRef]

32. Fargnoli, M.; Lombardi, M. Preliminary Human Safety Assessment (PHSA) for the improvement of the behavioral aspects of safety climate in the construction industry. *Buildings* **2019**, *9*, 69. [CrossRef]

33. Fargnoli, M.; Lombardi, M. Building Information Modelling (BIM) to enhance occupational safety in construction activities: Research trends emerging from one decade of studies. *Buildings* **2020**, *10*, 98. [CrossRef]

34. Kouris, E.-G.S.; Kouris, L.-A.S.; Konstantinidis, A.A.; Kourkoulis, S.K.; Karayannis, C.G.; Aifantis, E.C. Stochastic dynamic analysis of cultural heritage towers up to collapse. *Buildings* **2021**, *11*, 296. [CrossRef]

35. Shehu, R. Implementation of pushover analysis for seismic assessment of masonry towers: Issues and practical recommendations. *Buildings* **2021**, *11*, 71. [CrossRef]

36. Aşıkoğlu, A.; Vasconcelos, G.; Lourenço, P.B. Overview on the nonlinear static procedures and performance-based approach on modern unreinforced masonry buildings with structural irregularity. *Buildings* **2021**, *11*, 147. [CrossRef]

37. Guleria, D.; Kaur, G. Bibliometric analysis of ecopreneurship using VOSviewer and RStudio Bibliometrix, 1989–2019. *Libr. Hi Tech.* **2021**, *39*, 1001–1024, *ahead-of-print*. [CrossRef]

38. Noyons, E.C.M.; Moed, H.F.; Luwel, M. Combining mapping and citation analysis for evaluative bibliometric purposes: A bibliometric study. *J. Am. Soc. Inf. Sci.* **1999**, *50*, 115–131. [CrossRef]

The Relationship between Wind Pressure and Pressure Coefficients for the Definition of Wind Loads on Buildings

Vincenzo Picozzi, Antonio Malasomma, Alberto Maria Avossa and Francesco Ricciardelli *

Department of Engineering, University of Campania "Luigi Vanvitelli", 81031 Aversa, Italy; vincenzo.picozzi@unicampania.it (V.P.); antonio.malasomma@unicampania.it (A.M.); albertomaria.avossa@unicampania.it (A.M.A.)
* Correspondence: friccia@unicampania.it

Abstract: Wind induced pressures on buildings are the product of a velocity pressure and a pressure coefficient. The way in which these two quantities are calculated has changed over the years, and Design Codes have been modified accordingly. This paper tracks the evolution of the approach to wind loading of buildings from the practice in the 1950s, mainly referring to the Swiss Code SIA, to the most recent advances including probabilistic methods, internet databases, and advanced modelling of meteorological phenomena.

Keywords: wind pressure coefficients; wind load; design codes; wind tunnel tests; aerodynamic database

1. Introduction

Broadly speaking, the action exerted by the wind on a body is proportional to the wind velocity pressure through an aerodynamic coefficient, accounting for the way in which the body interacts with the flow. In the ideal case in which the flow is laminar and the body is streamlined, the surface pressure can be expressed as:

$$w = q \cdot c \tag{1}$$

where $q = 0.5\rho v^2$ is the velocity pressure, and $c = c(M)$ is the pressure coefficient, depending on the location M where pressure is measured. This is not quite the case for Civil construction in general and for buildings in particular. Indeed, wind in the low atmosphere is characterized by a turbulent boundary layer flow, in which the mean wind speed is variable with the height above the ground, and to which a three-component turbulence is superimposed. In addition, civil constructions quite seldom meet the requirement of a streamlined shape, being instead bluff bodies. The bluff shape causes flow separation, generating additional turbulence to the oncoming one, the so-called signature turbulence, whose characteristics are related to the aerodynamics of the building and to a lesser extent to the characteristics of the oncoming wind. Finally, the mean and fluctuating properties of the wind flow cannot be defined through a deterministic approach, but rather need a probabilistic treatment. Combination of the three aspects above makes Equation (1) the general expression of a physical law, yet unable to alone give a quantitative definition of the load.

The structure of Equation (1) seems to separate well that which derives from the characteristics of the flow from the effects of aerodynamics, yet this separation is not unique, and lends itself to many possible interpretations, as well as to potential misunderstandings. In fact, the meaning of the two terms appearing to the hand right side of the equation must be properly defined from both the physical and the statistical points of view.

In this paper, the evolution of Equation (1) from its first use to modern applications is briefly outlined. For use of designers making their way through Codes of Practice, the meaning and use of Code equations are also explained.

2. Early Studies on Building Aerodynamics

With the aim of experimentally measuring wind loads on simple objects, in 1871 the first wind tunnel was built by F. H. Wenham. The results of his tests on flat inclined plates were then used by W. Unwin, who first attempted to evaluate wind pressures on building roof surfaces [1]. In doing this, a first major error arose, that of assuming that the load measured on an isolated element remains the same when the element becomes part of an assemblage; this is not quite true, as the pressure distribution is related to the overall geometry, and not merely of that of the detail where it is measured. The first wind tunnel for civil engineering applications was built in 1890 in Melbourne, Australia, by W. C. Kernot with the purpose of measuring wind pressures on a flat plate orthogonal to the flow. In the coming years, wind tunnels were built also in Denmark by J. O. V. Irminger (1893) and in France by A. G. Eiffel (1909), both aimed at assessing wind loads on civil structures. Aerodynamic studies began to develop rapidly, and the first heavier-than-air flight was achieved in 1903, making aerodynamics the crucial issue in the development of aeronautics. For more than 50 years civil and aeronautical aerodynamics, though differing from each other, were investigated in the same experimental facilities as it had not yet been recognized that the flow encountered by aircraft flying at hundreds or thousands of meters of height is quite different from that hitting ground-based Civil constructions. This misunderstanding is at the base of perhaps the major mistake made in earlier times when evaluating wind loads on Civil structures.

In the early 1900s, the need for specific studies on the pressures exerted by the wind on buildings began to arise. Until the 1950s, the pressure distribution on plates with different shapes, dimensions and pitch angles were investigated in wind tunnels, and the results were used to evaluate the loading of the upwind surfaces of building. Only later, the important role of suction on the leeward surfaces when evaluating the overall forces due to wind was acknowledged [2–4]. Irminger [2] first carried out several experiments on rectangular model buildings with sloped roofs, showing the pressure pattern along the middle section of the tested models. Then, Irminger and Nøkkentved [5,6] used flow visualization to show that (i) the upwind face was subject to (over)pressure; that (ii) the leeward and side faces, as well as the downwind roof slope were subject to negative pressure (or suction); and that (iii) the upwind slope was exposed to either positive or negative pressures depending on its inclination. Moreover, the dependency of the pressure distribution on the ratio between width, depth, and height of the building was also highlighted. In their experiments, Irminger and Nøkkentved [5,6] and Nøkkentved [7] acknowledged the role of the wind tunnel floor roughness in influencing the wind speed profile and thus affecting the distribution and the intensity of wind pressures on model buildings.

In the meantime, starting from 1928 the first regulations on building design due to wind loading were introduced in Europe. More or less at the same time, on the US the American Society of Civil Engineering (ASCE) started working at recommendation for 'Wind Bracing in Steel Buildings', incorporating all the available data and studies [8]. The values of the pressure coefficients were based on a collection of measurements made in wind tunnels with smooth flow conditions, and on models often detached from the tunnel floor; therefore, despite the detailed description of the pressure pattern they provide, such measurement are now known to be useless as wrong.

The first attempt to compare wind tunnel measurements with full-scale data was made by Bailey [9], showing quantitative differences between the results coming from the two approaches. Based on the work of Nøkkentved [7], Bailey and Vincent [10] made one of the first experiments in a boundary layer wind tunnel, simulating the flow in the low atmosphere, finding good agreement with full-scale measurements. The turning point in the assessment of wind pressures on buildings was the work of Jensen in 1950s. Continuing the work of Nøkkentved, Jensen [11] clarified the role of ground roughness in generating wind turbulence, and first pointed out the need and set the rules for properly scaling the atmospheric boundary layer in the wind tunnel. Jensen's model law states that the ratio h/z_o (also known as Jensen Number, *Je*) between the building height, *h*, and the roughness

length, z_o, should be the same in wind tunnel as it is in full scale. Despite the work of Jensen, it took many years before that tests in boundary layer wind tunnel became commonly available, and in 1956 one of the first wind Codes (SIA 160) was published in Switzerland, still incorporating pressure and force coefficients measured in smooth flow [12].

3. The Modern Wind Engineering Approach

Besides the error in modelling the flow in the wind tunnel, until the 1960s the assessment of wind loads was based on the wrong hypothesis of steady wind resulting in steady pressures. This is now known not to be true, especially even in the case of bluff geometries causing flow separation, therefore a fluctuating separated shear layer and a turbulent wake. These aerodynamic features produce surface pressure fluctuations on the body, even when the flow in which this is immersed is laminar; broadly speaking, the wind velocity fluctuations induced by separation are referred to as signature turbulence. Before the spread of the use of Extreme Value statistics, Equation (1) was meant as the combination of the largest value of the velocity pressure at the site (often coinciding with the largest value ever measured, clearly depending on the measuring technique, on the length of the observation window, as well as on the inherent randomness of the quantity) and an average value of the pressure coefficient. This, of course, led to neglecting both the oncoming and signature turbulence.

In the 1960s, the various aspects of the wind loading of structures were integrated together into a comprehensive theory by Davenport [13], setting the stage for the Alan G. Davenport Wind Loading Chain [14,15], and starting the era of modern Wind Engineering. In this process played their role the use of boundary layer wind tunnels and the establishment of a series of International Conferences on *Wind Effects on Buildings and Structures* (now International Conference on Wind Engineering, ICWE) allowing the exchange of ideas and research results.

Davenport [16] first observed the need for a statistical approach to wind loading, introducing the concept of "basic design wind speed", defined as an "extreme value statistics of the wind speed averaged over a minute". In this definition, two notions were introduced: (1) the need for defining an averaging period for wind speeds, and nor rather considering instantaneous values; the latter, in fact, are not only affected by the measuring technique, but do not necessarily produce extreme effects on the structure, if their duration is too short; (2) the need for an Extreme Value (EV) analysis to evaluate the return wind speed, i.e., a fractile of the yearly maxima associated with a specified probability of exceedance. The choice of one minute as averaging period was justified by the wrong assumption that the average size of turbulent eddies was between 1.2 and 1.8 km, corresponding to a time scale of 60 s when the wind speed is 20 m/s and 30 m/s, respectively; therefore averaging over a minute would have cancelled the turbulent fluctuations out. This is now known not to be true, as values in the order of 50 to 300 m apply to the turbulence scale during synoptic storms. However, more than that, what was lacking in the first work of Davenport was an appropriate treatment of the effects of turbulence on the wind loads.

Later, Davenport [13] better recognized the structure of the atmospheric turbulence and its impact on the wind loading. He proposed that the instantaneous wind speed is represented as the sum of a mean wind speed U averaged over a longer period, T, and a zero-mean turbulent component $u'(t)$, averaged over a shorter period, τ:

$$V(t) = U + u'(t) = U \cdot \left[1 + \frac{u'(t)}{U} \right] \tag{2}$$

In so doing, the peak wind speed is represented as the product of the mean wind speed and a gust factor G_u:

$$\hat{V} = U \cdot [1 + g_u I_u] = U \cdot G_u \tag{3}$$

where $I_u = \sigma_u/U$ is the turbulence intensity, and g_u is the velocity peak factor, indicating the average number of standard deviations σ_u the peak wind speed exceeds the mean value. The peak factor was found to be a function of the averaging period and of the average rate ν_u at which the instantaneous speed up-crosses the mean value; when the turbulent fluctuations can be approximated by a Gaussian process:

$$g_u = \sqrt{2\log(\nu_u T)} + \frac{0.5772}{\sqrt{2\log(\nu_u T)}} \tag{4}$$

Based on the available measurements of the spectrum of the atmospheric turbulence, it is found that g_u ranges between 2.8 and 2.9.

This procedure implies the choice of the averaging period and of the duration of the gust. Based on the Van der Hoven spectrum of the horizontal wind speed [17], Davenport [14] found it appropriate to use an averaging period of 1 h, accounting for the macro-meteorological fluctuations, and a duration of the gust of 3 s, accounting for micro-meteorological fluctuations. In doing so, the mean wind speed was to be meant as the driving statistical quantity, to be evaluated by applying EV analysis to site-specific meteorological data, and the gust factor was to incorporate all the effects coming from ground surface roughness.

Applying the quasi-steady theory, i.e., assuming that the instantaneous value of the surface pressure in turbulent flow coincides with what it would be if the flow were laminar and the wind speed equal to the instantaneous turbulent speed, the instantaneous surface pressure at a point on the building is given by:

$$w(t) = 0.5\rho V^2(t) \cdot \bar{c}_p = 0.5\rho U^2 \cdot \left[1 + \frac{u'(t)}{U}\right]^2 \cdot \bar{c}_p \tag{5}$$

where $\bar{c}_p$ is to be meant as the mean value of the measured pressure coefficient. Upon linearization of Equation (5), one obtains:

$$w(t) \simeq 0.5\rho U^2 \cdot \left[1 + 2\frac{u'(t)}{U}\right] \cdot \bar{c}_p \tag{6}$$

and the corresponding peak surface pressure $\hat{w}$ is:

$$\hat{w}_{lin} = \bar{w}_{lin} \cdot [1 + 2g_u I_u] = \bar{w}_{lin} \cdot G_{w,lin} \tag{7}$$

where $\bar{w}_{lin} = 0.5\rho U^2 \cdot \bar{c}_p$ and where $G_{w,lin}$ is a linearized gust loading factor, transforming the mean load into a peak load.

The linearization in Equation (6) is based on the assumption of small turbulence, i.e., that $u'(t) \ll U$, and brings two major simplifications: first, the mean surface pressure coincides with the surface pressure associated with the mean wind speed; second, the fluctuating surface pressure is proportional to the turbulent component, $w'_{lin}(t) \propto u'(t)$ and $\tilde{w}_{lin} = 2I_u \bar{w}_{lin}$. This latter assumption allows expressing the spectrum of the surface pressure fluctuations directly from the spectrum of the atmospheric turbulence: $S_w \propto S_{u'}$. In case of high turbulence, linearization cannot be considered acceptable any more, and this makes all further steps much more complicated. From Equation (5), the mean surface pressure turns out to be:

$$\bar{w} = 0.5\rho \overline{[U + u'(t)]^2} \cdot \bar{c}_p = 0.5\rho U^2 \cdot \bar{c}_p + 0.5\rho \sigma_u^2 \cdot \bar{c}_p = \bar{w}_{lin} \cdot [1 + I_u^2] \tag{8}$$

indicating that the bias in the mean surface pressure arising from linearization is $\bar{w}/\bar{w}_{lin} = 1 + I_u^2$. The RMS of the surface pressure is:

$$\tilde{w}^2 = \overline{[w(t) - \bar{w}]^2} = \tilde{w}_{lin}^2 \cdot [1 + 0.5I_u^2] \tag{9}$$

In so doing, the bias in the variance of surface pressure arising from linearization is $\tilde{w}^2/\tilde{w}_{lin}^2 = 1 + 0.5I_u^2$; it can be very accurately defined as $\tilde{w}/\tilde{w}_{lin} \cong 1 + 0.25I_u^2$. Since the bias is a systematic error, then it can be used as a correction factor for Equation (7), accounting for the linearization of both mean value and variance of surface pressure.

Using the same format as Equation (3), the peak surface pressure is written as:

$$\hat{w} = \tilde{w} \cdot \left[1 + g_w \frac{\tilde{w}}{\tilde{w}}\right] = \tilde{w} \cdot \left[1 + 2g_w I_u \frac{\sqrt{1 + 0.5I_u^2}}{1 + I_u^2}\right] = \tilde{w} \cdot G_w \tag{10}$$

where g_w is the surface pressure peak factor, and G_w is the gust loading factor. The bias in the peak surface pressure can be calculated as the ratio of Equations (10) and (7), and to evaluate it one would need to know the exact value of g_w. On the other hand, a linearized version of g_w can be obtained by equating G_w in Equation (10) and $G_{w,lin}$ in Equation (7):

$$g_{w,lin} = g_u \cdot \frac{1 + I_u^2}{\sqrt{1 + 0.5I_u^2}} \cong g_u \cdot \frac{1 + I_u^2}{1 + 0.25I_u^2} \tag{11}$$

ranging between 2.8 and 3.2 when the turbulence intensity ranges between 0 and 0.4. The exact value of g_w cannot be calculated in closed form; numerical analyses based on the turbulence spectrum of Eurocode 1 show that, again when the turbulence intensity ranges between 0 and 0.4 and assuming $\tau = 3$ s, it ranges between 2.8 and 3.9. A value of 3.5 is adopted by Eurocode 1.

Figure 1 contains a sketch of the long term spectrum of surface pressure at a point, as derived from the velocity spectrum of Van der Hoven. In addition to the pressure fluctuations associated with the macro-meteorological and turbulent fluctuations of the wind speed, it contains also the fluctuations deriving from signature turbulence. The approach of Davenport, based on a mean pressure coefficient and a gust factor, in fact incorporates only the effects of the oncoming turbulence, but not those of signature turbulence. The magnitude of the latter term depends on the aerodynamic features and on the point at which the pressure is measured. For streamlined structures and for points on the windward faces the effect of signature turbulence is low to negligible; for bluff structures and for points in the separated flow region the effects of signature turbulence can be high.
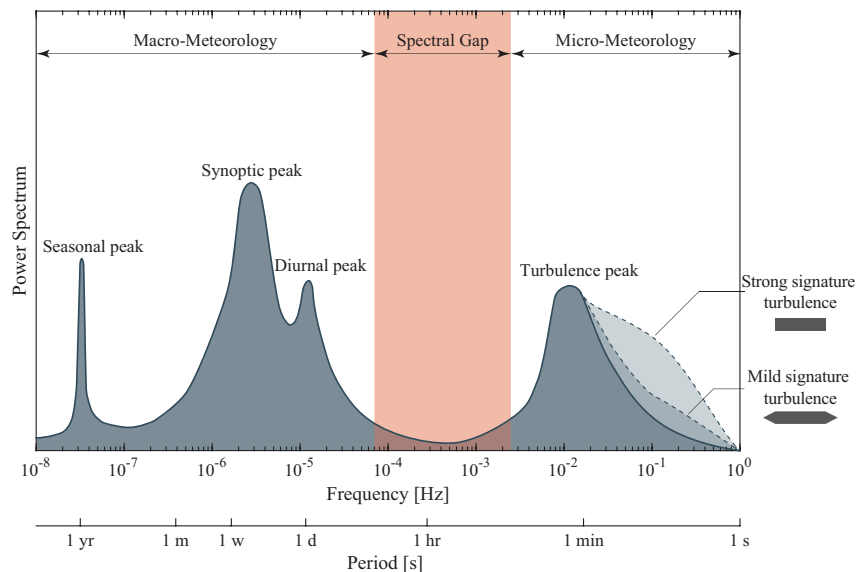
Figure 1. Surface pressure spectrum.

4. Enhanced Probabilistic Approach

The approach of Davenport was first validated by measurements performed by Dalgliesh [18] on a 45-story office building, showing that at all points on the windward side of the structure the PDF of (positive) pressures agreed with the Gaussian assumption. However, at the only measurement point on the leeward surface the PDF of (negative) pressures departed from Gaussianity. This aspect was then deeply investigated by Peterka and Cermak [19], who measured the pressure at hundreds of points on the four vertical walls and on the roof of a tall building wind tunnel model. They found that pressures can be grouped in two categories:

1. on the windward surface, the surface pressure is positive and its PDF is close to being Gaussian; this behaviour is more generally found at points where $\bar{c}_p > -0.1$;
2. on the surfaces exposed to separated flow, the PDF of pressures departs from being Gaussian and the left tail tends to an exponential form; this happens when $\bar{c}_p < -0.25$.

On the other hand, according to studies on low-rise buildings [20,21], Holmes [22] showed that even on the windward walls pressures can be non-Gaussian, this effect being more evident for large values of the turbulence intensity of the oncoming flow. From a practical point of view, this translates into peak factors larger than those evaluated by Equation (4), reaching values potentially as large as 10.

It was then clear that turbulent fluctuations do not immediately translate into pressure fluctuations, at least at points where the flow is separated, and this suggested a revision of the quasi steady approach. Based on the observation that it is impossible to separate the components of the pressure fluctuation deriving from the oncoming turbulence from those deriving from signature turbulence, an alternative to the Davenport's approach is that of combining the mean velocity pressure with a tail statistics of the pressure coefficient. A first attempt in this direction was that of Lawson [23], who proposed to determine the design value of pressure coefficients as those corresponding to the 5×10^{-4} fractile of the parent distribution. The chosen probability level corresponds to the largest gust in one hour having a duration of 1.8 s, as suggested by Eaton and Mayne [24].

Once it is recognized that the pressure coefficient is to be calibrated as a value corresponding a low probability of exceedance, then the question arises of whether it is more appropriate to consider the parent population or to apply Extreme Value (EV) analysis. For the latter option, it is observed that the domain of attraction of parents with an exponential tail is the Type I EV distribution or Gumbel distribution [25].

In their pioneering work, Cook and Mayne [26] tried to find a statistical model from which to derive the pressure coefficients, as alternative to the use nominal values (corresponding to mean values) as reported in the UK Code of Practice for wind load [27]. They proposed a design approach in which the definition of both wind speed (or velocity pressure) and pressure coefficients is based on the Spectral Gap [17]:

*   The design value of wind speed is obtained as an EV statistics of the wind speed, U, averaged over a period T of 10 min or 1 h, including all fluctuations of the macro-meteorological peak;
*   The design value of the pressure coefficient, c_p, is the peak value within the averaging period T, including all the micro-meteorological fluctuations of the incident wind turbulence, as well as those coming from signature turbulence.

As already pointed out by Davenport [14], in this case the peak pressure coefficient is also not to be confused with a maximum instantaneous value measured at a point, but it is rather a statistics the time- and space-averaged instantaneous values:

$$c_{p,\tau,A}(t) = \frac{1}{A}\frac{1}{\tau}\int_A \int_{t-\tau/2}^{t+\tau/2} c_p(a,\bar{t})\,\mathrm{d}\bar{t}\,\mathrm{d}a \tag{12}$$

The duration τ and the averaging area A shall be related to the capacity that the load has to produce an effect; for example, the load duration needed to produce damage to cladding elements is smaller than that needed to produce damage on structural elements

having larger tributary areas. The averaging duration and averaging area can be related with each other, once the convective nature of the process is recognised. A common relationship between the characteristic dimension $l = \sqrt{A}$ of the averaging area and the averaging duration is provided by the *TVL* formula [28]:

$$\tau U = 4.5l \tag{13}$$

The choice either A or τ allows the use of Equations (12) and (13). Common practice is to select A as the tributary area of the structural member or cladding element under consideration.

Therefore, in the approach of Cook and Mayne both mean wind speed and pressure coefficients have to be understood as statistical variables and their design values need to be assessed by EV analysis. The mean wind speed is usually evaluated with a yearly probability of exceedance equal to 0.02, corresponding to a return period $R = 50$ yrs; the same yearly probability of exceedance applies also to wind loads. Therefore the statistics of the pressure coefficient has to be chosen such that combined with a velocity pressure having a yearly probability of exceedance of 0.02 provides a wind load having also a yearly probability of exceedance of 0.02. Assuming a Type I EV distribution for both the annual maximum wind speed and the coefficient of pressure, Cook and Mayne [26] recommended the use of the 78% fractile of peak pressure coefficients. The Cook–Mayne coefficient was established for the UK wind climate and is used worldwide. Indeed, if a more reliable value is to be obtained, then it should be calibrated on the specific climate of the site of interest.

5. Calibration of Pressure Coefficients

5.1. Codification Procedures

EV analysis for the evaluation of the design pressure coefficients has been accepted worldwide. An exhaustive literature review of the evolution and of the geographic differences in the evaluation of pressure coefficients was presented by Gavanski et al. [29], while a state-of-the-art of the methods to estimate the peak pressures was made by Gavanski and Cook [30]. In Europe, the method of Cook and Mayne is widely used for the evaluation of the maximum and minimum pressure coefficients. Despite this, the sources of building pressure coefficients include both, largest measured peaks [31] and 78% fractiles [32] resulting from EV analysis [33,34]. In fact, the current version of Eurocode 1 [35], proposes two sets of pressure coefficients for the assessment of (1) local pressures on cladding and roofing elements ($c_{pe,1}$, for loaded areas of $1 \, \mathrm{m}^2$ corresponding to the largest measured peaks) and (2) wind loading on resistant structural members ($c_{pe,10}$, for loaded areas of $10 \, \mathrm{m}^2$, corresponding to 78% fractiles).

Current Codes and Standards incorporate the gust factor approach by using an equivalent form of Equation (7), expressing the characteristic wind load at a point M as:

$$w(M) = q_{m,ref} \cdot G_{w,lin} \cdot c_p(M) \tag{14}$$

where $q_{m,ref} = 0.5 \cdot \rho \cdot v_m^2(z_{ref})$ and $v_m(z_{ref})$ are the mean velocity pressure and mean wind speed at height z_{ref} above the ground, corresponding to a yearly probability of exceedance of 0.02, or a return period $R = 50$ yrs, respectively, and $c_p(M)$ is the representative value of the pressure coefficient at the point:

$$c_p(M) = \frac{\hat{p}(M)}{\hat{q}(z_{ref})} \tag{15}$$

where $\hat{p}(M)$ is the peak relative surface pressure measured in the wind tunnel at point M, and $\hat{q}(z_{ref})$ is the peak velocity pressure measured in the wind tunnel at height z_{ref} above the tunnel floor. Therefore, the height z_{ref} to be used in Equation (14) should be the same as that used for the normalization of the pressure coefficient in Equation (15).

Unlike the gust factor approach of Davenport, the method of Cook and Mayne accounts for wind gustiness through the pressure coefficients. These incorporate the effects

of both the oncoming and signature turbulence, and may strongly deviate from a Gaussian behaviour. Instead of Equation (14), the wind loading turns out to be:

$$w(M) = q_{m,ref} \cdot c_{p,(78)}(M) \tag{16}$$

where $c_{p,(78)}(M)$ indicates the 78% fractile of the pressure coefficient at point M.

Comparing Equations (14) and (16) one obtains:

$$c_p(M) = \frac{c_{p,(78)}}{G_{w,lin}} \tag{17}$$

The normalization procedure in Equation (17) gives rise to the so-called pseudo-steady pressure coefficient, highlighting the fact that it is calibrated within the steady-state method.

Figure 2 sketches the parent and the EV distributions of the pressure coefficient. The figure should help understanding the probabilistic nature of the pressure coefficients and the differences between mean ($\bar{c}_p$), 78%-fractile ($c_{p,(78)}$) and pseudo-steady (c_p) pressure coefficients.
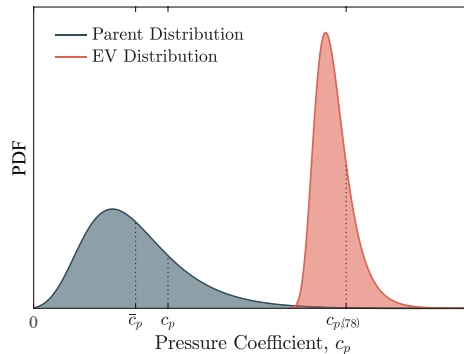
Figure 2. Sketch of the parent and EV distributions of the pressure coefficient.

5.2. Pressure Coefficients Analysis

Codes and Standards provide pressure coefficients c_p for rectangular buildings with flat roofs with different corner arrangement (sharp, curved, mansard, and with parapets) as well as with pitched roofs. When the geometry of interest is not covered by the Code or Standard, it is necessary to resort to wind tunnel tests to quantify the pressure coefficients.

The result of a wind tunnel test is a dataset consisting of time histories $c_p(M; t)$ of the pressure coefficients at a number of measurement points M on the model building surfaces. The instantaneous pressure coefficient is calculated as:

$$c_p(M; t) = \frac{p(M; t) - p_o}{q_{m,ref}} \tag{18}$$

in which $p(M; t)$ is the absolute surface pressure measured at point M and time t, and p_o is the static air pressure in the region outside the influence of the body (barometric pressure). In most cases, the reference height z_{ref} for pressures is taken equal to the building height h, therefore $q_{m,ref} = q_{m,h}$. In some cases, the pressure coefficients are normalized with respect to a reference wind tunnel height z_{wt}. In the latter case, preliminary to the statistical treatment of the data, the measurements must be converted to the reference height z_{ref}:

$$c_p(M; t) = \frac{q_{m,wt}}{q_{m,ref}} \cdot c_{p,wt}(M; t) \tag{19}$$

in which $c_{p,wt}(M;t)$ is the pressure coefficient normalized with respect to the velocity pressure $q_{m,wt}$ at the height z_{wt}.

The datasets provided by wind tunnel tests are sampled at frequency f_s, corresponding to a sampling time $1/f_s$ usually smaller than the averaging period τ. Therefore the time histories of the measured pressure coefficients must first be converted into time histories of τ-averaged pressure coefficients, also corresponding to area-average as per the TVL formula. Thus, a moving-average is applied to the time series:

$$c_{p,A}(M;t) = \frac{1}{\tau}\int_{t-\tau/2}^{t+\tau/2} c_p(M;\bar{t})\,\mathrm{d}\bar{t} \tag{20}$$

corresponding to low-pass filtering the measured time series at a frequency $1/\tau$. For example, Cook [32] referred to a load duration $\tau = 1\,\mathrm{s}$ and to a common design wind speed for the UK $U = 22.5\,\mathrm{m/s}$, which correspond to an averaging area $A = 12.5\,\mathrm{m}^2$ (or a characteristic dimension $l = 5\,\mathrm{m}$, corresponding to the diagonal of a square area). By doing this, the values given in Eurocode 1 as $c_{pe,10}$ are obtained (where the subscript e stands for *external*, as opposed to i used for *internal* pressures). On the other hand, when wind tunnel time series of the point pressure coefficients are available, Equation (20) must be evaluated with:

$$\tau = 4.5\frac{\sqrt{A}}{v_{m,ref}} \tag{21}$$

where A is the tributary area of the loaded structural element, and $v_{m,ref}$ is the expected value for the design mean wind speed.

The concept of tributary area applies to secondary structural elements or cladding elements; therefore, it is in the order of few square meters. For main structural elements and for foundation loads, where the tributary area is much larger, besides the use of Equation (20), the reduction in the resulting loads arising from the lack of coherence of the oncoming flow is accounted for through a background factor. This issue was first addressed by Davenport [13], who introduced the notion of background factor B^2, taking into account not only the lack of correlation of the oncoming flow turbulence, but also the vertical variation of the mean wind speed. In particular, the background factor is expressed as a function of the ratio $\sqrt{A_l}/L_u$ between the characteristic dimension of the loaded area A_l and the turbulent length scale L_u. In so doing, within the gust factor approach, the equivalent (or peak) load W_{lin} is given by:

$$W_{lin} = 0.5\rho U^2 \cdot c_p \cdot G_{W,lin}(A_l) \cdot A_l \tag{22}$$

where:

$$G_{W,lin}(A_l) = 1 + 2g_{W,lin}I_u\sqrt{B^2(A_l)} \tag{23}$$

is the gust loading factor depending on the loaded area, and $g_{W,lin}$ is the associated peak factor. It is clear that when the characteristic dimension of the structure is small compared with the dimension of the turbulent eddies, then $B^2 \to 1$. Similar to $g_{w,lin}$, a value of 3.5 is adopted by Eurocode 1 also for $g_{W,lin}$. A recent summary can by found in Liu et al. [36].

For the equivalent load, only a linearized version is given; this derives from the fact that the background factor in Equation (23) is derived following a stochastic approach in the frequency domain, in fact needing a linear relationship between the wind velocity fluctuations and the surface pressure fluctuations.

Finally, once the time series of pressure coefficients are normalized with respect the reference height z_{ref}, and filtered according to the load duration τ, then EV analysis can be performed. When a Type I EV distribution is used for the extremes of the pressure coefficient, then the Gumbel scale μ_M and shape β_M parameters are evaluated at each measurement point M. Then, the 78% fractile of the pressure coefficient is evaluated as:

$$c_{p,(78)}(M) = \mu_M + 1.4 \cdot \beta_M \tag{24}$$

5.3. Example

The above procedure is applied to pressure measurements on the flat roof of a building with dimensions $b = 24.40$ m, $d = 38.10$ m, $h = 12.20$ m, to evaluate the pressure coefficients $c_{p,1}$ for roof cladding and $c_{p,10}$ for structural elements. The raw data are taken from the NIST database [37]. First, a moving-average is applied to the original time series by considering a mean wind speed of 26.5 m/s, giving $\tau = 0.25$ s for $c_{p,1}$ and $\tau = 0.76$ s for $c_{p,10}$. Then, the Gumbel parameters μ_M and β_M in Equation (24) are calibrated based on the filtered time series, and the values of $c_{p,(78)}$ are calculated.

Figures 3a–d and 4a–d show the contour plots of pressure coefficients $c_{p,1}$ and $c_{p,10}$, respectively, evaluated as in Equation (17), for wind angles of incidence of $0°$, $15°$, $30°$, and $45°$. Figures 3e and 4e show the envelope of the calculated values, together with the zoning proposed by Eurocode 1.

With the purpose of assessing roofing elements, the envelope of Figure 3e can be used, as what we are interested in is the maximum wind load obtained from an omnidirectional analysis. For secondary structural members with small to moderate tributary areas, up to about 10 m², the $c_{p,10}$ envelope of Figure 4e can still be used. However, in the case of larger tributary areas, i.e., for main structural elements or for foundation loads, the background factor needs to be considered. In this case, the pressure coefficients $c_{p,10}$ provided by the loading patterns of Figures 4a–d shall be used for directional analysis, in conjunction with a background factor $B(A_l = b \cdot d)$.

In Table 1, a comparison of the area-averaged coefficients from the analysis of NIST data (CW) and Eurocode 1 values (EC1) is presented. The discrepancy between the corresponding values can be partly ascribed to the fact that the values given in Eurocode 1 apply to different ratios $b{:}d{:}h$; therefore, they must in some way smooth out the differences between one case and another.

(a)

(b)

(c)

(d)
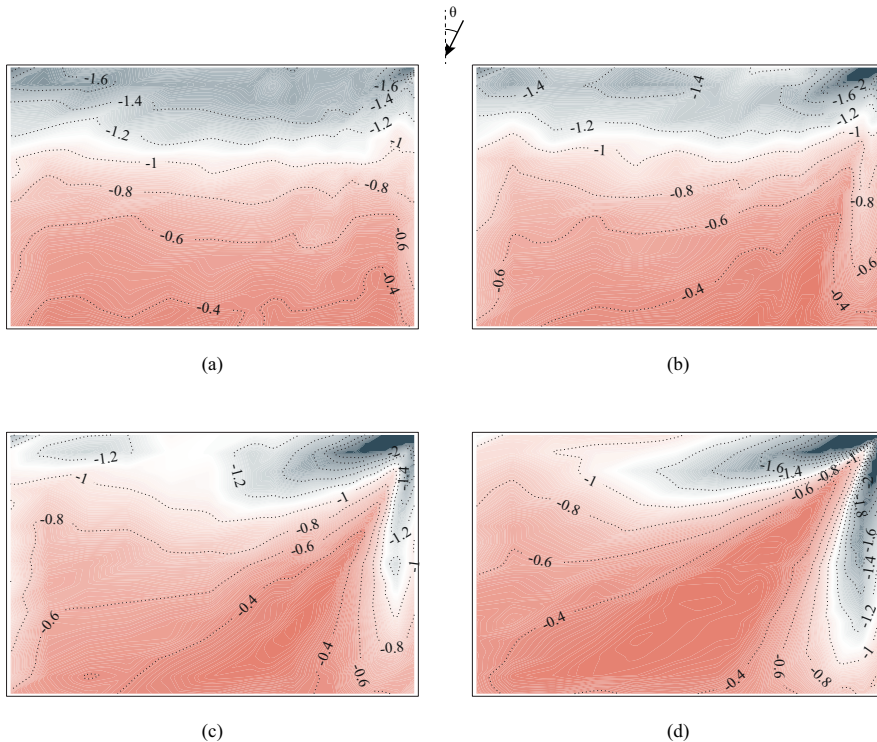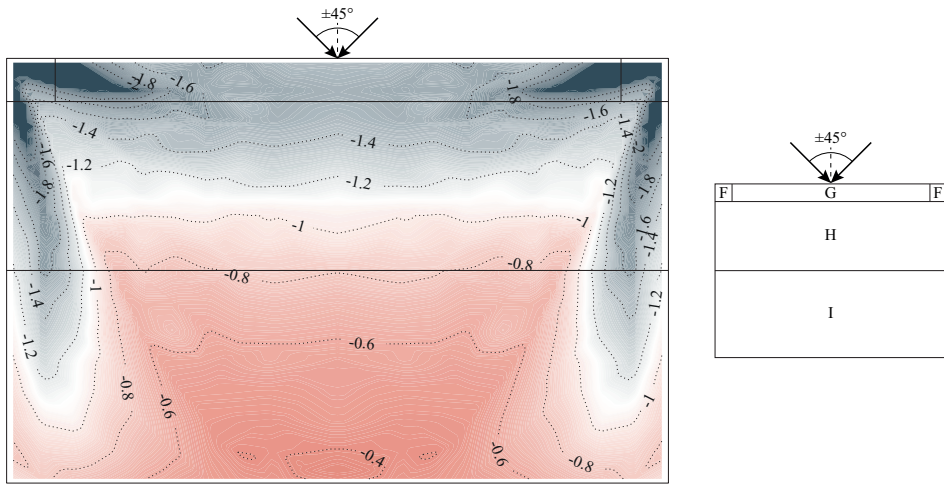
Figure 3. *Cont.*

(e)

Figure 3. Pressure coefficients $c_{p,1}$ ($\tau = 0.25\,$s) for wind angles $\theta = 0°$ (**a**), $\theta = 15°$ (**b**), $\theta = 30°$ (**c**), and $\theta = 45°$ (**d**). Envelope of $c_{p,1}$ for $\theta = 0°$, $\pm15°$, $\pm30°$, $\pm45°$, and Eurocode 1 loading zones (**e**).
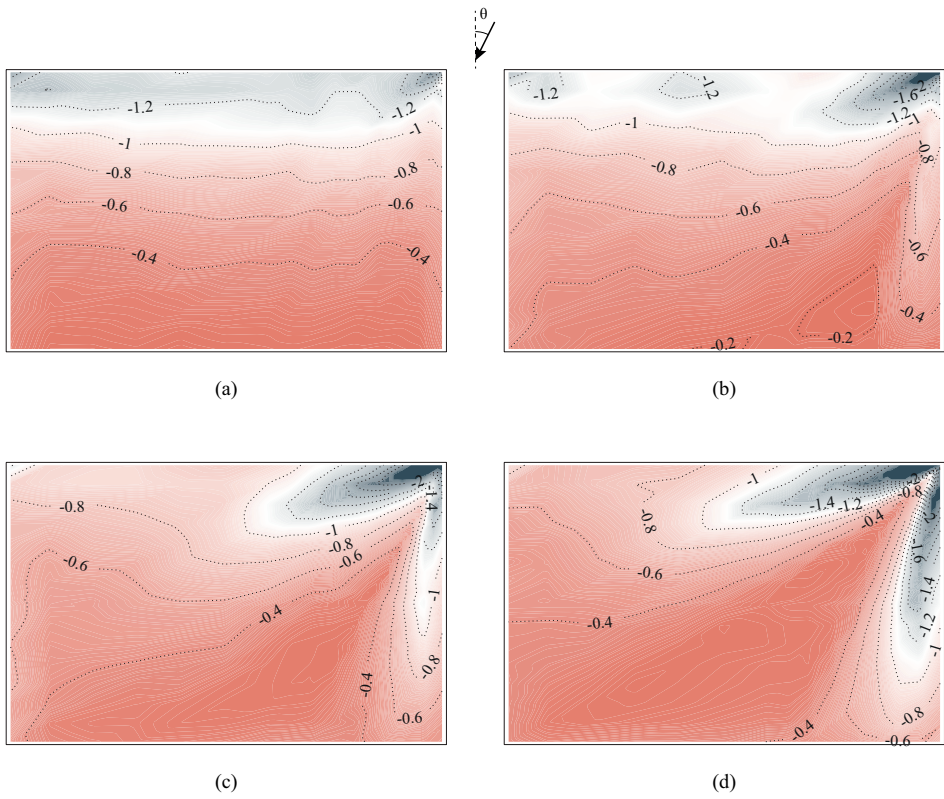
(a)

(b)

(c)

(d)

Figure 4. *Cont.*
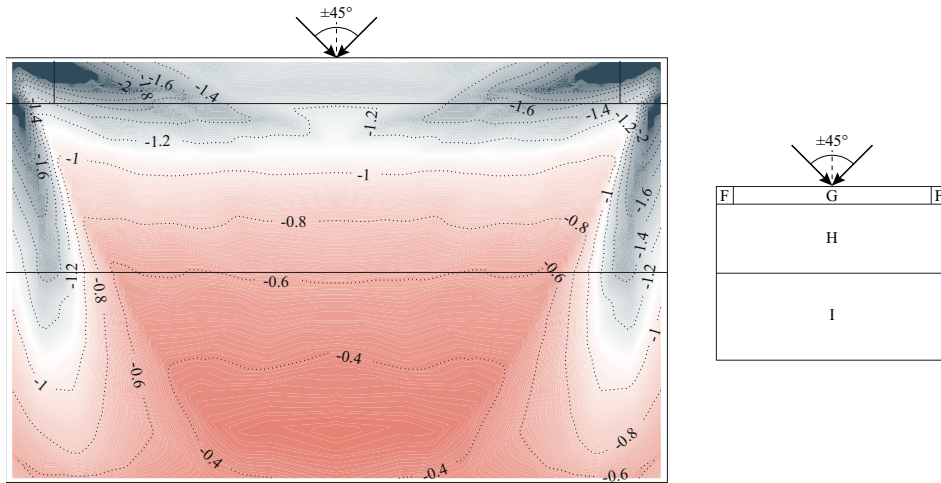
(e)

Figure 4. Pressure coefficients $c_{p,10}$ ($\tau = 0.76$ s) for wind angles $\theta = 0°$ (**a**), $\theta = 15°$ (**b**), $\theta = 30°$ (**c**), and $\theta = 45°$ (**d**). Envelope of $c_{p,10}$ for $\theta = 0°$, $\pm 15°$, $\pm 30°$, $\pm 45°$, and Eurocode 1 loading zones (**e**).

Table 1. Comparison of area-averaged coefficients from the analysis of NIST data (Current Work, *CW*) and Eurocode 1 values (*EC1*).

Roof Zone	$c_{p,1}$		$c_{p,10}$	
	CW	EC1	CW	EC1
F	−2.18	−2.5	−1.96	−1.8
G	−1.52	−2.0	−1.25	−1.2
H	−1.11	−1.2	−0.91	−0.7
I	−0.53	−0.2	−0.37	−0.2

6. Future Developments

According to the procedures developed through the years, the assessment of the wind load on rigid buildings requires the knowledge of both return velocity pressure and statistics of pressure coefficients. As already pointed out, pressure coefficients available in current Codes and Standards suffer from a number of deficiencies:

1. They refer to a rather narrow variety of geometries, often limited to rectangular plan buildings with constant height; for geometries that can be schematized as an assemblage of rectangular elements, empirical criteria are given to extend the use of pressure coefficients measured for rectangular buildings;
2. The statistical definition of the available pressure coefficients is not always clear, and seldom complies with Equation (24);
3. The duration of the load τ used in Equation (12), usually between 1 s and 3 s, had in some cases proven inadequate when assessing cladding loads in areas of strong negative pressures, a smaller value being more appropriate. This is the effect of high suctions being strongly non-Gaussian; therefore, featuring high peak factors;
4. The use of envelopes of pressure coefficients averaged over small areas for the assessment of main structural members and foundation load proves inaccurate; as an alternative, a more refined directional analysis using influence coefficients would be appropriate.

On the other hand, velocity pressures also suffer from a number of limitations:

1. Extreme wind maps are often old, and produced with heterogeneous data and heterogeneous (and often out-of-date) statistical methods;
2. There is often non appropriate consideration of the various storm mechanisms;
3. Very seldom the measurements are continuous, therefore giving rise to an underestimation of the design wind speed as an effect of downsampling.

In recent years, the development of Web and Information Technologies has led to new opportunities for more reliable procedures in the assessment of structural safety. At the beginning of the 21st century, the University of Notre Dame founded the NatHaz (Natural Hazards) Modeling Laboratory with the aim "to quantify load effects caused by various natural hazards on structures and to develop innovative strategies to mitigate and manage their effects" [38]. The NatHaz website was published, providing a collection of aerodynamic and damping datasets, online design modules for low- and high-rise buildings, and other features for buildings design to wind load. At the same time, the National Institute of Standards and Technology (NIST) developed a Database-Assisted Design (DAD) software for low- and high-rise buildings, freely available on the NIST website [39]. The software of both Institutions are based on the availability of aerodynamic databases. In this framework, NIST and the Tokyo Polytechnic University (TPU) provided data collections to create databases of pressure coefficients (aerodynamic database) and mechanical properties of buildings.

The NIST database collects data measured at the Boundary Layer Wind Tunnel Laboratory (BLWTL) of the University of Western Ontario (UWO); it is the result of a joint study conducted by NIST and Texas Tech University (TTU) entitled 'Windstorm Mitigation Initiative: Wind Tunnel Experiments on Generic Low Buildings' [37]. Instead, the TPU database is part of the 21st Century Center of Excellence Program named 'Wind Effects on Buildings and Urban Environment' [40]. The characteristics of the wind tunnel tests are summarized in Table 2 for both aerodynamic databases. As discussed in Section 5.2, the data provided in the databases can be used to calculate point surface pressure coefficients and area-averaged surface pressure coefficients on roof and wall surfaces, as well as foundation loads on low-rise buildings. Aerodynamic databases can be expanded in the future, to incorporate data for less regular geometries; these can come either from systematic studies on a variety of geometries (e.g., [41]), or from specific project-related analyses (e.g., [42]).

Table 2. Main aerodynamic databases for isolated low-rise buildings.

	Unit	NIST [37]	TPU [40]
Sampling Frequency *, f_s	Hz	500	500
Sampling Period *, T_s	s	100	18
10 cm Wind Speed *, $v_{m,10}$	m/s	8.8	7.4
Length Scale, λ_l		1:100	1:100
Velocity Scale, λ_v		1:4	1:3
Roughness Category		Open Country, Suburban	Suburban
Width × Depth, $b \times d$	m	12.2 × 19.0, 24.4 × 38.1, 15.2 × 30.5, 15.2 × 53.3, 36.6 × 57.1, 48.8 × 76.2	16.0 × 16.0, 16.0 × 24.0, 16.0 × 40.0
Height, h	m	3.7, 4.9, 5.5, 7.3, 9.7, 12.2	4.0, 8.0, 12.0, 16.0
Roof Slope, α	°	1.2, 2.4, 4.8, 14, 27	0, 4.8, 9.4, 14, 18.4, 21.8, 26.7, 30, 45

* model scale.

Currently wind tunnel tests are considered the reliable tool for investigating building aerodynamics, the main concern with Computational Fluid Dynamics (CFD) being the difficulty in calibrating simulations and validating their results. However, with the purpose of building aerodynamic databases, a joint effort within the scientific community might be able to produce standard criteria for simulations, the results of which may in a future complement wind tunnel data.

On the other hand, research is currently being developed towards the possibility of using reanalysis data for the definition of extreme wind climate at sites of interest. Numerical Weather Prediction (NWP) models simulate the physics of the atmosphere using available observations, and calculate meteorological variables in a three-dimensional grid extending from the surface to the stratosphere. These models have traditionally been used for weather forecasting, but they may also be rerun to produce a set of historical data. For example, the Integrated Forecast System (IFS) at the European Centre for Medium-Range Weather Forecasts has been rerun to produce a global reanalysis from 1979 to present at a horizontal resolution of 31 km, known as the ERA5 reanalysis [43]. The resolution of ERA5 is too coarse for calculating extreme values at a specific site, and downscaling to a higher resolution is hence required. This can be accomplished by rerunning the NWP model at higher resolution within the ERA5 dataset, which is called dynamical downscaling. An example, the NORA10 dataset [44] was created by running a NWP model with 11 km resolution, covering most of Northern Europe. The dataset is currently being updated with new model runs at 3 km resolution. Dynamical downscaling has the advantage that the physical consistency between the different variables is retained, but it is computationally demanding therefore it is not suitable to produce a long dataset. A cheaper alternative is running a high-resolution model for a shorter period, and use the short dataset for finding a statistical relationship between the short high-resolution dataset and the long low-resolution dataset. This method is called statistical downscaling [45].

The quality of these modelled dataset depends on the NWP model used and on its resolution, as well as on the methods used in statistical downscaling and interpolation; validation of the data against observation is clearly necessary for these datasets to become of practical use. In particular, it is observed that some models tend to underestimate the strongest winds. Not all NWP datasets include wind speed and direction as an explicit output. Examples of datasets of possible use when assessing wind loads are: the SMHI HARMONIE-ALADIN, covering the entire of Europe for the period 1961 to 2016 at a horizontal resolution of 11 km [46]; the MESCAN-SURFEX analysis, covering the period from 1961 to 2015 at 5 km spatial resolution [47]; the NORA10/NORA3 datasets, covering the period 1957 to 2002 for Scandinavia, Britain and parts of Northern Europe at 11 km resolution and the period 1995 to 2020 at a 3 km resolution [44]; and the Klinogrid dataset, providing hourly wind speed and wind direction on a 1 km resolution grid for the period 1957 to 2015 [45].

The visionary Wind Engineer can therefore think of a future in which web-based apps will access online databases to retrieve aerodynamic and meteorological data, and combine them together to obtain the "best" estimate of the wind load on a project structure; and machine learning and big data analytics could be the tools to achieve that. How far that future can be, and whether we will ever see it we do not know.

Author Contributions: Conceptualization, F.R. and A.M.A.; methodology, V.P.; software, V.P.; validation, A.M. and A.M.A.; formal analysis, A.M.; investigation, A.M.; data curation, V.P.; writing—original draft preparation, V.P., A.M., A.M.A. and F.R.; writing—review and editing, F.R. and A.M.A.; visualization, V.P.; supervision, F.R. All authors have read and agreed to the published version of the manuscript.

Institutional Review Board Statement: Not applicable.

Informed Consent Statement: Not applicable.

Data Availability Statement: Publicly available datasets were analyzed in this study. This data can be found here: NIST Aerodynamic Database (accessed on 20 November 2021).

Conflicts of Interest: The authors declare no conflict of interest.

References

1. Stoney, B. *The Theory of Stresses in Girders and Similar Structures with Practical Observations on the Strength and Other Properties of Materials*; Longmans, Greend and Co.: London, UK, 1886.
2. Irminger, J. Experiments on Wind Pressure. In Minutes of the Proceedings of the Institution of Civil Engineers; Institution of Civil Engineers: London, UK, 1894; Volume 118, pp. 468–472.
3. Stanton, T. On the resistance of plane surfaces in a uniform current of air. In *Minutes of the Proceedings of the Institution of Civil Engineers*; Institution of Civil Engineers: London, UK, 1904; Volume 156, pp. 78–126.
4. Eiffel, G. *The Resistance of the Air and Aviation: Experiments Conducted at the Champ-de-Mars Laboratory*; Dunot & Pinat: Paris, France, 1909.
5. Irminger, J.; Nøkkentved, C. *Wind-Pressure on Buildings: Experimental Researches (1st Series)*; Ingeniørvidenskabelige Skrifter, A 23; Danmarks Naturvidenskabelige Samfund: Copenaghen, Denmark, 1930.
6. Irminger, J.; Nøkkentved, C. *Wind-Pressure on Buildings: Experimental Researches (2nd Series)*; Ingeniørvidenskabelige Skrifter, A 42; Danmarks Naturvidenskabelige Samfund: Copenaghen, Denmark, 1936.
7. Nøkkentved, C. *Variation of the Wind-Pressure Distribution on Sharp-Edged Bodies*; Report 8, The Structural Research Laboratory, Royal Technical College: Copenhagen, Denmark, 1936.
8. Committee on Steel of the Structural Division. Wind Bracing in Steel Buildings: Final Report of Sub-Committee No. 31. *Trans. Am. Soc. Civ. Eng. ASCE* **1940**, *105*, 1713–1739. [CrossRef]
9. Bailey, A. Wind Pressures on Buildings. Ph.D. Thesis, Colorado State University, Fort Collins, CO, USA, 1976.
10. Bailey, A.; Vincent, N. Wind-pressures on buildings including effects of adjacent buildings. *J. Inst. Civ. Eng.* **1943**, *20*, 243–275. [CrossRef]
11. Jensen, M. The Model Law for Phenomena in Natural Wind. *Ingeniøren, Int. Ed.* **1958**, *2*, 121–158.
12. Swiss Society of Engineers and Architects (SIA). *SIA 160, Normen für die Belastungsannahmen, die Inbetriebnahme und die Ueberwachung der Bauten*; SIA: Zurich, Switzerland, 1956.
13. Davenport, A. The application of statistical concepts to the wind loading of structures. *Proc. Inst. Civ. Eng.* **1961**, *19*, 449–472. [CrossRef]
14. Davenport, A. The relationship of wind structure to wind loading. In Proceedings of the Symposium No. 16—Wind Effects on Buildings and Structures, Teddington, UK, June 1963; Her Majesty's Stationery Office: London, UK, 1963; pp. 53–111.
15. IAWE. Announcement of the Alan G. Davenport Wind Loading Chain. Available online: http://www.iawe.org/about/Wind_Loading_Chain.pdf (accessed on 20 November 2021).
16. Davenport, A. Rationale for Determining Design Wind Velocities. *J. Struct. Div.* **1960**, *2475.ST5*, 39–68. [CrossRef]
17. Van der Hoven, I. Power spectrum of horizontal wind speed in the frequency range from 0.0007 and 900 cycles per hour. *J. Meteorol.* **1957**, *14*, 160–164. [CrossRef]
18. Dalgliesh, A.M. Statistical Treatment of Peak Gusts on Cladding. *J. Struct. Div.* **1971**, *97*, 2173–2187. [CrossRef]
19. Peterka, J.A.; Cermak, J.E. Wind Pressures on Buildings—Probability Densities. *J. Struct. Div.* **1975**, *101*, 1255–1267. [CrossRef]
20. Holmes, J.D.; Best, R.J. *Wind Pressures on an Isolated High-Set House*; Wind Engineering Report 1/78; James Cook University of North Queensland: Queensland, Australia, 1978.
21. Stathopoulos, T.; Surry, D. Probability Distributions for Wind and Pressure for Low Buildings in Simulated Atmospheric Flow. In Proceedings of the 7th Canadian Congress of Applied Mechanics, Sherbrooke, CA, USA, 27 May–1 June 1979; pp. 565–566.
22. Holmes, J.D. Non-Gaussian Characteristics of Wind Pressure Fluctuations. *J. Wind Eng. Ind. Aerodyn.* **1981**, *7*, 103–108. [CrossRef]
23. Lawson, T.V. The Measurement of Short Term Average Pressure in a Wind Tunnel Investigation. *J. Wind. Eng. Ind. Aerodyn.* **1975**, *1*, 233–238.
24. Eaton, K.J.; Mayne, J.R. The Measurement of Wind Pressures on Two-Storey Houses at Aylesbury. *J. Ind. Aerodyn.* **1975**, *1*, 67–109. [CrossRef]
25. Gumbel, E.J. *Statistics of Extremes*; Columbia University Press: New York, NY, USA, 1958.
26. Cook, N.J.; Mayne, J.R. A Novel Working Approach to the Assessment of Wind Loads for Equivalent Static Design. *J. Wind Eng. Ind. Aerodyn.* **1979**, *4*, 149–164. [CrossRef]
27. British Standards Institution. *Basic Data for the Design of Buildings Chapter V. Loading—Part 2. Wind Loads*; BSI: London, UK, 1972.
28. Lawson, T.V. *Wind Effects on Buildings, Volume 1: Design Applications*; Applied Science Publisher: London, UK, 1980.
29. Gavanski, E.; Gurley, K.; Kopp, G. Uncertainties in the Estimation of Local Peak Pressures on Low-Rise Buildings by Using the Gumbel Distribution Fitting Approach. *J. Struct. Eng.* **2016**, *142*, 04016106. [CrossRef]
30. Gavanski, E.; Cook, N. Evaluation of XIMIS for Assessing Extreme Pressure Coefficients. *Front. Built Environ.* **2019**, *5*, 48. [CrossRef]
31. Stathopoulos, T. Turbulent Wind Action on Low-Rise Buildings. Ph.D. Thesis, The University of Western Ontario, London, ON, Canada, 1979.
32. Cook, N.J. *The Designer's Guide to Wind Loading of Building Structures, Part 2*; Building Research Establishment, Butterworths: London, UK, 1990.
33. Geurts, C. *External Pressure Coefficients and Peak Factor for Buildings in ENV 1991-2-4: Wind Loads*; TNO Report 2000-CON-DYN-R2021; TNO Building and Construction Research: Delft, The Netherlands, 2000.

34. Geurts, C.; Blackmore, P.; Hansen, S.; Hortmanns, M.; Sedlacek, G.; Spehl, P.; van Staalduinen, P. Transparency of Pressure and Force Coefficients. In Proceedings of the 3rd European & African Conference on Wind Engineering, Eindhoven, NL, USA, June 2001; pp. 165–172.

35. CEN. *EN1991-1-4, Eurocode 1: Actions on Structures—Part 1–4: General Actions—Wind Actions*; European Committee for Standardization (CEN): Brussels, Belgium, 2005.

36. Liu, Y.; Kopp, G.A.; Chen, S.F. An examination of the gust effect factor for rigid high-rise buildings. *Front. Built Environ.* **2020**, *6*, 221. [CrossRef]

37. Ho, T.; Surry, D.; Morrish, D.; Kopp, G. The UWO contribution to the NIST aerodynamic database for wind loads on low buildings. Part 1: Archiving format and basic aerodynamic data. *J. Wind Eng. Ind. Aerodyn.* **2005**, *1*, 1–30. [CrossRef]

38. University of Notre Dame. NatHaz Modeling Laboratory. Available online: https://nathaz.nd.edu (accessed on 20 November 2021).

39. National Institute of Standards and Technology (NIST). NIST Aerodynamic Database. Available online: https://www.nist.gov/el/materials-and-structural-systems-division-73100/nist-aerodynamic-database (accessed on 20 November 2021).

40. Tamura, Y. TPU Aerodynamic Database. Available online: http://wind.arch.t-kougei.ac.jp/system/eng/contents/code/tpu (accessed on 20 November 2021).

41. Rizzo, F.; Ricciardelli, F. Design pressure coefficients for circular and elliptical plan structures with hyperbolic paraboloid roof. *Eng. Struct.* **2017**, *139*, 153–169. [CrossRef]

42. Rizzo, F.; Sepe, V.; Ricciardelli, F.; Avossa, A. Wind pressures on a large span canopy roof. *Wind Struct.* **2020**, *30*, 299–316.

43. Hersbach, H.; Bell, B.; Berrisford, P.; Hirahara, S.; Horányi, A.; Muñoz-Sabater, J.; Nicolas, J.; Peubey, C.; Radu, R.; Schepers, D.; et al. The ERA5 global reanalysis. *Q. J. R. Meteorol. Soc.* **2020**, *146*, 1999–2049. [CrossRef]

44. Reistad, M.; Breivik, O.; Haakenstad, H.; Aarnes, O.; Furevik, B.; Bidlot, J. A high-resolution hindcast of wind and waves for The North Sea, The Norwegian Sea and The Barents Sea. *J. Geophys. Res.* **2011**, *116*, C5. [CrossRef]

45. Haakenstad, H.; Haugen, J. A 15-Year High Resolution Meteorological Dataset for Risk Assessment in Southern Norway. MET Report 5/2017; The Norwegian Meteorological Institute, 2017. Available online: https://www.met.no/publikasjoner/met-report/met-report-2017 (accessed on 20 November 2021).

46. Ridal, M.; Olsson, E.; Unden, P.; Zimmermann, K.; Ohlsonn, A. HARMONIE Reanalysis Report of Results and Dataset. Deliverable D2.7 of the UERRA Project 2017. Available online: http://www.uerra.eu/component/dpattachments/?task=attachment.download&id=297 (accessed on 20 November 2021).

47. Bazile, E.; Abida, R.; Verelle, A.; Le Moigne, P.; Szczypta, C. MESCAN-SURFEX Surface Analysis. Deliverable D2.8 of the UERRA Project 2017. Available online: http://www.uerra.eu/component/dpattachments/?task=attachment.download&id=399 (accessed on 20 November 2021).

MDPI

Article

Contemporary and Novel Hold-Down Solutions for Mass Timber Shear Walls

Thomas Tannert [1,*] and Cristiano Loss [2]

[1] Wood Innovation Research Laboratory, School of Engineering, University of Northern British Columbia, Prince George, BC V2N 4Z9, Canada

[2] Sustainable Engineered Structural Solutions Laboratory, Wood Science, University of British Columbia, Vancouver, BC V6T 1Z4, Canada; cristiano.loss@ubc.ca

* Correspondence: thomas.tannert@unbc.ca

Abstract: 'Mass timber' engineered wood products in general, and cross-laminated timber in particular, are gaining popularity in residential, non-residential, as well as mid- and high-rise structural applications. These applications include lateral force-resisting systems, such as shear walls. The prospect of building larger and taller timber buildings creates structural design challenges; one of them being that lateral forces from wind and earthquakes are larger and create higher demands on the 'hold-downs' in shear wall buildings. These demands are multiple: strength to resist loads, lateral stiffness to minimize deflections and damage, as well as deformation compatibility to accommodate the desired system rocking behaviour during an earthquake. In this paper, contemporary and novel hold-down solutions for mass timber shear walls are presented and discussed, including recent research on internal-perforated steel plates fastened with self-drilling dowels, hyperelastic rubber pads with steel rods, and high-strength hold-downs with self-tapping screws.

Keywords: cross-laminated timber; self-tapping screws; internal-perforated steel plates; hyperelastic bearing pads; proprietary connections

1. Introduction

1.1. Mass Timber Construction

Growing environmental concerns and emphasis on resource efficiency, combined with the need to mitigate the impacts from urban population growth, renewed the interest to use the renewable material wood for non-residential and tall buildings [1]. Recent developments of innovative materials, connectors, and systems contributed to a resurgence in the use of wood as a structural material. On the material level, the introduction of cross-laminated timber (CLT), a plate-type engineered wood product which can be used in structural wall or floor assemblies, has been labelled a 'game changer' [2]. A landmark on the connection level was the establishment of self-tapping screws (STS) as the state of the art in wood connector technology [3]. Finally, on the systems level, the concept of hybrid structures, which integrate wood with different materials to form a system that makes use of each material's strength and stiffness and overcomes their individual weaknesses, offers great potential to overcome the current height limitations of timber-only buildings [4]. Publications, such as *Technical Guide for the Design and Construction of Tall Wood Buildings* [5] and *Use of Timber in Tall Multi-Storey Buildings* [6] and recently built examples from around the world (e.g., [7–10]) show that wood has the potential to expand into construction segments that are the traditional stronghold of steel and concrete.

Mass timber products in general, and CLT in particular, provide architects and engineers with opportunities to expand the use of wood in structures beyond low- and mid-rise residential construction. Compared with traditional lumber products with small cross sections, engineered mass timber panels offer better fire resistance, homogeneity in mechanical properties, and dimensional stability when exposed to changes in environmental

conditions [11]. The high in-plane strength and stiffness of CLT panels make them suitable for diaphragms or shear walls as part of the lateral force-resisting system (LFRS), even in earthquake-prone regions [12]. Compared with steel and concrete buildings, buildings with wood LFRS are lighter and attract lower seismic loads; however, they are usually more flexible and more vulnerable against overturning forces [13].

1.2. Mass Timber Shear Walls

In North America, based on the current state of knowledge, mass timber structures have been incorporated into the (unpublished) 2020 National Building Code of Canada (NBCC) [14] for gravity-load systems in buildings up to 12 stories, and the 2021 International Building Code [15] for gravity-load systems in buildings up to 18 stories. In addition, the NBCC 2020 will adopt CLT shear walls as seismic LFRS and refers to the Canadian Standard for Engineering Design in Wood (CSA O86) [16] for detailing provisions intended to ensure that rocking is the energy dissipative kinematic mechanism.

These design provisions are tailored to platform-type construction, illustrated in Figure 1a, where each floor acts as a platform for the floor above. The walls at each floor act as an independent rocking system with connections to the floor below; vertical joints connect the individual panels within the wall assembly [17]. Platform-type construction requires a large number of panels to be handled on-site, and a large number of connections between panels and floors, hold-down (HD) deformations accumulate at each level, as do the compression perpendicular to grain stresses on the floor panels. In contrast, balloon-type shear wall systems consist of continuous panels over multiple floors, with the intermediate floors framing into their face (Figure 1b). This construction type eliminates perpendicular to grain bearing between floors, provides walls with slender panel aspect ratios, and requires fewer HD and shear bracket connections over the height of a building [17]. To date, however, only limited research is available on the seismic performance of balloon-type CLT construction (e.g., [18]), and implementation of standardized design provisions is still outstanding.

(**a**)   (**b**)
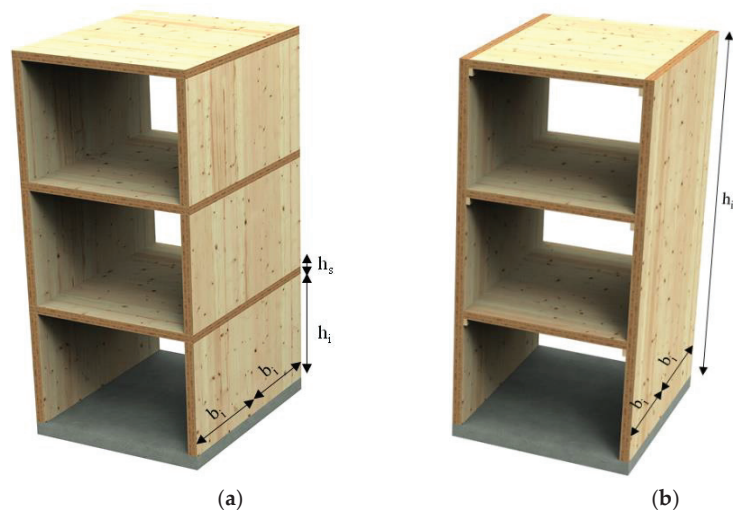
Figure 1. Platform-type (**a**) and balloon-type (**b**) construction (schematic produced by Andrea Roncari (UBC student, reprinted with permission)).

In platform-type structures, connections to the floor below are provided with brackets and HDs to resist sliding and (uplift), respectively. The vertical wall panel-to-panel connections typically use plywood splines or half-lap joints (Figure 2). The latter components are usually designed to provide ductility and energy dissipation [19,20]. The research findings

on platform-type CLT shear walls (e.g., [21,22]) can be summarized as follows: (1) Their structural performance in terms of strength, stiffness, ductility, and energy dissipation is governed by the connections; (2) adequate seismic performance and ductile behaviour can be achieved with proper detailing; (3) rocking kinematic motion is preferred to dissipate the energy; (4) the CLT wall panel deformation is negligible under in-plane lateral loading.
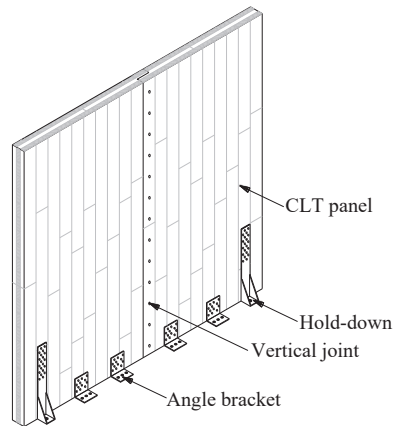
Figure 2. CLT shear wall connections (schematic produced by David Owolabi (UBC student, reprinted with permission)).

1.3. Objectives

HD solutions—when designed elastically and installed at both top and bottom of the panels—ensure continuity in the transfer of the load to the foundation, allow activating the energy-dissipative function of the vertical joint connections, and—when designed for this purpose—add ductility and energy dissipation to the LFRS through plastic failure in the fasteners. The objectives of this paper are to summarize the state of the art in HD technology for mass timber shear walls and present recent research on novel HD solutions.

2. Contemporary and Novel Hold-Down Solutions

2.1. Nailed Steel Brackets

Early studies by Ceccotti et al. [23] were pivotal to establishing connection details for CLT shear walls anchored using light steel plates nailed to the panels. Subsequent research formed the basis of the design of HDs and brackets to prevent wall uplift and sliding at its base [24]. Conventional metal cold-shaped HDs were proven adequate for low-rise buildings [25,26] when accepting a certain degree of damage in the joints and residual deformation in the timber assembly. Figure 3a,b show typical failures of commercially available non-resilient bracket connectors under reversed cyclic loading. Although the HD was designed for the required strength, the lack of resilience may result in local brittle wood failure. With such designs, the connection cannot be restored, and replacement could become uneconomic. Larger steel straps with an increased number of nails can provide higher strength and stiffness and shift the failure mode into the strap (Figure 3c); however, such HDs, when insufficiently sized, have been shown to be prone to high strength degradation under cyclic loading, particularly buckling [27]. The uplift force–displacement curve, shown in Figure 3d, illustrates the typical pinching behaviour of nailed HDs with significant loss of stiffness in unloading under reversed-cyclic loads.
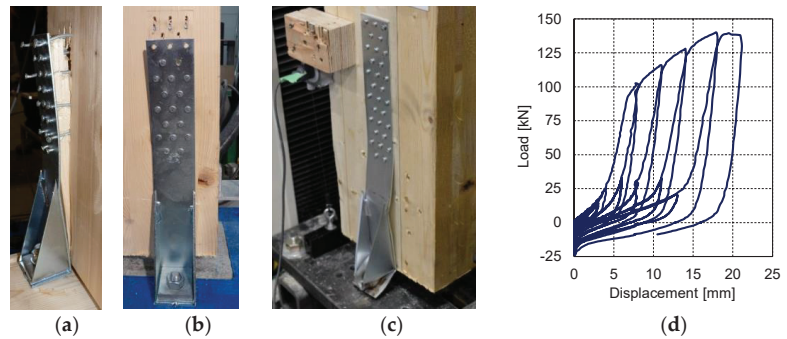
Figure 3. Nailed HDs: (**a**) brittle wood failure; (**b**) nail yielding; (**c**) steel bracket yielding (photo credit: (**a**,**b**) Cristiano Loss; (**c**) Thomas Tannert); (**d**) uplift force–displacement behaviour.

2.2. Dowelled Slotted-In Steel Plates

Dowelled slotted-in steel plates, varying the fastener spacing and the loaded end distance, were studied as HDs for mass timber shear walls [28–30]. It was possible to design large-scale HDs with ductile behaviour, as shown in Figure 4b; however, brittle wood failure (tear-out) was observed in some tests. It was also observed that ductility increased with the row spacing and end distance of fasteners; however, dimension constraints have to be observed when placing HDs close to the wall corner. Reinforcements using STS around the HDs were shown effective to reduce the likelihood of brittle failure and increase strength and ductility. However, the deformations developed through the yielding of steel and wood crushing, with permanent damage in the CLT panels and fasteners, require repair of dowelled slotted-in steel plates HDs after major earthquakes. HD ductility significantly increased when the out-of-plane opening of CLT lamellas was inhibited using bolted threaded rods. The behaviour of dowelled slotted-in steel plates in multiple-shear arrangements was studied [31], including sequential failure modes of the fasteners and detailing, to reduce the opening up of the side layers in the timber member. This type of HD is being applied in practice; an example (Begbie Elementary school in Vancouver, Canada) is shown in Figure 4c.
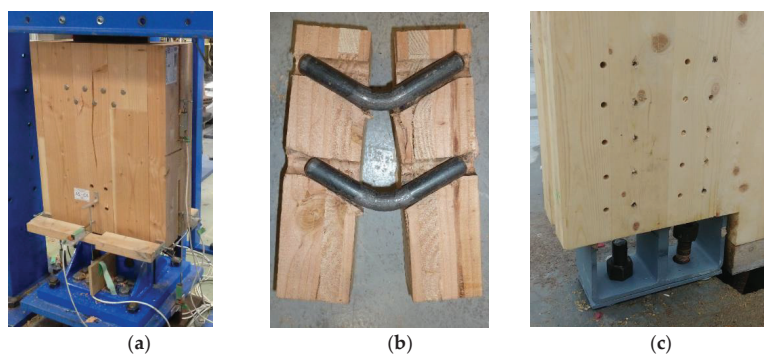
Figure 4. Dowelled slotted-in steel plates: (**a**) HD test setup; (**b**) ductile steel yielding and wood crushing failure modes (photo credit: (**a**,**b**) Justin Brown; (**c**) Fast + Epp, reprinted with permission).

2.3. Pinching-Free Connectors

Pinching-free connectors (PFCs) were proposed as alternative HD-to-timber connections with slender fasteners, with the aim to eliminate the loss of stiffness in unloading under reversed-cyclic loads [32]. PFCs were designed using stocky fasteners and steel side plates; the latter were held down using a spring-type system, as shown in Figure 5a. The

result is a ratcheting system in which each fastener remains elastic, while wall deformation is dictated by spring elongation. Regardless of uplift displacement demand in the HD, the ratcheting system ensures a perpetual surface contact between the fastener and wood element. Plastic deformation develops only through embedment in wood (Figure 5b), leading to better accuracy in predicting the behaviour of connectors. PFCs were also found to be effective in reducing peak deformation when compared with the conventional connectors, beyond 50% lower, with negligible pinching [32] (Figure 5c).
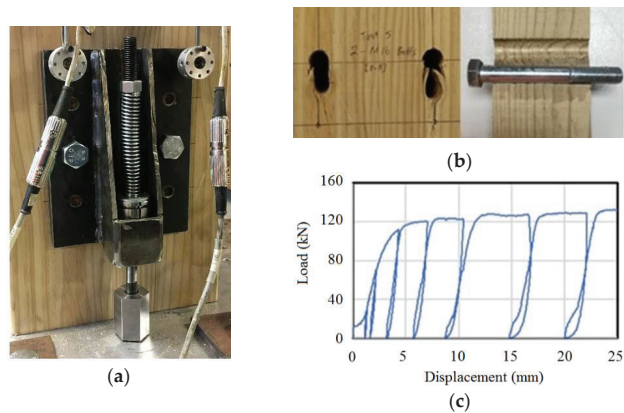
Figure 5. Pinching-free connectors: (**a**) as-built HD connector; (**b**) local failure with only crushing (photo credit: Nicholas Chan, reprinted with permission); (**c**) pinching-free load–displacement.

2.4. X-RAD System

The proprietary X-RAD system [33] was developed to connect CLT panels at their corners and to the foundation using steel plates, such as L-shape profiles (Figure 6a). X-Rad connectors have a hardwood block encased in a cold-formed metal box, machined to accommodate six STS, installed at two angles of inclination to capture shear forces and tension and ensure reliable stress flow into the CLT elements [34]. Experimental campaigns characterized the mechanical behaviour of the X-RAD connection under monotonic and cyclic loading [34]. From the observed failure modes, shown in Figure 6b, together with typical force–displacement curves, the first yielding of ductile members occurred; the system ultimately collapsed due to the block-shear failure mode of the internal plate. Experimental behaviour of X-RAD loaded in tension showed a static ductility of 6 or higher, making it suitable when used as dissipative HD connectors in CLT shear walls [35].
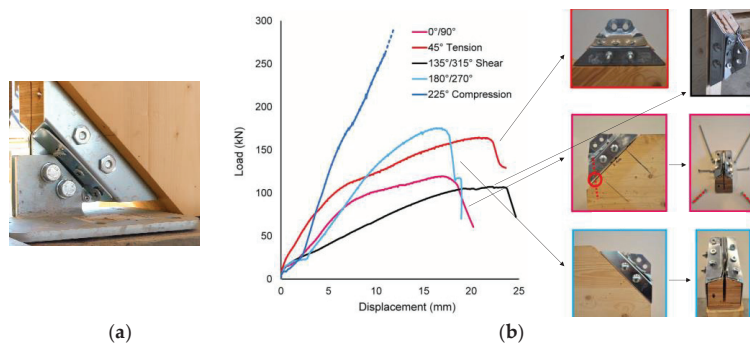
Figure 6. X-RAD system: (**a**) HD connector (photo credit: Rothoblaas, reprinted with permission); (**b**) force–displacement curves and failure modes (photo credit: Andrea Polastri, reprinted with permission).

2.5. Holz–Stahl–Komposit System

The proprietary Holz–Stahl–Komposit (HSK) system [36], originally developed for Glulam member connections, was modified in its layout for use as HD for CLT shear walls [37]. The HSK system is based on adhesively bonded perforated steel plates, inserted inside precut slots in the mass timber panels. The system's strength, stiffness, and ductility are governed by the steel plate material properties, while the adhesive bond and mass timber panel are capacity protected and designed to remain free of damage. From a design perspective, research showed that ductile failure modes develop when plastic behaviour in predefined ductile zones is observed, leaving all timber elements undamaged [38] (Figure 7a). The uplift load–displacement curves exhibited significant permanent deformations after each loading cycle (Figure 7b). The system has been successfully implemented in the Wood Innovation Design Centre in Prince George, Canada (Figure 7c).

(**a**)   (**b**)   (**c**)
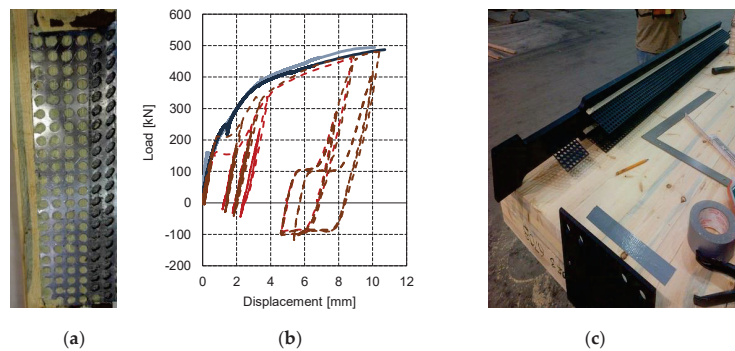
Figure 7. HSK-based HD: (**a**) steel plate after testing; (**b**) uplift force–displacement curve; (**c**) installed HD (photo credit: (**a**), Xiaoyue Zhang; (**c**), Robert Malczyk, reprinted with permission).

2.6. Internal Hollow Steel Tubes

Internal-bearing connections can minimize the risk of brittle failure in CLT panels; a noteworthy HD solution applying this concept consists of hollow steel tubes embedded into CLT panels [26,39]. The detailing consists of welding a coupler to the top of the tube, placing the tube into a panel hole of the same diameter, and attaching a tie-down steel rod to the coupler as an anchor to the floor below (Figure 8a). The components are reasonably easy to install, can be readily inspected, and can potentially be replaced.

(**a**)   (**b**)
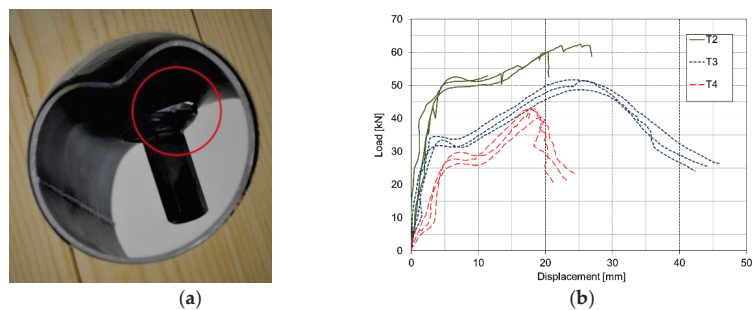
Figure 8. Steel tube HD: (**a**) typical failure (photo credit: Johannes Schneider, reprinted with permission); (**b**) load–displacement curves.

Experimental investigations indicated that this HD, when installed in CLT shear walls, could avoid damage to the wood and brittle failure (Figure 8a). While the ultimate failure exhibited undesirable buckling of the steel tube, the concept of an internal load-bearing mechanism was deemed the main advantage since the CLT panel was not damaged at

all. Resulting load–displacement curves using three different diameters (T2 = 50.8 mm, T3 = 76.2 mm, and T4 = 101.6 mm) are illustrated in Figure 8b. Subsequent numerical work optimized the steel tube connector geometry for a target load of 90 kN [40]. To explore the steel tube as a viable HD solution for tall buildings and higher demands, it was proposed to employ two or three steel tubes in a group.

2.7. Slip–Friction Devices

Slip–friction devices, consisting of a steel plate encased in the timber element and two built-in side steel plates held together with bolts and disc springs, were proposed as HD for mass timber shear walls [41]. Friction is developed at the contact surfaces between the steel plates. A stable, symmetric friction–slip behaviour was shown with the use of abrasive-resistant steel as slotted plates and mild steel for side plates. High dissipation energy capability can be attained in the system without pinching. Friction–slip connections made of abrasive-resistant steel as slotted plates and mild steel for side plates studied in [42] showed better performance than those using brass shims, having behaviour not affected by the loading rate. The experiments on rigid shear walls equipped with symmetric friction–slip joints further showed that connection with high slot lengths (slippage length) tended to exhibit self-centring behaviour [42].

CLT shear-walls equipped with slip–friction joints as HD displayed the desired flag-shaped hysteretic behaviour, shown in Figure 9b, although exhibiting limited self-centring capabilities [43]. Slip-friction connectors were further advanced into resilient slip friction (RSF) connectors [44,45] which provide a damage-free self-centring solution for CLT shear walls, avoiding downtime and repair costs due to earthquakes. In the RSF device, the two cap plates and two slotted plates assure elastic–plastic behaviour of the joint, while bolts and Belleville washers are used to create a controlled pressure between the plates. The self-centring capacity is enabled by the zigzag-like connection interface between the cap and slotted plates (Figure 9a). Nonlinear time–time history analyses showed that buildings with RSF HD exhibited low damage during moderate-to-severe seismic events [46]. The system, commercialized under the name 'Tectonus', has been used in recent structures such as the Fast + Epp building in Vancouver (Figure 9c).

| (a) | (b) | (c) |
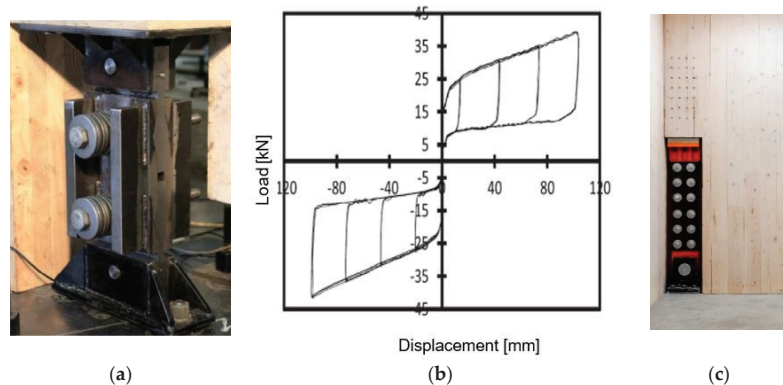
Figure 9. RSF HD: (**a**) close-up view; (**b**) force–displacement (photo credit: Ashkan Hashemi, reprinted with permission); (**c**) commercial application (photo credit: Fast + Epp, reprinted with permission).

2.8. Volume Damping Devices

Damper-based HDs were studied with a focus on glulam walls anchored at their base, using high-force-to-volume damping devices (HF2VDDs) made of a steel shaft sliding within a tube [47,48] (Figure 10a). The damping and energy dissipation are provided by an extruded lead mounted around the shaft. System-scale wall tests were performed on glulam shear walls with HF2VDD HDs installed using inclined self-tapping screws and anchored to the foundation through bolts. Tested full-scale specimens confirmed that such walls

can exhibit a high level of energy dissipation with low pinching. Severe crushing at the panel base laid on the plate foundation was observed, indicating a need for reinforcements in wood.
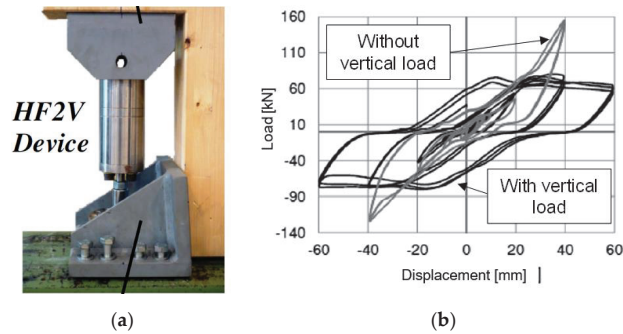
Figure 10. Damper-based HD: (**a**) close-up view of the damper device (photo credit: Geoffrey Rodgers, reprinted with permission); (**b**) typical load–displacement curve.

2.9. Self-Tapping Screw Connections

Recent research at the Wood Innovation Research Laboratory (WIRL) at the University of Northern British Columbia (UNBC) investigated CLT shear walls with STS connections as HD, shear bracket, and panel-to-panel connection. The objective was to determine the strength, stiffness, and ductility of a rocking wall system as a function of the number of STS in these connections. Component level connection tests (Figure 11a) and full-scale shear wall tests were conducted. HDs were tested with two (HD-2), six (HD-6), and nine (HD-9) screws. Quasi-static monotonic and reversed cyclic tests were conducted. The typical HD failure mode (fastener yielding) is illustrated in Figure 11b. The corresponding hysteresis behaviour of the HD connections, combined with a representative monotonic curve, presented in Figure 11c, showed nonlinear behaviour in terms of degradation and pinching. Until capacity, the HD showed little stiffness degradation; beyond capacity, distinct degradation in cyclic reloading stiffness was observed.
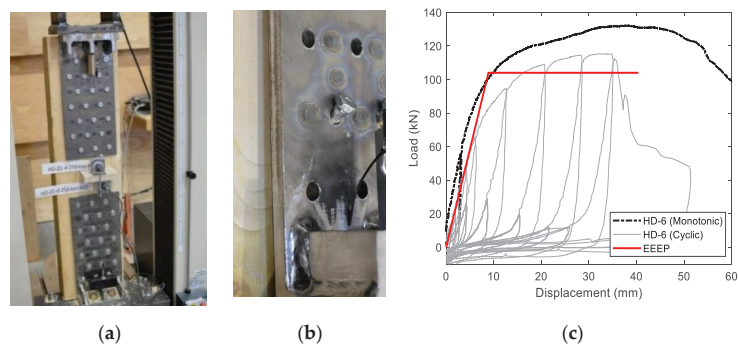
Figure 11. (**a**) HD with STS; (**b**) failure mode (photo credit: Thomas Tannert); (**c**) force–displacement curves.

As expected, strength was a linear function of the number of STS. The average strength values for HD-6 and HD-9 were about 3.1 and 4.5 times those for HD-2, under the monotonic tests. Similar trends were observed in yield strength. The elastic stiffness increased with the number of screws: HD-6 and HD-9 were about 2.5 and 5 times stiffer than HD-2. HDs with fewer screws showed higher ductility, e.g., the ductility of HD-2 was 42% and 16% higher than HD-6 and HD-9 under monotonic loading, and 79% and 47% higher under cyclic

loading. Most importantly, the results corresponded to those of previous research [49] confirming that STS in energy-dissipative connections are severely overdesigned and are likely to remain elastic during seismic design level events. Based on these results, there is a clear need to better define the relevant design parameters for the use of STS in energy-dissipative connections. Designers should consult with manufacturers about the availability of test data.

2.10. Internal Perforated Steel Plates

Timber connections combining slotted-in steel-plates with dowel-type fasteners avoid the use of adhesives [50] and, when combined with perforated steel plates, can also avoid the common dowel yielding and wood crushing failure mechanisms. Research on perforated steel plates as end-brace connections in timber frames [51,52] and as base shear connectors in CLT shear walls [53] verified their suitability as energy-dissipative components. As an alternative to common dowels, self-drilling dowels (SDDs) can simplify the installation and allow drilling through the whole assembly, including the steel plate, without predrilling [54]. If SDD connections are combined with internal-perforated steel plates (IPSPs) and designed with sufficient overstrength, then the desired ductility can be achieved through plate yielding [55]. The viability of using IPSPs with SDDs was demonstrated at the material and component levels. Different steel plate geometries were studied, and the most important parameter was found to be perforation length, with longer perforations exhibiting larger deformation capacity but being weaker and less stiff [56].

Recent research at the UNBC investigated HDs with IPSPs and SDDs. The objective was to determine the strength, stiffness, and ductility of a rocking wall system while designing the SDD connections with sufficient overstrength so that all energy dissipated was concentrated by the steel plates. IPSPs were welded to L-shaped steel profiles (Figure 12a). Then, IPSPs were inserted into 5 mm by 150 mm slots in the middle layer of the CLT, and eight 7 mm × 133 mm SDDs were used to fasten the IPSPs. One monotonic test and three half-cyclic tests were conducted. The hold-downs failed by yielding the steel 'bridges', as shown in Figure 12a, the HD uplift force–displacement curves are illustrated in Figure 12b. After an initial stiff and linear phase, the steel plates started deforming, with a pronounced drop in stiffness. The cyclic HD force–displacement hysteretic curves showed stiffness degradation per cycle, the load consistently increased until ultimate capacity was reached, and after the subsequent cycle, the specimens failed.
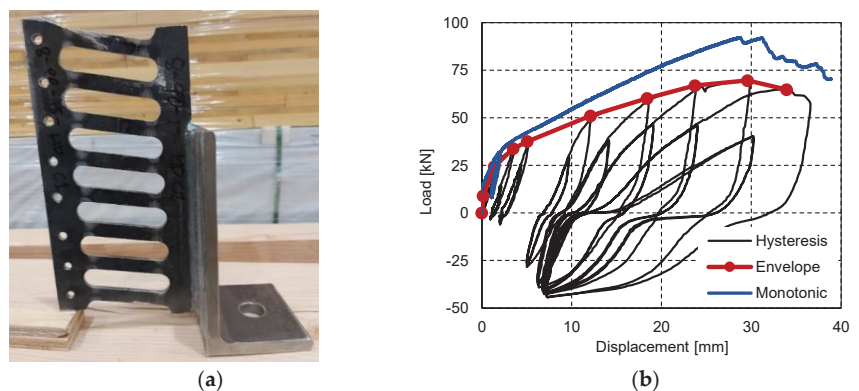
Figure 12. (**a**) Deformed HD with IBSP (photo credit: Thomas Tannert); (**b**) force–displacement curves.

2.11. Hyperelastic Pads with Internal Steel Rods

In 2019, capacity design principles for CLT shear walls were introduced into CSA O86, specifying that 'Energy dissipative connection shall be designed to ensure that all

principle inelastic deformations and all principle energy dissipation occurs in: (a) connections between vertical joints of adjacent shearwall segments; and (b) shear connections of shearwalls to foundations or floors underneath, in uplift only.' While no specific definitions are provided for 'principle inelastic deformations and principle energy dissipation', HDs have to be interpreted as nondissipative connections which shall be capacity protected by designing them to remain elastic under the force and displacement demands that are induced in them when the energy-dissipative connections reach the 95th percentile of their ultimate resistance. To comply with these Canadian design provisions (it is beyond the scope of this paper to discuss how meaningful these provisions are, and how likely they are to be changed again), there is a need to develop HD solutions with high load-carrying and deformation capacities while remaining elastic.

A material with such properties is hyperelastic rubber; therefore, it can be considered as a potential HD solution for CLT shear walls. The structural performance of internal-bearing hyperelastic HD for CLT shear walls was evaluated by Asgari et al. [57]. The components of the HD include the elastomeric bearing layers, steel plates, and a steel rod with nuts, as illustrated in Figure 13a. Recent research at the UNBC investigated CLT shear walls with hyperelastic pads and internal steel rods as HD. The objective was to determine the strength, stiffness, and ductility of a rocking wall system, where all energy dissipation occurs in the vertical panel-to-panel connections. Herein, only the HD tests, conducted to determine their performance parameters for the shear wall design, are presented and discussed. The rubber's effective compressive mechanical properties as functions of shape factor and loading speed and its load–displacement behaviour under quasistatic monotonic, repeated serviceability, and reversed cyclic loading for a given target load, herein 120 kN, were investigated [58]. The performance of a hyperelastic HD (Figure 13b) demonstrated that the assembly can achieve the performance to remain elastic. Ductile HD failure can be achieved as long as the steel rod is the weakest link in the setup. However, all other members must be capacity protected to avoid brittle failure. In further research [58], the performance of a hyperelastic HD was investigated at the component level, with different sizes of rubber pads. The tests demonstrated that (1) the HD can remain elastic under rocking kinematics provided that the elastic limit of the steel rod is not exceeded; (2) failure of the rod is the subsequent desired ductile mode; (3) sufficient CLT width can prevent undesired brittle failure mode before steel yielding; (4) increasing the rubber pad thickness reduces the HD stiffness; (5) increasing the rubber pad width increases the HD stiffness. Based on the results of the investigations presented herein, a capacity-design procedure for the hyper-elastic hold-downs was proposed.
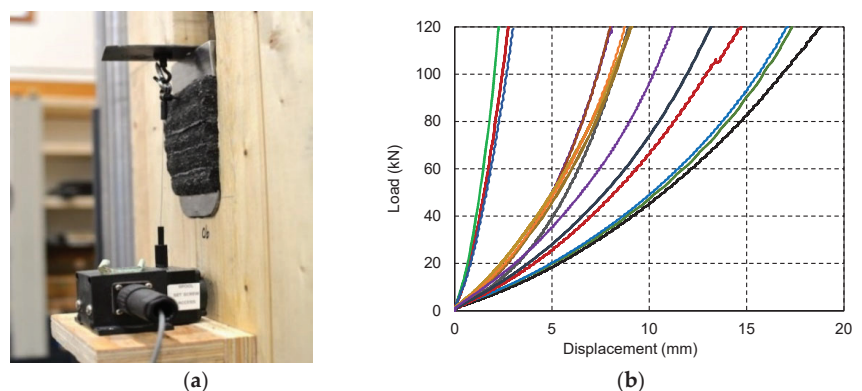
Figure 13. (**a**) Deformed HD (photo credit: Thomas Tannert); (**b**) force–displacement curves.

3. Discussion

The prospect of building larger and taller timber buildings creates higher demands on the 'hold-downs' in shear wall buildings. These demands are multiple: strength to resist loads, stiffness to minimize deflections during wind events, as well as deformation compatibility to facilitate the desired rocking motion during an earthquake.

Contemporary and novel hold-down solutions for mass timber shear walls were presented herein. Metal cold-shaped HDs attached with nails or screws were proven adequate for low-rise buildings when accepting a certain degree of damage in the joints and residual deformation in the timber assembly. It was shown that dowelled slotted-in steel plates can provide large-scale HDs with ductile behaviour, with high strength and stiffness; however, brittle CLT failure (tear-out) has to be prevented with sufficient spacing or wood reinforcements. HDs that rely on fastener yielding and wood crushing to dissipate energy exhibit pronounced pinching behaviour. Pinching-free HD connectors were developed to eliminate the loss of stiffness in unloading under reversed-cyclic loads, relying on a ratcheting system where the fasteners remain elastic, while wall deformation is dictated by the spring elongation. Larger capacities can be achieved using the proprietary X-RAD system in which CLT panels are connected at their corners and to the foundation, using customized steel plates. While the yielding of ductile steel members is the first failure mode, the system ultimately collapses due to the block-shear failure mode of the CLT panel. The proprietary HSK system, based on adhesively bonded perforated steel plates, inserted inside precut slots, avoids any exterior penetration of the mass timber panels. Ductile failure modes develop in predefined steel zones, and damage to the timber is avoided.

Internal-bearing connections can minimize the risk of brittle wood failure; a noteworthy HD solution applying this concept consists of hollow steel tubes embedded into CLT panels. The concept of an internal load-bearing mechanism was deemed the main advantage since the CLT panel was not damaged at all. Slip–friction devices, consisting of a steel plate encased in the timber element and two built-in side steel plates held together with bolts and disc springs, provide a stable, symmetric, pinching-free, and flag-shaped hysteretic behaviour, with high-dissipation energy capability. Slip–friction connectors were further advanced into resilient slip–friction connectors, which provide a damage-free self-centring solution for CLT shear walls. Damper-based HDs, made of a steel shaft sliding within a tube, provide a high level of energy dissipation with low pinching. Recent research investigated internal-perforated steel plates fastened with self-drilling dowels, hyperelastic rubber pads with steel rods, and high-strength STS assemblies.

The findings from the latter studies are of particular interest, as STSs are now considered the state-of-the-art approach in mass timber construction [3,59]. In platform-type construction, a capacity design philosophy is normally employed to avoid brittle wood failure modes and system collapse. The dissipative components are designed to be ductile, while the nondissipative components are overdesigned [12,60]. Current design practices designate the (nailed or screwed) shear connections between coupled CLT shear wall panels as the primary energy-dissipative components; these connections are designed using established procedures, including standardized modification factors. The UNBC research confirmed previous findings [49] regarding the inherent conservatism in these standardized design procedures with STS connections being up to six times stronger than their calculated design values. As a consequence, these energy-dissipating connections may remain elastic during seismic events, resulting in a much stiffer LFRS than assumed when estimating the overall structural behaviour. Based on these results, there is a clear need for further research to better define the relevant design parameters for the use of STS in energy-dissipative connections. Designers should consult with manufacturers about the availability of test data. Recent (e.g., [60]) and ongoing research in this area focuses on developing capacity-based procedures such that energy dissipation occurs in designated connections in the desired sequence, while brittle elements remain elastic. Such procedures will provide design guidance so that structural engineers beyond the early adaptors become confident in utilizing the renewable resource wood in their projects.

References

1. Green, M.; Karsh, J.E. *Tall Wood—The Case for Tall Wood Buildings*; Wood Enterprise Coalition: Vancouver, BC, Canada, 2012.
2. Karacabeyli, E.; Gagnon, S. *Cross-Laminated Timber (CLT) Handbook*; FPInnovations: Vancouver, BC, Canada, 2019.
3. Dietsch, P.; Brandner, R. Self-tapping screws and threaded rods as reinforcement for structural timber elements–A state-of-the-art report. *Constr. Build. Mater.* **2015**, *97*, 78–89. [CrossRef]
4. Pan, Y.; Tannert, T.; Kaushik, K.; Xiong, H.; Ventura, C. Seismic Performance of a Proposed Wood-Concrete Hybrid System for High-rise Buildings. *Eng. Struct.* **2021**, *238*, 112194. [CrossRef]
5. Karacabeyli, E.; Lum, C. *Technical Guide for the Design and Construction of Tall Wood Buildings in Canada*; Special Publication (SP-55E); FPInnovations: Vancouver, BC, Canada, 2014.
6. Smith, I.; Frangi, A. *Use of Timber in Tall Multi-Storey Buildings*; SED 13; IABSE: Zurich, Switzerland, 2014; ISBN 978-3-85748-133-8.
7. Malo, K.A.; Abrahamsen, R.B.; Bjertnæs, M.A. Some structural design issues of the 14-story timber framed building 'Treet' in Norway. *Eur. J. Wood Wood Prod.* **2016**, *74*, 407–424. [CrossRef]
8. Woschitz, R.; Zotter, J. High-rise timber building HoHo Vienna–The structural concept. *Österr. Ing. Archit. Z.* **2017**, *162*, 63–68.
9. Connolly, T.; Loss, C.; Iqbal, A.; Tannert, T. Feasibility Study of Mass-Timber Cores for the UBC Tall Wood Building. *Buildings* **2018**, *8*, 98. [CrossRef]
10. Staub-French, S.; Pilon, A.; Poirier, E.; Teshnizi, Z.; Fallahi, A.; Moudgil, M.; Tannert, T.; Froese, T. Design Process Innovation on Brock Commons Tallwood House. *Constr. Innov.* **2021**, *22*, 23–40.
11. Brandner, R.; Flatscher, G.; Ringhofer, A.; Schickhofer, G.; Thiel, A. Cross laminated timber: Overview and development. *Eur. J. Wood Prod.* **2016**, *74*, 331–351. [CrossRef]
12. Tannert, T.; Follesa, M.; Fragiacomo, M.; González, P.; Isoda, H.; Moroder, D.; Xiong, H.; van de Lindt, J.W. Seismic Design of CLT Buildings. *Wood Fiber Sci.* **2018**, *50*, 3–26. [CrossRef]
13. Loss, C.; Tannert, T.; Tesfamariam, S. State-of-the-art review of displacement-based seismic design of timber buildings. *Constr. Build. Mater.* **2018**, *191*, 481–497. [CrossRef]
14. National Research Council Canada. *NBCC—National Building Code of Canada*; National Research Council Canada: Ottawa, ON, Canada, 2020.
15. International Code Council, Inc. *IBC—International Building Code*; International Code Council, Inc.: Washington, DC, USA, 2021.
16. CSA Group. *CSA O86—Engineering Design in Wood*; CSA Group: Mississauga, ON, Canada, 2019.
17. Shahnewaz, M.; Dickof, C.; Tannert, T. Seismic Behaviour of Balloon Frame CLT Shearwalls with Different Ledgers. *ASCE J. Struct. Eng.* **2021**, *147*, 04021137. [CrossRef]
18. Chen, Z.; Popovski, M. Mechanics-based analytical models for balloon-type cross-laminated timber (CLT) shear walls under lateral loads. *Eng. Struct.* **2019**, *208*, 109916. [CrossRef]
19. Shen, Y.; Schneider, J.; Tesfamariam, S.; Stiemer, S.F.; Chen, Z. Cyclic behavior of bracket connections for cross-laminated timber (CLT): Assessment and comparison of experimental and numerical models studies. *J. Build. Eng.* **2021**, *39*, 102197. [CrossRef]
20. Jalilifar, E.; Koliou, M.; Pang, W. Experimental and Numerical Characterization of Monotonic and Cyclic Performance of Cross-Laminated Timber Dowel-Type Connections. *J. Struct. Eng.* **2021**, *147*, 04021102. [CrossRef]
21. Nolet, V.; Casagrande, D.; Doudak, G. Multipanel CLT shearwalls: An analytical methodology to predict the elastic-plastic behavior. *Eng. Struct.* **2019**, *179*, 640–654. [CrossRef]
22. Deng, P.; Pei, S.; van de Lindt, J.W.; Amini, M.O.; Liu, H. Lateral behavior of panelized CLT walls: A pushover analysis based on minimal resistance assumption. *Eng. Struct.* **2019**, *191*, 469–478. [CrossRef]
23. Ceccotti, A.; Sandhaas, C.; Okabe, M.; Yasumura, M.; Minowa, C.; Kawai, N. SOFIE project—3D shaking table test on a seven-storey full-scale cross-laminated timber building. *Earthq. Eng. Struct. Dyn.* **2013**, *42*, 2003–2021. [CrossRef]
24. Dujic, B.; Aicher, S.; Zarnic, R. Investigation on in-plane loaded wooden elements—Influence of loading on boundary conditions. *Otto Graf J.* **2005**, *16*, 259–272.

25. Popovski, M.; Pei, S.; van de Lindt, J.W.; Karacabeyli, E. Force modification factors for CLT structures for NBCC. In *Materials and Joints in Timber Structures*; RILEM Bookseries 9; Aicher, S., Reinhardt, H.W., Garrecht, H., Eds.; Springer: Dordrecht, The Netherlands, 2014; pp. 543–553.

26. Schneider, J. Conventional and novel timber steel hybrid connections: Testing, performance and assessment. Ph.D. Thesis, University of British Columbia, Vancouver, BC, Canada, 2015.

27. Benedetti, F.; Rosales, V.; Opazo-Vega, A.; Norambuena-Contreras, J.; Jara-Cisterna, A. Experimental and numerical evaluation of hold-down connections on radiata pine Cross-Laminated-Timber shear walls: A case study in Chile. *Eur. J. Wood Wood Prod.* **2019**, *77*, 79–92. [CrossRef]

28. Ottenhaus, L.-M.; Li, M.; Smith, T.; Quenneville, P. Mode Cross-Over and Ductility of Dowelled LVL and CLT Connections under Monotonic and Cyclic Loading. *J. Struct. Eng.* **2018**, *144*, 04018074. [CrossRef]

29. Ottenhaus, L.-M.; Li, M.; Smith, T. Structural performance of large-scale dowelled CLT connections under monotonic and cyclic loading. *Eng. Struct.* **2018**, *176*, 41–48. [CrossRef]

30. Brown, J.R.; Li, M. Structural performance of dowelled cross-laminated timber hold-down connections with increased row spacing and end distance. *Constr. Build. Mater.* **2021**, *271*, 121595. [CrossRef]

31. Bocquet, J.-F.; Epinal, F.; Lemaître, R.; Bader, T.K. Design recommendations and example calculations for dowel-type connections with multiple shear planes. *Des. Connect. Timber Struct.* **2018**, *241*, 241–295.

32. Chan, N.; Hashemi, A.; Zarnani, P.; Quenneville, P. Pinching-Free Connector for Timber Structures. *J. Struct. Eng.* **2021**, *147*, 04021036. [CrossRef]

33. RothoBlaas. *X-RAD Manual*; RB: Cortaccia, Bolzano, Italy, 2018.

34. Polastri, A.; Giongo, I.; Piazza, M. An innovative connection system for CLT structures. *Struct. Eng. Int.* **2017**, *27*, 502–511. [CrossRef]

35. Polastri, A.; Giongo, I.; Angeli, A.; Brandner, R. Mechanical characterization of a prefabricated connection system for Cross Laminated Timber structures in seismic regions. *Eng. Struct.* **2018**, *167*, 705–715. [CrossRef]

36. Bathon, L.; Bletz-Mühldorfer, O.; Schmidt, J.; Diehl, F. Fatigue performance of adhesive connections for wooden wind towers. In *Joints in Timber Structures*; Springer: Dordrecht, The Netherlands, 2014; Volume 9, pp. 375–380.

37. Zhang, X. Seismic design of timber steel hybrid high-rise buildings. Ph.D. Thesis, University of British Columbia, Vancouver, BC, Canada, 2017.

38. Zhang, X.; Popovski, M.; Tannert, T. High-capacity hold-down for mass-timber buildings. *Constr. Build. Mater.* **2018**, *164*, 688–703. [CrossRef]

39. Schneider, J.; Tannert, T.; Tesfamariam, S.; Stiemer, S.F. Experimental assessment of a novel steel tube connector in cross-laminated timber. *Eng. Struct.* **2018**, *177*, 283–290. [CrossRef]

40. Mpidi Bita, H.; Tannert, T. Numerical Optimisation of Novel Connection for Cross-Laminated Timber Buildings. *Eng. Struct.* **2018**, *175*, 273–283. [CrossRef]

41. Loo, W.Y.; Quenneville, P.; Chouw, N. A numerical study of the seismic behaviour of timber shear walls with slip-friction connectors. *Eng. Struct.* **2012**, *34*, 233–243. [CrossRef]

42. Loo, W.Y.; Quenneville, P.; Chouw, N. A new type of symmetric slip-friction connector. *J. Constr. Steel Res.* **2014**, *94*, 11–22. [CrossRef]

43. Hashemi, A.; Masoudnia, R.; Quenneville, P. Seismic performance of hybrid self-centring steel-timber rocking core walls with slip friction connections. *J. Constr. Steel Res.* **2016**, *126*, 201–213. [CrossRef]

44. Hashemi, A.; Zarnani, P.; Masoudnia, R.; Quenneville, P. Seismic resistant rocking coupled walls with innovative Resilient Slip Friction (RSF) joints. *J. Constr. Steel Res.* **2017**, *129*, 215–226. [CrossRef]

45. Hashemi, A.; Zarnani, P.; Masoudnia, R.; Quenneville, P. Experimental Testing of Rocking Cross-Laminated Timber Walls with Resilient Slip Friction Joints. *J. Struct. Eng.* **2018**, *144*, 04017180. [CrossRef]

46. Hashemi, A.; Zarnani, P.; Quenneville, P. Earthquake resistant timber panelised structures with resilient connections. *Structures* **2020**, *28*, 225–234. [CrossRef]

47. Wrzesniak, D.; Rodgers, G.W.; Fragiacomo, M.; Chase, J.G. Experimental testing of damage-resistant rocking glulam walls with lead extrusion dampers. *Constr. Build. Mater.* **2016**, *102*, 1145–1153. [CrossRef]

48. Vishnupriya, V.; Rodgers, G.W.; Mander, J.B.; Chase, J.G. Precision Design Modelling of HF2V Devices. *Structures* **2018**, *14*, 243–250. [CrossRef]

49. Sullivan, K.; Miller, T.H.; Gupta, R. Behavior of cross-laminated timber diaphragm connections with self-tapping screws. *Eng. Struct.* **2018**, *168*, 505–524. [CrossRef]

50. Tuhkanen, E.; Ojamaa, M. Early experimental investigations on slotted-in steel plate connections with self-perforating dowels in CLT. *Wood Mat. Sci. Eng.* **2019**, *16*, 102–109. [CrossRef]

51. Daneshvar, H.; Dickof, C.; Letarte, J.P.; Niederwestberg, J.; Spencer, J.; Chui, Y.H. Seismic performance of end brace connections in ductile braced timber frame. In Proceedings of the International Network on Timber Engineering Research (INTER), Tacoma, WA, USA, 26–29 August 2019.

52. Dickof, C.; Jackson, R.; Daneshvar, H.; Niederwestberg, J.; Chui, Y.H. Perforated plates as dissipative connections in mass timber seismic force resisting systems. In Proceedings of the World Conference on Timber Engineering (WCTE), Santiago, Chile, 11–14 January 2021.

53. Daneshvar, H.; Niederwestberg, J.; Letarte, J.-P.; Dickof, C.; Chui, Y.H. Seismic Performance of base shear connections in cross laminated timber shearwalls. In Proceedings of the World Conference on Timber Engineering (WCTE), Santiago, Chile, 11–14 January 2021.
54. Dong, W.; Li, M.; He, M.; Li, Z. Experimental testing and analytical modeling of glulam moment connections with self-drilling dowels. *J. Struct. Eng.* **2021**, *147*, 04021047. [CrossRef]
55. Nicolas, J.H. Pilot Study of a High Capacity Ductile Seismic Hold-Down for Cross-Laminated Timber. Master's Thesis, Montana State University, Bozeman, MT, USA, 2019.
56. Drexler, M.; Dires, S.; Tannert, T. Internal Perforated-steel-plate connections for CLT shear walls. In Proceedings of the World Conference on Timber Engineering, Santiago, Chile, 11–14 January 2021.
57. Asgari, H.; Tannert, T.; Ebadi, M.M.; Loss, C.; Popovski, P. Hyperelastic hold-down solution for CLT shear walls. *Constr. Build. Mater.* **2021**, *289*, 123173. [CrossRef]
58. Ajibola, O.A. High-capacity hyperelastic hold-down for cross-laminated timber shear walls. In *Project Report*; University of Northern British Columbia: Prince George, BC, Canada, 2021.
59. Brown, J.R.; Li, M.; Tannert, T.; Moroder, D. Experimental study on orthogonal joints in cross-laminated timber with self-tapping screws installed with mixed angles. *Eng. Struct.* **2021**, *228*, 111560. [CrossRef]
60. Casagrande, D.; Doudak, G.; Masroor, M. A proposal for capacity-based design of multi-storey CLT buildings. In Proceedings of the International Network on Timber Engineering Research (INTER), Online Conference, 16–19 August 2021.

buildings

Physics-Based Ground Motion Simulations for the Prediction of the Seismic Vulnerability of Masonry Building Compounds in Mirandola (Italy)

Nicola Chieffo [1], Marco Fasan [2], Fabio Romanelli [3], Antonio Formisano [4,*] and Giovanni Mochi [5]

[1] Faculty of Architecture and Urbanism, Politehnica University of Timişoara, 300223 Timişoara, Romania; nicola.chieffo@student.upt.ro

[2] Department of Engineering and Architecture, University of Trieste, 34127 Trieste, Italy; mfasan@units.it

[3] Department of Mathematics and Geosciences, University of Trieste, 34128 Trieste, Italy; romanel@units.it

[4] Department of Structures for Engineering and Architecture, University of Naples "Federico II", 80125 Napoli, Italy

[5] Department of Civil and Environmental Engineering, University of Perugia, 06123 Perugia, Italy; giovanni.mochi@unipg.it

* Correspondence: antoform@unina.it

Abstract: The current paper aims at investigating the seismic capacity of a masonry building aggregate in the historical centre of Mirandola based on a reliable ground motion simulation procedure. The examined clustered building is composed of eleven structural units (SUs) mutually interconnected to each other, which are made of brick walls and are characterized by wooden floors poorly connected to the vertical structures. Non-linear static analyses are performed by adopting the 3Muri software to characterize the seismic capacity of both the entire aggregate and the individual SUs. In this framework, a multi-scenario physics-based approach is considered for the definition of the seismic input in terms of broadband seismic signals inclusive of source and site effects. Finally, the incidence of the seismic input variability is discussed for the prediction of the global capacity response of the case study building.

Keywords: masonry building aggregates; seismic vulnerability assessment; seismic hazard analysis; non-linear static analysis; fragility curves

1. Introduction

The repeated occurrence of devastating seismic events has raised the technical-scientific sensitivity towards the issue of the protection of human lives and exposed buildings [1,2]. Generally, existing buildings represent the weakest vulnerable part of urban systems since they are susceptible to damage under seismic phenomena. Throughout the various construction eras, they have preserved techniques and structural details typical of a systematic design procedure conceived to resist, predominantly, gravitational actions only [3,4]. Therefore, existing unreinforced masonry (URM) buildings intrinsically present potential vulnerability factors due to multiple aspects related to the nature of the basic material, geometric complexity, construction heterogeneity and absence of appropriate seismic protection devices, that alter the entire architectural, functional and structural system [5,6].

In general, it was observed that several historical centres are characterized by an ancient building heritage having an inadequate safety level against earthquakes. In the urban centres, the existing construction typologies are frequently grouped in aggregate configurations, and the constructive matrix of structural units (SUs) is the living representation of a well-consolidated design practice that is very vulnerable to seismic actions [7–10].

Generally, the seismic capacity offered by single SUs is considerably different from that of the entire building aggregate. So, accounting for the highly non-linear response of

SUs only, without considering the interactions with adjacent constructions, can inevitably lead to a wrong seismic assessment [11–17]. For this reason, it is mandatory to consider, preferably with simplified structural models, the intrinsic peculiarities of the SUs and their mutual interactions due to the aggregate effect to correctly foresee their vulnerability level. Different engineering computational models are developed to predict the mechanical behaviour of these historic masonry structures subjected to seismic loads. These evaluation techniques are based on sophisticated approaches, such as the discrete elements method (DEM), which is a mechanical method providing a realistic prediction of the structural seismic response. This method estimates well load capacity, stiffness, and failure hierarchy of masonry structures through highly effective mathematical computational solutions [18–20].

However, the behaviour of masonry structures of historical centres also depends on the seismic hazard level of the site. Principally, the type of earthquake (near-field or far-field), the type of seismic signal and related accelerations (vibratory or impulsive), and the type of fault mechanism directly influence the structural performance of this construction technology in each geographical area. Generally, the seismic hazard analyses, whether based on either a probabilistic or a deterministic approach, are based on the use of simplified correlations (i.e., ground motion prediction equations (GMPE)) for the evaluation and prediction of the ground shaking [21–24]. These formulations, obtained by data-regression analysis deriving from historical events, provide a statistical distribution of the ground motion intensity measure (e.g., spectral acceleration) as a function of multiple parameters, such as the magnitude of the earthquake, M_w, and the site-source distance, R. Furthermore, the effects of the ground motion variability (e.g., inter- or intra-event) plays an essential role in the seismic hazard analysis [25,26]. Therefore, in the first instance (inter-event phenomenon), having identified the peculiarities of the scenario (e.g., magnitude, focal mechanism and the geometry of the fault plane), the variability of the ground motion is correlated to the different possible sources rupture processes. Afterwards, having fixed the reference scenario and a specific rupture process, the spatial variability (site-to-site) of the intensity measure depends mainly on the propagation of the seismic wave through different soil layers. Overall, it is clear that the spatial variability of seismic motion is a fundamental component for the seismic risk analysis of both urban and infrastructural systems for the quantification of expected losses [27–29].

With such an attempt, the present work aims to provide an exhaustive evaluation of the seismic vulnerability of masonry building aggregates through a case study placed in Mirandola. To this purpose, a refined modelling procedure for the propagation of seismic waves is used. It starts from the knowledge of the seismogenic sources and the geomorphological properties of the investigated site, taking into account the rupture process of the seismic source, as well as the site effects associated with the simulated scenarios, using a web application developed by the Department of Mathematics and Geosciences of the University of Trieste. The performed ground motion simulations, being independent of the definition of a ground motion intensity measure (e.g., macroseismic intensity, PGA, Housner intensity, etc.), result to be independent of the standard approach based on the use of GMPE equations. Different kinematic rupture processes on the fault plane are parameterized by varying the slip field, nucleation point and rupture velocity to take also into consideration the source stochastic component in the distribution of the ground motion at the site(s), and the implicit consequences on the global seismic response of the SUs placed in aggregated condition.

2. Activity Framework

2.1. The Historical Centre of Mirandola

The historic compartment of Mirandola is one of the oldest urban centres on the Italian peninsula. It developed over the centuries based on a spontaneous urban planning process that gave it the first "Forma Urbis", apparently casual, but responding to accurate settlement details prepared for the creation of roads and public spaces necessary for civil and public life, where important bureaucratic activities were carried out for the entire

community. The historic centre of Mirandola is a tangible representation of the spatial configuration of a well-defined urban project starting from the early Middle Ages. The city was built as a fortified city with a well-structured and organized conformation of the historical settlements. The urban conformation of the municipality started from the construction of buildings of public interest (e.g., churches and palaces around the Castle of Pico), conceived with new architectural and functional elements to create a global planimetric structure more meticulous and responsive to the concept of the city. The city was connected to the neighbouring villages while maintaining the conformation of the main roads. In general, the buildings were arranged in a grouped configuration and bordered on the main façade, thus presenting a free front for external view and access, and an opposite front overlooking the internal pertinence area (Figure 1) [30].
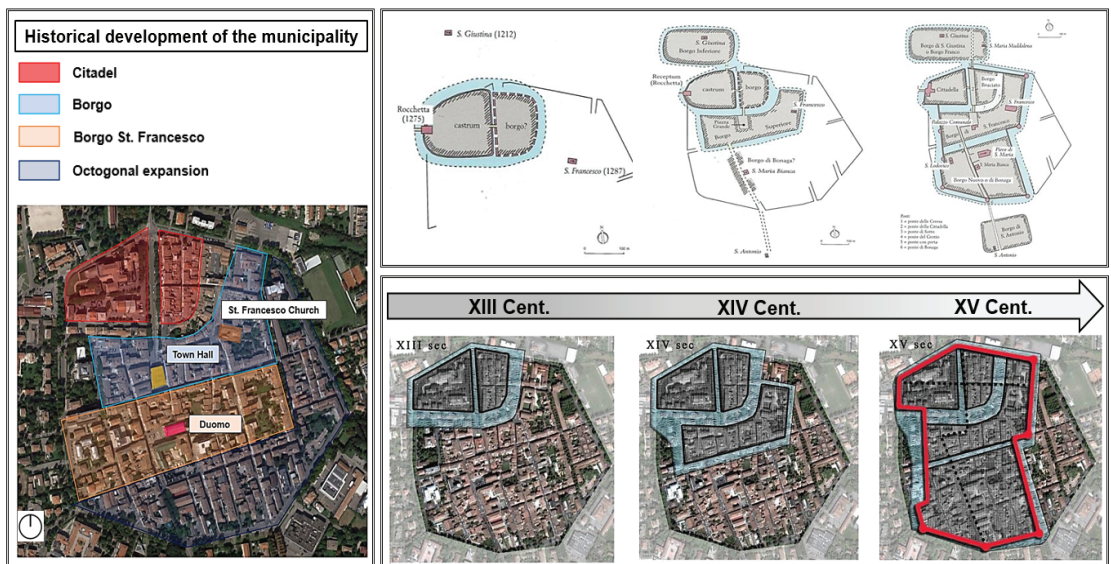
Figure 1. Historical urban conformation of the city of Mirandola [30]. On the left, a bird-eye view of the city, in which the highlighted areas indicate the urban expansion process, is illustrated. On the right, the urban development started from the "ancient village" (XIII Century) to the complete configuration of the citadel (XV Century).

Nowadays, the union of the villages and the organization of new districts have kept the original planimetric configuration of the unchanged octagonal city (Figure 2).

The historic centre is mainly characterized by masonry buildings, erected in a clustered conformation, in which the coexistence of construction heterogeneities, sometimes incongruous, has led to the manifestation of material degradation.
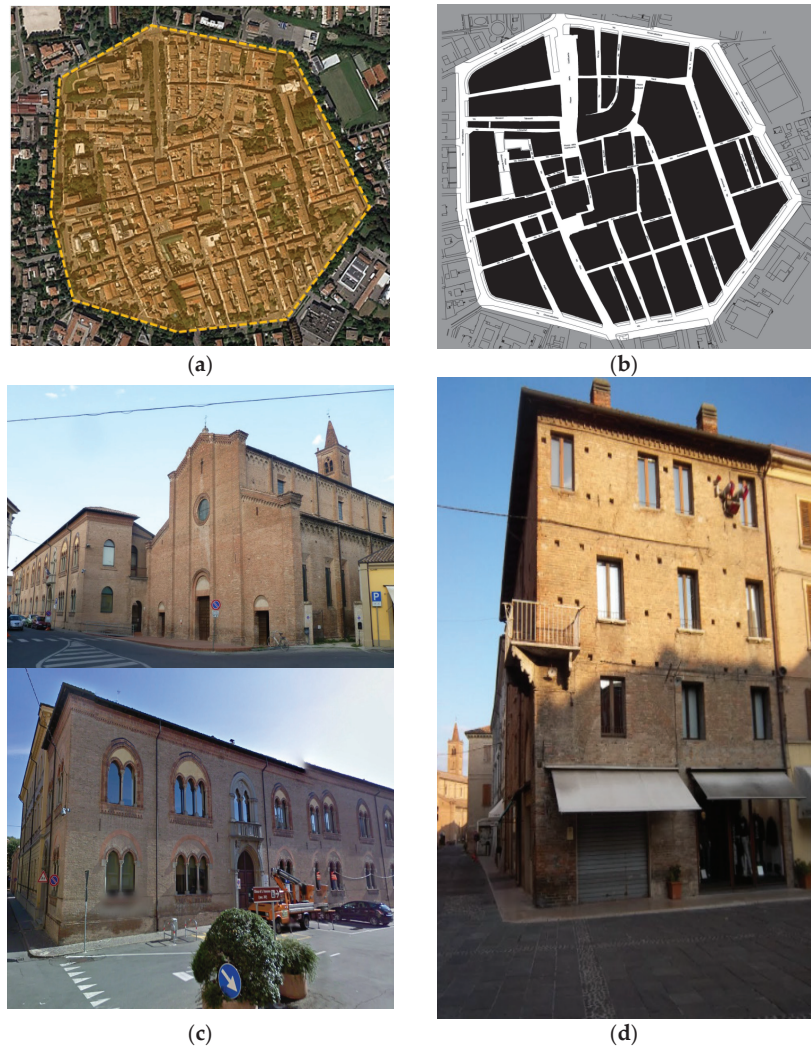
Figure 2. Octagonal compartment and urban blocks plan of the city (**a**,**b**) [30]; (**c**,**d**) some building typologies in the city centre.

2.2. Main Features of the Case Study Building Compound

The historic centre of Mirandola is made up of 43 urban areas composed of buildings erected and conceived in the aggregate configuration.

The configuration of the current building stock highlights how the size of the built-up area is correlated to the evolution of the city foreseen in the Recovery Plan approved in July 2001. However, although Mirandola did not have a radial expansion, it is noted that the dimensional variation of the building aggregates is linked to the transition from the first expansion phase of the city with a quadrangular plan to the second one with an octagonal urbanized distribution [30,31]. In particular, the buildings located in the historic centre are mainly characterized by a construction uniformity of vertical structures, made of solid brick walls, with the presence of semi-rigid and deformable floors, which represents the most widespread construction typology of the historic centres of the Emilia-Romagna Region [10].

Concerning the case study aggregate, it is an existing complex masonry building with a non-regular shape composed of 11 SUs (Figure 3a). The clustered units forming the aggregate occupy different structural positions. In particular, as reported in Figure 3b, two SUs (called SU1 and SU11) occupy corner positions, nine cells (from SU2 to SU10) are placed in intermediate positions, and only SU7 occupies the heading position.
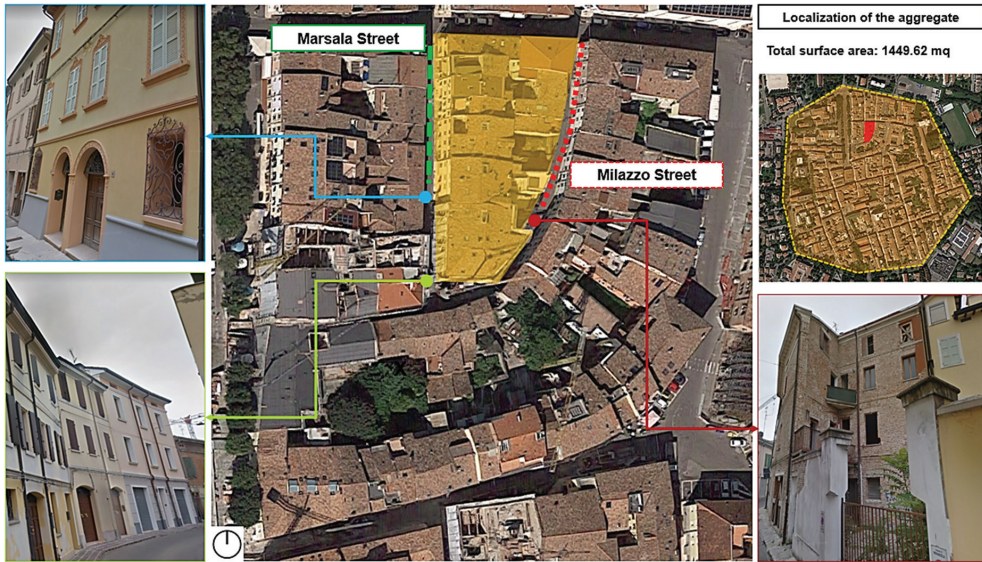
(**a**)

(**b**)

Figure 3. Localization of the case study aggregate (**a**) and identification of clustered structural units (SUs) (**b**).

On average, the number of floors of the various SUs varies from 2 to 4 above ground, with an average inter-floor height of 2.80 m [30].

The brick masonry walls have an average thickness ranging from 0.24 m to 0.50 m. The horizontal structures are mainly made up of wooden elements with upper double planking. For these elements, a design vertical load, F_d, of 5.5 KNm^{-2} has been estimated, considering the fundamental load combination at the ultimate limit state (ULS) [30].

Regarding the physical conditions of the building aggregate, it is noted that SUs have common walls simply juxtaposed to each other. In addition, the pushing effects of the roofing systems could trigger the overturning of the main façades. This phenomenon is very common in historical buildings since, in the case of earthquakes, the masonry walls, poorly connected to the structure top level, are subjected to horizontal pushing actions deriving from roof, which usually activate out-of-plane mechanisms.

Concerning the material degradation, along the facades facing the main streets, even if partial detachments of the plaster are evident, they do not compromise the functional statics of the building compound.

The mechanical properties of the structural elements characterizing the case study building are deduced from the indications prescribed in Table C8.5.I of the Italian NTC18 standard [32]. Due to the absence of accurate on-site test procedures, the mechanical characteristics of the masonry are reduced by assuming a confidence factor, FC, equal to 1.35, corresponding to a LC1 (limited) knowledge level.

Specifically, for the mechanical parameters (f_m, τ_0, f_{v0}), the minimum values of the intervals are reported in Table C8.5.I of the Italian standard are considered [32], while for the elastic moduli (E and G), the mean values are used. The mechanical parameters of solid brick masonry walls are summarized in Table 1.

Table 1. Mechanical characteristics of masonry material for inspected SUs [32].

Mechanical Properties		
Average compressive strength	f_m	2.60 Nmm^{-2}
Average shear strength	f_{v0}	0.13 Nmm^{-2}
Young modulus	E	1500 Nmm^{-2}
Shear elasticity modulus	G	600 Nmm^{-2}
Dead weight	W	18 KNm^{-3}

3. Ground Motion Selection

3.1. Seismological Structural Model

To take into account the entire variability of structural behaviour from elastic to inelastic, up to global collapse [33,34], as well as the record-to-record variability (variability related to the mechanism of the seismic source, path attenuation effects and local site), ground motion records must be properly selected and, if necessary, scaled to a certain seismic intensity level to provide relatively stable estimates of the median values of the damage thresholds for the investigated structure.

For the seismic input definition, with the physics-based approach followed here, the modelling of the propagation of seismic waves for the estimation of the seismic hazard requires a prior characterization of the mechanical properties of the soil layers crossed by the waves generated by a seismogenic source. In this regard, the XeRIS web application, as proposed in [35,36], is used to compute the seismic wavefield responsible for structural damage. The modelling of the ground motion scenarios is based on the modal summation (MS) technique, as described in [37], which considers the vibrational modes of the layered medium excited by a seismic source, providing a rapid computational procedure for an adequate simulation of the ground motion in the case of a far-field event. Therefore, in the case of near-field events, the discrete wave number (DWN) technique is used according to the theory proposed in [38]. Nevertheless, these techniques allow for a very efficient calculation of synthetic seismograms in laterally homogeneous layered models, taking into account anelastic attenuation. Thus, the proposed site-specific geological model has been defined starting from the soil structure provided by the Italian Accelerometric Archive, ITACA, [39] considering a soil class C, then adopting the mechanical layers parameters

(thickness, density, P and S waves velocity, and attenuation) discussed in [40], which represent the geological setting of the investigated area.

3.2. Fault Scenarios

The calculation of a fault-based ground-shaking scenario allows modelling, at a specific site, the ground motion caused by an earthquake with an extended fault. The computational technique used is based on the theory proposed by [41], where the seismogenic sources are modelled as a set of sub-sources, with a specific scaling source spectra law, also to predict the effects related to the kinematic rupture process (i.e., directivity).

Moreover, some of the kinematic parameters are made by varying the nucleation point, rupture velocity and slip field, and also take into consideration the source stochastic component [42,43].

Four different sources (Mirandola (MIR), Finale Emilia (FE), Veronese (VR) and Ferrara (FE)) are selected from the Web-GIS application DISS (Database of Individual Seismogenic Sources) [44] to compute the seismic input at the selected site. The sources have rectangular geometry of length, L, and width, W, with a variable distance between 1.9 km up to 44 km about the reference site, identified as MR (Lon (°): 11.06 and Lat (°): 44.88—geographical position of the study aggregate). In particular, Mirandola's source descends solely on the evidence of the recent tectonic activity of the Arc of Ferrara [45]. The 29 May 2012 earthquake in the Emilia-Romagna region of Italy, which was the second main shock of the Emilian sequence, activated this seismogenic source, producing a detectable uplift of the buried Mirandola anticline. The final geometry of the fault adopted is the one validated in the study proposed by [40]. The Finale Emilia seismic source was formed after the occurrence of the 20th May 2012 earthquake, which was the first mainshock of the Emilian sequence giving rise to a detectable uplift of the associated buried anticline. The Veronese source was generated following the 3rd January 1117 Verona earthquake, which was perhaps the strongest event that occurred in the Po Valley. The data collected in both historical and instrumental catalogues have shown that the seismicity of the Po Valley is concentrated mainly along the foothills and the buried thrust fronts of the northern Apennines and the southern Alps [46]. Finally, concerning the existence of the Ferrara's source, it dates back to the earthquake that occurred on 17th November 1570 based on data relating to both the recent tectonic activity of the Ferrara Arch [45], and from the subsoil geological structure [47]. Thus, based on the above considerations, some of the characteristics of the four considered seismic sources are reported in Table 2.

Table 2. Some characteristics of the four selected seismogenic sources [40,44]. The acronyms are related to: edi = epicentral distance; depth = focal depth of the earthquake occurred; strike = defines the orientation of the fault counter-clockwise till the North; dip = represents the inclination of the fault plane; rake = the direction the hanging wall moves during rupture measured relative to the fault strike; sre = represents the angle formed between the focal point and the site.

ID	Source	M_w	L (km)	W (km)	edi (km)	Depth (km)	Strike (°)	Dip (°)	Rake (°)	Sre (°)
1	MIR	6.0	22	12	1.90	8.9	95	60	90	69
2	FE	6.1	10	6.4	20.7	6.2	115	43	90	195
3	VR	6.7	30	14	43.8	7.5	248	40	90	74
4	FR	5.5	5.1	4.0	34.6	2.9	88	50	90	179

Furthermore, a map of the location of the case study building (MR) to source configuration has been presented in Figure 4, where the dark blue line identifies the top of the fault projection. The light blue circle (positioned in the centre of the fault projection) is the fault reference point, and the orange area is associated with the area where the position of the nucleation point of the rupture (red dot) is allowed to vary.
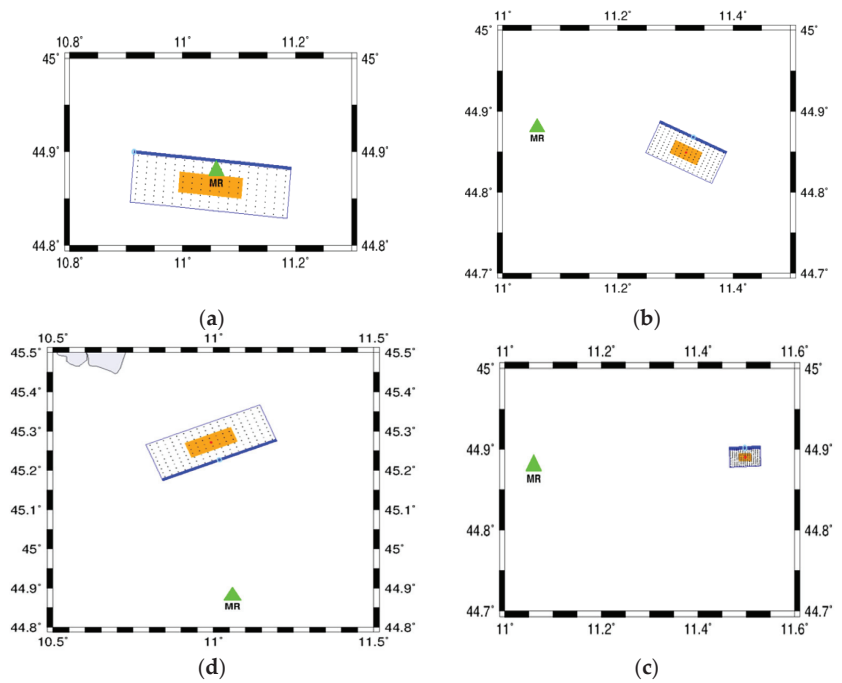
Figure 4. The investigated source-site configurations; (**a**) MIR: $M_w = 6.0$, edi = 1.9 km; (**b**) FE: $M_w = 6.1$, edi = 20.7 km; (**d**) VR: $M_w = 6.7$, edi = 43.8 km; (**c**) FR: $M_w = 5.5$, edi = 34.6 km.

Subsequently, starting from the definition of the above-introduced seismic sources, the modelled seismic scenarios consider the moment magnitude, the position of the nucleation point, and the mean rapture velocity, V_s. The simulation proposed is based on the Monte-Carlo technique for the quantification of the distribution of the final slip, considering 100 statistical realizations and assuming the random variability of the nucleation point of coordinates (X, Y) (the maximum allowable variation is $\pm 1/3$ of the fault length (X direction) and $\pm 1/3$ of the fault width (Y direction)).

The simulation of the source rupture processes has been performed using the PUL-SYN06 algorithm based on the theory presented in [41,48].

For a sake of example, the fault rupture scenarios generated by four realizations (i.e., #1, #50, #90, #100) out of 100 for the Mirandola (MIR) source, are shown in Figure 5. For each simulated rupture scenario, a 2D final slip map function is derived. The sub-source grid is made up of 17×9 crosses in which the red dot represents the nucleation point, the dark blue indicates the high slip of the fault, and the white contours (isochrones) represent the time-domain slip rupture propagation of a non-stationary random process.
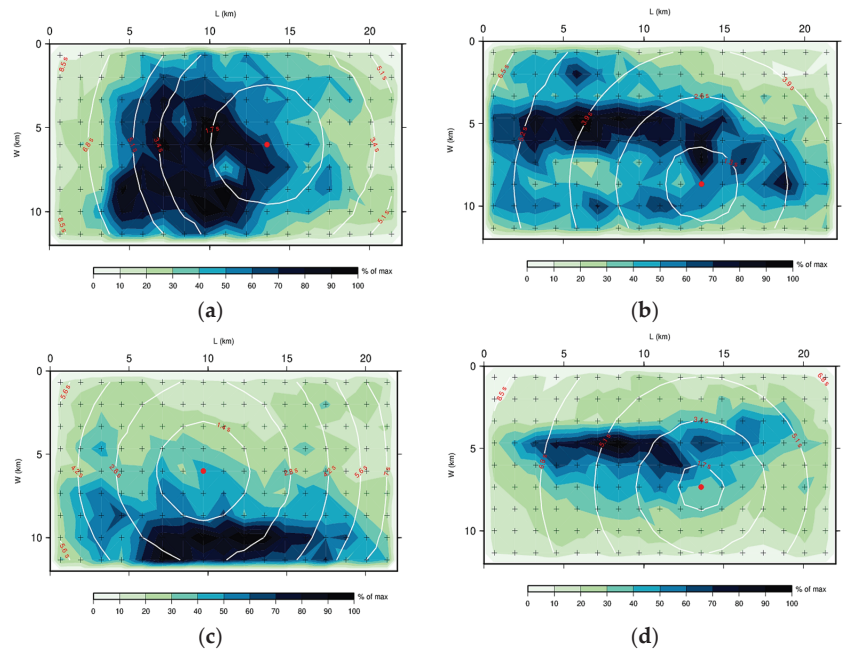
Figure 5. Four examples of fault-slip rupture processes were generated for the Mirandola source, varying the position of the nucleation point and the number of realization processes; (**a**) MIR: M_w = 6.0, #1; (**b**) MIR: M_w = 6.0, #50; (**c**) MIR: M_w = 6.0, #90; (**d**) MIR: M_w = 6.0, #100.

3.3. Maximum Credible Seismic Input (MCSI)

For the assessment of the seismic vulnerability of the considered case study, an appropriate calculation procedure is presented to predict the expected hazard for the site of interest.

For earthquake engineering purposes, the maximum credible seismic input (MCSI) represents a reliable estimation of the expected ground shaking level for a specific site, independently of the occurrence rate of earthquakes that could affect the investigated area. In particular, the proposed methodology [37,43] does not use empirical equations, such as GMPE, to derive the intensity measure (e.g., PGA or SA, PGV, PGD engineering parameters), but takes into consideration the seismic scenarios generated by independent seismic sources providing realistic ground motions in the time domain (either as a response spectrum or as a set of seismograms). Nevertheless, the use of source spectra [41] introduces a stochastic element in the proposed methodology; therefore, to define the MCSI spectrum, the uncertainties correlated to the hazard estimation must be considered.

Physics-based synthetic engineering parameters can be calculated through knowledge of the earthquake generation process and the propagation of seismic waves in an inelastic soil profile.

In this regard, the structural and topographical heterogeneities, as well as the influence of the source rupture process (slip distribution and rupturing velocity of the fault), were evaluated using the XeRIS web application, as proposed in [35].

Regarding the physical definition of the MCSI response spectrum, it is described in [29,42] where, for each seismogenic source, *n*-scenarios (in terms of magnitude, epicentre distance and focal mechanism of the earthquake) have been considered, the obtained *n*-spectral acceleration values (SA) have been compared, and the maximum median has been selected, as depicted in Figure 6.
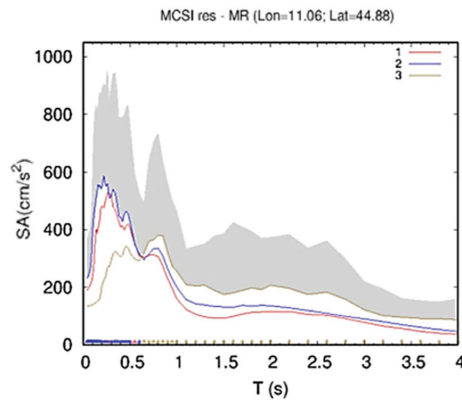
ID	Source	M_w	L (km)	W (km)	edi (km)	depth (km)	strike (°)	dip (°)	rake (°)	sre (°)
1	MIR	6.0	22	12	1.90	8.9	95	60	90	69
2	FE	6.1	10	6.4	20.7	6.2	115	43	90	195
3	VR	6.7	30	14	43.8	7.5	248	40	90	74

Figure 6. Simulated maximum credible seismic input (MCSI) for the selected sources. The grey band identifies the MCSI, as defined in [43], which is controlled by three sources: curves 1, 2 and 3 are the median spectra obtained from one hundred realizations of the rupture process for the sources MIR, FE and VR, respectively.

4. A Mechanical Vulnerability Assessment Model

4.1. Global Behaviour of the Case Study Aggregate

The case study compound has been numerically analysed using the 3Muri software founded on the Frame Macro-Elements (FME) theory (Figure 7) [49]. This methodological approach assumes that masonry walls are considered as a set of one-dimensional macro-elements (columns, beams, and nodes) mutually interconnected. The resistance criteria of the deformable elements have been assumed based on the requirements of EN 1998-3 [50], which establish maximum threshold values of 0.4% and 0.6% for shear failure and flexural collapse, respectively. The analyses were carried out along the two main global directions of the building, X and Y.

(**a**)   (**b**)
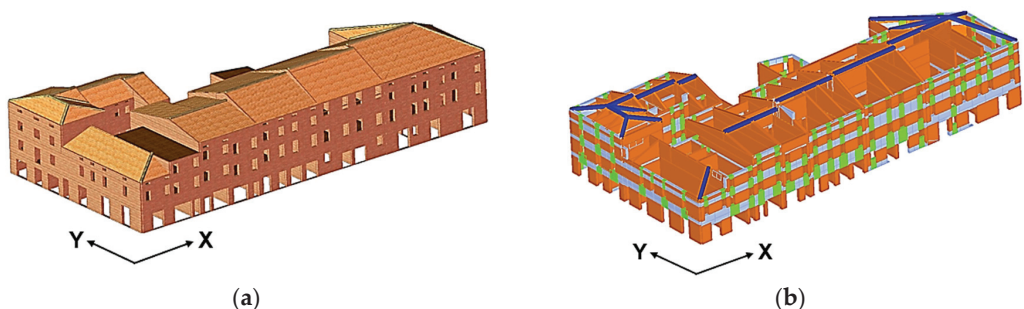
Figure 7. Representation of the case study aggregate: solid (**a**) and macro-element (**b**) models.

The above-introduced simulations were interrupted when the shear strength decay was equal to 20% of the maximum shear capacity, as reported in the NTC18 standard [32].

To this purpose, two different distributions of seismic forces and four combinations (±X, ±Y) have been considered, neglecting the influence of accidental eccentricities in the calculation procedure. The results in terms of capacity curves are presented in Figure 8.
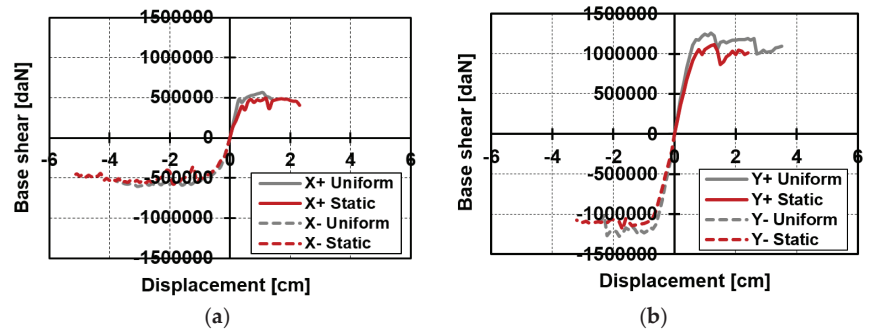
Figure 8. Capacity curves in (**a**) ±X and (**b**) ±Y directions.

From the gotten results, it was observed how the aggregate provides a better structural capacity in the transverse direction Y, rather than in the orthogonal one X. In particular, the ultimate displacements achieved in the positive Y direction (Y⁺) are approximately two times higher than the corresponding ones detected in the perpendicular X-direction referred to the uniform distribution of the forces.

Conversely, in the negative X direction (X⁻), an increase of the displacements was observed, compared to the Y direction.

In particular, the static condition (X⁻ 1st Mode) has shown an ultimate displacement, d_u, equal to −5.18 cm, which is approximately 61% greater than the analogous displacement attained in the direction Y (d_u = −3.18 cm). Regarding the maximum base shear threshold, it was noted that in the Y direction, the maximum strength is approximately two times greater than the corresponding value in direction X. This discrepancy in terms of global behaviour (e.g., displacements and maximum shear thresholds) in the two analyses directions is due to the irregular planimetric conformation of the entire building conjunctly with a higher presence of masonry resistant area.

Finally, for a global view of the vulnerability threshold and expected damage concerning the examined building, two indices were analysed: the vulnerability index (V_I) and the damage index (DI). With this intention, the vulnerability index, V_I, is intended as the ratio between the acceleration capacity, PGA_{Ci}, intended as the peak acceleration that determines the achievement of the ultimate limit state (ULS) condition based on the return periods, Tr, and the corresponding acceleration demand, PGA_{Di}, related to the spectral coordinates of the site where the construction is located. In the specific case, the 3 Muri software [49] automatically estimates the maximum spectral acceleration, starting from the definition of the elastic response spectrum (Tr = 475 year) for the site of interest (Mirandola) having assumed a soil class C, as reported in the Italian Accelerometric Archive, ITACA [39]. Consequently, the damage index has been evaluated, taking into account the mathematical formulation proposed in [51]:

$$DI = \frac{\mu_{max} - 1}{\mu_d - 1} = \frac{d_{max} - d_y}{d_u - d_y} \tag{1}$$

where μ_{max} and μ_d are the required and available ductility associated with the structural system, respectively, which can be expressed in terms of displacements; d_{max} represents the required displacement, evaluated for $T_i < T_C$, based on the area equivalence criterion; and d_y and d_u are the yielding and ultimate displacements associated with the SDoF system, respectively.

The numerator of the above-mentioned formulation indicates how the maximum displacement, d_{max}, deviates from the elastic one, while the denominator provides indications about the type of failure mechanisms (e.g., when the ultimate displacement, d_u, is comparable to d_y, the fragile mechanism is activated, vice versa, ductile ones). Thus,

congruently to what has been introduced, the synthesis of the results has been depicted in Figure 9.
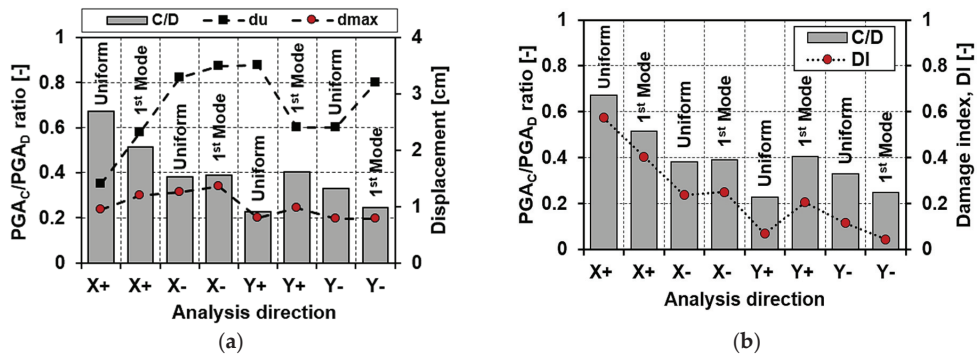
Figure 9. Estimated mechanical vulnerability index (V_I) (**a**) and damage index (DI) (**b**).

First, the achieved results presented in Figure 9a have shown that the worst-case scenario is attained for the direction X^+ (uniform), which corresponds to a C/D ratio equal to 0.67. Similarly, in the direction Y (Y^+ 1st Mode), the expected vulnerability level is 0.40 (e.g., medium-low level).

Concerning the damage index DI, as reported in Figure 9b, it has been observed that the value of 0.57 is reached for a uniform distribution of forces in the X^+ direction, since the difference between the maximum displacement demand, d_{max}, and the corresponding yielding displacement, d_y, is influenced by the achievement of a premature plastic displacement threshold.

Subsequently, the vulnerability indexes have been associated with the estimated damage index, DI, and then correlated to the damage thresholds provided by the European Macroseismic Scale, EMS-98 [52,53], as reported in Table 3.

Table 3. Correlation between DI and European Macroseismic Scale (EMS-98) damage levels.

DI	Damage Description	Damage Grade EMS-98
$0 < DI < 0.3$	Null	D0
$0.3 < DI < 0.6$	Slight	D1
$0.6 < DI < 0.8$	Moderate	D2
$0.8 < DI < 1.0$	Near-Collapse	D3
$1.0 < DI$	Collapse	D4-D5

Force Distribution	PGA_C/PGA_D [-]	DI [-]	EMS-98
X^+ (Uniform)	0.7	0.6	D2
X^- (1st Mode)	0.5	0.4	D1
X^- (Uniform)	0.4	0.2	D0
X^- (1st Mode)	0.4	0.3	D1
Y^+ (Uniform)	0.2	0.1	D0
Y^+ (1st Mode)	0.4	0.2	D0
Y^- (Uniform)	0.3	0.1	D0
Y^- (1st Mode)	0.2	0.0	D0

In Figure 10, the validation between the real damages detected after the Emilia-Romagna earthquake and the corresponding ones derived from the mechanical analysis procedure evaluated at the ultimate displacement, du, referring to the ULS (ultimate limit state) combination, has been provided.

Figure 10. Validation of the mechanical model by comparison between real damages and numerical ones (**a**,**b**).

The damages detected [30] are characterized by the widespread distribution of cracks in the main façade that affect the vertical structures.

More specifically, there is a propensity to damage identified mainly in the spandrel elements, since they have no tensile strength (instead guaranteed by a steel tie-rod or reinforced concrete ring beam) towards the combined effects induced by both bending and shear.

Congruently to what was discussed in the above-introduced comparison, it is possible to appreciate how the simulated structural model provides a global damage level not dissimilar to that really detected in the case study aggregate.

4.2. Capacity Response of Building Structural Units

This section analyses the seismic behaviour of the individual structural units in the aggregate configuration using a numerical procedure based on the capacity curve reconstruction process derived from that of the whole aggregate. This methodological approach allows estimation of the propensity to damage of the SUs, considering their interaction in the aggregate configuration and, therefore, accounting for their contribution in terms of both stiffness and mass. Thus, after assessing the seismic response of the whole aggregate along with the main analysis directions, the behaviours of the reference cells included in the aggregate have been evaluated. In particular, the clustered SUs response has been achieved by adopting a step-by-step simulation process by considering as base shear,

V_b^i, the analytical sum of the base reactions of the piers of the reference case study unit and, as displacement, the average value of the displacements of the selected monitoring nodes, D_m^i, at the top floor. The analytical formulations, adopted for the definition of the MDoF capacity curves, are presented according to the study proposed in [5,54,55]:

$$\begin{cases} V_b^i = \sum_{j=1}^{N} |V_j| \\ D_m^i = \dfrac{\left| \sum_{j=1}^{N} D_j \right|}{|N|} \end{cases} \tag{2}$$

having assumed $|V_j|$ as the absolute value of the base shear force associated with the j-th node at the i-th step, D_j as the absolute value of the top displacement associated with the j-th node at the i-th step, and N as the total number of the nodes at the base of the masonry piers.

The resulting curves in both analysis directions, X and Y, after a bi-linearization process, have been plotted in Figure 11.
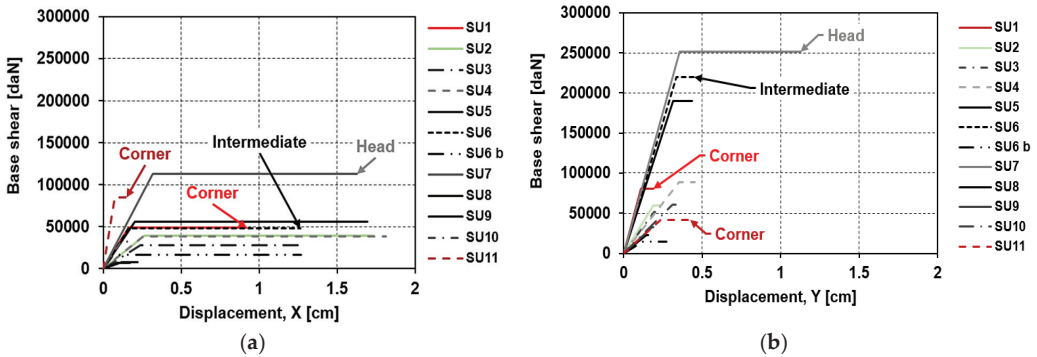
Figure 11. Bilinear curves for the selected SUs in X (**a**) and Y (**b**) analysis directions.

From the acquired results, it appears that the behaviour of the SUs in the two analysis directions is quite heterogeneous. In particular, the head units have been denoted with black-grey, the corner units in red, and a black scale colour has been adopted for the other intermediate units. The capacity parameters expressed in terms of forces and displacements for each of the analysed SUs are presented in Table 4.

From the obtained results, it has been observed that, in the X direction, the head unit (SU7) has higher stiffness and strength than the other building units which occupy intermediate and corner positions, respectively.

This circumstance has been revealed since the corner and intermediate units are affected by the beneficial effect of mutual structural confinement, while the head unit is constrained only on one side, thus resulting in greater susceptibility to displacements. In terms of displacements, it was noted that the SU7 (head) provides displacements comparable to the SU5 (intermediate), which has a higher mass due to the presence of contiguous SUs.

Moreover, in the Y direction, it has been observed that the SU7 provides a higher contribution in terms of displacement capacity than the other cells due to the interconnected confinement effect provided by the adjacent SUs. Furthermore, by comparing the maximum shear threshold of the SU7 in the two directions, it can be seen that, in the Y direction, the structural cell has an increased shear strength of about 44% compared to the corresponding threshold achieved in the orthogonal direction.

Table 4. Capacity parameters for the investigated SUs.

Position	SUs ID	Dir. X			Dir. Y		
		d_y [cm]	d_u [cm]	F_{max} [daN]	d_y [cm]	d_u [cm]	F_{max} [daN]
Corner	1	0.2	0.9	49,120	0.1	0.2	80,529
Intermediate	2	0.3	1.7	39,175	0.2	0.2	60,121
Intermediate	3	0.2	1.3	27,625	0.2	0.2	51,357
Intermediate	4	0.3	1.8	38,578	0.4	0.5	88,310
Intermediate	5	0.2	1.7	56,030	0.3	0.4	190,361
Intermediate	6	0.2	1.3	48,122	0.3	0.4	219,884
Intermediate	6b	0.1	1.3	16,133	0.1	0.3	14,598
Head	7	0.3	1.6	112,831	0.4	1.1	251,410
Intermediate	8	0.1	0.2	7694	0.1	0.2	22,418
Intermediate	9	0.1	0.2	6615	0.2	0.2	32,505
Intermediate	10	0.1	0.2	32,723	0.3	0.3	60,920
Corner	11	0.1	0.2	84,476	0.2	0.4	41,891

4.3. Analysis of the Capacity Parameters

To interpret the different global responses of the examined structural units, the main capacity parameters (stiffness, ductility, shear strength, mass and vibration period) have been plotted and correlated to each other, as reported in Figure 12.
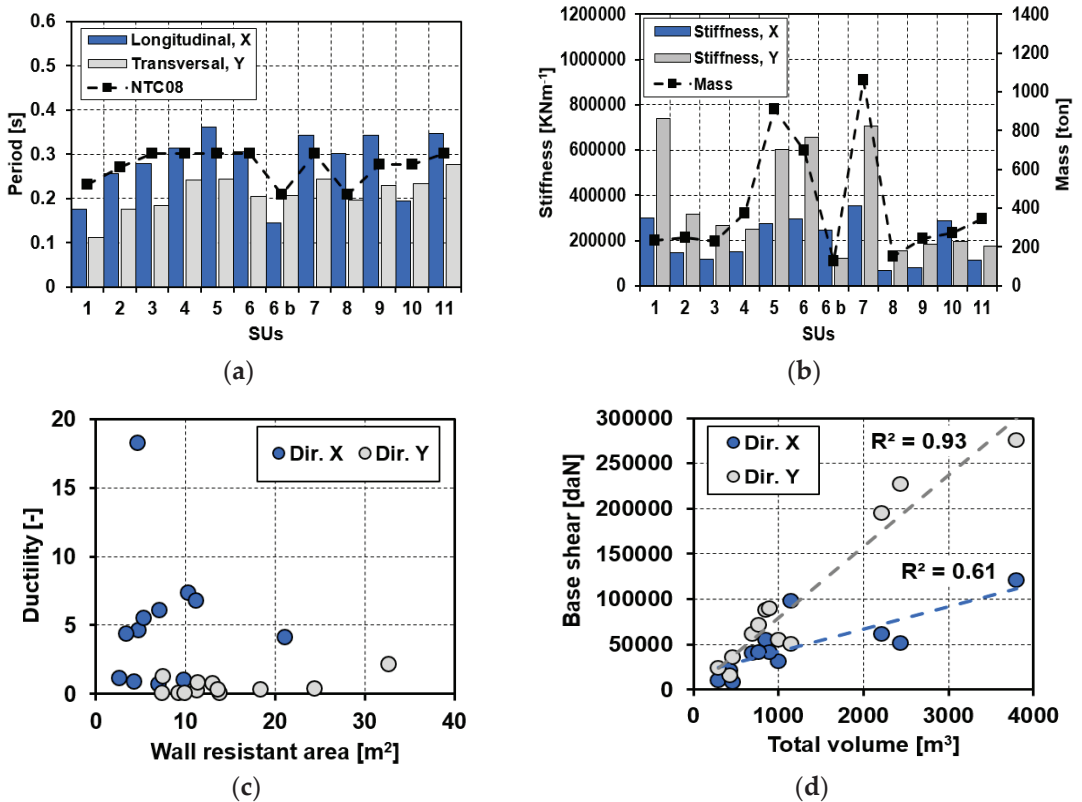
Figure 12. Capacity of the SUs in terms of (**a**) vibration period, (**b**) stiffness and mass, (**c**) ductility displacements vs. wall resistant area, and (**d**) base shear vs. total volume.

First of all, the vibration period of the single structural units analysed, taking into account their contribution in terms of mass and stiffness, has been appropriately compared with the simplified formulation derived from the NTC18 standard [32] (see Figure 12a). From the comparison, it has been noted that in the two analysis directions, the periods associated with the single SUs are heterogeneous with a higher incidence in the X direction, where they exceed the corresponding period provided by the NTC18 standard [32].

However, it is worth pointing out that the NTC18 standard [32] provides a simplified formulation for estimating the vibration period of buildings considered as isolated structures, without considering the aggregate effect. Thus, it is noted that the SUs 1, 2, 3, 6b, 8, 9 and 10 have a low seismic mass-to-stiffness ratio, presenting a reduced vibration period compared to the other structural cells examined in the same analysis direction. Conversely, in Y direction, the vibration period is, on average, 24% lower compared to the analogue values examined in the orthogonal direction.

This circumstance denotes that, in the transverse direction, the stiffness associated with the single SUs is on average 79% higher than that obtained in the X direction, as depicted in Figure 12b. As far as the displacement ductility is concerned, it has been correlated to the wall resistant area (see Figure 12c) to consider the incidence of the structural resistant area ($W_{R.A}$) on the expected ductility (μ). From the results achieved, it was observed that in the X direction, the point cloud is quite homogeneous for $2.0 < \mu < 7.0$, which corresponds to a wall resistant area $W_{R.A}$ enclosed in the range between 2.60 m^2 and 21.0 m^2. On the contrary, due to the higher number of wall panels, in the Y direction, the wall resistant area is within 7.40 m^2 and 32.0 m^2 and reduces the corresponding displacement.

Finally, in Figure 12d, the correlation between the maximum shear force and the total volume of SUs is shown. The analysis of the results in both analysis directions has revealed how the linear regression function presents a direct proportionality between the monitored parameters. The regression coefficient (R^2) is robust, assuming values greater than 0.5 in both examined cases, taking into account all the building-to-building variability in terms of mass, stiffness, and in-elevation interaction.

4.4. Vulnerability Assessment for the Bilinear Elasto-Plastic SUs Models

Following the above-introduced sections, the generation of MCSI spectra was implemented according to the soil structural model and fault scenario selected [56]. In particular, the MCSI has been defined in terms of the response spectrum to accomplish the engineering seismic verification of the case study masonry compound.

With this intent, according to [29,42], the MCSI response spectrum, taking into account the stochastic nature of the algorithm implemented by the XeRIS tool [35], is evaluated at the 95th percentile, based on the number of realizations of the fault rupture process considered. Therefore, by defining the maximum credible seismic input, the maximum contribution in terms of seismic hazard is offered by the Mirandola source (MIR, see Table 4) due to a reduced site-source distance. In these circumstances, the source spectrum derived from the rapture process of the Mirandola source represents the maximum expected MCSI for the generated scenario, enveloping, for periods of interest, the spectra generated by the other sources considered. The derived spectra for both the 50th and 95th percentile (median and maximum), are presented in Figure 13a, with their regularized shape according to the Italian seismic code as illustrated in Figure 13b. Finally, in Figure 13c, the design response spectra for the Mirandola site [32] have been presented, assuming soil class C and Tr = 475 years.
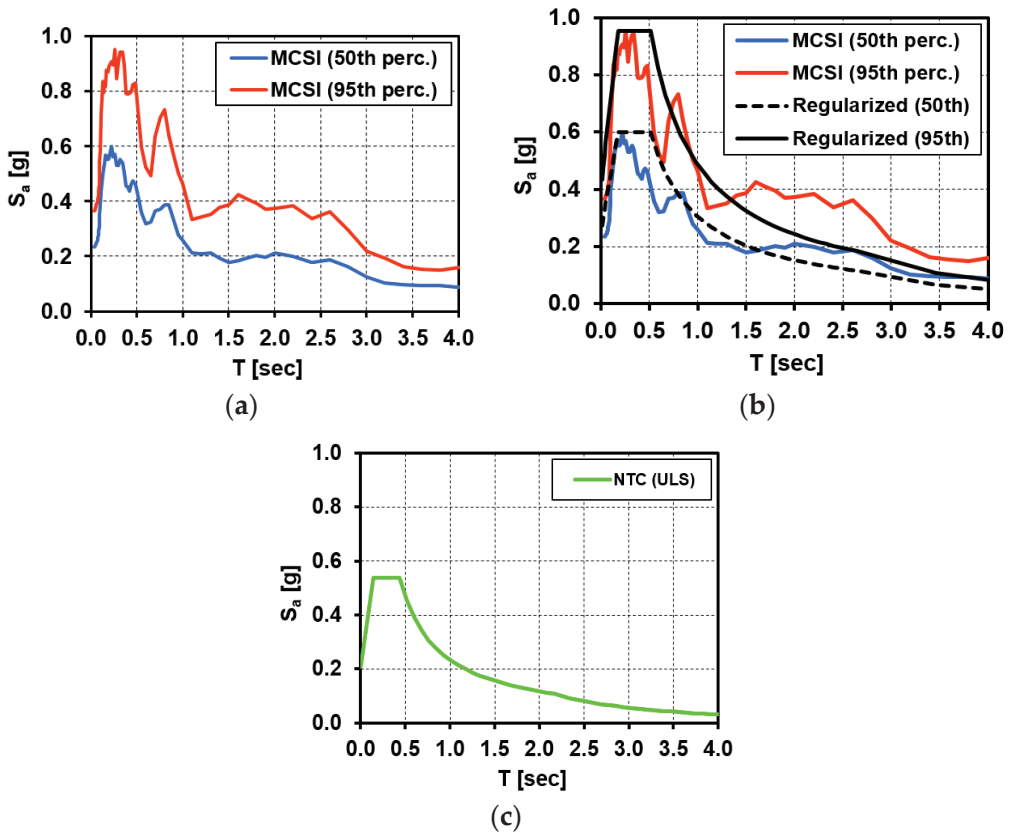
Figure 13. MCSI spectra at (**a**) the 50th and 95th percentile, (**b**) regularization response spectra, and (**c**) design response spectrum for the Mirandola site.

Consequently, the N2 method [57–59] has been adopted for the evaluation of the seismic performance of the single SUs in aggregate conditions by adopting the above-introduced MCSI spectrum. The method combines non-linear static analysis and the response spectrum approach to derive the ADRS (acceleration displacement response spectrum) domain, as reported in Figure 14. Moreover, the seismic verification is carried out by estimating the vulnerability index, appropriately evaluated as the ratio between the seismic demand, D_i, and the relative capacity, C_i, provided by the studied structures.

The results presented have shown how the expected vulnerability is heterogeneous in both analysis directions, depending on the structural position of SUs, as discussed in Sections 3.1 and 3.2. For the sake of example, a detailed application of the N2 method to the head unit is depicted in Figure 15, where also the ADRS obtained using the source spectra is compared with the corresponding spectrum derived from the NTC18 standard [32].
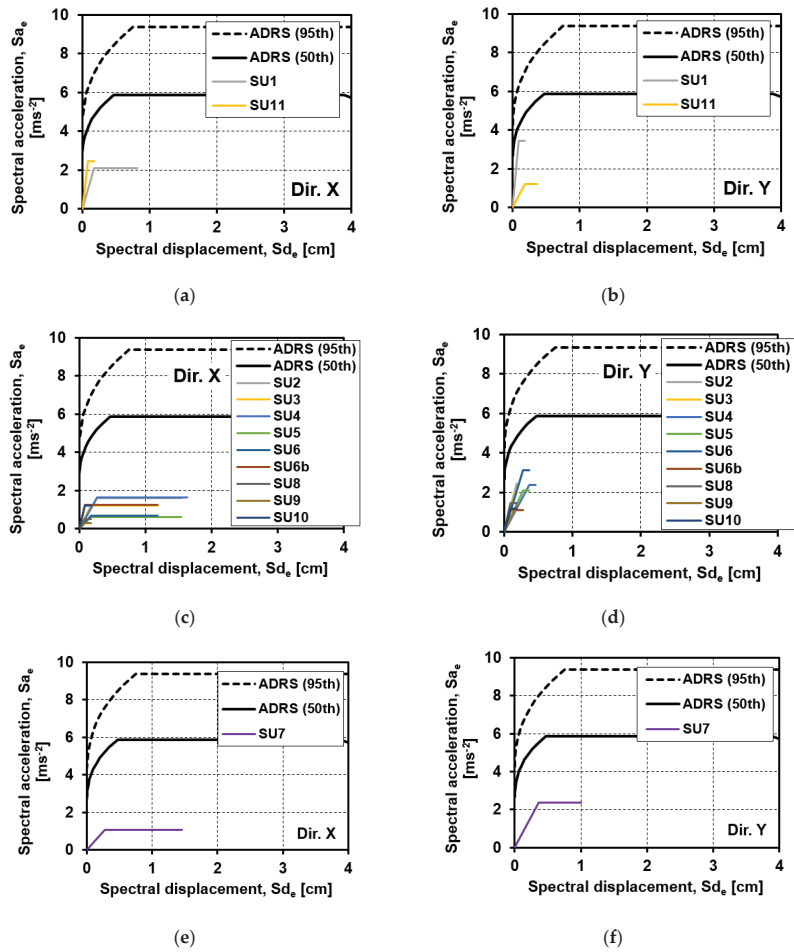
Figure 14. Capacity curves of SUs in the ADRS plane; (**a**) Corner SUs, X dir.; (**b**) Corner SUs, Y dir.; (**c**) Intermediate SUs, X dir.; (**d**) Intermediate SUs, Y dir.; (**e**) Head SU, X dir.; (**f**) Head SU, Y dir.
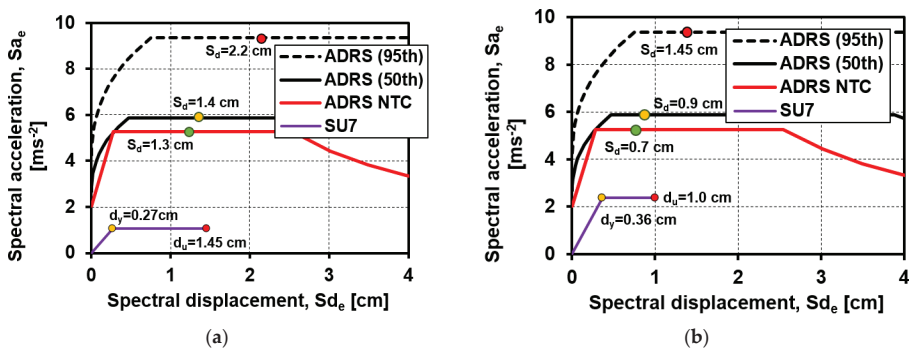
Figure 15. Seismic checks of the head SU in the ADRS plane in (**a**) X and (**b**) Y directions, considering the worst mechanical analysis case; (**a**) Head SU, X dir.; (**b**) Head SU, Y dir.

From the obtained results, it is noted that, in the transverse direction, there is an increase of both strength (55%) and stiffness (40%) concerning the longitudinal direction response. Subsequently, the results obtained by applying the ADRS spectrum, derived from the NTC18 standard [32], have revealed how the verification in the X direction provides a D/C ratio equal to 0.83 while, considering MCSI at the 50th percentile, the mechanical vulnerability, D/C, is equal to 0.96, with an increase of 14%. In the Y direction, it is noted as D/C |$_{NTC18}$ = 0.7, while the corresponding value obtained by MCSI is equal to 0.9, with an increase of 22%. Moreover, the ADRS spectrum achieved from the MCSI evaluated at the 95th percentile provides unsafe conditions, since the seismic checks are not satisfied (D/C > 1) in both analysis directions.

In conclusion, the N2 method verifications implemented through the proposed approach to derive seismic spectra have provided results on the safe side, in comparison to those provided by the standard code.

4.5. Fragility Assessment

In this section, the mean fragility curves of the different SUs have been derived. The fragility curves define the probability that a given damage state, d_{Si}, is equalled or exceeded by a specific intensity measure. The adopted methodology considers as intensity measure the spectral displacement, S_d, according to the following Equation (3) [10,55,60]:

$$P(d \geq d_{Si} | S_d) = \Phi \cdot \left[\frac{1}{\beta} \cdot \ln \left(\frac{S_d}{\overline{S_d}} \right) \right] \tag{3}$$

where Φ [●] stands for the cumulative normal distribution, while the denominator and β are the median and the standard deviation of the corresponding normal distribution, respectively. The damage thresholds have been assumed according to the theory proposed by [3,60] as a function of the structure yielding and ultimate displacements.

Moreover, to reduce the number of uncertainties deriving from the deterministic approach, a single value has been assumed for the standard deviation.

Specifically, the standard deviation has been set as equal to the displacement ductility, μ, multiplied for a fixed correlation coefficient equal to 0.45. Thus, the damage states and the standard deviations have been identified, as reported in Table 5.

Table 5. Definition of damage levels and the corresponding standard deviation.

Damage Levels DS$_i$		
D1	$0.7 \cdot d_y$	Slight
D2	$1.5 \cdot d_y$	Moderate
D3	$0.5 \cdot (d_y + d_u)$	Near Collapse
D4-D5	d_u	Collapse
Standard deviation β		
$0.45 \cdot \ln(\mu)$		

The expected damage levels are in line with the assumption proposed in the framework of the Risk-UE project [61], which is generally used in many seismic risk studies on European building stocks in prone cities. Therefore, the fragility functions have been derived, taking into consideration the average displacements of the above-mentioned case study SUs, as depicted in Figure 16.
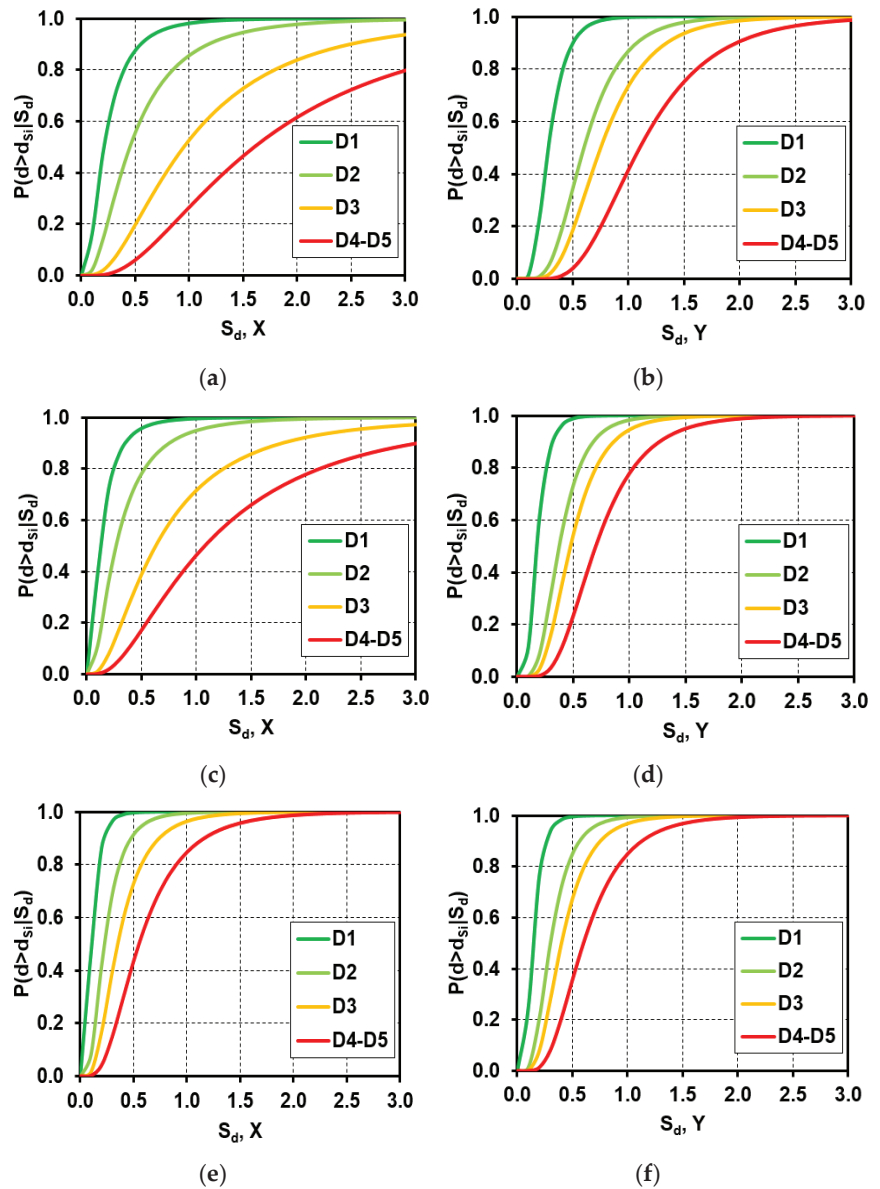
Figure 16. Fragility curves for the examined structural units in X (**a**–**e**) and Y (**b**–**f**) directions; (**a**) Head SUs; (**b**) Head SUs; (**c**) Intermediate SUs; (**d**) Intermediate SUs; (**e**) Corner SUs; (**f**) Corner SUs.

The obtained results clearly show how the corner structural unit provides damage probabilities higher than those of the other SUs occupying intermediate and head positions. In the specific case, the corner unit, despite having a number of floors less than the contiguous structural cells, has a reduced lateral constraint guaranteed by the adjacent structural units, so that the torsional phenomena limit the displacement capacity and, consequently, the expected damage is much more pronounced. Regarding the torsional effects, they are strictly correlated by the addition of structural mass rates offered by

the contiguous SUs, resulting in a non-uniform distribution of the resistant elements in the plane.

Therefore, the more pronounced eccentricity between the centre of gravity and centre of stiffness triggered the premature failure of the masonry wall panels, confirming the damage level depicted in Section 4.1.

5. Conclusions

The research work analysed the seismic vulnerability of an unreinforced masonry building aggregate located in the historic centre of Mirandola using a physics-based simulation approach.

The first step aims to characterize the expected hazard for the site of interest, based on the physics-based ground motion simulations. To this end, the web application XeRIS has been adopted. The starting point was the definition of the soil structure profile to model the propagation of the seismic waves for the estimation of the seismic hazard. In this regard, parametric studies were conducted both on the geological structural model and on the configurations of the selected seismic sources.

The proposed structural model contains the specific geological properties of the investigated area. Subsequently, four different sources (Mirandola (MIR), Finale Emilia (FE), Veronese (VR) and, Ferrara (FE)), were selected to derive the MCSI source spectrum by adopting a stochastic seismic scenario that considers all the possible variability related to the moment magnitude, the position of the nucleation point, and the mean slip rapture velocity.

The second step concerned the evaluation of the global seismic behaviour of the examined masonry compound through non-linear static analyses. The different global behaviour (e.g., displacements and maximum shear thresholds) in the two analysis directions is mainly due to the irregular planimetric configuration of the entire building conjunctly to the higher presence of resistant wall areas. Subsequently, concerning the global response, two synthetic parameters, namely the vulnerability index (V_I) and the damage index (DI), were analysed. To this end, the vulnerability index, V_I, was mechanically estimated directly by extrapolating the results from the 3Muri software, which once defined the elastic response spectrum for the site of interest. From the results achieved, it was shown that the X^+ (uniform) direction provides a PGA_C/PGA_D ratio equal to 0.70 while, in the transverse direction (Y^+ 1st Mode), the vulnerability stands at 0.40 (e.g., medium-low level). As far as the damage index (DI) is concerned, it has been used for establishing a failure hierarchy based on the analyses performed. In particular, it has been found that the selected parameter varied in the range between 0.1 and 0.6, which mainly corresponds to a ductile (bending) crisis of the structural elements and the corresponding damage level according to the EMS-98 scale.

Consequently, the seismic behaviour of the individual structural units in the aggregate configuration was analysed using a numerical procedure based on the reconstruction process of the capacity curves derived from those of the entire aggregate. This methodological approach allows estimation of the damage propensity of the single SUs, considering their interaction in the aggregate, so taking into account the contribution given by SUs adjacent to the investigated one in terms of both stiffness and mass.

The performed analyses provided important insight into the correlation between shear force and ductility. It has been observed that, by correlating the base shear force and the total volume of the single SUs, there is a direct proportionality among the monitoring parameters. However, the ductility tends to decrease as the total resistant area of walls in Y direction increases up to 35 m^2.

Consecutively, the seismic verification was implemented using the bilinear elasto-plastic curves of SUs. To this purpose, the ADRS domain was adopted for the MCSI spectrum (derived at 50th and 9th percentile). In the first instance, the acquired results showed that the expected vulnerability is heterogeneous in the analysis directions, providing unsatisfactory results using the ADRS at the 95th percentile (worst-case scenario).

Furthermore, to propose a suitable example regarding the performance of the SUs towards the seismic action, the investigated head unit was considered as a reference case for conducting the seismic verification in terms of demand and capacity displacements. In this regard, the ADRS obtained using the source spectra were compared with the corresponding spectrum derived according to the Italian design code. From the obtained results, it was noticed that, in the transverse direction, an increase of both strength (55%) and stiffness (40%) concerning the longitudinal direction was found.

The seismic verification in the longitudinal direction, obtained by applying the ADRS domain derived from the Italian NTC18 standard, provided a D/C ratio equal to 0.83, while, considering MCSI at the 50th percentile, the mechanical vulnerability, D/C, was equal to 0.96, with an increase of 14%. Moreover, in the Y direction, it was seen as $D/C|_{NTC18} = 0.7$, while the corresponding value obtained by MCSI was equal to 0.9, with an increase of 22%.

This aspect demonstrated how the displacement demands achieved by adopting the simulated scenario provide conforming results concerning the prediction of the code spectrum vulnerability procedure.

Finally, the mean fragility curves were derived for the different SUs investigated. The results showed how the corner structural unit provides higher damage probabilities than the other SUs occupying intermediate and head positions. Firstly, this outcome was due to the reduced lateral constraint guaranteed by the adjacent structural units, and, secondly, by the induced effect of the torsional phenomena strictly correlated to the addition of structural mass rates offered by the contiguous SUs, resulting in a non-uniform distribution of the resistant elements in the plane.

Overall, based on the results presented, this research topic provided complete information concerning the adoption of a specific procedure based on ground motion simulations for the seismic assessment of URM buildings.

For this reason, this study represents an initial first step that can provide clear insights into the causes of collapse observed in masonry structures after destructive earthquakes. In this framework, future developments should be oriented to the simulation of other seismic scenarios characterized by different fault mechanisms, epicentre distances, hypocentre depths, and ground amplification, to have a greater consistency on the effects caused by a possible earthquake on a larger building dataset.

Author Contributions: Conceptualization, N.C., F.R., M.F. and A.F.; methodology, N.C., F.R., M.F. and A.F.; software, N.C. F.R. and M.F.; validation, N.C., F.R., M.F. and A.F.; formal analysis, N.C.; investigation, N.C., F.R., M.F. and A.F.; resources, A.F.; data curation, A.F. and G.M.; writing—original draft preparation, N.C., F.R. and M.F.; writing—review and editing, N.C., F.R., A.F. and G.M; visualization, N.C.; supervision, F.R. and A.F.; project administration, A.F. and G.M. All authors have read and agreed to the published version of the manuscript.

References

1. Dolce, M.; Prota, A.; Borzi, B.; da Porto, F.; Lagomarsino, S.; Magenes, G.; Moroni, C.; Penna, A.; Polese, M.; Speranza, E.; et al. Seismic risk assessment of residential buildings in Italy. *Bull. Earthq. Eng.* **2021**, *19*, 1–34. [CrossRef]
2. da Porto, F.; Donà, M.; Rosti, A.; Rota, M.; Lagomarsino, S.; Cattari, S.; Borzi, B.; Onida, M.; De Gregorio, D.; Perelli, F.L.; et al. Comparative analysis of the fragility curves for Italian residential masonry and RC buildings. *Bull. Earthq. Eng.* **2021**, *19*, 1–44. [CrossRef]

3. Lagomarsino, S.; Cattari, S.; Ottonelli, D. The heuristic vulnerability model: Fragility curves for masonry buildings. *Bull. Earthq. Eng.* **2021**, *19*, 3129–3163. [CrossRef]
4. Masi, A.; Lagomarsino, S.; Dolce, M.; Manfredi, V.; Ottonelli, D. Towards the updated italian seismic risk assessment: Ex-posure and vulnerability modelling. *Bull. Earthq. Eng.* **2021**, *19*, 3253–3286. [CrossRef]
5. Formisano, A.; Chieffo, N.; Vaiano, G. Seismic Vulnerability assessment and strengthening interventions of structural units of a typical clustered masonry building in the campania region of Italy. *GeoHazards* **2021**, *2*, 101–119. [CrossRef]
6. Clementi, G.-E.F.; Formisano, A.; Milani, G.; Ubertini, F. Structural health monitoring of architectural heritage: From the past to the future advances. *Int. J. Arch. Herit.* **2021**, *15*, 1–4. [CrossRef]
7. Grillanda, N.; Valente, M.; Milani, G. Adaptive NURBS based local failure analyses of retrofitted masonry aggregates. In *AIP Conference Proceedings*; AIP Publishing LLC: Melville, NY, USA, 2021; Volume 2343, p. 080003.
8. Bernardini, C. Identification of Minimum Unit of Analsis for Seismic Performance Assessment of Masonry Buildings in Ag-gregate. Ph.D. Thesis, University of Florence, Florence, Italy, 2019.
9. Battaglia, L.; Ferreira, T.M.; Lourenço, P.B. Seismic fragility assessment of masonry building aggregates: A case study in the old city Centre of Seixal, Portugal. *Earthq. Eng. Struct. Dyn.* **2021**, *50*, 1358–1377. [CrossRef]
10. Chieffo, N.; Formisano, A.; Mochi, G.; Mosoarca, M. Seismic vulnerability assessment and simplified empirical formulation for predicting the vibration periods of structural units in aggregate configuration. *Geosciences* **2021**, *11*, 287. [CrossRef]
11. Cima, V.; Tomei, V.; Grande, E.; Imbimbo, M. Seismic vulnerability of italian historical towns: The case of borgo san rocco. In *Advances in Science and Technology*; Trans Tech Publications Ltd.: Freienbach, Switzerland, 2021; Volume 109, pp. 1–7.
12. Jiménez, B.; Saloustros, S.; Pelà, L. Seismic vulnerability index method for hybrid timber–masonry structures. Numerical calibration and application to the city of Valparaíso, Chile. *J. Build. Eng.* **2021**, *44*, 103185. [CrossRef]
13. Angiolilli, M.; Lagomarsino, S.; Cattari, S.; Degli Abbati, S. Seismic fragility assessment of existing masonry buildings in ag-gregate. *Eng. Struct.* **2021**, *247*, 113218. [CrossRef]
14. Leggieri, V.; Ruggieri, S.; Zagari, G.; Uva, G. Appraising seismic vulnerability of masonry aggregates through an automated mechanical-typological approach. *Autom. Constr.* **2021**, *132*, 103972. [CrossRef]
15. Ruggieri, S.; Cardellicchio, A.; Leggieri, V.; Uva, G. Machine-learning based vulnerability analysis of existing buildings. *Autom. Constr.* **2021**, *132*, 103936. [CrossRef]
16. Rapone, D.; Brando, G.; Spacone, E.; De Matteis, G. Seismic vulnerability assessment of historic centers: Description of a pre-dictive method and application to the case study of scanno (Abruzzi, Italy). *Int. J. Archit. Herit.* **2018**, *12*, 7–8. [CrossRef]
17. Roca, P.; Cervera, M.; Gariup, G.; Pelà, L. Structural analysis of masonry historical constructions. Classical and advanced approaches. *Arch. Comput. Methods Eng.* **2010**, *17*, 299–325. [CrossRef]
18. Ferrante, A.; Giordano, E.; Clementi, F.; Milani, G.; Formisano, A. FE vs. DE modeling for the nonlinear dynamics of a historic church in central Italy. *Geosciences* **2021**, *11*, 189. [CrossRef]
19. Ferrante, A.; Schiavoni, M.; Bianconi, F.; Milani, G.; Clementi, F. Influence of stereotomy on discrete approaches applied to an ancient church in Muccia, Italy. *J. Eng. Mech.* **2021**, *147*, 04021103. [CrossRef]
20. Salachoris, G.P.; Magagnini, E.; Clementi, F. Mechanical characterization of "Scaglia Rossa" stone masonry through exper-imental and numerical analyses. *Constr. Build. Mater.* **2021**, *303*, 124572. [CrossRef]
21. Anderson, J.G.; Cotton, F.; Bindi, D. A ground motion based procedure to identify the earthquakes that are the most relevant for probabilistic seismic hazard analysis. *Earthq. Spectra* **2021**, *37*, 762–788. [CrossRef]
22. Rodríguez-Castellanos, A.; Ruiz, S.E.; Bojórquez, E.; Reyes-Salazar, A. Influence of spectral acceleration correlation models on conditional mean spectra and probabilistic seismic hazard analysis. *Earthq. Eng. Struct. Dyn.* **2021**, *50*, 309–328. [CrossRef]
23. Ordaz, M.; Salgado-Gálvez, M.A.; Giraldo, S. R-CRISIS: 35 years of continuous developments and improvements for proba-bilistic seismic hazard analysis. *Bull. Earthq. Eng.* **2021**, *19*, 2797–2816. [CrossRef]
24. Dávalos, H.; Miranda, E. A ground motion prediction model for average spectral acceleration. *J. Earthq. Eng.* **2021**, *25*, 319–342. [CrossRef]
25. Romanelli, F.; Altin, G.; Indirli, M. Spreading NDSHA application from Italy to other areas. In *Earthquakes and Sustainable Infrastructure*; Elsevier BV: Amsterdam, The Netherlands, 2022; pp. 175–194.
26. Brandmayr, E.; Vaccari, F.; Panza, G.F. Neo-deterministic seismic hazard assessment of Corsica-Sardinia block. *Rend. Lincei. Sci. Fis. E Nat.* **2021**, 1–10. [CrossRef]
27. D'Ayala, D.; Meslem, A.; Vamvatsikos, D.; Porter, K.; Rossetto, T.; Silva, V. Guidelines for Analytical Vulnerability Assessment-Low/Mid-Rise. *GEM Tech. Rep.* 2014. Available online: https://storage.globalquakemodel.org/resources/publications/ (accessed on 20 October 2021).
28. Barnaba, M. Physics-Based Seismic Input for Engineering Design and Risk Assessment. Ph.D. Thesis, University of Trieste, Trieste, Italy, 22 October 2021.
29. Panza, G.F.; Vaccari, F.; Romanelli, F.; Amadio, C.; Fasan, M.; Magrin, A. A seismological and engineering perspective on the 2016 Central Italy earthquakes. *Int. J. Earthq. Impact Eng.* **2016**, *1*, 395. [CrossRef]
30. Ricchiuto, F. *Strategie Valutative Della Vulnerabilità Sismica Degli Aggregati Edilizi in Relazione Alla Caratterizzazione Costruttiva: Risultanze Delle Analisi Sugli Aggregati Dell'Intero Centro Storico Di Mirandola*; University of Bologna: Bologna, Italy, 2013. (In Italian)

31. Formisano, A.; Mochi, G.; Chieffo, N. Empirical and mechanical analysis methods for seismic vulnerability assessment of clustered buildings of historical centres: A case study. In Proceedings of the 8th International Conference on Computational Methods in Structural Dynamic Analysis and Its Application to Performance-Based Earthquake Engineering, Athens, Greece, 28–30 June 2021. [CrossRef]

32. Ministry of Infrastructure and Transport. *Updating Technical Standards for Construction*; Official Gazette: Rome, Italy, 2018. (In Italian)

33. Vamvatsikos, D.; Cornell, C.A. The Incremental Dynamic Analysis and Its Application to Performance-Based Earthquake Engineering. In Proceedings of the 12th European Conference on Earthquake Engineering, London, UK, 9–13 September 2002; p. 479.

34. Lantada, N.; Pujades, L.G.; Barbat, A.H. Vulnerability index and capacity spectrum based methods for urban seismic risk evaluation. A comparison. *Nat. Hazards* **2008**, *51*, 501–524. [CrossRef]

35. Vaccari, F.; Magrin, A. A user-friendly approach to NDSHA computations. In *Earthquakes and Sustainable Infrastructure*; Elsevier BV: Amsterdam, The Netherlands, 2022; pp. 215–237. ISBN 978-0-12-823503-4.

36. Magrin, A.; Gusev, A.A.; Romanelli, F.; Vaccari, F.; Panza, G.F. Broadband NDSHA computations and earthquake ground motion observations for the Italian territory. *Int. J. Earthq. Impact Eng.* **2016**, *1*, 131. [CrossRef]

37. Panza, G.F.; Romanelli, F.; Vaccari, F. Seismic wave propagation in laterally heterogeneous anelastic media: Theory and applications to seismic zonation. In *Advances in Geophysics*; Dmowska, R., Saltzman, B., Eds.; Elsevier: Amsterdam, The Netherlands, 2001; Volume 43, pp. 1–95.

38. Pavlov, V.M. Matrix impedance in the problem of the calculation of synthetic seismograms for a layered-homogeneous isotropic elastic medium. *Izv. Phys. Solid Earth* **2009**, *45*, 850–860. [CrossRef]

39. Italian Accelerometric Archive v3.1. Available online: http://itaca.mi.ingv.it/ItacaNet_31/#/home (accessed on 6 October 2021).

40. Paolucci, R.; Mazzieri, I.; Smerzini, C. Anatomy of strong ground motion: Near-source records and three-dimensional physics-based numerical simulations of theMw6.0 2012 May 29 Po Plain earthquake, Italy. *Geophys. J. Int.* **2015**, *203*, 2001–2020. [CrossRef]

41. Gusev, A.A. Broadband kinematic stochastic simulation of an earthquake source: A refined procedure for application in seismic hazard studies. *Pure Appl. Geophys.* **2010**, *168*, 155–200. [CrossRef]

42. Fasan, M.; Magrin, A.; Amadio, C.; Panza, G.F.; Romanelli, F.; Vaccari, F.; Noè, S. A possible revision of the current seismic design process to overcome the limitations of standard probabilistic seismic input definition. In Proceedings of the 16th World Conference on Earthquake, 16WCEE 2017, Santiago, Chile, 9–13 January 2017; p. 12.

43. Rugarli, P.; Amadio, C.; Peresan, A.; Fasan, M.; Vaccari, F.; Magrin, A.; Romanelli, F.; Panza, G.F. Neo-Deterministic Scenario-Earthquake Accelerograms and Spectra: A NDSHA approach to seismic analysis. In *Engineering Dynamics and Vibrations: Recent Developments*; Jia, J., Paik, J.K., Eds.; CRC Press: Boca Raton, FL, USA, 2018; pp. 187–241.

44. Database of Individual Seismogenic Sources, V. 3.0. Available online: http://diss.rm.ingv.it/diss/ (accessed on 6 October 2021).

45. Vannoli, P.; Burrato, P.; Valensise, G. The seismotectonics of the Po Plain (Northern Italy): Tectonic diversity in a blind faulting domain. *Pure Appl. Geophys.* **2015**, *172*, 1105–1142. [CrossRef]

46. Guidoboni, E.; Ferrari, G.; Mariotti, D.; Comastri, A.; Tarabusi, G.; Valensise, G. Catalogue of Strong Earthquakes in Italy (461 B.C.-1997) and Mediterranean Area (760 B.C.-1500). *CFTI4Med*. 2007. Available online: http://storing.ingv.it/cfti/cfti5/html/info_EN.html (accessed on 20 October 2021).

47. Mantovani, E.; Viti, M.; Babbucci, D.; Tamburelli, C.; Vannucchi, A.; Baglione, M.; D'Intinosante, V.; Cenni, N. *Stima Aggiornata della Pericolosità Sismica in Toscana e aree Circostanti*; Universitas Studiorum: Milan, Italy, 2018; ISBN 978-88-336-9014-8.

48. De Natale, G.; Petrazzuoli, S.; Romanelli, F.; Troise, C.; Vaccari, F.; Somma, R.; Peresan, A.; Panza, G.F. Seismic risk mitigation at Ischia island (Naples, Southern Italy): An innovative approach to mitigate catastrophic scenarios. *Eng. Geol.* **2019**, *261*, 105285. [CrossRef]

49. STA DATA. *3Muri-Seismic Calculation of Masonry Structures*; STA DATA Srl: Turin, Italy. Available online: https://www.3muri.com/documenti/brochure/en/3Muri10.9.0_ENG.pdf (accessed on 20 October 2021).

50. EN 1998-3. Eurocode 8: Design of structures for earthquake resistance. In *Part 3: Assessment and Retrofitting of Buildings*; CEN: Bruxelles, Belgium, 2004; pp. 1–97.

51. Chieffo, N. Seismic Vulnerability Assessment of Historical Masonry Building under Near-Field Earthquake. Ph.D. Thesis, Politehnica University of Timisoara, Romania, Balkans, 27 August 2021.

52. Grünthal, G. The European macroseismic scale 1992: (up-dated MSK-scale). In *Cahiers du Centre Européen de Géodyna-Mique et de Séismologie 7*; Centre Européen de Géodynamique et de Séismologie: Luxembourg, 1998; p. 99.

53. Hadzima-Nyarko, M.; Morić, D.; Pavić, G.; Mišetić, V. Spectral functions of damage index (DI) for masonry buildings with flexible floors. *Teh. Vjesn.* **2018**, *25*, 181–187. [CrossRef]

54. Chieffo, N.; Formisano, A. Comparative seismic assessment methods for masonry building aggregates: A case study. *Front. Built Environ.* **2019**, *5*, 123. [CrossRef]

55. Chieffo, N.; Clementi, F.; Formisano, A.; Lenci, S. Comparative fragility methods for seismic assessment of masonry buildings located in Muccia (Italy). *J. Build. Eng.* **2019**, *25*, 100813. [CrossRef]

56. Hassan, H.M.; Fasan, M.; Sayed, M.A.; Romanelli, F.; ElGabry, M.N.; Vaccari, F.; Hamed, A. Site-specific ground motion modeling for a historical Cairo site as a step towards computation of seismic input at cultural heritage sites. *Eng. Geol.* **2020**, *268*, 105524. [CrossRef]
57. Fajfar, P.; Fischinger, M. N2-A Method for Non-Linear Seismic Analysis of Regular Buildings. In Proceedings of the Ninth World Conference in Earthquake Engineering, Tokyo, Japan, 2–9 August 1988; Volume 5, pp. 111–116.
58. Mosoarca, M.; Onescu, I.; Onescu, E.; Azap, B.; Chieffo, N.; Szitar-Sirbu, M. Seismic vulnerability assessment for the historical areas of the Timisoara city, Romania. *Eng. Fail. Anal.* **2019**, *101*, 86–112. [CrossRef]
59. Mosoarca, M.; Onescu, I.; Onescu, E.; Anastasiadis, A. Seismic vulnerability assessment methodology for historic masonry buildings in the near-field areas. *Eng. Fail. Anal.* **2020**, *115*, 104662. [CrossRef]
60. Cattari, S.; Lagomarsino, S.; Ottonelli, D. Fragility curves for masonry buildings from empirical and analytical models. In Proceedings of the 2nd Conference on Earthquake Engineering and Seismology, Istanbul, Turkey, 25–29 August 2014; pp. 25–29.
61. Mouroux, P.; Le Brun, B. RISK-UE project: An advanced approach to earthquake risk scenarios with application to different european towns. In *Assessing and Managing Earthquake Risk*; Springer: Berlin/Heidelberg, Germany, 2008; pp. 479–508.

Article

Novel Fuzzy-Based Optimization Approaches for the Prediction of Ultimate Axial Load of Circular Concrete-Filled Steel Tubes

Jinsong Liao [1,*]**, Panagiotis G. Asteris** [2,*]**, Liborio Cavaleri** [3]**, Ahmed Salih Mohammed** [4]**, Minas E. Lemonis** [2]**, Markos Z. Tsoukalas** [2]**, Athanasia D. Skentou** [2]**, Chrysanthos Maraveas** [5]**, Mohammadreza Koopialipoor** [6] **and Danial Jahed Armaghani** [7]

1   School of Construction Management, Chongqing Jianzhu College, Chongqing 400072, China
2   Computational Mechanics Laboratory, School of Pedagogical and Technological Education, 14121 Athens, Greece; mlemonis@hotmail.com (M.E.L.); tsoukalas6967@gmail.com (M.Z.T.); athanasiaskentou@hotmail.gr (A.D.S.)
3   Department of Engineering, University of Palermo, 90133 Palermo, Italy; liborio.cavaleri@unipa.it
4   Civil Engineering Department, College of Engineering, University of Sulaimani, Sulaymaniyah 46001, Iraq; ahmed.mohammed@univsul.edu.iq
5   Farm Structures Laboratory, Department of Natural Resources and Agricultural Engineering, Agricultural University of Athens, 11855 Athens, Greece; c.maraveas@maraveas.gr
6   Faculty of Civil and Environmental Engineering, Amirkabir University of Technology, Tehran 15914, Iran; mr.koopialipoor@aut.ac.ir
7   Department of Urban Planning, Engineering Networks and Systems, Institute of Architecture and Construction, South Ural State University, 76, Lenin Prospect, 454080 Chelyabinsk, Russia; danialarmaghani@susu.ru
*   Correspondence: liaojinsong1022@163.com (J.L.); asteris@aspete.gr (P.G.A.)

Abstract: An accurate estimation of the axial compression capacity of the concrete-filled steel tubular (CFST) column is crucial for ensuring the safety of structures containing them and preventing related failures. In this article, two novel hybrid fuzzy systems (FS) were used to create a new framework for estimating the axial compression capacity of circular CCFST columns. In the hybrid models, differential evolution (DE) and firefly algorithm (FFA) techniques are employed in order to obtain the optimal membership functions of the base FS model. To train the models with the new hybrid techniques, i.e., FS-DE and FS-FFA, a substantial library of 410 experimental tests was compiled from openly available literature sources. The new model's robustness and accuracy was assessed using a variety of statistical criteria both for model development and for model validation. The novel FS-FFA and FS-DE models were able to improve the prediction capacity of the base model by 9.68% and 6.58%, respectively. Furthermore, the proposed models exhibited considerably improved performance compared to existing design code methodologies. These models can be utilized for solving similar problems in structural engineering and concrete technology with an enhanced level of accuracy.

Keywords: CCFST; hybrid; prediction; FFA; DE; FS

1. Introduction

Concrete-filled steel tube (CFST) members make better utilization of steel and concrete than traditional bare steel or reinforced concrete structures. The steel tube gives confinement to the concrete infill, while the concrete infill prevents the inward buckling of the steel tube. CFST members have a long history of being used in a broad range of construction projects due to their efficiency as structural components. As an example, CFSTs have been utilized as (1) mega columns in super high-rise buildings, (2) chord members in long-span arch bridges, (3) bridge piers, (4) floodwall piling, and (5) underwater pipeline structures, as described by researchers like Wang et al. [1]. For the most part, the CFST components in these situations are utilized to support compressive forces.

When it comes to improving the compressive strength of CFST components, there are primarily two approaches that are used. Using bigger cross sections is one approach. However, it may increase structural weight (and as a result the seismic impact) and decrease useable space, making it a less feasible or cost-effective solution. Alternatively, high strength steel (i.e., with a yield stress higher than 525 MPa) and high strength concrete (i.e., with a compressive strength greater than 70 MPa) are two additional viable methods [AISC 360 [2]].

According to experts like Nishiyama et al. [3], Kim [4] and Han [5] and others, many studies have been carried out to examine the behavior of conventional-strength members of the CFST. Several researchers have experimented with the behavior of high-strength CFST columns facilitating their adoption in practice. For example, Cederwall et al. [6], Varma [7], Uy [8], Liu et al. [9], Mursi and Uy [10], Sakino et al. [11], Lue et al. [12], Aslani et al. [13], and Xiong et al. [14] have performed experimental testing on high-strength rectangular CFST short columns. Lai and Varma [15] reviewed these experiments and provided design equations for calculating the cross-sectional strength of high-strength rectangular CFST columns and also effective stress-strain relationships for the steel tube and concrete infill of such high-strength components.

Additional experimental tests on CFST columns were conducted by Gardner and Jacobson [16], Bergmann [17], O'Shea and Bridge [18], Schneider [19], O'Shea and Bridge [20], Giakoumelis and Lam [21], Sakino et al. [11], Zeghiche and Chaoui [22], Yu et al. [23], de Oliveira et al. [24], Liew and Xiong [25], Chen et al. [26]. The experimental results from previous studies have been employed in this study in order to build an experimental database. It is noted, however, that experiments featuring columns with fibers in the concrete, stainless or aluminum steel tubing, grease on the inner surface of the tubing, or concrete infill alone were excluded from this database.

Machine learning (ML) methods have been widely used in many civil engineering applications [27–55], particularly in compressive structures [56–59]. ML uses databases to develop models that can solve various linear and nonlinear problems with varying degrees of complexity. These methods, using computer processing, help considerably in solving problems more efficiently and quickly, and is introduced as a powerful alternative method for older, experimental and statistical models. An optimization and tree-based approach has been developed by Sarir et al. [60] to find out the maximum capacity of circular CFST members. Short CFST members' load-bearing capacity was predicted by Ahmadi et al. using an artificial neural network [61,62]. A gene expression model for predicting circular CFST capability was established by Güneyisi et al. [63] and Ipek and Güneyisi [64]. In the study of Moon et al. [65], the load-bearing behavior of circular CFST was also examined using a fuzzy logic model. According to Al-Khaleefi et al. [66], the fire resistance of CFST columns has also been studied using a machine learning method that considers material characteristics and loading circumstances. For sections other than circular, Ren et al. [67] recently published a study on the prediction of square CFST members, using support vector machines and particle optimization methods. While for the same section Tran et al. [68] used a neural network model to predict the ultimate load. Also, Lee et al. [69] used a categorical gradient boosting algorithm to predict the strength of both circular and rectangular CFSTs under concentric or eccentric loading. Zarringol et al. [70] used ANN for the same problem. It can be concluded from these studies that ML methods prove quite promising in investigating the mechanical behavior of structures made up of CFST members.

In this research, the major goal is to develop a regression machine learning model for compressive circular CFST, particularly in contemporary buildings. This was achieved using a hybridizing fuzzy system (FS) with two optimization algorithms known as the firefly algorithm (FFA) and differential evolution (DE). The input data consist of column length, cross-section diameter and steel tube thickness in addition to concrete compressive and steel yield stress. Precise quality metrics such as root mean-squared-error (RMSE), and coefficient of determination (R^2) were utilized throughout the model's testing/validation

phase. The FS-FFA and FS-DE models were evaluated and compared with existing design code methodologies to highlight the best predictive model for the examined problem.

2. Research Significance

CFST design can be done using different methods and codes around the world. Accurate, faster, and less costly design is one of the priorities of any structural project. Due to the fact that an accurate CFST design has important effects on the stability of structures, examining different techniques could give a better understanding of their effects and behaviour. Therefore, this research, using a new generation of computational methods developed by learning machines, is aimed at coming up with a practical solution to the aforementioned problem. Using a combination of FS and optimization algorithms (i.e., FFA and DE), new predictive models can be developed to more accurately and quickly evaluate CFST design. Optimal solutions of hybrid models consisting of these conditions can be used for new conditions and provide acceptable results considering practical applications in industrial fields.

3. Short Literature Review on Design Codes

The design of circular CFST columns is already supported by several steel and composite codes, available worldwide. Such codes include EN1994 [71] in Europe, AISC 360 [72] in the USA, AIJ [73] in Japan. Besides providing the squash load that is relevant for short columns, design codes also provide methodologies to predict the resistance against flexural buckling, which becomes the critical failure mode for long, slender columns. Local buckling of the steel tube is also a failure mode relevant for thin-walled steel sections. It is typically covered by placing section slenderness limits and depending on them, either accounting for a reduced effective steel sectional area (i.e., EN1994 [71]), or limiting the ultimate stress the composite section may reach (i.e., AISC 360 [72]). Regarding squash load, which involves the plastic strength of the steel and concrete parts of the CFTS section, the influence of the increased concrete confinement provided by the circular tube is typically expressed through an increase of the concrete strength contribution. The following formulas describe the squash loads, for the EN1994 [71], AISC 360 [72], AIJ [73] design codes (ignoring any safety factors):

$$N_p^{EN1994} = \begin{cases} \eta_a f_y A_s + \left(1 + \eta_c \frac{t f_y}{d f_c'}\right) f_c' A_c & , \overline{\lambda} < 0.5 \\ f_y A_s + f_c' A_c & , \overline{\lambda} \geq 0.5 \end{cases} \quad (1)$$

$$N_p^{AISC360} = f_y A_s + 0.95 f_c' A_c \quad (2)$$

$$N_p^{AIJ} = 1.27 f_y A_s + 0.85 f_c' A_c \quad (3)$$

Factors η_a and η_c account for the member slenderness $\overline{\lambda}$. For slender columns, the squash loads given above fail to represent the ultimate compressive load. In such cases, buckling phenomena emerge that cause an earlier failure, depending on the global column slenderness. The methodologies provided by the aforementioned design codes are differentiated in this context. Due to space limitations the relevant expressions are not reproduced herein however.

All design codes place specific limits on their field of application. These are related to material strength limits, steel tube slenderness, global slenderness or steel to concrete ratio. Table 1 presents the relevant application limits for the codes examined.

Table 1. Design codes application limits, related to circular CFSTs.

Code	f_y (MPa)	f_c' (MPa)	Section Slenderness	Other
EN1994 [71]	$235 \leq f_y \leq 460$	$25 \leq f_c' \leq 50$	$\frac{d}{t} \leq 90\frac{235 \text{ MPa}}{f_y}$	$0.2 \leq \frac{A_s f_y}{N_p} \leq 0.9$
AISC 360 [72]	$f_y \leq 525$	$21 \leq f_c' \leq 69$	$\frac{d}{t} \leq \frac{0.31 E_s}{f_y}$	$A_s \geq 0.01 A_{sc}$
AIJ [73]	$235 \leq f_y \leq 355$	$18 \leq f_c' \leq 60$	$\frac{d}{t} \leq 1.5\frac{23500 \text{ MPa}}{\sqrt{\min\{f_y; 0.7 f_u\}}}$	$\frac{L_e}{B} \leq 50$

A_{sc}, A_s, and A_c are the areas of the total cross section, the steel tube and the concrete core, respectively L_e is the column effective length.

4. Modeling Approaches

4.1. Fuzzy System (FS)

A chapter titled "fuzzy sets" by Professor Lotfizadeh in 1965 presented the fuzzy theory [74]. Initially, his primary objective was to create a more accurate model of how natural language processing works. Fuzzy sets, fuzzy events, fuzzy numbers, and phases are only a few of the innovations he made to mathematics and engineering thanks to these ideas. A rule base, which includes If–Then rules created by application specialists, constitutes FS's core component [75]. Membership functions are used to deploy the fuzzy sets. For the FS process, the most popular fuzzifiers are Gaussian, Singleton, and Triangular. In addition, the most often used defuzzifiers in the literature are center of gravity, center average, and maximum. Fuzzy logic principles govern the firing of If–Then rules while the inference engine is operating. A fuzzy rule has the following syntax [76]:

$$If\ x_1\ is\ A_1\ and \ldots x_n\ is\ A_n\ then\ Y\ is\ B \tag{4}$$

Fuzzy sets in U R (U is the input space) are Ai and V R (V is the output space) are B, and X is equal to the product of the variables in the input space and the variables in the output space, respectively. There are two types of FS controller: closed-loop and open-loop. The product inference engine and Gaussian fuzzifier were used in the following ways:

$$f_{1(x)} = \begin{cases} \exp[-\frac{1}{2}\left(\frac{x-m_1}{\sigma}\right)] & x \leq m_1 \\ 1 & otherwise \end{cases} \tag{5}$$

$$f_{2(x)} = \begin{cases} 1 & x \leq m_2 \\ \exp[-\frac{1}{2}\left(\frac{x-m_1}{\sigma}\right)] & otherwise \end{cases} \tag{6}$$

4.2. Firefly Algorithm (FFA)

Yang was the first to propose FFA as a nature-inspired, meta-heuristic algorithm [77]. Engineers have used this method to address a variety of issues. The most critical aspects of the FFA process are the formulation of attraction and the change in light intensity. Fireflies will operate virtually independently in FFA modelling, which is advantageous for parallel implementation in particular. Fireflies in this algorithm tend to congregate closer to the optimum, making it superior to the particle swarm optimization (PSO) and the genetic algorithm (GA) [76,78]. Figure 1 depicts FFA's foundation for a better understanding. Several studies, including Yang [77], Zhang and Wu [79], and Apostolopoulos and Vlachos [80], go into great depth regarding FFA. Reviewing past research shows that the FFA may be utilized as a powerful tool for engineering optimization in almost all fields [81,82]. Gholizadeh and Barati [83], for example, used the PSO, FFA, and harmony search (HS) to explore the size and form optimization of truss systems. In terms of optimizing the size and geometry of truss structures, FFA outperformed PSO and HS.

START

Generate Initial population of fireflies $x=(x_1, \ldots, x_n)$

Determine Intensity (I) at objective function f(xi)

While *t<MaxIter*

    For i=1:n

      For j=1:n

        If $I_j > I_i$

            Move fireflies i and j in d-dimension

        End if

        Attractiveness varies with distance r via exp [−γr]

        Evaluate new solution and update light intensity

        End

      End

    Rank the fireflies and find the current best

  End

END

Figure 1. Base of firefly algorithm (FFA).

4.3. Differential Evolution (DE)

Storn and Price (1997) first proposed the concept of differential evolution (DE) as a stochastic population-based search technique [84]. NP members are randomly selected from the original population (parents) before the search may begin. Using crossover, mutation, and selection operators, the DE technique then produces a new population (i.e., offspring). This iteration's members are chosen by comparing how similar they are to the previous iteration's members. This cycle is repeated until the desired outcome is achieved. The following sections describe the major stages of this algorithm [84].

4.3.1. Generating the Initial Population

If the problem's decision variables are indicated by D, the initial population vector is produced with a random size N*D inside the decision variables allowed range, according to the following equation:

$$x_{io} = x_{imin} + round(\varphi_i \times x_{imax} - x_{imin}), \ i = 1, \ldots, NP \tag{7}$$

There are lower and higher limits on the choice variables x_{imin} and x_{imax}, respectively, while index i is a random number between 0 and 1.

4.3.2. Mutation

To carry out the mutation procedure, the following equation is used:

$$v_{i,G+1} = x_{r1,G} + F \times (x_{r2,G} - x_{r3,G}) \tag{8}$$

There are three randomly selected members of the population in this case, and the scaling factor F ranges from zero to two, giving us a mutant vector $v_{i,G+1}$ and three randomly picked members of the population.

4.3.3. Crossover

This operator combines the modified particles with the members of the target group that were chosen in the first stage as follows:

$$u_{ij,G+1} = \begin{cases} v_{ji,G+1} & r<Cr \ or \ j=rn_i \\ x_{ji,G} & otherwise \end{cases} \tag{9}$$

where $j = 1, 2, \dots, D$; $\in r_j$ [0, 1] is the random number; C_r stands for the crossover constant $\in$ [0, 1]; and $\in rn_i$ (1, 2, $\dots$, D) is the randomly chosen index.

4.3.4. Selection

Once all operators have been initialised to their respective goal functions, a new measurement vector and target member are created. If the measurement vector's value exceeds the target member's, the member is promoted to the next generation. If this does not happen, the target member will be added to the population of the following generation. Figure 2 depicts the DE's pseudo-code.

START

Initialize the random population Xi, G i=1,...,NP

Evaluate f(Xi,G) i=1,...,NP

For *G=1:MaxIter*

    For i=1:NP

        Select randomly $x_{r1,G}$, $x_{r2,G}$, $x_{r3,G}$

        For j=1:D

        If rand j (0,1)<CR

        $v_{ji,G+1} = x_{r1,G} + F \times (x_{r2,G} - x_{r3,G})$

        Else

        $v_{ji,G+1} = x_{ji,G}$

        End if

        End For

        If f($v_{ji,G+1}$) <=f(Xi,G)

            $x_{i,G+1} = v_{i,G+1}$

        Else

            $x_{i,G+1} = x_{i,G}$

        End if

    End for

End *For*

END

Figure 2. Pseudo-code of the differential evolution (DE).

4.4. Hybridization of FS

The CCFST is predicted using two hybrid FS-FFA and FS-DE in this research. Five characteristics were utilized as inputs in the hybrid FS modelling procedure, with CCFST ultimate load being the output. The proposed FS-FFA and FS-DE models were trained and tested using 328 datasets of data in the training phase and 82 datasets of data in the testing phase. Fuzzy-based modifications to FFA and DE are suggested in this research to remove or minimize model drawbacks. In this structure, the member (population) of optimization algorithms in each step may affect each other's movements. For determining progress in the program, we used two metrics to indicate how close the algorithms are getting to the ideal answer. We call this loop counter (iteration) Count and its value is decided by

expertise or via trial and error [85]. The fuzzy controller will have to deal with this last problem. The following is an introduction to the delta parameter:

$$Delta^i = F\left(Best^i\right) - F\left(TBest^{i-1}\right) \tag{10}$$

Iteration *i* yields *Best^i*, which is the best solution, whereas iteration *i*−1 yields *TBest^{i−1}*, which is the best solution. One of the benefits of the hybrid FS is that it regulates the fundamental database, i.e., physics of the examined problem. As a result, convergence speed may be improved by making the appropriate initial adjustments. A MATLAB programme was used to implement the hybrid FS model's code. The following equation is used to standardize datasets before beginning hybrid FS modelling:

$$Xnorm = \frac{X - Xmin}{Xmax - Xmin} \tag{11}$$

where *X*, *Xmin*, and *Xmax* represent the parameters' real values, minimum and maximum values, respectively, while *Xnorm* represents the parameter's normalized value. FS-FFA modeling's most critical parameters are Npop (swarm size), Alpha (mutation coefficient), Gamma (light absorption coefficient), Beta (attraction coefficient base value) and Maxiter (maximum number of iterations), according to prior research [81,82,85]. Parameters' number of iteration, crossover constant and population (Npop) are also effective for the DE algorithm [84,86]. Following the trial and error technique, Npop of FFA was set to 50, Npop of DE was set to 80, Alpha was set to 0.25, Gamma was set to 1, crossover constant was set to 0.8, Beta was set to 2, and the number of iterations for both algorithms was set to 500. Figure 3 depicts the steps involved in putting hybrid FS into practice.
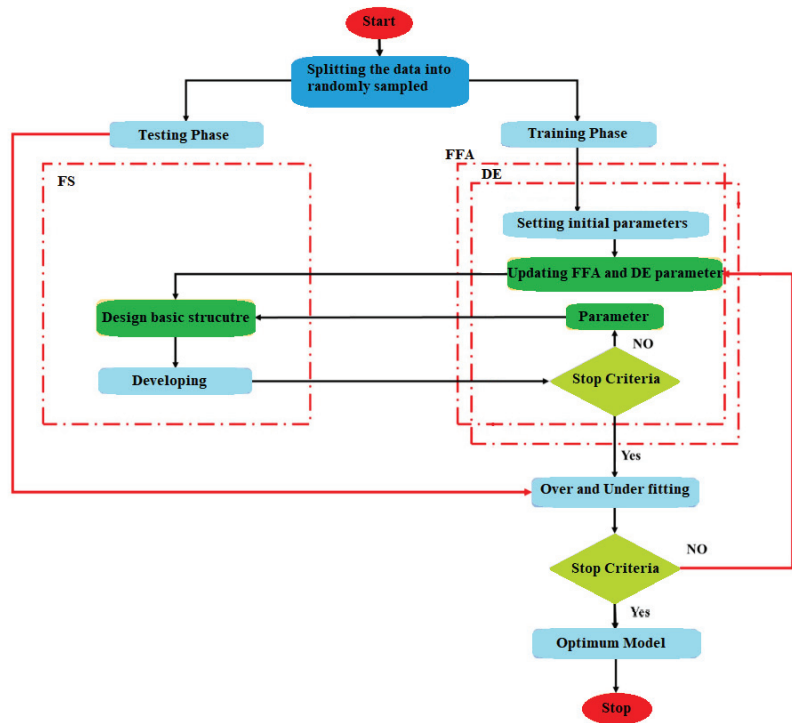
Figure 3. The general flowchart developed in this research.

5. Data Setup

A variety of sources were used to compile the database for this study such as Wang et al. [87], Geng [88], Dong et al. [89], Wang et al. [90], Chen et al. [91], Yang et al. [92], Wang et al. [93], Wei et al. [94] Hoang and Fehling [95], He et al. [96]. These sources include axial compression tests on circular CFST columns that make up 410 samples in total (whole used datasets for modeling are presented in Appendix A). Several geometrical factors and mechanical characteristics were utilized in these tests to investigate the failure of CFST columns under axial stress. These are column length (L), diameter (D), and thickness (t) as geometrical input variables. Additionally, the steel tube yield stress (fy) and the compressive strength (fc) of the filling concrete are the material specific variables representing their mechanical properties. The only output of the problem is the CFST column ultimate experimental axial compressive load (Pexp). Table 2 shows a statistical examination of the dataset.

Table 2. General information of dataset.

Parameter	Unit	Min	Average	Max	SDT
L	mm	180	720.73	4000	594.56
D	mm	60	169.41	550	74.04
t	mm	0.86	4.47	16.72	2.59
fy	MPa	184.8	388.38	1153	170.29
fc	MPa	23.2	74.98	188.1	44.01
Pexp	KN	215	2992.71	29590	3213.2

6. Development of the Hybrid Models

The performance of FS-FFA and FS-DE models is discussed in this part, presenting how well it can predict the circular CFST ultimate compressive load. In order to do this, three quantitative standard statistical performance measures, namely R^2, the a20-index, and RMSE, have been used, as described by Equations (12)–(14) [52,58,97–102]:

$$RMSE = \sqrt{\frac{1}{n} \sum_{i=1}^{n} \left(y_{fr,i} - \hat{y}_{fr,i} \right)^2} \tag{12}$$

$$R^2 = 1 - \frac{\sum_{i=1}^{n} \left(y_{fr,i} - \hat{y}_{fr,i} \right)^2}{\sum_{i=1}^{n} \left(y_{fr,i} - \overline{y}_{fr,i} \right)^2} \tag{13}$$

$$a20 - index = \frac{m20}{n} \tag{14}$$

where, the predicted and measured values for n data are indicated by $\hat{y}_{fr,i}$ and $y_{fr,i}$, respectively, and $m20$ is the number of samples with a value of (experimental value)/(predicted value) ratio, between 0.80 and 1.20. The best performance of the models is achieved when the errors (*RMSE*) are zero and the R^2 is close to one. The performance of the developed FS-FFA and FS-DE is presented in Table 3 in terms of R^2, *RMSE*, and a20-index. The optimal model values have been optimally picked having as objective to achieve the best possible performance metrics.

Table 3. The final result of hybrid fuzzy system (FS) models.

Model	Training			Testing		
	a20-Index	R^2	RMSE	a20-Index	R^2	RMSE
FS-FFA	0.9604	0.9854	482.0362	0.8659	0.9880	415.4471
FS-DE	0.9634	0.9571	655.4708	0.8659	0.9876	419.4502

In Table 3, it can be shown that the proposed FS-FFA and FS-DE have a good performance for predicting CFST values. In the training section, the performance of the FS-FFA model seems better in terms of RMSE and a20-index, compared to the FS-DE model whereas the latter scores a higher R^2 value. However, in the test section, the performance of the two models proves more closely matched, with the FS-FFA achieving slightly better metrics. Given that the FS-FFA model has been able to provide better predictions in both sections, it becomes the preferred one for the estimation of circular CFST ultimate compressive load. Figures 4 and 5 show separately for the training and the testing datasets graphs of predicted vs. experimental loads for both hybrid models. It can be seen that both models exhibit a consistent performance throughout the range of available compressive loads.
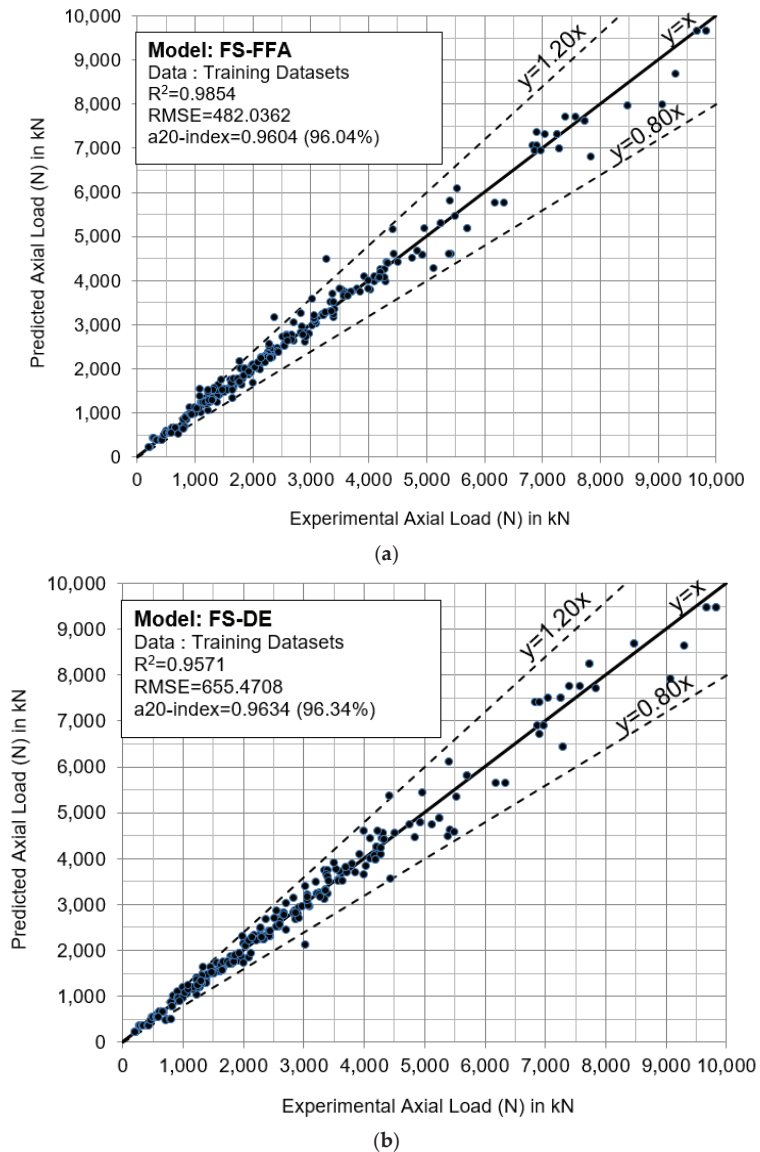
Figure 4. Results of training phase: (**a**) FS-FFA model, (**b**) FS-DE model.
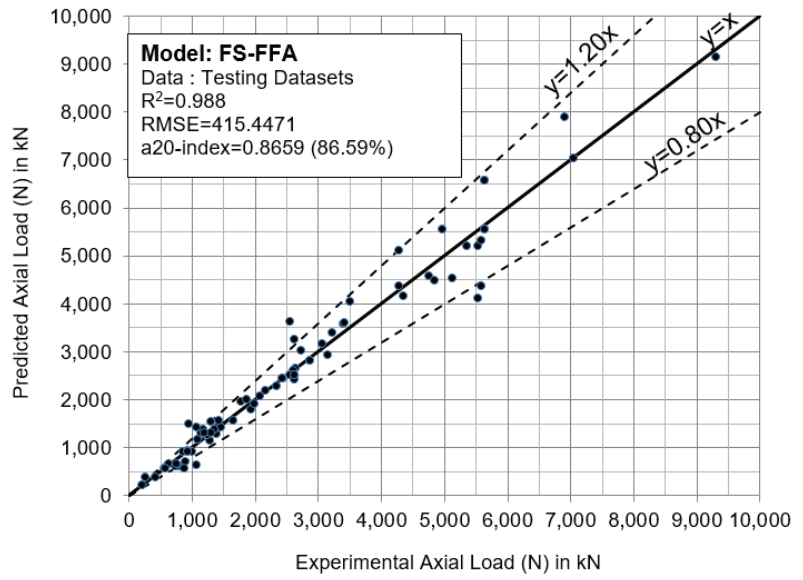
(**a**)
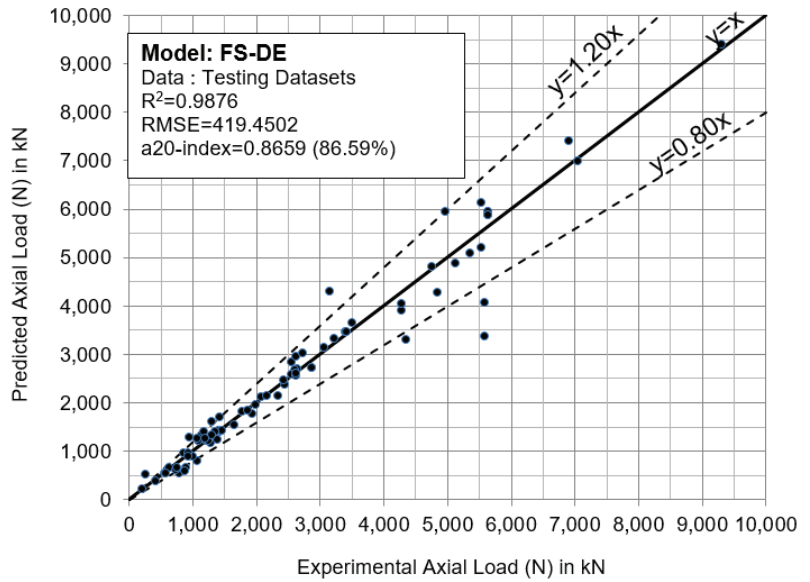
(**b**)

Figure 5. Results of testing phase: (**a**) FS-FFA model, (**b**) FS-DE model.

7. Discussion

7.1. Comparison against Alternative Hybrid Models

In this section, a comparison is made between the developed hybrid models with the base model and the other two traditional hybrid models. Given that optimization algorithms have different performances for each problem, it is possible to identify their differences and compare their performances by examining several algorithms together. Therefore, two hybrid models, FS-genetic algorithm (GA) and FS-particle swarm optimization (PSO), were developed to compare with the two developed models in this study. The findings showed that the FS-FFA, FS-DE, FS-GA, and FS-PSO models outperformed FS in terms of prediction accuracy for training data by 9.68%, 6.58%, 5.68%, and 1.56% respectively. Among the hybrid models, the FS-FFA model provided the best performance according to the various criteria for predicting circular CFST ultimate load values.

7.2. Comparison against Design Codes

In this section a comparison between the two developed models against the predictions of the three design codes, mentioned earlier in the text (EN1994, AISC360 and AIJ) is presented. The design code calculations were performed ignoring any safety factors. Also, the calculations were not focused on the squash load only but took into account the relevant for more slender columns buckling failure methodologies available in each code.

Table 4 presents the performance indices for the two developed models and the respective ones for the design codes. The results correspond to the designated testing datasets among the specimens in the experimental database, amounting to 82 specimens. The various models in the Table are ranked according to their RMSE index. It appears that the two developed models achieve a considerable improvement in almost all indices, compared to the design codes. In particular the improvement from the best performing code which proves the Japanese AIJ [73], is remarkable for both the RMSE and a20-index. A marginal improvement is also found in terms of R^2 index. Among design codes, the AIJ [73] achieves improved performance compared to the other codes.

Table 4. Performance indices on the testing datasets.

Ranking	Model	a20-Index	R^2	RMSE
1	FS-FFA	0.8659	0.9880	415.4471
2	FS-DE	0.8659	0.9876	419.4502
3	AIJ [73]	0.6341	0.9842	786.3858
4	EN1994 [71]	0.5732	0.9681	1119.6477
5	AISC 360 [72]	0.3659	0.9814	1330.6249

Figure 6 illustrates for the two hybrid models and for the examined design codes, the individual experimental vs. predicted load values for all specimens in the testing datasets. It can be visually inspected that the FS-FFA hybrid model achieves a better fit to the experimental values, with less outliers, over the entire range of specimens.

7.3. Limitations and Future Works

This research developed several hybrid models using artificial intelligence to predict the ultimate compressive load of CCFST columns. These models are based on data collected from laboratory works of previous research. Given that the structure of models is highly dependent on the number of parameters, their types must be taken into account in measuring and using such data. Laboratory outline data reduce the accuracy of prediction. On the other hand, the purpose of this study is to develop non-linear models to more accurately evaluate the target parameter. Therefore, a balance between the input data and their statistical characteristics must be elaborated. By doing this, a wider range of data can be analyzed and a model with higher power can be developed. Since these models

have used two optimization algorithms to improve the performance of the base model, some other optimization techniques such as the whale optimization algorithm can be examined to increase the base model performance. The base model in this research was made using the FS model, which has special features, while by changing the basic model to other predictive models such as neuro-fuzzy, new results can be achieved. The last future direction of this research can be related to increasing the number of data samples with circular cross sections to develop a new model with a level of more generalization.
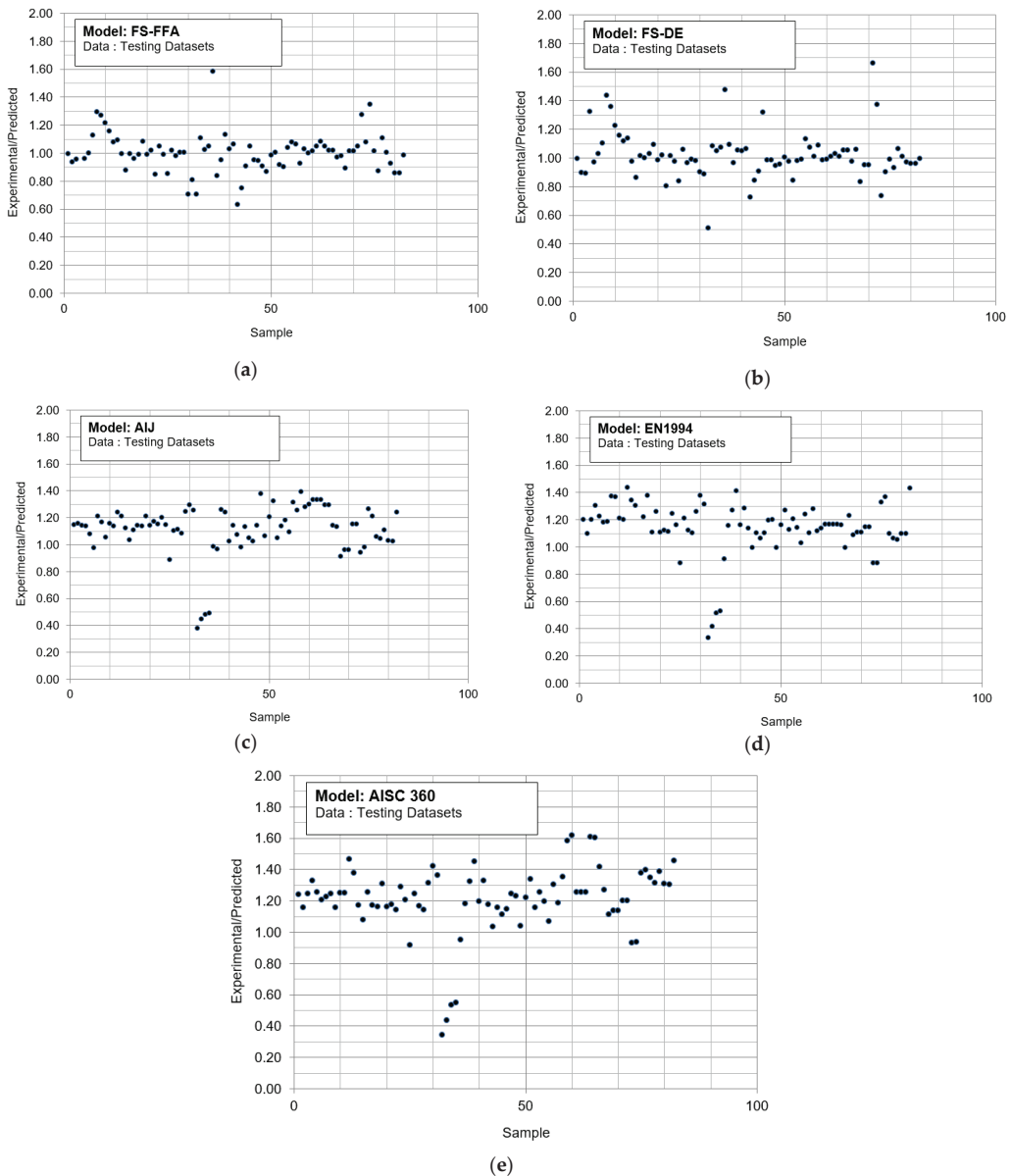
Figure 6. Experimental vs. predicted ratios: (**a**) the FS-FFA model, (**b**) the FS-DE model, (**c**) the AIJ design code model [73], (**d**) the EN1994 design code model [71], (**e**) the AISC360 design code model [72].

8. Conclusions

In this study, a novel artificial intelligence-based prediction model is used to correctly evaluate CCFST columns' axial compression capacity. FS and two recent nature meta-heuristic optimization methods known as FFA and DE were combined to create two hybrid FS-FFA and FS-DE models. It was also combined with two common optimization techniques, the GA and PSO. An extensive database of 410 experimental tests for the CCFST columns was gathered from openly available papers for this research project. A statistical and visual analysis was undertaken to determine the effectiveness and correctness of the findings, and the following conclusions can be reached.

According to the research findings, the suggested hybridization models outperformed the basic FS model when it came to resolving the axial compression capacity problem. The findings showed that the FS-FFA, FS-DE, FS-GA, and FS-PSO models outperformed FS in terms of prediction accuracy for training data by 9.68%, 6.58%, 5.68%, and 1.56%, respectively. According to all performance assessments, the new suggested FS-FFA model is optimal for the prediction of the axial compression capacity of CCFTS columns, with improved RMSE and a20-index compared with FS-DE. Additionally, the proposed model achieved a significantly improved prediction of the ultimate compressive load compared to available design code predictions. In particular, RMSE of the FS-FFA model was reduced by 47% from AIJ [73] and more from the EN1994 [71] and AISC360 [72], whereas a20-index was also considerably increased.

The base model in this research was made using the FS model, which has special features, while by changing the basic model to other predictive models such as neuro-fuzzy, new results can be achieved. The last future direction of this research can be related to increasing the number of data samples with circular cross sections to develop a new model with a greater generalization level.

This model's performance and machine learning methods are largely reliant on the database used. However, a more sophisticated and bigger database may have significant effects on the hybrid FS model's final outcomes. Other optimization techniques such as the whale optimization algorithm can be examined to increase the base model performance. Furthermore, other sections' geometries of CFTS, such as squares and round-ended squares, can also be investigated by the proposed hybrid models in this research. Close form equations of this issue using machine learning models will be very beneficial to engineering in the future.

Author Contributions: Conceptualization, P.G.A., M.K., A.S.M. and D.J.A.; Data curation, P.G.A., M.K., A.S.M., M.E.L., A.D.S. and C.M.; Formal analysis, J.L., M.K., A.S.M., L.C., M.Z.T. and A.D.S.; Supervision, P.G.A., A.S.M. and D.J.A.; Writing—original draft, P.G.A., M.K., A.S.M., D.J.A. and J.L.; Writing—review and editing, P.G.A., L.C., M.K., A.S.M., D.J.A., J.L., M.E.L., M.Z.T. and C.M. All authors have read and agreed to the published version of the manuscript.

Institutional Review Board Statement: Not applicable.

Informed Consent Statement: Not applicable.

Data Availability Statement: The data presented in this study are available in Appendix A.

Conflicts of Interest: The authors confirm that this article content has no conflict of interest.

Nomenclature

DE	differential evolution
D	diameter
HS	harmony search
CFST	concrete-filled steel tubular

CCFST   circular concrete-filled steel tubular
FS   fuzzy systems
FFA   firefly algorithm
fc   the compressive strength
fy   the steel tube yield stress
PSO   particle swarm optimization
L   column length
t   thickness
GA   genetic algorithm
R2   coefficient of determination
RMSE   root mean square error
Pexp   ultimate axial compressive load
Npop   population
ML   machine learning

Appendix A

Table A1. The database used for analysis in this study.

Dataset Number	fc (MPa)	D (mm)	L (mm)	t (mm)	fy (MPa)	Pexp (KN)
1	34.04	60	180	1.48	307	215
2	51.3	101.9	305.7	3.03	371	926
3	34.08	60	180	1.48	307	220
4	164.4	114.3	200	6.3	428	2866
5	103.4	100	300	1.9	404	1100
6	103.4	100	300	1.9	404	1125
7	103.4	100	300	1.9	404	1170
8	51.3	101.5	304.5	3.03	371	859
9	23.1	101.6	304.8	3.03	371	635
10	23.2	101.6	304.8	3.03	371	635
11	40	101.6	304.8	3.03	371	864
12	93.6	114.57	300	3.99	343	1308
13	34.1	101.7	203.3	3.07	605.1	1112.10
14	40	101.7	305.1	3.03	371	803
15	48.3	165	562.5	2.82	363.3	1759
16	23	101.8	305.4	3.03	371	679
17	23.2	101.8	305.4	3.03	371	632
18	40.2	101.6	304.8	3.03	371	864
19	51	101.9	305.7	3.03	371	926
20	34.08	60	180	1.48	307	215
21	25.4	108	324	6.47	853	2275
22	56.99	114.3	342.9	6	342.95	1425.3
23	40.5	108	324	6.47	853	2402
24	43.9	108	1296	4	336	839
25	43.92	108	324	4	336	1235
26	77	108	324	6.47	853	2713
27	40.5	109	327	6.47	853	2446

Table A1. *Cont.*

Dataset Number	fc (MPa)	D (mm)	L (mm)	t (mm)	fy (MPa)	Pexp (KN)
28	25	114	1250	5.91	486	1177
29	37	114	850	1.79	266	515
30	37	114	850	6	486	1334
31	31.9	114.09	300.5	3.85	343	948
32	97.2	114.26	300	3.93	343	1359
33	57.6	114.29	300	3.75	343	1067
34	31.7	114.3	1143	3.35	287.3	563.6
35	31.7	114.3	342.9	3.35	287.3	816.2
36	31.7	114.3	1143	6	343	909.7
37	31.7	114.3	800.1	6	343	1000.4
38	31.7	114.3	571.5	6	343	1218.7
39	31.75	114.3	342.9	3.35	287.33	816.2
40	31.75	114.3	342.9	6	342.95	1380
41	56.9	114.3	342.9	3.35	287.33	995.7
42	25.4	108	324	6.47	853	2275
43	57	114.3	1143	3.35	287.3	904.2
44	57	114.3	571.5	3.35	287.3	937
45	57	114.3	342.9	3.35	287.3	995.7
46	57	114.3	800.1	6	343	1244.4
47	57	114.3	571.5	6	343	1389.3
48	86.1	114.3	342.9	6	343	1673.9
49	86.2	114.3	1143	3.35	287.3	1200
50	86.2	114.3	571.5	3.35	287.3	1281.4
51	86.2	114.3	1143	6	343	1389.1
52	86.2	114.3	800.1	6	343	1509.3
53	86.2	114.3	571.5	6	343	1564.7
54	86.21	114.3	342.9	3.35	287.33	1242.2
55	86.21	114.3	342.9	6	342.95	1673.9
56	88.8	114.3	342.9	3.35	287.3	1136.20
57	88.8	114.3	571.5	3.35	287.3	1180.70
58	102.4	114.3	1143	3.35	287.3	1481.2
59	102.4	114.3	800.1	3.35	287.3	1513.5
60	102.4	114.3	571.5	3.35	287.3	1598.9
61	102.4	114.3	342.9	3.35	287.3	1610.6
62	102.4	114.3	1143	6	343	1613.5
63	102.4	114.3	800.1	6	343	1788.9
64	102.4	114.3	571.5	6	343	1827.1
65	102.43	114.3	342.9	3.35	287.33	1610.6
66	102.43	114.3	342.9	6	342.95	1943.4
67	107.2	114.3	300	2.74	235	1295.10

Table A1. *Cont.*

Dataset Number	fc (MPa)	D (mm)	L (mm)	t (mm)	fy (MPa)	Pexp (KN)
68	107.2	114.3	600	5.9	355	1968.10
69	164.35	114.3	200	6.3	428	2595
70	164.35	114.3	200	6.3	428	2866
71	37.5	60	180	1.48	307	215
72	173.5	114.3	250	3.6	403	2340
73	173.5	114.3	250	3.6	403	2422
74	173.5	114.3	250	6.3	403	2610
75	31.4	114.43	300	3.98	343	948
76	57.6	114.49	299.3	3.75	343	1038
77	98.9	114.54	300	3.84	343	1359
78	40.2	101.7	305.1	3.03	371	803
79	34.7	114.88	300.5	4.91	365	1380
80	89.2	115	300	4.92	365	1787
81	57.6	115.02	300.5	5.02	365	1413
82	104.9	115.04	300	4.92	365	1787
83	23.2	101.8	305.4	3.03	371	679
84	34.08	120	360	1.48	307	610
85	34.08	120	360	1.48	307	660
86	36.6	159	650	5	390	2120
87	64.2	159	650	4.8	433	2210
88	56.1	165	581	2.82	363.3	2040
89	110.6	121	370	5	295	2016
90	116.7	121	370	5	295	1996
91	25.4	122	366	4.54	576	1509
92	25.4	122	366	4.54	576	1509
93	40.2	122	366	4.54	576	1657
94	40.5	122	366	4.54	576	1657
95	40.5	122	366	4.54	576	1663
96	40.5	122	366	4.54	576	1663
97	77	122	366	4.54	576	2100
98	77.2	122	366	4.54	576	2100
99	110.6	127.4	390	5.7	295	2217
100	116.7	127.4	390	5.7	295	2266
101	116.7	127.4	390	8.5	295	3106
102	42.1	133	465	2.9	325	476
103	42.1	133	465	4.5	325	492
104	42.1	133	465	4.5	325	576
105	42.2	133	2730	4.5	325	282
106	42.2	133	2730	4.5	325	293
107	42.2	133	1670	4.5	325	335

Table A1. *Cont.*

Dataset Number	fc (MPa)	D (mm)	L (mm)	t (mm)	fy (MPa)	Pexp (KN)
108	42.2	133	1670	4.5	325	347
109	42.2	133	1670	4.5	325	412
110	42.2	133	1670	4.5	325	430
111	42.2	133	465	2.9	325	466
112	42.2	133	465	2.9	325	476
113	42.2	133	465	4.5	325	500
114	42.2	133	465	4.5	325	559
115	42.2	133	465	4.5	325	576
116	42.2	133	465	4.5	325	591
117	42.2	133	1862	4.5	325	715
118	42.2	133	2793	4.5	325	784
119	42.2	133	2793	4.5	325	800
120	95	133	405	5	295	2002
121	110.6	133	405	5	295	2142
122	116.7	133	405	5	295	2178
123	28.2	140	635	6.68	537	2715
124	52.5	140	420	4.42	1020.00	3020
125	52.5	140	420	8.36	813	4436
126	52.5	140	420	10.46	773	5420
127	125	140	420	6.21	359	3202
128	125	140	420	8.19	389	3354
129	125	140	420	8.19	389	3398
130	125	140	420	11.58	367	4104
131	125	140	420	11.58	367	4300
132	125	140	420	4.42	1020.00	4312
133	125	140	420	4.42	1020.00	4516
134	125	140	420	16.72	389	5120
135	125	140	420	6.27	1153.00	5386
136	125	140	420	8.36	813	5502
137	125	140	420	10.46	773	6187
138	125	140	420	10.46	773	6339
139	40.5	149	447	2.96	308	1080
140	77	149	447	2.96	308	1781
141	77.1	149	447	2.96	308	1781
142	95	152	465	5.5	295	2662
143	116.7	152	465	5.5	295	2851
144	170	152.4	942.9	8.8	392.6	3919.9
145	170	152.4	551.9	8.8	392.6	4200.8
146	178.4	152.4	940.2	6.3	373.4	3584.7
147	178.4	152.4	552.7	6.3	373.4	4033

Table A1. *Cont.*

Dataset Number	fc (MPa)	D (mm)	L (mm)	t (mm)	fy (MPa)	Pexp (KN)
148	178.8	152.4	943.8	8.8	392.6	4099.8
149	180.9	152.4	949.7	5	445.9	3383.4
150	182.8	152.4	950.5	5	445.9	3995.7
151	182.8	152.4	540.7	5	445.9	4224
152	185.7	152.4	947.3	6.3	373.4	3535.3
153	185.7	152.4	554.7	6.3	373.4	3808
154	185.7	152.4	951.3	8.8	392.6	4178.7
155	185.7	152.4	559.7	8.8	392.6	4288.5
156	185.8	152.4	951.3	5	445.9	3724.1
157	185.8	152.4	548.5	5	445.9	3997.5
158	188.1	152.4	553	6.3	373.4	3692.8
159	188.1	152.4	948.5	6.3	373.4	3861.1
160	42	152.6	304.9	4.93	633.4	2909.10
161	43.4	152.6	304.9	4.9	633.4	2913.60
162	37.5	120	360	1.48	307	660
163	36.6	159	650	6.8	402	2830
164	36.6	159	650	10	355	3400
165	64.1	159	650	4.8	433	2210
166	38	165	571	2.82	363.3	1649
167	37.5	120	360	1.48	307	660
168	48.3	190	658	1.52	306.1	1841
169	48.2	165	562.5	2.82	363.3	1759
170	64.5	159	650	4.8	433	2240
171	93.6	159	650	5	390	2970
172	93.6	159	650	10	355	3400
173	93.8	159	650	5	390	2970
174	93.8	159	650	6.8	402	3410
175	106	159.6	3500	4.98	270	1454
176	71	159.7	2500	5.2	281	1562
177	101	159.7	3000	4.97	275	1636
178	70	159.8	2000	5.01	283	1650
179	73	159.8	3000	5.1	276	1468
180	100	159.8	2500	5.01	275	1818
181	102	159.8	4000	4.97	270	1333
182	45	159.9	4000	4.98	281	1091
183	40	160.1	2000	4.98	280	1261
184	74	160.1	3500	4.98	276	1326
185	100	160.1	200	4.99	275	2550
186	41	160.2	2500	4.96	281	1244
187	71	160.2	4000	5.02	281	1231

Table A1. *Cont.*

Dataset Number	fc (MPa)	D (mm)	L (mm)	t (mm)	fy (MPa)	Pexp (KN)
188	43	160.3	3000	5	270	1236
189	99	160.3	2000	5.03	281	2000
190	158.46	164.2	652	2.5	377	3501
191	64.3	159	650	4.8	433	2210
192	38.1	165	571	2.82	363.3	1649
193	64.2	159	650	4.8	433	2240
194	48.1	165	562.5	2.82	363.3	1759
195	38.1	190	657	1.13	185.7	1308
196	37.5	120	360	1.48	307	610
197	34	120	360	1.48	307	660
198	95.8	168.6	645	3.9	363	3339
199	56.4	165	581	2.82	363.3	2040
200	67.9	165	500	2.76	350	2250
201	67.94	165	500	2.81	350	2160
202	67.94	165	500	2.76	350	2250
203	77	165	571	1.82	363.3	2608
204	34.08	180	540	1.48	307	1280
205	80.2	165	580.5	2.82	363.3	2295
206	108	165	577.5	2.82	363.3	2673
207	74.7	190	663.5	0.86	210.7	2451
208	29.5	165.2	200	3.7	366	1630.56
209	43.5	165.2	200	3.7	366	1676.42
210	43.5	165.2	200	3.7	366	1737.94
211	58	165.2	200	3.7	366	2094.15
212	58	165.2	200	3.7	366	2221.62
213	81.6	165.2	200	3.7	366	2511.3
214	81.6	165.2	200	3.7	366	2922.24
215	158.7	168.1	645	8.1	409	5254
216	48.2	190	658	1.52	306.1	1841
217	36.2	168.6	645	3.9	363	1771
218	56.3	165	581	2.82	363.3	2040
219	95.8	168.6	645	3.9	363	3339
220	165.49	168.6	648	3.9	363	4216
221	77.1	190	664	0.86	210.7	2553
222	158.75	168.7	645	5.2	405	4751
223	151.9	168.8	650	5.7	452	4930
224	56.4	190	664.5	0.86	210.7	1940
225	167.87	169	645	4.8	399	4330
226	38.2	165	571	2.82	363.3	1649
227	34	180	540	1.48	307	1280

Table A1. *Cont.*

Dataset Number	fc (MPa)	D (mm)	L (mm)	t (mm)	fy (MPa)	Pexp (KN)
228	38.2	216.5	649.5	6.61	452	4200
229	34.08	180	540	1.48	307	1311
230	37.2	180	540	1.48	307	1280
231	64.4	159	650	4.8	433	2210
232	37.5	180	540	1.48	307	1311
233	158.46	189	756	3	398	4837
234	38	190	657.5	0.86	210.7	1240
235	38	190	657	1.13	185.7	1308
236	38.1	190	657.5	0.86	210.7	1240
237	108	190	660	1.94	256.4	3360
238	38.1	190	659.5	1.94	256.4	1652
239	38.2	190	657.5	0.86	210.7	1240
240	41.1	300	900	2.96	279	3277
241	77.1	165	571	2.82	363.3	2608
242	48.1	190	658	1.52	306.1	1841
243	151.91	168.8	650	5.7	452	4930
244	77.2	190	656	1.94	256.4	3083
245	56.1	190	664.5	0.86	210.7	1940
246	56.2	190	661.5	1.13	185.7	1862
247	56.2	190	664.5	0.86	210.7	1940
248	56.2	190	655.5	1.94	256.4	2338
249	56.4	190	661.5	1.13	185.7	1862
250	165.5	168.6	648	3.9	363	4216
251	37.5	180	540	1.48	307	1280
252	74.2	190	657.5	0.86	210.7	2433
253	113.5	190	660	2	271.9	3360
254	113.5	165	577.5	3	364.3	2673
255	74.7	190	663.5	1.94	256.4	2592
256	77	190	664	0.86	210.7	2553
257	77	190	658	1.52	306.1	2830
258	77	222	666	6.47	843	7304
259	167.9	169	645	4.8	399	4330
260	77.1	190	658	1.52	306.1	2830
261	77.1	190	656	1.94	256.4	3083
262	39.2	318.4	955.2	10.37	335	7742
263	24.3	216.5	649.5	6.61	452	3568
264	80.1	190	662.5	1.13	185.7	2295
265	80.2	190	663.5	1.52	306.1	2602
266	80.2	190	658.5	1.52	306.1	2870
267	85.1	450	1350.00	2.96	279	11,665

Table A1. *Cont.*

Dataset Number	fc (MPa)	D (mm)	L (mm)	t (mm)	fy (MPa)	Pexp (KN)
268	108	190	661	1.13	185.7	3220
269	108	190	661.5	1.52	306.1	3260
270	38.2	190	659.5	1.94	256.4	1652
271	108.1	190	661.5	1.13	185.7	3220
272	40.5	222	666	6.47	843	5714
273	113.5	190	660	1.15	184.8	3058
274	113.5	190	662	0.95	211.2	3070
275	113.5	190	661.5	1.55	315.3	3260
276	25.4	337	1011.00	6.47	823	8475
277	46.7	216.4	649.2	6.61	452	4283
278	24.1	216.5	649.5	6.61	452	3568
279	56.4	190	655.5	1.94	256.4	2338
280	38.1	216.5	649.5	6.61	452	4200
281	41.1	337	1011	6.47	823	9835
282	108	219	708	6.3	300	5410
283	148.8	219.1	600	6.3	300	6838
284	163	219.1	600	6.3	300	6915
285	174.5	219.1	600	6.3	300	7569
286	175.4	219.1	600	6.3	300	7407
287	185.1	219.1	600	5	380	7837
288	185.1	219.1	600	10	381	9085
289	25.4	222	666	6.47	843	4964
290	108.2	190	661	1.13	185.7	3220
291	26.9	550	1000.00	16	546	28,830
292	77	222	666	6.47	843	7304
293	77.2	190	658	1.52	306.1	2830
294	40.5	238	714	4.54	507	3583
295	40.5	238	714	4.54	507	3647
296	25.4	239	717	4.54	507	3035
297	74.7	190	657.5	0.86	210.7	2433
298	34.08	240	720	1.48	307	2150
299	34.08	240	720	1.48	307	2300
300	41.1	337	1011.00	6.47	823	9668
301	37.5	240	720	1.48	307	2150
302	41.1	361	1083	4.54	525	7260
303	38.2	190	657	1.13	185.7	1308
304	25.4	301	903	2.96	279	2382
305	80.3	301	903	2.96	279	5540
306	52.2	318.3	954.9	10.37	335	9297
307	39.1	318.4	955.2	10.37	335	7742

Table A1. *Cont.*

Dataset Number	fc (MPa)	D (mm)	L (mm)	t (mm)	fy (MPa)	Pexp (KN)
308	77	190	656	1.94	256.4	3083
309	24.2	318.5	955.5	10.37	335	6901
310	92.3	323.9	1000.00	5.6	443.9	11,481
311	25.4	337	1011	6.47	823	8475
312	34.01	240	720	1.48	307	2300
313	41.1	337	1011	6.47	823	9668
314	158.75	168.1	645	8.1	409	5254
315	37.5	240	720	1.48	307	2300
316	41.1	337	1011.00	6.47	823	9835
317	85.1	337	1011	6.47	823	13,776
318	41.1	360	1080	4.54	525	7045
319	85.1	360	1080	4.54	525	11,505
320	37.2	240	720	1.48	307	2300
321	41.1	361	1083.00	4.54	525	7260
322	25.4	450	1350	2.96	279	4415
323	41.1	450	1350	2.96	279	6870
324	41.1	450	1350	2.96	279	6985
325	85.1	450	1350	2.96	279	11,665
326	108	190	660	1.13	185.7	3058
327	40.5	222	666	6.47	843	5714
328	26.9	550	1000.00	16	546	29,590
329	37.5	60	180	1.48	307	215
330	103.4	100	300	1.9	404	1085.00
331	51.3	101.5	304.5	3.03	371	859
332	33.9	101.7	203.3	3.07	605.1	1067.60
333	23.2	101.8	305.4	3.03	371	632
334	40.5	109	327	6.47	853	2446
335	25	114	1280	5.94	486	1285
336	37	114	850	3.35	291	785
337	37	114	850	4.44	332	902
338	31.7	114.3	800.1	3.35	287.3	736.8
339	31.7	114.3	571.5	3.35	287.3	749.4
340	31.7	114.3	342.9	6	343	1380
341	31.9	114.3	300	3.85	343	998
342	57	114.3	800.1	3.35	287.3	932.9
343	57	114.3	1143	6	343	1141.3
344	57	114.3	342.9	6	343	1425.3
345	86.2	114.3	800.1	3.35	287.3	1206.5
346	86.2	114.3	342.9	3.35	287.3	1242.2
347	102.4	114.3	342.9	6	343	1943.4

Table A1. *Cont.*

Dataset Number	fc (MPa)	D (mm)	L (mm)	t (mm)	fy (MPa)	Pexp (KN)
348	105.5	114.3	571.5	3.35	287.3	1407.10
349	105.5	114.3	342.9	3.35	287.3	1453.10
350	107.2	114.3	600	2.74	235	1296.60
351	107.2	114.3	300	5.9	355	1989.90
352	173.5	114.3	250	6.3	403	2633
353	98.9	114.37	299.5	3.85	343	1182
354	34.7	114.43	300	3.82	343	929
355	84.1	114.5	300	3.84	343	1359
356	79.6	114.6	300	3.99	343	1308
357	77.1	190	662	1.13	185.7	2630
358	95	127.4	390	8.5	295	2544
359	110.6	127.4	390	8.5	295	2623
360	42.2	133	2730	4.5	325	268
361	42.2	133	1670	4.5	325	416
362	42.2	133	465	4.5	325	568
363	42.2	133	465	4.5	325	582
364	42.2	133	1862	4.5	325	882
365	52.5	140	420	6.27	1153.00	4274
366	125	140	420	6.21	359	3215
367	125	140	420	16.72	389	5135
368	125	140	420	6.27	1153.00	5354
369	95	127.4	390	5.7	295	2078
370	25.4	149	447	2.96	308	941
371	40.5	149	447	2.96	308	1064
372	110.6	152	465	5.5	295	2734
373	178.8	152.4	549.8	8.8	392.6	4354.1
374	93.8	159	650	10	355	3400
375	77.1	190	662.5	1.13	185.7	2630
376	80	190	658.5	1.52	306.1	2870
377	158.5	164.2	652	2.5	377	3501
378	67.9	165	500	2.81	350	2160
379	41	160.2	3500	4.97	273	1193
380	29.5	165.2	200	3.7	366	1428.32
381	36.2	168.6	645	3.9	363	1771
382	158.7	168.7	645	5.2	405	4751
383	158.5	189	756	3	398	4837
384	38.2	190	659.5	1.94	256.4	1652
385	56.4	190	661.5	1.13	185.7	1862
386	56.4	190	655.5	1.94	256.4	2338
387	74.7	190	657.5	0.86	210.7	2433

Table A1. *Cont.*

Dataset Number	fc (MPa)	D (mm)	L (mm)	t (mm)	fy (MPa)	Pexp (KN)
388	77.1	190	664	0.86	210.7	2553
389	93.8	159	650	6.8	402	3410
390	125	140	420	8.36	813	5531
391	77.1	190	662	1.13	185.7	2630
392	77	165	571	2.82	363.3	2608
393	80.2	190	658.5	1.52	306.1	2870
394	108	190	662	0.86	210.7	3070
395	46.7	216.4	649.2	6.61	452	4283
396	25.4	222	666	6.47	843	4964
397	40.4	222	666	6.47	843	5638
398	40.5	222	666	6.47	843	5638
399	77	238	714	4.54	507	5578
400	77	238	714	4.54	507	5578
401	41.1	300	900	2.96	279	3152
402	80.3	301	903	2.96	279	5540
403	52.2	318.3	954.9	10.37	335	9297
404	24.2	318.5	955.5	10.37	335	6901
405	85.1	337	1011.00	6.47	823	13,776
406	41.1	360	1080.00	4.54	525	7045
407	85.1	360	1080.00	4.54	525	11,505
408	25.2	361	1083.00	4.54	525	5633
409	25.4	361	1083	4.54	525	5633
410	26.9	550	1000.00	16	546	29,050

References

1. Wang, F.; Han, L.; Li, W. Analytical behavior of CFDST stub columns with external stainless steel tubes under axial compression. *Thin-Walled Struct.* **2018**, *127*, 756–768. [CrossRef]
2. Design, A.S. Specification for structural steel buildings. *AISC Dec.* **1999**, *27*, 1–210.
3. Nishiyama, I. *Summary of Research on Concrete-Filled Structural Steel Tube Column System Carried out under the US-Japan Cooperative Research Program on Composite and Hybrid Structures*; Building Research Institution: Uttarakhand, India, 2002.
4. Kim, D.K. A Database for Composite Columns. 2005. Available online: http://hdl.handle.net/1853/7126 (accessed on 20 May 2005).
5. Han, L.H. *Concrete Filled Steel Tube Structures-Theory and Application*; Science Press: Beijing, China, 2007.
6. Cederwall, K.; Engstrom, B.; Grauers, M. High-strength concrete used in composite columns. *Spec. Publ.* **1990**, *121*, 195–214.
7. Varma, A.H. *Seismic Behavior, Analysis, and Design of High Strength Square Concrete Filled Steel Tube (CFT) Columns*; Lehigh University: Bethlehem, PA, USA, 2001.
8. Uy, B. Strength of short concrete filled high strength steel box columns. *J. Constr. Steel Res.* **2001**, *57*, 113–134. [CrossRef]
9. Liu, D.; Gho, W.-M.; Yuan, J. Ultimate capacity of high-strength rectangular concrete-filled steel hollow section stub columns. *J. Constr. Steel Res.* **2003**, *59*, 1499–1515. [CrossRef]
10. Mursi, M.; Uy, B. Strength of slender concrete filled high strength steel box columns. *J. Constr. Steel Res.* **2004**, *60*, 1825–1848. [CrossRef]
11. Sakino, K.; Nakahara, H.; Morino, S.; Nishiyama, I. Behavior of centrally loaded concrete-filled steel-tube short columns. *J. Struct. Eng.* **2004**, *130*, 180–188. [CrossRef]
12. Lue, D.M.; Liu, J.-L.; Yen, T. Experimental study on rectangular CFT columns with high-strength concrete. *J. Constr. Steel Res.* **2007**, *63*, 37–44. [CrossRef]
13. Aslani, F.; Uy, B.; Tao, Z.; Mashiri, F. Behaviour and design of composite columns incorporating compact high-strength steel plates. *J. Constr. Steel Res.* **2015**, *107*, 94–110. [CrossRef]

14. Xiong, M.-X.; Xiong, D.-X.; Liew, J.Y.R. Axial performance of short concrete filled steel tubes with high-and ultra-high-strength materials. *Eng. Struct.* **2017**, *136*, 494–510. [CrossRef]
15. Lai, Z.; Varma, A.H. High-strength rectangular CFT members: Database, modeling, and design of short columns. *J. Struct. Eng.* **2018**, *144*, 4018036. [CrossRef]
16. Gardner, N.J.; Jacobson, E.R. Structural behavior of concrete filled steel tubes. *J. Proc.* **1967**, *64*, 404–413.
17. Bergmann, R. Load introduction in composite columns filled with high strength concrete. In *Tubular Structures VI*; Routledge: Oxfordshire, UK, 2021; pp. 373–380.
18. O'Shea, M.D.; Bridge, R.Q. Circular thin-walled tubes with high strength concrete infill. In Proceedings of the Composite Construction in Steel and Concrete III, New York, NY, USA, 9–14 June 1996; pp. 780–793.
19. Schneider, S.P. Axially loaded concrete-filled steel tubes. *J. Struct. Eng.* **1998**, *124*, 1125–1138. [CrossRef]
20. O'Shea, M.D.; Bridge, R.Q. Design of circular thin-walled concrete filled steel tubes. *J. Struct. Eng.* **2000**, *126*, 1295–1303. [CrossRef]
21. Giakoumelis, G.; Lam, D. Axial capacity of circular concrete-filled tube columns. *J. Constr. Steel Res.* **2004**, *60*, 1049–1068. [CrossRef]
22. Zeghiche, J.; Chaoui, K. An experimental behaviour of concrete-filled steel tubular columns. *J. Constr. Steel Res.* **2005**, *61*, 53–66. [CrossRef]
23. Yu, Q.; Tao, Z.; Wu, Y.-X. Experimental behaviour of high performance concrete-filled steel tubular columns. *Thin-Walled Struct.* **2008**, *46*, 362–370. [CrossRef]
24. de Oliveira, W.L.A.; De Nardin, S.; de Cresce El, A.L.H.; El Debs, M.K. Influence of concrete strength and length/diameter on the axial capacity of CFT columns. *J. Constr. Steel Res.* **2009**, *65*, 2103–2110. [CrossRef]
25. Liew, J.Y.R.; Xiong, D.X. Effect of preload on the axial capacity of concrete-filled composite columns. *J. Constr. Steel Res.* **2009**, *65*, 709–722. [CrossRef]
26. Chen, G.; Xu, Z.; Yang, Z.; Tian, Z. Experimental study on behavior of short steel tubular columns filled with ultra-high strength concrete mixed with stone-chip subjected to axial load. *J. Build. Struct.* **2011**, *32*, 82–89.
27. Tang, D.; Gordan, B.; Koopialipoor, M.; Jahed Armaghani, D.; Tarinejad, R.; Thai Pham, B.; Huynh, V. Van seepage analysis in short embankments using developing a metaheuristic method based on governing equations. *Appl. Sci.* **2020**, *10*, 1761. [CrossRef]
28. Ye, J.; Koopialipoor, M.; Zhou, J.; Armaghani, D.J.; He, X. A novel combination of tree-based modeling and monte carlo simulation for assessing risk levels of flyrock induced by mine blasting. *Nat. Resour. Res.* **2020**, *30*, 225–243. [CrossRef]
29. Yang, H.; Wang, Z.; Song, K. A new hybrid grey wolf optimizer-feature weighted-multiple kernel-support vector regression technique to predict TBM performance. *Eng. Comput.* **2020**, 1–17. [CrossRef]
30. Zhou, J.; Chen, C.; Wang, M.; Khandelwal, M. Proposing a novel comprehensive evaluation model for the coal burst liability in underground coal mines considering uncertainty factors. *Int. J. Min. Sci. Technol.* **2021**, *31*, 799–812. [CrossRef]
31. Zhou, J.; Qiu, Y.; Khandelwal, M.; Zhu, S.; Zhang, X. Developing a hybrid model of Jaya algorithm-based extreme gradient boosting machine to estimate blast-induced ground vibrations. *Int. J. Rock Mech. Min. Sci.* **2021**, *145*, 104856. [CrossRef]
32. Zhou, J.; Li, X.; Mitri, H.S. Classification of rockburst in underground projects: Comparison of ten supervised learning methods. *J. Comput. Civ. Eng.* **2016**, *30*, 4016003. [CrossRef]
33. Asteris, P.G.; Cavaleri, L.; Ly, H.-B.; Pham, B.T. Surrogate models for the compressive strength mapping of cement mortar materials. *Soft Comput.* **2021**, *25*, 6347–6372. [CrossRef]
34. Harandizadeh, H.; Armaghani, D.; Asteris Panagiotis, G.; Gandomi, A.H. TBM performance prediction developing a hybrid ANFIS-PNN predictive model optimized by imperialism competitive algorithm. *Neural. Comput. Appl.* **2021**, *33*, 16149–16179. [CrossRef]
35. Mohammed, A.S.; Asteris, P.G.; Koopialipoor, M.; Alexakis, D.E.; Lemonis, M.E.; Armaghani, D.J. Stacking ensemble tree models to predict energy performance in residential buildings. *Sustainability* **2021**, *13*, 8298. [CrossRef]
36. Armaghani, D.J.; Mamou, A.; Maraveas, C.; Roussis, P.C.; Siorikis, V.G.; Skentou, A.D.; Asteris, P.G. Predicting the unconfined compressive strength of granite using only two non-destructive test indexes. *Geomech. Eng.* **2021**, *25*, 317–330.
37. Ke, B.; Khandelwal, M.; Asteris, P.G.; Skentou, A.D.; Mamou, A.; Armaghani, D.J. Rock-burst occurrence prediction based on optimized Naïve Bayes models. *IEEE Access.* **2021**, *9*, 91347–91360. [CrossRef]
38. Asteris, P.G.; Lourenço, P.B.; Hajihassani, M.; Adami, C.-E.N.; Lemonis, M.E.; Skentou, A.D.; Marques, R.; Nguyen, H.; Rodrigues, H.; Varum, H. Soft computing-based models for the prediction of masonry compressive strength. *Eng. Struct.* **2021**, *248*, 113276. [CrossRef]
39. Yang, H.; Koopialipoor, M.; Armaghani, D.J.; Gordan, B.; Khorami, M.; Tahir, M.M. Intelligent design of retaining wall structures under dynamic conditions. *STEEL Compos. Struct.* **2019**, *31*, 629–640.
40. Asteris, P.G.; Lemonis, M.E.; Le, T.-T.; Tsavdaridis, K.D. Evaluation of the ultimate eccentric load of rectangular CFSTs using advanced neural network modeling. *Eng. Struct.* **2021**, *248*, 113297. [CrossRef]
41. Nguyen, N.-H.; Vo, T.P.; Lee, S.; Asteris, P.G. Heuristic algorithm-based semi-empirical formulas for estimating the compressive strength of the normal and high performance concrete. *Constr. Build. Mater.* **2021**, *304*, 124467. [CrossRef]
42. Asteris, P.G.; Lemonis, M.E.; Nguyen, T.-A.; Van Le, H.; Pham, B.T. Soft computing-based estimation of ultimate axial load of rectangular concrete-filled steel tubes. *Steel Compos. Struct.* **2021**, *39*, 471.
43. Colesanti, C.; Wasowski, J. Investigating landslides with space-borne Synthetic Aperture Radar (SAR) interferometry. *Eng. Geol.* **2006**, *88*, 173–199. [CrossRef]

44. Asteris, P.G.; Skentou, A.D.; Bardhan, A.; Samui, P.; Lourenço, P.B. Soft computing techniques for the prediction of concrete compressive strength using Non-Destructive tests. *Constr. Build. Mater.* **2021**, *303*, 124450. [CrossRef]
45. Asteris, P.G.; Skentou, A.D.; Bardhan, A.; Samui, P.; Pilakoutas, K. Predicting concrete compressive strength using hybrid ensembling of surrogate machine learning models. *Cem. Concr. Res.* **2021**, *145*, 106449. [CrossRef]
46. Bardhan, A.; Gokceoglu, C.; Burman, A.; Samui, P.; Asteris, P.G. Efficient computational techniques for predicting the California bearing ratio of soil in soaked conditions. *Eng. Geol.* **2021**, *291*, 106239. [CrossRef]
47. Parsajoo, M.; Armaghani, D.J.; Mohammed, A.S.; Khari, M.; Jahandari, S. Tensile strength prediction of rock material using non-destructive tests: A comparative intelligent study. *Transp. Geotech.* **2021**, *31*, 100652. [CrossRef]
48. Parsajoo, M.; Armaghani, D.J.; Asteris, P.G. A precise neuro-fuzzy model enhanced by artificial bee colony techniques for assessment of rock brittleness index. *Neural. Comput. Appl.* **2021**, 1–19. [CrossRef]
49. Pham, B.T.; Nguyen, M.D.; Nguyen-Thoi, T.; Ho, L.S.; Koopialipoor, M.; Quoc, N.K.; Armaghani, D.J.; Van Le, H. A novel approach for classification of soils based on laboratory tests using Adaboost, Tree and ANN modeling. *Transp. Geotech.* **2020**, *27*, 100508. [CrossRef]
50. Mohamad, E.T.; Koopialipoor, M.; Murlidhar, B.R.; Rashiddel, A.; Hedayat, A.; Armaghani, D.J. A new hybrid method for predicting ripping production in different weathering zones through in-situ tests. *Measurement* **2019**, *147*, 106826. [CrossRef]
51. Cai, M.; Koopialipoor, M.; Armaghani, D.J.; Thai Pham, B. Evaluating slope deformation of earth dams due to earthquake shaking using MARS and GMDH techniques. *Appl. Sci.* **2020**, *10*, 1486. [CrossRef]
52. Huang, J.; Koopialipoor, M.; Armaghani, D.J. A combination of fuzzy Delphi method and hybrid ANN-based systems to forecast ground vibration resulting from blasting. *Sci. Rep.* **2020**, *10*, 1–21. [CrossRef] [PubMed]
53. Guo, H.; Zhou, J.; Koopialipoor, M.; Armaghani, D.J.; Tahir, M.M. Deep neural network and whale optimization algorithm to assess flyrock induced by blasting. *Eng. Comput.* **2019**, *37*, 173–186. [CrossRef]
54. Xu, C.; Gordan, B.; Koopialipoor, M.; Armaghani, D.J.; Tahir, M.M.; Zhang, X. Improving performance of retaining walls under dynamic conditions developing an optimized ANN based on ant colony optimization technique. *IEEE Access* **2019**, *7*, 94692–94700. [CrossRef]
55. Yang, H.Q.; Xing, S.G.; Wang, Q.; Li, Z. Model test on the entrainment phenomenon and energy conversion mechanism of flow-like landslides. *Eng. Geol.* **2018**, *239*, 119–125. [CrossRef]
56. Huang, L.; Asteris, P.G.; Koopialipoor, M.; Armaghani, D.J.; Tahir, M.M. Invasive weed optimization technique-based ANN to the prediction of rock tensile strength. *Appl. Sci.* **2019**, *9*, 5372. [CrossRef]
57. Lu, S.; Koopialipoor, M.; Asteris, P.G.; Bahri, M.; Armaghani, D.J. A novel feature selection approach based on tree models for evaluating the punching shear capacity of steel fiber-reinforced concrete flat slabs. *Materials* **2020**, *13*, 3902. [CrossRef]
58. Asteris, P.G.; Koopialipoor, M.; Armaghani, D.J.; Kotsonis, E.A.; Lourenço, P.B. Prediction of cement-based mortars compressive strength using machine learning techniques. *Neural Comput. Appl.* **2021**, *33*, 13089–13121. [CrossRef]
59. Gao, J.; Koopialipoor, M.; Armaghani, D.J.; Ghabussi, A.; Baharom, S.; Morasaei, A.; Shariati, A.; Khorami, M.; Zhou, J. Evaluating the bond strength of FRP in concrete samples using machine learning methods. *Smart Struct. Syst.* **2020**, *26*, 403–418.
60. Sarir, P.; Chen, J.; Asteris, P.G.; Armaghani, D.J.; Tahir, M.M. Developing GEP tree-based, neuro-swarm, and whale optimization models for evaluation of bearing capacity of concrete-filled steel tube columns. *Eng. Comput.* **2019**, *37*, 1–19. [CrossRef]
61. Ahmadi, M.; Naderpour, H.; Kheyroddin, A. ANN model for predicting the compressive strength of circular steel-confined concrete. *Int. J. Civ. Eng.* **2017**, *15*, 213–221. [CrossRef]
62. Ahmadi, M.; Naderpour, H.; Kheyroddin, A. Utilization of artificial neural networks to prediction of the capacity of CCFT short columns subject to short term axial load. *Arch. Civ. Mech. Eng.* **2014**, *14*, 510–517. [CrossRef]
63. Güneyisi, E.M.; Gültekin, A.; Mermerdaş, K. Ultimate capacity prediction of axially loaded CFST short columns. *Int. J. Steel Struct.* **2016**, *16*, 99–114. [CrossRef]
64. Ipek, S.; Güneyisi, E.M. Ultimate axial strength of concrete-filled double skin steel tubular column sections. *Adv. Civ. Eng.* **2019**, *2019*. [CrossRef]
65. Moon, J.; Kim, J.J.; Lee, T.-H.; Lee, H.-E. Prediction of axial load capacity of stub circular concrete-filled steel tube using fuzzy logic. *J. Constr. Steel Res.* **2014**, *101*, 184–191. [CrossRef]
66. Al-Khaleefi, A.M.; Terro, M.J.; Alex, A.P.; Wang, Y. Prediction of fire resistance of concrete filled tubular steel columns using neural networks. *Fire Saf. J.* **2002**, *37*, 339–352. [CrossRef]
67. Ren, Q.; Li, M.; Zhang, M.; Shen, Y.; Si, W. Prediction of ultimate axial capacity of square concrete-filled steel tubular short columns using a hybrid intelligent algorithm. *Appl. Sci.* **2019**, *9*, 2802. [CrossRef]
68. Tran, V.-L.; Thai, D.-K.; Kim, S.-E. Application of ANN in predicting ACC of SCFST column. *Compos. Struct.* **2019**, *228*, 111332. [CrossRef]
69. Lee, S.; Vo, T.P.; Thai, H.-T.; Lee, J.; Patel, V. Strength prediction of concrete-filled steel tubular columns using Categorical Gradient Boosting algorithm. *Eng. Struct.* **2021**, *238*, 112109. [CrossRef]
70. Zarringol, M.; Thai, H.-T.; Thai, S.; Patel, V. Application of ANN to the design of CFST columns. *Structures* **2020**, *28*, 2203–2220. [CrossRef]
71. The European Union. *European C. for Design of Composite Steel and Concrete Structures*; CEN: Salt Lake City, UT, USA, 1994.
72. Committee, A. *Specification for Structural Steel Buildings*; ANSI/AISC 360-10; American Institute of Steel Construction: Chicago, IL, USA, 22 June 2010.

73. AIJ. Recommendations for design and construction of concrete filled steel tubular structures. *Open J. Civ. Eng.* **1997**, *3*, 3.
74. Zadeh, L.A. A fuzzy-algorithmic approach to the definition of complex or imprecise concepts. *Int. J. Man. Mach. Stud.* **1976**, *8*, 249–291. [CrossRef]
75. Wang, L.-X. *A Course in Fuzzy Systems*; Prentice-Hall International, Inc.: Hoboken, NJ, USA, 1999.
76. Ali, M.M.; Khompatraporn, C.; Zabinsky, Z.B. A numerical evaluation of several stochastic algorithms on selected continuous global optimization test problems. *J. Glob. Optim.* **2005**, *31*, 635–672. [CrossRef]
77. Yang, X.-S. Firefly algorithm, stochastic test functions and design optimisation. *Int. J. Bio-Inspired Comput.* **2010**, *2*, 78–84. [CrossRef]
78. Kaur, M.; Ghosh, S. Network reconfiguration of unbalanced distribution networks using fuzzy-firefly algorithm. *Appl. Soft Comput.* **2016**, *49*, 868–886. [CrossRef]
79. Zhang, Y.; Wu, L. A novel method for rigid image registration based on firefly algorithm. *Int. J. Res. Rev. Soft Intell. Comput.* **2012**, *2*, 141–146.
80. Apostolopoulos, T.; Vlachos, A. Application of the firefly algorithm for solving the economic emissions load dispatch problem. *Int. J. Comb.* **2010**, *2011*. [CrossRef]
81. Koopialipoor, M.; Fahimifar, A.; Ghaleini, E.N.; Momenzadeh, M.; Armaghani, D.J. Development of a new hybrid ANN for solving a geotechnical problem related to tunnel boring machine performance. *Eng. Comput.* **2019**, *36*, 345–357. [CrossRef]
82. Koopialipoor, M.; Noorbakhsh, A.; Noroozi Ghaleini, E.; Jahed Armaghani, D.; Yagiz, S. A new approach for estimation of rock brittleness based on non-destructive tests. *Nondestruct. Test. Eval.* **2019**, *34*, 354–375. [CrossRef]
83. Gholizadeh, S.; Barati, H. A comprative study of three metaheuristics for optimum design of trusses. *Int. J. Optim. Civ. Eng.* **2012**, *2*, 3.
84. Hancer, E.; Xue, B.; Zhang, M. Differential evolution for filter feature selection based on information theory and feature ranking. *Knowl. Based Syst.* **2018**, *140*, 103–119. [CrossRef]
85. Bidar, M.; Sadaoui, S.; Mouhoub, M.; Bidar, M. Enhanced firefly algorithm using fuzzy parameter tuner. *Comput. Inf. Sci.* **2018**, *11*, 26–51. [CrossRef]
86. Mai, S.H.; Seghier, M.E.A.B.; Nguyen, P.L.; Jafari-Asl, J.; Thai, D.-K. A hybrid model for predicting the axial compression capacity of square concrete-filled steel tubular columns. *Eng. Comput.* **2020**, 1–18. [CrossRef]
87. Wang, Y.; Geng, Y.; Ranzi, G.; Zhang, S. Time-dependent behaviour of expansive concrete-filled steel tubular columns. *J. Constr. Steel Res.* **2011**, *67*, 471–483. [CrossRef]
88. Geng, Y.; Wang, Y.; Chen, J. Time-dependent behaviour of steel tubular columns filled with recycled coarse aggregate concrete. *J. Constr. Steel Res.* **2016**, *122*, 455–468. [CrossRef]
89. Dong, J.F.; Wang, Q.Y.; Guan, Z.W. Structural behaviour of recycled aggregate concrete filled steel tube columns strengthened by CFRP. *Eng. Struct.* **2013**, *48*, 532–542. [CrossRef]
90. Wang, Y.; Chen, J.; Geng, Y. Testing and analysis of axially loaded normal-strength recycled aggregate concrete filled steel tubular stub columns. *Eng. Struct.* **2015**, *86*, 192–212. [CrossRef]
91. Chen, J.; Wang, Y.; Roeder, C.W.; Ma, J. Behavior of normal-strength recycled aggregate concrete filled steel tubes under combined loading. *Eng. Struct.* **2017**, *130*, 23–40. [CrossRef]
92. Yang, Y.-F.; Ma, G.-L. Experimental behaviour of recycled aggregate concrete filled stainless steel tube stub columns and beams. *Thin-Walled Struct.* **2013**, *66*, 62–75. [CrossRef]
93. Wang, Y.; Geng, Y.; Chang, Y.; Zhou, C. Time-dependent behaviour of recycled concrete filled steel tubes using RCA from different parent waste material. *Constr. Build. Mater.* **2018**, *193*, 230–243. [CrossRef]
94. Wei, J.; Luo, X.; Lai, Z.; Varma, A.H. Experimental behavior and design of high-strength circular concrete-filled steel tube short columns. *J. Struct. Eng.* **2020**, *146*, 4019184. [CrossRef]
95. Le Hoang, A.; Fehling, E. Numerical study of circular steel tube confined concrete (STCC) stub columns. *J. Constr. Steel Res.* **2017**, *136*, 238–255. [CrossRef]
96. He, L.; Zhao, Y.; Lin, S. Experimental study on axially compressed circular CFST columns with improved confinement effect. *J. Constr. Steel Res.* **2018**, *140*, 74–81. [CrossRef]
97. Koopialipoor, M.; Jahed Armaghani, D.; Haghighi, M.; Ghaleini, E.N. A neuro-genetic predictive model to approximate overbreak induced by drilling and blasting operation in tunnels. *Bull. Eng. Geol. Environ.* **2017**, *78*, 981–990. [CrossRef]
98. Koopialipoor, M.; Ghaleini, E.N.; Tootoonchi, H.; Jahed Armaghani, D.; Haghighi, M.; Hedayat, A. Developing a new intelligent technique to predict overbreak in tunnels using an artificial bee colony-based ANN. *Environ. Earth Sci.* **2019**, *78*, 165. [CrossRef]
99. Yu, C.; Koopialipoor, M.; Murlidhar, B.R.; Mohammed, A.S.; Armaghani, D.J.; Mohamad, E.T.; Wang, Z. Optimal ELM–Harris Hawks optimization and ELM–Grasshopper optimization models to forecast peak particle velocity resulting from mine blasting. *Nat. Resour. Res.* **2021**, *30*, 2647–2662. [CrossRef]
100. Koopialipoor, M.; Nikouei, S.S.; Marto, A.; Fahimifar, A.; Armaghani, D.J.; Mohamad, E.T. Predicting tunnel boring machine performance through a new model based on the group method of data handling. *Bull. Eng. Geol. Environ.* **2018**, *78*, 3799–3813. [CrossRef]
101. Armaghani, D.J.; Koopialipoor, M.; Bahri, M.; Hasanipanah, M.; Tahir, M.M. A SVR-GWO technique to minimize flyrock distance resulting from blasting. *Bull. Eng. Geol. Environ.* **2020**, *79*, 4369–4385. [CrossRef]
102. Armaghani, D.J.; Yagiz, S.; Mohamad, E.T.; Zhou, J. Prediction of TBM performance in fresh through weathered granite using empirical and statistical approaches. *Tunn. Undergr. Space Technol.* **2021**, *118*, 104183. [CrossRef]

Pareto-Based Bi-Objective Optimization Method of Sensor Placement in Structural Health Monitoring

Shao-Xiao Nong [1,2], Dong-Hui Yang [2,*] and Ting-Hua Yi [2]

[1] State Key Laboratory of Mechanical Behavior and System Safety of Traffic Engineering Structures, Shijiazhuang Tiedao University, Shijiazhuang 050043, China; nshaox@163.com

[2] School of Civil Engineering, Dalian University of Technology, Dalian 116023, China; yth@dlut.edu.cn

* Correspondence: dhyang@dlut.edu.cn

Abstract: For a practical structural health monitoring (SHM) system, the traditional single objective methods for optimal sensor placement (OSP) cannot always obtain the optimal result of sensor deployment without sacrificing other targets, which creates obstacles to the efficient use of the sensors. This study mainly focuses on establishing a bi-objective optimization method to select the sensor placement positions. The practical significance of several single-objective criteria for OSP is firstly discussed, based on which a novel bi-objective optimization method is proposed based on the Pareto optimization process, and the corresponding objective functions are established. Furthermore, the non-dominated sorting genetic algorithm is introduced to obtain a series of the Pareto optimal solutions, from which the final solution can be determined based on a new defined membership degree index. Finally, a numerical example of a plane truss is applied to illustrate the proposed method. The Pareto optimization-based bi-objective OSP framework presented in this study could be well suited for solving the problem of multi-objective OSP, which can effectively improve the efficiency of the limited sensors in SHM system.

Keywords: structural health monitoring; optimal sensor placement; bi-objective optimization; Pareto optimization; non-dominated sorting genetic algorithm

1. Introduction

In recent decades, more and more long-span bridges and other large civil infrastructures have been constructed all over the world. To guarantee the normal operation and safety of the civil structures during their service life, structural health monitoring (SHM) system are widely applied, especially for long-span bridges and skyscrapers, which can obtain information with respect to the structural behavior and environmental actions [1–4]. A complete SHM system consists of three subsystems, namely a sensor subsystem, data acquisition and transmission subsystem and data management subsystem. The sensor subsystem is usually composed of various accelerometers, which are placed on the different positions to directly acquire the structural vibration and modal parameters. The rationality of sensor placement is crucial for the SHM system to identify the structural behavior and evaluate the structural performance [5–8]. Although increasing the number of the deployed sensors will obtain more data related to the structural behaviors and environmental actions, it will sacrifice the economy of SHM systems and also cause difficulty for the data analysis. Therefore, it is necessary to carry out research on the optimal sensor placement (OSP) to obtain enough information about structural responses with a finite number of sensors yet without compromising the reliability and precision of the monitoring-based structural analysis [9–12].

The research on OSP for SHM can be categorized into two groups: the first group concentrates on single-objective optimization, which considers only one criterion and the corresponding objective function; the second group is focused on multi-objective criteria for OSP. Since the 1970s, many researchers have realized the necessity of OSP for

structural monitoring. Shah and Udwadia carried out research on the sensor locations for identification of dynamic systems [13]. After more than 10 years of development in this research field, researchers have established explicit objectives for sensor placement. For the purpose of structural modal observability, several criteria have been proposed by researchers [14,15]. Kammer proposed the effective independence (EI) method, which can maximize the determinant of the Fisher information matrix to minimize the structural parameter estimation error [16]. Papadopoulos and Garcia researched the structural modal kinetic energy method, which can considerably increase the signal-to-noise ratio for the recorded data obtained by the sensors [17]. To guarantee the modal independence, the modal assurance criterion was proposed to maximize the angle between different modal vectors [18]. Li et al. revealed the relationship between two sensor placement methods, i.e., modal kinetic energy and EI [19]. Yi et al. carried out quantitative research on the optimal algorithm for OSP, which considerably improved the effectiveness of the optimization process [20,21]. In recent years, an increasing number of researchers have focused on OSP for novel monitoring techniques. Thiene et al. proposed an OSP algorithm for attaining the maximum area coverage within a sensor network, taking into account the physical properties of Lamb wave propagation [22]. A transducer placement scheme based on wave propagation was also proposed by Salmanpour et al. [23].

The criteria for OSP mentioned above can usually satisfy only a single requirement. To simultaneously fulfill the various requirements of sensor placement for SHM, it is essential to establish a multi-objective criterion and corresponding optimization method for OSP, which is a research focus that ia already attracting the attention of researchers worldwide. Casciati et al. studied the power management criterion of wireless sensors for SHM systems [24]. Sankary and Ostfeld proposed a multi-objective optimal criterion for wireless sensor placement, which could considerably improve the quality of the modal information obtained by the sensors and reduce the energy consumption of the sensor network as much as possible [25]. Soman et al. proposed a multi-objective optimal strategy for sensor placement considering the structural modal identification and mode shape expansion, which has been implemented to deploy various types of sensors on a long-span bridge [26]. Azarbayejani et al. studied the required sensor quantity for an SHM system based on the information entropy and the cost of the sensor equipment [27]. Cha et al. conducted research on the optimal placement positions of the active control devices and sensors of a framework structure, in which a multi-objective genetic algorithm was applied to realize the objectives of reducing the cost and enhancing the effectiveness of the active control strategy [28]. Soman et al. further presented a multi-objective optimization strategy for a multi-type sensor placement for SHMs of long span bridges, which also verified the effectiveness of the genetic algorithm in solving the joint optimization [26]. Ostachowicz et al. systematically reviewed the traditional sensor placement metrics for three commonly used monitoring techniques. In addition, they discussed the different optimization algorithms and multi-objective optimization for OSP [29].

Once the criteria of OSP are selected, the objective function can be determined, and the OSP problem can be transformed into a mathematical optimization problem [30,31]. To obtain the final sensor placement positions, the optimal problem needs to be solved through various optimization algorithms. The intelligent optimization algorithms are usually used to solve OSP problems. The genetic algorithm is one of the most popular methods and has been applied by several researchers to solve OSP problems in the fields of SHM [32,33]. Beygzadeh et al. proposed an improved genetic algorithm for OSP to detect the structural damage [34]. In addition, many other bioinspired algorithms, physics-inspired algorithms and geography-based techniques have been studied, including the monkey algorithm, simulated annealing, firefly algorithm, and particle swarm, which have also been applied by many researchers to solve OSP problems [20,35]. For the single-objective optimization of sensor placement, the objective function is usually established based on a single criterion, which usually cannot satisfy multiple requirements simultaneously. Although the optimization results can satisfy one criterion well, they may not be suitable for another optimization

criterion. The traditional multi-objective optimization method of sensor placement usually transforms multi-objective problems into single-objective problems through simple mathematical operations such as addition and multiplication. The transformation process introduces weight coefficients, which will subjectively affect the optimization results of sensor placement.

Pareto optimization is an effective method for solving multi-objective problems and has been effectively applied by researchers to solve the optimal problem of camera placement for automated visual inspection under a multi-objective framework. Considering that most of the previous studies on the multi-objective optimization of sensor placement simply transform the multi-objective functions to a single-objective function through a mathematical operation, this paper presents a study on the Pareto optimization-based multi-objective sensor placement method for SHM. The paper is organized as follows: (i) the traditional OSP single-objective criteria and the corresponding objective functions are studied; (ii) the basic mechanism of Pareto optimization is researched, and the bi-objective functions are established based on single-objective criteria for the Pareto optimization; (iii) the update of non-dominated sorting genetic algorithm (NSGA-II) is introduced to solve the Pareto optimization for sensor placement, and the iterative process is proposed; (iv) a comprehensive evaluation index is introduced to access the Pareto final solutions for multi-objective OSP, and the evaluation criteria are studied for multiple alternative sensor placement schemes; and (v) the proposed bi-objective optimization method for sensor placement is validated through a numerical example of a plane truss.

2. Single-Objective Criteria for Sensor Placement

2.1. Criterion of Minimum Estimation Error of Modal Coordination (EI Criterion)

According to the structural dynamic theory, the dynamic responses of linear elastic structures can be represented as the superposition of different modes, as shown in Equation (1).

$$y = \Phi q = \sum_{i=1}^{m} q_i \Phi_i \tag{1}$$

where Φ is the matrix of structural modes; q is the vector of modal coordinates; Φ_i is the ith vector in the matrix Φ; q_i is the ith elements in the vector q; and m is the structural model order under consideration.

Assuming y in Equation (1) is the dynamic behavior measured by the sensors deployed at the corresponding positions on the structures, the least squares estimation of q can be calculated according to Equation (2).

$$\hat{q} = \left[\Phi^T \Phi \right]^{-1} \Phi^T y \tag{2}$$

where $\hat{q}$ is the estimation of q according to the sensor measurement y. If the measurement noise is further considered for the sensor placement, the real structural responses can be represented as Equation (3).

$$y = \Phi q + \omega = \sum_{i=1}^{m} q_i \Phi_i + \omega \tag{3}$$

where ω is the stationary Gaussian white noise with the variance σ^2. Assuming the measurement noises are independent between different sensors, the covariance matrix of the estimation error can be represented as Equation (4).

$$J = E\left[\left(q - \hat{q} \right) \left(q - \hat{q} \right)^T \right] = \left[\frac{1}{\sigma^2} \Phi^T \Phi \right]^{-1} = \left[\frac{1}{\sigma^2} Q \right]^{-1} \tag{4}$$

where E is the expected value and Q is the Fisher information matrix. Maximizing Q will lead to minimization of the covariance matrix, which will result in the best estimation of $\boldsymbol{q}$. Kammer (1991) proposed the largest determinant of the Fisher information matrix as the criterion to determine the selected sensor positions, which is defined as the EI method.

2.2. Criterion of Maximum Structural Modal Kinetic Energy (MSMKE Criterion)

For the purpose of modal identification, accelerometers are usually deployed at the positions where the structure has the strongest vibration responses, which can increase the signal to noise ratio, resulting in the accurate identification of the structural modal parameters. Therefore, the modal kinetic energy can be represented as Equation (5).

$$\boldsymbol{MKE} = \boldsymbol{\Phi}^T \boldsymbol{M} \boldsymbol{\Phi} = \begin{bmatrix} \sum\limits_{i=1}^{n} MKE_{i1} & \cdots & 0 \\ \vdots & \ddots & \vdots \\ 0 & \cdots & \sum\limits_{i=1}^{n} MKE_{im} \end{bmatrix} \tag{5}$$

where $\boldsymbol{\Phi}$ is the matrix of structural modes; $\boldsymbol{M}$ is the matrix of structural mass; and the matrix diagonal element $\sum\limits_{i=1}^{n} MKE_{ij}$ is the sum of the modal kinetic energies of all the freedoms with respect to the jth structural mode. The off-diagonal elements of the matrix $\boldsymbol{MKE}$ are all zero, which means that one structural mode cannot induce modal kinetic energy on another mode. MKE_{ij} is the contribution of the ith freedom to the modal kinetic energy on the jth structural mode, which can be represented as Equation (6).

$$MKE_{ij} = \Phi_{ij} \sum_{k=1}^{n} M_{ik} \Phi_{kj} \tag{6}$$

where Φ_{ij} is the ith element of the jth structural mode; M_{ik} is the element of the structural mass matrix; and n is the structural freedom. According to the contributions of the different structural freedoms to the modal kinetic energy with respect to the target structural modals, the sensor placement positions can be determined to obtain the strongest modal kinetic energy.

2.3. Criterion of Structural Modal Independence (SMI Criterion)

For the purpose of the modal test, the theoretical structural mode vectors obtained at the selected sensor positions should be independent of each other, which can guarantee differentiability of the identified structural modes. Carne and Dohrmann proposed the $\boldsymbol{MAC}$ matrix as a criterion to access the differences quantitatively between the structural modes [18]. The element in the $\boldsymbol{MAC}$ matrix is presented as Equation (7).

$$MAC_{ij} = \frac{\left| \boldsymbol{\Phi}_i^T \boldsymbol{\Phi}_j \right|}{\sqrt{\left(\boldsymbol{\Phi}_i^T \boldsymbol{\Phi}_i \right) \left(\boldsymbol{\Phi}_j^T \boldsymbol{\Phi}_j \right)}} \tag{7}$$

where MAC_{ij} is the elements in the ith line and the jth column of the $\boldsymbol{MAC}$ matrix and $\boldsymbol{\Phi}_i$ and $\boldsymbol{\Phi}_j$ are the ith and jth structural mode vectors, respectively.

The values of elements in the $\boldsymbol{MAC}$ matrix are all between 0 and 1, where 0 represents no correlation between the two structural modes. When the elements in $\boldsymbol{MAC}$ approach 1, there is a strong correlation between the two structural modes, which means that the two modes cannot be easily distinguished. Therefore, the selected sensor placement positions should minimize the maximum off-diagonal element in the $\boldsymbol{MAC}$ matrix, which is defined as the SMI criterion.

3. Pareto Based Bi-Objective OSP

3.1. Theory of Pareto-Based Bi-Objective Optimization

The bi-objective optimization is obviously different from the single-objective optimization. For the optimization problem with a single-objective function, any different solutions can be compared with each other so that there is always an optimal solution to the problem. However, for the multi-objective problem, the results obtained according to the different objective functions will conflict with each other. Therefore, an optimal solution for all the objective functions cannot usually be achieved. In this case, a series of solutions exist that are equally good for the multi-objective optimization problem, which means that any of the solutions cannot be improved on any one of the objective functions without sacrificing the others. These solutions are called Pareto optimal solutions, which constitute the Pareto front. For a bi-objective optimization problem, the Pareto front $P(z^0)$ can be described as Equation (8). It is assumed that Z is a set of feasible solutions for the bi-objective optimization problem. If a point $z' \in Z$ is preferred to another point $z^0 \in Z$, z' dominates z^0, which can be written as $z' \succ z^0$.

$$P(z^0) = \left\{ z^0 \in Z : \left\{ z' \in Z : z' \succ z^0, z' \neq z^0 \right\} = \varnothing \right\} \tag{8}$$

where $\varnothing$ is the empty set.

The Pareto front can provide a series of optimal solutions in which the non-dominated solutions are equally good for the multi-objective optimization problems when no preference is prescribed for any of the objective demands, namely, any one of the objectives cannot be improved without sacrificing the others. Therefore, Pareto optimization is superior to the current method in terms of whether single or multiple demands exist for OSP. This paper concentrates on the following two aspects: (i) constructing the Pareto optimization objective function according to the multiple demands in OSP and (ii) efficiently solving the multi-objective optimization problems of OSP.

3.2. Bi-Objective Optimization Functions for Sensor Placement

The three single-objective functions above are constructed to decrease the identification errors of the modal parameters, increase the signal-to-noise ratio, and distinguish the different mode shapes. When more than one demand is prescribed for OSP, the multi-objective function can be constructed based on Pareto optimization. By combining the three single-objective functions, the bi-objective functions of Pareto optimization are constructed as follows:

(1)   Objective function for EI and MSMKE criteria

For the purpose of structural modal identification, the sensors need to be deployed at positions with strong vibration responses to increase the signal-to-noise ratio. In addition, the estimation error of the structural modal coordinates is an important criterion to assess the sensor placement. Therefore, a bi-objective function related to the two criteria mentioned above can be illustrated as Equation (9).

$$\begin{cases} f_1 = \frac{1}{|\boldsymbol{\Phi}^T \boldsymbol{\Phi}|} \\ f_2 = \frac{1}{AMKE} = \frac{1}{\frac{1}{n}\sum\limits_{i=i}^{n}\sum\limits_{j=1}^{m} MKE_{ij}} \\ \min\{f_1(\boldsymbol{x}), f_2(\boldsymbol{x})\} \end{cases} \tag{9}$$

where f_1 is positively proportional to the estimation error of the structural modal coordinates; f_2 is inversely proportional to the modal kinetic energy; $AMKE$ is the average structural modal kinetic energy; and $\min\{f_1, f_2\}$ is the Pareto bi-objective function for f_1 and f_2. When both the Fisher information matrix and MSMKE criterion are considered, the results of Pareto optimization can result in a series of solutions, by which it can be ensured that favorable modal kinetic energy of the monitoring points and the accurate

identification of modal parameters can be achieved simultaneously. The optimal solution for the objective function of f_1 can be obtained through the EI method. It is worth noting that there is a connection between the EI and MSMKE criteria, and Li et al. (2007) demonstrated that the EI is an iterated version of the MSMKE for the case of a structure with an equivalent identity mass matrix. This means that when the identity mass matrix is assumed for the structure, identical optimal sensor positions can be obtained for the EI and MKE criteria. However, for a nonidentity mass matrix, which is typical for real projects, obvious differences exist between the optimal solutions from the above two criteria. In this paper, the two most commonly used criteria (EI and MSMKE) are presented mainly to illustrate the implementation process of the Pareto bi-objective optimization of OSP and to verify the rationality.

(2)　Objective function for SMI and MSMKE criteria

For structural modal tests, structural modes should be distinguishable from each other. In addition, the strongest vibration should also be monitored. Therefore, sensors should be deployed to obtain both structural modal independence and large structural modal kinetic energy. Considering the criteria mentioned above, the bi-objective function based on Pareto optimization is presented in Equation (10).

$$\begin{cases} f_2 = \frac{1}{AMKE} \\ f_3 = \max\limits_{i \neq j}\left(MAC_{ij}\right) \\ \min\{f_3(\boldsymbol{x}), f_2(\boldsymbol{x})\} \end{cases} \tag{10}$$

where f_3 is the maximum of the off-diagonal elements in $\boldsymbol{MAC}$ matrix and $\min\{f_3, f_2\}$ is the Pareto bi-objective function for f_2 and f_3. When both the SMI and MSMKE are taken as the target demands of OSP, the Pareto optimization can lead to a series of solutions, which can ensure the favorable modal kinetic energy of the monitoring points and the independence of different mode shapes.

(3)　Objective function for EI and SMI

To minimize the estimate of the structural modal coordinates and structural modal independence, the objective functions f_1 and f_3 should be considered at the same time. Based on the Pareto optimization, the bi-objective function for the two criteria mentioned above can be illustrated as in Equation (11).

$$\begin{cases} f_1 = \frac{1}{|\boldsymbol{\Phi}^T\boldsymbol{\Phi}|} \\ f_3 = \max\limits_{i \neq j}\left(MAC_{ij}\right) \\ \min\{f_1(\boldsymbol{x}), f_3(\boldsymbol{x})\} \end{cases} \tag{11}$$

where $\min\{f_1(\boldsymbol{x}), f_3(\boldsymbol{x})\}$ is the Pareto bi-objective function for the criteria of f_1 and f_3. When both the Fisher information matrix and SMI are taken as the target demands of OSP, the Pareto optimization can lead to a series of solutions, which can ensure the accurate identification of the modal parameters and the independence of different mode shapes.

3.3. Solving of Pareto Based Bi-Objective OSP

The evolutionary algorithm is an ideal method for obtaining the Pareto optimal solutions. Srinivas and Deb proposed a non-dominated sorting genetic algorithm and its improved version [36]. Because the NSGA has the defect of high calculation complexity and the obtained satisfactory solutions could be lost during the optimization process, NSGA-II is adopted to solve the problem of Pareto-based bi-objective OSP. Due to the introduction of a fast non-dominated sorting in NSGA-II, the calculation complexity is reduced from $O(mN^3)$ to $O(mN^2)$. In addition, the concept of crowd distance is proposed to maintain the population diversity. The elitist strategy and a crowded-comparison approach are adopted, the population diversity can be maintained, and the loss of the satisfactory solutions can be

avoided during the optimization process. The general concept of NSGA-II can be described as follows: The population is firstly initiated, and a non-dominated sorting is carried out of all the individuals in the population. Based on the initial population, the process of selecting, mutation and crossover in genetic algorithms are performed to obtain the first generation. Starting from the second generation, the parent population is merged with the child population to maintain the population diversity. A fast non-dominated sorting is applied, in which an index of the crowding distance is introduced to sort the population and select the parent population combined with the non-dominated grade. The crowding distance can be presented as Equation (12). Finally, a new general child population is generated, and a new round non-dominated sorting and genetic process begins until the prescribed generation number is reached.

$$D(i) = \sum_{k=1}^{m} \frac{f_{i+1}(k) - f_{i-1}(k)}{f_{max}(k) - f_{min}(k)} \tag{12}$$

where $f_{i+1}(k)$ and $f_{i-1}(k)$ are the values of objective function k for $(i+1)$th and $(i-1)$th individuals in Pareto front; $f_{max}(k)$ and $f_{min}(k)$ are the maximum and minimum values of objective function k among all the individuals in a certain front. For the individual with the minimum value of the objective function, the crowding distance is defined as infinity, which indicates the priority over other individuals of the same non-dominated grade. The crowding distance considerably increases the calculation efficiency and solution robustness for multi-objective Pareto optimization. Therefore, the NSGA-II is applied in this research to solve the Pareto bi-objective function to obtain the optimal sensor placement positions.

Compared with the traditional genetic algorithm, when NSGA-II is applied to multi-objective OSP, non-dominated sorting, crowding distance estimation and crowding distance comparison operator are used to evaluate individual fitness. Further, a genetic algorithm is adopted to obtain the Pareto front iteratively which meets the requirements of the objective function. The specific implementation steps of the above algorithm are as follows:

(1)　Population initiation

An integer S is defined as the population size. The population (P_0) of the sensor placement cases, which contains S individuals, is created. For the subject of sensor placement, the binary encoding is applied to represent the sensor placement positions, of which '1' and '0' represent the positions with and without sensors, respectively.

It is worth noting that when the binary coding method in the genetic algorithm is used for the problems of OSP, the criteria of "Completeness", "Soundness" and "Non-redundancy" can be met for coding method selection: (i) encoding and decoding are simple to operate. The number of the candidate measuring points is equal to the number of the binary code, in which '1' and '0' represent the positions with and without sensors, respectively, as shown by Table 1; (ii) crossover and mutation are easy to realize. For the one-point-crossover, the crossover point is selected at random for one chromosome. The two parent chromosomes exchange the gene segments of each other before or after this crossover point, after which two new individuals are obtained (as shown in Figure 1). Moreover, mutation is also applied to change the binary code of one or more genes for a chromosome (as shown in Figure 2). Such a mutation operation represents that the sensors at those positions are installed or removed, which can avoid the problem of low efficiency and local optimum. (iii) The precision can be satisfied. For the optimization problem of the continuous function, the binary code method has the drawbacks of weak ability of local search and the Hamming Cliff problem. However, for the optimization problems of sensor placement, the discrete solutions constitute the solution set. Consequently, the drawbacks of the binary code method in GA can be avoided for OSP. Therefore, the binary coding method is adopted for NSGA-II in this research.

Table 1. Example of binary coding of sensor placement positions.

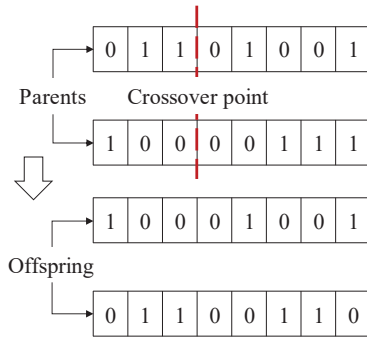| Position Number	Binary Code	With/Without Sensor
1	1	With
2	0	Without
. . .	. . .	. . .
$n-1$	0	Without
n	1	With

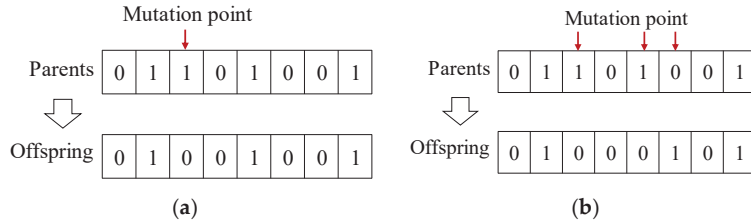
Figure 1. Example of single-point crossover.

Figure 2. Examples of mutation for binary code: (**a**) Single-point mutation; (**b**) multipoint mutation.

(2)   Non-dominated sorting and crowding distance of individuals

The objective functions (f_1, f_2) are calculated for all the individuals in the initial population, and the non-dominated grades (**G**) are obtained through the non-dominated sorting approach as follows: for each i and $j \in P_0$, if $f_1(i) < f_1(j)$ and $f_2(i) < f_2(j)$, individual i dominates individual j ($i \succ j$). If no individual dominates individual i in the population, the non-dominated grade rank 1 and all the individuals with the non-dominated grade 1 constitute the Pareto front 1. The same procedure is carried out for residual individuals iteratively, and the non-dominated grade of all the individuals can be obtained (as shown in Figure 3a). The smaller the number of non-dominated grade, the higher the fitness of individuals in the corresponding front.

For individuals with the same non-dominated grade, the concept of crowding distance is introduced to distinguish their fitness: firstly, individuals with the same dominated grade are sorted according to objective function values in ascending order of magnitude, and the crowding distance of individuals corresponding to the minimum and maximum function values after sorting is defined as infinite. The crowding distance of other individuals is calculated by Equation (12). As shown in Figure 3b, the crowded distance of the i-th individual ($D(i)$) in its front is the average side length of the dashed box. When individuals have the same level of dominance, a larger crowding distance represents better fitness.
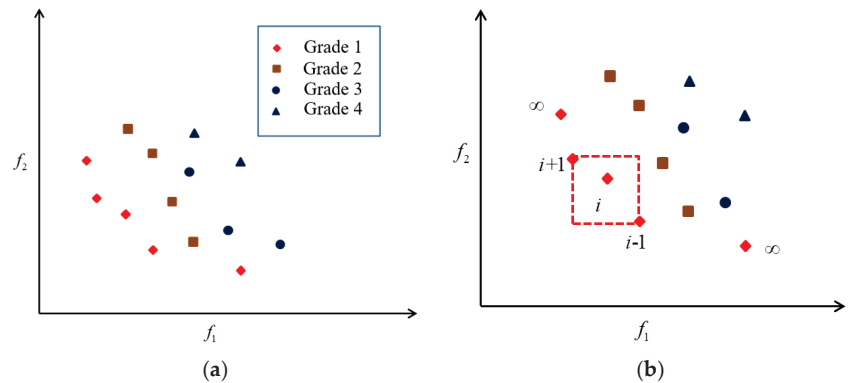
Figure 3. Non-dominated sorting and crowding distance: (**a**) non-dominated sorting; (**b**) crowding distance.

After obtaining the results of the non-dominated grade and crowding distances, all the individuals can be sorted according to the fitness: if $G(i) < G(j)$ or ($G(i) = G(j)$ and $D(i) > D(j)$), the i-th individual has a better fitness than the j-th one.

(3)   Selection

After all the individuals are sorted according to the fitness, the binary tournament selection method is used to select the parents ($\overline{P}_n$) in the population to produce the offspring. Two individuals were selected from the original population to compare the non-dominated grade and crowding distance, and the individuals with better fitness were selected as the parents for producing offspring. This procedure is repeated until the number of parents reaches half of the original population size.

(4)   Crossover and mutation

The offspring (C_n) are generated through crossover and mutation. To ensure that the number of sensors remains constant during the genetic process, the mutation method is used to randomly remove or supplement the sensors. Finally, the offspring individuals are added to the initial population, and the first S individuals with best fitness were preserved based on the non-dominated grade and crowd distance, which will produce the new population for the next generation. The iteration process above stops once the target number (N) of heredity generations is reached.

The flowchart of the NSGA-II applied in Pareto bi-objective optimization for OSP is shown in Figure 4.

3.4. Comprehensive Evaluation Criteria for Pareto Solutions of OSP

The solution set of a series of OSP schemes can be obtained by the proposed method above. When the engineer has no preference for any single target of senor placement, the obtained solutions are equally optimal in a Pareto sense. However, when some of the solutions in the optimal solution set reach optimum for a single objective function, the solutions degrade to the ones achieved through the traditional single-target sensor placement criteria, which is obviously contrary to the original intention of multi-objective sensor placement. Therefore, a comprehensive evaluation criterion is proposed to determine the final solution from the Pareto optimal solution set for sensor placement when there is no preference for any single criterion.
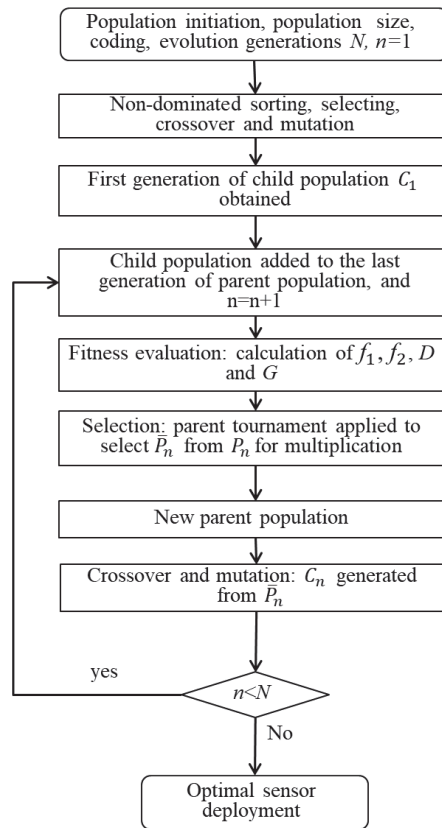
Figure 4. NSGA-II based Pareto bi-objective optimization.

For the problem of bi-objective OSP, the Pareto OSP solution set **F** can be expressed as Equations (13) and (14).

$$\mathbf{F} = [F_1(\mathbf{x}_1), F_2(\mathbf{x}_2), \ldots F_k(\mathbf{x}_k)] \tag{13}$$

$$F_k(\mathbf{x}_k) = [f_{k1}(\mathbf{x}_k), f_{k2}(\mathbf{x}_k)] \tag{14}$$

where $F_k(\bullet)$ is the k-th solution of the Pareto optimal solution set; f_{k1}, f_{k2} are the two objective function values; $\mathbf{x}_k$ is the vector of sensor placement positions corresponding to the k-th optimal solution. The ideal optimal solution of sensor placement is defined as Equation (15).

$$F^* = \left[f_1^*, f_2^*\right]$$
$$\text{s.t. } f_j^* = \min_{1 \leq i \leq k} \left(f_{ij}\right) \tag{15}$$

where f_{ij} is the j-th objective function value of the i-th solution in the Pareto solution set. Considering that the different objective functions of OSP are not easy to compare with each other because of their different units and magnitudes, the membership degree μ is defined to measure the closeness between the values of Pareto solutions and the ideal solutions for each objective function. When μ approaches 1, the Pareto solution tends to be the ideal solution for OSP. Because the solutions in the Pareto front for OSP can be considered to be randomly distributed, the normal distribution function is selected as the membership

function to evaluate the proximity between the Pareto solution and the ideal one. The membership degree vector $\widetilde{F}_i$ for each Pareto solution is shown as Equations (16) and (17).

$$\widetilde{F}_i = [\mu(f_{i1}), \mu(f_{i2})] \tag{16}$$

$$\mu(f_{ij}) = \exp\left[-\left(\frac{f_{ij} - f_j^*}{\frac{1}{k} \sum_{i=1}^{k} \left| f_{ij} - f_j^* \right|} \right)^2 \right] \tag{17}$$

On the basis of membership vector, a proximity index D is further defined to quantitatively assess the proximity between the Pareto solution and the ideal counterpart, as Equation (18).

$$D_i = \sqrt{\frac{1}{2} \sum_{j=1}^{2} \mu_{ij}^2} \tag{18}$$

4. Bi-Objective OSP for Plane Truss

4.1. Properties of Plane Truss

To verify the effectiveness of the bi-objective Pareto optimization for sensor placement, a plane truss is presented as an example to illustrate the application of the proposed method. There are 25 degrees of freedom (Dof) for the truss beam, the elevation of which is presented in Figure 5. The structural modal shapes were obtained through numerical analysis in a previous study. For the modal test, there are eight sensors to be deployed at eight positions selected from 25 candidates to obtain the structural experimental modal. The first four orders of structural modes are considered for the truss beam. Considering that the vertical modes are the main modes of the truss beam, the first four normalized modes are plotted (as shown in Figure 6) using the displacement along the directions of structural Dof number 4, 8, 12, 16 and 20, which are located at the lower side of the truss.
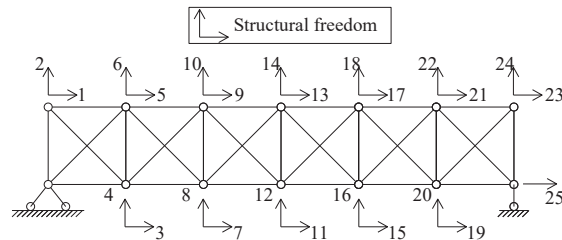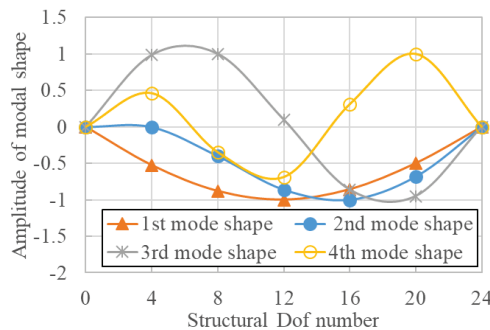

Figure 5. Structural freedom of the plane truss.

Figure 6. First four orders of vertical mode shapes.

4.2. OSP Proposals

For the sake of simplicity and convenience to illustrate the effectiveness of Pareto based bi-objective optimization, this paper assumes that the main concern of the OSP for the truss beam is to reduce the modal coordinate estimation error and increase the signal-to-noise ratio. In fact, considering any combination of two objective functions does not hinder the effectiveness of the Pareto-based bi-objective optimization method proposed in this paper. Considering EI and MSMKE as criteria of sensor placement, the corresponding bi-objective optimization function is established, and the Pareto optimization analysis is carried out for the OSP position of the plane truss.

To minimize the estimation error of the modal coordination and increase the signal-to-noise ratio of the recorded data, the EI and MSMKE should be considered during the process of OSP. Therefore, Equation (9) should be taken as the objective function for the Pareto bi-objective optimization. The NSGA-II is adopted to solve the bi-objective Pareto optimization considering the functions f_1 and f_2. During the iterative process, the initial population size of the sensor placement is set to 50. In addition, the crossover and mutation probability are set to 0.9 and 0.1, respectively. The target number of heredity generations is set to 200, which is the threshold used to control the iterative process. The corresponding convergence processes are shown in Figure 7. Compared with the global optimal solutions obtained through the exhaustive method, it can be observed that the two functions f_1 and f_2 converge to the optimal solution at the generations of 76 and 10, respectively. When the target heredity generation is reached, the iterative process of the NSGA-II terminates, and the Pareto front is output. In addition, the parents are selected through tournament selections to produce the offspring samples. The optimization is implemented according to the iterative process in Figure 4, and the results are plotted in Figure 8. To make comparisons with the results of single-objective functions, the results obtained based on the MSMKE and EI are also presented in Figure 8. Moreover, a traditional bi-objective function considering the EI and MSMKE is illustrated in Equation (19), which transforms the bi-objective optimization into a single-objective optimization. The optimal result of EI-MSMKE is also plotted in Figure 8.

$$\text{EI-MKE} = diag\left(\boldsymbol{\Phi}\left(\boldsymbol{\Phi}^T\boldsymbol{\Phi}\right)^{-1}\boldsymbol{\Phi}^T \right) \cdot diag\left(\boldsymbol{M}\boldsymbol{\Phi}\boldsymbol{\Phi}^T \right) \tag{19}$$
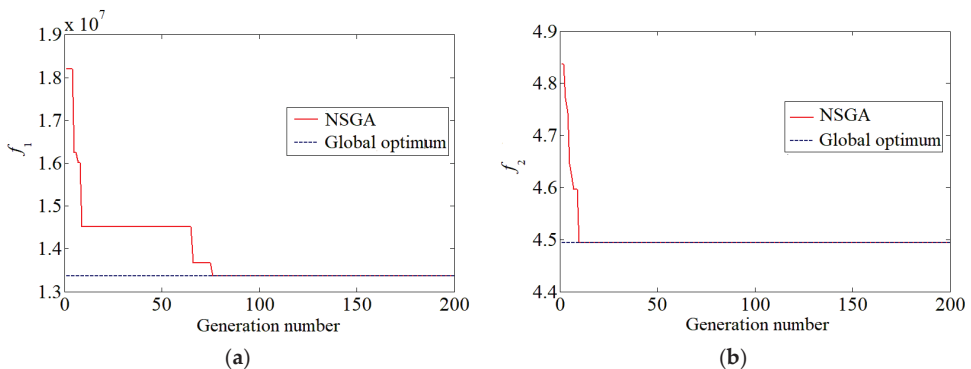

Figure 7. Convergence process of bi-objective optimization: (**a**) f_1; (**b**) f_2.

As presented in Figure 8, the optimal results for the EI, MSMKE and EI- MSMKE (points 'A', 'B' and 'C' in Figure 8) can all be found in the Pareto front, which means that the bi-objective Pareto optimal results can cover all the results obtained based on the single-objective and traditional bi-objective criteria. The Pareto optimization solved through the NSGA-II can achieve a solution as good as that of the single-objective function of the MSMKE, as shown by point 'C' in Figure 8. It is worth noting that the determinant of the

Fisher information matrix (point 'D' in Figure 8) obtained through the Pareto optimization is even larger than that obtained from the EI, which further verifies the efficiency of the NSGA-II to solve the bi-objective Pareto optimization problem for sensor placement. Moreover, the Pareto front can provide a series of sensor placement schemes that are not worse than the counterpart based on the traditional bi-objective criterion of EI- MSMKE ('B' in Figure 8). The sensor placement positions of 'B', 'C' and 'D' in the Pareto front are shown in Figure 9.
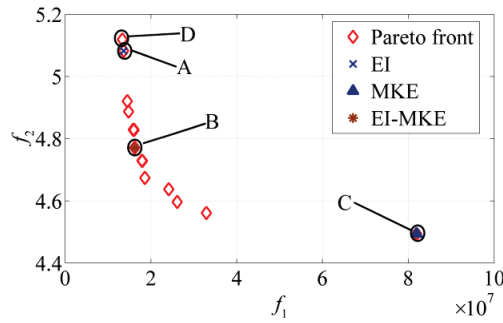

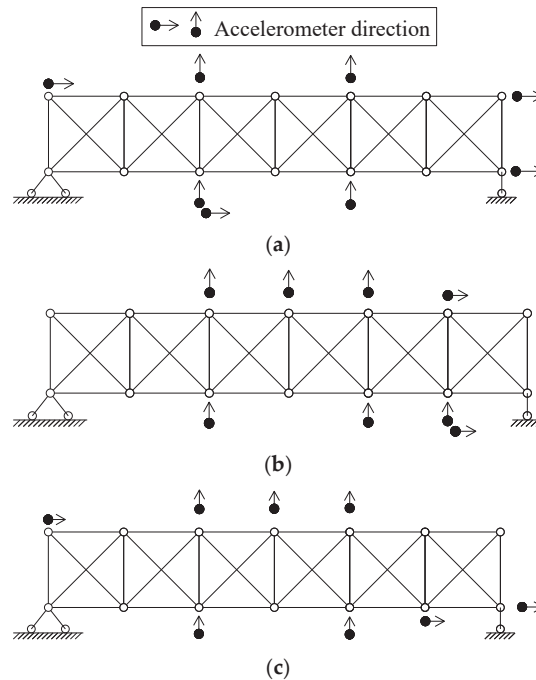**Figure 8.** Optimal solutions of sensor placement based on the criteria of EI and MSMKE.

Figure 9. Sensor placement proposals from Pareto front of EI and MSMKE: (**a**) solution 'D'; (**b**) solution 'B'; (**c**) solution 'C'.

4.3. Comprehensive Evaluation of OSP Schemes

The bi-objective optimization results show that the optimal solution set achieved through Pareto optimization method contains 16 equivalent OSP schemes. By adopting the evaluation criteria based on the membership degree index μ proposed above, the

solution from the Pareto optimal solution set, which is closest to the ideal solution, can be determined as the OSP scheme. As shown in Figure 10, solutions No. 14 and 15 have nearly the same value of index D which is the maximum one among all the solutions in Pareto front. It means that the two equivalent OSP solutions can provide alternative schemes when some positions of the structure are inconvenient to install the sensors, and the point 'B' in Figure 8 corresponds one of such optimal solutions. Consequently, considering reducing the identification error of modal parameters and increasing vibration signal intensity, the placement positions of the sensors corresponding to point 'B' in Figure 8 is optimal for the plane truss.
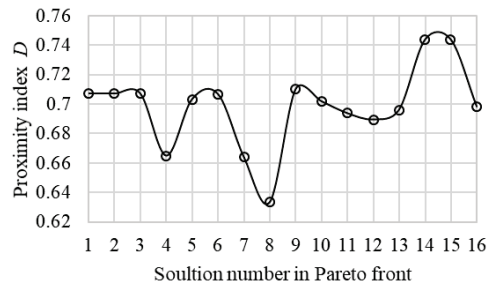

Figure 10. Proximity index D for each solution in Pareto front for OSP.

5. Conclusions

The traditional OSP method is based on single objective criterion, which is generally oriented to meet a single target of sensor placement. When more than one objective is considered to be satisfied, such as improving the identification accuracy of structural modal parameters, the vibration signal strength and the effect of modal reconstruction, the current OSP methods cannot achieve good results. This paper carried out a study on a Pareto-based bi-objective OSP method, and the proposed evaluation criteria of optimal solution can achieve satisfactory results for two objective functions at the same time. The bi-objective OSP method was finally verified through a numerical model of a plane truss. According to the analytical results and discussions, the following conclusions can be drawn:

Pareto optimization can comprehensively consider more than one objective function for OSP, such as the MSMKE, EI and structural modal independence. Compared with the traditional OSP method, the proposed method can make a compromise between the multiple objective functions, and all equally optimal solutions in a Pareto sense can be provided as alternatives for sensor placement, which also covers the sensor placement schemes obtained through the traditional single objective optimization methods.

The NSGA-II is suitable for solving the Pareto optimization problem of OSP for SHM. The bi-objective Pareto optimization of sensor placement can be effectively solved through the NSGA-II and all the equally optimal solutions for the bi-objective OSP can be achieved within a feasible number of generations. The proposed iterative process for the Pareto optimization based on the NSGA-II can be effectively applied to the bi-objective OSP. If more objective functions for OSP are considered, the proposed algorithm can still be effective through multi-objective Pareto optimization.

A comprehensive evaluation method based on membership degree index was proposed for multi-objective OSP, which can quantitatively analyze the proximity between the multiple alternative solutions provided by Pareto optimization and the ideal solutions. By selecting the Pareto optimal solution which has the largest value of proximity index D, the corresponding sensor placement scheme can be finally determined among a series of Pareto optimal solutions, and the OSP scheme can achieve good results in both the two objectives.

In this research, the Pareto-based bi-objective optimization functions are established according to three commonly used evaluation criteria for optimal sensor placement, which only involve the optimization of sensor placement positions. In the future, it would

be meaningful to carry out research on the multi-objective optimization for both the sensor number and location. In addition, if the evaluation criteria for different types of sensors are introduced to establish objective functions for OSP, the Pareto-based multi-objective optimization method proposed in this paper can be extended for the simultaneous optimization of the different types of sensors on the structure at the same time.

Author Contributions: Writing—original draft preparation, D.-H.Y. and S.-X.N.; writing—review and editing, D.-H.Y. and T.-H.Y.; supervision, T.-H.Y.; funding acquisition, D.-H.Y. and T.-H.Y. All authors have read and agreed to the published version of the manuscript.

Conflicts of Interest: The authors declare no conflict of interest.

References

1. Dharap, P.; Koh, B.-H.; Nagarajaiah, S. Structural Health Monitoring using ARMarkov Observers. *J. Intell. Mater. Syst. Struct.* **2006**, *17*, 469–481. [CrossRef]
2. Sun, L.; Shang, Z.; Xia, Y.; Bhowmick, S.; Nagarajaiah, S. Review of Bridge Structural Health Monitoring Aided by Big Data and Artificial Intelligence: From Condition Assessment to Damage Detection. *J. Struct. Eng.* **2020**, *146*, 04020073. [CrossRef]
3. Yang, D.-H.; Yi, T.-H.; Li, H.-N.; Zhang, Y.-F. Correlation-Based Estimation Method for Cable-Stayed Bridge Girder Deflection Variability under Thermal Action. *J. Perform. Constr. Facil.* **2018**, *32*, 04018070. [CrossRef]
4. Yang, D.-H.; Yi, T.-H.; Li, H.-N.; Zhang, Y.-F. Monitoring and analysis of thermal effect on tower displacement in cable-stayed bridge. *Measurement* **2018**, *115*, 249–257. [CrossRef]
5. Kim, S.; Frangopol, D.M. Multi-objective probabilistic optimum monitoring planning considering fatigue damage detection, maintenance, reliability, service life and cost. *Struct. Multidiscip. Optim.* **2018**, *57*, 39–54. [CrossRef]
6. Leyder, C.; Dertimanis, V.; Frangi, A.; Chatzi, E.; Lombaert, G. Optimal sensor placement methods and metrics–comparison and implementation on a timber frame structure. *Struct. Infrastruct. Eng.* **2018**, *14*, 997–1010. [CrossRef]
7. Ding, Z.; Li, J.; Hao, H.; Lu, Z.-R. Structural damage identification with uncertain modelling error and measurement noise by clustering based tree seeds algorithm. *Eng. Struct.* **2019**, *185*, 301–314. [CrossRef]
8. Nagarajaiah, S.; Yang, Y. Modeling and harnessing sparse and low-rank data structure: A new paradigm for structural dynamics, identification, damage detection, and health monitoring. *Struct. Control. Heal. Monit.* **2017**, *24*, e1851. [CrossRef]
9. Krishnamurthy, P.; Khorrami, F. Optimal Sensor Placement for Monitoring of Spatial Networks. *IEEE Trans. Autom. Sci. Eng.* **2016**, *15*, 33–44. [CrossRef]
10. Loutas, T.; Bourikas, A. Strain sensors optimal placement for vibration-based structural health monitoring. The effect of damage on the initially optimal configuration. *J. Sound Vib.* **2017**, *410*, 217–230. [CrossRef]
11. Pei, X.Y.; Yi, T.H.; Li, H.N. A multi-type sensor placement method for the modal estimation of structure. *Smart Struct. Syst.* **2018**, *21*, 407–420. [CrossRef]
12. Pakzad, S.N.; Fenves, G.L. Statistical Analysis of Vibration Modes of a Suspension Bridge Using Spatially Dense Wireless Sensor Network. *J. Struct. Eng.* **2009**, *135*, 863–872. [CrossRef]
13. Shah, P.C.; Udwadia, F.E. A Methodology for Optimal Sensor Locations for Identification of Dynamic Systems. *J. Appl. Mech.* **1978**, *45*, 188–196. [CrossRef]
14. Limongelli, M.P. Optimal location of sensors for reconstruction of seismic responses through spline function interpolation. *Earthq. Eng. Struct. Dyn.* **2003**, *32*, 1055–1074. [CrossRef]
15. Stephan, C. Sensor placement for modal identification. *Mech. Syst. Signal Process.* **2012**, *27*, 461–470. [CrossRef]
16. Kammer, D.C. Sensor placement for on-orbit modal identification and correlation of large space structures. *J. Guid. Control Dyn.* **1991**, *14*, 251–259. [CrossRef]
17. Papadopoulos, M.; Garcia, E. Sensor Placement Methodologies for Dynamic Testing. *AIAA J.* **1998**, *36*, 256–263. [CrossRef]
18. Carne, T.G.; Dohrmann, C.R.; Soc, E.M. A modal test design strategy for model correlation. In Proceedings of the 13th International Modal Analysis Conference, Albuquerque, NM, USA, 13–16 February 1995; Volume 2460, pp. 927–933.
19. Li, D.; Li, H.; Fritzen, C. The connection between effective independence and modal kinetic energy methods for sensor placement. *J. Sound Vib.* **2007**, *305*, 945–955. [CrossRef]
20. Yi, T.-H.; Li, H.-N.; Song, G.; Zhang, X.-D. Optimal sensor placement for health monitoring of high-rise structure using adaptive monkey algorithm. *Struct. Control. Heal. Monit.* **2015**, *22*, 667–681. [CrossRef]
21. Yi, T.-H.; Li, H.-N.; Zhang, X.-D. A modified monkey algorithm for optimal sensor placement in structural health monitoring. *Smart Mater. Struct.* **2012**, *21*, 21. [CrossRef]

22. Thiene, M.; Khodaei, Z.S.; Aliabadi, M.H. Optimal sensor placement for maximum area coverage (MAC) for damage localization in composite structures. *Smart Mater. Struct.* **2016**, *25*, 095037. [CrossRef]
23. Salmanpour, M.S.; Sharif Khodaei, Z.; Aliabadi, M.H. Transducer placement optimisation scheme for a delay and sum damage detection algorithm. *Struct. Control. Health Monit.* **2017**, *24*, e1898. [CrossRef]
24. Casciati, S.; Faravelli, L.; Chen, Z. Energy harvesting and power management of wireless sensors for structural control applications in civil engineering. *Smart Struct. Syst.* **2012**, *10*, 299–312. [CrossRef]
25. Sankary, N.; Ostfeld, A. Multiobjective Optimization of Inline Mobile and Fixed Wireless Sensor Networks under Conditions of Demand Uncertainty. *J. Water Resour. Plan. Manag.* **2018**, *144*, 04018043. [CrossRef]
26. Soman, R.N.; Onoufriou, T.; Kyriakides, M.A.; Votsis, R.A.; Chrysostomou, C.Z. Multi-type, multi-sensor placement opti-mization for structural health monitoring of long span bridges. *Smart Struct. Syst.* **2014**, *14*, 55–70. [CrossRef]
27. Azarbayejani, M.; El-Osery, A.; Taha, M.M.R. Entropy-based optimal sensor networks for structural health monitoring of a cable-stayed bridge. *Smart Struct. Syst.* **2009**, *5*, 369–379. [CrossRef]
28. Cha, Y.; Raich, A.; Barroso, L.; Agrawal, A. Optimal placement of active control devices and sensors in frame structures using multi-objective genetic algorithms. *Struct. Control. Heal. Monit.* **2011**, *20*, 16–44. [CrossRef]
29. Ostachowicz, W.; Soman, R.; Malinowski, P. Optimization of sensor placement for structural health monitoring: A review. *Struct. Health Monit.* **2019**, *18*, 963–988. [CrossRef]
30. Ahlawat, A.S.; Ramaswamy, A. Multiobjective Optimal Structural Vibration Control Using Fuzzy Logic Control System. *J. Struct. Eng.* **2001**, *127*, 1330–1337. [CrossRef]
31. Marsh, P.S.; Frangopol, D.M. Lifetime Multiobjective Optimization of Cost and Spacing of Corrosion Rate Sensors Embedded in a Deteriorating Reinforced Concrete Bridge Deck. *J. Struct. Eng.* **2007**, *133*, 777–787. [CrossRef]
32. Huang, Y.; Ludwig, S.A.; Deng, F. Sensor optimization using a genetic algorithm for structural health monitoring in harsh environments. *J. Civ. Struct. Heal. Monit.* **2016**, *6*, 509–519. [CrossRef]
33. Tan, P.; Dyke, S.J.; Richardson, A.; Abdullah, M. Integrated Device Placement and Control Design in Civil Structures Using Genetic Algorithms. *J. Struct. Eng.* **2005**, *131*, 1489–1496. [CrossRef]
34. Beygzadeh, S.; Salajegheh, E.; Torkzadeh, P.; Salajegheh, J.; Naseralavi, S.S. An Improved Genetic Algorithm for Optimal Sensor Placement in Space Structures Damage Detection. *Int. J. Space Struct.* **2014**, *29*, 121–136. [CrossRef]
35. Rao, A.R.M.; Anandakumar, G. Optimal placement of sensors for structural system identification and health monitoring using a hybrid swarm intelligence technique. *Smart Mater. Struct.* **2007**, *16*, 2658–2672. [CrossRef]
36. Srinivas, N.; Deb, K. Multiobjective optimization using non-dominated sorting in genetic algorithms. *Evol. Comput.* **1994**, *2*, 221–248. [CrossRef]

Suitability of Seismic Isolation for Buildings Founded on Soft Soil. Case Study of a RC Building in Shanghai

Francisco López Almansa [1],*,[†], Dagen Weng [2], Tao Li [2] and Bashar Alfarah [3]

[1] Architecture Technology Department, Technical University of Catalonia, Avda. Diagonal 649, 08028 Barcelona, Spain
[2] Research Institute of Structural Engineering and Disaster Reduction, Tongji University, Shanghai 200092, China; wdg@tongji.edu.cn (D.W.); ltlt52@gmail.com (T.L.)
[3] Civil and Environmental Engineering Department, Technical University of Catalonia, 08034 Barcelona, Spain; alfarah.bashar@gmail.com
* Correspondence: francesc.lopez-almansa@upc.edu
† Currently Associate Researcher Natural and Anthropogenic Risks Research Center, University Austral de Chile, Valdivia.

Abstract: Base (seismic) isolation is a promising technology for seismic protection of buildings and other constructions. Nowadays, it is accepted that such a technique is efficient and reliable; however, it has two major limitations: soft foundation soil, and tall buildings. The first issue restrains the seismic isolation spreading, given that soft soil is frequent in densely populated areas, and usually such a soil type concentrates the highest seismicity levels. This paper aims to contribute to demonstrating that base isolation, if properly implemented, can be suitable for soft soil. A representative case study is analyzed: a 6-story reinforced concrete (RC) building with base isolation that has recently been built in Shanghai. Since the building is founded on soft soil, concern regarding base isolation suitability arose; even the Chinese design code does not recommend this solution for soft soil. To clarify this issue, non-linear time-history analyses are carried out for a number of natural and artificial seismic inputs that represent the site seismicity; the superstructure behavior is linear, while nonlinearities are concentrated in the isolation layer. The adequacy of base isolation is assessed in the superstructure (in terms of reduction of interstory drift, absolute acceleration and shear force) and in the isolation layer (in terms of axial force, torsion angle and shear strain). The relevance of soil–structure interaction is discussed. The behavior when the mechanical parameters of the isolation units have experienced important changes is also analyzed. The major conclusion is that base isolation of ordinary mid-height RC buildings founded on soft soil can perform satisfactorily in medium seismicity regions.

Keywords: RC building; base isolation; seismic isolation; rubber bearing; soft soil; nonlinear dynamic analysis

1. Introduction

Base (seismic) isolation consists in uncoupling the construction under consideration from the foundation soil by using bearings that are flexible in the horizontal direction, being commonly termed as isolators (or isolation units). The resulting structure is divided into three parts: superstructure, isolation layer, and substructure; ordinarily, the isolation layer is situated right below the ground floor slab. Base isolation has been mainly considered for buildings and bridges; this study deals with seismically isolated buildings. The main effect of seismic isolation of buildings is an important elongation of their fundamental period, thus reducing significantly the spectral ordinate. Moreover, given that most of the drift displacement is concentrated in the isolation layer, additional damping can be easily incorporated; as a result, the spectral ordinate is further lowered.

The suitability of base isolation has been repeatedly proven by theoretical studies, laboratory testing, and observation of the seismic performance of actual buildings under strong seismic events. Therefore, nowadays such technology is recognized worldwide, being incorporated into the major design codes. However, although seismic isolation performs satisfactorily in most of the situations, it has two major limitations: high-rise buildings, and soft foundation soil. This paper deals with the second limitation; this choice is based on the important number of buildings in high seismicity regions that are founded in soft soil. Analyzing this limitation in more depth, it is widely accepted that base isolation is less efficient for soft soil [1–5]; the main reason for this prevention is that soft soil filters out short-period waves while it amplifies long-period components. Therefore, given the similarity between the wave predominant periods and the fundamental period of the isolated building, the ground motion in the superstructure could prove enlarged, instead of reduced. Several previous studies on this subject have been published [6–11].

Many design codes discourage the use of base isolation in soft soil [12–14]; sometimes, simplified design methods (equivalent static forces) are prevented, thus requiring the employment of more general strategies, typically non-linear time-history analysis [14]. This paper analyzes a representative case study, this being an isolated building in Shanghai; the particular interest of this case for China is discussed next.

The Wenchuan earthquake (12 May 2008) caused numerous casualties, principally students. Thereafter, concerns about the seismic safety of teaching buildings arose in China. In the Lushan earthquake (20 April 2013), a base-isolated hospital building experienced only minor damage and played a significant role in rescue work [15]; then, a broad pilot study on the seismic isolation of teaching buildings was undertaken. In the framework of this research effort, this paper investigates the rationality of using base isolation for buildings founded on soft soil. The aim is developing a strategy of verification and analyzing a relevant case study; no similar studies have been found in the technical literature.

The case study is a 6-story RC (reinforced concrete) building with rubber isolators and viscous dampers that had been recently constructed in Shanghai [16,17]. The building had been designed for seismic intensity degree 7 according to the current Chinese code [12], whose design input peak accelerations are 0.10 g and 0.22 g for moderate and rare earthquakes, respectively. Moderate and rare earthquakes correspond to a 10% and 2% possibility of being exceeded in 50 years, respectively. Given that the building is founded on soft soil, concern regarding the suitability of using base isolation arose; noticeably, the Chinese code [12] does not recommend this solution for that soil condition. This paper evaluates numerically the seismic performance of the isolated building; therefore, the study refers only to the after-construction stage. The performance is assessed through non-linear time-history analyses of the building being shaken by a number of seismic inputs; such analyses are performed with the software SAP2000 v16.0 [18]. These input accelerograms are selected to represent the site seismicity, mainly accounting for the soil conditions. In the analyses, the behavior of the superstructure is modelled as linear, while nonlinearities are concentrated in the isolation layer. The need for considering soil–structure interaction (SSI) is discussed, and SSI numerical simulations are carried out. Notably, given that the objective of the paper is to investigate the suitability of base isolation in buildings founded on soft soil, other soil types are not considered.

The adequacy of base isolation is assessed in both the superstructure and the isolation layer. In the superstructure, the appropriateness of base isolation is judged in terms of the reduction of interstory drift, absolute acceleration, and shear force. In the isolators, the correctness is evaluated in terms of axial force and lateral displacement (shear strain); for this purpose, the prescriptions of the Chinese code [12] and the European regulations for base isolation [19,20] and for rubber bearings [21] are considered.

2. Building under Consideration

2.1. Superstructure

The structure of the analyzed building is a RC frame; there are no shear walls or other structural or non-structural members that might provide significant lateral stiffening or strengthening. The building has six stories and one basement; the isolators are placed at the ground level, i.e., on the top of the basement columns. Figure 1 represents the analyzed building; Figure 1a displays a 3-D rendered view and Figure 1b exhibits a picture. Figure 1c,d refers to a typical floor plan layout; Figure 1c shows the architectural distribution and Figure 1d represents the structural configuration, indicating columns (black squares) and beams.
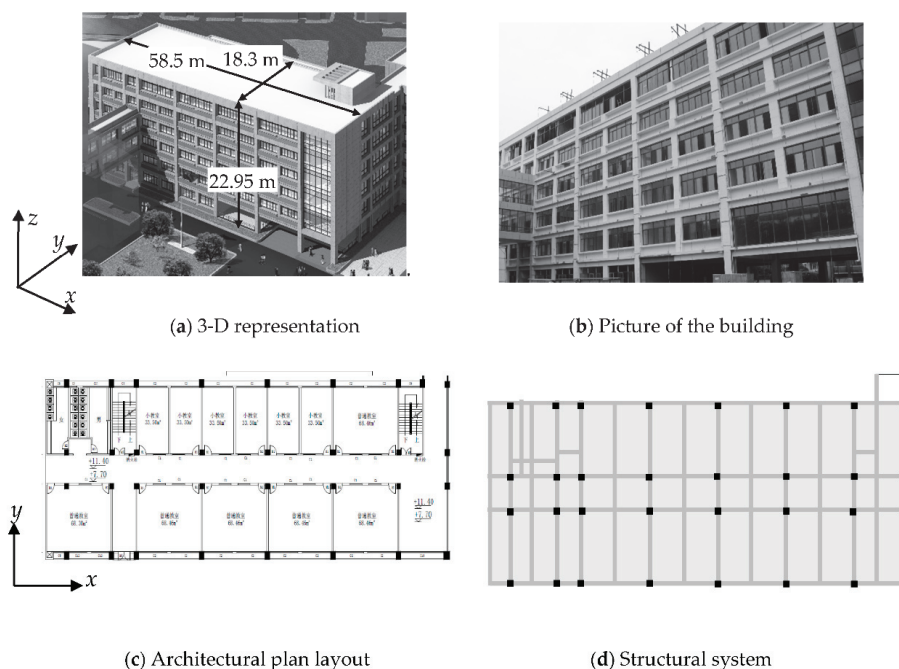

(**a**) 3-D representation

(**b**) Picture of the building

(**c**) Architectural plan layout

(**d**) Structural system

Figure 1. Analyzed case study building.

Figure 1 shows that the plan area is rectangular, and the configuration is essentially regular; as shown in Figure 1a, the building width, depth and height are 58.5 m, 18.3 m and 22.95 m, respectively. The columns have a constant rectangular cross section ranging between 60 cm × 70 cm (inner columns) and 90 cm × 90 cm (corner columns). The slabs are formed by rectangular beams that are 30 to 35 cm wide and 50 to 70 cm deep, and constant-depth slabs being 11 to 14 cm deep. The characteristic value of the concrete compressive strength is f_{ck} = 30 MPa and the deformation modulus is estimated as E_c = 30 GPa. The reference [16] contains deeper information on the structural parameters. The live (variable) gravity load is established according to the Chinese design code [22], ranging between 2 and 2.5 kN/m^2, except for stairs and other highly crowded areas. The seismic weight corresponds to the combination $D + 0.5 L$ where D and L account for dead (permanent) and live (variable) loads, respectively. For this loading level, the building mass is 9576 t; from the first to top (6th) floor, the masses are 1569, 1652, 1607, 1621, 1854 and 1273 t, respectively. To analyze the influence in the plan symmetry of irregular columns arrangements and other unevenness (e.g., balconies), the eccentricities between the mass and rigidity centers of each floor are determined: in the x direction, the eccentricity

ranges between 0.15% (first floor) and 0.70% (top floor) while in the *y* direction, it ranges between 3.75% (top floor) and 5.14% (first floor).

2.2. Isolation Layer

The isolation system is formed by the parallel combination of rubber bearings (isolation units) and viscous dampers; the sought damping ratio considers the recommendations in [23]. Two types of isolator are employed: ordinary natural rubber bearings and lead-rubber bearings, i.e., incorporating a central lead plug core to provide additional damping. Those devices are termed in this paper NRB (natural rubber bearing) and LRB (lead rubber bearing), respectively.

The rubber shear modulus is $G = 0.392$ N/mm^2 for all the devices; Table 1 displays the other main geometric and mechanic parameters of the rubber isolators.

Table 1. Rubber bearing parameters.

| Name	Diameter (mm)	Height (mm)	Rubber Layer Height (mm)	Rubber Height (mm)	Lead Plug Diameter (mm)	Horizontal Stiffness (kN/m)	Critical Shear Strain/Stress (%/MPa)	Yielding Force (kN)	After-Yielding Horizontal Stiffness (kN/m)
NRB700	700	451.5	5	200	-	742	280/8	-	-
NRB800	800	438.5	6	204	-	951	301/10	-	-
LRB700	700	451.5	5	200	160	1565	282/8	160	764
LRB800	800	438.5	6	204	160	1758	304/10	160	972

Two types of viscous damper are installed in the *x* and *y* directions, respectively; Table 2 displays their major parameters. Section 3.2 describes the meaning of such parameters.

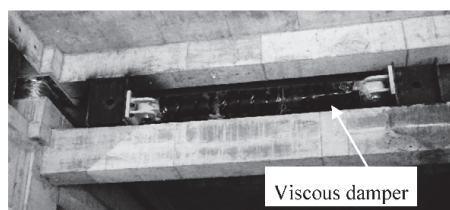**Table 2.** Parameters of the viscous dampers.

Direction	Exponent α	Initial Stiffness (kN/mm) *	Maximum Stroke (mm)	Damping Coefficient c (kN/(mm/s)$^{0.4}$)	Speed (mm/s)	Maximum Damping Force (kN)	Design Life (Years)
x	0.4	49	±350	70	600	900	50
y	0.4	42	±350	60	600	800	50

* Elastic combined axial stiffness of the supporting brace and internal damper portion.

Figure 2 contains pictures and sketches of the installation of the rubber bearings and the viscous dampers. Figure 2a,b represent a pair of isolators and a damper, respectively; Figure 2b shows that the viscous dampers are installed (between two adjoining isolators) connecting the ground floor slab (superstructure) with the basement columns (substructure). Figure 2c displays the plan layout of isolators and dampers. Figure 2c shows that isolators and dampers are arranged symmetrically; as well, dampers and LRBs (bearings with lead plugs) are located near the building perimeter, thus providing torsion damping and stiffness.
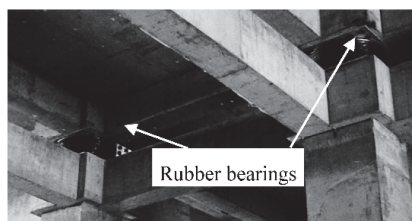
| (**a**) Rubber bearings | (**b**) Viscous damper |

Figure 2. *Cont.*

O,□: Natural rubber bearings   ◉,■: Lead-rubber bearings   ———: Viscous damper

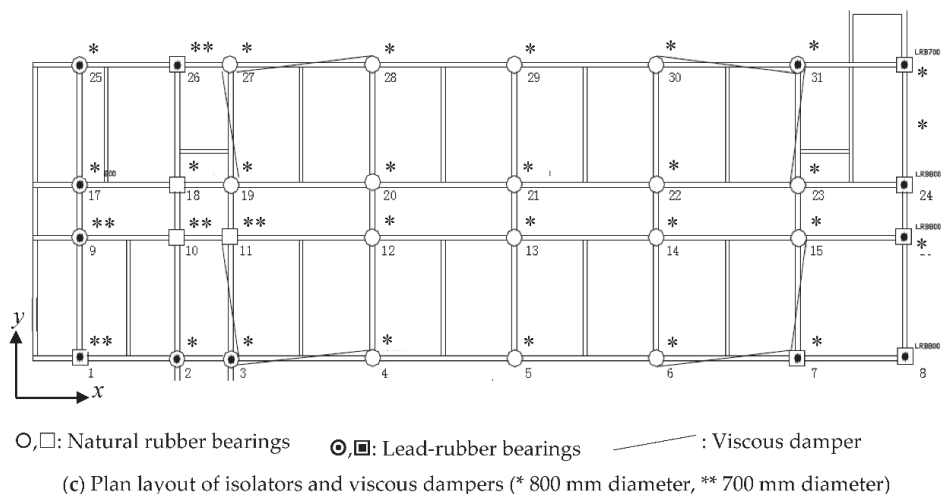(**c**) Plan layout of isolators and viscous dampers (* 800 mm diameter, ** 700 mm diameter)

Figure 2. Installation of isolators and dampers in the building.

2.3. Soil and Foundation

As the soil is soft, the building is founded on piles. Each pile is 600 mm in diameter and 28 m deep. The bedrock in Shanghai is often located 200~300 m underground, being covered by thick quaternary unconsolidated sediments. For categorization purposes, the soil is divided into 9 layers, and each layer is split into several sub-layers. At the bottom of the piles (28 m depth), the soil condition is classified as layer 7-1, "grey clay silt"; the weighted harmonic average shear wave velocity down to 30 m (v_{s30}) ranges between 84 and 256 m/s [24]. For the seismic design, the soil is categorized as type IV; this is the softest class, according to the Chinese code [12]. Section 3.3 discusses more deeply the ground parameters that are relevant to the soil–structure interaction.

3. Numerical Modeling of the Isolated Building Dynamic Behavior

3.1. Model of the Superstructure

The building lateral dynamic behavior is described with a linear 3D model implemented in the SAP2000 v16.0 software package [18]. Beams and columns are represented by frame elements, and slabs are modeled with shell elements. The rigid diaphragm effect is indirectly considered by the high in-plane stiffness of slabs. The stiffness of the members is determined based on their gross sectional parameters, although reduced to account for cracking; the corresponding reducing coefficient is 0.5 for beams, and 1 for columns and slabs [25]. Noticeably, that reduction is unnecessary in the Chinese code [12]. Figure 3 displays an overview of the building model. The damping is described by a classical Rayleigh model; the mass and stiffness coefficients are selected for a damping ratio 0.05 in the first two modes.

3.2. Model of Isolators and Dampers

The behavior of the natural and lead-rubber bearings is described by linear and hysteretic bilinear models, respectively. Table 1 displays the main parameters of both models; their torsional stiffness is neglected.

Regarding the dampers, their behavior is represented by a nonlinear viscous damping model:

$$f = c\,\dot{x}^{\alpha} \tag{1}$$

In Equation (1), f represents the damper force; the values of the damping coefficient c and the exponent α are listed in Table 2. Equation (1) can be considered as a modification of the classical linear Maxwell model [26,27], where the stiffness coefficient has been neglected.
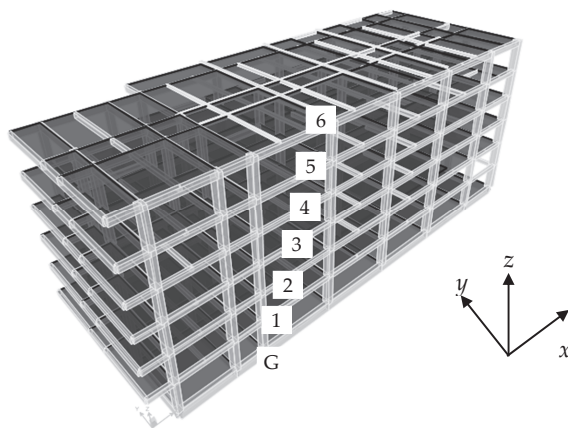

Figure 3. Spatial (3-D) model of the building structure.

3.3. Soil–Structure Interaction Modelling

A number of studies on the relevance of SSI in base-isolated buildings have been reported [6,8,9,11,28–30]. These studies conclude that the consideration of SSI is not necessary, unless the soil is very soft and the building is relatively stiff; moreover, commonly, the SSI effect is rather beneficial. Therefore, the above studies seem to indicate that, given the high lateral flexibility of the isolated building, SSI might be neglected. However, for the sake of safety, a simplified SSI study is performed herein. SSI is described with an uncoupled linear spring model [31]; such a model consists in representing the interaction by six springs that connect each pile cap to the adjoining soil.

The axial stiffness of each pile is calculated by two approaches: (a) it is assumed that the piles rest on a rigid bedrock, therefore, their stiffness is $E_p A_p/L_p$ (E_p, A_p and L_p refer to modulus of deformation, cross section area and length of the pile, respectively), and (b) since the piles do not actually reach the bedrock, only the friction stiffness is accounted for. In this last case, the vertical stiffness K_{vf} of a pile can be calculated by the formulation proposed in [32]:

$$K_{vf} = 1.8\, E_s\, D_p\, \lambda^{0.55}\, \eta^{-b} \tag{2}$$

In Equation (2), E_s is the soil modulus of elasticity, D_p is the pile diameter, λ is the ratio between the pile length and diameter ($\lambda = L_p/D_p$), η is the ratio between the soil and pile moduli of elasticity ($\eta = E_p/E_s$), and the exponent b is given by $b = \lambda/\eta$. In the analyzed case, $E_p = 26$ GPa, $L_p = 28$ m, $D_p = 0.60$ m, and E_s is calculated after the shear modulus G_s based on the weighted average shear wave velocity (v_s) and the soil density (ρ_s) on the top 28 m. Table 3 displays the soil properties of each layer in the top 28 m:

Table 3. Parameters of the soil layers in the top 28 m.

Layer Type	Cumulated Depth (m)	Density (kg/m³)	Shear Wave Velocity (m/s)
Filled earth	4.2	1870	112
Muddy-silty clay	9.5	1820	128
Muddy clay	22.5	1760	178
Muddy-silty clay	32.8	1800	245

Table 3 shows that, in this case, the average values of the shear wave velocity and density are v_s = 171.8 m/s and ρ_s = 1795 kg/m^3, respectively; therefore: G_s = 53 MPa, and, by assuming that the Poisson ratio is ν = 0.25, E_s = 132.5 MPa. Finally, $E_p \, A_p/L_p$ = 263 kN/mm and K_{vf} = 338 kN/mm; thus, the friction stiffness (K_{vf}) is 1.29 times higher than the axial one ($E_p \, A_p/L_p$), what is consistent with the estimations in [33]. Finally, for each cap, the vertical spring stiffness is obtained as the sum of those of each pile.

The rotational stiffness with respect to the horizontal axes are determined, from the vertical stiffness of each pile, by equilibrium conditions. For each cap, the torsional and horizontal stiffness are determined, in terms of the soil parameters and foundation dimensions, as indicated in [34]. The soil damping effect is neglected; this is a conservative assumption, since it would decrease the base shear force.

4. Modal Analysis of the Building

Linear modal analyses of the building under fixed-base and isolation conditions are carried out by using the models described in the previous section. Table 4 displays the periods and modal mass ratios of the first six modes of the base-isolated building, and of the first three modes of the fixed-base building; φ accounts for twist angle (torsion). Given that the incorporation of the isolation layer adds three new modes, in Table 4 the first three modes of the fixed-base building are associated with the 4th, 5th and 6th modes of the base-isolated building, respectively. In the isolated building, the periods are calculated for the effective secant stiffness (of the lead-rubber isolators) that correspond to 100% shear strain. In Table 4, the highlighted values correspond to the biggest component of each mode, in terms of modal mass factor.

Table 4. Modal parameters of the building under fixed-base/isolated conditions.

Mode No.	Period (s)	Modal Mass Factor x	Modal Mass Factor y	Modal Mass Factor φ
-/1	-/3.586	-/0.046	**-/0.910**	-/0.03561
-/2	-/3.528	**-/0.940**	-/0.053	-/0.0039
-/3	-/2.983	-/0.011	-/0.029	**-/0.96049**
1/4	1.229/0.571	0.010/7.25×10^{-7}	**0.717**/0.004	0.074/1.142
2/5	1.163/0.502	**0.621**/2.29×10^{-3}	0.046/1.02×10^{-6}	0.156/2.23×10^{-6}
3/6	1.106/0.177	0.196/7.08×10^{-8}	0.037/0.39×10^{-6}	**0.569**/8.59×10^{-8}

Table 4 provides the following remarks:

- **Fixed-base building**. The first mode corresponds basically to motion along the y direction (also some torsion), the second mode involves motion along the x direction (there is torsion as well), and the third mode contains mainly torsion. The relatively long period of the third mode (1.106 s) indicates a low torsional stiffness; this is coherent with the absence of any important stiffening element in the façades. Therefore, further verifications are carried out. The simplified expression for regular reinforced concrete frames that are contained in the European [19] and American [35] codes (among others) provide a fundamental period equal to 0.676 s; since the building is rather flexible (as base isolation allows for significant reductions in the lateral design forces), the difference among this value and those in Table 4 is feasible. For further verification, the building has been also modelled with the PKPM Chinese software code [36]; the obtained periods are highly similar to those from SAP.
- **Base-isolated building**. The first three modes correspond basically to motion along the y, x and φ directions, respectively. Such modes gather most of the mass; this indicates a rather satisfactory performance of base isolation, since those modes correspond basically to rigid-body motion (i.e., without any structural damage).

■ **Fixed-base vs. base-isolated building**. Comparison among the periods of the first three modes of the base-isolated building and those of the fixed-base building shows that base isolation elongates the periods as expected. Similar comparison among the modal mass factors shows that the base-isolated building vibrates more symmetrically; this can be read as a proper design of the isolation system, in the sense that the slight plan asymmetry of the fixed-base building is corrected in the isolated solution.

Table 5 displays the periods and modal mass ratios of the first six modes of the base-isolated building; such information is obtained for two conditions: by considering and neglecting SSI (Section 3.3). In Table 5, the values of the mass ratio that are smaller than 10^{-3} are indicated as "-"; SSI-a and SSI-b correspond to the consideration of axial and friction stiffness of the piles, respectively (Section 3.3). As in Table 4, the highlighted values correspond to the biggest component, in terms of modal mass factor, of each mode. Table 5 shows that the influence of SSI on the periods and modal mass ratios of the first three modes can be ignored. Also, comparison between both models of SSI shows little influence of the vertical stiffness of piles; therefore, the SSI results are reliable.

Table 5. Modal parameters of the base-isolated building considering and without considering soil–structure interaction (SSI).

Mode No.	Period (s)			Modal Mass Factor x			Modal Mass Factor y			Modal Mass Factor φ		
	SSI-a	SSI-b	No SSI	SSI-a	SSI-b	No SSI	SSI-a	SSI-b	No SSI	SSI-a	SSI-b	No SSI
1	3.603	3.608	3.586	0.032	0.053	0.046	**0.942**	**0.877**	**0.910**	0.023	0.067	0.036
2	3.544	3.540	3.528	**0.957**	**0.922**	**0.940**	0.036	0.067	0.053	0.004	0.008	0.004
3	2.892	3.178	2.983	0.008	0.022	0.011	0.018	0.052	0.029	**0.972**	**0.921**	**0.961**
4	0.443	0.661	0.571	0.002	-	-	-	0.003	0.004	-	-	-
5	0.306	0.600	0.502	-	0.002	-	0.004	-	-	0.001	0.001	-
6	0.193	0.580	0.177	-	0.001	-	-	-	-	-	0.003	-

5. Seismic Inputs for the Dynamic Analyses

Representative accelerograms are selected according to the former and current Shanghai design codes [37]. Two sets of seven trios of accelerograms (i.e., in two horizontal directions and in vertical direction) are chosen. Each set is composed of five natural earthquake records and two artificial inputs; the records are taken from the PEER database [38], and the artificial inputs are created by modifying recorded accelerograms. The accelerograms of the first set correspond to soil with predominant period 0.9 s and are scaled to 1 m/s^2 (moderate earthquake); for the second set, the soil period is 1.1 s and the acceleration is 2.2 m/s^2 (rare earthquake). Tables 6 and 7 display the main features of both sets, respectively; the information in such Tables is described next. In the left column, "NR" accounts for "Natural Record" while "AW" means "Artificial Wave". x/y directions correspond to strong/weak components, respectively. PGV and PGD refer to Peak Ground Velocity and Displacement, respectively. I_A is the Arias intensity [39] given by $I_A = \frac{\pi}{2g} \int \ddot{x}_g^2 \, dt$, where $\ddot{x}_g$ is the input ground acceleration; the Arias intensity is an estimator of the input severity. I_D is the dimensionless seismic index [40] given by $I_D = \frac{\int \ddot{x}_g^2 \, dt}{PGA \cdot PGV}$; I_D accounts for the relevance of the velocity pulses. The Trifunac duration is the elapsed time between 5% and 95% of the Arias intensity I_A [41]. The closest distance corresponds to the shortest way to the rupture surface. The hypocentral distance is the straight separation between the hypocentre and the recording station. v_{s30} is the harmonic weighted average shear wave velocity in the top 30 m; this parameter characterizes the soil type.

Table 6. Seismic inputs for soil predominant period 0.9 s and scaled to maximum acceleration 1 m/s^2.

Code	Earthquake	Date	M_w	Hypocentral Depth (km)	Station	Component		PGV (m/s)	PGD (cm)	I_A (m/s)	I_D	Trifunac Duration (s)	Closest Distance (km)	Hypocentral Distance (km)	v_{s30} (m/s)
NR0.9-3	Kocaeli, Turkey	17-08-1999	7.51	15.0	USAK	x	USK090	0.272	4.831	0.451	10.36	35.52	226.7	237.0	274.5
						y	USK180	0.310	7.700	0.264	5.32	35.36			
NR0.9-4	Hector Mine, USA	16-10-1999	7.13	5.0	San Bernardino Fire Station #9	x	0688c090	0.262	3.967	0.317	7.56	20.44	108.0	114.8	271.4
						y	0688a360	0.123	7.532	0.280	14.22	28.10			
NR0.9-5	Denali, USA	03-11-2002	7.9	4.9	Anchorage New Fire Station #7	x	1734090	0.262	3.967	0.499	11.89	31.72	275.9	296.55	274.5
						y	1734360	0.228	2.060	0.561	15.37	29.80			
NR0.9-6	Chichi, Taiwan	20-09-1999	6.02	18.0	CHY039	x	CHY039-N	0.197	14.260	0.349	11.06	35.70	46.8	52.53	201.2
						y	CHY039-E	0.244	18.919	0.299	7.65	36.72			
NR0.9-7	Chichi, Taiwan	20-09-1999	7.62	18.0	CHY059	x	CHY059-N	0.185	14.162	0.398	13.44	38.56	86.3	88.53	191.1
						y	CHY059-E	0.190	6.717	0.361	11.87	33.94			
AW0.9-2	Loma Prieta, USA	18-10-1989	6.93	17.5	Foster City Menhaden Court	x	MEN270	0.272	2.138	0.317	7.28	22.08	45.4	68.0	126.4
						y	MEN360	0.242	2.211	0.308	7.95	20.10			
AW0.9-1	Hokkaido, Japan	29-11-2004	7.1	48	HKD085	x	HKD085EW	0.274	2.127	0.344	7.84	41.68	98.1	-	150.0
						y	HKD085NS	0.242	2.762	0.183	4.72	33.04			

Table 7. Seismic inputs for soil predominant period 1.1 s and scaled to maximum acceleration 2.2 m/s^2.

Code	Earthquake	Date	M_w	Hypocentral Depth (km)	Station	Component		PGV (m/s)	PGD (cm)	I_A (m/s)	I_D	Trifunac Duration (s)	Closest Distance (km)	Hypocentral Distance (km)	v_{s30} (m/s)
NR1.1-3	Imperial Valley, USA	15-10-1979	7.62	10.0	El Centro Array #12	x	H-E12140	0.443	25.937	1.390	8.91	19.38	17.9	33.5	196.9
						y	H-E12230	0.284	20.607	0.975	9.75	19.14			
NR1.1-4	Chichi, Taiwan	20-09-1999	7.62	6.8	CHY058	x	CHY058-E	0.467	34.299	3.615	21.97	45.64	59.8	91.4	237.6
						y	CHY058-N	0.490	32.451	2.896	16.78	45.88			
NR1.1-5	Chichi, Taiwan	20-09-1999	7.62	6.8	CHY090	x	CHY090-E	0.446	28.146	2.917	18.57	38.78	58.4	89.8	201
						y	CHY090-N	0.556	40.618	2.569	13.12	45.32			
NR1.1-6	Chichi, Taiwan	20-09-1999	7.62	6.8	KAU008	x	KAU008-E	0.575	68.312	3.230	15.95	46.06	107.0	143.7	285.9
						y	KAU008-N	0.633	57.951	3.054	13.70	46.06			
NR1.1-7	Chichi, Taiwan	20-09-1999	7.62	6.8	KAU058	x	KAU058-E	0.584	76.979	3.172	15.42	40.16	107.8	143.3	201
						y	KAU058-N	0.717	72.504	4.263	16.88	46.84			
AW1.1-2	Morgan Hill	24-04-1984	6.19	8.5	Foster City APEEL 1	x	A01040	0.450	55.382	1.528	9.64	26.82	53.9	55.0	116.4
						y	A01310	0.552	50.816	1.558	8.01	26.56			
AW1.1-1	Hokkaido, Japan	26-09-2003	8.0	42	HKD066	x	HKD066EW	0.423	34.131	1.202	8.07	39.74	226.5	-	116.1
						y	HKD066NS	0.396	45.887	1.756	12.59	45.56			

The natural records in Tables 6 and 7 are selected based on the similarity between their individual response spectra and the code design spectra. Figure 4 displays response spectra of natural selected inputs (grey line) together with the code design spectrum (black line). Noticeably, all the spectra in Figure 4 correspond to records scaled to 1 m/s²; therefore, the plots in Figure 4c,d are reduced by a factor of 2.2. Figure 4 shows a rather satisfactory fit between the spectra of the scaled inputs and the code spectrum, particularly in the main (*x*) direction.

(**a**) Inputs in *x* direction for soil predominant period 0.9 s

(**b**) Inputs in *y* direction for soil predominant period 0.9 s

(**c**) Inputs in *x* direction for soil predominant period 1.1 s

(**d**) Inputs in *y* direction for soil predominant period 1.1 s
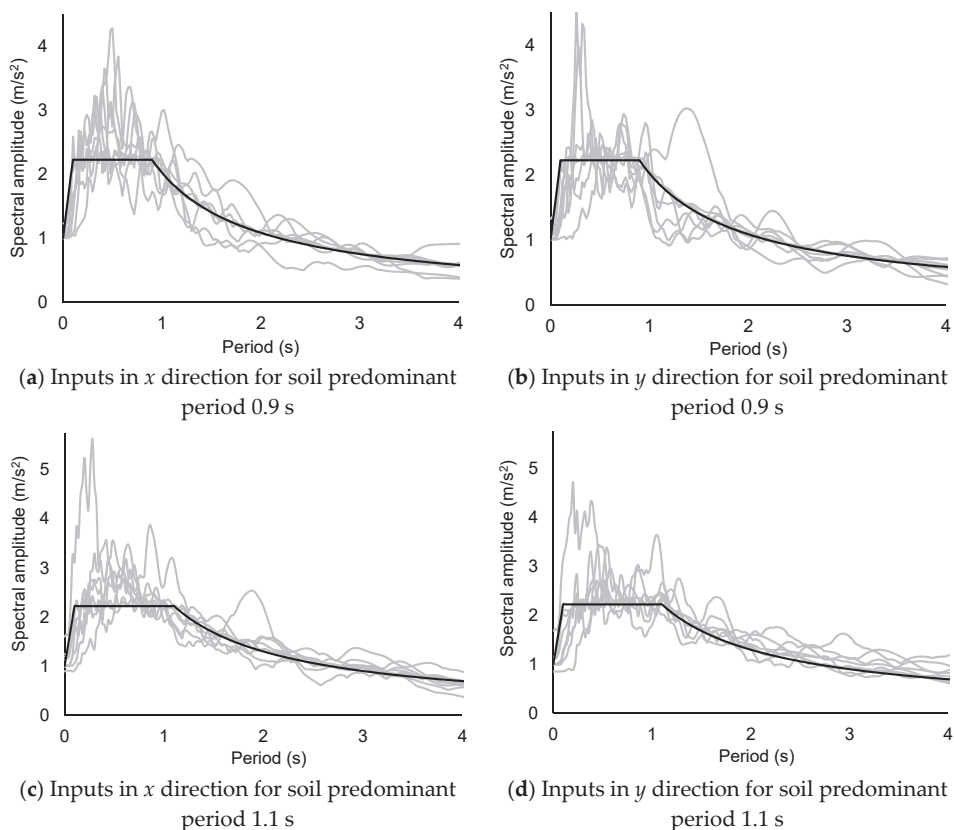
Figure 4. Comparison between the response spectra of the natural selected inputs and the code design spectra.

The artificial inputs are generated to fit the design spectrum, according to [12]. The fitting is established through 100 control points with logarithmic distribution in the interval [2 Δt, 10 s], where Δt = 0.02 s. The tolerance is 5%, in terms of quadratic error.

6. Time-History Analysis

6.1. Global Description of the Analyses

This section discusses the results of the time-history analyses for the inputs described in Section 5; the *x/y* input components are applied in *x/y* directions (Figure 2), respectively. As discussed in [42], the most meaningful results in the superstructure are the drift angle, shear force and absolute acceleration; in the isolators, the axial forces, shear strain and torsion angle are also significant.

The dynamic analyses are performed by implementing the numerical model described in Section 3 in SAP2000 v16.0 software package [18]. The building (superstructure) behavior is linear,

the non-linearities are concentrated in the isolation layer. The analyses consider the simultaneous actuation of both horizontal input components. The time integration is performed using non-linear modal analysis; the time step is $\Delta t = 0.02$ s. The second-order effects have not been considered; it is observed that such effects do not over-magnify the relative displacements in the isolators, although can increase the moments significantly, sometimes more than 10%. It should be kept in mind that any numerical model is always affected by epistemic (and random) uncertainties as discussed in [43,44].

6.2. General Overview of the Results

Figure 5 displays representative displacement time-history responses, and hysteresis loops of a natural rubber bearing (Figure 5a,d), a lead-rubber bearing (Figure 5b,e), and a viscous damper (Figure 5c,f); the labeling of isolators and damper refers to Figure 2c. All the plots in Figure 5 correspond to the input NR1.1-7 in the x direction (Table 7). Figure 5 shows a regular behavior; the similarity among the time-history plots in Figure 5a–c confirms the rigid diaphragm effect of the ground floor slab. On the other hand, the hysteresis loops in Figure 5d indicate a linear behavior, without any encompassed area; the loops in Figure 5e have almost quadrilateral shape, typical of the plastification of metals. Finally, the shape of the hysteresis loops in Figure 5f is closer to a rectangle than to an ellipse, this being consistent with the value of exponent α ($\alpha = 0.4$, Table 2).

(**a**) Displacement time-history for NRB No. 27

(**b**) Displacement time-history for LRB No. 32

(**c**) Displacement time-history for dampers Nos. 27, 28

(**d**) Hysteresis loops of NRB No. 27 (**e**) Hysteresis loops of LRB No. 32

(**f**) Hysteresis loops of dampers Nos. 27, 28
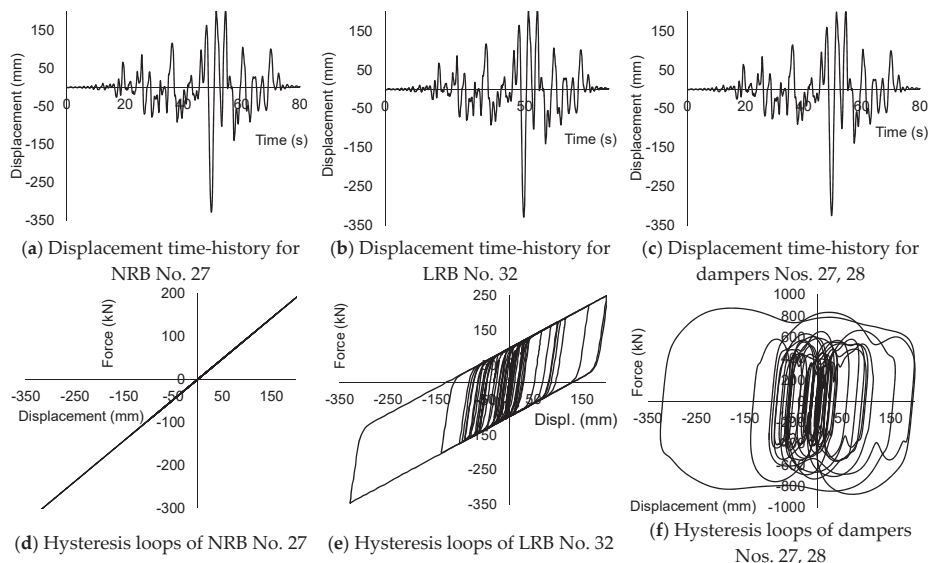
Figure 5. Dynamic responses of two isolators and a damper for input NR1.1-7 in the x direction (Table 7).

Under fixed-base and base isolation conditions, Tables 8 and 9 display average results for the "small" inputs NR0.9-3, NR0.9-6 and AW0.9-1 (Table 6), and the "big" inputs NR1.1-5, NR1.1-7 and AW1.1-1 (Table 7), respectively. Tables 8 and 9 consider three cases: (a) input in x direction, (b) input in y direction, and (c) simultaneous actuation of x and y inputs; these situations are denoted by "x", "y" and "$x + y$", respectively. Each table contains, for every story, the maximum values of the following quantities: (a) drift angle, (b) shear force normalized with respect to the supported weight (shear coefficient) and (c) absolute acceleration normalized with respect to the maximum input acceleration; such maxima refer to the shaking duration. Noticeably, the results for fixed-base conditions are obtained by assuming a linear behavior of the building structure; they are included only for comparison purposes. Finally, the drift angle in the isolators is equivalent to the rubber shear strain, i.e., the ratio between drift displacement and rubber height (Table 1).

Table 8. Average maximum * response values for the records NR0.9-3, NR0.9-6 and AW0.9-1 (Table 6).

Story	Input Direction	Drift Angle (%)		Shear Force/ Supported Weight		Absolute Acceleration/ Input Acceleration	
		Fixed-Base	Base Isolation	Fixed-Base	Base Isolation	Fixed-Base	Base Isolation
Ground	x	-	22.0 **	-	0.042	1	1.035
	y	-	42.5 **	-	0.052	1	1.034
	$x + y$	-	46.5 **	-	0.059	1	1.124
1	x	0.306	0.161	0.147	0.054	1.178	0.726
	y	0.247	0.193	0.122	0.058	0.963	0.745
	$x + y$	0.350	0.219	0.170	0.069	1.088	0.749
2	x	0.472	0.160	0.174	0.054	1.347	0.481
	y	0.452	0.219	0.134	0.058	1.031	0.569
	$x + y$	0.559	0.240	0.197	0.072	1.230	0.543
3	x	0.464	0.133	0.200	0.054	1.405	0.438
	y	0.468	0.195	0.147	0.058	1.277	0.530
	$x + y$	0.553	0.210	0.221	0.069	1.399	0.513
4	x	0.408	0.106	0.222	0.054	1.819	0.580
	y	0.410	0.157	0.159	0.058	1.517	0.615
	$x + y$	0.486	0.169	0.241	0.070	1.758	0.607
5	x	0.277	0.068	0.238	0.055	2.188	0.694
	y	0.296	0.108	0.170	0.059	1.721	0.736
	$x + y$	0.340	0.114	0.257	0.071	2.041	0.696
6	x	0.147	0.036	0.262	0.059	2.426	0.762
	y	0.176	0.063	0.188	0.062	1.923	0.831
	$x + y$	0.192	0.066	0.282	0.076	2.242	0.774

* "Maximum" refers to along the input duration. ** Drift displacement divided by rubber height (shear strain).

Table 9. Average of maximum * response values for the records NR1.1-5, NR1.1-7 and AW1.1-1 (Table 7).

Story	Input Direction	Drift Angle (%)		Shear Force/ Supported Weight		Absolute Acceleration/ Input Acceleration	
		Fixed-Base	Base Isolation	Fixed-Base	Base Isolation	Fixed-Base	Base Isolation
Ground	x	-	128.0 **	-	0.095	1	0.763
	y	-	132.0 **	-	0.105	1	1.035
	$x + y$	-	168.5 **	-	0.126	1	0.947
1	x	0.772	0.308	0.379	0.103	1.215	0.568
	y	0.903	0.381	0.387	0.115	1.073	0.731
	$x + y$	1.066	0.434	0.457	0.133	1.199	0.621
2	x	1.139	0.307	0.415	0.103	1.539	0.470
	y	1.656	0.433	0.453	0.115	1.636	0.497
	$x + y$	1.919	0.475	0.516	0.141	1.633	0.502
3	x	1.095	0.255	0.465	0.103	1.826	0.438
	y	1.726	0.384	0.520	0.115	2.152	0.480
	$x + y$	2.018	0.415	0.591	0.133	2.210	0.509
4	x	0.960	0.204	0.513	0.104	2.012	0.497
	y	1.541	0.310	0.580	0.116	2.586	0.523
	$x + y$	1.803	0.335	0.660	0.134	2.658	0.542
5	x	0.659	0.131	0.564	0.106	2.330	0.562
	y	1.118	0.213	0.631	0.118	2.992	0.582
	$x + y$	1.311	0.227	0.716	0.135	3.082	0.578
6	x	0.356	0.068	0.630	0.115	2.733	0.604
	y	0.668	0.125	0.708	0.126	3.433	0.631
	$x + y$	0.786	0.130	0.797	0.145	3.463	0.625

* "Maximum" refers to along the input duration. ** Drift displacement divided by rubber height (shear strain).

From the information in Tables 8 and 9, Figure 6 depicts, for further clarity, vertical profiles of drift angles (Figure 6a,c) and normalized absolute accelerations (Figure 6b,d). The results in Figure 6 correspond to the "$x + y$" cases.

(**a**) Drift angle for inputs for soil period 0.9 s

(**b**) Absolute acceleration/input acceleration for inputs for soil period 0.9 s

(**c**) Drift angle for inputs for soil period 1.1 s

(**d**) Absolute acceleration/input acceleration for inputs for soil period 1.1 s
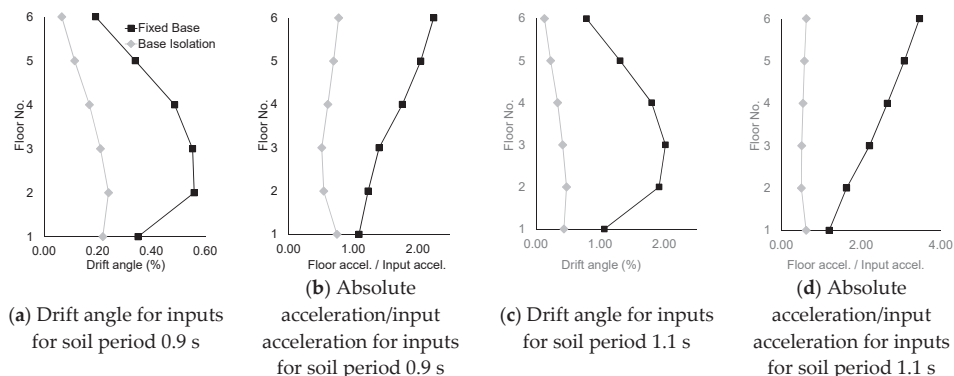
Figure 6. Vertical profiles of drift angles and absolute accelerations for combined $x + y$ inputs.

Table 10 displays the maximum drift angle, shear force and absolute acceleration for each input in Tables 8 and 9. The maxima in Table 10 refer to both the building height (1st to 6th stories) and the shaking duration. As in Tables 8 and 9, the shear force and absolute acceleration are normalized with respect to the supported weight and the maximum input acceleration, respectively. Again, as in Tables 8 and 9, the results for fixed-base conditions are obtained by supposing that the structure behaves linearly and, thus, are included only for comparison. For the base-isolated building, Table 10 displays also the ratios between the absorbed energies (E_ζ, E_{HD}, E_{HI}) and the input energy E_I. E_ζ, E_{HD} and E_{HI} are the energy dissipated by the structural damping, the viscous dampers and the rubber bearings, respectively; at the end of the shake, the energy balance reads $E_I \approx E_\zeta + E_{HD} + E_{HI}$.

Table 10. Maximum and cumulated response values for the selected inputs.

Input			Maximum * Drift Angle (%)		Maximum * Shear Force/Supported Weight		Maximum * Accel./Input Acceleration		E_ζ/E_I (Struct. Damp.)	E_{HD}/E_I (Dampers)	E_{HI}/E_I (Isolators)
Code	Period (s)	Direction	Fixed-Base	Base Isolation	Fixed-Base	Base Isolation	Fixed-Base	Base Isolation	Base Isolation		
NR0.9-3	0.9	x	0.388	0.108	0.151	0.042	2.79	0.771	0.196	0.551	0.247
		y	0.293	0.169	0.099	0.057	1.707	0.886	0.176	0.507	0.312
		$x + y$	0.400	0.168	0.156	0.058	2.281	0.723	0.177	0.508	0.313
NR0.9-6	0.9	x	0.363	0.108	0.148	0.044	2.493	0.716	0.151	0.557	0.292
		y	0.416	0.137	0.133	0.049	2.457	0.799	0.165	0.509	0.326
		$x + y$	0.388	0.151	0.164	0.061	2.394	0.812	0.148	0.525	0.327
AW0.9-1	0.9	x	0.271	0.113	0.101	0.041	1.996	0.799	0.165	0.565	0.262
		y	0.296	0.157	0.114	0.050	1.813	0.809	0.192	0.519	0.285
		$x + y$	0.421	0.184	0.148	0.059	2.052	0.788	0.167	0.552	0.276
NR1.1-5	1.1	x	0.689	0.191	0.317	0.083	2.531	0.656	0.145	0.532	0.322
		y	1.299	0.308	0.391	0.104	3.422	0.66	0.156	0.491	0.351
		$x + y$	1.460	0.294	0.410	0.117	3.652	0.665	0.151	0.532	0.316
NR1.1-7	1.1	x	1.028	0.265	0.444	0.123	3.212	0.628	0.154	0.531	0.314
		y	1.451	0.359	0.432	0.131	4.032	0.740	0.190	0.489	0.315
		$x + y$	1.632	0.332	0.444	0.154	4.166	0.782	0.176	0.527	0.297
AW1.1-1	1.1	x	0.716	0.174	0.301	0.079	2.457	0.528	0.138	0.533	0.328
		y	0.980	0.359	0.294	0.080	2.843	0.492	0.144	0.488	0.366
		$x + y$	1.280	0.282	0.410	0.106	2.571	0.428	0.137	0.519	0.342

* "Maximum" refers to both the building height and the input duration.

To analyze the time evolution of the energy balance, Figure 7 represents the time-histories of the energies E_I, E_ζ, E_{HD} and E_{HI} (Table 10) for the input NR0.9-6 (Table 6); "Input Energy", "Damping Energy", "Dampers Energy" and "Isolators Energy" account for E_I, E_ζ, E_{HD} and E_{HI}, respectively.
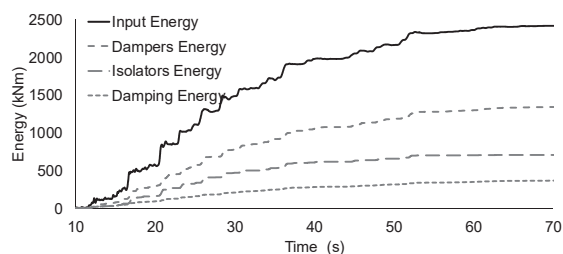
Figure 7. Time-history of the energy components for the input NR0.9-6 (Table 6).

Tables 8–10, and Figures 6 and 7 provide the following remarks:

- **Drift angle in the superstructure**. Except in few cases, the isolation reduces the drift displacements; for the 0.22 g inputs (Table 9), that lessening is higher in the top stories. In base isolation conditions, the drift is rather moderate, even for the strongest inputs (Table 9); this trend confirms that the assumption of linear behavior for the superstructure is correct. Finally, comparison between the results for inputs with maximum acceleration 0.1 g and 0.22 g shows that the reduction generated by the isolation is greater for the strongest inputs; this difference can be explained by the non-linear behavior of the lead-rubber bearings: the higher the shear strain, the higher the equivalent damping and the lower the effective secant stiffness, thus leading to a more intense isolation.

- **Drift angle in the isolators**. The shear strains for the inputs with acceleration 0.22 g (Table 9) are more than 2.2 times higher than those for the inputs with 0.1 g (Table 8). Obviously, this circumstance implies non-linear behavior of the lead-rubber bearings. On the other hand, no relevant permanent displacements are observed; this can be read as a satisfactory behavior of the isolation units.

- **Shear coefficient in the superstructure**. The isolation diminishes significantly the story shear forces; that decreasing is higher for the top stories and the strongest inputs. For the base-isolated building, the shear coefficient is near-constant along the building height; this seems to indicate a high participation of the first mode.

- **Base shear coefficient**. As expected, the isolation reduces appreciably the base shear force. For the less severe inputs (0.1 g, Table 8), the diminution ranges between 55% ("*y*" case) and 70% ("*x*" case); for the strongest inputs (0.22 g, Table 9), the lessening is roughly 75% in all the cases. This difference can be explained by the non-linear behavior of the lead-rubber bearings.

- **Absolute acceleration in the superstructure**. The absolute acceleration at the ground floor (above the isolation layer) is not reduced, compared to the driving input; in numerous cases, it is even slightly increased. This undesired circumstance might be due to the soft soil influence. However, in the other floors, the absolute acceleration is decreased, compared to the fixed-base case; more precisely, as is common in seismically isolated buildings, the reduction is higher in the top stories. As well, such decreasing is more important for the inputs with acceleration 0.22 g (Table 9). It is well known that the spectral ordinate is roughly equivalent to the ratio between the ground and the top floor acceleration; accordingly, the percentages of reduction of the top floor absolute acceleration and the base shear force are rather similar.

- **Dissipated energy**. Table 10 shows that the percentage of energy dissipated at the isolation interface ($E_{HD} + E_{HI}$, corresponding to viscous dampers and lead-rubber bearings, respectively) is above 80% of the input energy, being slightly higher for the stronger inputs (Table 9). Comparison with the ordinary values of the ratio between the input and hysteretic energies [45] shows

that this percentage is clearly above the common demands in terms of energy contributable to damage. Plots from Figure 7 show that the maximum values are obtained at the end of shake; this observation confirms that, for energy-based design, using the final values of energy is an adequate strategy.

■ **Simultaneity of the *x* and *y* inputs**. As expected, for both the fixed-base and base-isolated buildings, the average drift ratios and shear coefficients for the simultaneous action of the *x* and *y* inputs are bigger than those generated by the *x* and *y* inputs acting separately. Conversely, regarding the absolute acceleration, the balance is unclear; this apparent inconsistency can be explained by the small building asymmetry (Section 2.1), as any unidirectional input can generate responses containing *x*, *y* and torsion (φ) components (Table 4). Broadly speaking, the strategy of combining the full value in one direction with 30% of the value in the orthogonal direction seems to be sufficiently conservative.

6.3. Results for the Rubber Bearings

Apart from the general considerations in Section 6.2, this subsection discusses the performance of the rubber bearings in terms of buckling instability and shear deformation. Table 11 shows, for the isolators Nos. 29, 32, 24 and 17 (Figure 2), the maximum values of axial force, torsion angle and drift displacement. The displayed results correspond to the seismic inputs in Table 10; the axial force generated by the gravity loads (combination *D* + 0.5 *L*) is also shown (bottom row). In a similar way to Table 8 through Table 10, results for "*x*", "*y*" and "*x* + *y*" inputs are presented; herein, results corresponding to the combination of the responses in "*x*" and "*y*" directions are also shown. These combinations are obtained according to the European regulations [19]; two empirical criteria are considered: SRSS (square root of sum of squares), and *X* + 0.3*Y* or *Y* + 0.3*X*. *X* and *Y* represent the effect of the inputs in *x* and *y* directions, respectively. For the axial force and torsion angle, the combinations are $\sqrt{X^2 + Y^2}$, on one hand, and *X* + 0.3*Y* or *Y* + 0.3*X*, on the other hand; for the drift displacements, the combinations are $\sqrt{X^2 + (0.3Y)^2}$ and $\sqrt{(0.3X)^2 + Y^2}$. Comparison among the cases "Combination" and "*x* + *y*", shows low correlation; in some cases, the simplified values for "Combination" are over-conservative while in other cases they are extremely under-conservative. This shows that the usual empirical combination criteria are not always on the safe side.

The results in Table 11 are used next to check, in terms of buckling instability and maximum shear strain, the requirements of the Chinese code [12] and the European regulation [20] (8.2.3.4).

Buckling stability. The Chinese code [12] indicates that the average drift displacement in the rubber isolators should not exceed 0.55 times the rubber diameter. This condition is fulfilled in almost all the cases; more precisely, that threshold is only (slightly) exceeded in one case (corresponding to a "*x* + *y*" case). The Chinese code does not explicitly require consideration of that coincident actuation; for this unclear situation, the European regulation [21] is considered instead. In that code, it is required that the demanding axial force does not exceed the critical load of each isolator unit; such force is given by $P_{cr} = \lambda \, G \, A_r \, a' \, S/T_q$, where $\lambda = 1.1$ (for circular devices), *G* is the rubber shear deformation modulus, A_r is the rubber bearing plan area, a' is the device diameter, *S* is the shape factor (ratio between the diameter of the device and the thickness of each rubber layer) and T_q is the total rubber thickness. By neglecting (conservatively) the stiffening effect of the lead plug, the following two values of the critical load are obtained:

$$700 \text{ mm diameter } P_{cr} = 2.10 \times 10^4 \text{ kN}$$
$$800 \text{ mm diameter } P_{cr} = 2.80 \times 10^4 \text{ kN}$$

Table 11 shows that the maximum axial forces in the 700 and 800 mm isolators are $N_{Ed,max}$ = 4536 kN (device No. 24, input NR1.1-7, case "*x* + *y*") and $N_{Ed,max}$ = 6099 kN (device No. 17, input NR1.1-7, case "*x* + *y*"), respectively; thus, in both cases $N_{Ed,max} < P_{cr}/4$. On the other hand, [21] prescribes that it should be also checked that $\delta \leq 0.7$, where δ is the ratio between the design drift displacement d_{bd} and the device diameter; the design drift is conservatively taken as the

maximum value in Table 11: δ = 0.7 and 0.61 for 700 and 800 mm isolators, respectively. Therefore, this criterion is fulfilled in both types of device.

Maximum shear strain. In the European code [21], the maximum design shear strain is given by $\varepsilon_{t,d} = \varepsilon_{c,E} + \varepsilon_{q,max} + \varepsilon_{\alpha,d}$; in this expression, $\varepsilon_{c,E} = 6\, S/A_r\, E'_c$, $E'_c = 3\, G\, (1 + 2\, S^2)$, $\varepsilon_{q,max} = d_{bd}/T_q \leq 2.5$, and $\varepsilon_{\alpha,d} = 0.003\, (a'^2 + b'^2)\, t_r/2\, \Sigma\, t^3_r$, where $a' = b'$ (for circular devices), and t_r is the thickness of each rubber layer. For the 700 mm diameter isolators, $E'_c = 2882$ MPa, and for the 800 mm ones, $E'_c = 2614$ MPa; then:

$$700 \text{ mm diameter } \varepsilon_{t,d} = \varepsilon_{c,E} + \varepsilon_{q,max} + \varepsilon_{\alpha,d} = 4.77$$
$$800 \text{ mm diameter } \varepsilon_{t,d} = \varepsilon_{c,E} + \varepsilon_{q,max} + \varepsilon_{\alpha,d} = 4.90$$

Since both above results are smaller than $7/\gamma_m$ (where γ_m is a safety factor, being $\gamma_m = 1$ in this case), this criterion is fulfilled.

Table 11. Maximum * response values for the bearings No. 29 (NRB **), 32 (LRB ***), 24 (LRB **) and 17 (LRB **).

Input			Axial Force (kN)				Torsion Angle (rad)	Drift Displacement (mm)
Code	Period (s)	Input Direction	No. 32	No. 24	No. 29	No. 17		
NR0.9-3	0.9	x	338.1	266.5	12.7	409	0.00129	44
		y	467.8	921.5	430.3	789.1	0.00176	104
		Combination	577.2	1001.5	434.1	911.8	0.00180	105
		x + y	645.5	1010.9	424.7	713.9	0.00175	103
NR0.9-6	0.9	x	361.2	284.4	13.8	408.2	0.00129	46
		y	370.2	738	342.3	630.7	0.00143	76
		Combination	517.2	823.3	346.4	753.2	0.00143	77
		x + y	681.8	935.1	294.6	527.3	0.00127	89
AW0.9-1	0.9	x	398.6	315.7	10.5	343.9	0.00136	42
		y	246.5	484.8	226.9	415	0.00164	76
		Combination	472.6	579.5	230.1	539.0	0.00164	77
		x + y	298.4	397.5	218.3	567.1	0.00161	86
NR1.1-5	1.1	x	594	466.9	22.3	717.4	0.00229	186
		y	839.7	1669.2	772.3	1435.4	0.00321	255
		Combination	1028.6	1809.3	779.0	1650.6	0.00320	261
		x + y	1188.6	1849.8	695.9	1367.8	0.00290	272
NR1.1-7	1.1	x	712.7	564.7	24.4	959.2	0.00317	329
		y	967.5	1938.1	882.6	1661.5	0.00375	355
		Combination	1201.7	2107.5	889.9	1949.3	0.00375	369
		x + y	1013.6	1971.3	918.5	2368.8	0.00391	491
AW1.1-1	1.1	x	606.9	477.3	15.6	543	0.00208	163
		y	499.7	990.7	458.5	849	0.00258	182
		Combination	786.1	1133.9	463.2	1011.9	0.00258	189
		x + y	624	1052	449.2	1309.5	0.00237	247
D + 0.5 L	-	-	2755.4	2565	4349	3730	-	-

* "Maximum" refers to the input duration. **/*** 800/700 mm diameter.

6.4. Influence of Soil–Structure Interaction

To investigate the SSI effect, Table 12 displays, for the inputs in Table 10, the base shear coefficient in the building (ratio between the base shear force and the building weight), and the shear strain in the rubber bearings (ratio between the isolators drift displacement and the rubber height). Three situations are considered in Table 12: fixed-base without SSI, base isolation with SSI, and base isolation without SSI; like in Table 8 through Table 10, the fixed-base results are determined by assuming linear behavior, and are only displayed for reference. SSI-a and SSI-b have the same meaning than in Table 5. Comparison between the results for base isolation with and without SSI shows that its effect is only moderate, both in terms of base shear and shear strain; therefore, it can be globally concluded that SSI does not play a leading role. The results for both SSI models are rather similar, thus showing little influence of the piles' vertical stiffness. Comparison between the results for base isolation and fixed-base

shows that in all the cases the isolation reduces significantly the base shear; hence, its performance is satisfactory.

Table 12. Maximum * base shear coefficient and rubber shear strain with and without SSI.

Input			Base Shear Force/Building Weight			Shear Strain (%)	
Code	Period (s)	Direction	Fixed-Base without SSI	Base Isolation with SSI-a/SSI-b	Base Isolation without SSI	Base Isolation with SSI-a/SSI-b	Base Isolation without SSI
NR0.9-3	0.9	x	0.148	0.041/0.042	0.041	23.40/23.63	22.28
		y	0.097	0.044/0.060	0.056	63.68/58.95	50.18
NR0.9-6	0.9	x	0.145	0.043/0.044	0.043	23.63/23.18	23.18
		y	0.131	0.032/0.048	0.048	37.80/37.78	37.80
AW0.9-1	0.9	x	0.099	0.044/0.042	0.041	22.50/22.50	20.93
		y	0.112	0.035/0.048	0.049	37.35/37.35	37.35
NR1.1-5	1.1	x	0.311	0.085/0.086	0.081	94.28/94.50	92.93
		y	0.384	0.097/0.100	0.102	126.76/126.38	127.53
NR1.1-7	1.1	x	0.436	0.123/0.120	0.121	164.93/164.70	164.25
		y	0.423	0.134/0.126	0.128	177.53/177.53	177.75
AW1.1-1	1.1	x	0.295	0.079/0.081	0.078	83.70/83.70	81.45
		y	0.290	0.072/0.080	0.079	88.43/88.65	90.90

* "Maximum" refers to the input duration.

6.5. Influence of Changes of the Isolation Units' Parameters

This section discusses the behavior of the isolation system when the parameters of the isolation units are modified due to heating, rate of loading, scragging, aging, environmental conditions, and manufacturing irregularities. Given the absence of specific prescriptions in the Chinese regulations, the recommendations of [14] are considered. These documents propose a conservative formulation, to be used when no more specific information is available. The major mechanical parameters of the rubber bearings are modified with a factor (λ) that accounts for the aforementioned issues; both maximum and minimum values of λ need to be considered. In NRB, the λ factor affects the stiffness; their maximum and minimum values are 1.83 and 0.77, respectively. In LRB, the λ factor affects the post-yield stiffness and the yielding force; their maximum and minimum values are 1.83/1.84 and 0.77, respectively (1.83 and 1.84 correspond to post-yield stiffness and yielding force, respectively). To analyze the performance of the base isolation under these extreme conditions, Table 13 displays, as in Table 12, the base shear coefficient and the shear strain in the isolation units for the inputs in Table 10. In Table 13, "Lower bounds" and "Upper bounds" refer to the maximum and minimum values of the λ factor, respectively. To understand the results from Table 13, it should be kept in mind that λ > 1 corresponds to stiffer and more resistant devices, while λ < 1 refers to opposite situations.

Results in Table 13 reflect a regular and expected behavior, in which the stiffer and more resistant devices (upper bounds) lead to higher base shear force and lower shear strain (i.e., less intense isolation). Comparison with Table 12 shows that their results (normal condition of the rubber bearings) lie in between those for the lower and upper bounds, and that in all the cases the base isolation reduces significantly the base shear; this last property can be read as a proper performance of the base isolation, even under extreme modifications in the parameters of the rubber bearings. The only exception to the aforementioned regularity is that, for the input NR1.1-5 in the *y* direction, the shear strain under normal conditions (Table 12) is higher than the corresponding values in Table 13. This circumstance can be explained by the high uncertainties inherent to any non-linear dynamic (time-history) analysis.

Table 13. Maximum * base shear coefficient and shear strain in the rubber for modified parameters of the isolators.

	Input		Base Shear Force/Building Weight		Shear Strain (%)	
Code	Period (s)	Direction	Lower Bounds	Upper Bounds	Lower Bounds	Upper Bounds
NR0.9-3	0.9	x	0.037	0.052	23.95	17.01
		y	0.049	0.074	59.81	38.42
NR0.9-6	0.9	x	0.039	0.059	25.41	20.42
		y	0.043	0.058	40.47	24.08
AW0.9-1	0.9	x	0.036	0.055	23.07	18.80
		y	0.044	0.065	40.81	28.22
NR1.1-5	1.1	x	0.069	0.114	96.97	71.95
		y	0.078	0.149	117.49	113.48
NR1.1-7	1.1	x	0.109	0.159	188.27	117.88
		y	0.118	0.162	209.78	126.85
AW1.1-1	1.1	x	0.067	0.109	85.76	65.52
		y	0.067	0.108	94.80	73.10

* "Maximum" refers to the input duration.

7. Conclusions

Aiming to confirm the suitability of seismic isolation in soft soil, this paper presents a numerical analysis on the performance of a rubber-isolated 6-story RC teaching building in Shanghai. The verification consists in performing non-linear time-history analyses for a number of seismic inputs that are selected to represent the site seismicity, taking into consideration the soil conditions. Two sets of seven inputs each are considered; in the first and second sets, the inputs are normalized to maximum acceleration of 0.1 g and 0.22 g, respectively. A simplified uncoupled linear model represents the soil–structure interaction. The performance is analyzed even when the mechanical parameters of the isolation units have experienced important changes.

The general conclusion of this study is that, in the analyzed case study, the isolation performs satisfactorily, both in terms of demand on the isolation system and on the superstructure. Specific conclusions are discussed next.

- ■ **Global**. Isolation reduces significantly the base shear force, being more efficient for the strongest inputs; also, the SSI effect is rather negligible. Additionally, the simultaneous actuation of both input horizontal components is compared with the usual simplified combination criteria; it is concluded that they frequently underestimate the demand.
- ■ **Isolation layer**. The demand on the isolators is checked in terms of buckling instability and shear strain; on the other hand, the percentage of hysteretic energy that is dissipated by the isolation interface is high, clearly above common demands. Finally, it is observed that there are no relevant permanent displacements.
- ■ **Superstructure**. Relative displacements, shear forces and absolute accelerations are significantly reduced, except the ground floor accelerations.

This research seems to point out that base isolation, if properly designed and implemented, can be an efficient solution for ordinary mid-height RC buildings founded on soft soil and located in medium seismicity regions, like Shanghai. This conclusion may support the promotion of seismic isolation in soft soils; notably, these terrains are particularly frequent in numerous densely populated urban areas.

Author Contributions: Data curation, T.L.; Formal analysis, D.W.; Methodology, F.L.A.; Resources, B.A. All authors have read and agreed to the published version of the manuscript.

List of Symbols

A_r	Rubber bearing plan area
a', b'	Rubber bearing diameter
b	Exponent is given by $b = \lambda/\eta$ (Equation (2))
c	Dampers damping coefficient
D, L	Dead (permanent) and live (variable) loads
d_{bd}	Design drift displacement
E_c, E_s, E'_c	Concrete (soil, rubber) deformation modulus
E_p, A_p, L_p	Modulus of deformation, cross section area and length of a pile
E_ζ, E_{HD}, E_{HI}	Energy dissipated by the structural damping, the viscous dampers and the rubber bearings
f	Damper force (Equation (1))
f_{ck}	Characteristic value of the concrete compressive strength
G, G_s	Rubber (soil) shear modulus
I_A, I_D	Arias Intensity, dimensionless seismic index (Table 6)
K_{vf}	Vertical stiffness of a pile
$N_{Ed,max}$	Demanding axial force in the isolator units (rubber bearings)
P_{cr}	Critical load for each isolator unit (rubber bearing)
PGA, PGD, PGV	Peak Ground Acceleration (Displacement, Velocity)
S	Shape factor of a rubber bearing (ratio between the diameter of the device and the thickness of each rubber layer)
T_q	Total rubber thickness of a rubber bearing
t_r	Thickness of each rubber layer of a rubber bearing
v_s	Weighted harmonic average shear wave velocity (v_{s30} refers to the top 30 m)
x_g	Ground displacement
x, y	Horizontal coordinates along the longitudinal and transverse directions of the building (Figures 1, 2 and 4). Directions of the strong/weak components of the seismic inputs (Tables 6 and 7).
α	Exponent (Equation (1))
Δt	Time step
δ	Ratio between the design drift displacement (d_{bd}) and the device (rubber bearing) diameter
$\varepsilon_{t,d}$, $\varepsilon_{c,E}$, $\varepsilon_{q,max}$, $\varepsilon_{\alpha,d}$	Shear strain coefficients for the rubber bearing
φ	Torsion angle
γ_m	Safety factor for the rubber bearings ($\gamma_m = 1$)
λ	Ratio between the pile length and diameter ($\lambda = L_p/D_p$, Equation (2)). Coefficient for the critical load of an isolator unit (rubber bearing). Factor modifying the mechanical parameters of the rubber bearings.
η	Ratio between the soil and pile moduli of elasticity ($\eta = E_p/E_s$, Equation (2))
ρ_s	Soil density

References

1. Kelly, J.M. Aseismic base isolation: Review and bibliography. *Soil Dyn. Earthq. Eng.* **1986**, *5*, 202–217. [CrossRef]
2. Buckle, I.G.; Mayes, R.L. Seismic isolation: History, application, and performance. A world overview. *Earthq. Spectra* **1990**, *6*, 161–202. [CrossRef]
3. Koh, H.M.; Song, J.; Ha, D.H. Cost effectiveness of seismic isolation for bridges in low and moderate seismic region. In Proceedings of the 12th World Conference on Earthquake Engineering (12WCEE), Auckland, New Zealand, 30 January–4 February 2000; p. 1100.
4. Deb, S.K. Seismic base isolation—An overview. *Curr. Sci.* **2004**, *87*, 1426–1430.
5. Higashino, M.; Okamoto, S. (Eds.) *Response Control and Seismic Isolation of Buildings*; Taylor & Francis: Milton Park, UK, 2006.
6. Constantinou, M.; Kneifati, M. Dynamics of Soil-Base-Isolated-Structure Systems. *J. Struct. Eng. ASCE* **1988**, *114*, 211–221. [CrossRef]

7.   Vlassis, A.G.; Spyrakos, C.C. Seismically isolated bridge piers on shallow stratum with soil–structure interaction. *Comput. Struct.* **2001**, *79*, 2847–2861. [CrossRef]

8.   Spyrakos, C.C.; Koutromanos, I.A.; Maniatakis, C.A. Seismic response of base-isolated buildings including soil–structure interaction. *Soil Dyn. Earthq. Eng.* **2009**, *29*, 658–668. [CrossRef]

9.   Spyrakos, C.C.; Maniatakis, C.A.; Koutromanos, I.A. Soil-structure interaction effects on base-isolated buildings founded on soil stratum. *Eng. Struct.* **2009**, *31*, 729–737. [CrossRef]

10.   Enomoto, T.; Yamamoto, T.; Ninomiya, M.; Miyamoto, Y.; Navarro, M. Seismic Response Analysis of Base Isolated RC Building Building Considering Dynamical Interaction Between Soil and Structure. In Proceedings of the 15th World Conference on Earthquake Engineering (15WCEE), Lisbon, Portugal, 24–28 September 2012; p. 3611.

11.   Alavi, E.; Alidoost, M. Soil-Structure Interaction Effects on Seismic Behavior of Base-Isolated Buildings. In Proceedings of the 15th World Conference on Earthquake Engineering (15WCEE), Lisbon, Portugal, 24–28 September 2012; p. 4982.

12.   GB50011. *Code for Seismic Design of Buildings*; Ministry of Housing and Urban-Rural Development: Beijing, China, 2010.

13.   E.030. *Norma Técnica de Edificación E.030 Diseño Sismorresistente*; Ministerio de Vivienda, Construcción y Saneamiento: Madrid, Spain, 2014.

14.   ASCE 7–16. *Minimum Design Loads and Associated Criteria for Buildings and Other Structures*; American Society of Civil Engineers: Reston, VA, USA, 2016.

15.   Zhou, Y.; Wu, C.X.; Zhang, C.L. Analysis and Design of Seismic Isolation Structure in Outpatient Building of the Lushan County People's Hospital. *Build. Struct.* **2013**, *43*, 23–27. (In Chinese)

16.   Weng, D.; Zhang, S.; Hu, X.; Chen, T.; Zhou, Y. *Seismic Isolation Design Soil of a Teaching Building for Shanghai Foreign Language School*; Research Institute of Structural Engineering and Disaster Reduction, Tongji University: Shanghai, China, 2012. (In Chinese)

17.   Weng, D.; Tao, L.; Alfarah, B.; López-Almansa, F. Nonlinear time-history analysis of a base-isolated RC building in Shanghai founded on soft soil. In Proceedings of the 16th World Conference on Earthquake Engineering (16WCEE), Santiago de Chile, Chile, 9–13 January 2017; p. 2634.

18.   *CSI Analysis Reference Manual for SAP2000®, ETABS®, and SAFE®*; CSI (Computers and Structures, Inc.): Berkeley, CA, USA, 2010.

19.   EN 1998-1. *Eurocode 8: Design of Structures for Earthquake Resistance*; European Committee for Standardization: Brussels, Belgium, 2004.

20.   EN 15129. *Anti-Seismic Devices*; European Committee for Standardization: Brussels, Belgium, 2009.

21.   EN 1337-3. *Structural Bearings. Part 3: Elastomeric Bearings*; European Committee for Standardization: Brussels, Belgium, 2005.

22.   GB50009. *Load Code for Design of Building Structures*; Ministry of Housing and Urban-Rural Development: Beijing, China, 2010.

23.   Inaudi, J.A.; Kelly, J.M. Optimum damping in linear isolation systems. *Earthq. Eng. Struct. Dyn.* **1993**, *22*, 583–598. [CrossRef]

24.   DGJ 08-37. *Code for Investigation of Geotechnical Engineering*; Shanghai Geotechnical Investigations & Design Institute Co, Ltd.: Shanghai, China, 2012.

25.   FEMA 356. *Prestandard and Commentary for the Seismic Rehabilitation of Buildings*; Federal Emergency Management Agency: Washington, DC, USA, 2000.

26.   Castaldo, P.; De Iuliis, M. Optimal integrated seismic design of structural and viscoelastic bracing-damper systems. *Earthq. Eng. Struct. Dyn.* **2014**, *43*, 1809–1827. [CrossRef]

27.   Ou, J.P.; Long, X.; Li, Q.S. Seismic response analysis of structures with velocity-dependent dampers. *J. Constr. Steel Res.* **2007**, *63*, 628–638. [CrossRef]

28.   Luco, J.E. Effects of soil–structure interaction on seismic base isolation. *Soil Dyn. Earthq. Eng.* **2014**, *66*, 167–177. [CrossRef]

29.   Hatami, F.; Nademi, H.; Rahaie, M. Effects of Soil-Structure Interaction on the Seismic Response of Base Isolated in High-Rise Buildings. *Int. J. Struct. Civ. Eng. Res.* **2015**, *4*, 237–242. [CrossRef]

30.   Sayyad, S.T.; Bhusare, V. Effectiveness of base isolator in high-rise building for different soil conditions using FEM. *Int. J. Sci. Dev. Res.* **2016**, *1*, 291–295.

31. FEMA 273. *NEHRP Guidelines for the Seismic Rehabilitation of Buildings*; Federal Emergency Management Agency: Washington, DC, USA, 1997.
32. Gazetas, G.; Makris, N. Dynamic pile-soil-pile interaction. Part I: Analysis of axial vibration. *J. Earthq. Eng. Struct. Dyn.* **1991**, *20*, 115–132. [CrossRef]
33. ATC-40. *Seismic Evaluation and Retrofit of Concrete Buildings*; Applied Technology Council: Redwood City, CA, USA, 1996.
34. Gazetas, G. Formulas and charts for impedances of surface and embedded foundations. *J. Geotech. Eng. ASCE* **1991**, *117*, 1363–1381. [CrossRef]
35. *UBC (Uniform Building Code)*; International Council of Building Officials: Lansing, MI, USA, 1997.
36. PKPM. SATWE Users' Manual. 2014. Available online: http://www.pkpm.cn/ (accessed on 12 December 2020).
37. DGJ 08-9. *Code for Seismic Design of Buildings*; Tongji University Shanghai Urban Construction and Communication Commission: Shanghai, China, 2013.
38. PEER. *Users Manual for the PEER Ground Motion Database Web Application*; Technical Report; Pacific Earthquake Engineering Research Center (PEER): Berkeley, CA, USA, 2011.
39. Arias, A. *A Measure of Earthquake Intensity. Seismic Design for Nuclear Power Plants*; MIT Press: Cambridge, MA, USA, 1970; pp. 438–443.
40. Manfredi, G. Evaluation of seismic energy demand. *Earthq. Eng. Struct. Dyn.* **2001**, *30*, 485–499. [CrossRef]
41. Trifunac, M.D.; Brady, A.G. Study on the duration of strong earthquake ground motion. *Bull. Seismol. Soc. Am.* **1975**, *65*, 581–626.
42. Gomase, O.; Bakre, S. Performance of Non-Linear Elastomeric Base-Isolated building structure. *Int. J. Civ. Struct. Eng.* **2011**, *2*, 280–291.
43. Castaldo, P.; Gino, D.; Mancini, G. Safety formats for non-linear finite element analysis of reinforced concrete structures: Discussion, comparison and proposals. *Eng. Struct.* **2019**, *193*, 136–153. [CrossRef]
44. Haukaas, T.; Gardoni, P. Model uncertainty in finite-element analysis: Bayesian finite elements. *J. Eng. Mech.* **2011**, *137*, 519–526. [CrossRef]
45. López Almansa, F.; Yazgan, U.; Benavent Climent, A. Design energy input spectra for moderate-to-high seismicity regions based on Turkish registers. *Bull. Earthq. Eng.* **2013**, *11*, 885–912. [CrossRef]

Review

Experimental Campaigns on Mechanical Properties and Seismic Performance of Unstabilized Rammed Earth—A Literature Review

Ana Perić, Ivan Kraus *, Jelena Kaluđer and Lucija Kraus

Faculty of Civil Engineering and Architecture Osijek, Josip Juraj Strossmayer University of Osijek, Vladimira Preloga 3, 31000 Osijek, Croatia; aperic@gfos.hr (A.P.); jkaluder@gfos.hr (J.K.); lucija@gfos.hr (L.K.)
* Correspondence: ikraus@gfos.hr

Abstract: Earthen architecture has a significant share in the world's fund of both residential architecture and cultural heritage. It provides a home to more than half of the world's population and can be found in seismically active areas. Empirically acquired knowledge on building with rammed earth (RE) has usually been passed down from generation to generation by word of mouth, with no written scientific grant for the load-bearing capacity and resistance of structural elements. Today, many countries still do not have standards for the design of RE structures. In the development of new as well as existing design standards, the results of experimental research play a significant role. The focus of this study was on unstabilized RE, which is locally available material with low embodied energy. This paper elaborates experimental campaigns, within which meticulous techniques were employed to provide new knowledge on RE for use in earthquake-prone areas. Furthermore, this paper includes: (i) ranges of values of mechanical properties determined on RE specimens from all over the world; (ii) a comparative summary of experimental research conducted on walls and buildings to assess their seismic performance; (iii) an overview of standards and testing methods used in experiments; and (iv) recommendations for further research.

Keywords: state-of-art; unstabilized rammed earth; mechanical properties; seismic performance; experimental tests

1. Introduction

Earth constructions contribute to a significant and important share in the world's residential architecture and cultural heritage [1–3]. Earthen architecture provides a home to more than half of the world's population [4]. About one third of all constructions globally contain earth as a construction element [5]. Moreover, homes made of earth can be found in both seismically quiet and active areas [2,6–12].

The first houses in the world were built in an improvised way by applying material found in the immediate surroundings or obtained by digging basements, wells, or watering pits for cattle [11]. Empirically acquired knowledge on building with earth has been passed down from generation to generation by word of mouth, with no written scientific information for load-bearing capacity and resistance of structural elements. The industrialization process and development of new technologies has resulted in modern materials used in construction in accordance with constantly improved design standards. Moreover, the oral tradition of sharing empirical knowledge was replaced with code-based architecture, the behavior of which is predicted and planned by computer software.

Among the other types of vernacular earth-building techniques, earthen architecture includes adobe [12–14], cob [15,16], compressed earth block [17–19], and rammed earth (RE) [4,10,11]. However, this paper focused only on the unstabilized RE building technique. It is considered that this building technique is one of the most important earth-building techniques both in traditional and modern earth architecture [4]. Moreover, vernacular

unstabilized RE buildings are still important on the global scale and need to be protected from disappearing [20].

Building with RE consists of pouring moistened soil in layers inside a wooden or metal formwork and compacting it by using a manual or pneumatic rammer to form walls [3,21,22]. Sassu et al. [19] demonstrated an innovative, very reproducible procedure for making earth blocks using a manual press. This procedure could potentially be used in the preparation of RE specimens for testing material properties. The formwork can be removed later and placed to a new construction location or to a new part of a future house. The soil composition varies and strongly depends on building location, which is demonstrated in the next chapter. However, it is known that RE suitable soil always comprises clay, silt, and sand [4,6,7].

In the unstabilized RE construction technique, clay acts as a natural binder that holds together larger particles once the formwork is removed. In contrast, the stabilized rammed earth (SRE) construction technique uses modern industrially produced binders such as hydraulic or calcium lime, cement, or asphalt emulsions [6,21]. Modern stabilizers in SRE have a favorable effect on its strength, durability, and resistance to external actions (e.g., earthquakes), however, at the same time, they reduce the possibility to fully recycle RE as a building material and increase its embodied energy. This paper only deals with unstabilized RE as it is a low-cost material available practically everywhere. Moreover, it does not contain artificial binders and can be returned to nature en block. When compared to modern materials, unstabilized RE has become competitive as it greatly supports sustainability and low energy consumption [5,11,23]. Despite its advantages, unstabilized RE possesses relatively poor mechanical properties and low seismic resistance.

Eastern Croatia has been taken as an example of seismically active areas with many houses made by the RE technique [11,24]. Although being more than 100 years old, many of these houses have withstood the devastation of war and natural disasters. Through field research, the authors have learned that many such houses are still in use for housing or as outbuildings. However, experimental research of the load-bearing capacity of RE walls or houses in Croatia has not been carried out yet, and the techniques of making soil mixtures and building with RE are neglected or forgotten. Another challenge of building with RE in Croatia is the lack of relevant norms. These are just some of the issues related to building with RE in Croatia as well as in some other European Union member states [7,25].

As already pointed out, a significant amount of earthen architecture is located in seismically active areas. However, despite the growing volume of research, a lack of knowledge regarding the mechanical properties and seismic resistance of RE still exists not only in the European Union, but also in most countries around the world. The most likely culprit for this situation is to be found in the uniqueness and high variability of properties of local material used in RE, but also in the lack of coded methods and procedures.

Only the synergy between numerical and experimental research methods can contribute to the development of codes for the design of RE structures. They both complement each other. Numerical methods are used for the preliminary design and prediction of the behavior of real structures. However, input data determined by experimental tests are required to define the numerical models. Experiments are conducted to verify the validity of numerical models, and to gain new knowledge on the behavior of real structures. Finally, numerical methods are relatively inexpensive and suitable for the implementation of rapid parametric studies. In contrast, experimental methods are often very expensive and rarely harmless, but can provide superior insight into the actual behavior and failure mechanisms of real structures. There have been many numerical studies on the seismic behavior of RE structures conducted recently [26–28]. The data from the available peer-reviewed papers collected in the following chapters will facilitate the implementation of further similar studies.

The aim of this paper is twofold. First, to collect the key experimental data from cutting-edge laboratories to facilitate the implementation of numerical studies but also norms and codes, and second, to define niches for future experimental research in the

field of URE. This paper encompasses: (i) an overview of both norms and testing methods used in experiments on small-scale RE specimens from all over the world; (ii) an overview of experimentally tested RE walls and buildings allowing easier calibrations and validations of both numerical and analytical models; (iii) insight into the minimum and maximum values of mechanical properties that can be expected in load-bearing RE walls and buildings; (iv) data that can enable machine learning aided by artificial intelligence; and (v) recommendations for further research.

To gain a better understanding of the mechanical properties of RE, this paper begins with a description and interpretation of the fundamental physical properties of RE available in the reviewed literature. Emphasis was placed on the particle size distribution, moisture content, and dry density as these properties are provided in most of the reviewed literature. Moreover, it is well known that these properties directly affect the mechanical properties of the soil, so they were considered first. Then, the mechanical properties of RE were placed under the loupe. The third part of the paper describes the experimental research conducted on models and mockups made of URE. Finally, the niches for further research are highlighted.

2. Digest on Physical Characteristics of RE

2.1. Particle Size Distribution (PSD)

The fundamental description of an earth mixture suitable for RE construction can be provided through PSD. PSD is usually mentioned in papers dealing with RE, so it is also observed in this paper as the first factor. PSD governs the compaction behavior of the soil, its maximum dry density, and finally unconfined compressive strength UCS [29]. Particle size ranges defined according to Knappett and Craig [30] were used in this study. As RE usually contains clay, silt, and sand particles, special attention was given to particle sizes between 0 and 2 mm. However, it should be noted that some mixtures described in the available literature [4,6,31–33] even contained gravel and cobbles, however, in very low quantity. Table 1 presents the PSD curves of 39 earth mixtures described in 23 studies conducted in Australia, Asia, and Europe. Table 1 indicates natural materials originated from different parts of the world and man-made earth mixtures produced for construction.

As presented in Table 1, the PSD for RE mixtures showed high dispersion. On average, natural mixtures contained 12.83% of clay, 23.73% of silt, 42.92% of sand, and 18.89% of gravel. Man-made mixtures predominantly consisted of sand particles.

Figure 1 shows data on the PSD of soils and soil mixtures used in Australia, France, and Portugal (Table 1). To the authors' best knowledge, RE architecture in those countries is common, so special attention was given to studies from these countries. In addition, most of the observed PSD curves in this study were obtained from studies particularly conducted in the above-mentioned countries. However, New Zealand should also be mentioned here as a country with a long tradition of building earthen houses, but also as a country that has the most comprehensive earth building standards in the world (http://www.earthbuilding.org.nz/ accessed on 13 August 2021). In Figure 1, natural material is presented by continuous lines, while man-made soil mixtures are presented by dashed lines. As expected, Figure 1 shows that PSD for each observed country vary significantly. In the context of the PSD of local material used for RE, it is presumed that it varies not only because of the geological location of the building site, but also because of the local builders' empirical knowledge and preferences when selecting a suitable soil for building.

Table 1. PSD for RE-suitable soils and soil mixtures.

Study By	Country	Type	Clay (%)	Silt (%)	Sand (%)	Gravel (%)
[2]	Bhutan	Natural	20.2	17.9	48.1	13.8
			26.5	20.5	23.0	30.0
			9.0	12.0	70.0	9.0
[4]	Portugal	Natural	16.0	23.0	33.7	27.3
			10.0	17.3	47.7	25.0
			12.5	22.8	26.8	37.9
			17.5	30.7	11.0	39.5
[6]	Turkey	Man-made	47.5	1.6	5.9	44.3
[10]	UK and Ireland	Man-made	10.0	15.1	54.4	16.3
			2	11.5	79.0	7.5
[29]	Hong Kong	Natural	10	40.7	48.8	0.5
			4	10.8	66.2	19.0
[31,32]	France	Natural	3.5	31.0	49.5	13.3
[33]	France	Natural	8.2	27.9	47.4	13.3
			20.0	8.3	59.8	11.9
[34]	Australia	Man-made	18.7	15.3	55.1	10.9
			16.3	25.1	49.4	9.2
	France	Natural	19.9	64.5	15.0	0.8
[35]	France	Natural	16.0	49.5	34.5	0
		Man-made	0	6.6	60.5	26.6
[36]	Australia	Man-made	N/A	N/A	60.0	10.0
			0	0	50.0	50.0
[37]	Australia	Natural	0	0	75.5	68.0
			0	0	24.5	32.0
[38]	France	Natural	23.5	61.7	14.7	0.1
[39,40]	France	Natural	19.9	64.6	15.5	0
			5.6	13.7	45.8	35.0
[41]	Portugal	Natural	5.2	15.3	58.5	21.0
			4.5	13.8	58.8	23.0
			11.5	12.4	52.6	23.5
[42]	Portugal	Man-made	14.2	15.6	32.6	37.7
[43]	Portugal	Man-made	7.4	27.7	44.9	20.0
[44]	Spain	Natural	0	0	76.0	24.0
			0	0	80.0	20.0
[45]	UK and Ireland	Natural	23.0	26.8	29.7	20.5
[46]	France	Natural	34.3	4.0	24.8	0
			17.4	18.6	64.0	0
			26.3	30.0	43.8	0
Average value			13.2	24.4	43.1	19.9
Min (non-zero)		Natural	2.0	4.0	11.0	0.1
Max			34.3	64.6	79.0	68.0
Average value			14–3	11.6	51.9	22.4
Min (non-zero)		Man-made	7.4	1.6	5.9	9.2
Max			47.5	32.5	90.0	50.0

Earlier studies [29,42,47] presented Houben and Guillard's envelope (HGE in Figure 1) on PSD that indicated soils suitable for use in RE construction. The same envelope was used in this paper, as shown in Figure 1. It can be observed from Figure 1 that not even one PSD curve obtained from Australia and merely one PSD curve obtained from France respects the limits defined by the envelope. However, most of the PSD curves obtained from Portugal fit well inside the envelope proposed by Houben and Guillard. The PSD of all man-made soil mixtures from Australia were above the upper envelope threshold, except in the range of coarse silt and fine sand, where they were located within the recommended envelope. Moreover, Figure 1 shows that natural soils from Australia lack clay and fine silts, but that sand content is between the recommended upper and lower threshold. Soils A5—A7 had to be stabilized by cement as the clay content was negligible.
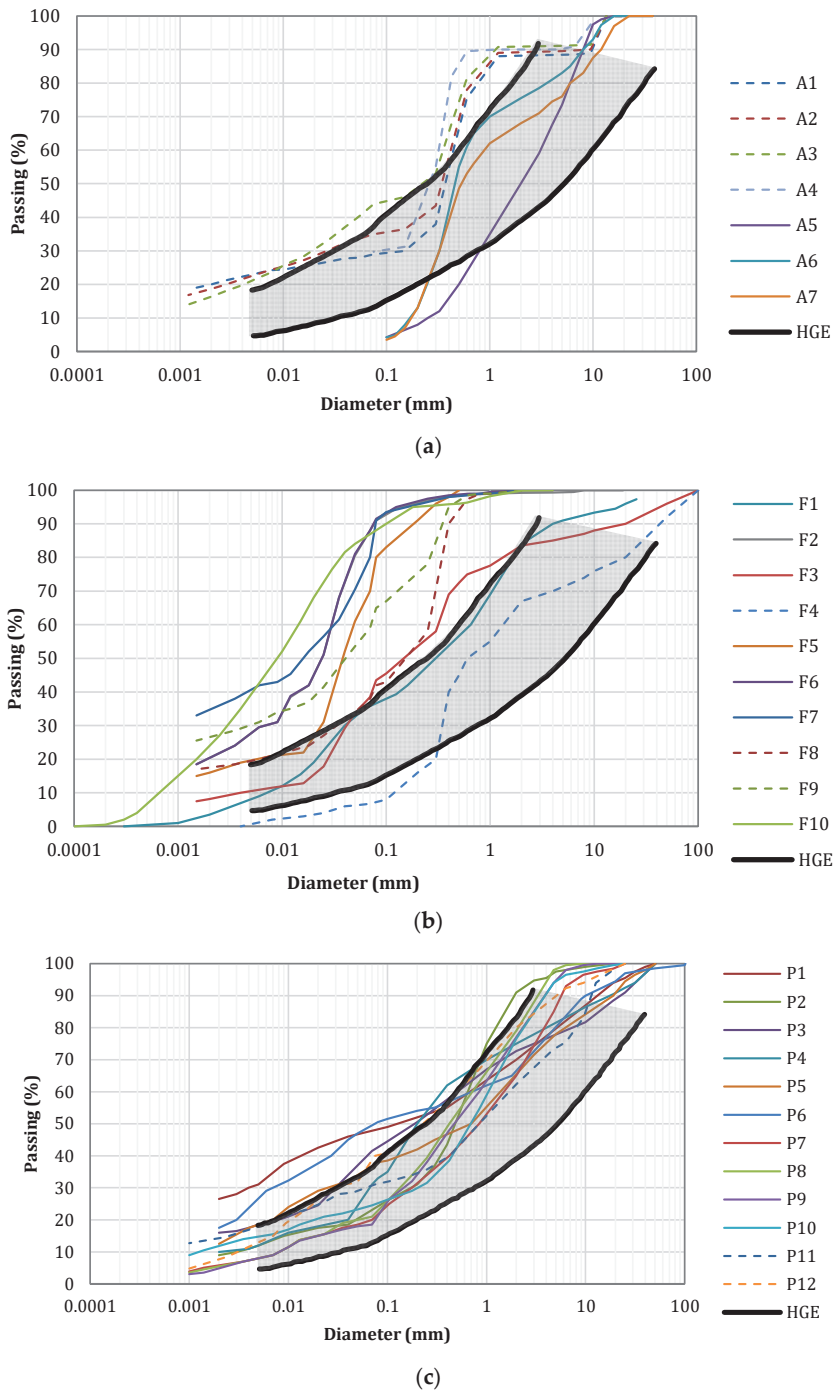
Figure 1. PSD for soils and soil mixtures used in RE structures in: (**a**) Australia: A1—A3 [34], A4 [36]; A5—A7 [37]; (**b**) France: F2 [31], F1 [34], F5—F7 [35], F3 [40], F8—F10 [46], F4 [48]; and (**c**) Portugal: P1—P6 [4], P7—P10 [41], P11 [42], P12 [43].

However, it should be noted that Houben and Guillard's envelope has the strictest limit on the amount of smaller particles that RE-suitable soil may contain. Observing the PSD curves of soils used in recent experiments, as given in Figure 1, led to the conclusion that there is still no consensus on how many smaller particles a soil suitable for RE construction should contain.

2.2. Moisture Content and Dry Density

Determination of moisture and dry density is usually performed in one or two consecutive steps. In addition to PSD, moisture and dry density are also among the key factors that greatly influence the value of UCS [49–53].

Due to its porous structure, RE has the ability to absorb moisture from the air and/or the substructure on which it rests (e.g., foundation and/or foundation soil). Likewise, RE can release moisture when heated. By observing Figure 2, it can be seen that moisture content in the specimens used to determine UCS ranged from 0.7 to 12.0%, whereas dry density ranged from 1530 to 2155 kg/m^3. Mean moisture content equaled 4.53% and dry density was 1969 kg/m^3.

(**a**)

(**b**)
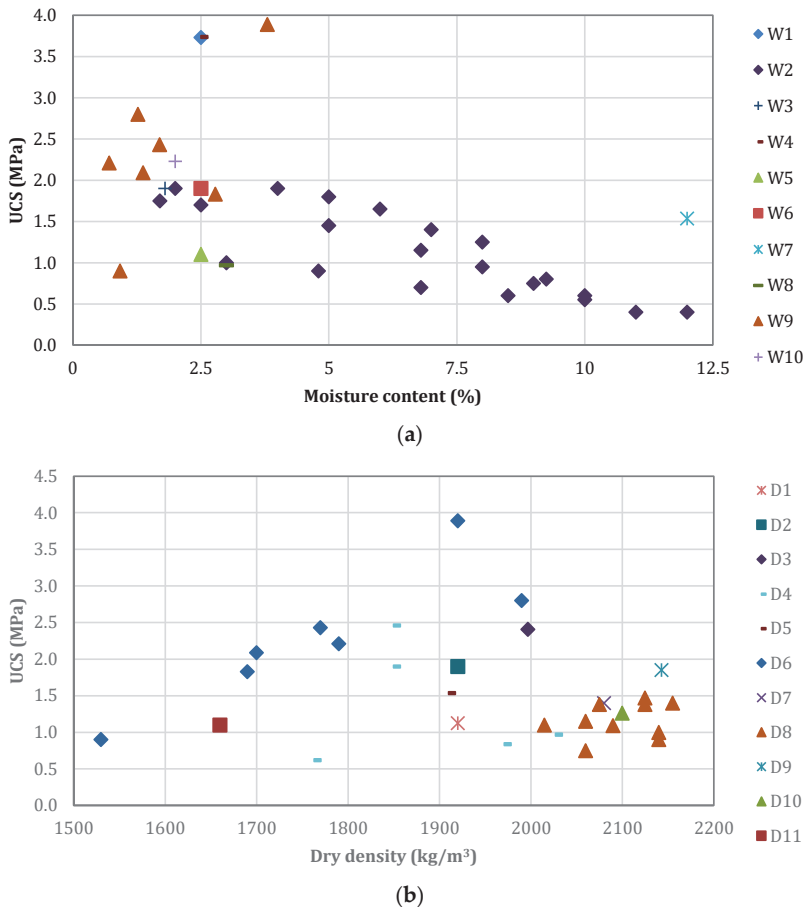
Figure 2. UCS value depending on (**a**) moisture: W1 [1], W2 [20], W3 [21], W4 [26,54], W5 [39], W6 [55], W7 [56], W8 [57], W9 [58], W10 [59]; and (**b**) dry density: D1 [20], D2 [21], D3 [49], D4 [51], D5 [56], D6 [58], D7 [60], D8 [61], D9 [62], D10 [63], D11 [64].

In an intuitive way of thinking, it would be concluded that UCS would be higher at larger dry density and/or lower moisture content. However, Figure 2 does not show such trend. Higher UCS is usually followed by lower percentage of moisture content, but this does not always appear to be the case. The relationship between UCS and dry density is even less apparent with all values dispersed. It is assumed that UCS is also affected by the size of test sample and by PSD as well as by energy and the method of compaction.

3. Experimental Campaigns on Mechanical Properties of RE

3.1. Unconfined Compressive Strength and Young's Modulus of Elasticity

Usually determined in a pair, unconfined compressive strength (USC) and Young's modulus of elasticity, E, make the most important mechanical characteristics for describing structural materials.

Methods for testing concrete have been used by many authors to determine mechanical properties of RE [2,56,65]. While considering those properties, Table 2, defined by Tomičić [66], overviews the different shapes and dimensions of concrete specimens that result in different UCS. Meticulous testing of UCS by using different specimens ought to be carried out to determine if the same principle is also valid for RE. To the authors' best knowledge, up until today, such testing has only been presented by Maniatidis and Walker [51], and El-Nabouch [67]. In both of these studies, higher values of UCS were obtained on small cylindrical specimens with respect to the values obtained on larger prismatic counterparts (Table 3). A 150 mm cube was used as a reference specimen in Table 2 as it is one of the recommended test specimens according to the European standards for concrete. The possibility of using the results obtained by testing specimens of other dimensions and shapes as orientation data is not excluded.

Table 2. UCS of concrete depending on dimensions and shape of the specimen.

Specimen Dimensions (mm)		The Ratio of UCS of 150 mm Cube to Specimen of Different Dimensions
Cube $a/a/a$	100	0.95
	150	1.00
	200	1.05
	300	1.14
Cylinder d/h	100/200	1.23
	150/300	1.26
	200/400	1.33
	100/100	1.07
	150/150	1.10
	200/200	1.16

Note: a is the cube side length; d is the specimen diameter; h is the height of specimen.

Over the past 26 years, studies have been carried out to determine UCS and modulus of elasticity, the results of which are presented in Tables 3 and 4, respectively. Usually, UCS is determined by unconfined compression test on small prismatic or cylindrical specimens of various dimensions, and rarely on wallets or full-scale walls (Table 3). To the authors' best knowledge, in only one study [46] dealing with RE, UCS and modulus of elasticity were determined by triaxial tests.

For some authors [51,68], the cylindrical shape of specimens is by far superior. As there are no corners, cylindrical specimens are easier to manufacture and better compacted, thus having higher density, higher compression strength, and higher modulus than prismatic specimens. However, "true" compressive strength of RE walls is, in some instances, smaller than the one determined on cylindrical specimens. This is the reason why some authors [21,32,37] agree on the limitations of cylindrical specimens when determining the compression strength of RE.

Table 3. UCS values obtained at different age, along with description of methods, specimens, and norms employed.

Study By	Method	Specimen: $h/w/t$ (mm); d/h (mm)	No. of Specimens Tested per Mixture	UCS (MPa)	Age (Days)	Norm
[1,69]	UCT	500/500/110	N/A	3.73	28	DIN 18945
[2]	CT	92 to 96/163 to 200	N/A	0.53 *	30	ASTM C39/C39M-17b
[3]	UCT	150/230	N/A	1.00	32	N/A
[8]	CT	800/300/300	4	1.24 *	90	GB/T 50129-2011
[21]	CST	160/300	3	1.90 *	N/A	N/A
[26,54]	AXCT	500/500/110	5	3.74 *	N/A	N/A
[39]	UCT	500/250/250	3	1.10 *	N/A	N/A
[41]	CT	100/200	N/A	0.38 *	27–35	N/A
[50]	UCT	75/150	3	1.77 *	28	ASTM D2166/D2166M-16
[51]	UCT	100/200	N/A	2.46	28	N/A
		300/600		1.90	28–42	
		600/300/300		0.81 *	28–42	
[52]	CT	100/20/20	N/A	2.03 *	28	N/A
[53]	CST	92/180	N/A	0.68 *	120	ASTM C39
[56]	CT	150/150/150	N/A	0.67	1	BS 1881–108:1983
				2.04	7	
				1.90	28	
[58]	CT	200/200/200	3	0.42 *	7	N/A
			3	1.38 *	28	
			3	2.31 *	90	
[59]	UCT	75/150	10	2.23 *	28	N/A
[60]	UCT	100/200	3	1.40 *	28	N/A
[61]	UCT	100/100/100	16	1.16 *	28	NZS 4298:1998
[62]	UCT	75/150	5	1.85 *	90	ASTM D2166/D2166M
[63]	AXCT	100/200	6	1.26 *	27–35	N/A
[64]	CT	100/100/100	6	1.10 *	38	IS 4332 Part 5
[70]	UCT	100/200	5	2.03 *	28	NF EN 12390-4
[71]	UCT	39/80	N/A	1.04 *	28	ASTM D 2166
[72]	CT	150/NA	8	3.18 *	N/A	N/A
	DFJ	1130/2100/380	N/A	3.10		
	MPT	1130/2100/380	N/A	4.15 *		
[68]	UCT	200/400	3	2.00 *	60	N/A
		500/250/250	5	1.15 *		
[73]	UXCT	150/150/150	6	0.60 *	26	Bulletin 5: Earth wall construction
[74]	AXCT	505/499/117	5	3.70 *	N/A	N/A
[75]	CT	600/600/600	3	1.36 *	N/A	N/A
Average value				1.72		
Min				0.38		
Max				4.15		

Note: d is the specimen diameter; h is the height of the specimen; t is the thickness of the specimen; w is the width of the specimen; AXCT is the axial compression test; CST is the compressive strength test; CT is the compression test; DFJ is the double flat-jack test; MPT is the mini-pressuremeter test; UCT is the unconfined compression test; UXCT is the uniaxial compression test; * average value.

Table 4. Modulus of elasticity (*E*) values obtained at different age, along with description of methods, specimens, and norms employed.

Study By	Method	Specimen: *h/w/t* (mm); *d/h* (mm)	No. of Specimens Tested per Mixture	*E* (MPa)	Age (Days)	Norm
[1,69]	UCT + LVDTs + ARAMIS	500/500/110	N/A	4143	28	DIN 1408-5
[2]	Derived from CT results	From σ-ε plot	N/A	63.36 *	30	N/A
[3]	UCT (5–30% UCS)	From σ-ε plot	N/A	67	32	N/A
	UST	2750–3600/7200/600		462.20	32	BS 1881-203-Part 203
[8]	Linear regression below 0.8σ_max	From σ-ε plot	1	243	90	N/A
[20]	UCT (0–20% UCS)	From σ-ε plot	N/A	569.05 *	N/A	N/A
[21]	CT + extensometers + LVDTs	160/300	3	500 *	N/A	N/A
[26,54]	AXCT + LVDTs	From σ-ε plot	5	4206.80 *	N/A	N/A
[41]	Linear fitting σ-ε curve (5–30% UCS)	From σ-ε plot	N/A	118.18 *	27–35	N/A
[51]	Derived from UXCT (from σ-ε plot)	100/200 600/300/300	N/A	160 65 *	28 28–42	N/A
[52]	Derived from CT results	From σ-ε plot	N/A	54.61 *	28	N/A
[53]	Derived from CT results	N/A	N/A	72.92 *	120	ASTM C39
[59]	Derived from UCT results + LVDTs	From σ-ε plot	10	143 *	28	N/A
	UST	75/150	N/A	2426	28	ASTM C5697
[62]	Calculated according to norm	Estimated	5	34 *	90	ASTM C469/C469M-14
[63]	Derived from AXCT results	From σ-ε plot	6	1034 *	27–35	N/A
[70]	Derived from UCT results	From σ-ε plot	5	340 *	28	N/A
[71]	UCT	61.8/125	N/A	102.68 *	28	N/A
[72]	Derived from CT results	N/A	8	359.03 *		
	Derived from DFJ results	From σ-ε plot	N/A	3170.66	N/A	N/A
	PT	From σ-ε plot	N/A	1394		
	MPT	Estimated	N/A	45.90 *		
[68]	DIC	200/400 500/250/250	3 5	763 * 365 *	60	N/A
[73]	Derived from UXCT results	From σ-ε plot	6	40	26	N/A
[74]	Derived from AXCT results	From σ-ε plot	5	4207 *	N/A	N/A
[75]	Derived from CT results	N/A	3	57 *	N/A	N/A
Average value				900.23		
Min				34		
Max				4207		

Note: *d* is the specimen diameter; *h* is the height of the specimen; *t* is the thickness of the specimen; *w* is the width of the specimen; σ-ε is stress-strain; σ_max is maximum stress; AXCT is the axial compression test; CT is the compression test; DFJ is the double flat-jack test; DIC is digital image correlation; MPT is the mini-pressuremeter test; PT is potentiometric transducers; UCT is the unconfined compression test; UST is ultrasonic test; UXCT is the uniaxial compression test; * average value.

Yamin et al. [76] proposed that the specimen scale does not considerably affect the mechanical properties of RE. It was later observed that larger specimens yield lower UCS [51,65]. Namely, a reduction in UCS in larger specimens can be explained by using larger fractions of soil, which requires greater compaction effort. For this reason, Ciancio and Gibbings [37] recommended making cylindrical specimens out of SRE at least three times larger than the maximum particle size of the used soil.

In some instances [2,53], instead of ramming the specimen inside mold, cylindrical specimens were extracted from the walls, usually by a drilling machine with diamond core bits. This technique can save time and attempts to replicate manufacturing the wall better than ramming separate specimens. However, according to Ciancio and Gibbins [37], this technique is not recommended for unstabilized RE as it may severely damage the specimen.

Another important feature is the age of the specimen at the time of testing. Figure 3 shows the average value of UCS and standard deviation with respect to the age of the specimen at the time of testing. Above the columns in Figure 3, numbers in brackets show the number of specimens tested at a particular age. Researchers usually follow the norms for concrete and test specimens after 28 days, as shown in Figure 3. Lilley and Robinson [56] tested cubes at the ages of 24 h, seven days, and 28 days to conclude that after seven days, UCS increased to the value of around 2 MPa, but then decreased for 10% after 28 days, particularly if the used soil contained more than 15% of clay. However, Schroeder [58] suggested that the determination of UCS should be carried out after 90 days, since the drying of RE takes longer than the drying of concrete.
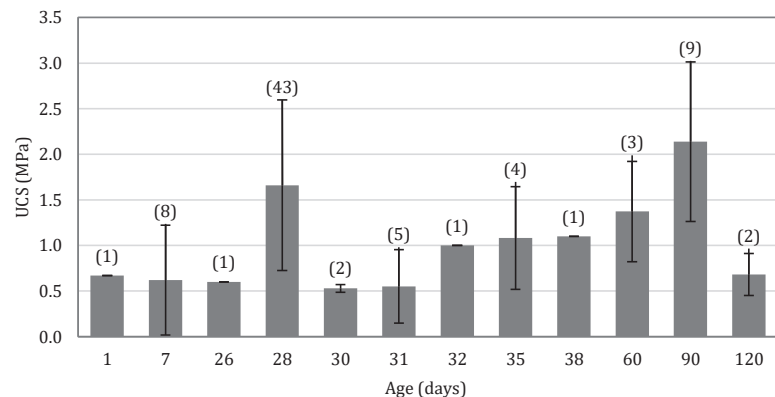
Figure 3. Average value of UCS with respect to the age of the specimen at the time of testing.

Based on the graph shown in Figure 3, neither definite trend nor conclusion on the ideal age for the testing of UCS can be made. However, it was calculated that the standard deviation of UCS at the age of 28 days was equal to 0.93 MPa. Furthermore, the number of tested specimens clearly plays an important role when determining the standard deviation. The combination of different techniques and possibly different compositions of the local soil used for earth architecture can be blamed for such a large dispersion of the measured UCS. Moreover, to the authors' best knowledge, no study has been conducted on several-year-old specimens produced in laboratories. For this reason, it is suggested to test specimens of controlled material at various periods of time.

It is known that the UCS of RE is strongly dependent on granulometry, especially on the clay percentage in the mixture [1,69]. The type of clay can also influence the UCS of RE [52]. When it comes to particle composition, Liu and Tong [71] proposed empirical expression (1) for calculating UCS based on the ratio of fine aggregates to coarse aggregates:

$$UCS = -0.033\omega^2 + 0.376\omega + 0.297 \tag{1}$$

where ω is ratio of fine aggregates (silt and clay) to coarse aggregates (sand and gravel).

According to Liu and Tong [71], UCS is maximal when ω equals 5.77 because the intake of fine aggregates is then sufficient enough to wrap around coarse aggregates, but not immoderate so that coarse aggregates loose contact.

As presented in Tables 3 and 4, tests are being carried out in accordance with different norms and recommendations. In the majority of observed countries, norms for determining mechanical properties of RE have not been developed yet. Thus, in most cases, researchers are using norms to determine the mechanical properties of concrete (Table 2). Exceptions are experimental campaigns conducted in Australia and New Zealand, where norms for RE constructions are already in use.

Table 3 presents the list of studies conducted over the past 25 years, along with methods for the description of specimens used for determining UCS. For each study, the average value of UCS was calculated and, if known, the norm by which UCS testing was performed is provided.

Determining modulus of elasticity usually goes hand-in-hand with determining UCS. To plot the stress–strain curve, deformation is measured by extensometers or, more commonly, by LVDTs during testing. Miccoli et al. [1,69] measured deformations by using ARAMIS in pair with LVDTs. From the σ–ε curve, the modulus of elasticity is determined by linear fitting curve between 5 and 30% UCS [3,41,42] or between 0 and 20% UCS for the secant modulus [20]. Furthermore, in two recent studies [3,59], the dynamic modulus of elasticity was determined by an ultrasonic test on full-scale walls, yielding much greater values of modulus when compared with static modulus determined on small scale specimens made from the same material.

Table 4 presents studies published over the past 13 years. The same table presents the test methods and describes the specimen used to determine the modulus of elasticity. In most cases, the modulus was determined from the compression tests, with a few exceptions being the axial and uniaxial compression test or calculating the modulus according to norm. For each study presented in Table 4, the average value of the modulus of elasticity is listed in MPa and, if known, the norm according to which the testing was performed is provided.

Figure 4 presents the data gathered from 25 studies, providing information on the measured modulus of elasticity and UCS. Significant scatter of values implicates high dependency of RE mechanical characteristics on many factors such as granulometry and composition of mixture, specimen shape and size, compaction energy, compaction technique, the age at which the testing was conducted, etc. A large scatter in the value of the modulus of results can be noted, which was also pointed out in [47].
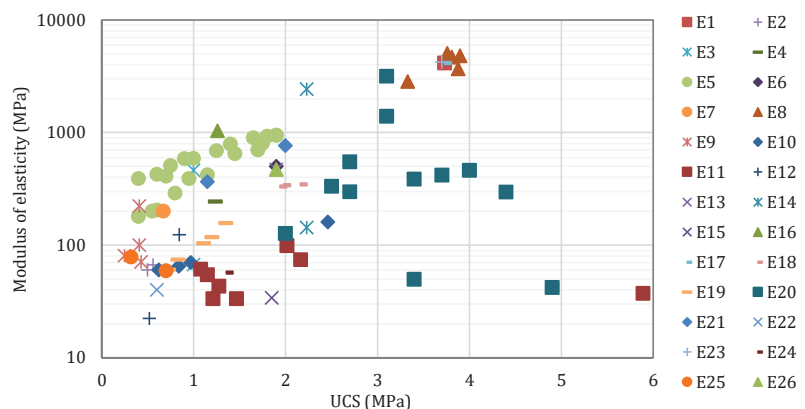
Figure 4. The relationship between UCS and modulus of elasticity: E1 [1], E2 [2], E3 [3], E4 [8], E5 [20], E6 [21], E7 [25], E8 [26,54], E9 [41], E10 [51], E11 [52], E12 [53], E13 [55], E14 [59], E15 [62], E16 [63], E17 [69], E18 [70], E19 [71], E20 [72], E21 [68], E22 [73], E23 [74], E24 [75], E25 [76], E26 [77].

3.2. Tensile Strength

When talking about the seismic capacity of RE construction, having information about the tensile strength is one of the key elements. Similar to concrete, an Achilles' heel of RE is its significantly lower tensile strength as opposed to the compressive strength. In addition, it has been proven [49,65] that the interface between two layers of RE has even lower tensile strength than the RE layer, thus making the interfaces as critical places in RE structures.

Table 5 overviews some studies published over the past seven years that have dealt with the determination of RE tensile strength. As in the case with UCS, specimens of various shapes and dimensions were observed, and each study employed a different norm.

Table 5. Tensile strength values obtained at different age, with description of methods, specimens, and norms employed.

Study By	Type	Method	Specimen: h/w/t (mm); d/h (mm)	No. of Specimens Tested per Mixture	f_t (MPa)	Age (Days)	Norm
[2]	RE	ST	92 to 96/163 to 200	N/A	0.09 *	30	ASTM C496/C496–17
[21]	RE	ST	160/300	3	0.20 *	N/A	N/A
[49]	RE	DT	50 (middle 45)/140	19	0.24 *	28	N/A
		ST	50/50	23	0.30 *	28	JGS 2551-2009
[53]	RE	ST	92/180	N/A	0.08 *	120	ASTM C496
[59]	RE	ST	75/150	10	0.24 *	28	N/A
[70]	RE	ST	100/200	5	0.40 *	28	NF EN 12390-6
[71]	RE	ST	39/80	N/A	0.22 *	28	ASTM D 2166
[42]	SRE	3P	150/600/150	-	-	42	N/A
		ST	150/300			28	
[65]	SRE	4P	100/400/100 150/400/150	-	-	28	AS 1012.10
		3P	50/200/50		-	28	
[78]	SRE	3P	100/350/100	-	-	N/A	JSCE-SF4
[79]	SRE	3P	40/160/40	-	-	N/A	N/A
Average value					0.22		
Min					0.08		
Max					0.40		

Note: *d* is the specimen diameter; *h* is the height of the specimen; *t* is the thickness of the specimen; *w* is the width of the specimen; 3P is the three-point bending test; 4P is the four-point bending test; DT is the direct tension; ST is the splitting tensile test; * average value.

Four references studying SRE have been included in Table 5 to present methods used for the testing of tensile strength and corresponding norms, if applicable. For those tests, no results were presented in Table 5 because SRE was not a focus of this review.

As presented in Table 5, two different methods prevail: the splitting tensile test (i.e., Brazilian test) that uses cylindrical specimens, and the three-point bending test that uses prismatic specimens. Exception was found in one study [49], in which direct tension test was applied in addition to splitting tensile test. The direct tension test was conducted on cylindrical specimens, where the diameter was smaller in the middle part. The reason for choosing this method is the apparent underestimation of tensile strength during splitting testing [80]. Although using the same method almost ten years later, Araki, Koseki, and Sato [49] did not observe much of a difference.

In Table 5, the average value of tensile strength is listed for each reviewed study and, if known, the norm by which the test was performed is given respectively.

When not determined experimentally, tensile strength was estimated as the function of UCS. It was suggested that tensile strength may be estimated equal to 10% of UCS value [21], but also as being equal to 20% of the UCS value [71]. These recommendations are shown as linear functions in Figure 5. Figure 5 demonstrates that tensile strength for RE with UCS higher than 1 MPa can be well estimated as 10% of UCS, while for RE with UCS lower than 1 MPa, it is more appropriate to estimate tensile strength equal to 20%

UCS. However, as Figure 5 demonstrates, there is no clear relationship between tensile strength and UCS.
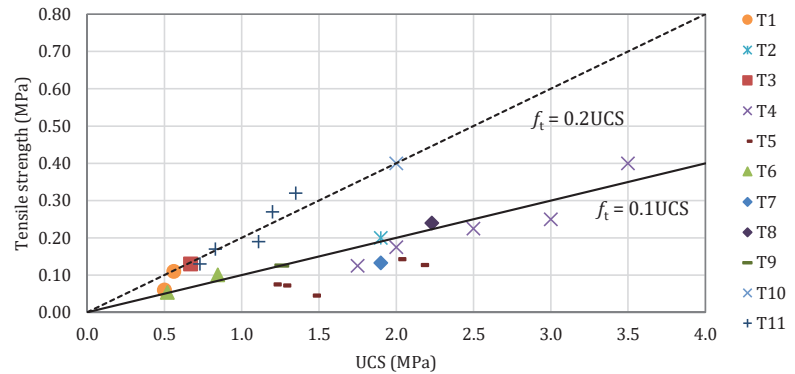
Figure 5. The relationship between UCS and tensile strength: T1 [2], T2 [21], T3 [25], T4 [49], T5 [52], T6 [53], T7 [55], T8 [59], T9 [63], T10 [70], T11 [71].

3.3. Shear Strength

The shear strength of RE is essential for the design of resilient and safe structures in seismically active areas. For the testing of RE shear strength, geotechnical and masonry testing techniques are usually employed.

The most common test for determining shear strength is the diagonal compression test, carried out in accordance with the norms for the design of masonry structures. Specimens observed and listed in Table 6 are similar in geometry. However, a scaled diagonal compression test was performed in one study [81].

Table 6. Shear strength values obtained at different age, along with description of methods, specimens, and norms employed.

Study By	Method	Specimen: $h/w/t$ (mm)	No. of Specimens Tested per Mixture	f_s (MPa)	Age (Days)	Norm
[1,26,54,69]	DCT	500/500/110	5	0.71 *	N/A	ASTM E 519-10
[21]	MC	N/A	N/A	0.18	N/A	N/A
[41]	DCT	550/550/200	N/A	N/A	46	ASTM E 519
[63]	DCT	550/550/200	11	0.15 *	84	ASTM E 519-02
[74]	DCT	505/499/117	5	0.70 *	N/A	ASTM E 519-10
[82]	DST	60/60/20	6	2.20 *	7	BS EN 1377-7:1990
Average value				0.79		
Min				0.15		
Max				2.20		

Note: h is the height of the specimen; t is the thickness of the specimen; w is the width of the specimen; DCT is the diagonal compression test; DST is the direct shear test; MC is the Mohr–Coulomb criterion; * average value.

Another approach to the determination of the shear strength employs a geotechnical procedure. T.-T. Bui et al. [21] defined the shear strength as a function of cohesion, normal stress, and friction angle, according to the Mohr–Coulomb criterion. In the same study, they concluded that shear strength could be estimated as 10% of UCS. Furthermore, Corbin and Augarde [82] suggested that shear strength should be determined from the direct shear box test, while in two other studies [46,83], shear strength was determined by using the triaxial test on cylindrical specimens.

Table 6 lists nine studies that describe the methods for the determination of shear strength on RE specimens, in which the diagonal compression test is preferred. For each

study, the average value of shear strength is listed and, if known, the norm by which the test was performed is given.

3.4. Cohesion and Friction Angle

When building with RE, it is crucial to perceive geotechnical parameters such as cohesion and friction angle (Table 7), especially when constructing the computational model of a RE structure. Experimentally, cohesion and friction angle are usually determined from the direct shear test, which can be used for the assessment of cohesion and friction angle of the interface (IF). IF is the surface between two layers of RE. Values for IF properties are almost exclusively lower than the counterparts determined for RE layers (LAY). Namely, the friction angle of IF equals around 90% of the friction angle of the layer, while cohesion of IF equals around 80% of the layer cohesion, according to El-Nabouch, Bui, Perrotin et al. [40].

Table 7. Cohesion and friction angle values of the RE layer (LAY) and interface (IF) obtained at different age, with description of methods, specimens, and norms employed.

Study By	Type	Method	Specimen: $h/w/t$ (mm); d/h (mm)	No. of Specimens Tested per Mixture	c (kPa)	φ (°)	Age (Days)	Norm
[21]	LAY	MC	N/A	N/A	170.0	51.0	N/A	-
[40]	LAY	DST	35/100/100 450/500/500	N/A	214.0 * 31.0	44.3 * 37.3	60 60	NF P 94-071-1 NF P 94-071-1
[58]	LAY	CT	hourglass-shaped specimens	N/A	9.81	N/A	N/A	DIN V 18952
[82]	LAY	DST	20/60/60	6	118.0 *	54.1 *	7	BS EN 1377-7:1990
[84]	LAY	DMT	76.2/147.2	N/A	134.0	41.0	N/A	N/A
[40]	IF	DST	450/500/500	N/A	24.0	34.8	60	N/A
[62]	IF	DST	150/150/180	3	50.0 *	65.0 *	90	ASTM D3080/D3080M, ASTM D5321
Average value Min Max	LAY				112.8 9.8 214.0	45.5 37.3 54.1		
Average value Min Max	IF				37 24.0 50.0	49.9 34.8 65.0		

Note: d is the specimen diameter; h is the height of the specimen; t is the thickness of the specimen; w is the width of the specimen; CT is the cohesion test; DMT is the drained monotonic triaxial test; DST is the direct shear test; MC is the Mohr–Coulomb criterion; * average value.

To determine cohesion values, Nowamooz and Chazallon [84] used the drained monotonic triaxial test, while Schroeder [58] used the cohesion test published by Richard Niemeyer in 1944 and adopted in the German norm. The cohesion test appears to be a simplified version of the direct tension test that uses special hourglass-shaped specimens.

When experiments cannot be conducted, cohesion can be estimated by applying the Mohr's circles theory for tensile and compressive (UCS) strengths as 14% of UCS [21]. In some studies, cohesion was taken as equal to tensile strength [55,77,85] or as a fraction of tensile strength [1,26].

El-Nabouch, Bui, Perrotin et al. [40] studied the influence of specimen size on cohesion and friction angle to conclude that larger specimens provide lower values of cohesion and friction angle due to high variation of the moisture content inside large specimens.

Table 7 lists seven studies that describe the methods and norms for the assessment of cohesion and friction angle. Three of those studies also provide information on IF characteristics. For each observed study, the average value of cohesion and friction angle are listed, and if known, the norms by which the tests were performed are given.

4. Experimental Campaigns on Seismic Performance

Each experimental study is preceded by the definition of: (i) sample geometry; (ii) modeling and scaling techniques; (iii) building technology; (iv) load input; and (v) measurement of data of interest.

Tables 8 and 9 provide a chronological overview of experimental studies conducted on mock-up RE structures over the past 12 years. The observed studies were conducted to primarily determine the crack patterns, seismic capacity, drift ratios, failure mode, load-displacement relationships, stiffness degradation as well as to assess the equivalent viscous damping and the effects of layer thickness and drying period on the RE shear resistance. All were measured and assessed in laboratory conditions on available measuring devices. In most cases, experimental tests performed on seismic tables are the only ones to provide insight into the overall seismic behavior of the structure and the associated mechanical and dynamic properties. For instance, damping ratio value for RE was expressed in only one observed study conducted by using a shaking table [75]. The determined damping ratio was estimated to be 9.81% during low intensity shaking. This is a relatively high value when compared to the same quantity obtained experimentally on real RE structures in the field [7], where the value of damping ratio ranged between 2.5 and 4%.

Table 8. Specimen geometry, loading methods, and maximum load attained by country and study observed.

Study By	Specimen	Type	No. of Specimen	Geometry $h/w/t$ (m)	σ_v (MPa)	Testing Method	Dir. of Loading	Δu (%)	F_{max} (kN)
[1,54]	Solid wall	Scaled	3	1.30/1.05/0.25	0.56	CSCT	In-plane	0.13–0.14	59–78
[2]	Solid wall	Real	1	1.20/1.20/0.60	0	ST	In-plane	0.08 *	13.5
[6]	Solid wall	Scaled	1	1.50/1.50/0.20	0	LRCL	In-plane	0.15 *	52–54
[8]	Building	Scaled	2	1.50/2.15/0.20 1.50/2.45/0.20	N/A	TBL	X and Y direction	N/A N/A	N/A N/A
[21]	Solid wall	Scaled	1	1.00/1.00/0.30	MI	VCIL	In-plane	N/A	112
[32]	Solid wall	Real	3	2.30/varies/0.50 (L shaped)	0	DM	N/A	N/A	N/A
[53]	Solid wall	Real	1	2.87/5.53/0.60	0	PD	Out-of-plane	0.17	30
[57,68]	Solid wall	Scaled Scaled	2 2	1.50/1.50/0.25 1.00/1.50/0.25	0.10, 0.20, 0.30	PM	In-plane	0.20 * 0.35 *	40–42 36–52
[75]	Building	Real	1	2.10/2.60/0.40 2.10/2.40/0.40	N/A	TBL	X and Y direction	N/A N/A	N/A N/A
[86]	Solid wall	Real	3	1.80/2.50/0.40	0.018, 0.048, 0.067	LRCL	In-plane	0.08–0.25	17–33
	Wall with openings	Real	1	3.45/7.00/0.60	0.010	LRCL	In-plane	0.08	59–76

Note: h is the height of the specimen; t is the thickness of the specimen; w is the width of the specimen; Δu is the inter-storey drift; σ_v is the vertical compressive stress at the top of the specimen; F_{max} is the maximum load attained during testing; CSCT is the cyclic shear-compression test; DM is the dynamic measurements; LRCL is the lateral reversed cyclic loading; MI is monotonically increasing; PD is the pull-down test; PM is the pushover method; VCIL is the vertical concentrated increasing load; ST is the shear test; TBL is the shaking table.

To simulate the vertical stress at the top of RE mock-up structures resulting from the dead loads (e.g., self-weight of roof) and the live loads (e.g., snow and wind), there were concrete blocks, vertically orientated hydraulic presses and/or steel profiles employed. Vertical compressive stress of 0.30 MPa applied at the top of the wall in tests conducted by El-Nabouch et al. [68] corresponded to the stress created by the self-weight of structural and non-structural loads and live loads in upper two stories of a three-storey RE house. On the other hand, vertical compressive stress of 0.56 MPa was applied at the top of the specimens tested by Miccoli, Müller, and Pospíšil [54] corresponding to 15% of the mean value of UCS determined before the test. Namely, high values of vertical compressive stress were used in tests to prevent possible rocking and flexural failure mechanisms [54,68], but also to enforce a shear-type behavior [54]. Many of the experiments listed in Table 8 did not employ any vertical stress at the top of RE mock-up structures. This configuration can correspond to RE walls that serve as an infill of load-bearing frame structures.

Table 9. Specimen geometry, preparation, and time of curing by country and study observed.

Study By	Specimen	Type	Scale	Type of Formwork	Compaction Method	$d_{lay,0}$ (m)	d_{lay} (m)	t_{cur} (Days)	Country
[1,54]	Wall	Scaled	N/A	Plywood	Mechanically compacted with a rammer	0.15	0.10	ca. 60	Germany
[2]	Wall	Real	1:1	Wooden planks	Manual ramming	0.24 0.12	0.12 0.06	ca. 30	Bhutan
[6]	Wall	Scaled	N/A	N/A	Pneumatic rammer	N/A	0.15–0.20	30	Turkey
[8]	Building	Scaled	1:2	N/A	N/A	N/A	7.5	ca. 90	China
[21]	Wall	Scaled	N/A	N/A	N/A	N/A	0.15	148 to 155	France
[32]	Wall	Real	1:1	Metal	Pneumatic rammer	N/A	N/A	3 to 53	France
[53]	Solid wall	Real	1:1	Shutter planks	Manual ramming	0.24	0.12	ca. 120	Bhutan
[57,68]	Wall	Scaled	1:2	Steel	Pneumatic rammer	N/A	N/A	ca. 60	France
[75]	Building	Real	1:1	N/A	N/A	N/A	N/A	N/A	China
[86]	Solid wall	Real	1:1	Wood	Manual ramming	N/A	N/A	N/A	Columbia
	Wall with openings	Real	1:1						

Note: ca. stands for circa (around); d_{lay} is the layer thickness after ramming; $d_{lay,0}$ is the layer thickness before ramming; and t_{cur} is the time of curing.

In the context of seismic performance assessment, different limit states are defined for structures subjected to horizontal forces until failure [68,86]. Inter-storey drift can be used to assess a limit state. With the occurrence of cracking (i.e., with leaving the elastic region), the first limit state can be defined. Definition of other limit states depend on the extent of damage, the degree of stiffness or strength degradation as well as on the width of cracking.

For the walls and one-storey buildings observed here, inter-storey drift, Δu, can be obtained as the top horizontal displacement normalized by the height of the observed structure. Inter-storey drifts at leaving the elastic region are listed in Table 8. In the absence of inter-storey drift values available in the reviewed literature, the authors approximated inter-storey drift values from cyclic load-displacement or pushover curves. In case when cyclic load-displacement curves are used, only the positive (pushing) direction was observed. Inter-storey drift values determined by the authors are marked with an asterisk in Table 8. In this study, only inter-storey drifts for the first limit state were defined as there was not enough available data in the literature observed to assess inter-storey drifts for higher limit states. Table 8 indicates the conservative lower bound of cracking inter-storey drift for RE walls as 0.08%.

Out of the 11 experimental studies listed in Table 8, only three studies examined the out-of-plane behavior of RE walls, while only one study investigated the behavior of RE walls with openings. To the authors' best knowledge, only two studies were conducted by using shaking tables to provide the full insight into the seismic performance of RE mock-ups. This suggests limited knowledge on the out-of-plane behavior of RE walls and behavior of RE walls with openings for seismically active areas. Furthermore, there is limited knowledge on the behavior of corners in RE structures (i.e., joints of RE walls meeting from two perpendicular directions).

The most common height of tested walls is 1.50 m, which refers to a 1:2 scale model of a real RE building, considering that the height of the floor in a real building is 3 m [11,57]. The same conclusion regarding the scaling can be determined based on wall thickness. Namely, RE walls in real structures are usually between 0.40 and 0.60 m thick [11,24,42,57]. Walls tested in 1:2 scale have a thickness ranging between 0.20 and 0.30 m. Table 8 indicates that the conservative lower bound of the maximum horizontal load that 1:2 scaled RE

walls can attain is 40 kN. On the other hand, real scale RE structures show a pronounced scattering of maximum horizontal load attained during testing.

The size of the laboratory and the ability to make models outdoors has a major impact on the model scale. Real scale models can provide the most accurate data, but such models require significant human, material, and financial resources. In the case of using small-scale models, it is necessary to follow the scaling rules. Except for the study of Zhou and Liu [8], other reviewed studies did not refer to the scaling rules employed in experiments. Almost all studies listed in Table 9 provided only the scale at which the model was derived.

From the studies listed in Table 9, it was not possible to establish whether the thickness of the RE layer was scaled when scaling the global geometry of the specimen (i.e., it was not possible to establish whether the number of RE layers was scaled when scaling the global geometry of wall samples). This is an important issue because it is known that the zones between the RE layers are weak points in RE structures [40,68].

Today, although there are advanced technologies that allow for the creation of models of walls and houses, many of the research projects listed in Table 9 used traditional methods employing wood formwork and manual ramming. By applying such building techniques, more faithful replicas of traditional constructions can be created.

The RE mock-ups were first tested after 30 days. This test time corresponds to the standard test time for concrete specimens [87]. However, many experiments were conducted after a curing period of two or more months.

5. Outlook and Perspectives

This study addressed the experimental campaigns conducted in different countries worldwide to determine the mechanical properties and assess the seismic performance of RE. It provides a report on the experimental campaigns conducted during the last 20 years within which meticulous techniques were used to obtain new knowledge on RE for use in earthquake prone areas.

The study included:

i.   A short survey on the key physical properties of RE that can influence its mechanical properties and consequently its seismic performance;
ii. A survey of peer-reviewed literature to identify the norms and testing methods used in various experiments to determine the mechanical properties of RE;
iii. Data collection from peer-reviewed literature to define the minimum and maximum values of mechanical properties that can be expected in load-bearing RE walls and buildings; and
iv. An overview of experimentally tested RE walls and buildings from all over the world.

The main conclusions regarding the physical properties of RE are the following:

i.   On average, natural soil mixtures for RE used in experimental campaigns consist of 12.83% clay, 23.73% silt, 42.92% sand, and 18.89% gravel. Man-made soil mixtures predominantly consist of sand particles; and
ii. Based on ten peer-reviewed studies, it was concluded that moisture content in specimens used to determine UCS ranged from 0.7 to 12, whereas dry density ranged from 1530 to 2155 kg/m^3. Mean moisture content equaled 4.53% and dry density was 1969 kg/m^3.

When considering the experimental campaigns on mechanical properties, the main conclusions are as follows:

i.   The observed values of UCS ranged from 0.38 to 4.15 MPa, with the average value being 1.72 MPa;
ii. Values of modulus of elasticity ranging from 40 to 4207 MPa were recorded, pointing out a large disperse of results, with the average value being equal to 932.30 MPa;
iii. A survey conducted on 31 peer-reviewed research papers showed that there is no standardized mold for the determination of UCS of RE. Molds of different sizes and shapes were used to determine UCS;

iv.   Values of tensile strength ranging from 0.08 to 040 MPa were noted, with the average value being equal to 0.22 MPa;

v.   Values of shear strength ranging from 0.15 to 2.20 MPa were noted, with the average value being equal to 0.77 MPa;

vi.   Values of cohesion of RE layer ranged from 9.81 to 214 kPa, with the average value being equal to 101.10 kPa;

vii. Values of friction angle of RE layers ranged from 37.3° to 54.11°, with the average value being equal to 44.16°;

viii. In most of the cases observed in the literature, reviewed ASTM norms were employed to determine the mechanical properties of RE; and

ix.   Researchers usually follow the norms for concrete and test RE specimens for mechanical properties after 28 days of curing.

The main conclusions regarding the experimental campaigns conducted to assess the seismic performance of RE structures are as follows:

i.   Many of the experimental campaigns did not employ any vertical stress at the top of the RE mock-up structures. However, when applied, the vertical stress ranged from 0.1 to 0.56 MPa;

ii.   The most common height of tested walls is 1.50 m, which refers to a 1:2 scale model of a real RE building. Walls tested in 1:2 scale have a thickness ranging between 0.20 and 0.30 m;

iii. RE mock-ups are usually tested after 30 days of curing;

iv.   For RE walls in general, a conservative lower bound of cracking inter-storey drift equal to 0.08% was indicated based on 11 observed experimental campaigns;

v.   For 1:2 scaled RE walls, a conservative lower bound of maximum horizontal load equal to 40 kN was indicated based on eight different solid walls experimentally tested until failure; and

vi.   The damping ratio determined by the shaking table test was estimated to be 9.81% for a RE structure subjected to low intensity shaking. This is relatively high value when compared to the same quantity obtained experimentally on real RE structures in the field, where the value of damping ratio ranged between 2.5 and 4%.

The following niches for future experimental research in the field of RE are defined:

i.   It was learned that different shapes and dimensions of specimens can dictate different values of UCS. Meticulous testing of UCS on different RE specimens ought to be carried out to clearly determine if the same principles determined for concrete are also valid for RE;

ii.   There is no clear relationship between tensile strength and UCS;

iii. There is very limited knowledge on damping ratio of RE;

iv.   Limited data on the sheer strength, cohesion, and friction angle for RE is available in the peer-reviewed literature; and

v.   From the peer-reviewed literature, it was not possible to establish whether the thickness of the RE layer was scaled when scaling the global geometry of the specimen (i.e., it was not possible to establish whether the number of RE layers was scaled when scaling the global geometry of wall samples). This could be an important issue because it is known that the zones between the RE layers are weak points in RE structures.

Author Contributions: Conceptualization, A.P. and I.K.; methodology, I.K. and J.K.; formal analysis, A.P. and I.K.; investigation, A.P., I.K., J.K. and L.K.; resources, A.P., I.K., J.K. and L.K.; writing—original draft preparation, A.P. and I.K.; writing—review and editing, A.P., I.K., J.K. and L.K.; visualization, A.P., I.K. and L.K.; supervision, I.K.; project administration, I.K.; funding acquisition, I.K. All authors have read and agreed to the published version of the manuscript.

Conflicts of Interest: The authors declare no conflict of interest.

References

1. Miccoli, L.; Drougkas, A.; Müller, U. In-plane behaviour of rammed earth under cyclic loading: Experimental testing and finite element modelling. *Eng. Struct.* **2016**, *125*, 144–152. [CrossRef]
2. Shrestha, K.C.; Aoki, T.; Miyamoto, M.; Wangmo, P. In-plane shear resistance between the rammed earth blocks with simple interventions: Experimentation and finite element study. *Buildings* **2020**, *10*, 57. [CrossRef]
3. Silva, R.A.; Mendes, N.; Oliveira, D.V.; Romanazzi, A.; Domínguez-Martínez, O.; Miranda, T. Evaluating the seismic behaviour of rammed earth buildings from Portugal: From simple tools to advanced approaches. *Eng. Struct.* **2018**, *157*, 144–156. [CrossRef]
4. Gomes, M.I.; Gonçalves, T.D.; Faria, P. Unstabilized rammed earth: Characterization of material collected from old constructions in south portugal and comparison to normative requirements. *Int. J. Archit. Herit.* **2014**, *8*, 185–212. [CrossRef]
5. Mateus, L.; Veiga, M.D.; de Brito, J. In situ characterization of rammed earth wall renders. *Int. J. Archit. Herit.* **2015**, *9*, 430–442. [CrossRef]
6. Arslan, M.E.; Emiroğlu, M.; Yalama, A. Structural behavior of rammed earth walls under lateral cyclic loading: A comparative experimental study. *Constr. Build. Mater.* **2017**, *133*, 433–442. [CrossRef]
7. Bui, Q.-B.; Hans, S.; Morel, J.-C.; Do, A.-P. First exploratory study on dynamic characteristics of rammed earth buildings. *Eng. Struct.* **2011**, *33*, 3690–3695. [CrossRef]
8. Zhou, T.; Liu, B. Experimental study on the shaking table tests of a modern inner-reinforced rammed earth structure. *Constr. Build. Mater.* **2019**, *203*, 567–578. [CrossRef]
9. Arrigoni, A.; Beckett, C.T.S.; Ciancio, D.; Pelosato, R.; Dotelli, G.; Grillet, A.C. Rammed Earth incorporating Recycled Concrete Aggregate: A sustainable, resistant and breathable construction solution. *Resour. Conserv. Recycl.* **2018**, *137*, 11–20. [CrossRef]
10. Jaquin, P.A.; Augarde, C.; Gallipoli, D.; Toll, D.G. The strength of unstabilised rammed earth materials. *Geotechnique* **2009**, *59*, 487–490. [CrossRef]
11. Lončar-Vicković, S.; Stober, D. *Tradicijska Kuća Slavonije i Baranje*; Ministarstvo turizma Republike Hrvatske, Sveučilište Josipa Jurja Strossmayera u Osijeku, Građevinski fakultet Osijek: Osijek, Croatia, 2011. Available online: https://mint.gov.hr/UserDocsImages//arhiva//150514_Slavonija_Baranja.pdf (accessed on 13 August 2021).
12. Momin, S.; Lovon, H.; Silva, V.; Ferreira, T.M.; Vicente, R. Seismic Vulnerability Assessment of Portugese Adobe Buildings. *Buildings* **2021**, *11*, 200. [CrossRef]
13. Aguilar, R.; Noel, M.F.; Ramos, L.F. Integration of reverse engineering and non-linear numerical analysis for the seismic assessment of historical adobe buildings. *Autom. Constr.* **2019**, *98*, 1–15. [CrossRef]
14. Niroumand, H.; Zain, M.F.M.; Jamil, M. Various Types of Earth Buildings. *Procedia Soc. Behav. Sci.* **2013**, *89*, 226–230. [CrossRef]
15. Vinceslas, T.; Hamard, E.; Razakamanantsoa, A.; Bendahmane, F. Further development of a laboratory procedure to assess the mechanical performance of cob. *Environ. Geotech.* **2016**, *7*, 200–207. [CrossRef]
16. Hamard, E.; Cazacliu, B.; Razakamanantsoa, A.; Morel, J.-C. Cob, a vernacular earth construction process in the context of modern sustainable building. *Build. Environ.* **2016**, *106*, 103–119. [CrossRef]
17. Mostafa, M.; Uddin, N. Effect of banana fibers on the compressive and flexural strength of compressed earth blocks. *Buildings* **2015**, *5*, 282–296. [CrossRef]
18. Hema, C.; Messan, A.; Lawane, A.; Van Moeseke, G. Impact of the Design of Walls Made of Compressed Earth Blocks on the Thermal Comfort of Housing in Hot Climate. *Buildings* **2020**, *10*, 157. [CrossRef]
19. Sassu, M.; Romanazzi, A.; Giresini, L.; Franco, W.; Ferraresi, C.; Quaglia, G.; Orefice, E. Production procedures and mechanical behaviour of interlocking stabilized compressed earth blocks (ISCEBs) manufactured using float ram 1.0 press. *Eng. Solid Mech.* **2018**, *6*, 89–104. [CrossRef]
20. Bui, Q.-B.; Morel, J.-C.; Hans, S.; Walker, P. Effect of moisture content on the mechanical characteristics of rammed earth. *Constr. Build. Mater.* **2014**, *54*, 163–169. [CrossRef]
21. Bui, T.-T.; Bui, Q.-B.; Limam, A.; Maximilien, S. Failure of rammed earth walls: From observations to quantifications. *Constr. Build. Mater.* **2014**, *51*, 295–302. [CrossRef]
22. Narloch, P.; Woyciechowski, P. Assessing cement stabilized rammed earth durability in a humid continental climate. *Buildings* **2020**, *10*, 26. [CrossRef]
23. Soudani, L.; Woloszyn, M.; Fabbri, A.; Morel, J.-C.; Grillet, A.C. Energy evaluation of rammed earth walls using long term in-situ measurements. *Sol. Energy* **2017**, *141*, 70–80. [CrossRef]
24. Živković, Z. *Hrvatsko Tradicijsko Graditeljstvo*; Ministarstvo Kulture Uprava za Zaštitu Kulturne Baštine: Zagreb, Croatia, 2013. Available online: https://min-kulture.gov.hr/UserDocsImages//arhiva/Bastina//HTG_web.pdf (accessed on 13 August 2021).
25. Gomes, M.I.; Lopes, M.; De Brito, J. Seismic resistance of earth construction in Portugal. *Eng. Struct.* **2011**, *33*, 932–941. [CrossRef]
26. Miccoli, L.; Oliveira, D.V.; Silva, R.A.; Müller, U.; Schueremans, L. Static behaviour of rammed earth: Experimental testing and finite element modelling. *Mater. Struct. Constr.* **2015**, *48*, 3443–3456. [CrossRef]
27. Fagone, M.; Loccarini, F.; Ranocchiai, G. Strength evaluation of jute fabric for the reinforcement of rammed earth structures. *Compos. Part B Eng.* **2017**, *113*, 1–13. [CrossRef]
28. François, B.; Palazon, L.; Gerard, P. Structural behaviour of unstabilized rammed earth constructions submitted to hygroscopic conditions. *Constr. Build. Mater.* **2017**, *155*, 164–175. [CrossRef]

29. Lin, H.; Zheng, S.; Lourenço, S.D.N.; Jaquin, P. Characterization of coarse soils derived from igneous rocks for rammed earth. *Eng. Geol.* **2017**, *228*, 137–145. [CrossRef]

30. Knappett, J.A.; Craig, R.F. *Craig's Soil Mechanics*, 8th ed.; CRC Press: Boca Raton, FL, USA, 2012.

31. Bui, Q.-B.; Morel, J.-C. Assessing the anisotropy of rammed earth. *Constr. Build. Mater.* **2009**, *23*, 3005–3011. [CrossRef]

32. Bui, Q.-B.; Morel, J.-C.; Hans, S.; Meunier, N. Compression behaviour of non-industrial materials in civil engineering by three scale experiments: The case of rammed earth. *Mater. Struct. Constr.* **2009**, *42*, 1101–1116. [CrossRef]

33. Bui, Q.-B.; Morel, J.-C. First exploratory study on the ageing of rammed earth material. *Materials* **2015**, *8*, 1–15. [CrossRef]

34. Arrigoni, A.; Grillet, A.C.; Pelosato, R.; Dotelli, G.; Beckett, C.T.S.; Woloszyn, M.; Ciancio, D. Reduction of rammed earth's hygroscopic performance under stabilisation: An experimental investigation. *Build. Environ.* **2017**, *115*, 358–367. [CrossRef]

35. Bui, Q.-B.; Morel, J.-C.; Reddy, B.V.; Ghayad, W. Durability of rammed earth walls exposed for 20 years to natural weathering. *Build. Environ.* **2009**, *44*, 912–919. [CrossRef]

36. Ciancio, D.; Beckett, C.T.S.; Carraro, J.A.H. Optimum lime content identification for lime-stabilised rammed earth. *Constr. Build. Mater.* **2014**, *53*, 59–65. [CrossRef]

37. Ciancio, D.; Gibbings, J. Experimental investigation on the compressive strength of cored and molded cement-stabilized rammed earth samples. *Constr. Build. Mater.* **2012**, *28*, 294–304. [CrossRef]

38. Millogo, Y.; Aubert, J.-E.; Hamard, E.; Morel, J.-C. How Properties of Kenaf Fibers from Burkina Faso Contribute to the Reinforcement of Earth Blocks. *Materials* **2015**, *8*, 2332–2345. [CrossRef]

39. El-Nabouch, R.; Bui, Q.-B.; Plé, O.; Perrotin, P. Characterizing the shear parameters of rammed earth material by using a full-scale direct shear box. *Constr. Build. Mater.* **2018**, *171*, 414–420. [CrossRef]

40. El-Nabouch, R.; Bui, Q.-B.; Perrotin, P.; Plé, O. Shear parameters of rammed earth material: Results from different approaches. *Adv. Mater. Sci. Eng.* **2018**, *2018*, 8214604. [CrossRef]

41. Silva, R.A.; Oliveira, D.V.; Miranda, T.; Cristelo, N.; Escobar, M.C.; Soares, E. Rammed earth construction with granitic residual soils: The case study of northern Portugal. *Constr. Build. Mater.* **2013**, *47*, 181–191. [CrossRef]

42. Silva, R.A.; Oliveira, D.V.; Schueremans, L.; Miranda, T.; Machado, J. Effectiveness of the repair of unstabilised rammed earth with injection of mud grouts. *Constr. Build. Mater.* **2016**, *127*, 861–871. [CrossRef]

43. Silva, R.A.; Domínguez-Martínez, O.; Oliveira, D.V.; Pereira, E.B. Comparison of the performance of hydraulic lime- and clay-based grouts in the repair of rammed earth. *Constr. Build. Mater.* **2018**, *193*, 384–394. [CrossRef]

44. Serrano, S.; Rincón, L.; González, B.; Navarro, A.; Bosch, M.; Cabeza, L.F. Rammed earth walls in Mediterranean climate: Material characterization and thermal behaviour. *Int. J. Low Carbon Technol.* **2017**, *12*, 281–288. [CrossRef]

45. Tinsley, J.; Pavía, S. Thermal performance and fitness of glacial till for rammed earth construction. *J. Build. Eng.* **2019**, *24*, 1–8. [CrossRef]

46. Xu, L.; Wong, K.K.; Fabbri, A.; Champiré, F.; Branque, D. Loading-unloading shear behavior of rammed earth upon varying clay content and relative humidity conditions. *Soils Found.* **2018**, *58*, 1001–1015. [CrossRef]

47. Ávila, F.; Puertas, E.; Gallego, R. Characterization of the mechanical and physical properties of unstabilized rammed earth: A review. *Constr. Build. Mater.* **2021**, *270*, 1–12. [CrossRef]

48. Millogo, Y.; Morel, J.-C.; Aubert, J.-E.; Ghavami, K. Experimental analysis of Pressed Adobe Blocks reinforced with Hibiscus cannabinus fibers. *Constr. Build. Mater.* **2014**, *52*, 71–78. [CrossRef]

49. Araki, H.; Koseki, J.; Sato, T. Tensile strength of compacted rammed earth materials. *Soils Found.* **2016**, *56*, 189–204. [CrossRef]

50. Pakand, M.; Toufigh, V. A multi-criteria study on rammed earth for low carbon buildings using a novel ANP-GA approach. *Energy Build.* **2017**, *150*, 466–476. [CrossRef]

51. Maniatidis, V.; Walker, P. Structural capacity of rammed earth in compression. *J. Mater. Civ. Eng.* **2008**, *20*, 230–238. [CrossRef]

52. Mužíková, B.; Plaček Otcovská, T.; Padevět, P. Modulus of Elascity of Unfired Rammed Earth. *Acta Polytech. CTU Proc.* **2018**, *15*, 63–68. [CrossRef]

53. Wangmo, P.; Shrestha, K.C.; Miyamoto, M.; Aoki, T. Assessment of out-of-plane behavior of rammed earth walls by pull-down tests. *Int. J. Archit. Herit.* **2019**, *13*, 273–287. [CrossRef]

54. Miccoli, L.; Müller, U.; Pospíšil, S. Rammed earth walls strengthened with polyester fabric strips: Experimental analysis under in-plane cyclic loading. *Constr. Build. Mater.* **2017**, *149*, 29–36. [CrossRef]

55. Bui, Q.-B.; Limam, A.; Bui, T.-T. Dynamic discrete element modelling for seismic assessment of rammed earth walls. *Eng. Struct.* **2018**, *175*, 690–699. [CrossRef]

56. Lilley, D.M.; Robinson, J. Ultimate strength of rammed earth walls with openings. *Proc. Inst. Civ. Eng. Struct. Build.* **1995**, *110*, 278–287. [CrossRef]

57. El-Nabouch, R.; Bui, Q.-B.; Plé, O.; Perrotin, P.; Poinard, C.; Goldin, T.; Plassiard, J.P. Seismic Assessment of Rammed Earth Walls Using Pushover Tests. *Procedia Eng.* **2016**, *145*, 1185–1192. [CrossRef]

58. Schroeder, H. Moisture transfer and change in strength during the construction of earthen buildings. *Inf. Constr.* **2011**, *63*, 107–116. [CrossRef]

59. Toufigh, V.; Kianfar, E. The effects of stabilizers on the thermal and the mechanical properties of rammed earth at various humidities and their environmental impacts. *Constr. Build. Mater.* **2019**, *200*, 616–629. [CrossRef]

60. Arrigoni, A.; Pelosato, R.; Dotelli, G.; Beckett, C.T.S.; Ciancio, D. Weathering's beneficial effect on waste-stabilised rammed earth: A chemical and microstructural investigation. *Constr. Build. Mater.* **2017**, *140*, 157–166. [CrossRef]

61. Hall, M.; Djerbib, Y. Rammed earth sample production: Context, recommendations and consistency. *Constr. Build. Mater.* **2004**, *18*, 281–286. [CrossRef]
62. Kosarimovahhed, M.; Toufigh, V. Sustainable usage of waste materials as stabilizer in rammed earth structures. *J. Clean Prod.* **2020**, *277*, 1–10. [CrossRef]
63. Silva, R.A.; Oliveira, D.V.; Schueremans, L.; Lourenço, P.B.; Miranda, T. Modelling the Structural Behaviour of Rammed Earth Components. In *Civil-Comp Proceedings*; Civil-Comp Press: Stirlingshire, UK, 2014.
64. Tripura, D.D.; Singh, K.D. Characteristic Properties of Cement-Stabilized Rammed Earth Blocks. *J. Mater. Civ. Eng.* **2015**, *27*, 1–8. [CrossRef]
65. Ciancio, D.; Augarde, C. Capacity of unreinforced rammed earth walls subject to lateral wind force: Elastic analysis versus ultimate strength analysis. *Mater. Struct. Constr.* **2013**, *46*, 1569–1585. [CrossRef]
66. Tomičić, I. *Betonske Konstrukcije*; Društvo hrvatskih građevinskih inženjera: Zagreb, Croatia, 1996.
67. El Nabouch, R. Mechanical Behavior of Rammed Earth Walls under Pushover Tests/Comportement Mécanique des Murs en Pisé. Ph.D. Thesis, Université Grenoble Alpes, Grenoble, France, 2017.
68. El-Nabouch, R.; Bui, Q.-B.; Plé, O.; Perrotin, P. Assessing the in-plane seismic performance of rammed earth walls by using horizontal loading tests. *Eng. Struct.* **2017**, *145*, 153–161. [CrossRef]
69. Miccoli, L.; Müller, U.; Fontana, P. Mechanical behaviour of earthen materials: A comparison between earth block masonry, rammed earth and cob. *Constr. Build. Mater.* **2014**, *61*, 327–339. [CrossRef]
70. Koutous, A.; Hilali, E. Reinforcing rammed earth with plant fibers: A case study. *Case Stud. Constr. Mater.* **2021**, *14*, 1–15.
71. Liu, Q.; Tong, L. Engineering properties of unstabilized rammed earth with different clay contents. *J. Wuhan Univ. Technol. Mater. Sci. Ed.* **2017**, *32*, 914–920. [CrossRef]
72. Lombillo, I.; Villegas, L.; Fodde, E.; Thomas, C. In situ mechanical investigation of rammed earth: Calibration of minor destructive testing. *Constr. Build. Mater.* **2014**, *51*, 451–460. [CrossRef]
73. Porter, H.; Blake, J.; Dhami, N.K.; Mukherjee, A. Rammed earth blocks with improved multifunctional performance. *Cem. Concr. Compos.* **2018**, *92*, 36–46. [CrossRef]
74. Silva, R.A.; Oliveira, D.V.; Miccoli, L.; Schueremans, L. Modelling of Rammed Earth Under Shear Loading. In Proceedings of the SAHC 2014—9th International Conference on Structural Analysis of Historicak Constructions, Mexico City, Mexico, 14–17 October 2014.
75. Wang, Y.; Wang, M.; Liu, K.; Pan, W.; Yang, X. Shaking table tests on seismic retrofitting of rammed-earth structures. *Bull. Earthq. Eng.* **2017**, *15*, 1037–1055. [CrossRef]
76. Yamin, L.E.; Phillips, C.A.; Reyes, J.C.; Ruiz, D.M. Seismic behaviour and rehabilitation alternatives for adobe and rammed earth buildings. In Proceedings of the 13th World Conference on Earthquake Engineering, Vancouver, BC, Canada, 1–6 August 2004; pp. 1–10.
77. Bui, Q.-B.; Bui, T.-T.; Limam, A. Assessing the seismic performance of rammed earth walls by using discrete elements. *Cogent. Eng.* **2016**, *3*, 1–12. [CrossRef]
78. Bernat-Maso, E.; Gil, L.; Escrig, C. Textile-reinforced rammed earth: Experimental characterisation of flexural strength and thoughness. *Constr. Build. Mater.* **2016**, *106*, 470–479. [CrossRef]
79. Otcovska, T.; Padevět, P. Dependence of Tensile Bending Strength of Rammed Earth on Used Clay Composition and Amount of Mixture Water. *Adv. Mater. Res.* **2017**, *1144*, 48–53. [CrossRef]
80. Namikawa, T.; Koseki, J. Evaluation of tensile strength of cement-treated sand based on several types of laboratory tests. *Soils Found.* **2007**, *47*, 657–674. [CrossRef]
81. Ruiz, D.; López, C.; Unigarro, S.; Domínguez, M. Seismic Rehabilitation of Sixteenth- and Seventeenth-Century Rammed Earth-Built Churches in the Andean Highlands: Field and Laboratory Study. *J. Perform. Constr. Facil.* **2015**, *29*, 1–17. [CrossRef]
82. Corbin, A.; Augarde, C. Investigation into the shear behaviour of rammed earth using shear box tests. In Proceedings of the First International Conference on Bio-Based Building Materials, Clermont-Ferrand, France, 22–24 June 2015; pp. 93–98.
83. Cheah, J.S.J.; Walker, P.; Heath, A.; Morgan, T.K.K.B. Evaluating shear test methods for stabilised rammed earth. *Proc. Inst. Civ. Eng. Constr. Mater.* **2012**, *165*, 325–334. [CrossRef]
84. Nowamooz, H.; Chazallon, C. Finite element modelling of a rammed earth wall. *Constr. Build. Mater.* **2011**, *25*, 2112–2121. [CrossRef]
85. Bui, Q.-B.; Bui, T.-T.; Limam, A.; Morel, J.-C. Discrete element modeling of rammed earth wall. In *Rammed Earth Construction, Proceedings of the 1st International Conference on Rammed Earth Construction, ICREC 2015, Perth, Australia, 11–13 February 2015*; CRC Press: Boca Raton, FL, USA, 2015; pp. 57–61.
86. Reyes, J.C.; Yamin, L.E.; Hassan, W.M.; Sandoval, J.D.; Gonzalez, C.D.; Galvis, F.A. Shear behavior of adobe and rammed earth walls of heritage structures. *Eng. Struct.* **2018**, *174*, 526–537. [CrossRef]
87. Sorić, Z.; Kišiček, T. *Betonske Konstrukcije 1*; Građevinski fakultet: Zagreb, Croatia, 2014.

Experimental Investigation on Cement Mortar Bricks Manufactured with Fennel Wastes

Antonio Formisano * and Antonio Davino

Department of Structures for Engineering and Architecture, University of Naples "Federico II", Piazzale Vincenzo Tecchio 80, 80125 Naples, Italy; davino.ad@gmail.com
* Correspondence: antoform@unina.it

Abstract: Current practices supporting sustainable building design aim at reducing the expenditure of natural resources, such as raw materials, energy and water, in the production of construction supplies. In the current paper water is replaced by fennel centrifugate (FC) for the realization of cement mortar bricks. After having identified the most suitable cementitious pre-mixed over three potential candidates, the mechanical and physical characteristics of the FC bricks are compared to cement mortar bricks, prepared with regular water, by means of bending, compression at ordinary and high temperatures, imbibition and acoustic tests. From compared results, it is noticed that FC bricks have the same imbibition property, but tensile and compression (ordinary and high temperatures) resistances have about 20% less than the control specimen ones. The acoustic tests revealed a better response of FC bricks to the high frequencies greater than 1600 Hz. However, fennel fibres do not provide a manifest advantage, likely due to the small size of the centrifuged fragments that are not able to enhance the product tensile resistance.

Keywords: sustainable building; reuse; fennel wastes; cement mortar; green bricks

1. Introduction

The construction industry has a significant adverse impact on the environment, with serious worldwide implications. The European industry accounts for about 46% of the annual construction and demolition waste (CDW) according to Eurostat [1]. Similarly, the U.S. building industry contributes with 25% of non-industrial waste generation per year [2]. In China, the CDW reaches 30–40% of the total waste and recycling represents less than 5% [3]. From an environmental perspective, this category employs an enormous quantity of resources, including raw materials, energy and water [4–6]. The first are the focus of many researchers, which aim at recycling the building elements, either as isolated items or as components of novel products [7]. Several natural fibres, such as hemp, flax, jute and sisal, are currently being employed in fibre-reinforced composites [6], whose manufacturing method was widely investigated in literature [8–14].

Less attention has been paid to the use of water in the building industry, besides single case-studies, often performed in desertic or semi-desertic regions. Mekonnen and Hoekstra [15] reported that the overall trade of international virtual water (embodied in the production of food, fibre and non-food commodities) equals 26% of global water footprint. In particular, construction consumes 16% of the water, worldwide [7]. For what concerns the Mediterranean basin, the water availability is scarce and mainly based on mountain runoff water (50–90%) [16,17]. Thus, it is fundamental to preserve the water amount and quality, thereby safeguarding the accessible resources [18]. To this regard, the project aims at employing alternative plant-derived water sources in bricks manufacturing. The fennel (*Foeniculum vulgare*) bulb contains about 90 g of water per 100 g of raw product [19]. It is a biennial plant originating from southern Europe and, more generally, from the Mediterranean region. Nowadays, it is being cultivated worldwide due to its broad use [20].

In fact, fennel is employed in medicine [21–24], animal nutrition [25,26], pharmaceutics, cosmetics [27] and fashion industry [28]. Most importantly, fennel plantations can be grown in arid- and semi-arid regions of the planet [29]. In the production chain, the outermost rigid leaves are usually discarded for being too hard and fibrous. This selection results in the disposal of about 30% of the overall production for a total of around 70,000 tons per year only in the Southern regions of Italy [30].

The innovative pipeline presented by the paper aims at reducing the use of water in cement production by substituting it with water contained in fennel by-products. In this context, fennel centrifugate (FC) was employed as additive to cement mortars for bricks manufacturing. The experimental campaign consists in a preliminary investigation that intends to identify, among three types, the most suitable cement mortar. The compression and bending tests, as well as the economic evaluation, revealed the most appropriate type for the aims of this research. Consequently, a detailed characterization of the manufactured bricks was performed to evaluate potential physical and mechanical benefits provided by the supplement of fennel fibres. The investigations include bending, compression (at ordinary and high temperatures), soaking and acoustic tests.

In accordance with the Green Building Challenge process, the current work aims at: (1) reducing waste by employing a by-product of the agricultural industry, (2) employing less water in the process of cement-making by using fennel-centrifugate instead, (3) testing a new source of natural fibres (fennel), which are widely produced on the Italian territory and (4) fostering the use of local goods.

2. Materials and Methods

2.1. Experimental Setup

The experimental setup is summarized in the flow chart of Figure 1. Organization of work steps was done based on consultation of appropriate literature papers [31,32]. Briefly, a preliminary investigation was performed to settle the most suitable binding agent for a novel fennel-based composite material (phase I). After having defined the water content of fennel (%), three cement mortars (A, B and C) were tested. A total of 36 samples (see Section 2.3.1) were employed. The most appropriate combination was determined with compression and bending tests. Hence, a detailed physical and mechanical characterization of the obtained bricks was performed (phase II). For that, two sets of samples were prepared: (I) 24 parallelepiped samples for bending, compression and shrinkage tests. Four of these samples were cut and reshaped into 6 equally sized bricks and employed for imbibition and high temperature compression tests; (II) 12 cylindrical samples for acoustic tests (see Section 2.3.2).

2.2. The Fennel Water Content

Fennel leaves were centrifuged to obtain the fennel centrifugate (FC) and weighted on a precision balance (Wunder ACS-3M, Trezzo sull'Adda (Milan), Italy). The blend was placed in a muffle oven (FM22, Falc Instruments, Treviglio (Bergamo), Italy) at 105 °C for about 10 min to eliminate the water fraction and repeatedly weighted, until stabilization. The final weight of the dried samples was employed to calculate the fennel 'dry' mass (fibres, carbohydrates, lipids, calcium and vitamins) and the percentage of water. The same procedure was applied to the edible part of fennel.

2.3. Sample Preparation

All samples were prepared according to the UNI EN 196-1:2016 guidelines [33].
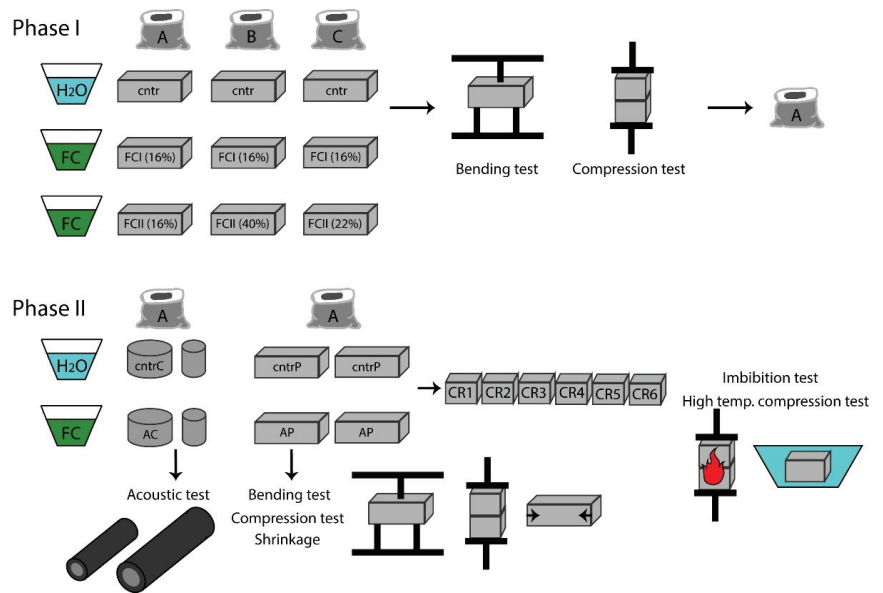
Figure 1. Overview of the experimental setup.

2.3.1. Phase I Samples

A total of 36 samples (Table 1, Figure 1) were prepared with one of three commercial cement mortars. Each matrix was combined with either water or FC to cast the following set of samples: (I) Control samples (cntr): 4 specimens/mortar. These samples were prepared by adding 16% tap water to the appropriate cement powder; (II) FC I: 4 specimens/mortar. In this case, exclusively the water obtained from fennel centrifugation was employed. To have a solid comparison between the obtained products, a fixed percentage (16%) was chosen. Such percentage was defined as the smallest value among the producers' indications of each cement matrix; (III) FC II: 4 specimens/mortar. The samples were prepared by replacing the percentage of water indicated by the producers with FC (16% for mortar A, 40% for B and 22% for C) (Figure 2).
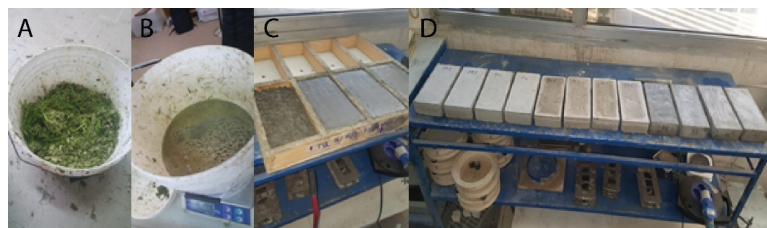
Figure 2. Preparation of FC (**A,B**) and casting of phase I specimens (**C,D**).

The casted samples were employed for compression tests. The two obtained fragments were reshaped and consequently joined with a high-strength cement mortar. The latter has mechanical characteristics superior to that used for the realization of the samples object of this research.

Table 1. Samples casted in phase I with 6 fennel-mortar combinations (cntr: control samples (mortar + tap water); FC I: mortar and 16% fennel centrifugate; FC II: mortar and variable % of fennel centrifugate).

	Cement Mortar		
	A	**B**	**C**
Control (16% H$_2$O)	cntrA1	cntrB1	cntrC1
	cntrA2	cntrB2	cntrC2
	cntrA3	cntrB3	cntrC3
	cntrA4	cntrB4	cntrC4
FC I (16% fennel centrifugate)	FCI_A1	FCI_B1	FCI_C1
	FCI_A2	FCI_B2	FCI_C2
	FCI_A3	FCI_B3	FCI_C3
	FCI_A4	FCI_B4	FCI_C4
FC II (variable % fennel centrifugate)	FCII_A1	FCII_B1	FCII_C1
	FCII_A2	FCII_B2	FCII_C2
	FCII_A3	FCII_B3	FCII_C3
	FCII_A4	FCII_B4	FCII_C4

2.3.2. Phase II Samples

Twenty-four parallelepiped-shaped specimens (Table 2) were prepared for shrinkage, bending and compression tests and 8 cylindrical specimens (Table 3), with 2 different diameters (98 mm for 4 blocks and 24 mm for other 4 blocks), for acoustic tests. The dimensions of this second group were dictated by the experimental setup for acoustic analyses, which require the insertion of the cylinders in steel tubes for impedance tests. The small and large diameters are required to investigate both low- and high-frequency acoustic waves. All samples (Figure 3) were prepared using mortar A and 16% fennel centrifugate instead of regular water, in accordance with the supplier's instructions. Tables 2 and 3 report the sample acronyms and dimensions, as well as the casting and dismantling dates.

Table 2. Parallelepiped (P)-shaped specimens for phase II (cntr: control samples, mortar A + water; AP: mortar A + fennel centrifugate bricks).

Acronym	Casting Date	Dimensions		Dismantling Date
		Length (mm)	Depth (mm)	
cntrP1	07/08/2019	250	120	17/09/2019
cntrP2	07/08/2019	250	120	17/09/2019
cntrP3	07/08/2019	250	120	17/09/2019
cntrP4	07/08/2019	250	120	17/09/2019
cntrP5	24/10/2019	250	120	19/11/2019
cntrP6	24/10/2019	250	120	19/11/2019
cntrP7	24/10/2019	250	120	19/11/2019
cntrP8	24/10/2019	250	120	19/11/2019
cntrP9	24/10/2019	250	120	19/11/2019
cntrP10	24/10/2019	250	120	19/11/2019
AP1	07/08/2019	250	120	17/09/2019
AP2	07/08/2019	250	120	17/09/2019
AP3	07/08/2019	250	120	17/09/2019

Table 2. *Cont.*

| Acronym | Casting Date | Dimensions | | Dismantling Date |
		Length (mm)	Depth (mm)	
AP4	07/08/2019	250	120	17/09/2019
AP5	07/08/2019	250	120	17/09/2019
AP6	07/08/2019	250	120	17/09/2019
AP7	07/08/2019	250	120	17/09/2019
AP8	07/08/2019	250	120	17/09/2019
AP9	07/08/2019	250	120	17/09/2019
AP10	07/08/2019	250	120	17/09/2019
AP11	07/08/2019	250	120	17/09/2019
AP12	07/08/2019	250	120	17/09/2019
AP13	07/08/2019	250	120	17/09/2019
AP14	07/08/2019	250	120	17/09/2019

Table 3. Cylindrical (C)-shaped specimens for phase II (cntr: control samples, mortar A + tap water; AC: mortar A + fennel centrifugate bricks).

| Acronym | Casting Date | Shape | | Dismantling Date | Weight (g) |
		Diameter (mm)	Height (mm)		
cntrC1	09/01/2020	98	50	22/01/2020	724
cntrC2	09/01/2020	98	48	22/01/2020	692
cntrC3	09/01/2020	98	55	22/01/2020	738
cntrC4	09/01/2020	28	51	22/01/2020	61
cntrC5	09/01/2020	28	51	22/01/2020	63
cntrC6	09/01/2020	28	50	22/01/2020	63
AC1	09/01/2020	98	49	22/01/2020	680
AC2	09/01/2020	98	52	22/01/2020	701
AC3	09/01/2020	98	51	22/01/2020	711
AC4	09/01/2020	28	51	22/01/2020	59
AC5	09/01/2020	28	52	22/01/2020	64
AC6	09/01/2020	28	49	22/01/2020	59

Figure 3. Centrifugation of fennel side-products (**A**) and preparation of cylindrical bricks for acoustic tests (**B**).

Two P-shaped control and two P-shaped fennel bricks were cut into 6 equally sized specimens (Table 4) for high temperature compression and imbibition tests.

Table 4. Cutting and reshaping of specific samples for high temperature compression and imbibition tests (cntr: control samples, mortar A + tap water; AP: mortar A + fennel centrifugate bricks).

Original Sample	Cut and Reshaped (C/R) Samples					
cntrP4	cntrP4_CR1	cntrP4_CR2	cntrP4_CR3	cntrP4_CR4	cntrP5_CR5	cntrP6_CR6
cntrP10	cntrP10_CR1	cntrP10_CR2	cntrP10_CR3	cntrP10_CR4	cntrP10_CR5	cntrP10_CR6
AP10	AP10_CR1	AP10_CR2	AP10_CR3	AP10_CR4	AP10_CR5	AP10_CR6
AP14	AP14_CR1	AP14_CR2	AP14_CR3	AP14_CR4	AP15_CR5	AP16_CR6

2.4. Testing Activities

The physical and mechanical tests (Section 2.4.1, Section 2.4.2, Section 2.4.3, Section 2.4.4, and Section 2.4.5) were carried out in the laboratory of the Department of Structures for Engineering and Architecture (DIST), Naples. The acoustic tests were entrusted to the company "Innovacustica Srl", Alvignano (Caserta, Italy) and performed at the laboratories located in in Casalnuovo di Napoli, Italy.

2.4.1. Bending Tests

Three-points bending tests were carried out with a 500 kN MTS 810 Universal Machine (Germany), as regulated by UNI EN 12390-5:2019 [34]. All 36 phase I- and 9 phase II-samples (3 cntr- and 6 FC-bricks) were tested for potential use in seismic areas. A concentrated force (loading speed v = 0.005 MPa/s) was applied in the middle of the specimen, which was constrained at the ends by two cylindrical supports. The distance between the support pins was 150 mm and the samples were perfectly centred inside the testing machine (Figure 4). In addition to measuring the displacement of the upper loading tool, a transducer located under the specimen reported the downward shift of the brick (Figure 4).
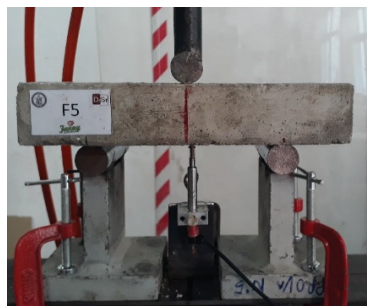
Figure 4. Setup for the three-points bending test.

The flexural strength f_{cf} was calculated with the following equation:

$$f_{cf} = \frac{3 \times F \times L}{2 \times d_1 \times d_2^2} \tag{1}$$

where F is maximum applied load, L is distance between the support pins, d_1 is the specimen's length and d_2 is the specimen's depth.

2.4.2. Compression Tests

The compression tests were carried out with a 500 kN MTS 810 Universal Machine (Germany), as regulated by the UNI EN 12390-3:2019 [35] standards for bricks (Figure 5). The top plate was designed to automatically align with the specimen. The load was increased at a speed of 50 N/s. The compressive strength was calculated by dividing the measured breaking load by the sample's cross-sectional area.

Figure 5. Setup for compression tests.

2.4.3. Shrinkage Tests

Shrinkage of control- and FC-bricks was calculated by measuring the dimensions at the dismantling date and after drying (28 days after dismantling), as regulated by UNI 11307:2008 [36].

2.4.4. Compression Test at High Temperatures

The samples were preheated at 200 °C and 600 °C in a muffle oven (FM22, Falc Instruments, Treviglio, Italy) prior to regular compression tests (as described in Section 2.4.2). The purpose is to evaluate the influence of high temperatures on the mechanical performances of samples by simulating a fire scenario. A pilot test was carried out to identify the procedure timing and potential temperature fluctuations. Three heating cycles were carried out on the cntrP4_CR1 specimen. The following thermoelectric probes were prepared (Figure 6A): (I) T1, inserted inside the specimen to a depth of 5 mm; (II) T2, inserted inside the specimen to a depth of 25 mm; (III) T3, inserted in the oven for the acquisition of the contact temperature. The data acquisition continued outside the oven to gain the cooling trend of the bricks. To reproduce the most realistic conditions and evaluate the cooling resulting from contact with the compression press, the pilot specimen was extracted from the oven and placed between two steel plates. Thus, it was possible to infer the temperature at which the brick fails under the compression test (Figure 6B).
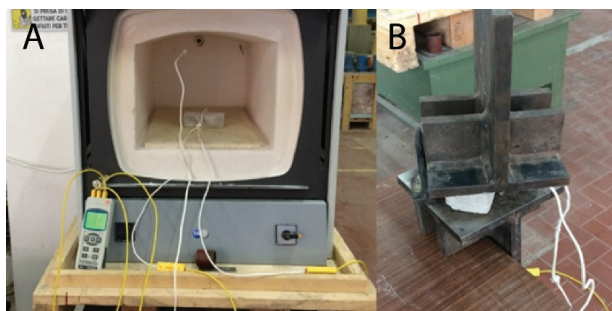
Figure 6. Thermoelectric probes for temperature monitoring (**A**) and temperature acquisition after extraction from the oven (**B**).

Figure 7 reports the pilot test with preheating at 600 °C. A temperature drop is observed after 102 min due to a voluntary opening of the oven. This was conceived to estimate the time required to restore the set temperature after extracting a sample.
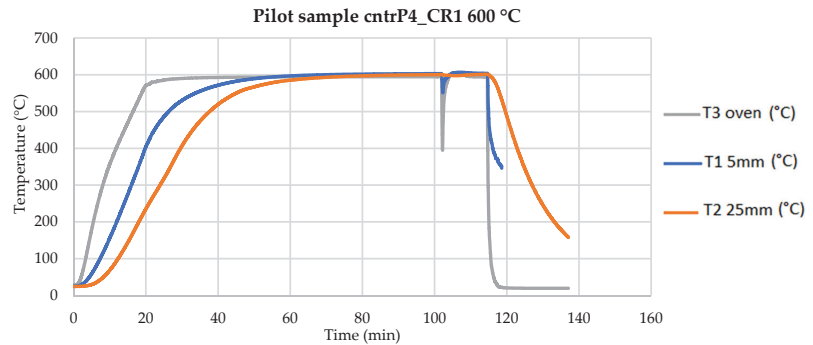
Figure 7. Pilot test at 600 °C.

2.4.5. Soaking Tests

In order to evaluate the amount of water absorbed by the bricks, they were placed under water for two weeks. Weight measurements were performed every 24 h [37].

2.4.6. Acoustic Tests

Transmission loss (TL) measurements were carried out using impedance tubes (Kundt tubes), according to the technical standard ASTM E2611-09 [38]. The instruments are listed in Table 5.

Table 5. Instruments employed to measure transmission loss.

Type	Model	Description
4 channels impedance tubes	BSWA SW 422	100 mm diameter tube with loudspeaker and 100 mm extension tube
4 channels impedance tubes	BSWA SW 477	30 mm diameter tube with loudspeaker and 30 mm extension tube
Microphones	BSWA MPA416	n. 4 1/4" microphones
Power Amplifier	BSWA TECH PA50	Power amplifier and signal generator
Sound card	BSWA TECH MC3242	4 channels DAQ Card
Sound calibrator	BSWA CA115	1000 Hz 114 dB sound calibrator

The investigated frequency range was 63–6300 Hz. The impedance tubes with diameters of 30 mm and 100 mm (Figure 8) covered, respectively, a complete range of 63–1800 Hz and 800–6300 Hz. In particular, the tube with a larger diameter was used for low frequencies, and the one with a smaller diameter was used for high frequencies.

The samples were intentionally casted with diameters smaller than the impedance tube to be coated with insulating material before insertion. The purpose was both to preserve the pipe from scratches and to create a layer of sound insulation between the mortar surface and the rigid surface of the steel pipe.
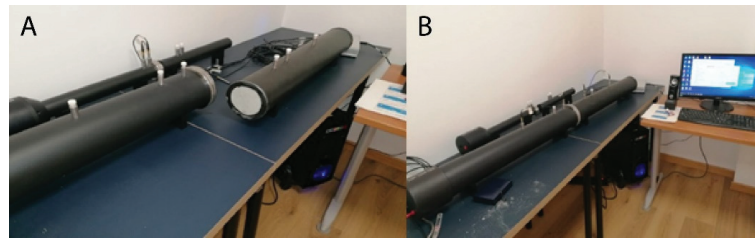
Figure 8. BSWA SW 422 and BSWA SW477 impedance tubes: (**A**) sample loading; (**B**) data acquisition.

3. Results

3.1. Phase I: Identifying the Ideal Fennel-Mortar Combination

3.1.1. Percentage of Water in Fennel Centrifugate (FC)

The centrifugate of fennel leaves was weighted in duplicate: FC1 (gross weight: 189.04 g) and FC2 (gross weight: 189.36 g). After incubation at 105 °C, the dried weights equalled 5.96 g and 5.99 g, respectively. Thus, the 'dry' mass corresponded to 7.5% of the fennel centrifugate and the water fraction to 92.5%. Concerning the edible part of fennel, 2.2 g of water-free mass were obtained for 100 g of starting material. The percentage of water-free mass (mainly fibres) was in line with the chemical composition tables of fennel [21]. The observed reduction possibly depended on the high content of fibres of the outer fennel leaves.

3.1.2. Flexural Strength Tests

The results in terms of flexural stress are summarized in Table 6. The specimens manufactured with mortar A or mortar B and 16% FC did not show great differences in terms of resistance compared to the control specimens. The greatest reduction in resistance was observed for mortar C. The overall best performances were registered for bricks prepared with the mortar A.

Table 6. Results of three-point bending flexural test in terms of flexural stress. The average values are reported with the standard deviation (SD).

Sample		Mortar A		Mortar B		Mortar C	
		Stress (MPa)	Average ± SD (MPa)	Stress (MPa)	Average ± SD (MPa)	Stress (MPa)	Average ± SD (MPa)
Control (16% H$_2$O)	1	4.14		2.34		6.72	
	2	3.11	3.39 ± 0.43	3.72	2.77 ± 0.55	4.65	5.76 ± 1.00
	3	3.16		2.53		6.79	
	4	3.16		2.50		4.86	
FC I (16% fennel centr.)	1	2.95		4.20		1.18	
	2	3.57	3.30 ± 0.42	2.00	2.81 ± 1.03	1.47	1.35 ± 0.12
	3	2.83		3.40		1.45	
	4	3.83		1.65		1.29	
FC II (variable % fennel centr.)	1	2.52		1.50		0.19	
	2	1.86	2.36 ± 0.39	0.96	1.05 ± 0.29	0.37	0.29 ± 0.08
	3	2.91		1.04		0.24	
	4	2.16		0.69		0.37	

3.1.3. Compression Tests

The results are summarized in Table 7. The highest strength values were obtained with mortar B. The specimens prepared with FC water displayed a drastic reduction in resistance of over 80%. Despite this decrease, for all blocks the average resistance values were greater than 5 MPa, which is the lowest admissible value for employing artificial blocks in the construction of load-bearing walls. This reduction was clearly marked for the samples assembled with mortar C. For mortar A-FC bricks, a 30% drop in resistance was observed with respect to the control specimens.

Table 7. Results of compression tests in terms of tensile strength. The average values are reported with the standard deviation (SD).

Sample		Mortar A		Mortar B		Mortar C	
		Stress (MPa)	Average ± SD (MPa)	Stress (MPa)	Average ± SD (MPa)	Stress (MPa)	Average ± SD (MPa)
Control (16% H$_2$O)	1	17.58	18.65 ± 0.65	32.48	36.15 ± 3.66	15.81	20.03 ± 3.44
	2	18.73		42.24		19.43	
	3	19.31		35.10		19.49	
	4	18.97		34.79		25.41	
FC I (16% fennel centr.)	1	11.40	12.92 ± 3.02	7.18	7.87 ± 3.98	1.13	1.35 ± 0.23
	2	15.05		10.45		1.58	
	3	8.86		12.15		1.58	
	4	16.54		1.71		1.11	
FC II (variable % fennel centr.)	1	14.14	12.66 ± 1.83	6.16	6.72 ± 1.98	0.82	0.58 ± 0.17
	2	14.14		5.92		0.41	
	3	12.73		10.02		0.66	
	4	9.65		4.77		0.44	

Based on the results of bending and compression tests, mortar A was chosen for the assembly of bricks. Thus, greater resistances were measured for mortar A when replacing regular water with fennel centrifugate. Furthermore, the costs of the mortar were lower.

3.2. Phase II: Physical and Mechanical Characterization of the Fennel-Mortara Composite Bricks
3.2.1. Shrinkage Tests

The average dimensions of all samples with the standard deviations are reported in Table 8. With respect to the original size (250 mm × 120 mm), the results did not show substantial differences in shrinkage between the control- and FC-samples (A).

Table 8. Average and standard deviation (SD) of shrinkage on all tested samples.

Sample	Width ± SD (mm)	Length ± SD (mm)
Control	249.0 ± 0.4	118.0 ± 0.7
A	249.0 ± 0.5	119.0 ± 0.7

Shrinkage is greatly influenced by the relative humidity of the surrounding environment and by the surface-to-volume ratio of the investigated element. Its extent is also conditioned by the installation method and the composition of the mortar, i.e., the water-to-cement ratio and the total amount of cement. An increase in concrete percentage causes an amplification of the phenomenon. It should be noted that shrinkage causes damaging cracks only in hyperstatically linked elements. For elements constrained in an isostatic manner, the damage is absent.

3.2.2. Bending Tests

The bending tests (Table 9) revealed a 21% reduction of the average bending tensile strength Δf_{ctf} for the samples supplemented with fennel centrifugate. The load-displacement and stress–strain (σ-ε) diagrams are presented in Figure 9A,B. It should be noted that the results did not show substantial differences between the displacements measured by the transducer and those recorded by the loading tool.

Table 9. Results of bending tests.

Acronym	Speed (mm/s)	Load$_{max}$ (KN)	f$_{ctf}$ (MPa)	Average $\pm$ SD (MPa)	Δf$_{ctf}$ (%)
cntrP1	0.05	4.64	4.37		
cntrP2	0.01	3.96	3.61	4.03 $\pm$ 0.32	-
cntrP3	0.005	4.40	4.12		
AP1	0.005	3.23	3.15		
AP2	0.005	2.43	2.69		
AP3	0.005	3.23	2.89	3.19 $\pm$ 0.35	−21.0
AP4	0.005	4.29	3.14		
AP5	0.005	3.70	3.68		
AP6	0.005	4.10	3.56		
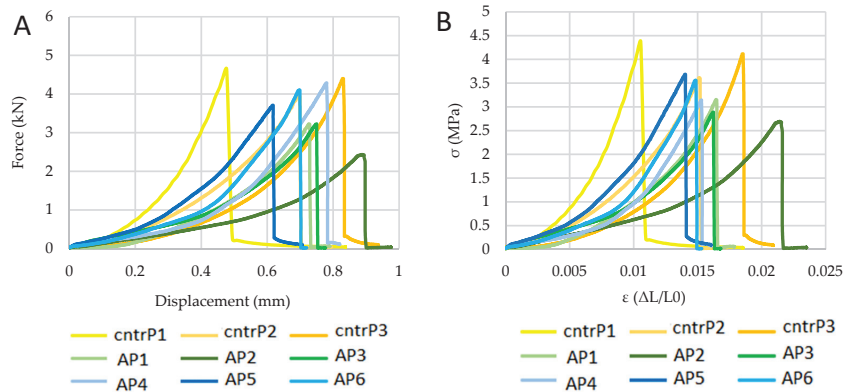
Figure 9. Results of bending tests in terms of load-displacement (**A**) and stress(σ)–strain(ε) (**B**). Yellow indicates control- and green/blue stands for FC-samples.

3.2.3. Compression Tests

On average, the specimens with additives provided a 17.8% decrease in compressive strength $\Delta\sigma_m$. The results are plotted in Figure 10 and reported in Table 10.
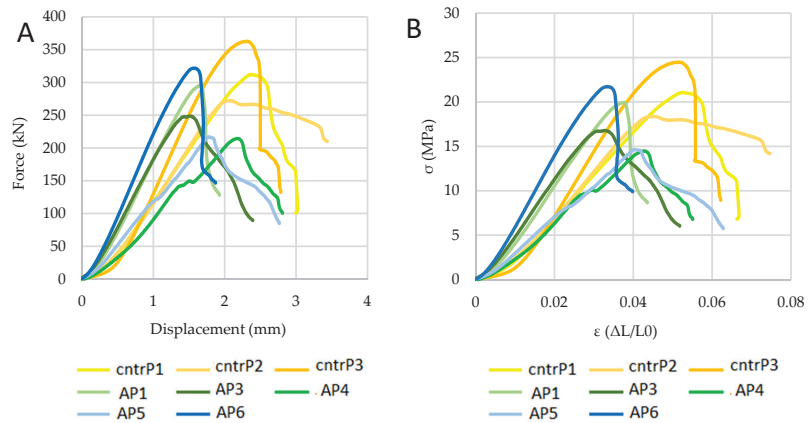
Figure 10. Results of compression tests in terms of load-displacement (**A**) and stress(σ)–strain(ε) (**B**). Yellow indicates control- and green/blue stands for FC-samples.

Table 10. Results of compression tests.

Acronym	Speed (mm/s)	Load$_{max}$ (KN)	σ (MPa)	Average ± SD (MPa)	Δσ$_m$ (%)
cntrP1	0.01	312.08	21.07	21.31 ± 2.50	-
cntrP2	0.01	272.23	18.38		
cntrP3	0.01	362.68	24.48		
AP1	0.01	295.68	19.96	17.52 ± 2.89	−17.8
AP3	0.01	248.81	16.80		
AP4	0.01	214.56	14.48		
AP5	0.01	217.09	14.65		
AP6	0.01	321.93	21.73		

3.2.4. Compression Tests at High Temperatures

The results on the 12 specimens, grouped according to the preheating temperature, are reported in terms of flexural stress–strain (σ-ε) diagrams in Figure 11. Based on the results obtained during the pilot test, it was possible to calculate the exact temperature of the specimen at both the beginning and the end of the test. The results are summarized in Tables 11 and 12.

Table 11. Overview of compression tests at 200 °C.

Samples at 200 °C							
Sample	T$_{sample}$ (°C)	Δt$_{start}$	T$_{start}$ (°C)	Δt$_{breakage}$	T$_{breakage}$ (°C)	σ$_{max}$ (MPa)	Average ± SD (MPa)
cntrP4_CR4	193.3	00:00:45	191.2	00:05:35	133.4	17.75	18.07 ± 0.23
cntrP4_CR2	193.3	00:00:32	192.0	00:06:43	119.8	18.27	
cntrP4_CR5	193.3	00:00:35	191.8	00:05:34	133.7	18.18	
AP10_CR1	193.3	00:00:37	191.7	00:04:09	152.7	13.73	14.68 ± 0.98
AP10_CR2	193.3	00:00:35	191.8	00:04:06	153.2	14.28	
AP10_CR3	193.3	00:00:38	191.7	00:04:06	153.2	16.02	
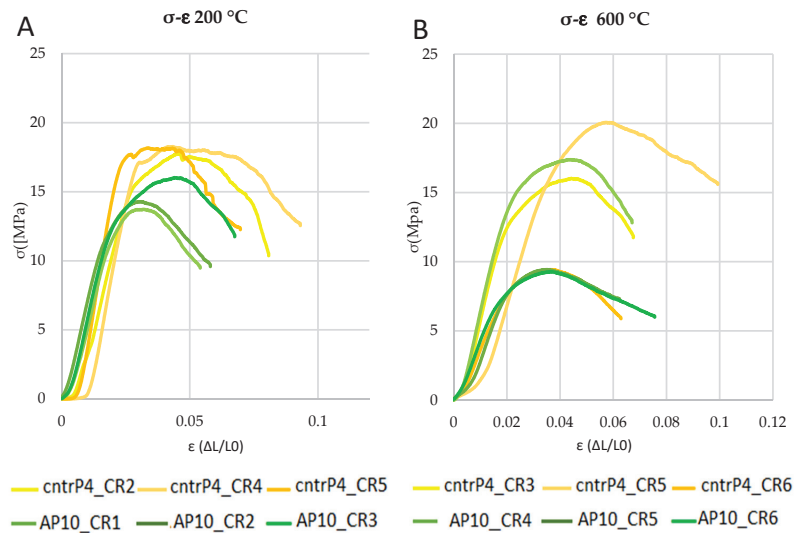
Figure 11. Load-displacement diagrams for samples preheated at 200 °C (**A**) and 600 °C (**B**). Yellow indicates control- and green stands for FC-samples.

Table 12. Overview of compression tests at 600 °C.

Sample	T_{sample} (°C)	Δt_{start}	T_{start} (°C)	$\Delta t_{breakage}$	$T_{breakage}$ (°C)	σ_{max} (MPa)	Average $\pm$ SD (MPa)
			Samples at 600 °C				
cntrP4_CR3	601.2	00:00:35	596.5	00:04:36	508.6	16.02	15.18 $\pm$ 4.38
cntrP4_CR6	601.2	00:00:39	596.5	00:04:27	512.9	9.44	
cntrP10_CR5	601.2	00:00:45	595.1	00:06:31	447.8	20.07	
AP10_CR4	601.2	00:00:35	596.5	00:04:37	508.6	17.38	12.03 $\pm$ 3.78
AP10_CR5	601.2	00:00:38	596.5	00:04:23	516.0	9.43	
AP10_CR6	601.2	00:00:34	597.2	00:05:05	492.5	9.28	

The obtained results were compared with the compression tests at room temperature described in the previous paragraph. The summary diagram of the trends is reported in Figure 12. The temperature decreased by 15% in control specimens and 35% in samples prepared with FC, along with the tension state. The specimens supplemented with FC presented stress values greater than 9 MPa at 600 °C, which overcomes the minimum resistance limit allowed in the seismic area (5 MPa).
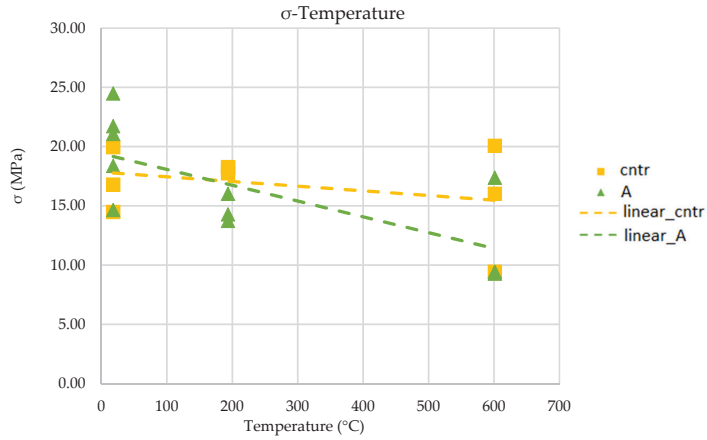
Figure 12. Comparison of test results in terms of compression stress vs. temperature. Yellow indicates control- and green FC-samples.

3.2.5. Soaking Tests

The results show a similar trend for control- and FC-bricks. The initial weight increased by 8% when compared to the initial weight. The plateau was reached after 48 h. Because of the great difference in size, and therefore in weight, the data are plotted in two different graphs (Figure 13).
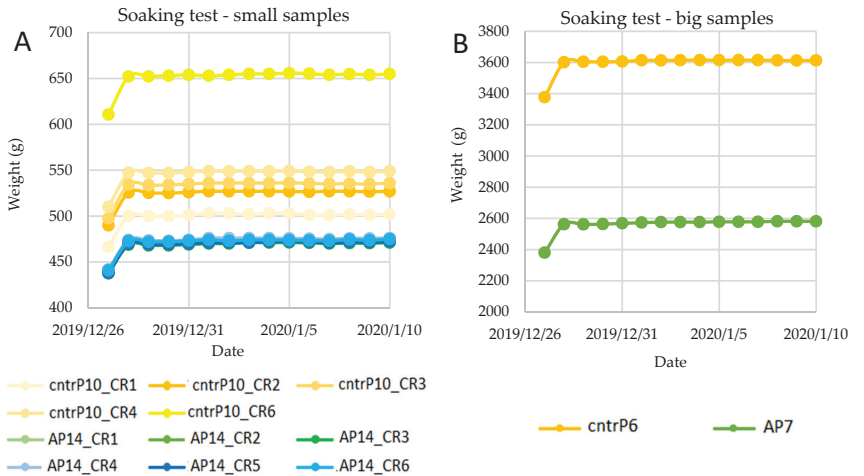
Figure 13. Soaking tests on small (**A**) and big (**B**) samples. Yellow indicates control- and green/blue FC-samples.

3.2.6. Acoustic Tests

An increase of sound insulation could be a potential benefit of the fennel fibrous components incorporated into the bricks. Figure 14 reports the transmission loss for all the investigated frequencies for control- and FC-samples.
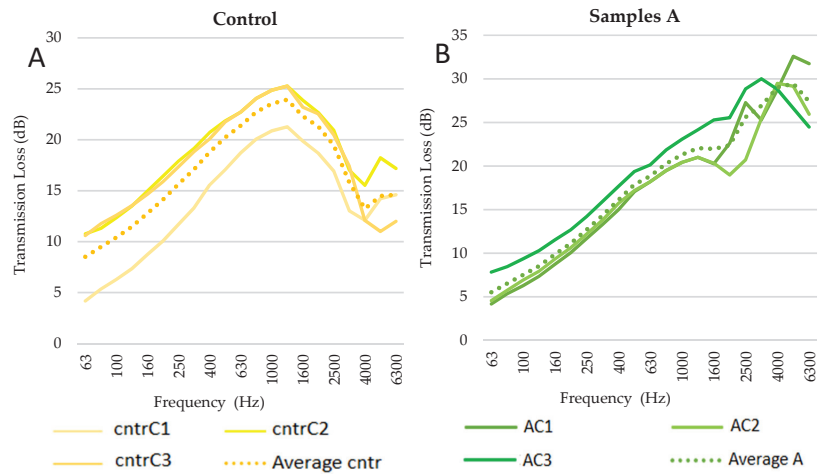
Figure 14. Transmission loss deriving from acoustic tests on control- (**A**) and FC-bricks (**B**). Yellow indicates control- and green FC-samples.

The TL curves present a similar trend. However, the curves of control samples are shifted towards higher frequencies, especially sample cntrC1. A possible explanation of this behaviour relies on the irregular circular shape of the specimens, which created gaps between the walls of the tube and the specimens. Future measurements can be improved by further reducing the specimen's diameter and better sealing the edges when inserting the samples into the tubes. To facilitate comparisons between the two groups, the TL averages obtained at each frequency are plotted in a single graph (Figure 15).
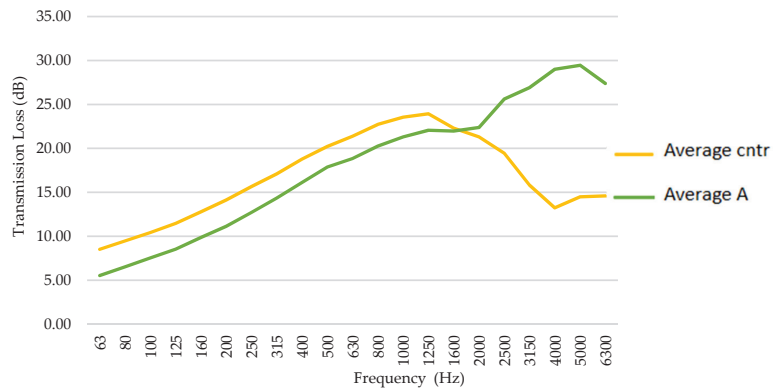
Figure 15. TL averages of control- (yellow) and FC-samples (green) plotted for all the measured frequencies.

At medium-low frequencies, of a major interest in the civil sector [39], the fennel centrifugate bricks display a behaviour comparable to controls. However, it provides a better insulation at higher frequencies.

4. Conclusions and Future Perspectives

The presented work aimed at supporting the use of fennel processing waste in the construction industry. Fennel centrifugate (FC) can be combined with matrices into bricks, which are environmentally sustainable due to the following reasons: (1) water is preserved, as it is replaced by fennel centrifugate; (2) agricultural waste is reduced by giving a second

life to fennel by-products that find less employment in satellite industries; (3) fennel fibres could be employed as additional source of natural fibres in building industry. Furthermore, the use of fennel by-products in building industry is in line with the current directives to prefer the employment of local goods.

The experimental campaign was designed to first identify, among three different mortar-fennel combinations, the most suitable one for the mentioned research objectives. Mortar A was chosen based on the physical and mechanical performances, as well as for the reduced cost. Thus, mortar A was employed for the preparation of a set of samples used in the second phase of testing. The latter was intended to provide a broader picture of the material performance. It was achieved that, for bricks manufactured with 16% of FC instead of water, mortar A is preferable to mortar B because of its significantly greater resistances (almost double). The bricks manufactured with mortar A did not show any significant reduction in size compared to the control specimens and, overall, there was a minimal shrinkage compared to the original dimensions. The bending tests highlighted a 20% reduction of tensile strength in the FC-bricks compared to the control specimens. The samples supplemented with fennel subjected to compression tests displayed a 17.8% resistance reduction compared to control specimens.

The same test performed at high temperature revealed a 15% reduction in compressive strength for the control specimens, which increased to 35% for FC bricks. Nonetheless, in both cases, at 600 °C the values were greater than 9 MPa, which exceeds the minimum resistance limit allowed in seismic areas (5 MPa).

The imbibition tests showed an increase of weight that equals 8% in mass for both control specimens and FC bricks after 24 h. After that period, the weight remained constant over the subsequent 14 days.

The acoustic tests showed that the insulation characteristics of the two types of materials are comparable. In particular, they showed a similar behaviour at low frequencies, which is of greater interest in the civil sector, but a better response at high frequencies.

In conclusion, the paper revealed that the replacement of water by fennel centrifugate for the preparation of cement mortar bricks results in products with performances equivalent to the ordinary mortar bricks. The addition of fibres did not produce evident benefits. This was probably due to the centrifugation process of fennel, which possibly results in too small fragments to give a significant contribution to tensile resistance. For this reason, further developments of the research will be devoted to investigating the effect of longer fennel fibres to improve the flexural strength of the tested bricks, as well as the long-term performances of tested products due to aging of the fennel particles contained in the used water. Moreover, a cost analysis will be done to evaluate the economic convenience of these bricks and a Life Cycle Assessment phase will be useful to quantify the energy spent for producing, using and dismantling the examined building products during their whole life. Results deriving from future research developments will be used to produce a new prototyping line able to generate a new type of green bricks for building constructions.

person of Eng. Antonio Vittorioso) for the kind provision of the pre-mixed types used in the current research. Finally, a special thank is devoted to the Innovacustica srl company, in the person of Eng. Marco Anniciello, for the execution of acoustic tests on the studied building products.

Conflicts of Interest: The authors declare no conflict of interest.

References

1. Eurostat. Generation of Waste by Waste Category, Hazardousness and NACE Rev 2 Activity. Available online: https://ec.europa.eu/eurostat/web/products-datasets/-/ENV_WASGEN (accessed on 1 July 2021).
2. Keeler, M.; Burke, B. *Fundamentals of Integrated Design for Sustainable Building*; John Wiley & Sons, Inc.: Hoboken, NJ, USA, 2009.
3. Huang, B.; Wang, X.; Kua, H.; Geng, Y.; Bleischwitz, R.; Ren, J. Construction and demolition waste management in China through the 3r principle. *Resour. Conserv. Recycl.* **2018**, *129*, 36–44. [CrossRef]
4. Heravi, G.; Fathi, M.; Faeghi, S. Multi-criteria group decision-making method for optimal selection of sustainable industrial building options focused on petrochemical projects. *J. Clean. Prod.* **2017**, *142*, 2999–3013. [CrossRef]
5. Birgisdóttir, H.; Rasmussen, F.N. *Introduction to LCA of Buildings*, 1st ed.; Danish Transport and Construction Agency: Copenhagen, Denmark, 2016.
6. Sanal, I.; Verma, D. Construction Materials Reinforced with Natural Products. In *Handbook of Ecomaterials*; Martínez, L., Kharissova, O., Kharisov, B., Eds.; Springer: Cham, Switzerland, 2017. [CrossRef]
7. The Worldwatch Institute. *Annual Report*; The Worldwatch Institute: Washington, DC, USA, 2006.
8. Maziz, A.; Tarfaoui, M.; Gemi, L.; Rechak, S.; Nachtane, M. A progressive damage model for pressurized filament-wound hybrid composite pipe under low-velocity impact. *Compos. Struct.* **2021**, *276*, 114520. [CrossRef]
9. Gemi, D.S.; Şahin, Ö.S.; Gemi, L. Experimental investigation of the effect of diameter upon low velocity impact response of glass fiber reinforced composite pipes. *Compos. Struct.* **2021**, *275*, 114428. [CrossRef]
10. Ivens, J.; Urbanus, M.; De Smet, C. Shape recovery in a thermoset shape memory polymer and its fabric-reinforced composites. *Express Polym. Lett.* **2011**, *5*, 254–261. [CrossRef]
11. Korotkov, R.; Vedernikov, A.; Gusev, S.; Alajarmeh, O.; Akhatov, I.; Safonov, A. Shape memory behavior of unidirectional pultruded laminate. *Compos. Part A Appl. Sci. Manuf.* **2021**, *150*, 106609. [CrossRef]
12. Vedernikov, A.; Safonov, A.; Tucci, F.; Carlone, P.; Akhatov, I. Pultruded materials and structures: A review. *J. Compos. Mater.* **2020**, *54*, 4081–4117. [CrossRef]
13. Yu, T.; Zhang, Z.; Song, S.; Bai, Y.; Wu, D. Tensile and flexural behaviors of additively manufactured continuous carbon fiber-reinforced polymer composites. *Compos. Struct.* **2019**, *225*, 111147. [CrossRef]
14. Czapski, P.; Jakubczak, P.; Bieniaś, J.; Urbaniak, M.; Kubiak, T. Influence of autoclaving process on the stability of thin-walled, composite columns with a square cross-section—Experimental and numerical studies. *Compos. Struct.* **2020**, *250*, 112594. [CrossRef]
15. Mekonnen, M.M.; Hoekstra, A.Y. *National Water Footprint Accounts: The Green, Blue and Grey Water Footprint of Production and Consumption*; UNESCO-IHE Institute for Water Education: Delft, The Netherlands, 2011.
16. De Jong, C.; Lawler, D.; Essery, R. Mountain hydroclimatology and snow seasonality and hydrological change in mountain environments. *Hydrol. Process.* **2009**, *23*, 955–961. [CrossRef]
17. Viviroli, D.; Dürr, H.H.; Messerli, B.; Meybeck, M.; Weingartner, R. Mountains of the world, water towers for humanity: Typology, mapping, and global significance. *Water Resour. Res.* **2007**, *43*, 1–13. [CrossRef]
18. Messerli, B.; Viviroli, D.; Weingartner, R. Mountains of the world—Vulnerable water towers for the 21st century. *Ambio Spec. Rep.* **2004**, *13*, 29–34. [CrossRef]
19. U.S. Department of Agriculture Agricultural Research Service. Composition of Foods. Raw, Processed, Prepared. USDA National Nutrient Database for Standard Reference, Release 23. Available online: https://www.ars.usda.gov/ARSUserFiles/80400535/DATA/sr23/sr23_doc.pdf (accessed on 1 July 2021).
20. Al-Snafi, A.E. The chemical constituents and pharmacological effects of Foeniculum vulgare—A review. *IOSR J. Pharm.* **2018**, *8*, 81–96.
21. Charles, D.J. Fennel. In *Antioxidant Properties of Spices, Herbs and Other Sources*; Springer: New York, NY, USA, 2012; pp. 287–293. [CrossRef]
22. Bokaie, M.; Farajkhoda, T.; Enjezab, B.; Khoshbin, A.; Karimi-Zarchi, M. Oral fennel (*Foeniculum vulgare*) drop effect on primary dysmenorrhea: Effectiveness of herbal drug. *Iran J. Nurs. Midwifery Res.* **2013**, *18*, 128–132. [PubMed]
23. Choi, E.M.; Hwang, J.K. Antiinflammatory, analgesic and antioxidant activities of the fruit of *Foeniculum vulgare*. *Fitoterapia* **2004**, *75*, 557–565. [CrossRef] [PubMed]
24. De Marino, S.; Gala, F.; Borbone, N.; Zollo, F.; Vitalini, S.; Visioli, F.; Iorizzi, M. Phenolic glycosides from *Foeniculum vulgare* fruit and evaluation of antioxidative activity. *Phytochemistry* **2007**, *68*, 1805–1812. [CrossRef]
25. Uslu, Ö.S.; Gedik, O. A Research on the using of fennel hay as animal feed additive. In Proceedings of the 2nd International Conference on Agriculture, Technology, Engineering and Sciences (ICATES 2019), Lviv, Ukraine, 18–20 September 2019.
26. Pałka, S.; Kmiecik, M.; Migdał, L.; Siudak, Z. The effect of a diet containing fennel (*Foeniculum vulgare* Mill.) and goat's-rue (*Galega officinalis* L.) on litter size and milk yield in rabbits. *Sci. Ann. Pol. Soc. Anim. Prod.* **2019**, *4*, 73–78. [CrossRef]

27. Ahmad, B.S.; Talou, T.; Saad, Z.; Hijazi, A.; Cerny, M.; Kanaan, H.; Chokr, A.; Merah, O. Fennel oil and by-products seed characterization and their potential applications. *Ind. Crops Prod.* **2018**, *111*, 92–98. [CrossRef]

28. Haddar, W.; Elksibi, I.; Meksi, N.; Mhenni, M.F. Valorization of the leaves of fennel (*Foeniculum vulgare*) as natural dyes fixed on modified cotton: A dyeing process optimization based on a response surface methodology. *Ind. Crops Prod.* **2014**, *52*, 588–596. [CrossRef]

29. Barros, L.; Cavalho, A.M.; Ferreira, I.C.F.R. The nutritional composition of fennel (*Foeniculum vulgare*): Shoots, leaves, stems and inflorescences. *LWT Food Sci. Technol.* **2010**, *43*, 814–818. [CrossRef]

30. Mariniello, L.; Giosafatto, C.V.L.; Moschetti, G.; Aponte, M.; Masi, P.; Sorrentino, A.; Porta, R. Fennel waste-based films suitable for protecting cultivations. *Biomacromolecules* **2007**, *8*, 3008–3014. [CrossRef] [PubMed]

31. Lionetto, F.; Moscatello, A.; Totaro, G.; Raffone, M.; Maffezzoli, A. Experimental and numerical study of vacuum resin infusion of stiffened carbon fiber reinforced panels. *Materials* **2020**, *13*, 4800. [CrossRef] [PubMed]

32. Vedernikov, A.; Nasonov, Y.; Korotkov, R.; Gusev, S.; Akhatov, I.; Safonov, A. Effects of additives on the cure kinetics of vinyl ester pultrusion resins. *J. Compos. Mater.* **2021**, *55*, 2921–2937. [CrossRef]

33. *EN 196-1:2016*; Methods of Testing Cement—Part 1: Determination of Strength. European Committee for Standardization: Brussels, Belgium, 2016.

34. *EN 12390-5:2019-08*; Testing Hardened Concrete—Part 5: Flexural Strength of Test Specimens. European Committee for Standardization: Brussels, Belgium, 2019.

35. *UNI EN 12390-3:2019*; Testing Hardened Concrete—Part 3: Compressive Strength of Test Specimens. European Committee for Standardization: Brussels, Belgium, 2019.

36. *UNI 11307:2008*; Testing for Hardened Concrete—Shrinkage Determination. UNI Italian Committee for Standardization (Ente Nazionale Italiano di Unificazione): Milan, Italy, 2008.

37. *UNI EN 13755:2008*; Natural Stone Test Methods. Determination of Water Absorption at Atmospheric Pressure. European Committee for Standardization: Brussels, Belgium, 2008.

38. *ASTM E2611-09*; Standard Test Method for Measurement of Normal Incidence Sound Transmission of Acoustical Materials Based on the Transfer Matrix Method. ASTM International: West Conshohocken, PA, USA, 2009.

39. Hopper, C.; Assous, S.; Wilkinson, P.B.; Gunn, D.A.; Jackson, P.D.; Rees, J.G.; O'Leary, R.L.; Lovell, M.A. Bioinspired low-frequency material characterisation. *Adv. Acoust. Vib.* **2012**, *2012*, 927903. [CrossRef]

Numerical Simulation and Design Recommendations for Web Crippling Strength of Cold-Formed Steel Channels with Web Holes under Interior-One-Flange Loading at Elevated Temperatures

Zhiyuan Fang [1], Krishanu Roy [1,2,*], Hao Liang [1], Keerthan Poologanathan [3], Kushal Ghosh [4], Abdeliazim Mustafa Mohamed [5,6] and James B. P. Lim [1,2]

[1] Department of Civil and Environmental Engineering, The University of Auckland, Auckland 1023, New Zealand; zfan995@aucklanduni.ac.nz (Z.F.); hlia929@aucklanduni.ac.nz (H.L.); james.lim@auckland.ac.nz (J.B.P.L.)

[2] School of Engineering, The University of Waikato, Hamilton 3216, New Zealand

[3] Faculty of Engineering and Environment, University of Northumbria, Newcastle upon Tyne NE7 7YT, UK; keerthan.poologanathan@northumbria.ac.uk

[4] Department of Civil Engineering, National Institute of Technology, South Sikkim 737139, Sikkim, India; kushal@nitsikkim.ac.in

[5] Department of Civil Engineering, College of Engineering, Prince Sattam Bin Abdulaziz University, Al-Kharj 16278, Saudi Arabia; a.bilal@psau.edu.sa

[6] Building & Construction Technology Department, Bayan University, Khartoum 210, Sudan

[*] Correspondence: krishanu.roy@auckland.ac.nz or krishanu.roy@waikato.ac.nz

Abstract: This paper investigates the interior-one-flange web crippling strength of cold-formed steel channels at elevated temperatures. The stress-strain curves of G250 and G450 grade cold-formed steel (CFS) channels at ambient and elevated temperatures were taken from the literature and the temperatures were varied from 20 to 700 °C. A detailed parametric analysis comprising 3474 validated finite element models was undertaken to investigate the effects of web holes and bearing length on the web crippling behavior of these channels at elevated temperatures. From the parametric study results, it was found that the web crippling strength reduction factor is sensitive to the changes of the hole size, hole location, and the bearing length, with the parameters of hole size and hole location having the largest effect on the web crippling reduction factor. However, the web crippling strength reduction factor remains stable when the temperature is changed from 20 to 700 °C. Based on the parametric analysis results, the web crippling strength reduction factors for both ambient and elevated temperatures are proposed, which outperformed the equations available in the literature and in the design guidelines of American standard (AISI S100-16) and Australian/New Zealand standard (AS/NZS 4600:2018) for ambient temperatures. Then, a reliability analysis was conducted, the results of which showed that the proposed design equations could closely predict the reduced web crippling strength of CFS channel sections under interior-one-flange loading conditions at elevated temperatures.

Keywords: web crippling; proposed equations; elevated temperatures; interior-one-flange loading; web hole; finite element analysis; cold-formed steel

1. Introduction

In recent years, the popularity of cold-formed steel (CFS) has increased in the construction industry, due to their numerous advantages, such as superior strength to weight ratio, stiffness, and ease of construction, when compared to hot-rolled steel structures [1–3]. The applications of these CFS members (particularly CFS channels) often include beams [4–7], columns [8–16], shear walls [17], and cladding systems [18]. However, localized web failure can occur near the web holes of CFS channels, especially under transverse concentrated

loads. The fire safety of these CFS channels is also essential to minimize the damage caused by fire-related accidents [2,19]. This paper intends to investigate the effect of fire loading on the interior-one-flange (IOF) web crippling strength of CFS channels with web holes.

Extensive research works are available in the literature on the web crippling strength of CFS channels at ambient temperatures [20–33]. However, very limited research studies are available in the literature for the IOF web crippling capacity of these CFS channels at elevated temperatures. In addition, no information is available in the current design standards of CFS, explaining how the effect of fire loading can reduce the web crippling capacity of CFS channels from ambient to elevated temperatures. The lack of design information makes it difficult for practicing engineers and researchers to predict the web crippling capacity of CFS channels subjected to one-flange loading at elevated temperatures.

Recent studies have started to focus on the material behavior of CFS sections at elevated temperatures. Imran et al. [34] recently proposed numerical equations to evaluate the strength reduction factors of square, rectangular, and circular CFS hollow sections at elevated temperatures. Coupons were cut from these hollow sections and loaded under temperatures ranging from 20 to 800 °C. The main aim of their study was to determine the reduction in material properties. Furthermore, Kankanamge and Mahendran [35] proposed the updated equations for reduction factors of the stress-strain relationship for both the normal and high strength steels of different grades at elevated temperatures. A similar study was completed by Ranawaka and Mahendran [36], who proposed empirical equations for determining the stress-strain relationship of both the normal and high strength steels at elevated temperatures. Chen and Young [37] reported mechanical property data for G550 and G450 grades of CFS sections by conducting tensile coupon tests under both the steady and transient temperature conditions. Lim and Young [38] used the stress-strain relationships of Chen and Young [37] to determine the effect of fire loading on the capacity of CFS bolted connections.

Alongside the studies reported in the literature on reduced mechanical properties of CFS sections at elevated temperatures, some researchers also focused on the structural behavior of different CFS sections at elevated temperatures and that are subject to different loading conditions. Multiple investigations have been completed to determine the effect of elevated temperatures on CFS beams. Landesmann and Camotim [39] presented a FE investigation on the distortional buckling behavior of CFS single-span lipped channel beams under elevated temperatures. Laim et al. [40] completed a study to understand the structural behavior of CFS beams in fire. Kankanamge and Mahendran [41] presented a validated FE model to determine the structural behavior of CFS lipped channel beams under bending at elevated temperatures.

The structural behavior of CFS columns at elevated temperatures has been studied by researchers to date. Gunalan et al. [31] carried out the experimental and numerical investigation on the local buckling behavior of CFS lipped and unlipped channel columns under simulated fire loading. Gunalan et al. [42] also presented a study on the flexural-torsional buckling interaction of CFS lipped channel columns at ambient and elevated temperatures. Ranawaka and Mahendran [43] conducted a study to determine the distortional buckling behavior of CFS lipped channel columns at elevated temperatures. Chen and Young [37] performed a numerical study to understand the behavior of CFS lipped channel columns at elevated temperatures. Feng and Wang [44] investigated the axial strength of CFS channel columns under ambient and elevated temperatures.

Of note, most of the research studies available in the current literature focus on the behavior of CFS sections under compression and torsional loading at elevated temperatures. No research is available in the literature that investigated the effects of web holes on the web crippling strength of CFS channels at elevated temperatures. Furthermore, the current design specifications, such as ASCE [45], EN 1993-1-1 [46], and BS 5950 [47] do not provide any guidelines for CFS channels with web holes at elevated temperatures. However, AISI [48] and AS/NZ:4600 [49] offer reduction factor equations for CFS channels with web holes under IOF and end-one-flange (EOF). However, these are focused on channels with

web holes that offset to the bearing edge and are applicable only at ambient temperatures. Lian et al. [29,30] proposed strength reduction factors for determining the reduced web crippling capacity of CFS channels with web holes subjected to IOF loading. However, the reduction factors of Lian et al. [29,30] are only applicable at ambient temperatures and do not cover the case of elevated temperatures. This issue is addressed in the current research.

This paper investigates the feasibility of using the same reduction factor equations of Lian et al. [29,30] from ambient temperatures to elevated temperatures. Figure 1 shows the symbol definitions used for the dimensions of CFS channels considered in this study. Based on the results of 3474 finite element (FE) models, the parametric effects of web holes and bearing length on the web crippling strength of CFS channels were investigated. From the parametric analysis results, design recommendations are proposed for the reduced IOF web crippling strength of CFS channels at elevated temperatures. Then, a comparison of results from the proposed equations and the equations of Lian et al. [29,30] and AISI [48] and AS/NZS [49] was made and showed that the proposed equations outperformed the others. Next, a reliability analysis was conducted, which showed that the proposed equations could closely predict the reduced web crippling strength of CFS channels when loaded with IOF loading at elevated temperatures.
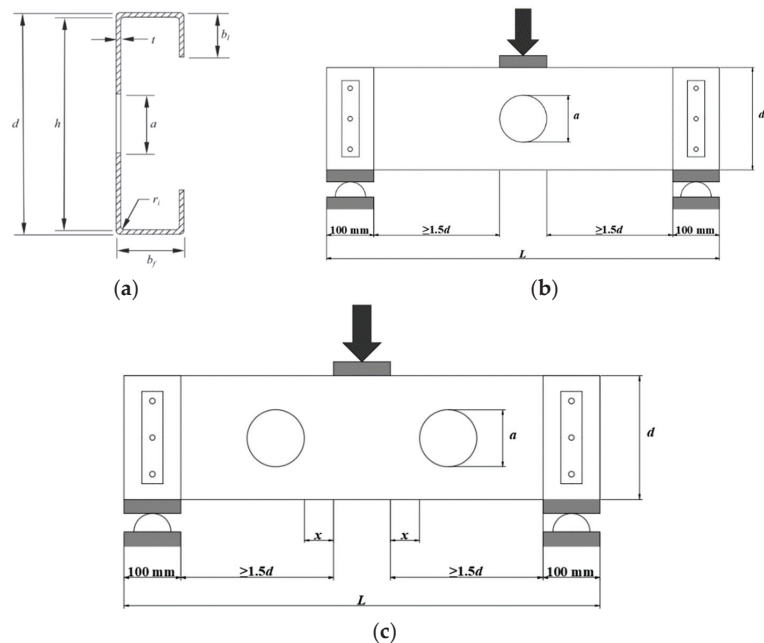
Figure 1. Definition of symbols and loading cases: (**a**) Section dimensions; (**b**) sections with centered holes from the bearing plate under IOF; (**c**) sections with offset holes from the bearing plate under IOF.

2. Summary of the Experimental Investigation

A total of 61 experimental test results of CFS channels with web holes subjected to IOF loading were reported in Lian et al. [29,30]. The cases of both fastened flange and unfastened flange are considered in the experimental tests. In addition, the hole of the specimens was located as centered beneath the bearing plate or with a horizontal clear distance to the near edge of the bearing plate. The experimental results matched well with the validated FE models in terms of failure modes and failure loads.

3. Numerical simulation

3.1. Development of the Finite Element Model

A nonlinear elasto-plastic FE model was developed using a finite element analysis (FEA) software named ABAQUS [50] to simulate the IOF web crippling behavior of CFS channels with web holes (see Figure 2). The CFS channels were modelled using S4R shell elements with a mesh size of 5 mm× 5 mm. In total, around 3000 elements were used. The upper endplate was modelled using rigid quadrilateral shell elements (R3D4) with a mesh size of 10 mm× 10 mm. In total, 350 elements were used to model the upper endplate. Figure 3 illustrates a typical FE mesh.
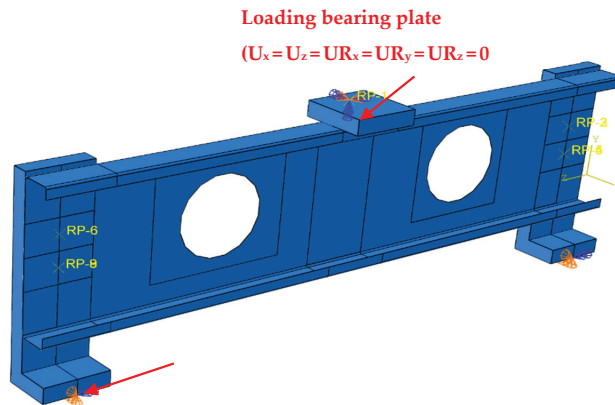
Figure 2. Boundary conditions used in FE models.
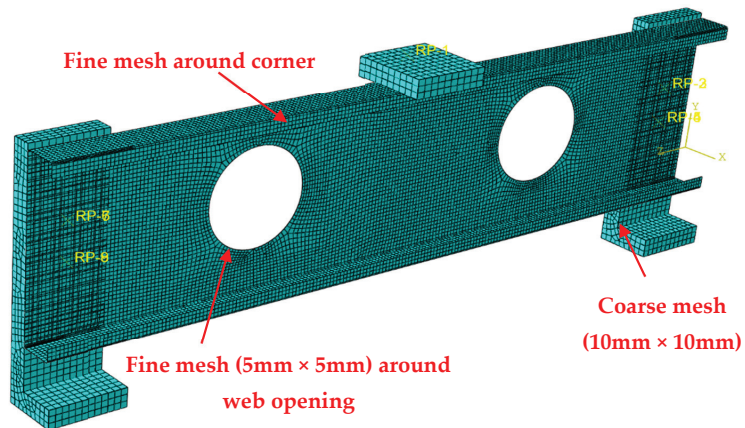
Figure 3. FE meshing types.

The stress-strain curves of 1.55 and 1.95 mm thick G250 CFS and 1.50 and 1.90 mm G450 steels at elevated and ambient temperatures were taken from Kankanamge and Mahendran [35] and used in the FE model.

The interface of bearing plate and channel section was modelled using the surface-to-surface contact option. The target surface was the bearing plate, whereas the contact surface was selected to be the channel section. No penetration of the two contact surfaces was permitted. Displacement control was applied to model the vertical load applied to the channels through the reference node of the top bearing plate. A similar modelling method was employed by Fang et al. [16], Chen et al. [51–53], and Roy et al. [54–56].

3.2. FE Validation

A total of 61 experimental test results of Lian et al. [29,30] were used to validate the FE model. As shown in Tables 1 and 2, the average ratios of experimental to FEA strengths (P_{EXP}/P_{FEA}) are 1.00 and 0.94, respectively for the CFS channels with unfastened and fastened flanges at ambient temperatures. Therefore, the FE models could closely predict the IOF web crippling strength of perforated CFS channels at ambient temperatures.

Table 1. Comparison of experimental results with FEA results for sections with unfastened flanges.

Specimen ID	Web	Flange	Lip	Bend Radius	Thickness	Hole Dia.	Bearing Length	Yield Stress	Exp. Load	FEA Result	
	d	b_f	b_l	r	t	a	N	f_y	P_{EXP}	P_{FEA}	P_{EXP}/P_{FEA}
	(mm)	(mm)	(mm)	(mm)	(mm)	(mm)	(mm)	(MPa)	(kN)	(kN)	
1	141.82	60.63	13.66	4.8	1.27	0.00	100	639.8	10.78	11.21	0.96
2	142.27	60.41	13.86	4.8	1.27	83.66	100	639.8	10.17	10.66	0.95
3	142.31	59.94	13.97	4.8	1.28	83.64	100	639.8	10.32	10.84	0.95
4	142.24	60.37	13.9	4.8	1.27	0.00	120	639.8	11.64	12.05	0.97
5	142.11	60.2	13.97	4.8	1.28	83.68	120	639.8	10.54	11.32	0.93
6	142.42	60.2	13.6	4.8	1.27	83.73	120	639.8	10.57	10.82	0.98
7	142.4	59.79	13.28	4.8	1.28	0.00	150	639.8	12.60	12.93	0.97
8	142.17	59.88	12.95	4.8	1.28	55.04	150	639.8	12.49	12.52	1.00
9	142.37	60.26	13.22	4.8	1.28	54.66	150	639.8	12.51	12.45	1.01
10	202.04	64.79	14.78	5	1.39	0.00	100	649.6	12.15	11.92	1.02
11	202.03	64.86	14.98	5	1.39	79.25	100	649.6	11.70	11.47	1.02
12	202.07	65.01	14.95	5	1.39	79.26	100	649.6	11.59	12.18	0.95
13	202.11	65.45	14.39	5	1.39	119.07	100	649.6	10.81	10.48	1.03
14	202	65	14.73	5	1.39	0.00	120	649.6	12.98	12.62	1.03
15	202	65.04	14.82	5	1.39	79.31	120	649.6	11.63	11.99	0.97
16	202.66	65.35	14.57	5	1.38	119.22	120	649.6	11.16	10.90	1.02
17	202	65.06	14.88	5	1.39	79.32	120	649.6	12.21	12.41	0.98
18	202.26	65.39	14.5	5	1.39	119.39	120	649.6	10.95	10.39	1.05
19	202.01	65.04	14.98	5	1.45	0.00	150	649.6	14.51	14.40	1.01
20	202.01	64.96	15.02	5	1.43	79.35	150	649.6	12.98	13.27	0.98
21	202	65.09	15	5	1.39	79.32	150	649.6	13.23	12.38	1.07
22	303.18	87.91	18.83	5	1.98	0.00	100	670.6	24.57	24.74	0.99
23	302.58	88.61	19.28	5	2.06	178.89	100	670.6	21.89	24.08	0.91
24	303.05	88.2	18.99	5	1.98	179.00	100	670.6	22.85	21.13	1.08
25	303.07	87.95	18.26	5	1.96	0.00	120	670.6	25.16	25.42	0.99
26	303.05	88.03	18.32	5	2.06	178.99	120	670.6	23.24	24.04	0.97
27	303.03	87.99	18.3	5	1.98	179.00	120	670.6	23.29	21.47	1.08
28	303.03	88.54	18.97	5	1.99	0.00	150	670.6	28.24	27.36	1.03
29	302.9	88.47	19.03	5	2.06	178.55	150	670.6	24.40	23.37	1.04
30	303.63	88.25	19.11	5	1.99	178.66	150	670.6	24.18	21.88	1.11
Average											1.00
COV											0.05

Table 2. Comparison of experimental results with FEA results for sections with fastened flanges.

Specimen ID	Web	Flange	Lip	Bend Radius	Thickness	Hole Dia.	Bearing Length	Yield Stress	Exp. Load	FEA Result	
	d	b_f	b_l	r	t	a	N	f_y	P_{EXP}	P_{FEA}	P_{EXP}/P_{FEA}
	(mm)	(mm)	(mm)	(mm)	(mm)	(mm)	(mm)	(MPa)	(kN)	(kN)	
1	142.49	60.33	13.79	4.8	1.29	0.00	100	639.8	11.14	12.21	0.91
2	142.56	60.11	13.78	4.8	1.29	84.67	100	639.8	10.89	11.85	0.92
3	142.48	60.06	13.7	4.8	1.29	83.59	100	639.8	10.97	11.39	0.96
4	142.38	60.21	13.68	4.8	1.29	0.00	120	639.8	12.33	13.13	0.94
5	142.26	60.22	13.67	4.8	1.29	83.78	120	639.8	11.97	12.53	0.96

Table 2. *Cont.*

Specimen ID	Web	Flange	Lip	Bend Radius	Thickness	Hole Dia.	Bearing Length	Yield Stress	Exp. Load	FEA Result	P_{EXP}/P_{FEA}
	d	b_f	b_l	r	t	a	N	f_y	P_{EXP}	P_{FEA}	
	(mm)	(mm)	(mm)	(mm)	(mm)	(mm)	(mm)	(MPa)	(kN)	(kN)	
6	142.53	60.29	13.91	4.8	1.29	83.77	120	639.8	11.69	11.83	0.99
7	142.18	60.12	13.19	4.8	1.28	0.00	150	639.8	13.48	14.11	0.96
8	142.35	60.07	13.2	4.8	1.28	55.26	150	639.8	13.04	13.88	0.94
9	142.42	60.07	13.13	4.8	1.28	55.20	150	639.8	13.28	13.72	0.97
10	201.99	64.87	14.76	4.8	1.38	0.00	100	649.6	13.35	13.88	0.96
11	202.01	64.96	14.76	4.8	1.37	79.36	100	649.6	12.42	13.07	0.95
12	202.22	65.44	14.42	4.8	1.37	119.41	100	649.6	11.73	12.90	0.91
13	202.11	64.92	14.99	4.8	1.37	79.30	100	649.6	12.60	14.65	0.86
14	201.79	65.68	14.64	4.8	1.37	119.45	100	649.6	12.18	12.83	0.95
15	202.05	64.99	14.82	4.8	1.41	0.00	120	649.6	14.60	15.47	0.94
16	201.98	65.1	14.92	4.8	1.38	79.32	120	649.6	13.36	14.25	0.94
17	201.76	65.4	14.62	4.8	1.39	119.51	120	649.6	12.98	14.22	0.91
18	202	65.16	15.02	4.8	1.39	79.36	120	649.6	13.94	15.73	0.89
19	202.42	65.36	14.4	4.8	1.39	119.41	120	649.6	12.44	13.57	0.92
20	202	64.93	15	4.8	1.41	0.00	150	649.6	16.16	16.71	0.97
21	202.01	64.88	14.98	4.8	1.38	79.31	150	649.6	14.63	15.51	0.94
22	202.02	64.88	14.79	4.8	1.38	79.32	150	649.6	14.96	16.21	0.92
23	303.2	88.24	18.66	4.8	1.96	0.00	100	670.6	25.26	27.60	0.92
24	303.44	88.38	19.34	5	1.9	178.91	100	670.6	22.95	25.04	0.92
25	303.45	88.57	19.26	5	1.91	178.42	100	670.6	24.26	24.48	0.99
26	303.5	88.53	18.36	5	1.93	0.00	120	670.6	26.40	28.53	0.93
27	303.28	88.79	18.55	5	1.9	178.73	120	670.6	23.74	26.43	0.90
28	303.02	88.77	18.48	5	1.9	178.69	120	670.6	24.18	24.64	0.98
29	303.85	88.71	18.41	5	1.9	0.00	150	670.6	28.13	29.39	0.96
30	303.19	88.32	19.09	5	1.96	178.45	150	670.6	25.66	29.16	0.88
31	303.08	88.42	19.06	5	1.9	178.40	150	670.6	24.89	24.94	1.00
Average											0.94
COV											0.03

4. Current Design Rules

The calculation procedure for reduced IOF web crippling strength is available in Lian et al. [29,30] and AISI [48] and AS/NZS [49]. However, the procedure is applicable at ambient temperatures and does not necessarily work for elevated temperatures.

4.1. Current Design Standards

For IOF loading, where any portion of a web hole is not within the bearing length, the reduction factor, *R*, can be calculated using Equation (1) of AISI [48] and AS/NZS [49] as follows:

$$R = 0.90 - 0.047\frac{a}{h} + 0.053\frac{x}{h} \leq 1 \tag{1}$$

where, *a*, *h*, and *x* denote the hole diameter, depth of flat portion of the web, and the nearest distance between the web hole and the edge of bearing, respectively.

4.2. Reduction Factor Equations

Lian et al. [29,30] proposed the IOF web crippling strength reduction factor equations for CFS channels with web holes at ambient temperatures. These equations are limited to CFS channels with parametric ranges of $h/t \leq 157.8$, $N/t \leq 120.97$, $N/h \leq 1.15$, and $a/h \leq 0.8$. Moreover, these equations may not work for determining the web crippling strength of CFS channels at elevated temperatures.

The IOF web crippling strength reduction factor equations are proposed based on 3474 validated FE models. Unlike the equations proposed by Lian et al. [29,30], the parameter N/h is included in equations for both the cases of offset-hole and center-hole CFS channels.

5. Parametric Analysis

Using the validated FE model of CFS channels with web holes at ambient temperatures (described in Section 3 of this paper), an extensive parametric analysis was conducted to investigate the effects of fire loading on its web crippling strength. In total, 3474 FEA models were analyzed. It should be noted that the parametric analysis is mainly conducted to find out which parameters would lead to an unignorable change.

The selected failure modes of some sections are shown in Figures 4 and 5, and the plot of displacement-web crippling strength is shown in Figure 6. It was observed in Figures 4 and 5 that the out-of-plane deformation of the webs occurred gradually at the early stage of loading and continued to increase until failure occurred. The failure pattern was symmetrical, and failure occurred due to the formation of a local yield zone under the bearing plate. Moreover, the deformation due to the web crippling of channel sections at ambient temperatures was very low, when compared to the channel sections at elevated temperatures. This comparison shows that for the case of elevated temperatures, the web crippling resistance decreases considerably. Figure 6 shows a typical example of the load-deflection curve obtained from the FEA for the specimens with both unfastened and fastened flanges at ambient and elevated temperatures. As the load increases, the linear behavior was seen initially until reaching the yield point. The maximum stress occurred in the upper corner between the flange and the web of channels. Beyond the yield point, the plastic behavior began to spread through the channel section. When reaching the maximum load, the post-buckling strength of the channel section was achieved. In addition, it can be seen from Figure 6 that the web crippling strength decreased dramatically when the temperatures increased.

(a)

(b)

(c)

(d)

(e)

(f)

(g)

(h)
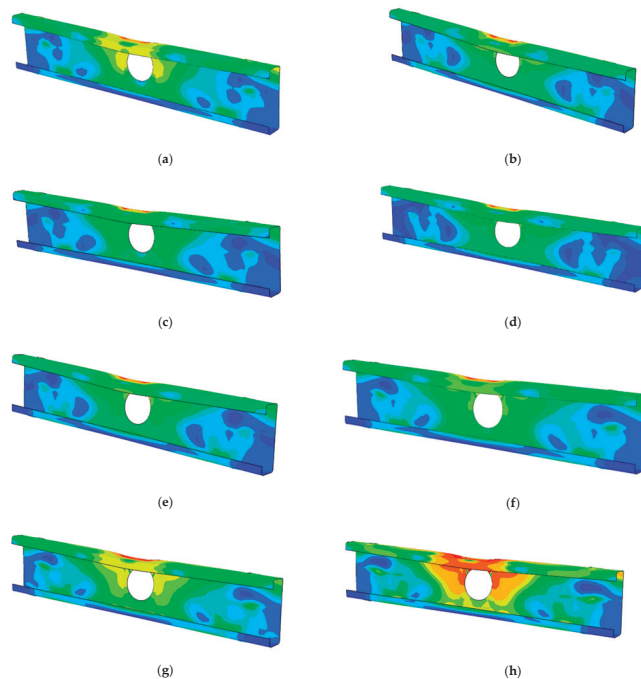
Figure 4. Failure modes of unfastened section (100 × 30 × 15-t1.55-N50-A0.6-FR) with the centered hole at different temperatures: (**a**) 20 °C; (**b**) 100 °C; (**c**) 200 °C; (**d**) 300 °C; (**e**) 400 °C; (**f**) 500 °C; (**g**) 600 °C; (**h**) 700 °C.
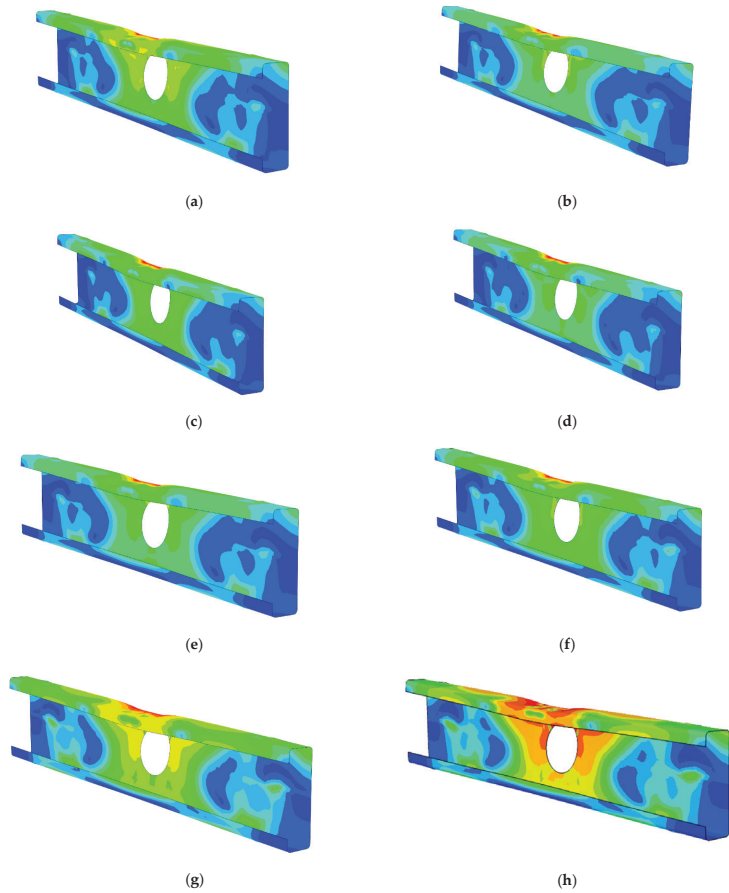
Figure 5. Failure modes of fastened section (100 × 30 × 10-t1.55-N50-A0.6-FX) with the centered hole at different temperatures: (**a**) 20 °C; (**b**) 100 °C; (**c**) 200 °C; (**d**) 300 °C; (**e**) 400 °C; (**f**) 500 °C; (**g**) 600 °C; (**h**) 700 °C.
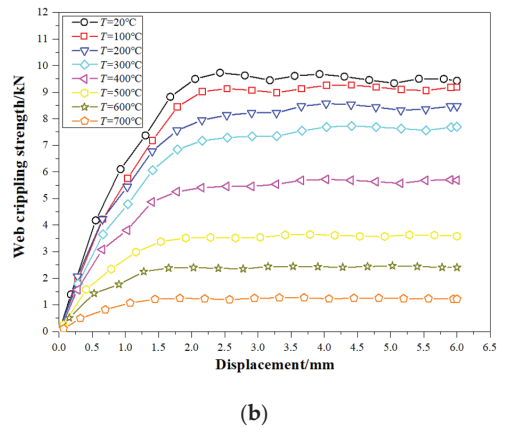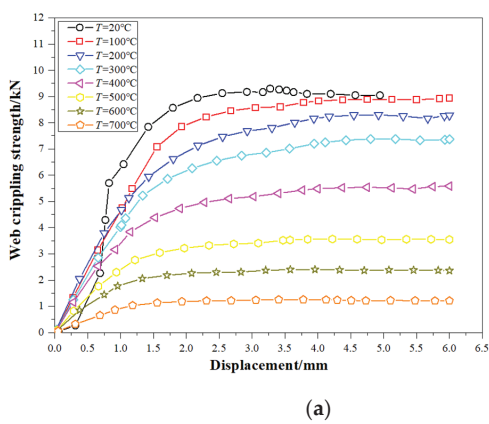
Figure 6. Load-displacement plot of selected sections under different temperatures for (**a**) unfastened section (100 × 30 × 15-t1.55-N50-A0.6-FR) with a centered hole and (**b**) fastened section (100 × 30 × 15-t1.55-N50-A0.6-FX) with a centered hole.

In addition, the detailed effects of each of these parameters on the web crippling strength of perforated CFS channels at elevated temperatures are discussed in the following sub-sections:

5.1. Effect of a/h, x/h and N/h Ratio

Figure 7 and Table 3 demonstrate the influence of the *a/h* ratio on the factor *R*. Figure 7 shows a decreasing trend in web crippling strength reduction factors as the *a/h* ratio increases from 0.2 to 0.8, with the change in the reduction factor as essentially identical for all temperatures groups. On the one hand, the factor *R* for offset-hole sections with unfastened and fastened flanges is identical, and the average factor *R* for these two sets of sections decreases from 0.97 to 0.81 and 0.96 to 0.92, respectively, when the ratio *a/h* rises from 0.2 to 0.8. The difference in factor *R* of centered-hole sections with unfastened and fastened flanges, on the other hand, is substantially higher. The average factor *R* for centered-hole sections with unfastened flanges reduced from 0.99 to 0.82, as indicated in Table 3. Meanwhile, when the *a/h* ratio was increased from 0.2 to 0.8, the factor *R* for CFS sections with fastened flanges reduced from 0.99 to 0.77.

(a) (b)
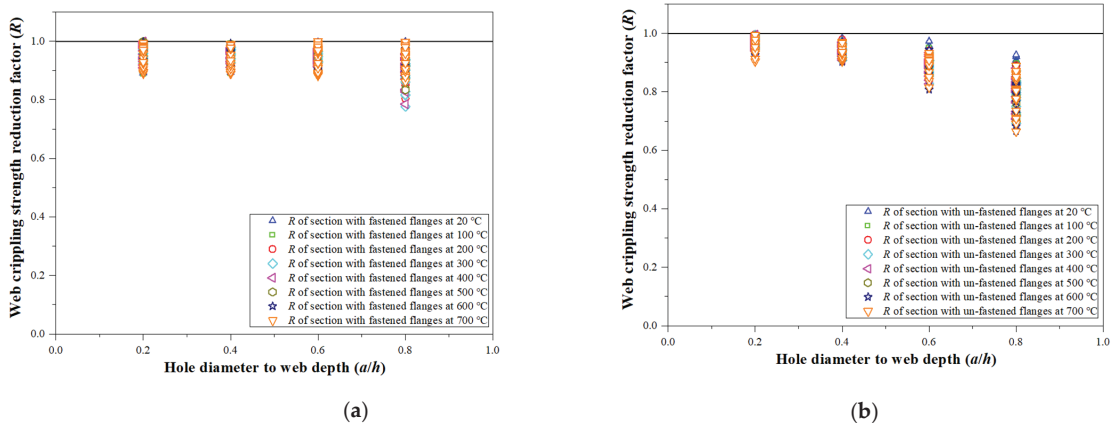
Figure 7. Web crippling strength reduction factor against *a/h* for cold-formed steel channel with (**a**) fastened flanges and offset web hole subjected to IOF and (**b**) unfastened flanges and offset web hole subjected to IOF.

Table 3. Average web crippling strength reduction factor (*R*) of investigated sections.

Hole Position		IOF Loading Condition	
		Unfastened Flanges	**Fastened Flanges**
Centered hole	*a/h* = 0.2	0.99	0.99
	a/h = 0.4	0.97	0.99
	a/h = 0.6	0.93	0.94
	a/h = 0.8	0.82	0.77
Offset hole	*a/h* = 0.2	0.97	0.96
	a/h = 0.4	0.94	0.96
	a/h = 0.6	0.88	0.95
	a/h = 0.8	0.81	0.92

The change in average factor *R* for offset-hole channels at varied temperatures remains steady between 0.85 and 0.99 as the *x/h* ratio is changed from 0.45 to 0.95.

The average factor *R* for sections with unfastened and fastened flanges decreased significantly by 4% and 5% on average for each set of *a/h* ratios, respectively, when the *N/h*

ratio was increased from 0.25 to 0.75. Figure 8 depicts the change in the factor *R* as the *N/h* ratio changes.

(**a**)

(**b**)

(**c**)

(**d**)
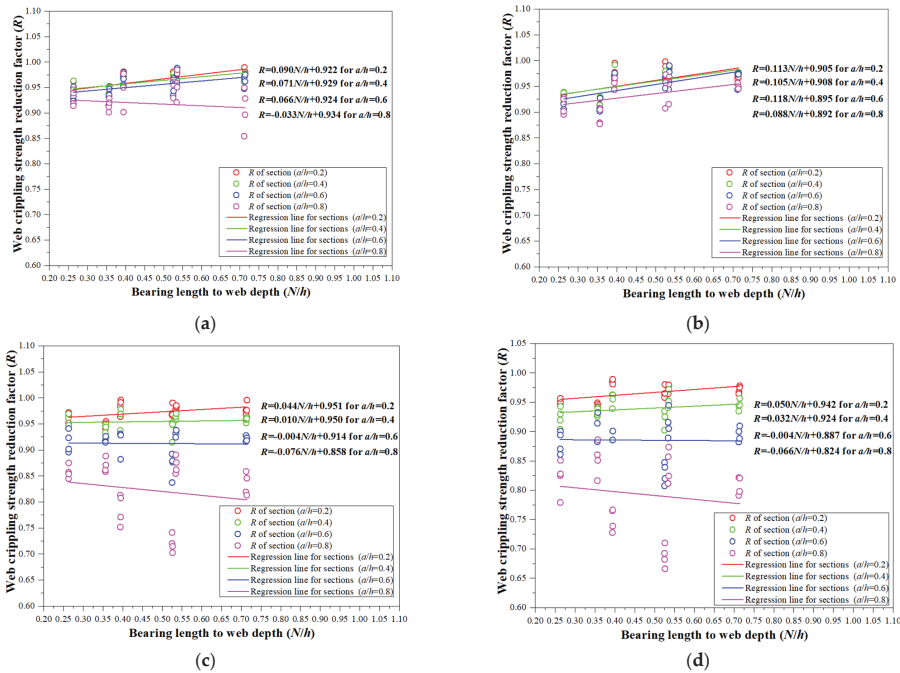
Figure 8. Web crippling strength reduction factor against *N/h* for cold-formed steel channel with (**a**) fastened flanges and offset web hole subjected to IOF at 200 °C; (**b**) fastened flanges and offset web hole subjected to IOF at 600 °C; (**c**) unfastened flanges and offset web hole subjected to IOF at 200 °C; (**d**) unfastened flanges and offset web hole subjected to IOF at 600 °C.

5.2. Effect of Fastened Flanges

With varied *a/h* ratios and hole positions, Figure 9 and Table 4 demonstrate the influence of fastened flanges on factor *R*. The average factor *R* of CFS channels with fastened flanges is larger (by 5.3%) than those with unfastened flanges for sections with offset web holes. On the other hand, factor *R* of centered-hole sections with fastened and unfastened flanges is fairly similar.
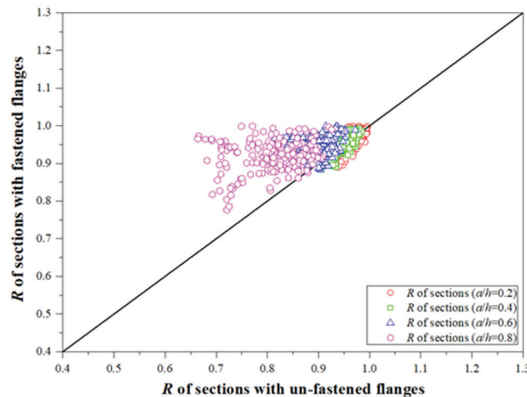
Figure 9. Web crippling strength reduction factor against unfastened/fastened flanges.

Table 4. Average web crippling strength reduction percentage (%) of investigated sections at elevated temperatures against ambient temperatures (*T* = 20 °C).

Temperatures		IOF Loading Condition	
		Unfastened Flanges	Fastened Flanges
Centered hole	T = 20 °C	-	-
	T = 100 °C	5.67	5.01
	T = 200 °C	6.41	5.08
	T = 300 °C	19.52	16.19
	T = 400 °C	38.31	36.44
	T = 500 °C	61.28	60.67
	T = 600 °C	81.81	81.73
	T = 700 °C	89.57	89.67
Offset hole	T = 20 °C	-	-
	T = 100 °C	5.15	4.23
	T = 200 °C	4.88	3.42
	T = 300 °C	18.12	14.02
	T = 400 °C	37.25	35.33
	T = 500 °C	60.97	59.93
	T = 600 °C	81.94	81.45
	T = 700 °C	89.60	89.65

5.3. Effect of Elevated Temperatures

At elevated temperatures, the web crippling strength decrease percentages for CFS sections with unfastened flanges are slightly larger than those with fastened flanges. Figure 10 shows that when the temperatures rise from 20 to 700 °C, the web crippling strength (*P*) of CFS sections decreases. In the meantime, Table 4 indicates the average web crippling strength drop (from 5% to 90%) for each investigated temperatures group.

(**a**)

(**b**)
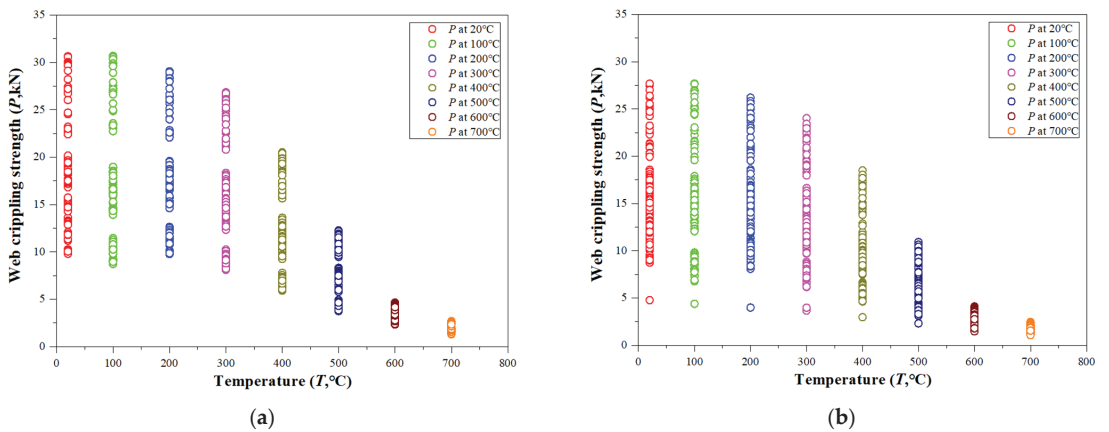
Figure 10. *Cont.*
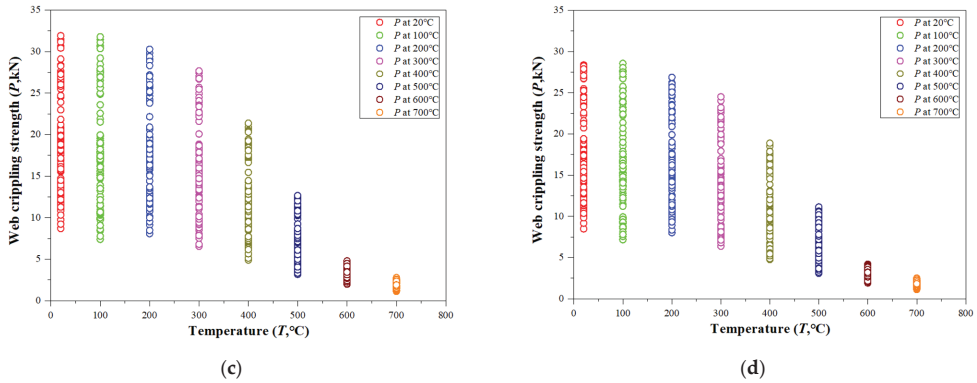
Figure 10. Web crippling strength against temperatures for cold-formed steel channel with (**a**) offset web hole and fastened flanges subjected to IOF; (**b**) offset web hole and unfastened flanges subjected to IOF; (**c**) centered web hole and fastened flanges subjected to IOF; (**d**) centered web hole and unfastened flanges subjected to IOF.

6. Proposed Design Equations and Reliability Analysis

The previous study showed that the FEA model was able to predict the web crippling strength of perforated CFS channels with more precision than the existing design guidelines. As a consequence of the FEA results, design equations in the form of web crippling strength reduction factors were proposed. The limits of the proposed equations are $h/t \leq 160$, $N/t \leq 120$, $N/h \leq 0.75$, and $a/h \leq 0.8$.

6.1. Design Equations

The FEA results of parametric analysis were used to propose design equations for CFS channels with unfastened and fastened flanges when loaded with IOF loading. The proposed equations included the variables, such as *a/h*, *x/h*, and *N/h*. Regression analysis was performed to develop these equations (Equations (2) and (3)) as shown below:

For CFS sections with centered holes:

$$R_{prop} = \alpha' - \gamma' \frac{a}{h} + \lambda' \frac{N}{h} \leq 1 \tag{2}$$

For CFS sections with offset holes:

$$R_{prop} = \beta' - \mu' \frac{a}{h} + \zeta' \frac{N}{h} + \xi' \frac{x}{h} \leq 1 \tag{3}$$

where, *α′*, *γ′*, *λ′*, *β′*, *μ′*, *ζ′*, and *ξ′* are the equation coefficients. The equation coefficient values for cold-formed steel channels are summarized in Table 5. The effect of *a/h*, *x/h*, and *N/h* on the reduced web crippling strength is considered in the equations.

Table 5. Proposed equations summary for the web crippling strength reduction factor.

Coefficients	IOF Loading Condition	
	Flange Unfastened to Support	**Flange Fastened to Support**
α′	1.128	1.214
γ′	0.378	0.537
λ′	0.010	0.010
β′	0.618	0.932
μ′	0.060	0.062
ζ′	0.047	0.084
ξ′	0.413	0.010

Table 5 shows that the results obtained from the proposed reduction factors (R_{prop}) could closely predict the web crippling failure load of the CFS sections. From Tables 6 and 7, it can be seen that the ratios for R/R_{prop} range from 1.00 to 1.05 and 0.98 to 1.06, for most of the unfastened sections and fastened sections, respectively. The average values of R/R_{prop} are 1.03, with COVs at 0.04 and 0.06, respectively for unfastened sections and fastened sections. Compared to the ratios calculated by the proposed equations of Lian et al. [29,30] (R/R_{Ying}) and AISI [48] and AS/NZS [49] ($R/R_{AISI\&AS/NZS}$), the average values of R/R_{prop} are lower with the lower coefficient of variations (COVs). The comparison shows that the proposed equations perform better than those from the other methods in predicting the IOF strength reduction factor (R) for both the case of ambient and elevated temperatures.

6.2. Reliability Analysis

A detailed reliability analysis was carried out using the methods outlined by Hsiao et al. [57] and Fang et al. [58–60]. In accordance with the American standard [48], when the reliability index of any equation is higher than or equal to the target reliability index 2.5, the equation can be considered reliable:

$$\beta = \frac{\ln(R_m/Q_m)}{\sqrt{V_R^2 + V_Q^2}} \tag{4}$$

where,

$$R_m = R_n M_m F_m P_m \tag{5}$$

$$Q_m = C(D_m + L_m) \tag{6}$$

$$V_R = \sqrt{V_M^2 + V_F^2 + V_P^2} \tag{7}$$

$$V_Q = \frac{\sqrt{D_m^2 V_D^2 + L_m^2 V_L^2}}{D_m + L_m} \tag{8}$$

Here, R_n is the nominal resistance, M_m, F_m, and P_m are the mean values of the dimensionless random variables reflecting the uncertainties in the material properties, the geometry of the cross section, and the prediction of the ultimate resistance, respectively. V_R and V_Q are the corresponding coefficients of variation. C is a deterministic influence coefficient. D_m and L_m are the mean values. V_D and V_L are the coefficients of variation of the dead load and live load, respectively.

As shown in Tables 8 and 9, the reliability index (2.53 and 2.70 for unfastened sections with centered and offset web holes, respectively; 2.71 and 2.59 for fastened sections with centered and offset web holes, respectively) determined for the proposed equations are all greater than the target reliability index of 2.5 as per the American standard [48] for CFS channels with unfastened and fastened flanges. This shows that the proposed equations are reliable when predicting the IOF web crippling strength of CFS channels with web holes at elevated temperatures. The reliability index for the equations proposed by Lian et al. [29,30] and AISI [48] and AS/NZS [49] were summarized in Tables 8 and 9. In addition, most of the calculated reliability index values of these two methods [29,30,48,49] are lower than the target index value (2.5). Furthermore, a comparison of the reliability index determined for the proposed equations with the reliability index of equations proposed by Lian et al. [29,30] and AISI [48] and AS/NZS [49] was conducted, showing that the proposed equations are more reliable than the equations from Lian et al. [29,30] and AISI [48] and AS/NZS [49], which is in line with the conclusion made in Section 6.1 of the paper.

Table 6. Comparison of proposed equations with other methods for sections with unfastened flanges.

Specimen	Failure Load P_{A0} (kN) No Hole	Reduction Factor $R = P_w/P_{A0}$		Reduction Factor $R_{AISI\&AS/NZS}$ by AISI&AS/NZS		Reduction Factor R_{Ying} by Ying et al.		Reduction Factor R_{prop} by Equation		$R/R_{AISI\&AS/NZS}$		R/R_{Ying}		R/R_{prop}	
		Centered Hole	Offset Hole	Centered Hole	Offset Hole	Centered Hole	Offset Hole	Centered Hole	Offset Hole	Centered Hole	Offset Hole	Centered Hole	Offset Hole	Centered Hole	Offset Hole
CFS channel sections at 20 °C															
200 × 60 × 30-t1.5-N100-A0.2-FR	20.01	0.99	0.97	0.93	0.93	0.96	-	-	0.95	0.94	0.96	0.97	-	-	0.98
200 × 60 × 30-t1.5-N100-A0.4-FR	20.01	0.96	0.93	0.92	0.92	0.91	0.96	0.98	0.90	0.96	0.98	0.95	1.03	1.02	0.96
200 × 60 × 30-t1.5-N100-A0.6-FR	20.01	0.88	0.86	0.90	0.90	0.86	0.90	0.91	0.85	1.03	1.05	0.97	1.04	1.03	0.98
200 × 60 × 30-t1.5-N100-A0.8-FR	20.01	0.75	0.75	0.89	0.89	0.80	0.83	0.83	0.79	1.18	1.19	1.07	1.12	1.10	1.06
Average										1.03	1.04	0.99	1.06	1.05	1.00
COV										0.09	0.09	0.05	0.04	0.04	0.04
CFS channel sections at 100 °C															
200 × 60 × 30-t1.5-N100-A0.2-FR	20.01	0.98	0.97	0.93	0.93	0.96	-	-	0.95	0.95	0.96	0.98	-	-	0.98
200 × 60 × 30-t1.5-N100-A0.4-FR	20.01	0.95	0.93	0.92	0.92	0.91	0.96	0.98	0.90	0.97	0.98	0.96	1.03	1.04	0.97
200 × 60 × 30-t1.5-N100-A0.6-FR	20.01	0.87	0.86	0.90	0.90	0.86	0.90	0.91	0.85	1.04	1.05	0.99	1.05	1.05	0.99
200 × 60 × 30-t1.5-N100-A0.8-FR	20.01	0.80	0.74	0.89	0.89	0.80	0.83	0.83	0.79	1.12	1.20	1.01	1.12	1.04	1.07
Average										1.02	1.05	0.98	1.07	1.04	1.00
COV										0.07	0.09	0.02	0.04	0.00	0.04
CFS channel sections at 200 °C															
200 × 60 × 30-t1.5-N100-A0.2-FR	20.01	0.95	0.97	0.93	0.93	0.96	-	-	0.95	0.98	0.96	1.01	-	-	0.98
200 × 60 × 30-t1.5-N100-A0.4-FR	20.01	0.91	0.91	0.92	0.92	0.91	0.96	0.98	0.90	1.01	1.00	1.00	1.05	1.08	0.98
200 × 60 × 30-t1.5-N100-A0.6-FR	20.01	0.83	0.84	0.90	0.90	0.86	0.90	0.91	0.85	1.08	1.08	1.03	1.07	1.09	1.01
200 × 60 × 30-t1.5-N100-A0.8-FR	20.01	0.78	0.72	0.89	0.89	0.80	0.83	0.83	0.79	1.14	1.23	1.03	1.16	1.06	1.10
Average										1.05	1.07	1.02	1.09	1.08	1.02
COV										0.06	0.10	0.01	0.05	0.01	0.05
CFS channel sections at 300 °C															
200 × 60 × 30-t1.5-N100-A0.2-FR	20.01	0.94	0.97	0.93	0.93	0.96	-	-	0.95	0.99	0.96	1.02	-	-	0.98
200 × 60 × 30-t1.5-N100-A0.4-FR	20.01	0.93	0.91	0.92	0.92	0.91	0.96	0.98	0.90	0.99	1.01	0.98	1.06	1.06	0.99
200 × 60 × 30-t1.5-N100-A0.6-FR	20.01	0.83	0.83	0.90	0.90	0.86	0.90	0.91	0.85	1.09	1.09	1.03	1.09	1.09	1.02

Table 6. *Cont.*

Specimen	Failure Load P_{A0} (kN) No Hole	Reduction Factor $R = P_w/P_{A0}$		Reduction Factor $R_{AISI\&AS/NZS}$ by AISI&AS/NZS		Reduction Factor R_{Ying} by Ying et al.		Reduction Factor R_{prop} by Equation		$R/R_{AISI\&AS/NZS}$		R/R_{Ying}		R/R_{prop}	
		Centered Hole	Offset Hole	Centered Hole	Offset Hole	Centered Hole	Offset Hole	Centered Hole	Offset Hole	Centered Hole	Offset Hole	Centered Hole	Offset Hole	Centered Hole	Offset Hole
200 × 60 × 30-t1.5-N100-A0.8-FR	20.01	0.78	0.72	0.89	0.89	0.80	0.83	0.83	0.79	1.14	1.23	1.03	1.16	1.06	1.10
Average										1.05	1.07	1.01	1.10	1.07	1.02
COV										0.07	0.10	0.02	0.04	0.02	0.05
CFS channel sections at 400 °C															
200 × 60 × 30-t1.5-N100-A0.2-FR	20.01	0.95	0.97	0.93	0.93	0.96	-	-	0.95	0.98	0.96	1.01	-	-	0.98
200 × 60 × 30-t1.5-N100-A0.4-FR	20.01	0.91	0.91	0.92	0.92	0.91	0.96	0.98	0.90	1.00	1.01	0.99	1.06	1.07	0.99
200 × 60 × 30-t1.5-N100-A0.6-FR	20.01	0.84	0.83	0.90	0.90	0.86	0.90	0.91	0.85	1.07	1.09	1.02	1.09	1.08	1.02
200 × 60 × 30-t1.5-N100-A0.8-FR	20.01	0.80	0.73	0.89	0.89	0.80	0.83	0.83	0.79	1.11	1.22	1.01	1.15	1.04	1.09
Average										1.04	1.07	1.01	1.10	1.06	1.02
COV										0.05	0.10	0.01	0.04	0.02	0.04
CFS channel sections at 500 °C															
200 × 60 × 30-t1.5-N100-A0.2-FR	20.01	0.99	0.97	0.93	0.93	0.96	-	-	0.95	0.94	0.96	0.97	-	-	0.98
200 × 60 × 30-t1.5-N100-A0.4-FR	20.01	0.97	0.93	0.92	0.92	0.91	0.96	0.98	0.90	0.95	0.99	0.94	1.04	1.01	0.97
200 × 60 × 30-t1.5-N100-A0.6-FR	20.01	0.89	0.85	0.90	0.90	0.86	0.90	0.91	0.85	1.01	1.07	0.96	1.06	1.02	1.00
200 × 60 × 30-t1.5-N100-A0.8-FR	20.01	0.76	0.73	0.89	0.89	0.80	0.83	0.83	0.79	1.17	1.22	1.06	1.14	1.10	1.09
Average										1.02	1.06	0.98	1.08	1.04	1.01
COV										0.09	0.10	0.05	0.05	0.04	0.05
CFS channel sections at 600 °C															
200 × 60 × 30-t1.5-N100-A0.2-FR	20.01	0.98	0.96	0.93	0.93	0.96	-	-	0.95	0.95	0.97	0.97	-	-	0.99
200 × 60 × 30-t1.5-N100-A0.4-FR	20.01	0.94	0.90	0.92	0.92	0.91	0.96	0.98	0.90	0.97	1.02	0.96	1.07	1.04	1.00
200 × 60 × 30-t1.5-N100-A0.6-FR	20.01	0.88	0.81	0.90	0.90	0.86	0.90	0.91	0.85	1.03	1.12	0.97	1.11	1.03	1.05
200 × 60 × 30-t1.5-N100-A0.8-FR	20.01	0.82	0.68	0.89	0.89	0.80	0.83	0.83	0.79	1.08	1.30	0.98	1.22	1.01	1.16
Average										1.01	1.10	0.97	1.13	1.03	1.05

Table 6. *Cont.*

Specimen	Failure Load P$_{A0}$ (kN)	Reduction Factor R = P$_w$/P$_{A0}$		Reduction Factor R$_{AISI\&AS/NZS}$ by AISI&AS/NZS		Reduction Factor R$_{Ying}$ by Ying et al.		Reduction Factor R$_{prop}$ by Equation		R/R$_{AISI\&AS/NZS}$		R/R$_{Ying}$		R/R$_{prop}$	
	no Hole	Centered Hole	Offset Hole	Centered Hole	Offset Hole	Centered Hole	Offset Hole	Centered Hole	Offset Hole	Centered Hole	Offset Hole	Centered Hole	Offset Hole	Centered Hole	Offset Hole
COV										0.05	0.13	0.01	0.07	0.01	0.07
CFS channel sections at 700 °C															
200 × 60 × 30–t1.5–N100–A0.2–FR	20.01	0.99	0.96	0.93	0.93	0.96	-	-	0.95	0.94	0.97	0.97	-	-	0.99
200 × 60 × 30–t1.5–N100–A0.4–FR	20.01	0.97	0.92	0.92	0.92	0.91	0.96	0.98	0.90	0.94	1.00	0.93	1.05	1.01	0.98
200 × 60 × 30–t1.5–N100–A0.6–FR	20.01	0.91	0.81	0.90	0.90	0.86	0.90	0.91	0.85	0.99	1.11	0.94	1.10	1.00	1.04
200 × 60 × 30–t1.5–N100–A0.8–FR	20.01	0.78	0.66	0.89	0.89	0.80	0.83	0.83	0.79	1.14	1.34	1.03	1.26	1.07	1.19
Average										1.00	1.10	0.97	1.14	1.03	1.05
COV										0.08	0.14	0.04	0.09	0.03	0.09

Table 7. Comparison of proposed equations with other methods for sections with fastened flanges.

Specimen	Failure Load P$_{A0}$ (kN)	Reduction Factor R = P$_w$/P$_{A0}$		Reduction Factor R$_{AISI\&AS/NZS}$ by AISI&AS/NZS		Reduction Factor R$_{Ying}$ by Ying et al.		Reduction Factor R$_{prop}$ by Equation		R/R$_{AISI\&AS/NZS}$		R/R$_{Ying}$		R/R$_{prop}$	
	No Hole	Centered Hole	Offset Hole	Centered Hole	Offset Hole	Centered Hole	Offset Hole	Centered Hole	Offset Hole	Centered Hole	Offset Hole	Centered Hole	Offset Hole	Centered Hole	Offset Hole
CFS channel sections at 20 °C															
200 × 60 × 30–t1.5–N100–A0.2–FX	20.01	0.97	0.97	0.93	0.93	0.94	-	-	0.97	0.96	0.96	0.97	-	-	1.00
200 × 60 × 30–t1.5–N100–A0.4–FX	20.01	0.96	0.96	0.92	0.92	0.93	0.98	1.00	0.96	0.96	0.96	0.97	1.02	1.05	1.00
200 × 60 × 30–t1.5–N100–A0.6–FX	20.01	0.93	0.94	0.90	0.90	0.92	0.95	0.90	0.94	0.97	0.96	0.99	1.01	0.96	1.01
200 × 60 × 30–t1.5–N100–A0.8–FX	20.01	0.74	0.86	0.89	0.89	0.91	0.91	0.79	0.93	1.21	1.03	1.23	1.06	1.07	1.08
Average										1.02	0.98	1.04	1.03	1.03	1.02
COV										0.11	0.03	0.11	0.02	0.05	0.04
CFS channel sections at 100 °C															
200 × 60 × 30–t1.5–N100–A0.2–FX	20.01	0.97	0.99	0.93	0.93	0.94	-	-	0.97	0.96	0.94	0.97	-	-	0.98

Table 7. *Cont.*

Specimen	Failure Load P_{A0} (kN)	Reduction Factor $R = P_w/P_{A0}$		Reduction Factor $R_{AISI\&AS/NZS}$ by AISI&AS/NZS		Reduction Factor R_{Ying} by Ying et al.		Reduction Factor R_{prop} by Equation		$R/R_{AISI\&AS/NZS}$		R/R_{Ying}		R/R_{prop}	
	No Hole	Centered Hole	Offset Hole	Centered Hole	Offset Hole	Centered Hole	Offset Hole	Centered Hole	Offset Hole	Centered Hole	Offset Hole	Centered Hole	Offset Hole	Centered Hole	Offset Hole
200 × 60 × 30-t1.5-N100-A0.4-FX	20.01	0.96	0.96	0.92	0.92	0.93	0.98	1.00	0.96	0.96	0.96	0.97	1.02	1.05	1.00
200 × 60 × 30-t1.5-N100-A0.6-FX	20.01	0.94	0.94	0.90	0.90	0.92	0.95	0.90	0.94	0.96	0.96	0.98	1.01	0.96	1.01
200 × 60 × 30-t1.5-N100-A0.8-FX	20.01	0.73	0.84	0.89	0.89	0.91	0.91	0.79	0.93	1.21	1.06	1.24	1.09	1.08	1.11
Average										1.02	0.98	1.04	1.04	1.03	1.02
COV										0.11	0.05	0.11	0.03	0.05	0.05
CFS channel sections at 200 °C															
200 × 60 × 30-t1.5-N100-A0.2-FX	20.01	0.97	0.98	0.93	0.93	0.94	-	-	0.97	0.96	0.95	0.97	-	-	0.99
200 × 60 × 30-t1.5-N100-A0.4-FX	20.01	0.96	0.96	0.92	0.92	0.93	0.98	1.00	0.96	0.96	0.96	0.97	1.02	1.05	1.00
200 × 60 × 30-t1.5-N100-A0.6-FX	20.01	0.88	0.93	0.90	0.90	0.92	0.95	0.90	0.94	1.03	0.97	1.05	1.02	1.02	1.02
200 × 60 × 30-t1.5-N100-A0.8-FX	20.01	0.68	0.80	0.89	0.89	0.91	0.95	0.79	0.93	1.31	1.11	1.34	1.14	1.16	1.16
Average										1.06	1.00	1.08	1.06	1.08	1.04
COV										0.14	0.07	0.15	0.06	0.06	0.07
CFS channel sections at 300 °C															
200 × 60 × 30-t1.5-N100-A0.2-FX	20.01	0.97	0.99	0.93	0.93	0.94	-	-	0.97	0.96	0.94	0.97	-	-	0.98
200 × 60 × 30-t1.5-N100-A0.4-FX	20.01	0.96	0.96	0.92	0.92	0.93	0.98	1.00	0.96	0.96	0.95	0.97	1.02	1.05	1.00
200 × 60 × 30-t1.5-N100-A0.6-FX	20.01	0.85	0.93	0.90	0.90	0.92	0.95	0.90	0.94	1.06	0.97	1.08	1.02	1.05	1.02
200 × 60 × 30-t1.5-N100-A0.8-FX	20.01	0.66	0.78	0.89	0.89	0.91	0.91	0.79	0.93	1.35	1.14	1.38	1.17	1.20	1.20
Average										1.08	1.00	1.10	1.07	1.10	1.05
COV										0.16	0.08	0.17	0.07	0.07	0.09
CFS channel sections at 400 °C															
200 × 60 × 30-t1.5-N100-A0.2-FX	20.01	0.97	0.98	0.93	0.93	0.94	-	-	0.97	0.96	0.95	0.97	-	-	0.99
200 × 60 × 30-t1.5-N100-A0.4-FX	20.01	0.96	0.96	0.92	0.92	0.93	0.98	1.00	0.96	0.96	0.95	0.97	1.02	1.05	1.00
200 × 60 × 30-t1.5-N100-A0.6-FX	20.01	0.87	0.93	0.90	0.90	0.92	0.95	0.90	0.94	1.04	0.97	1.06	1.02	1.03	1.01
200 × 60 × 30-t1.5-N100-A0.8-FX	20.01	0.68	0.79	0.89	0.89	0.91	0.91	0.79	0.93	1.31	1.13	1.34	1.16	1.17	1.19
Average										1.07	1.00	1.09	1.07	1.08	1.05

Table 7. *Cont.*

Specimen	Failure Load P_{A0} (kN) No Hole	Reduction Factor $R = P_w/P_{A0}$ Centered Hole	Offset Hole	Reduction Factor $R_{AISI\&AS/NZS}$ by AISI&AS/NZS Centered Hole	Offset Hole	Reduction Factor R_{Ying} by Ying et al. Centered Hole	Offset Hole	Reduction Factor R_{prop} by Equation Centered Hole	Offset Hole	$R/R_{AISI\&AS/NZS}$ Centered Hole	Offset Hole	R/R_{Ying} Centered Hole	Offset Hole	R/R_{prop} Centered Hole	Offset Hole
COV										0.15	0.08	0.15	0.07	0.06	0.08
CFS channel sections at 500 °C															
200 × 60 × 30-t1.5-N100-A0.2-FX	20.01	0.97	0.98	0.93	0.93	0.94	-	-	0.98	0.96	0.95	0.97	-	-	0.99
200 × 60 × 30-t1.5-N100-A0.4-FX	20.01	0.96	0.96	0.92	0.92	0.93	0.98	1.00	0.96	0.96	0.95	0.97	1.02	1.05	1.00
200 × 60 × 30-t1.5-N100-A0.6-FX	20.01	0.91	0.94	0.90	0.90	0.92	0.95	0.90	0.94	0.99	0.96	1.01	1.01	0.99	1.01
200 × 60 × 30-t1.5-N100-A0.8-FX	20.01	0.73	0.84	0.89	0.89	0.91	0.91	0.79	0.93	1.22	1.06	1.25	1.09	1.09	1.11
Average										1.03	0.98	1.05	1.04	1.04	1.03
COV										0.11	0.05	0.12	0.03	0.04	0.05
CFS channel sections at 600 °C															
200 × 60 × 30-t1.5-N100-A0.2-FX	20.01	0.97	0.99	0.93	0.93	0.94	-	-	0.98	0.96	0.94	0.97	-	-	0.99
200 × 60 × 30-t1.5-N100-A0.4-FX	20.01	0.96	0.96	0.92	0.92	0.93	0.98	1.00	0.96	0.96	0.95	0.97	1.02	1.05	0.99
200 × 60 × 30-t1.5-N100-A0.6-FX	20.01	0.95	0.95	0.90	0.90	0.92	0.95	0.90	0.94	0.95	0.95	0.97	1.00	0.94	1.00
200 × 60 × 30-t1.5-N100-A0.8-FX	20.01	0.80	0.91	0.89	0.89	0.91	0.91	0.79	0.93	1.12	0.98	1.14	1.00	0.99	1.03
Average										0.99	0.96	1.01	1.01	0.99	1.00
COV										0.07	0.01	0.07	0.01	0.04	0.02
CFS channel sections at 700 °C															
200 × 60 × 30-t1.5-N100-A0.2-FX	20.01	0.97	0.99	0.93	0.93	0.94	-	-	0.98	0.96	0.94	0.97	-	-	0.99
200 × 60 × 30-t1.5-N100-A0.4-FX	20.01	0.96	0.97	0.92	0.92	0.93	0.98	0.97	0.96	0.96	0.94	0.97	1.01	1.01	0.99
200 × 60 × 30-t1.5-N100-A0.6-FX	20.01	0.94	0.97	0.90	0.90	0.92	0.95	0.89	0.95	0.96	0.93	0.98	0.98	0.94	0.98
200 × 60 × 30-t1.5-N100-A0.8-FX	20.01	0.82	0.96	0.89	0.89	0.91	0.91	0.80	0.94	1.08	0.92	1.11	0.94	0.97	0.97
Average										0.99	0.93	1.01	0.98	0.98	0.98
COV										0.05	0.01	0.06	0.03	0.03	0.01

Table 8. Reliability analysis results (centered-hole sections).

	With Fastened Flanges	With Unfastened Flanges
Ratio of equations	$R_{\mathrm{FEA}}/R_{prop}$	$R_{\mathrm{FEA}}/R_{prop}$
Data number	381	415
Mean, P_m	1.00	1.00
Reliability index, β	2.71	2.53
Reliability index, β for AISI&AS/NZS	2.39	2.23
Reliability index, β for Ying et al.	2.70	2.12
Reliability index, φ	0.85	0.85

Table 9. Reliability analysis of the proposed equations (offset-hole sections).

	With Fastened Flanges	With Unfastened Flanges
Ratio of equations	$R_{\mathrm{FEA}}/R_{prop}$	$R_{\mathrm{FEA}}/R_{prop}$
Data number	756	748
Mean, P_m	1.00	1.01
Reliability index, β	2.59	2.70
Reliability index, β for AISI&AS/NZS	2.47	2.69
Reliability index, β for Ying et al.	2.42	2.63
Reliability index, φ	0.85	0.85

7. Summary and Conclusions

This study carried out a numerical investigation on the IOF web crippling behavior of CFS channels with web holes at elevated temperatures. The two popular carbon steel grades, i.e., G250 and G450 were used. A nonlinear FE model was developed for CFS perforated channels under IOF loading and was validated against the test results available in the literature for ambient temperatures. Using the validated FE model of perforated CFS channels at ambient temperatures, an extensive parametric analysis was undertaken to investigate the effects of fire loading on its web crippling strength. In total, 3474 FEA models were analyzed. In the parametric study, the effects of a/h, x/h, and N/h flange type and temperatures on the web crippling strength of CFS channels with web holes at elevated temperatures were discussed. According to the parametric study results, the web crippling strength reduction factor is sensitive to changes in the ratios of a/h, N/h, and x/h, with the ratios of a/h and x/h having the largest effects on the web crippling reduction factor. However, the web crippling strength reduction factor remains stable when the temperature is changed from 20 to 700 °C.

New design equations were developed to consider the effects of cross-sectional geometry, plate element, flange type, hole size, and hole position to obtain the IOF web crippling strength of CFS channels at elevated temperatures. The limits for the proposed equations are $h/t \le 160$, $N/t \le 120$, $N/h \le 0.75$, and $a/h \le 0.8$. Compared with the proposed equations of Lian et al. (2017), a new factor N/h was included to the proposed design equations on the strength reduction factor, which was ignored by Lian et al. (2017). In addition to the influence of cross-section and hole size parameters, other parameters, such as hole position and flange type also play an important role in the failure strength of the web. Therefore, these effects are included in the proposed equations. The comparison of results obtained from the current design standards and from the proposed equations of the current research and from Lian et al. (2017) showed that the equations developed in this research performed better than the other equations by at least 5% on the web crippling strength of both plain and perforated channels. Thereafter, a comprehensive reliability analysis was performed, which showed that the proposed design equations are capable of demonstrating a reliable limit state design on the web crippling performance of perforated CFS channel sections when calibrated with a resistance factor from the American standard.

Some limitations were set in this study, in terms of applicability of the proposed design equations. First, for the offset-hole sections used in this paper, the proposed equations should be considered for sections with two symmetrically offset web holes. Meanwhile, the hole sizes for each offset web hole should be equal. Second, in this paper, the proposed equations cover the typical IOF web crippling case. However, in real engineering practice, the loading and boundary conditions may vary. Third, only two typical carbon steel material properties were considered in the FE modelling. The structural behavior of channels with other grades of carbon steel should be investigated in the future. Finally, the prediction accuracy of proposed equations was only assessed based on the validated FEA. The experimental tests of CFS at elevated temperatures subjected to web crippling should be conducted in the future.

The limitations as mentioned above show the need of future studies in the following areas:

- For the case of sections with one offset web holes, and sections with two non-symmetrically offset web holes with different hole diameters, the web crippling coefficients of design equations are needed to be developed.
- In the case of sections with complicated loading and boundary conditions, the modification of web crippling coefficients of design standards should be made.
- The structural behavior of perforated channels with other grades of carbon steel should be investigated.
- The experimental tests of CFS channels subjected to web crippling at elevated temperatures should be conducted.

Author Contributions: Conceptualization, Z.F. and K.R.; data curation, Z.F. and H.L.; formal analysis, Z.F. and K.G.; methodology, Z.F., K.P. and A.M.M.; supervision, K.R., K.P., A.M.M. and J.B.P.L.; validation, Z.F. and H.L.; writing—original draft, Z.F.; writing—review & editing, Z.F., K.R. and J.B.P.L. All authors have read and agreed to the published version of the manuscript.

Institutional Review Board Statement: Not applicable.

Informed Consent Statement: Not applicable.

Data Availability Statement: Not applicable.

Conflicts of Interest: The authors declare no conflict of interest.

References

1. Lowe, D.; Roy, K.; Das, R.; Clifton, C.G.; Lim, J.B.P. Full scale experiments on splitting behavior of concrete slabs in steel concrete composite beams with shear stud connection. *Structures* **2020**, *23*, 126–138. [CrossRef]
2. Roy, K.; Lim, J.B.P.; Lau, H.H.; Yong, P.M.; Clifton, G.C.; Wrzesien, A.; Mei, C.C. Collapse behavior of a fire engineering designed single-storey cold-formed steel building in severe fires. *Thin-Walled Struct.* **2019**, *142*, 340–357. [CrossRef]
3. Mathieson, C.; Roy, K.; Charles, C.G.; Ahmadi, A.; Lim, J.B.P. Failure mechanism and bearing capacity of cold-formed steel trusses with HRC connectors. *Eng. Struct.* **2019**, *201*, 109741. [CrossRef]
4. Roy, K.; Lau, H.H.; Ting, T.C.H.; Chen, B.; Lim, J.B.P. Flexural capacity of gapped built-up cold-formed steel channel sections including web stiffeners. *J. Constr. Steel Res.* **2020**, *172*, 106154. [CrossRef]
5. Chen, B.S.; Roy, K.; Fang, Z.Y.; Uzzaman, A.; Raftery, G.; Lim, J.B.P. Moment capacity of back-to-back cold-formed steel channels with edge-stiffened holes, un-stiffened holes, and plain webs. *Eng. Struct.* **2021**, *235*, 112042. [CrossRef]
6. Chen, B.S.; Roy, K.; Fang, Z.Y.; Uzzaman, A.; Chi, Y.H.; Lim, J.B.P. Web crippling capacity of fastened cold-formed steel channels with edge-stiffened web holes, un-stiffened web holes and plain webs under two-flange loading. *Thin-Walled Struct.* **2021**, *163*, 107666. [CrossRef]
7. Fang, Z.Y.; Roy, K.; Murugesan, M.; Lim, J.B.P. Finite element analysis of cold-formed steel channels with web holes under end-one-flange loading at elevated temperatures. *Struct. Eng. Mech.* **2021**. under review.
8. Beulah Gnana Ananthi, G.; Roy, K.; Lim, J.B.P. Experimental and numerical investigations on axial strength of back-to-back built-up cold-formed steel angle columns. *Steel Compos. Struct.* **2019**, *31*, 601–615.
9. Schafer, B.W. Local, distortional, and euler buckling of thin-walled columns. *J. Struct. Eng.* **2002**, *128*, 289–299. [CrossRef]

10. Chi, Y.H.; Roy, K.; Chen, B.S.; Fang, Z.Y.; Uzzaman, A.; Beulah Gnana Ananthi, G.; Lim, J.B.P. Effect of web hole spacing on axial capacity of back-to-back cold-formed steel channels with edge-stiffened holes. *Steel Compos. Struct.* **2021**, *40*, 287–305.
11. Fang, Z.Y.; Roy, K.; Chen, B.S.; Sham, C.-W.; Hajirasouliha, I.; Lim, J.B.P. Deep learning-based procedure for structural design of cold-formed steel channel sections with edge-stiffened and un-stiffened holes under axial compression. *Thin-Walled Struct.* **2021**, *166*, 108076. [CrossRef]
12. Fang, Z.Y.; Roy, K.; Mares, J.; Sham, C.-W.; Chen, B.S.; Lim, J.B.P. Deep learning-based axial capacity prediction for cold-formed steel channel sections using Deep Belief Network. *Structures* **2021**, *33*, 2792–2802. [CrossRef]
13. Chen, B.S.; Roy, K.; Fang, Z.Y.; Uzzaman, A.; Pham, C.H.; Raftery, G.; Lim, J.B.P. Shear behavior and design cold-formed steel channels with edge -stiffened hole, un-stiffened hole, and plain web. *ASCE J. Struct. Eng.* **2021**, 04021268.
14. Nie, S.; Zhou, T.; Liao, F.; Yang, D. Study on axial compressive behavior of quadruple C-channel built-up cold-formed steel columns. *Struct. Eng. Mech.* **2019**, *70*, 499–511.
15. Roy, K.; Chen, B.S.; Fang, Z.Y.; Uzzaman, A.; Chen, X.; Lim, J.B.P. Local and distortional buckling behavior of back-to-back built-up aluminium alloy channel section columns. *Thin-Walled Struct.* **2021**, *163*, 107713. [CrossRef]
16. Roy, K.; Chen, B.S.; Fang, Z.Y.; Uzzaman, A.; Lim, J.B.P. Axial capacity of back-to-back built-up aluminium alloy channel section columns. *ASCE J. Struct. Eng.* **2021**, *148*, 04021265. [CrossRef]
17. Borzoo, S.; Ghaderi, S.R.M.; Mohebi, S.; Rahimzadeh, A. Nonlinear finite element modeling of steel-sheathed cold-formed steel shear walls. *Steel Compos. Struct.* **2016**, *22*, 79–89. [CrossRef]
18. Rosario-Galanes, O.; Godoy, L.A. Modeling of wind-induced fatigue of cold-formed steel sheet panels. *Struct. Eng. Mech.* **2014**, *49*, 237–259. [CrossRef]
19. Heva, Y.B.; Mahendran, M. Flexural-torsional buckling tests of cold-formed steel compression members at elevated temperatures. *Steel Compos. Struct.* **2013**, *14*, 205–227. [CrossRef]
20. Uzzaman, A.; Lim, J.B.P.; Nash, D.; Rhodes, J.; Young, B. Web crippling behavior of cold-formed steel channel sections with offset web holes subjected to interior-two-flange loading. *Thin-Walled Struct.* **2012**, *50*, 76–86. [CrossRef]
21. Uzzaman, A.; Lim, J.B.P.; Nash, D.; Rhodes, J.; Young, B. Cold-formed steel sections with web openings subjected to web crippling under two-flange loading conditions—part I: Tests and finite element analysis. *Thin-Walled Struct.* **2012**, *56*, 38–48. [CrossRef]
22. Uzzaman, A.; Lim, J.B.P.; Nash, D.; Rhodes, J.; Young, B. Cold-formed steel sections with web openings subjected to web crippling under two-flange loading conditions—Part II: Parametric study and proposed design equations. *Thin-Walled Struct.* **2012**, *56*, 79–87. [CrossRef]
23. Uzzaman, A.; Lim, J.B.P.; Nash, D.; Rhodes, J.; Young, B. Effect of offset web holes on web crippling strength of cold-formed steel channel sections under end-two-flange loading condition. *Thin-Walled Struct.* **2013**, *65*, 34–48. [CrossRef]
24. Uzzaman, A.; Lim, J.B.P.; Nash, D.; Young, B. Effects of edge-stiffened circular holes on the web crippling strength of cold-formed steel channel sections under one-flange loading conditions. *Eng. Struct.* **2017**, *139*, 96–107. [CrossRef]
25. Uzzaman, A.; Lim, J.B.P.; Nash, D.; Roy, K. Cold-formed steel channel sections under end-two-flange loading condition: Design for edge-stiffened holes, unstiffened holes and plain webs. *Thin-Walled Struct.* **2020**, *147*, 106532. [CrossRef]
26. Uzzaman, A.; Lim, J.B.P.; Nash, D.; Roy, K. Web crippling behavior of cold-formed steel channel sections with edge-stiffened and unstiffened circular holes under interior-two-flange loading condition. *Thin-Walled Struct.* **2020**, *154*, 106813. [CrossRef]
27. Lian, Y.; Uzzaman, A.; Lim, J.B.P.; Abdelal, G.; Nash, D.; Young, B. Effect of web holes on web crippling strength of cold-formed steel channel sections under end-one-flange loading condition—Part I: Tests and finite element analysis. *Thin-Walled Struct.* **2016**, *107*, 443–452. [CrossRef]
28. Lian, Y.; Uzzaman, A.; Lim, J.B.P.; Abdelal, G.; Nash, D.; Young, B. Effect of web holes on web crippling strength of cold-formed steel channel sections under end-one-flange loading condition—Part II: Parametric study and proposed design equations. *Thin-Walled Struct.* **2016**, *107*, 489–501. [CrossRef]
29. Lian, Y.; Uzzaman, A.; Lim, J.B.P.; Abdelal, G.; Nash, D.; Young, B. Web crippling behavior of cold-formed steel channel sections with web holes subjected to interior-one-flange loading condition-Part I: Experimental and numerical investigation. *Thin-Walled Struct.* **2017**, *111*, 103–112. [CrossRef]
30. Lian, Y.; Uzzaman, A.; Lim, J.B.P.; Abdelal, G.; Nash, D.; Young, B. Web crippling behavior of cold-formed steel channel sections with web holes subjected to interior-one-flange loading condition—Part II: Parametric study and proposed design equations. *Thin-Walled Struct.* **2017**, *114*, 92–106. [CrossRef]
31. Gunalan, S.; Bandula Heva, Y.; Mahendran, M. Local buckling studies of cold-formed steel compression members at elevated temperatures. *J. Constr. Steel Res.* **2015**, *108*, 31–45. [CrossRef]
32. Gunalan, S.; Mahendran, M. Experimental study of unlipped channel beams subject to web crippling under one flange load cases. *Adv. Steel Constr.* **2019**, *15*, 165–172.
33. Elilarasi, K.; Kasturi, S.; Janarthan, B. Effect of circular openings on web crippling of unlipped channel sections under end-two-flange load case. *Adv. Steel Constr.* **2020**, *16*, 310–320.
34. Imran, M.; Mahendran, M.; Keerthan, P. Mechanical properties of cold-formed steel tubular sections at elevated temperatures. *J. Constr. Steel Res.* **2018**, *143*, 131–147. [CrossRef]
35. Kankanamge, N.D.; Mahendran, M. Mechanical properties of cold formed steel at elevated temperatures. *Thin-Walled Struct.* **2011**, *49*, 26–44. [CrossRef]

36. Ranawaka, T.; Mahendran, M. Experimental study of the mechanical properties of light gauge cold-formed steels at elevated temperatures. *Fire Saf. J.* **2009**, *44*, 219–229. [CrossRef]
37. Chen, J.; Young, B. Experimental investigation of cold-formed steel material at elevated temperatures. *Thin-Walled Struct.* **2007**, *45*, 96–110. [CrossRef]
38. Lim, J.B.P.; Young, B. Effects of elevated temperatures on bolted moment-connections between cold-formed steel members. *Eng. Struct.* **2007**, *29*, 2419–2427. [CrossRef]
39. Landesmann, A.; Camotim, D. Distortional failure and DSM design of cold-formed steel lipped channel beams under elevated temperatures. *Thin-Walled Struct.* **2016**, *98*, 75–93. [CrossRef]
40. Laím, L.; Rodrigues, J.P.C.; Craveiro, H.D. Flexural behavior of axially and rotationally restrained cold-formed steel beams subjected to fire. *Thin-Walled Struct.* **2016**, *98*, 39–47. [CrossRef]
41. Dolamune Kankanamge, N.; Mahendran, M. Behavior and design of cold-formed steel beams subject to lateral–torsional buckling at elevated temperatures. *Thin-Walled Struct.* **2016**, *61*, 213–228. [CrossRef]
42. Gunalan, S.; Heva, Y.B.; Mahendran, M. Flexural–torsional buckling behavior and design of cold-formed steel compression members at elevated temperatures. *Eng. Struct.* **2014**, *79*, 149–168. [CrossRef]
43. Ranawaka, T.; Mahendran, M. Numerical modelling of light gauge cold-formed steel compression members subjected to distortional buckling at elevated temperatures. *Thin-Walled Struct.* **2010**, *48*, 334–344. [CrossRef]
44. Feng, M.; Wang, Y.C.; Davies, J.M. Structural behavior of cold-formed thin-walled short steel channel columns at elevated temperatures. Part 1: Experiments. *Thin-Walled Struct.* **2003**, *41*, 543–570. [CrossRef]
45. American Society of Civil Engineers. *ASCE/SEI 7-10—Minimum Design Loads for Buildings and Other Structures*; ASCE: Washington, DC, USA, 2005.
46. British Standards Institutions. *Eurocode 3: Design of Steel Structures*; BS EN 1993-1-1; BSI: London, UK, 2005.
47. British Standard Institution. *BS 5950—Structural Use of Steelwork in Buildings, Part 5—Code of Practice for the Design of Cold-Formed Sections*; BSI: London, UK, 1998.
48. AISI (American Iron and Steel Institute). *NAS S100—North American Specification for the Design of Cold-Formed Steel Structural Members*; NAS S100; AISI: Washington, DC, USA, 2016.
49. AS/NZS (Australian/New Zealand Standard). *AS/NZS 4600: 2018—Cold-Formed Steel Structures*; Jointly Published by Standards Australia: Sydney, Australia; Standards New Zealand: Wellington, New Zealand, 2018.
50. ABAQUS. *ABAQUS Version 6.14-2*; SIMULIA: Providence, RI, USA, 2018.
51. Chen, B.; Roy, K.; Uzzaman, A.; Raftery, G.M.; Lim, J.B.P. Parametric study and simplified design equations for cold-formed steel channels with edge-stiffened holes under axial compression. *J. Constr. Steel Res.* **2020**, *172*, 106161. [CrossRef]
52. Chen, B.; Roy, K.; Uzzaman, A.; Raftery, G.; Lim, J.B.P. Axial strength of back-to-back cold-formed steel channels with edge-stiffened holes, un-stiffened holes and plain webs. *J. Constr. Steel Res.* **2020**, *174*, 106313. [CrossRef]
53. Chen, B.; Roy, K.; Uzzaman, A.; Lim, J.B.P. Moment capacity of cold-formed channel beams with edge-stiffened web holes, un-stiffened web holes and plain webs. *Thin-Walled Struct.* **2020**, *157*, 107070. [CrossRef]
54. Roy, K.; Ho Lau, H.; Ting, T.C.H.; Chen, B.; Lim, J.B.P. Flexural behavior of back-to-back built-up cold-formed steel channel beams: Experiments and finite element modelling. *Structures* **2021**, *29*, 235–253. [CrossRef]
55. Roy, K.; Ting, T.C.H.; Lau, H.H.; Lim, J.B.P. Nonlinear behavior of axially loaded back-to-back built-up cold-formed steel un-lipped channel sections. *Steel Compos. Struct.* **2018**, *28*, 233–250.
56. Roy, K.; Ting, T.C.H.; Lau, H.H.; Lim, J.B.P. Experimental and numerical investigations on the axial capacity of cold-formed steel built-up box sections. *J. Constr. Steel Res.* **2019**, *160*, 411–427. [CrossRef]
57. Hsiao, L.; Yu, W.; Galambos, T.V. Load and resistance factor design of cold formed steel, calibration of the AISI design provisions. In *Ninth Progress Report, Civil Engineering Study 88-2*; University of Missouri-Rolla: Rolla, MO, USA, 1988.
58. Fang, Z.Y.; Roy, K.; Ma, Q.; Uzzaman, A.; Lim, J.B.P. Application of deep learning method in web crippling strength prediction of cold-formed stainless steel channel sections under end-two-flange loading. *Structures* **2021**, *33*, 2903–2942. [CrossRef]
59. Fang, Z.Y.; Roy, K.; Chi, Y.; Chen, B.; Lim, J.B.P. Finite element analysis and proposed design rules for cold-formed stainless steel channels with web holes under end-one-flange loading. *Structures* **2021**, *34*, 2876–2899. [CrossRef]
60. Fang, Z.Y.; Roy, K.; Uzzaman, A.; Lim, J.B.P. Numerical simulation and proposed design rules of cold-formed stainless steel channels with web holes under interior-one-flange loading. *Eng. Struct.* **2021**, 113566. [CrossRef]

Local Retrofit of Reinforced Concrete Structures by the ACM System

Stefano Sorace [1], Gloria Terenzi [2,*] and Elena Fuso [1]

[1] Polytechnic Department of Engineering and Architecture, University of Udine, 33100 Udine, Italy; stefano.sorace@uniud.it (S.S.); elena.fuso@uniud.it (E.F.)

[2] Department of Civil and Environmental Engineering, University of Florence, 50123 Firenze, Italy

[*] Correspondence: gloria.terenzi@unifi.it; Tel.: +39-55-275-8887

Abstract: During the last decades, low architectural impact strategies have been increasingly adopted in the seismic retrofit of reinforced concrete structures. Among the emerging technologies in this field, the active lateral confinement of columns, beams, and beam-to-column joints is gaining growing attention thanks to the localization of the interventions only on the members in unsafe conditions, the resulting small increase in size, and the limited demolition required for installation. The study presented herein is focused on the application of a highly performing confinement technology, named as ACM (Active Confinement of Masonry), which was conceived more than twenty years ago in Italy for masonry structures, and then successfully applied to reinforced concrete ones. A representative case study is examined in detail herein, i.e., a school built in the early 1960s in the Friuli Venezia Giulia area in Italy. A seismic assessment analysis of the building is carried out in its current state, also supported by preliminary diagnostic investigations, which highlights several seismic deficiencies, especially in terms of shear response of columns and beams. Thus, a retrofit hypothesis based on the installation of the ACM system is proposed, which allows attaining a substantial improvement in the seismic response capacities, while maintaining limited architectural intrusion. A detailed description of the case study characteristics and a synthesis of the time-history seismic analyses developed in original conditions are presented in this article, along with the design criteria, drawings of the interventions, and an evaluation of the resulting performance enhancement in retrofitted configuration.

Keywords: active confinement; reinforced concrete structures; local seismic retrofit strategies; ACM method; time-history analysis

1. Introduction

Frame buildings with a reinforced concrete (RC) structure designed in the 1960s normally show poor response capacities to earthquakes due to the absence of specific anti-seismic measures in their original design conception and detailing [1–3].

Innovative seismic retrofit strategies are now increasingly adopted for this class of building to limit architectural impact, working times, and costs of the interventions, as well as to upgrade their structural and non-structural seismic performance, as compared to traditional rehabilitation techniques. Among these innovative strategies, the ones based on the notion of active lateral confinement (ALC) of RC members are gaining growing attention from the academic and professional communities. Starting from early studies on concrete failure under biaxial compressive stress states [1], the concept of lateral confinement as a tool for increasing strength and ductility of RC members has been theoretically fixed by fundamental research contributions [4–8] and has progressively evolved up to date. This prompted the conception of several passive lateral confinement (PLC) retrofit strategies, based on the external installation of transversal steel reinforcements like hoops, straps, cages [9–15] or jackets [16–22], RC jackets [23–26], mortar jackets [27], or, after the successful

introduction of fibre reinforced polymer (FRP) materials in the broad field of structural rehabilitation, of perimeter wrapping with FRP layers or fabric sheets [28–34]. As an alternative, ALC technologies, which differ from PLC ones for the application of an initial confining pressure obtained by prestressing the lateral surface of the considered members—inspired to the classical "active hooping" strategy applied for centuries to stone and masonry columns—have been recently extended to RC structures too [35–48].

Among the ALC technologies, a pioneer role has been played by the ACM (Active Confinement of Masonry, "CAM" in Italian, registered trademark) technology, ideated more than twenty years ago in Italy for masonry structures [49,50], and later successfully adapted with effective results to RC ones. The system consists of stainless steel ribbons, shaped like thin strips, embracing and tying walls (masonry structures) or beams, columns, and beam-to-column joints (RC frame structures) by means of closed loops passing through transverse holes. The active confinement effect is generated by pre-tensioning the strips. The additional local stress states induced by pre-tension in the contact zones with the structural members are distributed by means of connection elements, such as flat and funnel-type plates, and angles.

Like other ALC technologies applied to RC structures, the advantages offered by the ACM system are represented by the localisation of demolitions in the perimeter zones around the beams, columns, and joints to be retrofitted, and a practically null addition of masses in the total dead mass computation for the building (Figure 1). Consistently, architectural intrusion, working times, and costs are remarkably reduced compared to traditional rehabilitation solutions, and benefits are obtained also in terms of seismic structural weights. At the same time, a distinguishing characteristic of the ACM system, in comparison to other ALC strategies, is that the strips are made of high-strength stainless steel, which helps limiting their thickness below one millimetre per strip while guaranteeing high pre-stress levels and preserving them from oxidation during their in-place lifespan. Moreover, the strips can be installed on beams, columns, and joints without discontinuities, and the system offers, in addition to lateral confinement, significant supplemental steel reinforcement.
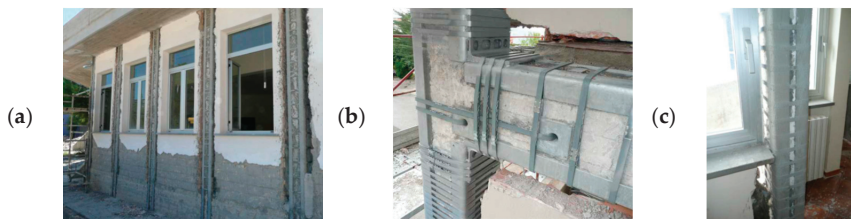
Figure 1. Images of a typical ACM-based retrofit intervention on a building with RC frame structure: view of a façade (**a**), a beam-to-column joint (**b**), and a column situated in proximity to two windows (**c**)—pictures taken from [50].

The study presented herein concerns a hypothesis of application of the ACM system to an Italian building of the early 1960s with RC frame structure, characterised by the typical seismic vulnerabilities of a wide class of reinforced concrete structures belonging to that period. As illustrated in Section 2, this was assessed by a non-linear time-history analysis carried out in current conditions, the results of which highlight remarkably unsafe stress states in most members at the basic design earthquake (BDE) level of seismic action, especially in terms of shear. Low ductility capacities of columns and beams also emerge in flexure, and unsafe conditions for about 40% of beam-to-column joints.

The ACM-based retrofit solution conceived for the case study building allows attaining safe stress states and a notably increased ductility in the retrofitted members, with limited demolition works of infills and partitions in contact with them and relatively low structural intervention costs, as discussed in Section 3.

2. Case Study Building

The considered building is a school situated in the town of Tolmezzo, Friuli-Venezia Giulia region, Italy. Its structural design dates back to 1960, and the construction works were completed in 1961. The general characteristics of the building and the results of the seismic assessment analysis carried out in current conditions are summarised below.

2.1. Geometrical and Structural Characteristics

The building has a rectangular plan, sized 13.5 m × 32.8 m, and is organised in four storeys above ground, with inter-storey heights of 3.36 m (ground storey), 3.65 (first), 3.62 (second), and 2.57 m (measured at the under-roof top). The structural plans of the first, second, and third floors and the roof are shown in Figures 2–5.
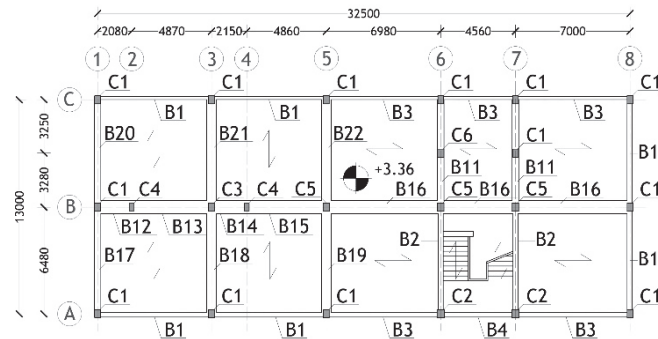
Figure 2. First floor structural plan.
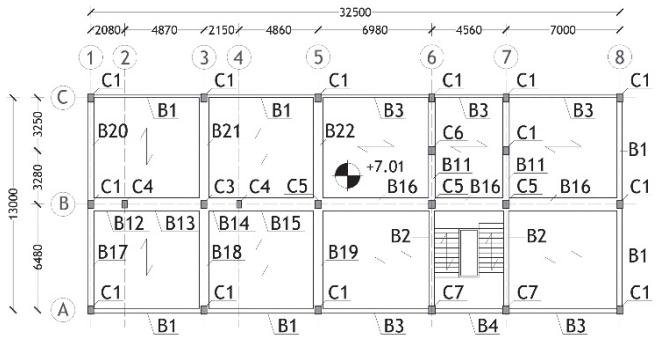
Figure 3. Second floor structural plan.
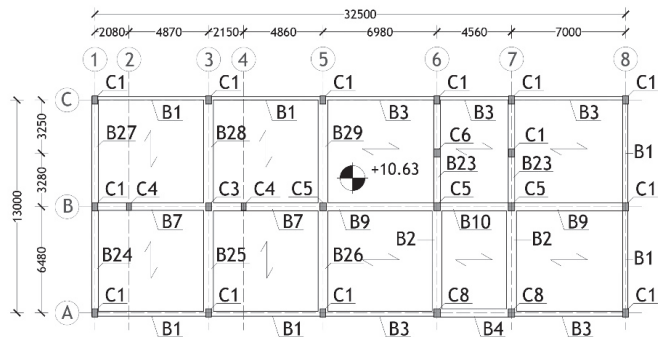
Figure 4. Third floor structural plan.
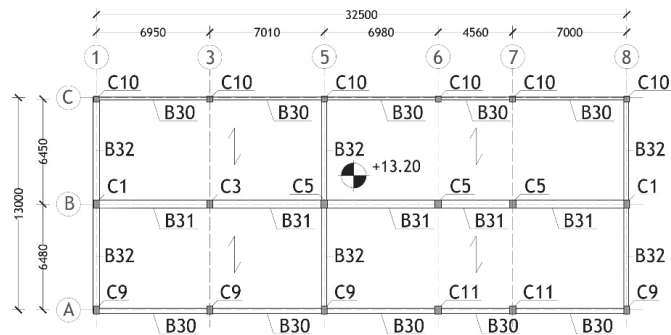
Figure 5. Roof structural plan.

The structure of the storey floors is made of 280 mm-high and 80 mm-wide RC joists parallel to the transversal direction in plan in the two left frame spans, and parallel to the longitudinal direction in the three remaining frame spans. The joists are placed at a mutual distance of 700 mm, as determined by the interposed clay lug bricks, and a 40 mm thick upper RC slab. The roof floor structure is made of "SAPAL"-type 370 mm-high reinforced clay lug bricks, integrated by on-site cast 350 mm-high RC ribs placed at a mutual distance of 1250 mm, and a 50 mm thick upper RC slab. Foundations are constituted by a mesh of inverse T-beams, with heights and flanges ranging from 700 mm to 1000 mm, and from 600 mm to 800 mm, respectively.

As part of the OSS (Seismic Observatory of Structures) programme promoted by the Italian Department of Civil Protection to structurally assess and monitor public buildings [51], a careful on-site mechanical investigation campaign was carried out on the case study one [52]. This campaign consisted of concrete cover demolitions (Figure 6a), pacometer tests (Figure 6b), and extraction of samples, for the reinforcing bars, and core drillings (Figure 7a) and Son-Reb tests (i.e., combined sclerometer—Figure 7b—and ultrasonic—Figure 7c—tests) for concrete.
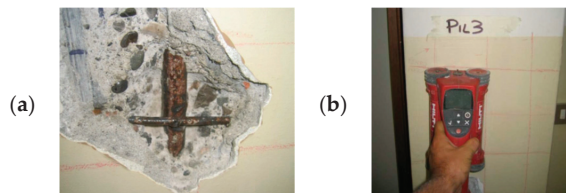
Figure 6. Images of a concrete cover demolition (**a**) and a pacometer test (**b**).
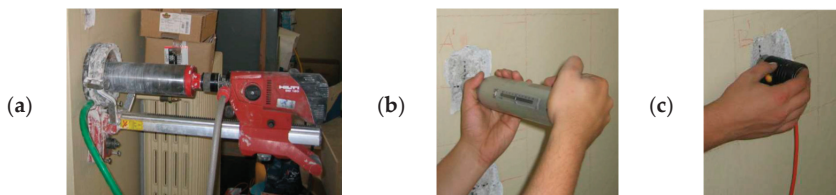
Figure 7. Images of a concrete core drilling (**a**), a sclerometer test (**b**), and an ultrasonic test (**c**).

The results of the tests highlighted the average values of yielding and ultimate stress values, f_{sy} and f_{su}, of 380 MPa and 500 MPa, respectively, and Young's modulus, E_s, of 204.000 MPa for steel; and the average values of cylindrical compressive strength, f_c, equal

to 20.3 MPa, Young's modulus, E_c, of 21.500 MPa, and strains at peak stress and at collapse, ε_c, and ε_{cu}, equal to 0.00156 and 0.00402, respectively, for concrete.

2.2. Time-History Evaluation Analysis

The seismic response of the building was evaluated by means of the finite element model displayed in Figure 8, generated by the SAP2000NL calculus program [53]. Concrete-type frame elements were used to model beams and columns, and shell elements for the flights of stairs. The in-plan axial stiffness of the floors was simulated by means of equivalent horizontal braces. The model does not include infills in contact with the structural members because the assessment analysis was essentially focused on the building performance at the BDE, the peak lateral displacements relevant to which would significantly damage them, as discussed below, thus, practically annulling the contribution of infills to the seismic response.
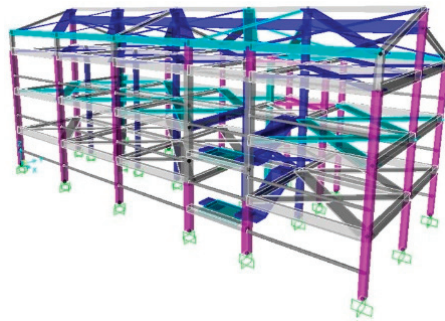
Figure 8. Finite element model of the structure.

The finite element model shown in Figure 8 was used for the analysis of the structure both in current state and in ACM-retrofitted conditions; the mechanical characteristics of concrete were changed when passing from the former to the latter, according to the criteria presented in Section 3.

A modal analysis of the structure was carried out in the first step of the assessment study, which highlighted three prevailing modes, and namely: a first translational mode along the longitudinal axis in plan, with vibration period of 0.32 s; and a second and a third mixed translational along the transversal axis in plan-rotational around the vertical axis modes, with periods of 0.23 s and 0.16 s, respectively. Nine modes are needed to obtain a summed effective modal mass greater than 85% of the total seismic mass of the building along the longitudinal (95%) and transversal (87%) axes, as well as around the vertical one (86%).

The non-linear time-history analyses were developed by adopting lumped plastic hinges at the end sections of beams, governed by a Takeda-type hysteretic relationship [54] and fibre-type plastic hinges—composed of concrete-type fibres and steel-type fibres—at the end sections of columns. For the latter, which allow an accurate consideration of the interaction between axial force and biaxial bending moment, a Mander-type [7] backbone curve and a Takeda-type hysteretic model were assumed for the concrete fibres, and a strain hardening elasto-plastic skeleton curve with hysteretic kinematic behaviour for the reinforcing steel fibres. A typical fibre model mesh of a column cross section is drawn in Figure 9, where the reinforcing bars are located by red dots encased in black circles.
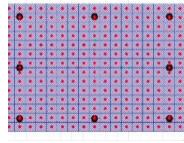
Figure 9. Fibre model of a column cross section.

The accelerograms used in the input for the time-history analyses were generated in seven groups of two horizontal components from the pseudo-acceleration response spectra referred to the municipality of Tolmezzo. In each analysis, a different pair of horizontal components was used in the input. The results were elaborated in mean terms over the response to the seven pairs. Attention is focused here on the response to the BDE, with a 10% probability of being exceeded over the reference time period V_R, fixed at 75 years by Italian Standards for school buildings [55]. The relevant response spectrum, referred to the soil conditions identified for the site of the building, and characterised by a peak ground acceleration of 0.284 g, is shown in Figure 10.
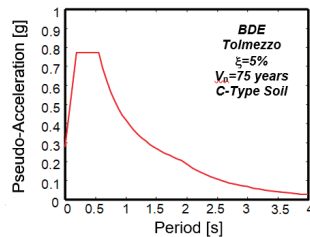
Figure 10. BDE-scaled pseudo-acceleration response spectrum for Tolmezzo.

A synthesis of the results of the analyses shows that the members in unsafe conditions are: 54 out of 84 columns in shear (namely, by referring to the plans in Figure 2 through Figure 5, 23 C1, 2 C2, 4 C3, 4 C4, 4 C5, 2 C6, 2 C7, 2 C8, 4 C9, 4 C10, and 2 C11-type columns), and 43 in combined axial force/biaxial flexure (21 C1, 2 C2, 4 C3, 2 C4, 10 C5, 2 C7, and 2 C8), with the maximum demand/capacity ratio (*DCR*) values of 3.49 (shear) and 2.26 (combined axial force/biaxial flexure); 42 out of 73 beams in shear (14 B1, 4 B2, 15 B3, 3 B4, 4 B7, 1 B9, and 1 B10-type beams), and 32 (14 B1, 4 B2, 13 B3, and 1 B9) in flexure, with the maximum *DCRs* of 2.6 (shear) and 2.01 (flexure); and 25 out of 60 beam-to-column joints (by referring to the nomenclature reported in Section 3.1, 3 B, 3 D, 3 H, 3 N, 3 P, 2 C, 2 G, 2 I, 2 O, 1 E, and 1 F-type joints), with the maximum *DCRs* of 2.74. At the same time, safe conditions are evaluated for the foundation beams, both in flexure and shear.

For the example of the plastic demand in columns, the bending moment-rotation cyclic response around the strong flexural axis of C1 column situated in the A5 alignment on the ground storey is plotted in Figure 11 for the most demanding of the seven input accelerograms.

The energy response time-histories of the structure obtained for the same input ground motion are graphed in Figure 12, highlighting a similar contribution of the plastic energy related to the inelastic response of the RC members and the modal (i.e., viscous damping matrix-related) energy dissipated by the structure.
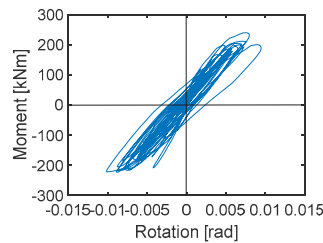
Figure 11. Bending moment-rotation response of C1 ground storey column belonging to A5 alignment around its strong flexural axis.
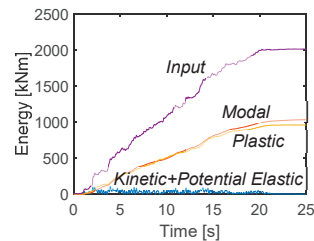
Figure 12. Energy time-histories of the structure.

The response in terms of lateral displacements is assessed by the maximum inter-storey drift values equal to about 1.3% of the inter-storey height in the longitudinal direction in plan, and 1.05% in the transversal direction, at the BDE. The corresponding values at the Serviceability Design Earthquake (SDE), characterised by 63% probability of being exceeded over V_R, are equal to 0.55% and 0.46%, respectively. Based on these results, negligible damage to non-structural elements (infills, partitions, finishes, and plants) is assessed at the SDE, and repairable damage at the BDE. This highlights an acceptable lateral displacement performance of the building, which does not prompt any interventions aimed at significantly increasing the horizontal translational stiffness of the structure.

In view of this, as well as of the remaining data drawn from the seismic assessment analysis in current conditions, a retrofit strategy aimed at improving the response capacities of beams, columns, and beam-to-column joints by means of local strengthening interventions, like the ACM-based one, was identified as the preferable option for the case study structure.

3. ACM-Based Retrofit Solution

The retrofit hypothesis was designed by computing the effects of the ACM-induced active confinement on the compression strength and ultimate strain of concrete. Relevant calculations were carried out by referring to the formulas provided by the Instructions for application of the Italian Technical Standards [56], recapitulated below.

3.1. Beams and Columns

In the following, symbol ρ_s is assumed to denote the transversal reinforcement volume ratio for discontinuous jacketing made of strips, given by $\rho_s = 2A_s \cdot (b + h)/(b \cdot h \cdot s)$, with A_s, s = transversal section and spacing of strips, b, h = RC section sides, and f_{ywd} the design yielding stress of the constituting stainless steel of strips (equal to 560 MPa for the basic ACM application conceived in this study). Based on this notation, the cylindrical compression strength of the confined concrete, f_{cc}, is obtained from the unconfined strength, f_c, as follows:

$$f_{cc} = f_c \cdot \left[1 + 3.7 \cdot \left(\frac{0.5 \cdot \alpha_n \cdot \alpha_s \cdot \rho_s \cdot f_{ywd}}{f_c} \right)^{0.86} \right] \tag{1}$$

where:

$$\alpha_n = 1 - \frac{(b - 2R)^2 + (h - 2R)^2}{3b \cdot h} \tag{2}$$

$$\alpha_s = \left(1 - \frac{s - h_s}{2b}\right) \cdot \left(1 - \frac{s - h_s}{2h}\right) \tag{3}$$

with h_s = strip height and R = manufacturing smoothing radium, which can be put as equal to:

$$R = \min\left(L_{ang}; 5t_{ang}\right) \tag{4}$$

where L_{ang}, t_{ang} are the side and thickness of the steel angles. The ε_{cc} strain at the peak stress and the ε_{ccu} ultimate strain of confined concrete are derived from the corresponding ε_c and ε_{cu} values in original unconfined conditions by means of the following relations:

$$\varepsilon_{cc} = \varepsilon_c \cdot \left[1 + 5\left(\frac{f_{cc}}{f_c} - 1\right)\right] \tag{5}$$

$$\varepsilon_{ccu} = \varepsilon_{cu} + 0.5 \cdot \frac{0.5\alpha_n \cdot \alpha_s \cdot \rho_s \cdot f_{ywd}}{f_{cc}} \tag{6}$$

When the intervention was designed, a decision was made to place the steel strips at the ends of each column in unsafe conditions, with the number of layers ranging from two to four, and constant spacing of 50 mm or 100 mm. For unsafe beams, two strip layers with a spacing of 100 mm were always adopted. The columns and beams subjected to the interventions are identified with different colours in the structural plans drawn in Figures 13–16. Therein, the labels "Full height ACM-strengthened" (in green) and "Web ACM-strengthened" (pink) mean that the lateral side of the strips is either limited to the out-of-depth portion of beams or extended to their whole height.
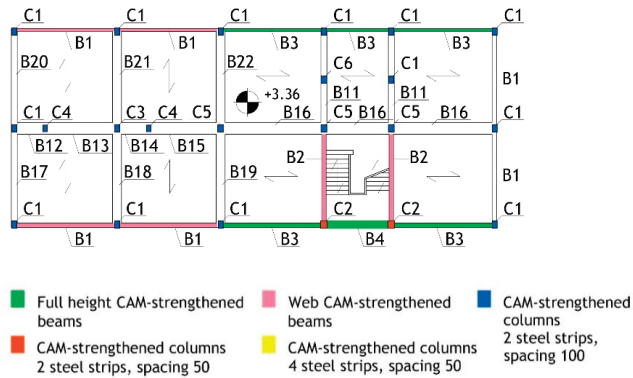
Figure 13. Localization of the interventions—ground storey—and nomenclature for all storeys.
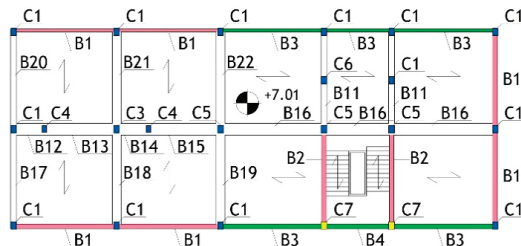
Figure 14. Localization of the interventions—first storey.
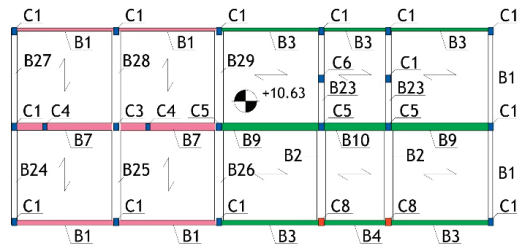
Figure 15. Localization of the interventions—second storey.
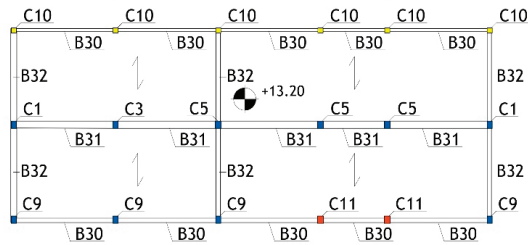
Figure 16. Localization of the interventions—third storey.

The f_{cc}, ε_{cc}, and ε_{ccu} values computed by means of Formulas (1), (5) and (6), respectively, are recapitulated in Table 1, for the columns subjected to the intervention, and Table 2, for beams. The f_{cc} values are about 10% to 50% greater than the f_c value of 20.3 MPa identified in current conditions, as mentioned in Section 2.1; at the same time, ε_{cc} and ε_{ccu} are about 180% to 415% greater than the corresponding ε_c and ε_{cu} values of 0.00156 and 0.00402, respectively, cited in Section 2.1 as well.

Table 1. Mechanical parameters of confined concrete—columns.

Column Type	Strips (Layers/Spacing)	f_{cc} (MPa)	ε_{cc}	ε_{ccu}
C1	2/100 mm	22.65	0.00314	0.01136
C2	2/50 mm	24.77	0.00413	0.01859
C3	2/100 mm	22.67	0.00315	0.01141
C4	2/100 mm	22.92	0.00327	0.01231
C5	2/100 mm	22.59	0.00311	0.01113
C6	2/100 mm	22.59	0.00311	0.01113
C7	4/50 mm	28.58	0.00606	0.03072
C8	2/100 mm	24.88	0.00423	0.01914
C9	2/100 mm	23.25	0.00343	0.01348
C10	4/50 mm	31.31	0.00739	0.03813
C11	2/50 mm	25.92	0.00474	0.02257

Table 2. Mechanical parameters of confined concrete—beams.

Beam Type	Strips (Layers/Spacing)	f_{cc} (MPa)	ε_{cc}	ε_{ccu}
B1	2/100 mm	23.79	0.0037	0.01541
B2	2/100 mm	24.14	0.00385	0.01663
B3/B4	2/100 mm	23.43	0.00352	0.01414
B7	2/100 mm	22.58	0.0031	0.01109
B9/B10	2/100 mm	22.57	0.00302	0.01048

The confinement effects in terms of moment-curvature response are demonstratively visualised in Figure 17 for column C1. Consistently with the results obtained for the compression strength and ultimate strain values, the diagram highlights an increase in peak moment and ultimate curvature equal to about 15% and 160%, respectively. This underlines a considerable improvement of bending moment capacity and a very high growth in ductility reached, thanks to the ACM-induced confinement action.
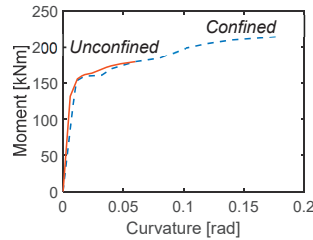
Figure 17. Bending moment-curvature diagram for C1 column referred to its strong flexural axis.

The bending moment (beams) and axial force-biaxial bending moment (columns) checks in retrofitted conditions were developed by replacing the original properties of concrete with the corresponding ones of confined concrete, for each strengthened member. The results of these checks, not reported in detail for brevity's sake, show *DCR* values below one, and, thus, safe conditions, for all beams and columns. Furthermore, plastic demand is reduced by up to 20% in the most stressed members, and by 18% in the complete structure, as highlighted by the hysteretic response of C1 ground storey column in Figure 18 and the energy time-histories in Figure 19, which replicate in retrofitted conditions the corresponding graphs plotted in Figures 11 and 12 for the current state. The reduction in the plastic demand is a consequence of the increased elastic response limits of beams and columns produced by the intervention, in addition to the enhancement of their strength capacities.
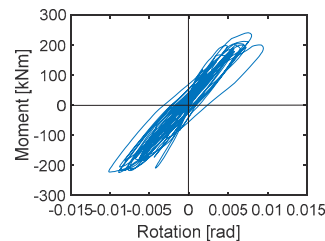
Figure 18. Bending moment-rotation response of C1 ground storey column belonging to A5 alignment around its strong flexural axis in retrofitted conditions.
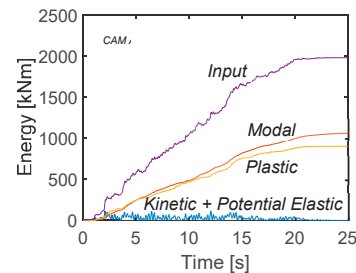
Figure 19. Energy time-histories of the structure in retrofitted conditions.

In order to develop shear checks on beams and columns, the contribution of the ACM system strips, $V_{Rsd,ACM}$, to the tensile shear strength was evaluated as follows [56]:

$$V_{Rsd,ACM} = 0.9 \cdot d \cdot \frac{2t_s}{s} \cdot b_s \cdot 0.5 f_{ywd} \cdot cot\theta \tag{7}$$

where d is the effective depth of the RC section, t_s and b_s are the thickness and width of strips, 0.5 is a reduction factor adopted to guarantee an elastic response of strips—and thus their effectiveness in limiting concrete crack width—with considerable margin, and θ is the angle of inclination of shear cracks with respect to the horizontal. In retrofitted conditions, the resultant shear strength in tension, $V_{Rsd,r}$, is given by the sum of $V_{Rsd,ACM}$ and the value in current state, $V_{Rsd,c}$. $V_{Rsd,ACM}$, and $V_{Rsd,c}$ are lower than the corresponding values of the shear strength in compression, $V_{Rcd,ACM}$ and $V_{Rcd,c}$, computed by considering, in relevant formulas, f_c in current state, and f_{cc} in retrofitted conditions. Therefore, the tensile values $V_{Rsd,c}$ and $V_{Rsd,r}$ were assumed in the stress state checks as shear strength measures. Relevant values are recapitulated in Tables 3 and 4 for the most stressed columns and beams, along with the shear demand values derived from the analysis, V_{Ed}, and the *DCR* values in current and retrofitted conditions, DCR_c and DCR_r. As highlighted by Tables 3 and 4, all members reach safe post-retrofit shear stress states, with the maximum DCR_r/DCR_c ratios (which give a direct measure of the maximum performance enhancement obtained thanks to the ACM-based intervention) ranging from about 2.8, for beams, to about 10, for columns.

Table 3. Shear demand, capacity values in current and retrofitted conditions, and relevant demand/capacity *DCR* ratios–selected columns.

Column	Storey	V_{Ed} (kN)	$V_{Rsd,c}$ (kN)	$V_{Rsd,r}$ (kN)	DCR_c	DCR_r
C1	Ground	113.4	59.8	275.3	1.90	0.41
C2	Ground	287.2	99.7	530.6	2.88	0.54
C4	Ground	105.2	53.6	247.5	1.96	0.43
C1	1	85.6	59.8	275.3	1.43	0.31
C3	1	110.4	74.7	290.2	1.48	0.38
C4	1	82.6	66.9	260.9	1.23	0.32
C7	1	186.9	78.9	653.7	2.37	0.29
C8	2	117.9	78.9	423.6	1.49	0.28
C10	3	143.7	41.1	435.2	3.49	0.33

Table 4. Shear demand, capacity values in current and retrofitted conditions, and relevant demand/capacity *DCR* ratios–selected beams.

Beam	Storey	V_{Ed} (kN)	$V_{Rsd,c}$ (kN)	$V_{Rsd,r}$ (kN)	DCR_c	DCR_r
B1	Ground	137.8	72.3	192.9	1.91	0.71
B2	Ground	125.6	59.8	137.4	2.60	0.91
B1	1	121.5	72.3	192.9	1.68	0.63
B2	1	132.1	59.8	137.4	2.36	0.96
B7	2	84.5	59.8	167.5	1.41	0.51

The design drawings of the interventions on beams, both for the case of "Full height" and "Web" ACM-strengthened ones, and columns are illustrated in Figures 20–22.
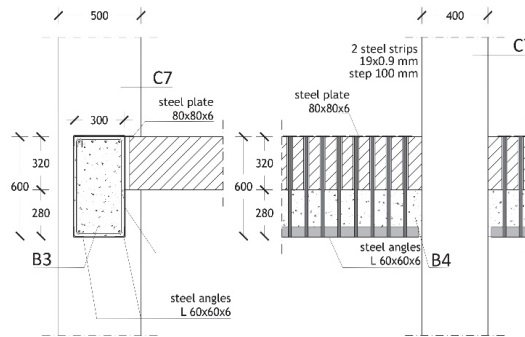
Figure 20. Full height ACM-strengthened beam.
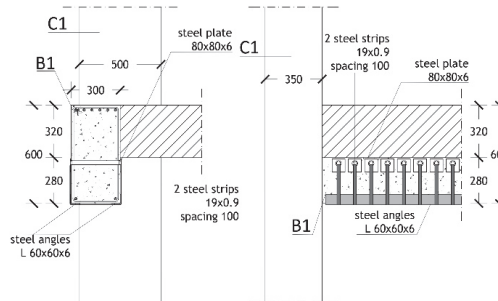
Figure 21. Web ACM-strengthened beam.
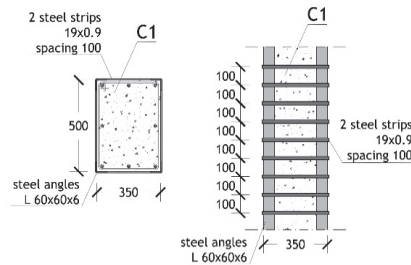
Figure 22. ACM-strengthened column.

3.2. Beam-to-Column Joints

Stress checks were carried out on all beam-to-column joints, as none of them meet the condition of a geometrically confined joint. According to [56], the two possible collapse mechanisms were evaluated, i.e., in tension and compression, showing that—as mentioned in Section 2—25 out of 60 joints are in unsafe conditions in the current state, with the maximum demand/capacity ratios of 2.74. Based on these results, the ACM system was applied to the unsafe joints too. The checks were replicated in retrofitted configuration, by means of the following relations:

$$\sigma_{nt} = \left| \frac{N}{2A_j} + \frac{\sigma_h}{2} - \sqrt{\left(\frac{N}{2A_j} + \frac{\sigma_h}{2} \right)^2 + \left(\frac{V_n}{A_j} \right)^2} \right| \leq 0.3\sqrt{f_{cc}} \tag{8}$$

$$\sigma_{nc} = \frac{N}{2A_j} + \frac{\sigma_h}{2} + \sqrt{\left(\frac{N}{2A_j} - \frac{\sigma_h}{2}\right)^2 + \left(\frac{V_n}{A_j}\right)^2} \leq 0.5 f_{cc} \tag{9}$$

where σ_{nt} and σ_{nc} are the principal tensile and compressive stresses, N is the axial force in the column above the joint, A_j is the area of the joint surface evaluated for the direction along which shear is considered, V_n is the total shear acting on the joint (given by the sum of the shear transmitted by the column above and the horizontal forces transferred by the upper face of the concurrent beams), and σ_h is the horizontal active confinement pressure exerted by the strips placed on the joint, expressed as follows:

$$\sigma_h = \frac{n_c \cdot n_s \cdot 2 \cdot A_s \cdot f_{ywd}}{b_j \cdot h_{jw}} \tag{10}$$

where n_c is the number of strip positions in the joint, n_s is the number of layers per each strip, and b_j, and h_{jw} are the effective width and height of the joint. The same type of strips as used to strengthen beams and columns was adopted for joints too. The spacing and number of layers per strip were calculated for each unsafe joint in current state by means of expressions (8)–(10). The design drawings of the intervention on the most stressed corner and perimeter joint, both situated in the ground storey and denoted with letters "B" and "N" in Figure 23, are illustrated in Figures 24 and 25. The quantity of strips requested for ground storey joint N (10 strip layers with 50 mm spacing) is the same as for the adjacent joint "O". All remaining perimeter joints are strengthened with a lower number of strips (from eight to two layers, and with spacing of 50 mm or 100 mm).
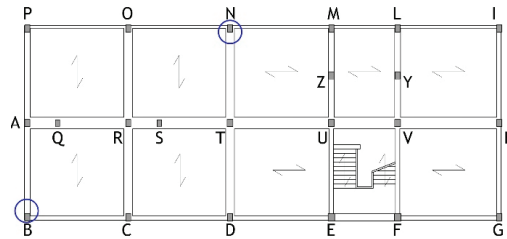
Figure 23. Numbering of beam-to-column joints.
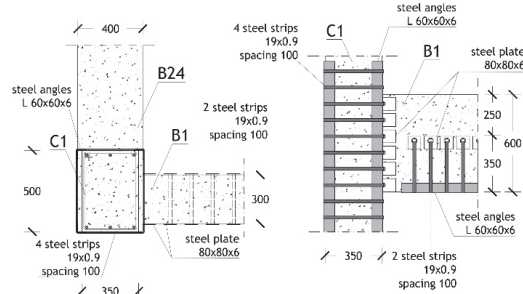
Figure 24. ACM-strengthened ground storey beam-to-column joint B.
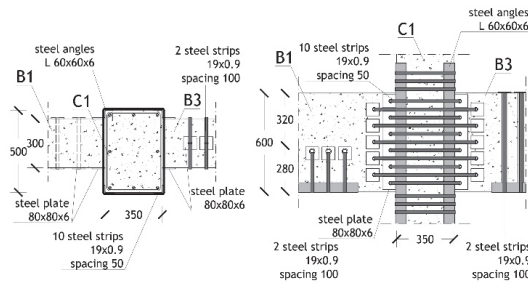
Figure 25. ACM-strengthened ground storey beam-to-column joint N.

The pre- and post-strengthening demand/capacity ratios for a selected set of most stressed joints, listed in Table 5, highlight that safe stress states are reached in retrofitted conditions, like for beams and columns.

Table 5. Demand/capacity DCR ratios—selected beam-to-column joints.

Joint Type	Storey	DCR_c	DCR_r
C	1	2.25	0.97
H	1	2.00	0.96
N	1	2.23	0.94
O	1	1.95	0.93
P	1	1.47	0.89
B	2	2.74	0.99
E	2	2.25	0.90
F	2	2.14	0.94

The cost of the structural intervention, demolition, and reconstruction of the involved portions of façade infills and partitions included, amount to about 150 Euro/m^2, i.e., 25–30% lower than the cost estimated for traditional retrofit strategies, like RC-based jacketing of beams, columns and joints, incorporation of additional earthquake-resistant structural members, etc. The latter strategy would also considerably increase the lateral stiffness of the structure, which is not motivated by the displacement performance in current state and, at the same time, could cause an unfavourable growth of storey shears.

Finishes, like plasters, paintings, and floor tiles are not included in cost computation, as they are included in the architectural renovation works planned for the building. At the same time, no interference with the thermal and electrical plants—and thus no additional related cost—is determined by the installation of the ACM system.

4. Conclusions

The study on the application of the ACM system to reinforced concrete structures presented in this article was aimed at evaluating, for a real building, all the aspects involved in the practical design of this retrofit strategy, as well as the actual levels of seismic improvement that it can offer. Indeed, although the use of the ACM was extended to RC structures several years ago, the literature on this technology is essentially limited to technical reports focused on the calculation of the interventions on single members, and relevant installation details.

The case study selected for this research is representative of the wide class of RC buildings designed in the 1960s without anti-seismic provisions, which causes a considerable earthquake-related vulnerability even when they are characterised by geometrical regularity and a simple and clearly conceived structural organization, like the examined school.

The results of the assessment analyses and the development of the ACM-based design hypothesis are summarised in the concluding remarks listed below.

- The response of the structure at the BDE level of seismic action highlights unsafe shear stress states in most beams and columns, with the maximum demand/capacity ratios reaching 2.6 in the former and 3.49 in the latter. Furthermore, about 40% of beams do not meet stress checks in flexure, and more than 50% of columns in normal force/biaxial flexure. About 40% of beam-to-column joints are in unsafe conditions too.

- On the other hand, thanks to the structural regularity of the building and to its low number of storeys, the response in terms of inter-storey drifts is not so poor.

- As a consequence of the combined stress states/drifts assessment, a local strengthening strategy, like the ACM, was evaluated as the preferable retrofit choice for the building.

- Thanks to the active confinement action offered by this technology, the intervention allows reaching a safe response of all members. This is obtained with a relatively small number of strips in all beams (two strip layers with 100 mm spacing) and columns (characterised by the same design output, except for two elements, where four strip layers and a 50 mm spacing are requested).

- A comparable quantity of strips is computed for most beam-to-column joints, except for the perimeter ones, where the number of strip layers exceptionally reaches a maximum of 10 for two of them, situated on the ground storey, and eight or six in four other perimeter joints. This is due to the total absence of stirrups and of any type of transversal reinforcement in the joints, which is typical of the RC structures of the time, causing a remarkably poor response capacity in tension in the most stressed ones.

- In addition to the effects on strength, the confinement action supplied by the ACM produces remarkable benefits in terms of ductility as well, as quantified by an increase in ultimate curvature in columns always greater than 100%, with the peak of 160%.

- The reliable cost analysis of a complete building offered in this study allowed an estimation of the amount of structural works which was 25–30% lower than the cost typically associated to traditional retrofit strategies. This is owed to fewer demolitions, as well as to quicker installation times required by the ACM.

- The localization of the intervention inherent to this retrofit strategy, and the practically null increase in the strengthened RC member sections, helps to avoid any appreciable increase in the lateral stiffness of the structural system, and, thus, any related growth in storey shears.

- The combined seismic performance enhancement/cost evaluation obtained as a final result of the study confirms the opportunity of a wider application of the ACM method to the seismic retrofit of RC frame structures in the next future.

Author Contributions: Conceptualization, S.S. and G.T.; methodology, S.S., G.T. and E.F.; software, E.F.; validation, S.S., G.T. and E.F.; formal analysis, G.T. and E.F.; investigation, S.S., G.T. and E.F.; resources, G.T.; data curation, G.T. and E.F.; writing—original draft preparation, S.S. and G.T.; writing—review and editing, S.S. and G.T.; funding acquisition, G.T. All authors have read and agreed to the published version of the manuscript.

Conflicts of Interest: The authors declare no conflict of interest.

Abbreviations

ACM	Active Confinement of Masonry ("CAM" in Italian, registered trademark)
ALC	active lateral confinement
PLC	passive lateral confinement
RC	reinforced concrete
BDE	Basic Design Earthquake
SDE	Serviceability Design Earthquake
DCR	demand/capacity ratio

References

1. Thermou, G.E.; Pantazopoulou, S.J. Assessment indices for the seismic vulnerability of existing R.C. buildings. *Earthq. Eng. Struct. Dyn.* **2011**, *40*, 293–313. [CrossRef]
2. Sorace, S.; Terenzi, G. Structural assessment of a modern heritage building. *Eng. Struct.* **2013**, *49*, 743–755. [CrossRef]
3. Sorace, S.; Terenzi, G. Motion control-based seismic retrofit solutions for a R/C school building designed with earlier Technical Standards. *Bull. Earthq. Eng.* **2014**, *12*, 2723–2744. [CrossRef]
4. Richart, F.A.; Brandtzaeg, A.; Brow, R.L. *A Study of the Failure of Concrete under Combined Compressive Stress*; University of Illinois Engineering Experiment Station Bulletin: Urbana, IL, USA, 1928.
5. Kent, D.C.; Park, R. Flexural members with confined concrete. *ASCE J. Struct. Div.* **1971**, *97*, 1969–1990. [CrossRef]
6. Desayi, P.; Iyengar, K.T.S.A.; Reddy, T.S. Equations for stress strain curve of concrete confined in circular steel spiral. *Mater. Struct. Test. Res.* **1978**, *11*, 33945. [CrossRef]
7. Mander, J.B.; Priestley, M.J.N.; Park, R. Theoretical stress strain model for confined concrete. *ASCE J. Struct. Eng.* **1988**, *114*, 1804–1826. [CrossRef]
8. Saatcioglu, M.; Razvi, S.R. Strength and ductility of confined concrete. *ASCE J. Struct. Eng.* **1992**, *118*, 1590–1607. [CrossRef]
9. Uy, B. Strength of reinforced concrete columns bonded with external steel plates. *Mag. Concr. Res.* **2002**, *54*, 61–76. [CrossRef]
10. Li, Y.F.; Chen, S.H.; Chang, K.C.; Liu, K.Y. A constitutive model of concrete confined by steel reinforcements and steel jackets. *Can. J. Civ. Eng.* **2005**, *32*, 279–288. [CrossRef]
11. Gimenez, E.; Adam, J.M.; Ivorra, S.; Calderon, P.A. Influence of strips configuration on the behavior of axially loaded RC columns strengthened by steel angles and strips. *Mater. Des.* **2009**, *30*, 4103–4111. [CrossRef]
12. Montuori, R.; Piluso, V. Reinforced concrete columns strengthened with angles and battens subjected to eccentric load. *Eng. Struct.* **2009**, *31*, 539–550. [CrossRef]
13. Nagaprasad, P.; Sahoo, D.P.; Rai, C.D. Seismic strengthening of RC columns using external steel cage. *Earthq. Eng. Struct. Dyn.* **2009**, *38*, 1563–1586. [CrossRef]
14. Roca, J.G.; Adam, J.M.; Calderon, P.A. Behavior of RC columns strengthened by steel caging under combined bending and axial loads. *Constr. Build. Mater.* **2011**, *25*, 2402–2412. [CrossRef]
15. Wang, L.; Kai-Leung, S.R. Theoretical and experimental study of plate-strengthened concrete columns under eccentric compression loading. *ASCE J. Struct. Eng.* **2013**, *139*, 350–359. [CrossRef]
16. Rodriguez, M.; Park, R. Seismic load tests of reinforced concrete columns strengthened by jacketing. *ACI Struct. J.* **1994**, *91*, 150–159.
17. Priestley, N.M.J.; Seible, F.; Xiao, Y.; Verma, R. Steel jacket retrofitting of reinforced concrete bridge columns for enhanced shear strength—Part 2: Test results and comparison with theory. *ACI Struct. J.* **1994**, *91*, 537–548.
18. Aboutaha, R.S.; Engelhardt, M.D.; Jirsa, J.O.; Kreger, M.E. Retrofit of concrete columns with inadequate lap splices by the use of rectangular steel jackets. *Earthq. Spectra* **1996**, *12*, 693–714. [CrossRef]
19. Xiao, Y.; Wu, H. Retrofit of reinforced concrete columns using partially stiffened steel jackets. *ASCE J. Struct. Eng.* **2003**, *129*, 725–732. [CrossRef]
20. Kaliyaperumal, G.; Sengupta, A.K. Seismic retrofit of columns in buildings for flexure using concrete jacket. *ISET Earthq. Techn. J.* **2009**, *46*, 77–107.
21. Lin, M.N.; Chen, P.C.; Tsai, K.C.; Yu, Y.J.; Liu, J.G. Seismic steel jacketing of rectangular RC bridge columns for the mitigation of lap splice failures. *Earthq. Eng. Struct. Dyn.* **2010**, *39*, 1687–1710. [CrossRef]
22. Belal, M.F.; Mohamed, H.M.; Morad, S.A. Behavior of reinforced concrete columns strengthened by steel jacket. *HBRC J.* **2015**, *11*, 201–212. [CrossRef]
23. Júlio, E.S.; Branco, F.; Silva, V.D. Structural rehabilitation of columns with reinforced concrete jacketing. *Prog. Struct. Eng. Mater.* **2003**, *5*, 29–37. [CrossRef]
24. Bousias, S.N.; Biskinis, D.E.; Fardis, M.N. Strength, stiffness and cyclic deformation capacity of concrete jacketed members. *ACI Struct. J.* **2007**, *104*, 521–531.
25. Vandoros, K.G.; Dritsos, S.E. Concrete jacket construction detail effectiveness when strengthening RC columns. *Constr. Build. Mater.* **2008**, *22*, 264–276. [CrossRef]
26. Sezen, H.; Miller, E.A. Experimental evaluation of axial behavior of strengthened circular reinforced-concrete columns. *J. Bridge Eng.* **2011**, *16*, 238–247. [CrossRef]

27. Foti, D.; Vacca, S. Mechanical behavior of concrete columns reinforced with rheoplastic mortar. *Mater. Constr./Build. Mater.* **2013**, *63*, 267–282. [CrossRef]
28. Lorenzis, L.D.; Tepfers, R. Comparative study of models on confinement of concrete cylinders with fiber-reinforced polymer composites. *ASCE J. Compos. Constr.* **2003**, *7*, 21937. [CrossRef]
29. Xiao, Y.; Wu, H. Compressive behavior of concrete confined by carbon fiber composite jackets. *J. Mater. Civ. Eng.* **2000**, *12*, 13946. [CrossRef]
30. Ilki, A.; Peker, O.; Karamuk, E.; Demir, C.; Kumbasar, N. FRP retrofit of low and medium strength circular and rectangular reinforced concrete columns. *J. Mater. Civ. Eng.* **2008**, *20*, 169–188. [CrossRef]
31. Rousakis, T.C.; Karabinis, A.I. Adequately FRP confined reinforced concrete columns under axial compressive monotonic or cyclic loading. *RILEM Mater. Struct.* **2012**, *45*, 957–975. [CrossRef]
32. Mazza, F.; Mazza, M. Seismic retrofitting of gravity-loads designed r.c. framed buildings combining CFRP and hysteretic damped braces. *Bull. Earthq. Eng.* **2019**, *17*, 3423–3445. [CrossRef]
33. Madotto, R.; Van Engelen, N.C.; Das, S.; Russo, G.; Pauletta, M. Shear and flexural strengthening of RC beams using BFRP fabrics. *Eng. Struct.* **2021**, *229*, 111606. [CrossRef]
34. Rossi, E.; Randl, N.; Mészöly, T.; Harsányi, P. Flexural strengthening with fiber-/textile-reinforced concrete. *ACI Struct. J.* **2021**, *118*, 97–107.
35. Krstulovic-Opara, N.; Thiedeman, P.D. Active confinement of concrete members with self-stressing composites. *ACI Struct. J.* **2000**, *97*, 297–308.
36. Triantafillou, T.C. Seismic retrofitting of structures with fibre-reinforced polymers. *Prog. Struct. Eng. Mater.* **2001**, *3*, 57–65. [CrossRef]
37. Mortazavi, A.; Pilakoutas, K.; Son, K.S. RC column strengthening by lateral pre-tensioning of FRP. *Constr. Build. Mater.* **2003**, *17*, 491–497. [CrossRef]
38. Saatcioglu, M.; Yalcin, C. External prestressing of concrete columns for improved seismic shear resistance. *ASCE J. Struct. Eng.* **2003**, *129*, 105770. [CrossRef]
39. Tamuzs, V.; Tepfers, R.; Chi-Sang, Y.; Rousakis, T.; Repelis, I.; Skruls, V.; Vilks, U. Behaviour of concrete cylinders confined by carbon-composite tapes and prestressed yarns. 1—Experimental data. *Mech. Compos. Mater.* **2006**, *42*, 13–32. [CrossRef]
40. Janke, L.; Czaderski, C.; Ruth, J.; Motavalli, M. Experiments on the residual load-bearing capacity of prestressed confined concrete columns. *Eng. Struct.* **2009**, *31*, 2247–2256. [CrossRef]
41. Andrawes, B.; Shin, M.; Wierschem, N. Active confinement of reinforced concrete bridge columns using shape memory alloys. *ASCE J. Bridge Eng.* **2010**, *15*, 81–89. [CrossRef]
42. Choi, E.; Nam, T.-H.; Yoon, S.J.; Cho, S.K.; Park, J. Confining jackets for concrete cylinder using NiTiNb and NiTi shape memory alloys wires. *Phys. Scr.* **2010**, *T139*, 014058. [CrossRef]
43. Shin, M.; Andrawes, B. Experimental investigation of actively confined concrete using shape memory alloys. *Eng. Struct.* **2010**, *32*, 656–664. [CrossRef]
44. Zuboski, G.R. Stress-Strain Behaviour for Actively Confined Concrete Using Shape Memory Alloys. Master's Thesis, Department of Civil Engineering, The Ohio State University, Columbus, OH, USA, 2013.
45. Holmes, N.; Niall, D.; O'Shea, C. Active confinement of weakened concrete columns. *Mater. Struct.* **2015**, *48*, 2759–2777. [CrossRef]
46. Tran, H.; Balandraud, X.; Destrebecq, J.F. Improvement of the mechanical performances of concrete cylinders confined actively or passively by means of SMA wires. *Arch. Civ. Mech. Eng.* **2015**, *15*, 292–299. [CrossRef]
47. Fakharifar, M.; Chen, G.; Wu, C.; Shamsabadi, A.; ElGawady, M.A.; Dalvand, A. Rapid repair of earthquake-damaged RC columns with prestressed steel jackets. *J. Bridge Eng.* **2016**, *21*, 4015075. [CrossRef]
48. Abdelrahman, K.; El-Hacha, R. Experimental investigation of RC columns confined with Ni–Ti shape memory alloy wires versus CFRP sheets. *Can. J. Civ. Eng.* **2021**, *48*, 925–940. [CrossRef]
49. Dolce, M.; Nigro, D.; Ponzo, F.C.; Marnetto, R. The CAM system for the retrofit of masonry structures. In Proceedings of the 7th International Seminar on Seismic Isolation, Passive Energy Dissipation and Active Control of Vibrations of Structures, Assisi, Italy, 2–5 October 2001; p. 9.
50. Marnetto, R.; Vari, A.; Leonori, M. *Il Sistema CAM—Consolidamento Strutturale Con Cuciture Inox*; 21mo Secolo: Milan, Italy, 2017. (In Italian)
51. Dolce, M.; Nicoletti, M.; De Sortis, A.; Marchesini, S.; Spina, D.; Talanas, F. Osservatorio Sismico delle Strutture: The Italian structural seismic monitoring network. *Bull. Earthq. Eng.* **2017**, *15*, 621–641. [CrossRef]
52. Dipartimento della Protezione Civile. Available online: https://www.protezionecivile.gov.it (accessed on 22 September 2021).
53. SAP2000NL. *Theoretical and Users' Manual*; Computers & Structures Inc.: Berkeley, CA, USA, 2021.
54. Takeda, T.; Sozen, M.A.; Nielsen, N.N. Reinforced concrete response to simulated earthquakes. *ASCE J. Struct. Div.* **1970**, *96*, 2557–2573. [CrossRef]
55. Ministry of Infrastructure and Transport. *Update of Technical Standards for Constructions*; Ministerial Decree, 17 January 2018, Ordinary supplement to G.U. no. 42, 20 February 2018; Ministry of Infrastructure and Transport: Rome, Italy, 2018. (In Italian)
56. Ministry of Infrastructure and Transport. *Instructions for the application of the Update of Technical Standards for Constructions*; Circular no. 7, 21 January 2019, Ordinary supplement to G.U. no. 35; Ministry of Infrastructure and Transport: Rome, Italy, 2019. (In Italian)

Absorption and Strength Properties of Short Carbon Fiber Reinforced Mortar Composite

Md. Safiuddin [1,2,3,*], George Abdel-Sayed [3] and Nataliya Hearn [3]

1   Angelo DelZotto School of Construction Management, George Brown College, 146 Kendal Avenue, Toronto, ON M5T 2T9, Canada

2   Department of Civil Engineering, Faculty of Engineering and Architectural Science, Ryerson University, 350 Victoria Street, Toronto, ON M5B 2K3, Canada

3   Department of Civil and Environmental Engineering, Faculty of Engineering, University of Windsor, 401 Sunset Avenue, Windsor, ON N9B 3P4, Canada; geosayed@yahoo.com (G.A.-S.); drhearn@gmail.com (N.H.)

*   Correspondence: msafiuddin@georgebrown.ca or safiq@yahoo.com; Tel.: +1-416-415-5000 (ext. 6692)

Abstract: This paper presents the water absorption and strength properties of short carbon fiber reinforced mortar (CFRM) composite. Four CFRM composites with 1%, 2%, 3%, and 4% short pitch-based carbon fibers were produced in this study. Normal Portland cement mortar (NCPM) was also prepared for use as the control mortar. The freshly mixed mortar composites were tested for workability, wet density, and entrapped air content. In addition, the hardened mortar composites were examined for compressive strength, splitting tensile strength, flexural strength, and water absorption at the ages of 7 and 28 days. The effects of different carbon fiber contents on the tested properties were observed. Test results showed that the incorporation of carbon fibers decreased the workability and wet density, but increased the entrapped air content in mortar composite. Most interestingly, the compressive strength of CFRM composite increased up to 3% carbon fiber content and then it declined significantly for 4% fiber content, depending on the workability and compaction of the mortar. In contrast, the splitting tensile strength and flexural strength of the CFRM composite increased for all fiber contents due to the greater cracking resistance and improved bond strength of the carbon fibers in the mortar. The presence of short pitch-based carbon fibers significantly strengthened the mortar by bridging the microcracks, resisting the propagation of these minute cracks, and impeding the growth of macrocracks. Furthermore, the water absorption of CFRM composite decreased up to 3% carbon fiber content and then it increased substantially for 4% fiber content, depending on the entrapped air content of the mortar. The overall test results suggest that the mortar with 3% carbon fibers is the optimum CFRM composite based on the tested properties.

Keywords: carbon fibers; fiber content; mortar composite; strength properties; water absorption

1. Introduction

Cement-based mortar is widely used because of its many beneficial properties, including good compressive strength, high fire resistance, ease of application, and low cost. Unfortunately, cement mortar possesses very low tensile and flexural strengths, limited ductility, and little resistance to cracking. It exhibits an elastic brittle behavior under tensile stresses. The primary reason for such weakness of cement mortar is its inability to resist the initiation and growth of cracks due to relatively low tensile strength [1]. Internal microcracks are inherently present in cement-based composites, such as mortar and concrete. When loaded, these microcracks propagate and gradually connect to each other. Due to poor tensile strength, the connectivity of microcracks increases and results in macrocracks that lead to the brittle fracture in cement-based composites. This inherent deficiency can be overcome by adding fibers, as they arrest the cracks and allow much larger deformation beyond the peak stress [2]. Many studies have reported that short fibers substantially

improve the performance of cement-based composites under tensile and flexural loadings [3–8]. Fibers with a length less than $\frac{1}{2}$ inch (12.7 mm) are generally defined as "short fibers" [9]. The incorporation of randomly distributed short fibers into cement-based materials increases their tensile and flexural strengths by preventing or controlling the initiation, propagation, and connectivity of cracks [10–14].

In the past, asbestos cement incorporating asbestos fibers was widely used as a fiber reinforced cement-based material [15]. Asbestos fibers were used in the construction industry for many years, particularly in thin sheet applications. Unfortunately, asbestos fibers were found to cause critical health issues, such as fibrosis and lung cancer [16]. Then researchers and practitioners looked for alternative fibers, which are medically safe for construction workers and the public. The quest for safe and sound fibers brought glass, cellulose, and steel fibers to the construction industry, but they showed certain durability issues. Glass fibers exhibited embrittlement and strength loss problems [17], cellulose fibers showed moisture sensitivity issues [18], and steel fibers exposed on the surface appeared to have corrosion problems [19]. The durability issues of the above-mentioned fibers steered the construction industry to find medically safe and physically durable fibers. Thereafter, many other fibers were incorporated into cement-based materials. Amongst these, polypropylene, polyvinyl alcohol, and carbon fibers are noteworthy.

Short carbon fibers appeared first in the construction industry of Japan, for use in cement composites, and became attractive due to their greater weatherability, thermal resistance, and long-term chemical stability compared to glass, polypropylene, and steel fibers; in addition, they exhibit good mixability and finishability when used in cement composites [20]. Carbon fibers are inert and medically safe for humans; they are physically strong like steel fibers and more durable than glass fibers in aggressive environments. Additionally, carbon fibers are lighter, and they provide higher strength than many other fibers despite their lower density [1]. Historically, polyacrylonitrile (PAN)-based carbon fibers were initially used in cement composites [21]. It can make cement-based composites more durable than polyvinyl alcohol and polypropylene due to a lower porosity, a smaller fraction of large capillary pores, and a less entrapped air content, contributing to a better impermeability [22]. However, PAN-based carbon fibers were cost-prohibitive and therefore its applications were not widespread in the construction industry. Such a barrier was removed with the invention of pitch-based carbon fibers. Due to lower prices, short pitch-based carbon fibers have been used for many building applications [20,23–25].

Extensive research studies have been carried out to investigate the tensile and flexural performance of carbon fiber reinforced cement composites [5,14,26]. In comparison, less emphasis has been placed on the compressive strength of carbon fiber composites. In the literature, the effect of carbon fibers on the compressive strength of cement-based composites is not definitive. Several studies reported that the compressive strength of cement-based composites decreases in the presence of carbon fibers [26–28]. In contrast, Li et al. [29], Zhang et al. [30] and Liu et al. [31] showed that carbon fibers can increase the compressive strength of cement-based composites, depending on the mix composition. Furthermore, limited studies have been performed to examine the absorption properties of carbon fiber reinforced cement composites, although they are quite important for certain applications, such as roof tiles, cladding walls, curtain walls, staircase walls, parapet walls, and domes, which frequently become in contact with moisture during the service life of buildings. Research on the optimization of carbon fiber content for cement-based composites is also scarce.

This study presents the performance of carbon fiber reinforced mortar (CFRM) composites with respect to absorption and strength properties. Short pitch-based carbon fibers were used to produce several mortar composites. The fresh mortars were tested for workability, wet density, and entrapped air content. Moreover, the hardened mortars were tested for water absorption, compressive strength, splitting tensile strength, and flexural strength. The effects of carbon fibers on the above-mentioned properties of mortar composites were examined. However, more emphasis was placed on the absorption and strength properties

of CFRM composites. Based on the test results, the optimum carbon fiber content for excellent performance and the best CFRM composite were identified.

2. Research Significance

The water absorption and strength properties (compressive strength, splitting tensile strength, and flexural strength) of CFRM composites were determined in the present study. These properties of CFRM composites are crucial for applications in walls (e.g., cladding walls, curtain walls, parapet walls, staircase walls), roofs, or the domes of buildings, due to exposure to snow, rain, storm, and wind loads as well as associated moisture. In this study, the effects of short pitch-based carbon fibers on the water absorption and strength properties of mortar composite were examined and the optimum fiber content was determined. Test results revealed that 3% carbon fibers provided the maximum improvement in the water absorption and compressive strength of mortar. CFRM composite including 3% carbon fibers also provided excellent splitting tensile strength and flexural strength. Hence, 3% carbon fiber can be considered as the optimum content for the best performance of CFRM composite with respect to water absorption and strength properties. Such an outcome will be useful for the mix optimization of CFRM composite. It is also hoped that the findings of this study will enrich the present state of knowledge on the use of carbon fibers and guide the construction industry towards producing and commercializing CFRM composites for various applications in buildings.

3. Materials and Methods

3.1. Constituent Materials of Various Mortar Composites

Air-dry sand (fine aggregate), normal Portland cement, silica fume, short pitch-based carbon fiber, superplasticizer, and tap water were used to produce CFRM composite mixes. The fineness modulus, saturated surface-dry (SSD) specific gravity, absorption, and total evaporable moisture content of sand were 1.97, 2.60, 1.60%, and 0.50%, respectively.

Cement conformed with the standard specification for ASTM Type I Portland cement [32]. Its specific gravity was 3.15. The chemical composition of the cement is given in Table 1. The amounts of magnesium oxide (MgO) and sulfur trioxide (SO_3) were less than the maximum permissible limits of 6% and 3%, respectively.

Table 1. Typical chemical composition of normal Portland cement and silica fume.

Normal Portland Cement		Silica Fume	
Chemical Component	**Mass Content (%)**	**Chemical Component**	**Mass Content (%)**
Calcium oxide (CaO)	64.5	Silicon dioxide (SiO_2)	91.1
Silicon dioxide (SiO_2)	20.0	Aluminum oxide (Al_2O_3)	1.4
Aluminum oxide (Al_2O_3)	5.6	Ferric oxide (Fe_2O_3)	1.2
Ferric oxides (Fe_2O_3 and FeO)	3.5	Calcium oxide (CaO)	0.4
Magnesium oxide (MgO)	2.0	Magnesium oxide (MgO)	0.9
Sulfur trioxide (SO_3)	1.5	Sodium oxide (Na_2O)	0.5
Alkaline oxide (Na_2O and K_2O)	0.9	Potassium oxide (K_2O)	1.5
Igneous loss	2	Igneous loss	3.0

Silica fume complied with the ASTM standard specification given in ASTM C1240-05 [33]. Its specific gravity was 2.20. The chemical composition of silica fume is shown in Table 1. The silica (SiO_2) content of silica fume was 91.1%, which is significantly more than 85%, the minimum required content, as specified in ASTM C1240-05 [33]. In addition, the available alkalis as Na_2O were 0.5% (less than the maximum permissible limit of 1.5%) and the igneous loss was 3% (less than the maximum permissible limit of 6%).

Chopped carbon fibers were used to prepare CFRM composites. They were 10 mm long and had a filament diameter of 17 μm. The specific gravity, tensile strength, and tensile modulus of carbon fibers were 1.85, 1770 MPa, and 180 GPa, respectively. The fibers were insoluble in water.

The tap water had a turbidity of 2.07 NTU and its total dissolved solids was 18 mg/L. A naphthalene-based superplasticizer was used with water to ensure the compactability of the freshly mixed mortar composites. The specific gravity of superplasticizer was 1.20 and it was 100% soluble in water.

3.2. Mix Proportions of Various Mortar Composites

In total, five mortar composites were designed with 0–4% carbon fibers based on a sand/binder ratio of 0.50 and a water/binder ratio of 0.35. The mortar composite with 0% carbon fiber was considered as the control mix and designated as NPCM (normal Portland cement mortar). The other four mortar composites included 1%, 2%, 3%, and 4% carbon fibers by volume and they were, respectively, designated as CFRM1, CFRM2, CFRM3, and CFRM4. All mortar composites included 15% silica fume as a partial replacement of cement. The weight-based amounts of the constituent materials for a unit volume (1 m^3) of mortar composite were determined based on the absolute volumes of all materials. The mix proportions of the mortar composites including the dosages of superplasticizer were finalized based on the trial mixes. The entrapped air content was included in the unit volume of mortar composite. For NPCM, 1% entrapped air content was assumed. In the cases of CFRM1, CFRM2, CFRM3, and CFRM4, the assumed entrapped air contents were 4%, 5%, 6%, and 7%, respectively. The mix proportions of various mortar composites are shown in Table 2. It is worth mentioning that the proportions of sand shown were applicable only in SSD condition. However, air-dry sand was used during batching. Air-dry sand absorbed some water during mixing. Conversely, liquid superplasticizer contributed some water to the mortar during mixing. Therefore, the amounts of water and air-dry sand were corrected for all mortar composites considering the water absorption of sand and the water contribution of superplasticizer.

Table 2. Mix proportions of various mortar composites.

Type of Mortar Composite	Cement (kg/m^3)	Sand (kg/m^3)	Silica Fume (kg/m^3)	Carbon Fiber (Vol. %)	Water (kg/m^3)	SP (%B)
NPCM	955.9	562.3	168.7	0	393.6	1
CFRM1	917.2	539.6	161.9	1	377.7	2
CFRM2	898.0	528.2	158.5	2	369.8	3
CFRM3	878.6	516.9	155.1	3	361.8	4
CFRM4	859.4	505.5	151.7	4	353.9	5

3.3. Preparation and Testing of Fresh Mortar Composites

The component materials were mixed in a pan-type mixer. The capacity of the mixer was 0.1 m^3 but the batch volume varied in the range of 0.028–0.032 m^3. Sand, cement, and silica fume were weighed, put in the mixer, and then mixed 1 min together by adding half of the water content. Keeping the mixer running, the remaining half of the water content blended with the dosage of superplasticizer was added gradually within 1 min, followed by additional mixing for 1 min. Thereafter, carbon fibers were manually spread in the running mixer by 2 min. This step was followed for all CFRM composites but skipped for NPCM. The mixing operation was completed by 4 min for NPCM and 6 min for CFRM composites. Immediately after the completion of mixing, the fresh mortar composites were sampled and tested for workability (slump), wet density, and entrapped air content. The details of these tests can be found in Safiuddin et al. [34].

3.4. Casting and Conditioning of Test Specimens

The fresh mortar composite mixes were used to prepare the test specimens. Beam, cylinder, and cube specimens were prepared for testing the hardened mortar composites. The beam specimens of 400 mm (length) × 75 mm (width) × 100 mm (height) dimensions were cast for the flexure test. The cylinder specimens of 100 mm (diameter) × 200 mm

(height) size were prepared for the compression and splitting tension tests. The smaller cubes for the water absorption test were not cast directly. They were processed from 150-mm parent cubes, which were cast and cured in water. At the day of testing, 150-mm parent cubes were cut to obtain 50-mm smaller cubes for the water absorption test. Six 50-mm cubes were obtained from a 150-mm parent cube.

Beam and parent cube specimens were cast in reusable cast iron molds whereas cylinder specimens were fabricated in single-use plastic molds. ASTM standard practice [35] was followed for molding the test specimens in the laboratory, with some exceptions for the control mortar. Three layers of filling were used for the cylinder and parent cube specimens whereas two layers were used in the case of beam specimens. A vibrating table was used for the compaction of CFRM composites. Each layer was vibrated until a thin layer of bleed water appeared on the surface. In the case of the control mortar (NPCM), all specimens were cast in one layer without any vibration, because the mortar was highly workable.

Beam and cube specimens were covered with wax papers and polyethylene sheets after 30 to 45 min from casting, and then left in their molds until the age of 24 h. The cylinder specimens were sealed immediately using the lids and left undisturbed for 24 h. All the specimens were removed from their molds at the age of 24 h, marked, and transferred for curing. ASTM standard practice [35] was followed in curing the specimens, except for using any calcium hydroxide in water. The demolded specimens were placed inside the curing tanks. Water curing by ponding was used to cure the specimens until the time of testing. The curing temperature was 23 ± 2 °C.

3.5. Testing of Various Hardened Mortar Composites

3.5.1. Compression Test

The compressive strength of hardened mortar composites was determined at the ages of 7 and 28 days in accordance with ASTM C39/C39M-01 [36]. Triplicate 100 mm (diameter) × 200 mm (height) cylinder specimens were used for each testing age. Prior to the compression test, the cylinders were dried at room temperature and capped by sulfur mortar in accordance with ASTM standard practice [37]. During testing, the test cylinders were placed individually in the center position of the lower platen of compression machine. Then uniaxial loading was applied steadily to increase the stress at a rate of 0.14 to 0.34 MPa/s. The maximum load taken by the individual specimen was indicated in the load scale. It was noted and used to compute the compressive strength. The average compressive strength was calculated from the strength values of triplicate cylinder specimens.

3.5.2. Splitting Tension Test

The splitting tensile strength of hardened mortar composites was determined at 7 and 28 days according to ASTM C496/C496M-04 [38]. Triplicate 100 mm (diameter) × 200 mm (height) cylinder specimens were used for every testing age. During testing, each cylinder was placed horizontally in the center position of the lower platen of compression machine. Two light wooden blocks were used to keep the specimen in the central position. The load was applied continuously and without shock to induce the stress at a constant rate within the range of 689 to 1380 kPa/min. The loading was continued until the failure of test specimen. The maximum applied load indicated by the testing machine was recorded and used to calculate the splitting tensile strength. The average splitting tensile strength was determined from the test results of triplicate cylinder specimens.

3.5.3. Flexure Test

The flexural strength of hardened mortar composites was examined at the ages of 7 and 28 days according to ASTM C1018-97 [39]. Duplicate 400 mm (length) × 75 mm (width) × 100 mm (height) beam specimens were used for each testing age. The beam specimens were tested immediately after removal from the curing tank. In each test case, the beam specimen was turned on its side with respect to its position as molded and was centered in the supporting block. Immediately, the load-applying block was brought onto

the beam specimen at the two third points. Then the load was applied continuously by a hydraulic jack until the breakage of the specimen. The loading system included a load-cell of 111.2 kN (25 kips) capacity. The maximum load for individual beam specimen was recorded during testing to calculate its flexural strength. The average flexural strength was determined from the test results of duplicate beam specimens.

3.5.4. Water Absorption Test

The water absorption of hardened mortar composites was tested at 7 and 28 days in accordance with Method A, as specified in ASTM C1195-03 [40]. Triplicate 50-mm cube specimens were used for each testing age. Before starting the test, the specimens were oven-dried at a temperature of 105 ± 5 °C for 24 h and then allowed to cool to room temperature for 30 min. The specimens were weighed separately and then immersed in distilled water at 23 ± 2 °C for 48 h. Thereafter, the specimens were removed from the water and weighed in SSD condition to determine the amount of absorbed water. The water absorption of each specimen was calculated based on it absorbed water and oven-dried weight. The average water absorption was obtained from the absorption results of triplicate cube specimens.

4. Test Results and Discussion

4.1. Fresh Properties

The slump, wet density, and entrapped air content results of various mortars are presented in Table 3. These fresh properties of mortar composites are not the focus of this study. The detailed discussion on the fresh properties can be found in Safiuddin et al. [34]. In general, the slump of mortar composite decreased with the increased volume content of carbon fibers. It implies that the increase in carbon fiber content lessened the workability of mortar due to large surface area and interlocking of the fibers. Hence, higher dosages of superplasticizer were required for CFRM composites, as evident from Table 3, to make them adequately workable for compaction by vibration. The use of the same dosage of superplasticizer was not practicable for all mortar composite mixes due to different contents of carbon fibers.

Table 3. Fresh properties of various mortar composites.

Type of Mortar Composite	Slump (cm)	Wet Density (kg/m³)	Entrapped Air Content (%)
NPCM	26.5	2070.7	1.0
CFRM1	19	1968.8	5.2
CFRM2	12.5	1947.7	6.4
CFRM3	6.5	1989.9	4.2
CFRM4	2.5	1905.5	7.9

The wet density of CFRM composite was lower than that of the control mortar composite (NPCM) due to the light weight of carbon fibers compared to the other solid ingredients of the mortar. Moreover, the entrapped air content was relatively high in the mortars including carbon fibers (refer to Table 3). The entrapped air content of mortar composite increased largely with the increase in carbon fiber content due to lower workability. It infers that the compaction effort was not enough to take all the entrapped air bubbles out of the CFRM composites possessing a lower slump. Relevantly, the increased entrapped air content caused to decrease the wet density of CFRM composite. However, it was noticed that the mortar composite with 3% carbon fibers had the highest wet density and the lowest entrapped air content compared to the other mortar composites including 1%, 2%, and 4% carbon fibers.

4.2. Compressive Strength

The average compression test results are given in Table 4. The effect of different carbon fiber contents on the compressive strength of mortar is presented in Figure 1. It is evident from Figure 1 that the compressive strength increased linearly with the incorporation of carbon fibers up to 3% fiber content, and then decreased sharply. Ohama et al. [41] obtained a similar trend of results for carbon fiber reinforced cement composites. In their study, the compressive strength also dropped beyond 3% fiber content. This suggests that the effect of carbon fibers is not always conducive to the compressive strength of mortar composite. It largely depends on the workability, degree of compaction, density, and entrapped air content of mortar. Even if the fibers increase the compressive strength, it is relatively low, as compared to the increases in splitting tensile strength and flexural strength. This is because the fibers cannot resist compressive load as effectively as they endure tensile and flexural loads.

Table 4. Compressive strength and strengthening factors of various mortar composites.

Type of Mortar	Compressive Strength (MPa)		Strengthening Factor	
	7 Days	28 Days	7 Days	28 Days
NPCM	34.37	39.05	1.00	1.00
CFRM1	40.04	49.77	1.15	1.28
CFRM2	44.76	56.75	1.30	1.45
CFRM3	49.11	62.99	1.43	1.61
CFRM4	34.94	47.72	1.02	1.22
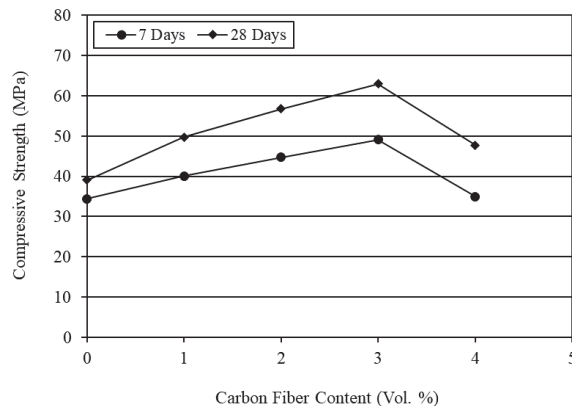
Figure 1. Effect of carbon fiber content on the compressive strength of mortar composite.

The strengthening factors of various CFRM composites for compression were found after dividing their compressive strength values by the compressive strength of NPCM and are shown in Table 4. It can be seen from Table 4 that 3% carbon fibers provided the maximum increase in compressive strength and the extent of strengthening was 61% at the age of 28 days. The wet density and entrapped air content results of the CFRM composite with 3% carbon fibers were linked with its highest compressive strength. In general, the rise in density and the reduction in entrapped air content increased the compressive strength. In contrast, the CFRM composite with 4% carbon fibers content (CFRM4) had a relatively low compressive strength; the strengthening factor for this mortar composite was about 22%, as evident from Table 4. The main reason for the lower compressive strength of CFRM4 is that the degree of compaction was not good because of the poor workability. Therefore, excessive air bubbles remained entrapped within the mix (refer to Table 3) and the density decreased, which eventually caused a negative effect on the compressive strength of mortar composite.

The reduction in the compressive strength of mortar for more than 3% carbon fibers can also be due to the retarding effect of superplasticizer as observed by Pigeon et al. [42]. Since a relatively high dosage of superplasticizer was used in the mix with 4% carbon fibers, it may alter the composition of calcium silicate hydrate (CSH, a strength-contributing hydration product) and retard the hydration of cement significantly, thus reducing the compressive strength of mortar. The overall results suggest that carbon fibers can improve the compressive strength of mortar if used with a volume content that does not cause any adverse effect on its workability and entrap excessive air bubbles inside the mix.

The ductility of mortar was much increased by carbon fibers, as reveled from the failure modes of different cylindrical specimens in compression test. NPCM exhibited a brittle failure as shown in Figure 2a. On the other hand, CFRM composite at first yielded and then progressively cracked as shown in Figure 2b. The standard compression test under uniaxial loading produced a combination of shear failure near the ends with lateral swelling and cracking in the central portion of the specimen. It suggests that the fibers had a reinforcing effect in the lateral direction. However, this effect was predominant in the CFRM composites with 3% and 4% fiber contents. It indicates that the fiber content has a significant influence on the lateral strain capacity and thereby on the ductility of CFRM composite.

(**a**)   (**b**)
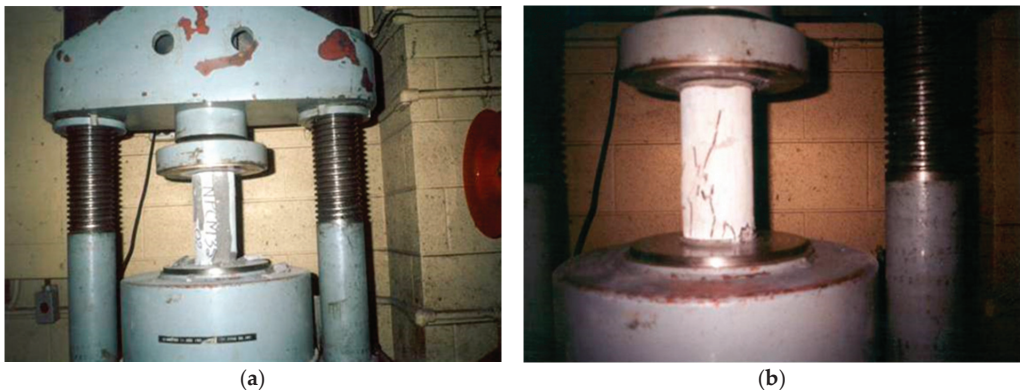
Figure 2. Failure mode of the specimens in compression test—(**a**) NPCM and (**b**) CFRM.

The increase in ductility as observed during the compression test was largely due to the increased resistance of carbon fibers against the growth of cracks. The resistance to crack propagation increased with a greater fiber content. Therefore, the improvement in ductility was significant with a greater fiber content. Shah and Chandra [43] showed that the volume of compressed concrete starts to dilate under loading, and this dilation is related to the slow growth of microcracks within the cement composite. The incorporation of carbon fibers in the cement mortar delayed and reduced the volume dilation. As a result, the improved ductility behavior of CFRM composite was noticed in the cylinder specimens under compression test.

4.3. Splitting Tensile Strength

The average results of splitting tension test are given in Table 5. The effect of different carbon fiber contents on the splitting tensile strength of mortar composite is presented in Figure 3. It is obvious from Figure 3 that the splitting tensile strength of CFRM composite increased almost linearly with the increase in carbon fiber content. A similar trend of increase in tensile strength was reported in several past studies [5,30,44–46].

Table 5. Splitting tensile strength and strengthening factors of various mortar composites.

Type of Mortar	Tensile Strength (MPa)		Strengthening Factor	
	7 Days	28 Days	7 Days	28 Days
NPCM	3.29	4.31	1.00	1.00
CFRM1	4.36	5.19	1.33	1.21
CFRM2	4.80	5.76	1.46	1.34
CFRM3	5.88	6.43	1.79	1.49
CFRM4	6.26	6.87	1.90	1.59
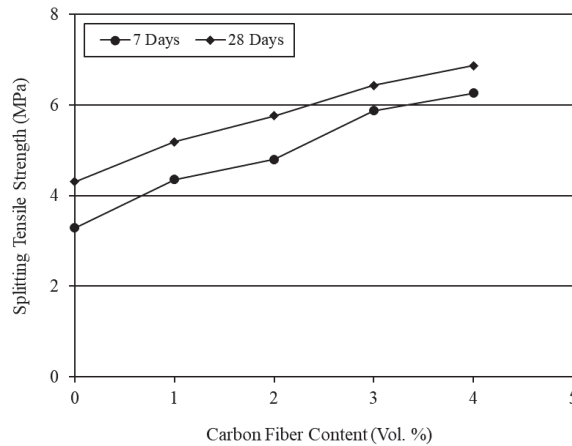
Figure 3. Effect of carbon fiber content on the splitting tensile strength of mortar composite.

The strengthening factors of various CFRM composites for tension were found after dividing their tensile strength by the tensile strength of NPCM and are shown in Table 5. It is evident from Table 5 that the splitting tensile strength of CFRM composite at 4% carbon fibers was 1.5 to 2 times greater than that of NPCM. This increase in tensile strength is due to the bridging action of carbon fibers during crack formation. However, the increase in tensile strength was less compared with the findings of other researchers who conducted direct tension test using dumbbell specimens [14,46]. The splitting tension test was conducted in the present study to determine the tensile strength of CFRM composite. Neville [47] mentioned that the splitting tension test yields a lower value of tensile strength in the case of mortar. This is perhaps due to the absence of large particles such as coarse aggregates near the surface onto which the load is applied. In addition, it can be seen from Table 5 that the rate of increase in splitting tensile strength was greater at the age of 7 days although the maximum tensile strength was obtained at 28 days. This is because the gain in tensile strength is usually high at early ages due to a higher degree of cement hydration, which slows down at later ages.

The increase in tensile strength is not attributed to the incorporation of carbon fibers alone. It does not only depend on the volume content of carbon fibers but also on the interfacial bond between the constituents. Katz et al. [48] and Park et al. [14] reported that the densification of the matrix surrounding carbon fibers improves their interfacial bond with the other solid ingredients of mortar and thereby enhances the pull-out strength of the fibers. The presence of silica fume in CFRM composite results in a densification of the matrix around carbon fibers and therefore the contact area between fibers and adjacent materials is increased and a stronger bond is established. The interfacial bond is also strengthened by additional CSH formed from the pozzolanic reaction between silica fume and calcium hydroxide ($Ca(OH)_2$), which is liberated during cement hydration [12]. The interlocking of sand particles and carbon fibers can also improve the interfacial bond; furthermore, some of the fine cement grains and finer silica fume particles might penetrate the holes or

surface grooves existing on the carbon fibers; consequently, the surface roughness of fibers increases and therefore the bond between carbon fibers and matrix can be enhanced [1]. All these effects might eventually lead to a greater improvement in the tensile strength of CFRM composite.

The ductile behavior of CFRM composite was also observed in the cylinder specimens under splitting tension test. The failure modes for NPCM and CFRM composites are shown in Figure 4. The cylinder specimens used in the splitting tension test of NPCM failed suddenly. The failure mode was brittle, and the cylinders were completely split as shown in Figure 4a. Conversely, the failure mode for the cylinders used in the splitting tension test of CFRM composites was ductile under the applied load. This was evidenced by the increased ability of the cylinders to deform markedly under the applied load without splitting. The cylinder specimens failed showing a visible vertical crack throughout the axis but did not fall apart, as obvious from Figure 4b.

(**a**) (**b**)
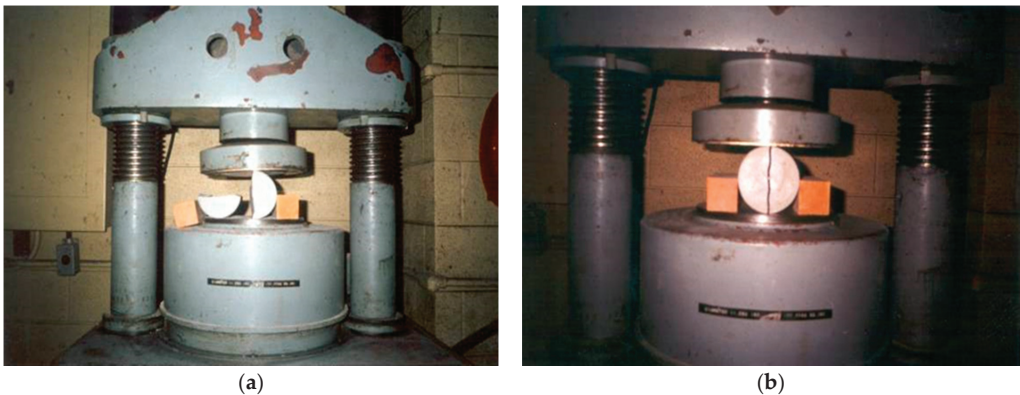
Figure 4. Failure mode of the specimens in splitting tension test—(**a**) NPCM and (**b**) CFRM.

4.4. Flexural Strength

The flexure test was conducted by third-point loading arrangement as shown in Figure 5. The third-point loading test usually gives more reliable results. This is because the probability of a weak element being subjected to the critical stress is considerably greater under two third-point loads [47]. In third-point loading, the middle-third of the beam is subjected to the maximum bending stress. Therefore, the critical crack may appear at any section within the middle third or it could start in the middle third and then extend to one of the two end-thirds of the beam. In the present study, all specimens failed with a fracture occurring completely within the middle third of the beams; such an example is shown in Figure 5. This indicates that the bottom face of the middle third of the beam experienced the maximum bending stress.

The average flexure test results are given in Table 6. The effect of carbon fibers is graphically presented in Figure 6. It is obvious from Figure 6 that the flexural strength of CFRM composite increased non-linearly with the increase in carbon fiber content. A similar trend was observed in several earlier studies [8,26,29,44,46].
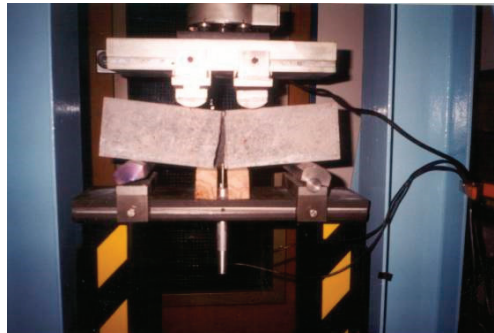
Figure 5. Failure mode of the specimen in flexure test.

Table 6. Flexural strength and strengthening factors of various mortar composites.

Type of Mortar	Flexural Strength (MPa)		Strengthening Factor	
	7 Days	28 Days	7 Days	28 Days
NPCM	4.22	5.85	1.00	1.00
CFRM1	6.68	8.04	1.58	1.37
CFRM2	7.74	9.01	1.83	1.54
CFRM3	8.50	9.93	2.01	1.70
CFRM4	8.99	10.41	2.13	1.78
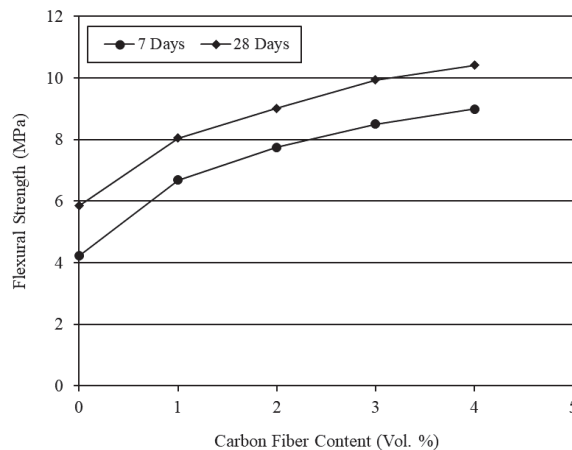
Figure 6. Effect of carbon fiber content on the flexural strength of mortar composite.

The strengthening factors of various CFRM composites for flexure were obtained after dividing their flexural strength values by the flexural strength of NPCM and are shown in Table 6. The incorporation of carbon fibers significantly increased the flexural strength of CFRM composite. It is also obvious from Table 6 that the strengthening factors were greater at 7 days, although the highest level of flexural strength was obtained at the age of 28 days. The mortar composite containing 4% carbon fibers provided the maximum flexural strength. In general, about a two-fold increase in flexural strength was observed for the carbon fibers at 4% volume content. The increase in flexural strength with the incorporation of carbon fibers is mainly due to the increased reinforcing and bonding effects of fibers resulting from the densified microstructure of mortar brought by silica fume and superplasticizer.

The flexural strength of CFRM composite was much higher than its splitting tensile strength, as evident from Figure 7. This is due to the disparity in the orientation of carbon fibers in test specimens. Sakai et al. [49] reported that carbon fibers tend to be oriented at right angle to the vibrational direction of a vibrator used during molding. However, this tendency is expected to be affected by the dimensions of the specimen. The compaction by vibration induced a degree of preferential 2D-fiber orientation parallel to the length of beam specimens, which were used for the flexure test. This was also evidenced by the presence of carbon fibers oriented at right angle to the fracture faces of the beam. Thus, the fiber orientation coincided with the direction of the major tensile stress and resulted in a greater flexural strength. On the other hand, the carbon fibers were oriented in a 3D-random fashion in the cylinder specimens used for the splitting tension test. This was confirmed as some of the carbon fibers were observed lying on the fracture (split) faces of the cylinder. Perhaps, the lower dimension (diameter) of the cylinder specimens lying in the horizontal plane during molding hindered the orientation of carbon fibers in a direction perpendicular to the pathway of vibration. Consequently, the reinforcing effectiveness of carbon fibers in the cylinder specimens was comparatively low towards the direction of the major tensile stress. Therefore, the lower values of splitting tensile strength were obtained for the mortar composites as compared to their flexural strength.
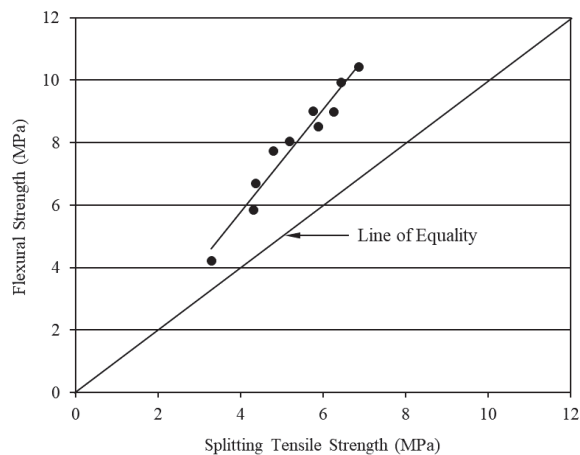
Figure 7. Flexural strength versus splitting tensile strength of CFRM composite.

The assumption of linear stress distribution in the beam specimens is another reason for the higher flexural strength of CFRM composites compared with their splitting tensile strength [1]. The flexural strength was calculated based on the elastic beam theory, in which the stress–strain relation is assumed to be linear. It implies that the ultimate flexural stress in the beam specimens is supposed to be proportional to the distance from its neutral axis. However, the linear stress–strain relation is no longer valid when the first crack appears. Therefore, the actual stress block between the first-crack and maximum loads becomes parabolic instead of being triangular. Thus, the ultimate flexural strength was overestimated because of the assumption of linear stress distribution. Furthermore, the maximum fiber stress reached in the flexure test may be higher than that in the splitting tension test because the fibers and other less-stressed materials near to the neutral axis of the beam specimen hinder the propagation of cracks. In particular, the carbon fibers aligned in the direction of the major tensile stress effectively slow down the formation of the first crack, impede the propagation of cracks, and thus delay the failure of test specimen. As a result, the ultimate flexural strength becomes greater than the splitting tensile strength.

4.5. Water Absorption

The average test results for water absorption are given in Table 7. The effect of carbon fiber content is shown in Figure 8. It can be seen from Figure 8 that the water absorption decreased with the incorporation of carbon fibers up to 3% fiber content, and then increased at 4% fiber content. Very few studies have been carried out to examine the water absorption of CFRM composite. Ohama et al. [41] performed the water absorption test for carbon fiber reinforced cement composite and found that the water absorption tends to decrease with increasing carbon fiber content up to 5%. In the present study, a reduction in the water absorption was observed for the mortar composites including 1–3% carbon fiber contents. In contrast, the water absorption of the CFRM composite with 4% carbon fibers was relatively high, as obvious from Figure 8.

Table 7. Water absorption and water resistance factors of various mortar composites.

Type of Mortar	Water Absorption (wt.%)		Water Resistance Factor	
	7 Days	28 Days	7 Days	28 Days
NPCM	14.44	13.80	1.00	1.00
CFRM1	14.33	13.47	1.01	1.03
CFRM2	13.67	12.68	1.06	1.09
CFRM3	12.45	11.23	1.16	1.23
CFRM4	15.41	15.56	0.94	0.89
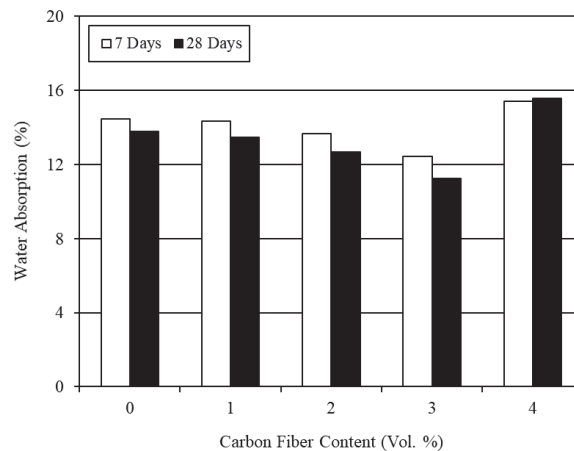
Figure 8. Effect of carbon fiber content on the water absorption of mortar composite.

The water resistance factors of various CFRM composites were found after dividing the water absorption of NPCM by the water absorption of each CFRM and are shown in Table 7. It is evident from Table 7 that the resistance to water absorption increased considerably at 3% carbon fiber content. On the contrary, the resistance to water absorption decreased for 4% carbon fiber content. This can be due to the increased number of capillary pores and air-voids existing in the mortar composite as realized from the test results of wet density and entrapped air content. The porosity largely governs the water absorption of mortar—the larger the porosity, the greater the water absorption. The density and entrapped air content results imply that the CFRM composite with 3% carbon fiber had lesser capillary pores and air-voids due to a higher degree of compaction at adequate workability. Hence, it provided the highest resistance to water absorption. Moreover, the water resistance factor at 28 days was higher than that at 7 days. This is because more CSH resulting from cement hydration and pozzolanic reaction filled in the capillary pores further, thus decreasing the porosity of mortar composite at 28 days.

The use of superplasticizer and silica fume in CFRM composite decreased the number of capillary pores in its matrix. Superplasticizer substantially decreases the water content and thus diminishes the overall porosity of mortar. It also reduces bleeding and thus assures a better adhesion among sand particles, carbon fibers, and cement paste. Moreover, silica fume contributes to reduce the porosity of mortar composite. It also improves the interfaces of sand particles and carbon fibers. However, all these improvements largely depend on the workability and degree of compaction. Workability and compaction play important roles in reducing the capillary pores and air-voids in mortar. As the mortar composite with 3% carbon fibers possessed adequate workability, the fresh mortar became well-compacted under vibration. Accordingly, the water absorption of the hardened mortar composite incorporating 3% carbon fibers decreased. Conversely, excessive capillary pores and air-voids were present in the mortar composite with 4% carbon fibers as it was too stiff in the fresh state for easy placing and sufficient compaction due to the poor workability. As a result, the maximum water absorption was obtained for CFRM4.

5. Optimum Fiber Content and Best Mortar Composite

The best mortar composite was derived by judging the overall performance in terms of workability (slump), wet density, entrapped air content, compressive strength, splitting tensile strength, flexural strength, and water absorption. The mortar composite with 3% carbon fibers (CFRM3) provided adequate slump for placing and compaction by vibration, had lower entrapped air content and higher wet density, gave the maximum compressive strength, possessed excellent splitting tensile strength and flexural strength, and offered reduced water absorption thus exhibiting the potential for excellent durability, compared with the other mortars incorporating 1%, 2%, and 4% carbon fibers. Therefore, the optimum content of carbon fibers was 3% and CFRM3 can be considered as the best mortar composite in the context of the present study.

6. Conclusions

The following conclusions are drawn based on the findings from the present study on CFRM composite.

1. The workability of mortar composite decreased with higher content of carbon fibers due to large surface area and interlocking of the fibers; consequently, the entrapped air content of CFRM composite was greater and therefore its wet density became lower than that of NPCM.
2. The compressive strength of mortar composite increased with the incorporation of carbon fibers when the fresh mortar was sufficiently workable and well-compacted; CFRM3 with 3% carbon fibers possessed the maximum level of compressive strength.
3. The splitting tensile strength and flexural strength of mortar composite increased significantly with higher content of carbon fibers due to their greater resistance to cracking and improved bond with the other solid constituents of the mortar.
4. Considerable strengthening was possible by reinforcing the cement mortar matrix with short pitch-based carbon fibers as they bridged the microcracks, resisted the propagation of these tiny cracks, and impeded the formation of macrocracks.
5. The incorporation of carbon fibers diminished the water absorption and thus enhanced the durability of mortar when a sufficient workability was maintained for good compaction.
6. The mortar composite with 3% carbon fibers can be considered as the optimum CFRM composite based on its performance with respect to workability, wet density, entrapped air content, compressive strength, splitting tensile strength, flexural strength, and water absorption.

References

1. Safiuddin, M.; Abdel-Sayed, G.; Hearn, H. *High Performance Mortars with Short Carbon Fibers: Properties and Mix Optimization*; Lambert Academic Publishing AG & Co. KG: Saarbrücken, Germany, 2010.
2. Betterman, L.R.; Ouyang, C.; Shah, S.P. Fiber-mortar interaction in microfiber-reinforced mortar. *Adv. Cem. Based Mater.* **1995**, *2*, 53–61. [CrossRef]
3. Dinh, N.H.; Park, S.-H.; Choi, K.-K. Effect of dispersed micro-fibers on tensile behavior of uncoated carbon textile-reinforced cementitious mortar after high-temperature exposure. *Cem. Concr. Compos.* **2021**, *118*, 103949. [CrossRef]
4. Du, Q.; Cai, C.; Lv, J.; Wu, J.; Pan, T.; Zhou, J. Experimental investigation on the mechanical properties and microstructure of basalt fiber reinforced engineered cementitious composite. *Materials* **2020**, *13*, 3796. [CrossRef]
5. Graham, R.K.; Huang, B.; Shu, X.; Burdette, E.G. Laboratory evaluation of tensile strength and energy absorbing properties of cement mortar reinforced with micro- and meso-sized carbon fibers. *Construct. Build. Mater.* **2013**, *44*, 751–756. [CrossRef]
6. Pierre, P.; Pleau, R.; Pigeon, M. Mechanical properties of steel microfiber reinforced pastes and mortars. *J. Mater. Civ. Eng.* **1999**, *11*, 317–324. [CrossRef]
7. Soroushian, P.; Khan, A.; Hsu, J.W. Mechanical properties of concrete materials reinforced with polypropylene or polyethylene fibers. *ACI Mater. J.* **1992**, *89*, 535–540.
8. Banthia, N.; Sheng, J. Strength and toughness of cement mortars reinforced with micro-fibers of carbon, steel, and polypropylene. In Proceedings of the Second Canadian Symposium on Cement and Concrete, University of British Columbia, Vancouver, BC, Canada, 24–26 July 1991; pp. 75–83.
9. Etbridge, M.D.; Krifa, M. Renewed focus on short fibers. In *Textile Topics*; International Textile Center, Texas Tech University: Lubbock, TX, USA, 2004; Volume 2004-3.
10. George, M.; Sathyan, D.; Mini, K.M. Investigations on effect of different fibers on the properties of engineered cementitious composites. *Mater. Today Proc.* **2021**, *42*, 1417–1421. [CrossRef]
11. Deng, M.; Dong, Z.; Zhang, C. Experimental investigation on tensile behavior of carbon textile reinforced mortar (TRM) added with short polyvinyl alcohol (PVA) fibers. *Construct. Build. Mater.* **2020**, *235*, 117801. [CrossRef]
12. Safiuddin, M.; Yakhlaf, M.; Soudki, K.A. Key mechanical properties and microstructure of carbon fibre reinforced self-consolidating concrete. *Construct. Build. Mater.* **2018**, *164*, 477–488. [CrossRef]
13. Toutanji, H.A.; El-Korchi, T.; Katz, R.N. Strength and reliability of carbon-fiber reinforced cement composites. *Cem. Concr. Compos.* **1994**, *2*, 15–21. [CrossRef]
14. Park, S.B.; Lee, B.I.; Lim, Y.S. Experimental study on the engineering properties of carbon fiber reinforced cement composites. *Cem. Concr. Res.* **1991**, *21*, 589–600. [CrossRef]
15. Marikunte, S.; Shah, S.P. High performance cement-based composites for the future. In *Fiber Reinforced Concrete: Modern Developments*; The University of British Columbia: Vancouver, BC, Canada, 1995; pp. 13–27.
16. Gilson, J.C. Health hazards of asbestos. *Compos.* **1972**, *3*, 57–59. [CrossRef]
17. Bentur, A. Mechanisms of potential embrittlement and strength loss of glass fiber reinforced cement composites. In Proceedings of the Symposium on Durability of Glass Fiber Reinforced Cement Concrete, Precast/Prestressed Concrete Institute, Chicago, IL, USA, 12–15 November 1985; pp. 109–123.
18. Soroushian, P.; Marikunte, S. Cellulose fiber reinforced cement composites: State-of-the-art. In Proceedings of the First Canadian University/Industry Workshop on Fibre Reinforced Concrete, Québec, BC, Canada, 28–29 October 1991; pp. 44–58.

19. ACI 544. *1R-96 (Reapproved 2002). Report on Fiber Reinforced Concrete*; American Concrete Institute: Detroit, MI, USA, 2002.
20. Banthia, N. Pitch-based carbon fiber reinforced cements: Structure, performance, applications and research needs. *Can. J. Civ. Eng.* **1992**, *19*, 26–38. [CrossRef]
21. Ali, M.A.; Majumder, A.J.; Rayment, D.L. Carbon fiber reinforcement of cement. *Cem. Concr. Res.* **1972**, *2*, 201–212. [CrossRef]
22. Wang, L.; He, T.; Zhou, Y.; Tang, S.; Tan, J.; Liu, Z.; Su, J. The influence of fiber type and length on the cracking resistance, durability and pore structure of face slab concrete. *Construct. Build. Mater.* **2021**, *282*, 122706. [CrossRef]
23. Akihama, S.; Suenaga, T.; Nakagawa, H. Carbon fiber reinforced concrete. *Concr. Int.* **1988**, *10*, 40–47. [CrossRef]
24. Morgan, D.R.; Razaqpur, A.G.; Crimi, J. Fibre reinforced concrete products. In *Advanced Composite Materials in Bridges & Structures*; Canadian Society for Civil Engineering: Montreal, QC, Canada, 1992; pp. 18–32.
25. Banthia, N.; Genois, I. Pitch-based carbon fiber reinforced cement composites. In *Fiber Reinforced Concrete: Modern Developments*; The University of British Columbia: Vancouver, QC, Canada, 1995; pp. 213–228.
26. Donnini, J.; Bellezze, T.; Corinaldesi, V. Mechanical, electrical and self-sensing properties of cementitious mortars containing short carbon fibers. *J. Build. Eng.* **2018**, *20*, 8–14. [CrossRef]
27. Niu, M.; Zhang, J.; Li, G.; Song, Z.; Wang, X. Mechanical properties of polyvinyl alcohol fiber-reinforced sulfoaluminate cement mortar containing high-volume of fly ash. *J. Build. Eng.* **2021**, *35*, 101988. [CrossRef]
28. Vipulanandan, C.; Garas, V. Electrical resistivity, pulse velocity, and compressive properties of carbon fiber-reinforced cement mortar. *J. Mater. Civ. Eng.* **2008**, *20*, 93–101. [CrossRef]
29. Li, Y.-F.; Lee, K.-F.; Ramanathan, G.K.; Cheng, T.-W.; Huang, C.-H.; Tsai, Y.-K. Static and dynamic performances of chopped carbon-fiber-reinforced mortar and concrete incorporated with disparate lengths. *Materials* **2021**, *14*, 972. [CrossRef]
30. Zhang, X.; Ge, L.; Zhang, Y.; Wang, J. Mechanical properties of carbon-fiber RPC and design method of carbon-fiber content under different curing systems. *Materials* **2019**, *12*, 3759. [CrossRef] [PubMed]
31. <named-content content-type="background:white">Liu, D.J.; Chen, M.J.; Xue, L.; He, F.; Hu, J. The effect of the carbon fiber on concrete compressive strength. *Adv. Mater. Res.* **2018**, *1145*, 106–111.
32. ASTM C150-07. *Standard Specification for Portland Cement*; ASTM International: West Conshohocken, PA, USA, 2007.
33. ASTM C1240-05. *Standard Specification for Use of Silica Fume as a Mineral Admixture in Hydraulic Cement Concrete, Mortar, and Grout*; ASTM International: West Conshohocken, PA, USA, 2005.
34. Safiuddin, M.; Abdel-Sayed, G.; Hearn, N. Effects of pitch-based short carbon fibers on the workability, unit weight, and air content of mortar composite. *Fibers* **2018**, *6*, 63. [CrossRef]
35. ASTM C192/C192M-06. *Standard Practice for Making and Curing Concrete Test Specimens in the Laboratory*; ASTM International: West Conshohocken, PA, USA, 2006.
36. ASTM C39/C39M-01. *Standard Test Method for Compressive Strength of Cylindrical Concrete Specimens*; ASTM International: West Conshohocken, PA, USA, 2001.
37. ASTM C617-98 (Reapproved 2003). *Standard Practice for Capping Cylindrical Concrete Specimens*; ASTM International: West Conshohocken, PA, USA, 2003.
38. ASTM C496/C496M-04. *Standard Test Method for Splitting Tensile Strength of Cylindrical Concrete Specimens*; ASTM International: West Conshohocken, PA, USA, 2004.
39. ASTM C1018-97. *Standard Test Method for Flexural Toughness and First-Crack Strength of Fiber-Reinforced Concrete (Using Beam with Third-Point Loading)*; ASTM International: West Conshohocken, PA, USA, 1998.
40. ASTM C1195-03. *Standard Test Method for Absorption of Architectural Cast Stone*; ASTM International: West Conshohocken, PA, USA, 2003.
41. Ohama, Y.; Amano, M.; Endo, M. Properties of carbon fiber reinforced cement with silica fume. *Concr. Int.* **1985**, *7*, 58–62.
42. Pigeon, M.; Pleau, R.; Azzabi, M.; Banthia, N. Durability of microfiber reinforced mortars. *Cem. Concr. Res.* **1996**, *26*, 601–609. [CrossRef]
43. Shah, S.P.; Chandra, S. Critical stress, volume change, and microcracking of concrete. *ACI J. Proc.* **1968**, *65*, 770–781.
44. Kim, T.-J.; Park, C.-K. Flexural and tensile strength developments of various shape carbon fiber-reinforced lightweight cementitious composites. *Cem. Concr. Res.* **1998**, *28*, 955–960. [CrossRef]
45. Zheng, Q.; Chung, D.D.L. Carbon fiber reinforced cement composites improved by using chemical agents. *Cem. Concr. Res.* **1989**, *19*, 25–41. [CrossRef]
46. Akihama, S.; Suenaga, T.; Banno, T. Mechanical properties of carbon fiber reinforced cement composites. *Int. J. Cem. Compos. Lightweight Concr.* **1986**, *8*, 21–33. [CrossRef]
47. Neville, A.M. *Properties of Concrete, Fourth Edition*; John Wiley & Sons Inc.: New York, NY, USA, 1996.
48. Katz, A.; Li, V.C.; Kazmer, A. Bond properties of carbon fibers in cementitious matrix. *J. Mater. Civ. Eng.* **1995**, *7*, 125–128. [CrossRef]
49. Sakai, H.; Takahashi, K.; Mitsui, Y.; Ando, T.; Awata, M.; Hoshijima, T. Flexural behavior of carbon fiber reinforced cement composite. In *Fiber Reinforced Concrete: Developments and Innovations*; ACI SP-142; American Concrete Institute: Detroit, MI, USA, 1994; pp. 73–89.

Development of Retrofitting Solutions: Remedial Wall Ties for Masonry Enclosure Brick Walls

Filipe Rebelo [1], António Figueiredo [1], Gonçalo Correia Lopes [1], Tiago Miguel Ferreira [2,*] and Romeu Vicente [1]

[1] RISCO, Department of Civil Engineering, University of Aveiro, Campus Universitário de Santiago, 3810-193 Aveiro, Portugal; filiperebelo@ua.pt (F.R.); ajfigueiredo@ua.pt (A.F.); gclopes@ua.pt (G.C.L.); romvic@ua.pt (R.V.)

[2] ISISE, Institute of Science and Innovation for Bio-Sustainability (IB-S), Department of Civil Engineering, Campus de Azurém, University of Minho, 4800-058 Guimarães, Portugal

* Correspondence: tmferreira@civil.uminho.pt

Abstract: The external envelope walls of a significant percentage of the residential building stock in Southern European countries is commonly constituted by infill masonry walls. However, thousands of square meters of this masonry wall typology presents severe issues of cracking and instability, related to the incorrect and deficient support conditions of the outer brick panel of the double-leaf wall solution. In this work, an experimental campaign divided in two phases has been performed to evaluate the effectiveness of two different remedial wall ties retrofitting techniques (*Solution A* and *Solution B*) used for double leaf horizontally hollowed clay brick masonry façades. The first phase of the experimental campaign was performed on 120 isolated specimens of horizontally hollowed clay bricks, resorting to post- and pre-NP EN 771-1 brick exemplars (that is, new and pre-existent aged bricks, respectively), as well as on 4 square wallettes, with a side length of 1.20 m, considered as representative of a real scale scenario, for evaluating the two remedial wall ties retrofitting techniques. The second phase of the experimental campaign was performed to fully characterize the different failure types as well as the slipping phenomena observed in the first phase of the experimental campaign, focusing solely on the retrofitting technique *Solution B* and comprises 24 tests performed on isolated specimens, resourcing to new and pre-existent aged bricks as well. The results obtained by the use of these techniques revealed an average anchorage strength value ranging from 0.25 to 2.5 kN for each tested tie-bar. *Solution B* reveals an increase of double of the anchorage strength value in comparison to *Solution A*. In this sense, the global results revealed a suitable applicability of both retrofit studied solutions.

Keywords: instability and cracking; infill walls; retrofitting; remedial wall ties; out-of-plane

1. Introduction

As a consequence of population and economic growth, an increasing demand for indoor thermal comfort and energy efficiency requirements has arisen, implying new challenges related to buildings' thermal performance in the European built environment [1]. Thus, during the last few decades, the typology of external infill masonry walls has notably been changing, ranging from the old-fashioned loadbearing massive stone masonry walls into increasingly lighter solutions, in the form of single leaf non-structural brick masonry infills and/or enclosure walls [2].

Although the increasing number of new successful alternative systems for enclosure walls, such as vertically perforated clay bricks [3], double-leaf horizontally hollowed clay brick masonry walls are still one of the most widely used constructive solutions for buildings' external envelope [2]. These non-loadbearing infill masonry walls are generally supported by a concrete framed structure constituted by columns, beams and slabs, presenting some evident advantages:

- When properly and effectively connected, both wall leafs contribute to the global resistance of the wall solution against horizontal actions;
- Enables thermal bridge correction solutions, with significant effectiveness in terms of thermal performance;
- Enables the protection of the insulation system (when placed within the air gap).

However, since these walls are seldom designed to withstand severe external loads but rather to perform an infilling function, their design is often neglected and insufficiently detailed [4]. Moreover, in addition to the non-structural pathological defects associated with infill masonry walls (generally comprising loss of water tightness, mould growth and the development of condensation issues), distortions may occur as well as excessive deformation as consequence of hygrothermal movements, leading to severe cracking or even to its collapse, compromising not only the buildings serviceability and functionality, but most importantly human life [5–7].

Concerning the critical role of buildings' external envelope walls in terms of protection from the environmental elements whilst assuring desirable indoor thermal comfort conditions to the building occupants, one of the most debatable measures in terms of constructive systems solutions has been the external thermal bridge correction by means of clay brick slips or veneer cladding, aligned with the underlying strategy of the European Union (EU) energy policy framework for reducing the environmental impacts and the ecological footprint, as well as to reduce energy consumption through improving energy efficiency in buildings without compromising the living quality standards [8,9]. Despite these constructive systems solutions contributing to the improvement of the buildings' façade thermal behavior, insufficient testing and technological validation has been responsible for a considerable amount of pathologies associated with deficient support conditions, and therefore severe cracking and instability of horizontally hollowed clay brick enclosure infill masonry walls have been observed. In Figure 1a, it is depicted how the disrespect of the rule to maintain a minimal partial width support over the concrete beam of at least 2/3 of the outer wall leaf, in accordance to [10], has led to numerous severe issues, imposing in some situations the demolition and re-construction of the external leaf of the wall [6,7].

Additional contributing factors responsible for cracking and instability problems observed in several buildings have been identified as the excessive weight of the exterior rendering, additional eccentric loads, wind loads, creep and shrinkage movements of the structure, masonry deformations and movements induced by heat and moisture, lack of wall ties, lack of building technology knowledge in the design phase, and non-specialized workmanship skills (particularly for singular points) [7].

When subjected to seismic actions, despite the masonry enclosure and infills walls being considered non-structural, several authors [7,11–13] have acknowledged their influence on the global behavior of the reinforced concrete frames under seismic loads, considering that their disregard in the design process of new buildings may induce local mechanisms in the structure. The abovementioned phenomena has recently been observed as consequence of several earthquake events, as referred to by [14]. Consequently, the lessons learnt about the influence of the non-structural masonry enclosure and infills walls on the buildings' structural response under seismic action have been the basis for important improvements of several structural design standards [15–19].

It should also be mentioned that the reduced wall support usually required to minimize thermal bridges due to structural elements is an issue when the building is subjected to seismic actions, since these masonry enclosure and infill walls exhibit a non-desirable and fragile out-of-plane behavior, resulting in the manifestation of severe cracking, which, in the worst case scenario, is responsible for the walls to completely detach and collapse, as observed in Figure 1b. Considering that the associated costs involved in repairing non-structural elements often exceeds the structural repair ones [7,14,20], the need to study and evaluate suitable measures in order to improve and assure the in-plane and out-of-plane integrity of enclosure and infill masonry walls, possibly subjected to seismic actions, is paramount to minimize the adverse consequences.

(**a**)

(**b**)
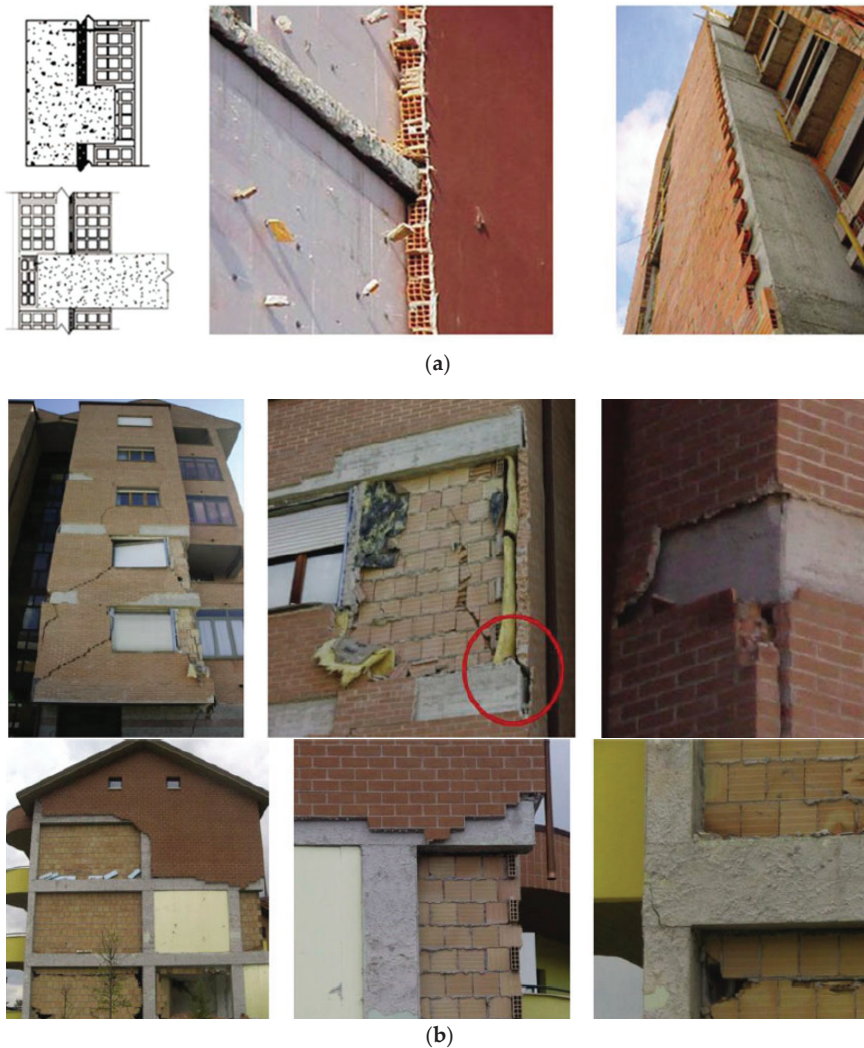
Figure 1. Examples of severe mechanical pathologies as consequence of: (**a**) inadequate correction of thermal bridges, using partially supported infill walls; (**b**) cracking and out of plane collapse of outer leaf of double-leaf cavity walls and veneer cladding walls [7].

Several strengthening intervention methods and retrofitting techniques applied in masonry enclosure and infill walls have been extensively addressed in the literature, such as the use of fibre reinforced polymers (FRP), engineered cementitious composites (ECC), textile reinforced mortars (TRM) and ferrocement and bed joints' reinforcement [4,21–24].

The present paper focuses on the using of the remedial wall tying retrofitting technique (by means of different techniques comparison), originally developed for Northern European clay brick veneer wall systems [25], and therefore adapted to the Southern European traditional horizontally hollowed clay brick masonry walls. Based on the experimental investigation herein presented, conduced within two different techniques—that is, *Solution A* based on the insertion of a remedial helicoidal tie through percussion, and *Solution B* based on the use of a cement grout sock on the extremities of the remedial wall tie—the effectiveness and adequacy of using this technique in real retrofitting interventions will

be thoroughly discussed in the following sections. To achieve the specific objective of fully assessing the adequacy and efficiency of the presented post-construction pinning techniques in future real retrofitting interventions, the experimental work presented in this paper comprises the following steps: (i) assess the retrofitting technique in laboratorial environment; (ii) evaluate the efficiency of the retrofitting solution on specimens constituted by post- and pre-NP EN 771-1 horizontally hollowed clay bricks (meaning, resourcing to new and pre-existent aged brick exemplars); (iii) evaluate the influence of different features of the retrofitting technique (such as sleeve introduction and grout injection) over the pull-out test results; and, finally, (iv) describe and catalogue the different failure types and the observed behavior of the two different techniques tested. Resourcing to new and pre-existent aged horizontally hollowed clay brick exemplars for testing purposes has been considered paramount to assess behavior and performance differences, since aged bricks (pre-NP EN 771-1) have already been exposed to different humidity, moisture and temperature conditions, therefore experiencing innumerable cycles of temperature charge and discharge, no longer comprising the initial (as when new) physical, chemical and mechanical characteristics, allowing this way the simulation of an approximated scenario to real post-construction retrofitting environment conditions. On the other hand, new horizontally hollowed clay bricks (post-NP EN 771-1) are expected to behave according to their optimal physical and mechanical characteristics. The results acquired for both retrofitting techniques are thoroughly presented and discussed.

2. Wall Tie Retrofitting Techniques

One of the techniques used during the construction process, specifically aimed at avoiding defects related to the lack of adequate support of the outer brick wall layer (see Section 1), has often been the use of steel wall ties, embedded into the mortar layers to connect the two brick wall leafs as well as for connecting the walls to confining and adjacent structural elements, such as concrete columns. However, the location of these steel connectors is frequently random and the wall ties are often inappropriate, revealing to be fragile, prone to corrosion and unable to aid draining internal condensation in the wall cavity [26].

The post-construction remedial wall tying arises therefore as one of the suitable retrofitting techniques, able of being successfully applied for these type of constructive solution for walls, improving its out-of-plane integrity as well as stability [27]. Among all of the solutions available in the construction market, this paper focuses on the comparative analysis of two particular solutions applied to horizontally hollowed clay brick cavity walls, hereinafter referred to as *Solution A* (as depicted in Figure 2a) and *Solution B* (as depicted in Figure 2b). *Solution A* is a based on the insertion of a remedial helicoidal tie that is inserted through percussion and connects the two wall leafs solely by friction. *Solution B* is based on the insertion of cement grout sock that constitutes an anchoring bulb on the extremities of the remedial wall tie.

(**a**) (**b**)
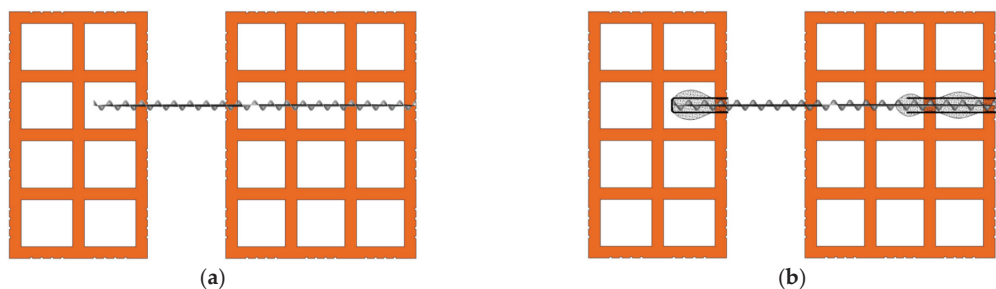
Figure 2. Functioning scheme of the two solutions considered: (**a**) Solution A—dry remedial wall tie in horizontally hollowed bricks; (**b**) Solution B—remedial wall tie using an expanded grout-filled sock in horizontally hollowed bricks.

The choice for these two solutions was motivated by the fact that they both present advantageous features (presented in Table 1) and have been applied extensively in retrofitting across Europe.

Table 1. Comparative analysis between *Solution A* and *Solution B:* features and benefits.

	Solution A	Solution B
Features	• Safe, quick and easy application; • Purely mechanical system (frictional resistance), do not requires the use of resins, grouts or mechanical expansion; • Efficient with the use of bricks, blocks, concrete, hard mortar and wood; • Efficient in cavity and solid walls, as well as hollowed and perforated materials; • Can be applied independently of the external environment and/or temperature.	• The capacity to fix the thin layer of the double leaf wall can be easily tested; • Effective in all constructive materials; • Excellent connection between tie and plaster; • Curing time mandatory for cementitious grout.
Benefits	• Low acquisition and installation cost; • High tensile resistance; • Flexible, able to absorb the natural movement of the structure; • Can be placed through the insulation system without affecting significantly its thermal efficiency; • Does not affect the external aspect of the masonry wall; • Low disturbance for the buildings' function and occupants.	• Efficient relation between cost and benefit, as well as performance; • Able to absorb natural building movements; • Efficient for the rehabilitation of tall buildings; • Does not affects the buildings' external appearance; • Does not disturb the buildings' occupants.

From the comparison between the two solutions, it is noteworthy that *Solution A* is expected to be a more economic tie solution, does not require skilled workmanship and presents higher productivity levels since it allows the execution of a larger number of ties in a shorter period of time. However, *Solution B* tends to be a more effective tie solution since the use of grout bulbs results in higher tensile strengths, but nevertheless comprises higher material costs, and since a curing period is mandatory, the process becomes slightly more time-consuming.

3. Methodology

The developed work of the experimental campaign performed in the scope of this study follows the methodological approach depicted in the schematic flowchart presented in Figure 3.

The work methodology is structured into two main phases, preceded by the geometric and mechanical properties characterization of the horizontally hollowed clay bricks to be used throughout the experimental campaign. The first phase of the experimental campaign was performed on 120 isolated specimens (depicted in Figure 6a) of horizontally hollowed clay bricks, resorting to post- and pre-NP EN 771-1 [28] brick exemplars (that is, new and pre-existent aged bricks, respectively, as explained in Section 1), meaning that a total of 120 specimens, divided in 30 specimens composed of new bricks and 30 specimens composed of pre-existent aged bricks for studying *Solution A*, and 30 specimens composed of new bricks and 30 specimens composed of pre-existent aged bricks for evaluate *Solution B*, were tested and each individual response has been assessed. Additionally, 4 square wallettes were constructed with a side length of 1.20 m (as depicted in Figure 6b) and tested for evaluating the two remedial wall ties retrofitting techniques (*Solution A* and *Solution B*). The second phase of the experimental campaign was performed to fully characterize the different failure types as well as the slipping phenomena observed in the first phase of the experimental campaign, focusing solely on the retrofitting *Solution B* and comprises 24 tests performed on isolated specimens, resourcing to new and pre-existent aged bricks

as well. Therefore, a series of compression tests have been performed according to the procedure presented in NP EN 772-1 [29] for mechanical characterization of the clay bricks. As for the two phases of the experimental campaign, a series of pull-out tests have been performed for both the isolated specimens and the wallettes, whose results obtained have been registered and discussed throughout the respective subsections.
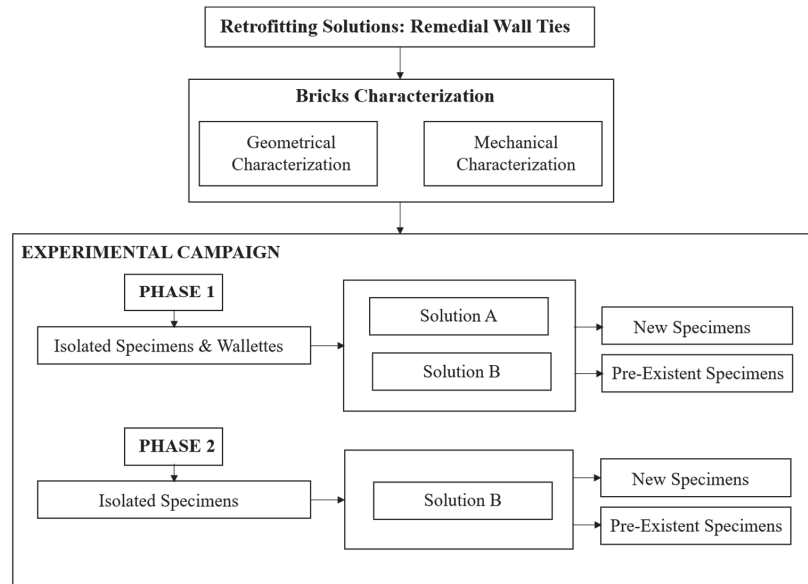
Figure 3. Flowchart diagram of the work methodology for the experimental campaign.

4. Characterization of the Clay Bricks

Two double-leaf cavity wall masonry specimens composed of two different formats of horizontally hollowed clay bricks were constructed and tests were performed for studying a common constructive solution, as referred to in the Introduction (see Section 1), considered to be representative of the majority of the building envelope walls existing in Southern European built environment. In order to enrich the discussion, two distinct frameworks were considered: pre- and post-European Standard NP EN 771-1 [28], in which the physical and mechanical features of the masonry units as well as its geometric tolerances are specified. In this sense, prior to the construction of the specimens, bricks used were geometrically and mechanically characterized according to the recommendations of the European Standard NP EN 772-1 [29]. The obtained results for the performed characterization are presented and discussed throughout the following subsections.

4.1. Geometrical Characterization

The geometrical characterization of the specimens was evaluated, based on a randomly selected group of six horizontally hollowed clay brick exemplars. The nomenclature used for the brick types is based on their representative measures (in (cm) unless otherwise stated) of $30 \times 20 \times 15$ and $30 \times 20 \times 11$ (meaning: Length $\times$ Height $\times$ Width), as depicted in Figure 4, both compliant with pre- and post-NP EN 771 1 [28] requirements. Regarding to length and height, the $30 \times 20 \times 15$ and $30 \times 20 \times 11$ bricks can present significant dimensional variations, ranging between 28.8 cm to 30.2 cm and between 18.4 cm and 19.6 cm, respectively. In the same line, in terms of width, the $30 \times 20 \times 15$ bricks can present dimensions ranging from 14.5 cm to 15.5 cm, while the $30 \times 20 \times 11$ bricks can

present dimensional variations ranging between 10.6 cm and 11.4 cm. The thickness of the bricks' wall and webs range from 0.8 cm to 1.0 cm.

(**a**)　　　　　　　　　　　　　　　　　　　(**b**)
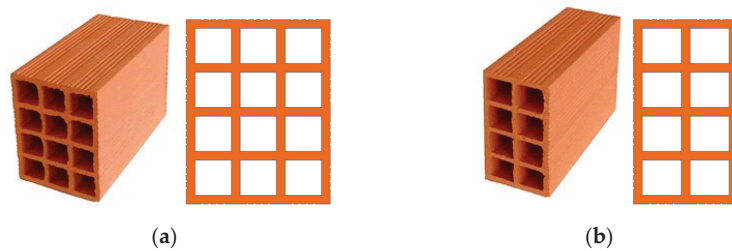
Figure 4. Formats of the horizontally hollowed clay bricks used in the experimental tests: (**a**) 30 × 20 × 15; and (**b**) 30 × 20 × 11.

4.2. Mechanical Characterization

The mechanical characterization of the horizontally hollowed clay brick specimens have been performed by means of a series of simple compression tests, complying with the standard procedure presented in EN 772 1 [29]. The acquired average values from the tests performed for the six bricks of each type, as well as the corresponding coefficients of variation are presented in Table 2. The compressive strength values of the Pre-NP EN 771-1 bricks are slightly higher due to the thicker inner septums/webs.

Table 2. Average compressive strength values.

Type of Brick	Average Compressive Strength (MPa)	Coefficient of Variation (%)
30 × 20 × 15 (Post-NP EN 771-1)	3.01	13
30 × 20 × 15 (Pre-NP EN 771-1)	3.79	26
30 × 20 × 11 (Post-NP EN 771-1)	1.72	14
30 × 20 × 11 (Pre-NP EN 771-1)	2.70	11

During the execution of the tests performed for mechanical characterization, four main types of failure were registered: detachment of the outer webs of the brick, global crushing, cracking of the inner webs and fractional shear. The four failure types were registered and presented in Figure 5.

(**a**)　　　　　　(**b**)　　　　　　(**c**)　　　　　　(**d**)
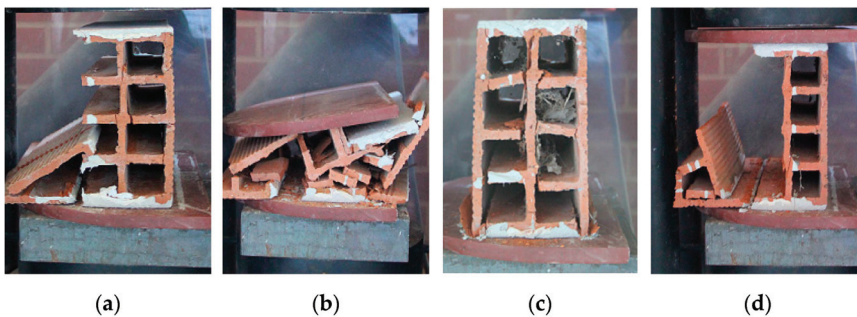
Figure 5. Types of failure observed: (**a**) detachment of the outer webs; (**b**) global crushing; (**c**) cracking of the inner webs; (**d**) fractional shear.

5. Experimental Campaign: Phase 1

The aim of the first phase of the experimental campaign has been to test the two distinct previously selected solutions of post-construction wall tying (that is, *Solution A* and *Solution B*), with the specific objective of evaluating its efficiency and to understand the main differences between the both solutions, in terms of mechanical behavior and execution procedure by means of material use and time consumption related to each application process. Considering these objectives, a total of 120 specimens (divided in 30 for each solution and for each one of the two sets of specimens, as explained in Section 3), were tested and each individual response has been assessed. Additionally, to evaluate the two post-construction wall tie techniques, four scaled specimens of masonry wallettes were constructed.

5.1. Preparation of the Test Specimens

The specimens were built and prepared following an assembly line analogy (depicted in Figure 6a). The specimen preparation started with the placement of the $30 \times 20 \times 11$ bricks. Secondly, polystyrene bars (XPS), previously prepared, were carefully placed on top of the first layer of bricks (see Figures 6a and 7), to simulate the air-gap space between layers. Finally, the specimen has been "closed" with the placement of the $30 \times 20 \times 15$ brick panel. To assure the functioning of the system and the correct application of the post construction wall tie, a set of wood boards and clamps were used to guarantee the stability of the bricks during the drilling process and the application of the solutions.

| (**a**) | (**b**) |
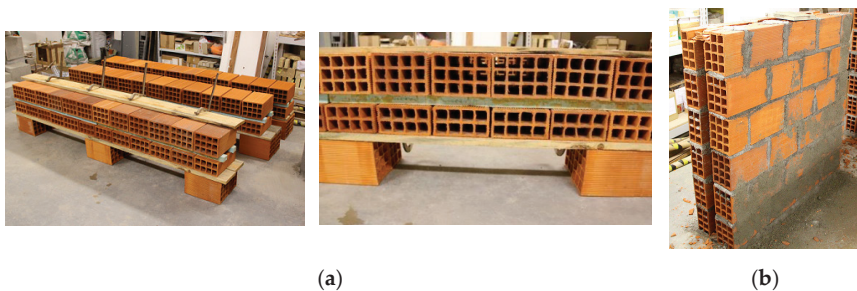
Figure 6. Test specimens and wallettes: (**a**) preparation of the isolated specimens; (**b**) masonry wallettes, adapted fom [30].
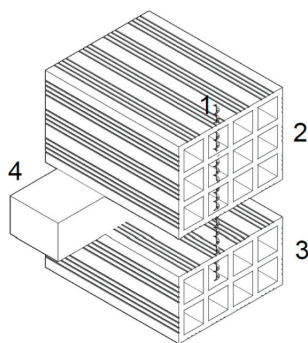
Figure 7. Schematic detail of an isolated specimens: (**1**) Steel tie rod; (**2**) $30 \times 20 \times 15$ brick; (**3**) $30 \times 20 \times 11$ brick; (**4**) XPS insulation bar.

Regarding the four masonry wallettes (see Figure 6b), their construction followed a similar sequence: (i) preparation of the brick laying mortar; (ii) positioning of the first row

of bricks; (iii) pre-wetting of the bricks; (iv) brick laying; (v) filling of the vertical head mortar joints; and (vi) rendering of the masonry wallettes.

5.2. Application of the Post-Construction Wall Tying for Single Isolated Specimens

5.2.1. Solution A

For the application of *Solution A*, the used steel tie rods were made of stainless steel with a helical format of 8 mm in diameter. As observable in Figure 8a, the first step consisted of pre-drilling the bricks resorting to a 5 mm drill. Secondly, the helical tie rods were placed into the pre-drilled holes, as seen Figure 8b. Regarding this procedure, it is worth mentioning that the insertion of the tie rods have been performed by crimping, i.e., by drilling with pulse, resorting to an adaptor coupled to the drill, specifically for this purpose.

| (**a**) | (**b**) |
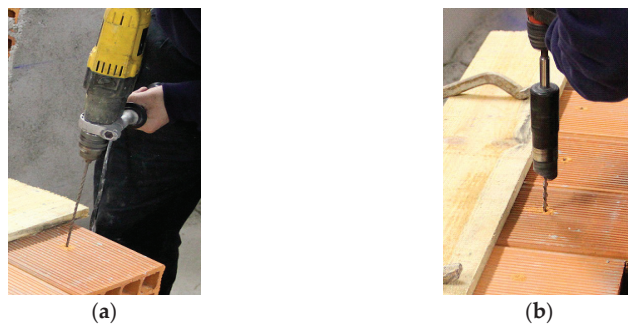
Figure 8. *Solution A* execution process: (**a**) pre-drilling of the brick; (**b**) crimping the steel rod into the brick.

5.2.2. Solution B

For the application of *Solution B*, special care has been taken during the insertion and positioning of the sleeves (either sock or plastic), necessary for the application of the grout. Otherwise, these jacks tend to be placed in an incorrect manner, leading either to the malfunctioning of the grout or making impossible its injection. It is worth noting that the injection is itself a particularly demanding task to perform, since its application has been made with the grout injection nozzle gun positioned vertically, making it difficult to control the grout introduction. Another important aspect that must be considered in this solution is the required curing time of the grout (28 days in the particular case of a cement-based grout). The execution steps followed for the application of *Solution B* are presented in Figure 9.

5.3. Application of Post Remedial Wall Ties on the Masonry Wallettes

The application of post remedial wall ties on the masonry wallettes has followed the same procedure used on the preparation of the isolated specimens. Particular precaution has been taken prior to drilling on the positioning of holes in order to avoid hitting the vertical head mortar joints. Additional concern considered during the implementation of this solution has been to assure that the adequate amount of grout was injected into each sock sleeve, in order to guarantee the formation of a suitable bulb. The shape of the grout bulb formed is independent of the direction of the grout injection. For the sake of comparison, this was verified before defining the first experimental testing procedure, when the injection was done for the two brick specimens (single isolated specimen) in the vertical direction and for the double leaf wall specimen in the horizontal direction. In both cases, the "egg" shaped grout bulb has always been formed because of two reasons: (i) the consistency of the injected grout, that is not excessively fluid; and (ii) the flexible sock that restrains and prevents an irregular shaped bulb from being formed.
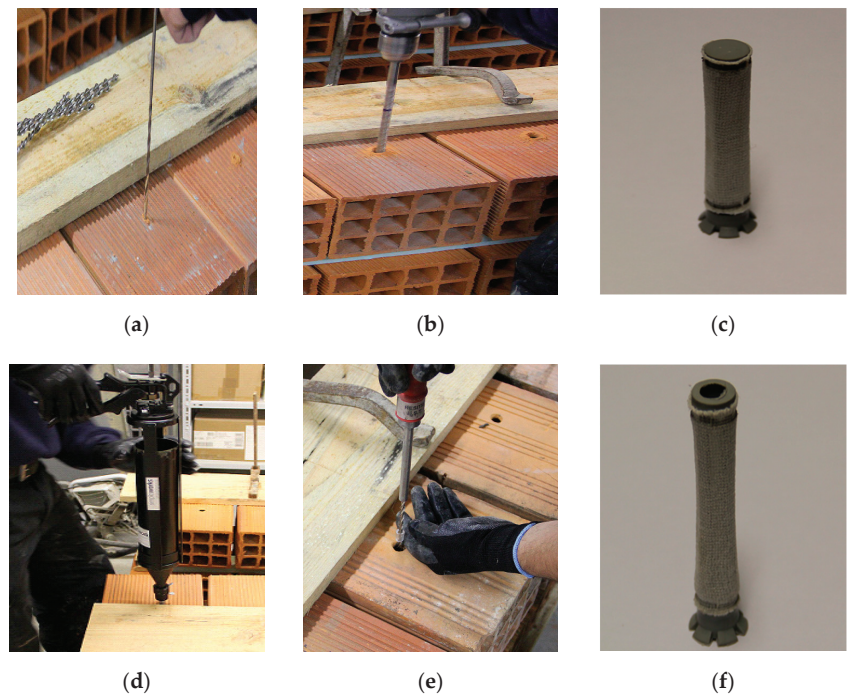
Figure 9. *Solution B* step-by-step execution process: (**a**) pre-drilling of the bricks with a 5 mm drill; (**b**) drilling of the bricks with a 14 mm drill; (**c**) placement of the closed-end sock sleeve into the 30 × 20 × 11 brick (inner brick); (**d**) filling of the sock sleeve with the cement based grout; (**e**) placement of the helical tie rod into the hole and the outer brick sock sleeve; (**f**) sock sleeve into the 30 × 20 × 15 brick (outer brick).

5.4. Description of the Pull-Out Tests

For the singular isolated specimens, the helical steel rod has been cut between both bricks (that is, in the air gap existing between the two brick panels), since this testing approach intends to pull-out the steel rods individually. The test has been performed resourcing to a 3 kN dynamometer for precision purposes. Regarding the wallette specimens, aiming to reproduce a real wall in a laboratory environment, they were constructed to test and identify pinning application constraints, limitations, as well as improvement measures for both techniques. For *Solution A* pull-out tests performed, a 3 kN dynamometer has been used, and for *Solution B*, a 16 kN dynamometer was used to take advantage of the resolution and precision of the equipment since, in the case of the pull-out tests for *Solution B*, these exceed the value of 3 kN.

A noteworthy aspect related to the testing set-up is that, in order to inject the grout into the sock sleeve, due to their additional extension, it was necessary to arrange an adapter for placing the injection gun, making it possible to apply the grout within the inner sock sleeve inserted into the 30 × 20 × 15 brick.

5.5. Analysis of the Results Obtained in the First Testing Campaign
5.5.1. Solution A

As previous referred to in Section 4, all the single brick specimens (including both new and pre-existent bricks) were tested according to the procedure defined in the standard NP EN 771-1 (CEN2006). Following to the methodology described in Section 3, the specimens were tested in pull-out and the record of relevant information from the tests, namely, load cell forces were collected and presented in Figure 10. From the results obtained, it is

shown that pre-existent brick specimens (designated in the plots as #cm ExiB, meaning, dimension of the brick type and pre-existent specimen) present, on average, a higher pull-out force in respect to new brick specimens (designated in the plots as #cm NewB, meaning dimension of the brick type and new specimen); and for new and pre-existent specimens of 30 × 20 × 15 brick type format, this force is higher with respect to the 30 × 20 × 11 brick format. Since *Solution A* is strictly dependent on frictional force mobilization of the helical steel bar, these results were somehow expectable considering the brick geometry of hollows and web thickness, higher in the case of the 30 × 20 × 15 bricks. When compared with the new specimens, pre-existent bricks present higher compressive strength (indicator of better mechanical behavior), and the thicker value of the webs is also higher, leading therefore to higher pull-out force in both formats. In addition, since brick formats 30 × 20 × 15 have three webs that are pierced, in respect to the two of the 30 × 20 × 11 brick format, higher frictional resistance is expected and consequently the pull-out values for the wider bricks are higher. The result values obtained for the pull-out tests performed in the wallettes were, on average, higher when compared with the obtained results for the single brick specimens.
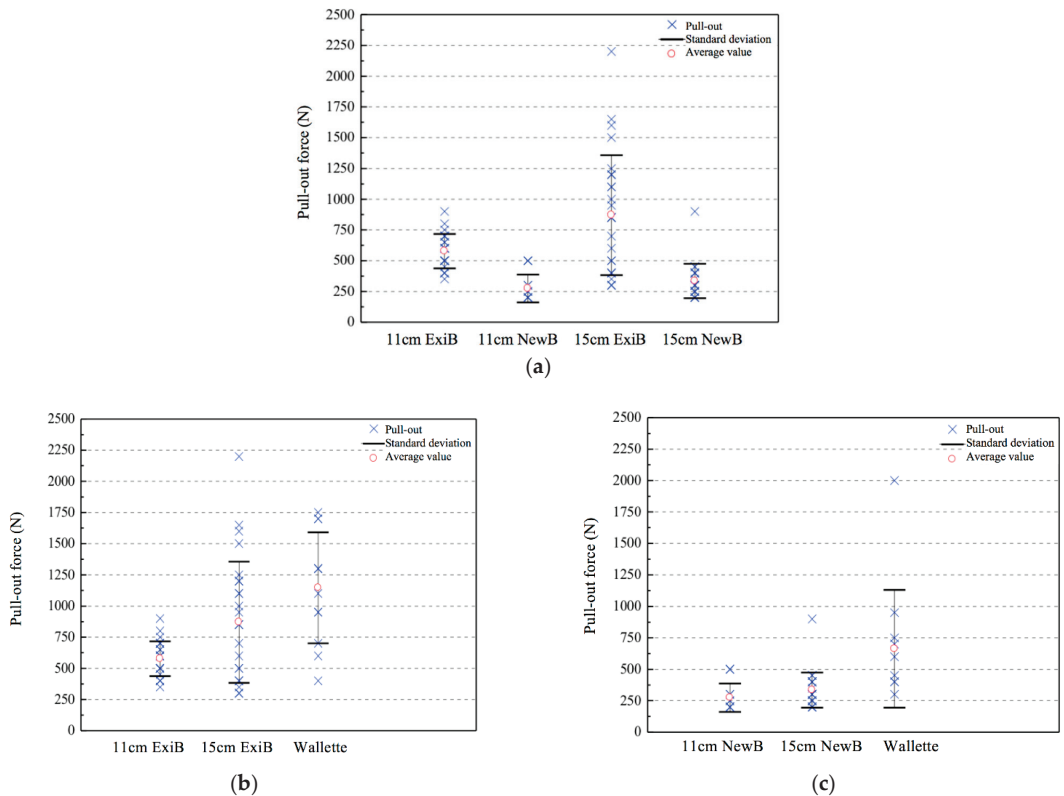
Figure 10. Pull-out tests of *Solution A*: (**a**) single brick specimens; (**b**) comparison for pre-existent brick wallette and single brick specimens; (**c**) comparison for new brick wallette and single brick specimens.

From the analysis of Figure 10, it is possible to observe—even though taking into account the difference in the testing methodology for the single brick specimens, for which the pull-out tests are done individually for each brick—that the pull-out force of the 30 × 20 × 15 brick format is 20% to 50% higher than the one of the 30 × 20 × 11 format. Comparing the pull-out forces obtained of the wallette and the 30 × 20 × 15 brick format, an increase between 40% to 95% was attained for the pull-out force in the wallette specimens,

proving that the mechanical pinning between bricks is beneficial for this type of horizontally hollowed brick geometry. However, further testing driven to better understand this relationship is encouraged.

From the analysis of Figure 11 it is possible to observe that pre-existent bricks specimens present, on average, higher compressive strength, when compared with new brick specimens. Thus, a direct correlation was observed in the attained results (compression and pull-out force), showing the same tendency of higher result values for the existent brick specimens. Finally, regarding the failure mode, all tests revealed that in *Solution A*, when applied to the wallettes, failure occurs exclusively by steel tie slippage.
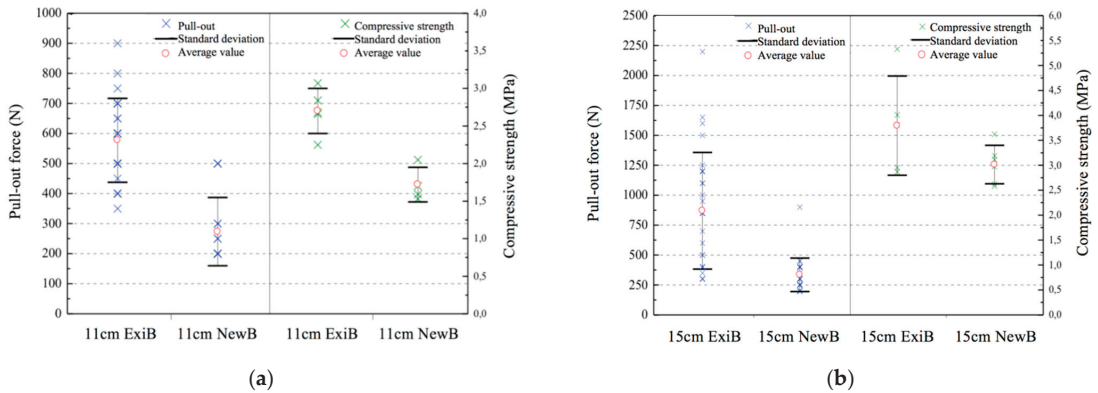
Figure 11. Relationship between pull-out force of single specimens and bricks' compressive strength: (**a**) brick format $30 \times 20 \times 11$; (**b**) brick format $30 \times 20 \times 15$.

5.5.2. Solution B

As previous referred to in Methodology (see Section 3), the testing framework and the number of specimens for *Solution B* was the same used for *Solution A*.

From the analysis of Figure 12, it is possible to conclude that both new and the pre-existing bricks specimens present higher pull-out force values for the specimens with $30 \times 20 \times 15$. Although the closed-end sock sleeve inserted into the inner leaf of the $30 \times 20 \times 11$ brick may, at first sight, allow a better formation of the grout bulb (due to the assured pressure of the grout injection nozzle gun), its effectively formed contact area between the grout bulb and the web of the brick may still be reduced. Furthermore, the fact that the sock sleeve, inserted into the outer leaf of the $30 \times 20 \times 15$ brick, is opened on both extremities (since the helical steel bar must pass through) and pierces two webs of the brick, may even be positive to the formation of one smaller additional bulb after the first inner web, leading to improved results.

The results obtained for the pull-out tests performed on the wallette specimens (new and pre-existent bricks) are depicted in Figure 12. The acquired results reveal that the pull-out force of the wallette is about 5% to 15% higher when compared with the force attained for the $30 \times 20 \times 15$ brick specimens.

Regarding the comparison between the compressive strength results with the pull-out forces, as depicted in Figure 13, *Solution B* do not exhibit the same tendency observed in *Solution A*, attaining higher values of the pull-out force when the compressive strength is also higher. In this sense, only the $30 \times 20 \times 15$ specimens reveals higher resistance in the pull-out tests when the compressive strength is higher as well. In opposition of *Solution A*, this wall tie execution technique strongly depends on other features, such as the grout quality and bulb formation into the hollowed bricks, tie insertion or bond to the grout, and, most importantly, on the quality of the execution, as will be discussed further.
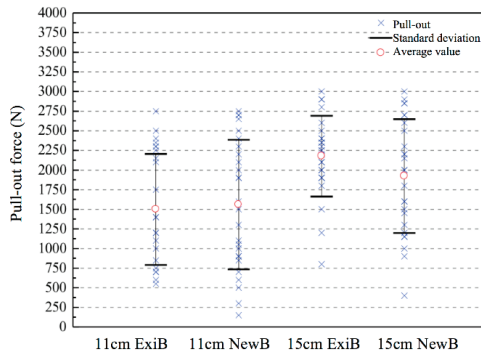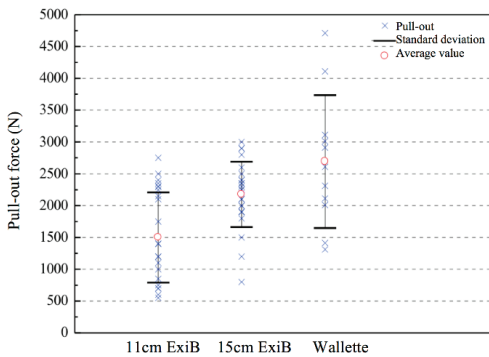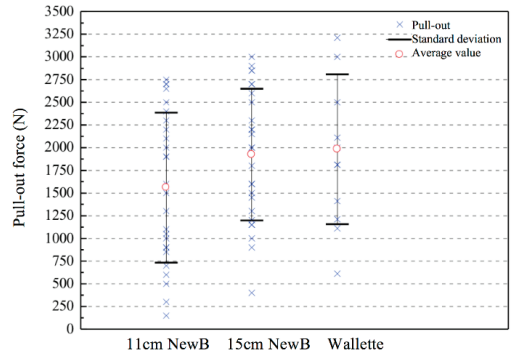
Figure 12. Pull-out tests of *Solution B*: (**a**) single brick specimens; (**b**) comparison for pre-existent brick wallette and single specimens; (**c**) comparison for new brick wallette and single specimens.
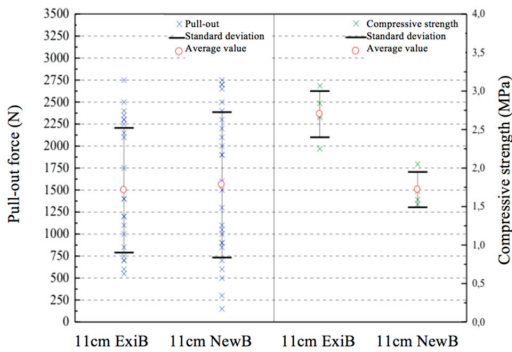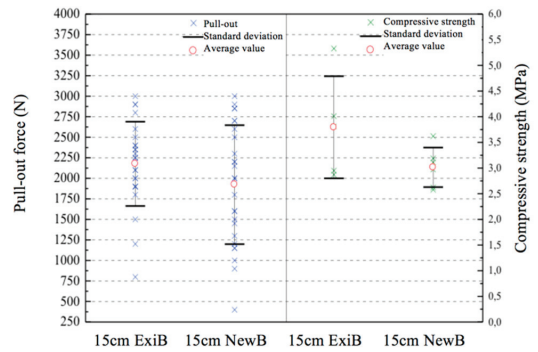
Figure 13. Relationship between pull-out force of single specimens and bricks' compressive strength: (**a**) brick format $30 \times 20 \times 11$; (**b**) brick format $30 \times 20 \times 15$.

From the pull-out tests performed on the specimens using *Solution B*, it was possible to identify three types of failure modes:

1. Fragile failure (FF): this type of failure appears when, during the test, abrupt loss of adhesion occurs between the tie-bar and the brick walls/webs, driven by the loss of

strength capacity of the brick to the pull-out force. Figure 14a presents an example of this failure, conditioned by the brick resistance.

2. Failure by tie-bar slippage (FTS): this type of failure arises when slippage of the tie-bar occurs within the grout. From Figure 14b, it is possible to verify that the brick web is intact without attaining the failure, and the sock sleeve is not moved from the initial position.

3. Global failure (GF): this type of failure occurs when the brick gradually weakens and fails, and the system solution (sleeve plus tie) slides along the brick web. In Figure 14c, it is observed the slippage of the solution relative to the hollowed brick web. It is also quite noticeable the slipping experienced once the initial position of the sock sleeve nears the right exterior web of the brick.

(**a**) (**b**) (**c**)
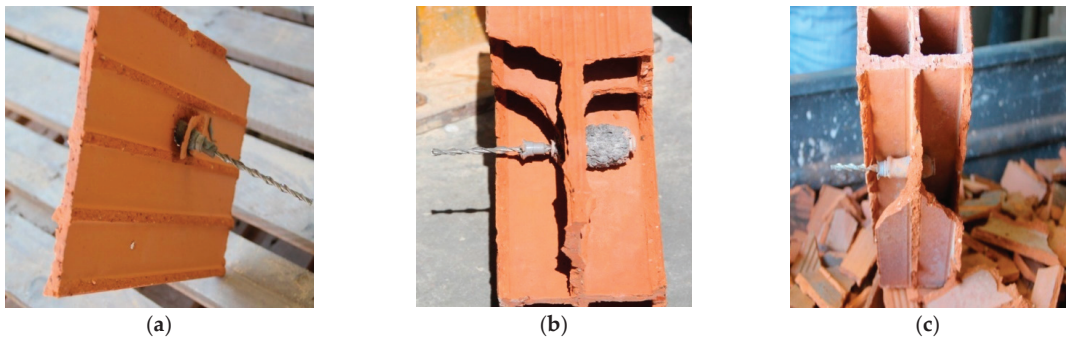
Figure 14. Types of failure observed: (**a**) fragile; (**b**) tie-bar slippage; (**c**) global.

6. Experimental Campaign: Phase 2

The second phase of the experimental campaign was developed to fully characterize the different failure types as well as the slipping phenomena attained in the previously phase of the experimental campaign. This second phase comprises 24 tests performed in isolated specimens from *Solution B* using new and pre-existent bricks. It is noteworthy that the preparation of the specimens and the application of the reinforcement wall tie solution have followed the procedure adopted for the first phase of the experimental campaign, previously described in Sections 3 and 5.

Regarding the pull-out tests, this second phase was performed with a different experimental setup, consisting of the use of a hydraulic jack of 300 kN, fixed to a steel frame coupled to a load cell with capacity of 25 kN in traction and compression (see Figure 15) that has been used to perform the experimental tests. At the top of the load cell, a steel grip was placed to clamp the steel helical tie (see Figure 15b). The specimens were constrained by a steel sheet fixed in the outer corners to the lower beam of the steel frame setup (Figure 15d).

At this experimental campaign, the tests were performed with the two bricks connected by the tie (see Figure 7). Thus, it allowed to attain the value of the pull-out strength of the entire solution. Finally, the tests were performed at a constant speed with a rate of 0.2 mm/s controlled by the displacement transducer of the hydraulic jack.

Based on the obtained results, individual plots (i.e., by specimen) of the pull-out strength vs. displacement recordings were generated considering the registered behavior in terms of strength evolution, slipping and global displacement. Table 3 presents the behaviors registered for three groups of new brick specimens tested (a representative test was chosen as example for each group of tests and it is depicted in the plot), whereas Table 4 presents the result for the two groups of pre-existent brick specimens.

(**a**)

(**b**)

(**c**)

(**d**)
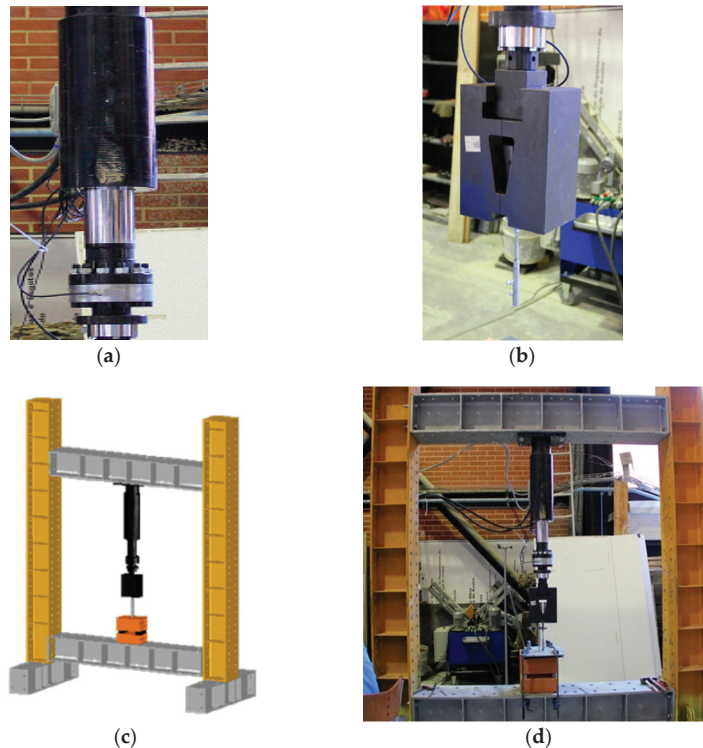
Figure 15. Test components: (**a**) hydraulic jack of 300 kN coupled to a load cell of 25 kN; (**b**) steel grip coupled to the load cell; (**c**) pull-out test apparatus; (**d**) full apparatus view.

Table 3. Pull-out test results of the three groups of new brick specimens.

New Brick Specimens
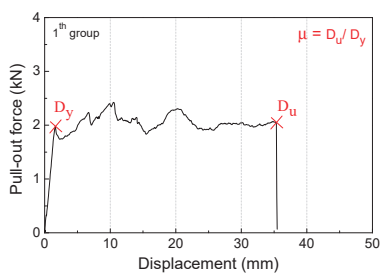
Obs.: Failure by slipping of the tie in the brick $30 \times 20 \times 11$ sock sleeve and slipping of the tie in the brick $30 \times 20 \times 15$ sock sleeve
D_y: 1.65 mm; D_u: 34.84 mm; μ: 21.12; $f_{max.}$: 2.42 kN
Slipping after yielding: 33.70 mm
In this group of tested specimens it was obtained, on average, a value of 2.7 kN for the maximum pull-out force and 11.74 for ductility. The abrupt decrease in strength represents the initiation of the tie slippage in the sleeve, leading to the global failure.
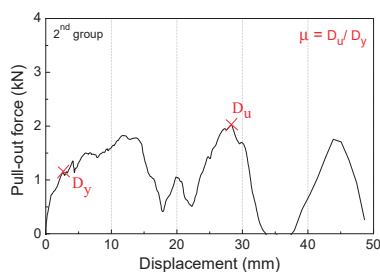
Obs.: Global failure
D_y: 2.61 mm; D_u: 28.32 mm; μ: 10.85; f_{max}: 2.02 kN
Slipping after yielding: 24.7 mm
For the second group of specimens, the average value obtained for the pull-out force was 1.9 kN and a ductility of 10.78 was also obtained. In general, the grout bulbs formed did not possess flaws (cracks, irregularities), showing a regular and consistent formation.

<div align="center">

Table 3. *Cont.*

</div>
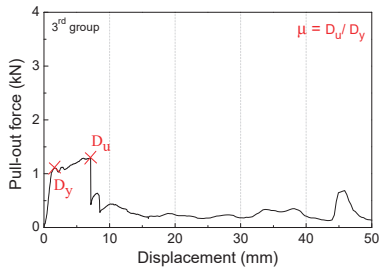
New Brick Specimens	
	Obs.: Brittle failure D_y: 1.84 mm; D_u: 7.08 mm; μ: 3.85; f_{max}: 1.29 kN Slipping after yielding: 4.16 mm The third group of isolated specimens of new bricks obtained an average value of 2.14 kN for the pull-out force and 3.11 for ductility. When the maximum pull-out force and yielding occurs is reached, the specimen no longer has capacity to attain pull-out strength values near this maximum.

Legend: D_y: displacement obtained in the maximum peak of strength; D_u: displacement obtained before the rupture; μ: ductility; f_{max}: maximum pull-out force.

In summary, and regarding the tests performed on new brick specimens, it has been possible to identify three types of failure modes:

1. Failure by tie slippage (FTS): approximately constant pull-out force during the test, and abrupt decrease in strength in the rupture;
2. Global failure (GF): the variation of the pull-out force during the test clearly indicates the instant when yielding occurs at each web of the bricks;
3. Fragile failure (FF): after the maximum value of the pull-out force is attained and yielding occurs, the specimen no longer has the capacity to attain pull-out strength values similar to the maximum peak of strength.

<div align="center">

Table 4. Pull-out test results of the two groups of pre-existent brick specimens.

</div>
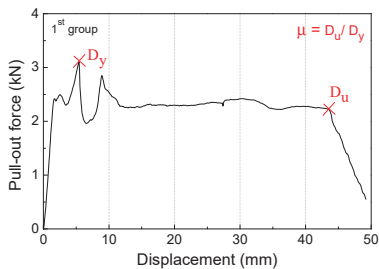
Pre-Existent Brick Specimens	
	Obs.: Sliding of the tie in the sleeve for both bricks D_y: 1.65 mm; D_u: 42.02 mm; μ: 25.47; f_{max}: 3.10 kN Slipping after yielding: 40.37 mm This group of tested specimens obtained an average value of 2.93 kN for the pull-out force and 12.74 for ductility. After the rupture, it was observed that certain sock sleeves were damaged, which corroborates the fact that there was slippage of the ties.
	Obs.: Brittle failure for the brick $30 \times 20 \times 11$ and slipping of the sock sleeve in the brick $30 \times 20 \times 15$. D_y: 1.49 mm; D_u: 17.29 mm; μ: 11.60; f_{max}: 1.67 kN Slipping after yielding: 15.80 mm In this second group, it was obtained, on average, a value of 2.90 kN for the pull-out force and 12.99 for ductility. Highlight that, firstly, a rupture of the first web was noticed, with an abrupt loss of strength. Then the second web of the brick was solicited; however, the maximum strength attained is 50% lower when compared with the maximum value obtained.
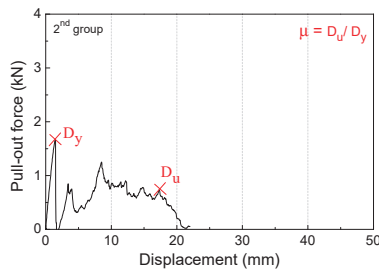
Legend: D_y: displacement obtained in the maximum peak of strength; D_u: displacement obtained before the rupture; μ: ductility; f_{max}: maximum pull-out force.

In summary, it was possible to identify two types of failure modes for the pre-existent brick specimens:

1. Failure by tie slippage (FTS): as in the previous group of new brick specimens, this type of failure was obtained;

2. Brittle failure (BF): the pull-out force does not reach values higher than the maximum previously obtained.

Regarding the quality control, as stated above in Section 5.2.2, special attention should be given to the grout injection process, as it strongly influences the effectiveness of the solution. However, there are other parameters presented to control, such as the grout workability time and preparation, which should have an adequate fluidity so that it can be easily injected in the sock sleeve. Another important factor that must be adequately controlled is the drilling process, which requires a careful execution to avoid undesirable damages in the bricks as well as to avoid undermining the steps to be carried out afterwards. Thus, a perpendicular drilling stance is mandatory to allow the introduction of the sock sleeves avoiding extra damages to the specimens. It is also important to control the drilling depth, since it is necessary to preserve the last web of the brick of the internal leaf (usually concerning the 30 × 20 × 11 brick format in the case of a double-leaf wall).

Regarding the execution of the sock sleeves strengthening technique piercing the brick, it should also be thoroughly controlled, since the risk of tearing the sock sleeves when passing through the webs or becoming deformed is possible.

7. Conclusions

This paper focused on the effectiveness of two different remedial wall ties retrofitting techniques with the purpose of tackling a recurrent problem concerning the instability of double-leaf masonry enclosure walls.

The potential advantages offered by the two studied solutions have proven the suitability and reliability of these retrofitting techniques to connect both wall leafs effectively, thus contributing to the global resistance of the existent wall solution against horizontal actions. Due to frequent deficient support conditions of the external envelope layer, the need of adequate connection between the two masonry wall leafs is crucial to mitigate the risk of collapse due to excessive deformation or seismic actions, ultimately compromising human life [31,32].

The work comprised an experimental campaign divided into two phases, preceded by the geometric and mechanical characterization of the horizontally hollowed clay bricks (30 × 20 × 15 and 30 × 20 × 11, new and pre-existent aged bricks) used throughout the study. To characterize the effectiveness of the remedial wall tie solutions, a total of 120 isolated specimens and 4 wallettes were executed and tested by performing the pull-out technique. Two different retrofit scenarios have been tested and compared, analyzing two solutions. *Solution A* is a based on the insertion of a remedial helicoidal tie that is inserted through percussion and connects the two wall leafs solely by friction. *Solution B* is based on the insertion of cement grout sock that constitutes an anchoring bulb on the extremities of the remedial wall tie.

From the attained results from Phase 1 of the experimental campaign, it is possible to conclude that pre-existent bricks specimens present higher compressive strength as well as pull-out force, when compared with new brick ones, revealing a direct correlation. Regarding the failure modes, all tests revealed that in *Solution A*, when applied to the wallettes, the failure occurs exclusively by steel tie slippage.

The technique of *Solution B* is strongly dependent on the grout quality and bulb formation into the hollowed bricks, tie insertion or bond to the grout, and on the quality of the execution.

The second phase of the experimental campaign revealed that no coherent rupture type was attained. In this sense, three different types of rupture have been observed, namely "failure by tie slippage" characterized by a constant value for pull-out force followed by an abrupt decrease in strength; "global failure," in which the pull-out test behavior reveals

a swing of the applied force, until the rupture occurs; and "fragile failure," where after the maximum value of the pull-out force is attained and yielding occurs, the specimen no longer has the capacity to attain pull-out strength values similar to the maximum peak of strength. This research has opened the discussion on various levels, starting from the need to rethink the technology and execution rules of facades and development of execution guidelines, especially in the cases of veneer wall solutions and erection of infill walls in seismic prone areas, as well as in the case of retrofitting to lead the way to the development of optimization these retrofitting approaches in terms of intervention cost-technical benefit.

References

1. Lee, J.H.; Yeo, M.-S. Condensation Control to Cope with Occupancy Activity and Effectively Mitigate Condensation in Unheated Spaces by Real-Time Sensor Control Strategy. *Sustainability* **2020**, *12*, 4033. [CrossRef]
2. Teni, M.; Krstić, H.; Kosiński, P. Review and comparison of current experimental approaches for in-situ measurements of building walls thermal transmittance. *Energy Build.* **2019**. [CrossRef]
3. Lourenço, P.; Vasconcelos, G.; Medeiros, P.; Gouveia, J. Vertically perforated clay brick masonry for loadbearing and non-loadbearing masonry walls. *Constr. Build. Mater.* **2010**, *24*, 2317–2330. [CrossRef]
4. Furtado, A.; Rodrigues, H.; Arêde, A.; Varum, H. Experimental tests on strengthening strategies for masonry infill walls: A literature review. *Constr. Build. Mater.* **2020**. [CrossRef]
5. Silva, L.M.; Marting, A.; Vasconcelos, G.; Lourenço, P.B. Paredes de Alvenaria de Fachada: Soluções e Sugestões de Melhoria de Desempenho. In Proceedings of the Seminário de Reabilitação de Fachadas, Guimarães, Portugal, 22 September 2016.
6. Vicente, R.; Da Silva, J.A.R.M. Defects of non-loadbearing masonry walls due to partial basal supports. *Constr. Build. Mater.* **2007**, *21*, 1977–1990. [CrossRef]
7. Vicente, R.; Rodrigues, H.; Varum, H.; Costa, A.; Da Silva, J.A.R.M. Performance of masonry enclosure walls: Lessons learned from recent earthquakes. *Earthq. Eng. Eng. Vib.* **2012**, *11*, 23–34. [CrossRef]
8. Directive 2018/844/EU of the European Parliament and of the Council of 30 May. *Off. J. Eur. Union* **2018**, *156*, 75–91.
9. Figueiredo, A.; Rebelo, F.; Castanho, R.A.; Oliveira, R.; Lousada, S.; Vicente, R.; Ferreira, V. Implementation and Challenges of the Passive House Concept in Portugal: Lessons Learnt from Successful Experience. *Sustainability* **2020**, *12*, 8761. [CrossRef]
10. Groupe de Coordination des Textes Techniques. *Parois et Murs en Maçonnerie de Petits Éléments*; DTU 20.1 (référence AFNOR DTUP10-202); Centre Scientifique et Technique du Bâtiment: Marne-la-Vallée, France, 1985.
11. Furtado, A.; Rodrigues, H.; Arêde, A.; Varum, H. Simplified macro-model for infill masonry walls considering the out-of-plane behaviour. *Earthq. Eng. Struct. Dyn.* **2016**, *45*, 507–524. [CrossRef]
12. Crisafulli, F.J.; Carr, A.J.; Park, R. Analytical modelling of infilled frame structures—A general review. *Bull. New Zeal. Soc. Earthq. Eng.* **2000**, *33*, 30–47. [CrossRef]
13. Rodrigues, H.; Varum, H.; Costa, A. Simplified Macro-Model for Infill Masonry Panels. *J. Earthq. Eng.* **2010**, *14*, 390–416. [CrossRef]
14. *The L'Aquila, Italy Earthquake of 6 April 2009—A Preliminary Field Report by EEFIT*; EEFIT: London, UK, 2009.
15. *Eurocode 8: Design of Structures for Earthquake Resistance—Part 1: General Rules, Seismic Actions and Rules for Buildings 2004*; European Committee for Standardization: Brussels, Belgium, 2004.
16. *Eurocode 6: Design of Masonry Structures—Part 11: General Rules for Reinforced and Unreinforced Masonry Structures 2005*; European Committee for Standardization: Brussels, Belgium, 2005.

17. *NEHRP Handbook for the Seismic Evaluation of Existing Buildings—A Prestandard, Federal Emergency*; FEMA 310; Federal Emergency Management Agency: Washington, DC, USA, 1998.
18. *Seismic Evaluation and Retrofit of Concrete Buildings—Technical Report*; ATC-40; Applied Technology Council: Redwood City, CA, USA, 1996.
19. *Assessment and Improvement of the Structural Performance of Buildings in Earthquakes*; New Zeland Society for Earthquake Engineering: Wellington, New Zeland, 2006.
20. *Earthquake Hazard Mitigation for Nonstructural Elements—Field Manual*; FEMA 74; Federal Emergency Management Agency: Washington, DC, USA, 2005.
21. Özgür, A.; Tatayoğlu, M.; Demirhan, M. Out-of-plane behavior of unreinforced masonry brick walls strengthened with CFRP strips. *Constr. Build. Mater.* **2012**, *35*, 614–624. [CrossRef]
22. Chen, W.; Yeh, Y.-K.; Hwang, S.-J.; Lu, C.-H.; Chen, C.-C. Out-of-plane seismic behavior and CFRP retrofitting of RC frames infilled with brick walls. *Eng. Struct.* **2012**, *34*, 213–224. [CrossRef]
23. Ozsayin, B.; Yilmaz, E.; Ispir, M.; Ozkaynak, H.; Yüksel, E.; Ilki, A. Characteristics of CFRP retrofitted hollow brick infill walls of reinforced concrete frames. *Constr. Build. Mater.* **2011**, *25*, 4017–4024. [CrossRef]
24. Kesner, K.; Billington, S.L. Investigation of Infill Panels Made from Engineered Cementitious Composites for Seismic Strengthening and Retrofit. *J. Struct. Eng.* **2005**. [CrossRef]
25. Memari, A.M.; Burnett, E.F.; Kozy, B.M. Seismic response of a new type of masonry tie used in brick veneer walls. *Constr. Build. Mater.* **2002**, *16*, 397–407. [CrossRef]
26. Graça, J. Intervenções em Fachadas: Novas Soluções Para Problemas Antigos. In Proceedings of the Seminário de Reabilitação de Fachadas, Guimarães, Portugal, 22 September 2016; pp. 73–82.
27. Mendes da Silva, J.A.R.; Carvalhal, M.; Vicente, R.D.S. Reforço mecânico de alvenaria de tijolo: Reabilitação de cunhais e grampeamento metálico pós-construção. In Proceedings of the Encontro Sobre Conservação e Reabilitação de Edifícios, Lisboa, Portugal, 26–30 May 2003; pp. 1329–1338.
28. *Specification for Masonry Units—Part 1: Clay Masonry Units*; NP EN 771-1; European Committee for Standardization: Brussels, Belgium, 2006.
29. *Methods of Test for Masonry Units—Part 1: Determination of Compressive Strength*; NP EN 772-1; European Committee for Standardization: Brussels, Belgium, 2002.
30. Ribeiro, S. Soluções de Reabilitação—Grampeamento de Paredes de Alvenaria. Master's Thesis, University of Aveiro, Aveiro, Portugal, 2013.
31. Aguado, J.L.P.; Ferreira, T.M.; Lourenço, P. The Use of a Large-Scale Seismic Vulnerability Assessment Approach for Masonry Façade Walls as an Effective Tool for Evaluating, Managing and Mitigating Seismic Risk in Historical Centers. *Int. J. Arch. Herit.* **2018**, *12*, 1259–1275. [CrossRef]
32. Ferreira, T.M.; Maio, R.; Costa, A.A.; Vicente, R. Seismic vulnerability assessment of stone masonry façade walls: Calibration using fragility-based results and observed damage. *Soil Dyn. Earthq. Eng.* **2017**, *103*, 21–37. [CrossRef]

Article

Earth to Earth: Patterns of Environmental Decay Affecting Modern *Pisé* Walls

Dirk H. R. Spennemann

Gulbali Institute, Charles Sturt University, P.O. Box 789, Albury, NSW 2640, Australia; dspennemann@csu.edu.au

Abstract: Rammed earth/*pisé* is an earth building technique with a deep history in several countries across the globe. In the past twenty years, *pisé* buildings have seen a resurgence in popularity, primarily because of their environmentally friendly, passive energy characteristics, but also due to the aesthetic appeal of the fabric. As with all other earth architecture, *pisé* is susceptible to decay by moisture ingress. This paper presents longitudinal observations on the decay of capped and uncapped *pisé* walls of an early twenty-first-century complex of four buildings in Albury (NSW, Australia). It can be shown that while surface treatment with water-repellent sealants prevents the ingress of penetrating damp, it also traps moisture (falling damp) in the fabric by restricting evaporation. This leads to internal cleavage between the consolidated and the unconsolidated fabric and accelerates the decay of uncapped walls. The future design of both stabilized and unstabilized external rammed earth walls must ensure effective protection from rainfall through well-proportioned overhanging eaves. While the capping of feature walls may be aesthetically pleasing, and thus architecturally desirable, it does not adequately protect the walling against long-term decay.

Keywords: building conservation; earth construction; environmental decay; modern architecture

1. Introduction

Historically, earth-walled buildings were common throughout the world [1,2], with many building techniques (wattle and daub, adobe, and *pisé*) still being practiced in many modern-day communities [3,4]. Vernacular earthen architecture was common, for example, in colonial settler communities in the Americas [5–7], as well as in Australia, where a number of techniques were practiced, such as pug-and-pine, cob, mudbrick, and *pisé* [8–11]. With increasing standards of living in the late nineteenth and early twentieth centuries and the associated public perceptions as to what constituted 'proper' architecture, however, earth-walled buildings became uncommon in the developed world.

While mudbrick homes have a long post-World War II history, particularly among people aspiring to alternative life styles [12], the international debate on climate change during the mid-1990s brought about a new emphasis on sustainable, energy efficient architecture. Consequently, the period saw a revival and adaptation of traditional vernacular earth building techniques in many countries [13–16], among them Australia [17–20].

One of the frequently expressed concerns in relation to earthen architecture is the longevity of such structures, particularly their resistance to various agents of environmental decay. Such considerations gain in importance in an era of global climate change where environmental extremes (droughts, floods, and fires) are becoming more frequent and more intense.

Several longitudinal studies have examined how historic earth-walled buildings decay, be they of pug-and-pine [8,10] adobe [21–23], or *pisé* construction [9]. This is of relevance to both the owners of the properties and to cultural heritage professionals tasked with the conservation of the structures. Setting aside research into seismic performance [24–26], there is, at present, no literature that examines the environmental decay processes that affect modern-day rammed earth construction.

A common method to prevent or restrict moisture ingress into concrete masonry, as well as rammed earth and other earthen constructions, is to treat the external surfaces with a deep-penetrating, substrate-bonding sealer. This treatment is commonly applied post-construction [27,28], but can also be applied retrospectively as a conservation treatment [29]. While laboratory tests confirm the suitability of the treatment to prevent penetrating moisture (driving rain and condensation), the long-term effects have not been examined in real-life situations.

Following a review of the general decay processes and the ways that they impact earthen construction, this paper will discuss the longitudinal effects of environmental decay acting on *pisé* structures

It will do so through a series of macroscopic examinations and diachronic observations of unprotected walls at a late twentieth-century complex of rammed earth buildings located in New South Wales, Australia, and by contrasting the findings with the decay affecting protected walls in the same complex.

2. Methodology

2.1. Study Site

Between 1997 and 1999, Charles Sturt University (CSU) erected the Environmental Sciences complex of buildings at Thurgoona (NSW)(−36.038013, 146.990988), using cement-strengthened rammed earth. While the majority of the walls are capped to prevent moisture ingress, eight shield/privacy walls remained uncapped. The six free-standing walls assessed for this study are all located on the northern side of buildings 761 and 762. For ease of reference, they have been numbered from W1 to W6, starting in the east. Each wall has two faces, an eastern (E) and a western (W). Two uncapped, but roofed, walls on the southern side of buildings 761 and 762 serve as controls (C1 and C2).

2.2. Assessment and Documentation

The assessment of the decay occurred in situ, examining the visual and tactile appearance of the walls, as well as their integrity when subjected to gentle physical-impact testing (with the blunt end of a broad marker pen). The documentation of the decay is based on two methodologies of macroscopic observation: measurements and stratigraphic recording.

The recording of the first wall surface (wall 1, eastern face) used a laser beam (Bosch PLL 1P) mounted on a robust tripod (Gitzo GT5561SGT with a G2270M three-way head), which was set up so that the beam was aligned parallel to the wall surface. Relative to that arbitrary line, measurements with 1 mm accuracy were taken, set in a 20 × 20 cm grid. A level of accuracy greater than 1 mm was deemed spurious given the irregularity of the wall surface.

The contour analysis of these detailed measurements led to the simplification of the recording method for the remaining five walls. The documentation was thereafter limited to the recording of the visible decay with a method akin to a standard archaeological/pedological stratigraphy, with measurements taken in a 40 × 20 cm grid.

Unless specified otherwise, all photos were taken by the author.

2.3. Environmental Settings

Albury has a warm, temperate climate, characterized by very warm to hot summers and cool to mild winters, with temperatures rarely dipping below 0 °C [30]. While a freeze–thaw action, one of the major destructive forces in colder climates, is very rare and thus not a concern in Albury, the walls do experience a large temperature variation during the summer. During the middle of summer, diurnal temperatures range from 15 °C at night to a maximum in the mid-40s during the day [30]. Temperatures in the direct sun, however, can be up to 25 °C higher (pers. obs.).

3. General Patterns of Decay of Unreinforced Rammed Earth and Adobe Walls

In the literature, the pattern and mechanics of the decay of earthen structures are well described [31–35]. In principle, the decay processes affecting *pisé* buildings are physical, chemical, and biological.

Pisé is a building technique whereby lumps of clayey soil with a high plasticity are placed between the formwork and then compacted using a stamper. This results in layers of clay/soil that alternate between low (bottom of layer) and high compaction (top) (Figure 1). The strength of the bonding between the layers depends on the amount of time the surface of the compacted layers is allowed to dry out and also the smoothness of the compacted surface before the next layer is applied (Figure 2).

(**A**)
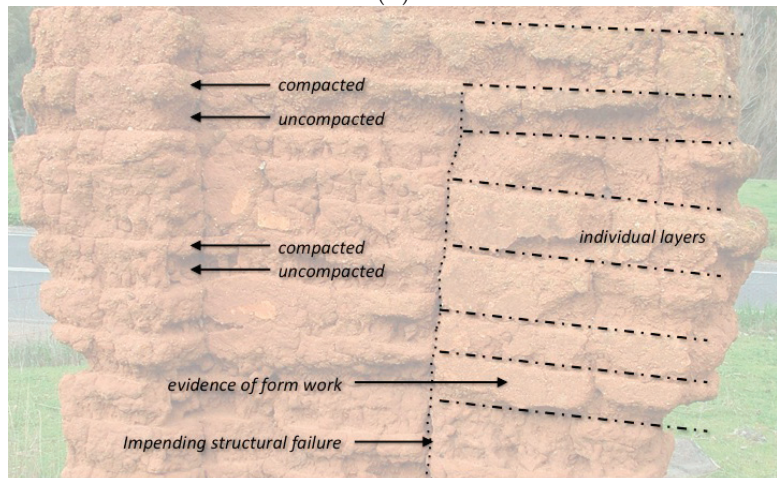
(**B**)

Figure 1. Influences of construction technique and quality of work on the preservation of *pisé* walls of a nineteenth-century ruin at Jugiong (NSW). (**A**) Photograph of a section of the northern face of the now collapsed southeastern wall block, as seen on 30 September 2005. The layers of fill and compaction are well evident. (**B**) Annotated interpretation of the image. Reprinted from Ref. [9].

Figure 2. The collapsed southeastern block as seen from the southeast on 30 September 2015. Note the clean breaks and lack of bonding between the compaction layers. Reprinted from Ref. [9].

Traditionally, the walls were then rendered with a fine clay/sand mixture and whitewashed. During the second half of the nineteenth century, Australian rural newspapers regularly carried columns that explained the technique to the colonial settler community [36–44].

Pisé work has some resistance against deterioration, and as long as the earthwork is not exposed to rain or surface moisture, long-lasting houses can be erected by this technique. The agents of decay are predominantly physical, with the bulk of the damage caused by rainfall and its derivatives. A *pisé* structure becomes susceptible to decay due to the ingress of water once it has lost its surface finish. *Pisé* buildings, which essentially consist of unfired loams or clays with a high hygroscopic index, will shrink and swell depending on the moisture content of the ambient air. Because of the high hygroscopic index, they are also very vulnerable to rising damp (Figure 3f) [45]. Subject to the duration of the immersion event, a flooding of the bottom part of the walling, be it riverine flooding or rainfall-induced sheet flooding significantly threatens the stability and integrity of a *pisé* structure. Walls may bulge under the weight of the roof once the clay becomes so wet that it reaches its plasticity limit.

Given the unconsolidated, compressed nature of *pisé* walls, damage to or loss of a roof allows rainfall to enter the unprotected top ends ('falling damp', Figure 3b). Prolonged wetness will accelerate the severity of the decay, depending on the intensity of the rainfall, as well as the pre-existing moisture content of the walling at the time of precipitation.

Vortexes created by winds (Figure 3a) can exacerbate the decay of the exposed wall tops (Figure 4). The high hygroscopic index of *pisé* walls also facilitates the ingress of penetrating damp caused by wind-driven rain as well as dew (Figure 3c). During heavy downpours, the lower parts of the walls are not only susceptible to general wetting but also to raindrops or hail pellets splashing off the ground through micro-impact (depending on raindrop velocity), which can, over time, dissolve the render and thus provide further avenues for moisture ingress (Figure 3d,e). This process is accelerated if the base of the walling has already been weakened by rising damp (Figure 3f). If left unchecked, this basal erosion eventually undermines the walling to such an extent that entire walls may topple or collapse (Figure 2).
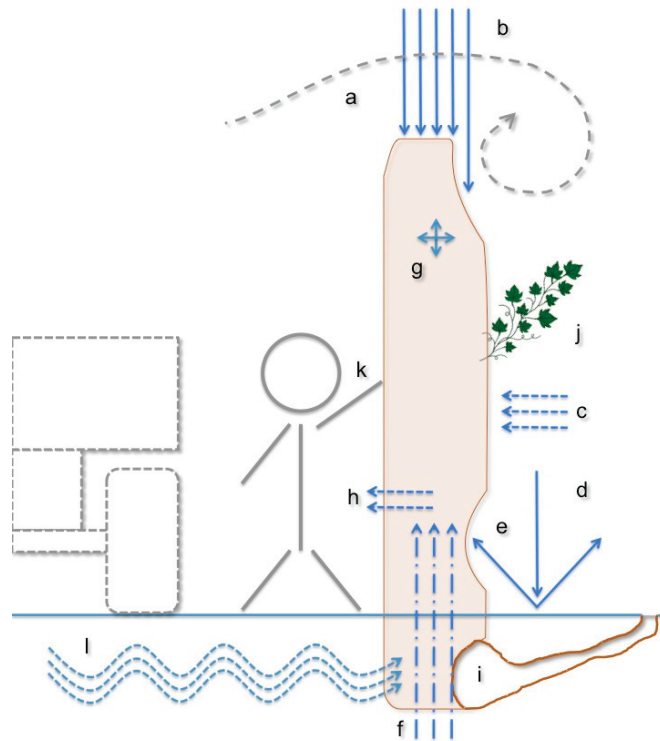
Figure 3. Schematic representation of the decay processes observed in *pisé* buildings after the roof has been removed/collapsed (see text for explanation). Reprinted from Ref. [9].

(**A**)   (**B**)
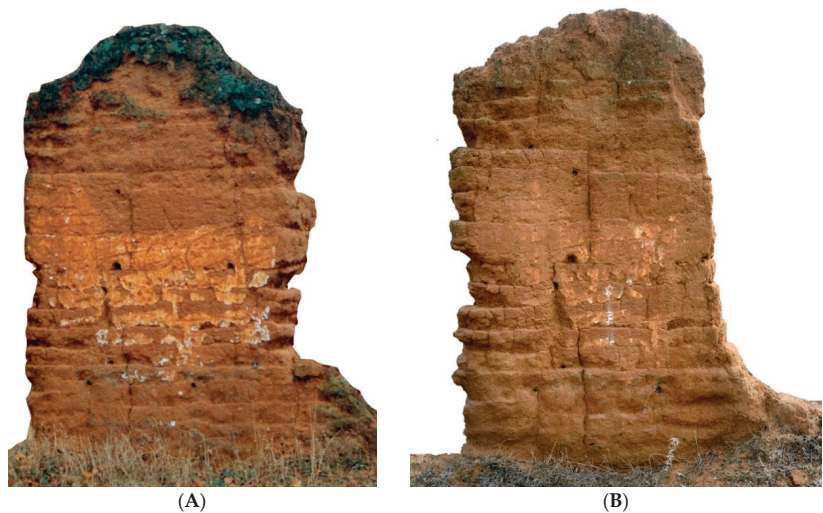
Figure 4. The southern face of the southeastern wall block at Jugiong (NSW). (**A**) Appearance on 15 February 1993; (**B**) appearance on 2 April 2015. Reprinted from Ref. [9].

Earth buildings can also be subject to a saline threat [46,47]. Depending on the level of ground moisture and the concentrations of water-soluble salts therein, this may lead to salt crystallization in the pore spaces and subsequent efflorescence. Repeated dehydration

and hydration events increase the problem, which will bring about a decay of the fabric through micro-erosion, which may, eventually, lead to structural failure (Figure 3h) [48].

It is important to note that the clay, as a binding agent of the walls, relies on the presence of moisture. Thus, *pisé* buildings should not be allowed to completely dry out, even if external moisture acts a major decay agent. In consequence, the introduction of a damp-proof course into traditionally erected *pisé* buildings could prove to be counter-productive as it might affect the stability of the structure. A total drying out of the walls would result in the separation of the sand and fine gravel that acts as an aggregate due to the shrinkage of the clay particles, resulting in a gradual granular erosion of the exposed surfaces. Structural cracking of the walling decreases its load-bearing capacity and stiffness (Figure 4). If structural unconformities exist, such as where poor quality of the initial construction work results in the walls lacking overlapping layers (Figure 1), the result may be large-scale cleaving of the wall segments.

On a more micro-scale level, the effects of the differential thermal expansion, such as the freeze–thaw action, of the components of the *pisé* may also need to be considered. This applies in particular to hot climates, where daytime surface temperatures on unshaded walls can exceed 65 °C, while nighttime temperatures drop to 20 °C or less; repeated differential thermal expansion between the core and the exposed surfaces of the walling may cause separation of the clay matrix and the aggregate. As the *pisé* earth mix is unfired, the bonds between the clay particles and the sand and fine gravel aggregate are weak. Differential bonding occurs in areas that exhibit variable compaction during the construction process, with the less compacted layers clearly more susceptible to granular erosion (Figure 1). This can be exacerbated if the surface of the aggregate particles is rounded and smooth rather than rough and textured. Moreover, the nature of the clay inclusions, such as gypsum, influences its bonding characteristics.

Finally, changes in the weight distribution of a roof may have severe or even catastrophic implications on the structural integrity of a building during seismic events, largely due to the low tensile strength of adobe and *pisé* walls. These are well described in the literature [49–51]. Given that the study area is not known for its seismic risk [52–55], we need not be overly concerned with these effects. It should be noted, however, that that destructive earthquakes affected the area in the nineteenth century [56,57].

Additional causes of decay that do not impact on the structures under discussion, but that may compromise other *pisè* structures, are the effects of vehicular traffic in close proximity, both chemical (CO_2 and SO_2 vehicle emissions) and mechanical (low-frequency ground vibrations) (Figure 3l); burrowing animals that can weaken the foundations and lower wall sections (Figure 3i); and vascular plants growing in cracks with expanding roots exerting lateral pressures in the fissures (Figure 3j) [9].

4. Modern Decay at Thurgoona (NSW)

In 1993, Charles Sturt University (CSU) acquired land at Thurgoona, 8.2 km northeast of the Albury CBD and commenced the green fields development of a campus. The initial suite of buildings was erected in an arc along the northern slope of a small knoll (Figure 5). The design concept aimed at making the development as environmentally neutral as possible. This entailed passive energy in the buildings, facilitated by the use of rammed earth construction, natural ventilation, and solar heating; the exclusive use of sustainably grown or recycled timber and other building materials (incl. fire-retardant wool carpets); the use of composting toilets with artificial wetlands for the purification of the effluent; the collection of surface runoff in large farm dams to prevent creek erosion; and the reuse of this water for landscape irrigation (using a windmill to pump it to a higher elevation) [19,58–64]. In total, fourteen rammed earth buildings were erected between 1997 and 2004 (Table 1).

Figure 5. The eastern wing of the Environmental Sciences building (Bldg 760) as seen from northwest.

Table 1. Chronology of rammed earth structures erected at Charles Sturt University Campus, Thurgoona, NSW, Australia.

Date	Event	Building (n°)
1993	Charles Sturt University acquires the site	
1995–1996 (May)	Student Pavilion Building	672
1997–1999 (Feb)	School of Environmental (and Information) Sciences Offices	760
1997–1999 (Feb)	Specialist teaching building (and computer lab)	761
1997–1999 (Feb)	Office building, a regional herbarium	762
1998	Network facility completed (telephone and computer switch)	754 (part)
1998–2000	Four eight-room student cottages and laundry block	680–684
1998 (Oct)–2001	Two-story teaching complex, including a 200-seat lecture theatre.	751
2001–2002 (Feb)	Two additional eight-room student cottages	685–686
2002–2003 (Jul)	Student Recreation Facility	752
2004 (Feb)–2005 (Jun)	School of Early Childhood Education Offices	763

The campus design received a number of awards and has been showcased as an example of sustainable architecture in a sustainable tertiary teaching environment [59,64]. The site development and architectural design influenced other buildings in the region, ref. [65] including a church and the associated priest's residence. In view of its architectural and social significance, the Environmental Sciences Building, a two-storey building housing 100 staff (Figure 5), was identified as culturally significant in a 2003 heritage study [66], and subsequently included as a protected heritage item in Albury City's Local Environmental Plan 2010 (schedule 5, item 330) [67].

In order to minimize the environmental impact, the original group of Environmental Sciences buildings is not sewered, but is serviced by a series of Clovis Multrum composting toilets. Public toilets are attached to buildings 761 and 762, and there is an additional, dedicated, staff toilet in building 762 (Figure 6). The design of the maintenance access to these toilets differs from that of the toilets of building 760. While the latter access is flush with the building, the toilets of buildings 761 and 762 have two protruding wing walls each, which provide visual screening and also prevent wind from accessing the system. These walls are fully exposed; they lack capping and also lack shading (Figures 6 and 7).

Figure 6. The School of Environmental Sciences building complex, Charles Sturt University, Thurgoona, showing the location of the buildings and the eight walls under discussion (1–6, C1, C2). Base image: Google Earth.

Figure 7. Uncapped *pisé* wing walls (walls 3 to 6), as seen from the northeast. Building 761 (right) and building 762 (left).

The buildings are erected on a slight slope, which provides the required depth for the toilet cavity that is dug into the slope (Figure 7). As a consequence, the free-standing wing walls exhibit a base of concrete blocks (400 × 200 × 200 mm) that follows the line of the slope, topped by a rammed earth wall (Figures 8–10). Each of the rammed earth walls was created in two sections: a short single-layered section adjacent to the building and a longer section projecting away from the structure, which exhibits three layers. These layers correlate with the original form boards. The top two layers are 600 mm high, while the bottom layer makes up the remainder of the wall height.

Figure 8. Wall 1 seen from the west. Note the accumulation of eroded debris at the base of the wall.

Figure 9. Wall 1 seen from the east.

Figure 10. Wing wall 3 seen from the east. Note the linear decay at left, indicating different layers of compaction.

4.1. The Construction of Buildings 760, 761, and 762 at Thurgoona

The buildings were constructed by Terry Wright Riverina Rammed Earth Constructions (Table Top, NSW, Australia), based on the designs by architects Marci Webster-Mannison and Chris McInerny [68]. While traditionally the soil for a *pisé* building would be obtained on site or close by, the soil used for the CSU buildings was sourced from a clay pit in Jindera (11 km northwest of the site). The testing of the supplied soil, as well as the resulting mixes, was carried out to the relevant standards, as prescribed at the time [69–76].

The specifications, as issued for the rammed earth buildings, are set out in Table 2. Similar specifications were issued for the subsequent buildings [77], including the projected School of Business, which was eventually erected for the School of Early Childhood Education (Bldg. 763) [78].

Table 2. Specifications for the buildings.

Constituent Materials	
Soil particle sizes	
Organic content	<2%
Clay and silt content	<20%
Sand content	≥50%
Coarse aggregate content	>30%
Water	Clean, fresh, free from impurities
Stabilizing agent	Cement (AS 3972) GP grade
Stabilized earth mix at placement	
Cement content (range)	max. 5% by weight
Adj. compressive strength (min.)	2.5 MPa
Moisture content (range)	8–16%
Dry density (t/m^3)	2.13
Liquid limit (max.)	35%
Plastic limit (max.)	20%
Plasticity index (max.)	12%
Linear shrinkage (max.)	5%
Plasticity index: linear shrinkage	2.5:1

The construction technique followed established principles [79] and entailed the erection of moveable sections of formwork, with the earth fill added with vibration and subsequent compaction and curing. The load-bearing external and internal walls of the buildings, irrespective of whether it was a double-storey (760) or a single storey office building (761, 762), are 300–310 mm thick. The internal partition walls have a thickness of 200 mm. By comparison, the screening walls (C1, C2) for the toilets of buildings 761 and 762 are also 300 mm thick (beveled to 210 mm). The final walls exhibited a very smooth, almost shiny, surface finish, caused by the clay particles being pressed against the smooth form boards. As the bolts fastening the form boards onto the support frame were recessed, the final wall surfaces show these recesses as small and low circular protrusions (Figure 11).

| (**A**) | (**B**) |

Figure 11. Uncapped, protected wall C1, screening the entrance to the external toilets of building 762: (**A**) frontal view seen from the south; (**B**) sideways view seen from the west.

To prevent the ingress of penetrating damp, silicone-based sealants were applied that made the inherently hydrophilic rammed earth construction more hydrophobic [27]. For buildings 752, 760, 761, and 762, Tech-dry® Plasticure was added to the rammed earth mix [68]. The product remains permanently bonded to the substrate, cannot be washed out, and reduces water absorption and efflorescence by over 80% [80]. For Building 763, the surfaces of the finished walls were treated with a water-repellent coating, a silane/siloxane sealer with a deep-penetrating, substrate-bonding clear impregnating finish that, theoretically, would prevent moisture ingress while allowing vapor transmission [68,78]. The interior walls that are not exposed to the elements have a smooth and shiny finish.

4.2. General Observations of Decay

Unlike traditional rammed earth, the structures constructed for CSU have a small admixture of Portland cement (Table 2), primarily to increase the structural strength required to hold the heavy concrete ceilings that were required for the innovative cooling and heating systems. Even though the walls are stronger, this does not imply that they are immune from decay.

The decay documented here has occurred in an incremental fashion but seems to have accelerated in the past few years (pers. obs). The decay of some of the walls is very obvious, with the loss of surface finish on most of the wall areas, the loss of fabric in some sections of the wall, and the concomitant accumulation of the gravelly component of the mix at the base of the wall (Figure 8).

4.3. Results of Decay Measurements and Observations

The standard or control sample, against which all decay could be assessed was provided by two free-standing walls, which were both privacy walls shielding the entrances to the male and female public toilets of buildings 761 and 762 (Figure 12).

Figure 12. Section of an external wall covered by a large overhanging roof. Note the details of the recessed bolts holding the form boards as well as the sections of form boards (Bldg 762).

At the time of construction, the wing walls were 200 mm thick, 1.65 m tall at their highest point, and measured between 3.6 m (walls 1 and 2) and 4.9 m in length (walls 3–6). The base of the walls is made up of one row of 200 mm-tall concrete blocks. The top of these wing walls is not only uncapped, but its surface is also rough and unfinished—and as such, a prime candidate for moisture ingress. As the main roof of the building extends over the walls and adjoining area, none of the wall surfaces is exposed to rainfall-derived moisture. Consequently, these walls have retained a very smooth, almost glossy surface (caused by the compression of clay particles against the form boards) and also show all the small circular protrusions that originate from the recessed bolt sections of the form boards. None of the six exposed wing walls examined for this study shows this level of preservation.

The eastern face of wall 1 (Figure 13A) is the one that has been studied in the most detail. It comprises a small section under the eaves, with a clear boundary of the form section and a larger section ending at 3.60 m from the wall of the building. While the small section was executed as one piece, the larger section shows three horizontal lines indicating the form board levels (Figure 12). The top half of the second wall segment exhibits extensive and largely uniform surface decay, exposing the coarse aggregate. The wall section closest to the northern wall of building 762 exhibits a small patch of original surface finish, located under and protected by the eave. All the measurements obtained relative to the laser beam (see methodology) were recalculated relative to the base value provided by this original surface.
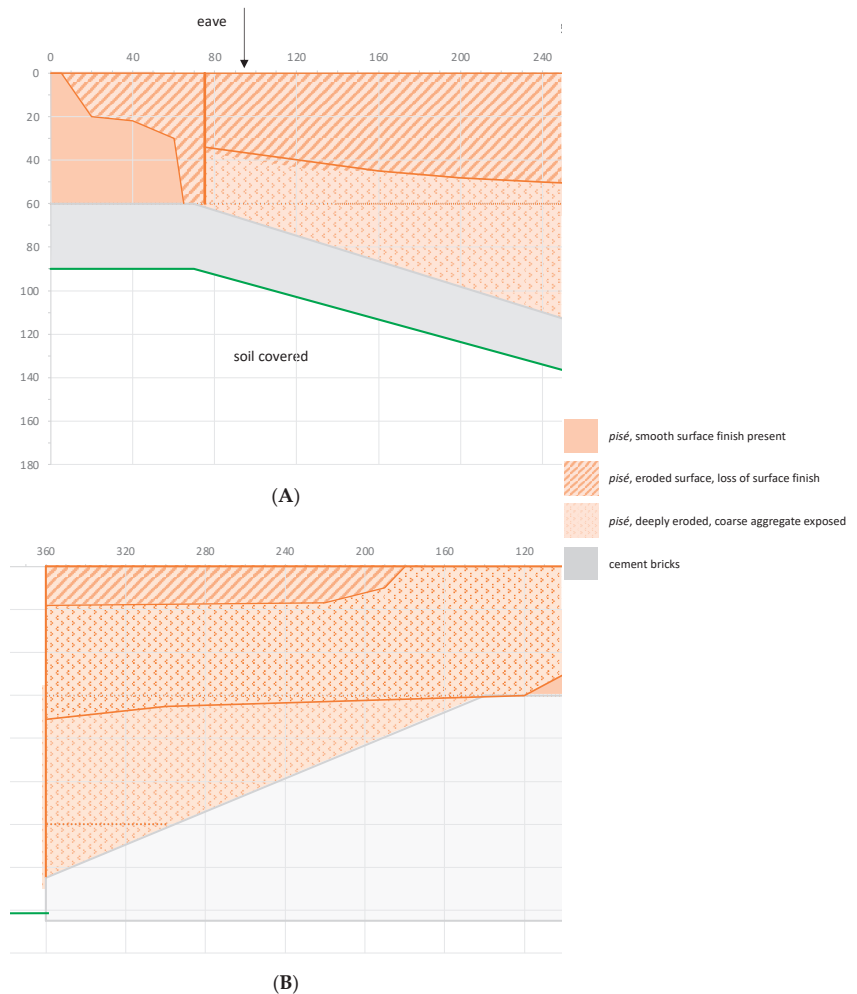
Figure 13. Schematic representation of the observed decay of wall 1: (**A**) eastern face; (**B**) western face.

Based on general observations, as well as experience gathered at the Jugiong site (Figures 2 and 4), it was expected that the wall would exhibit a general overall surface loss, resulting in a reduction in wall thickness, with the upper sections showing a greater loss than the lower sections. As the contour map shows, however, the reality is more complex (Figure 14). A small section, shielded by the eave, appears to have retained its original level. Compared to the control walls that are fully roofed (Figure 11), however, the surface of that section has experienced a loss of smoothness as well as the loss of form board details, indicating some degree of broadscale erosion. As expected, the very top of the walling exhibits the greatest loss of fabric, especially in the area just below the (guttered) drip-line of the eave. The upper section of the wall generally also shows major loss of fabric. A considerable quantity of erosion product, mainly fine- and coarse-grained aggregate, has accumulated at the base of the walls, with the finer clay particles washed out by rainfall. A general loss of surface was also observed in the lower section of that half of the wall closest to the dripline, while the lines between the form board levels are filled with coarser material and thus are prominently visible in the finished walls. In the exposed walls this infill has eroded out and allows for moisture to reside there.
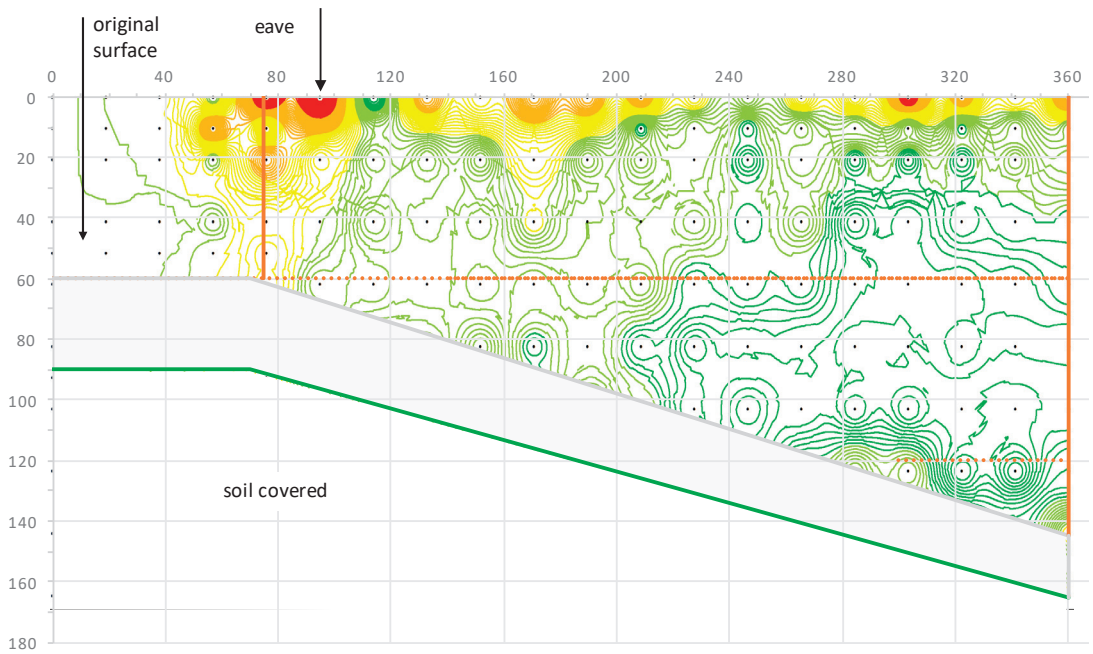
Figure 14. Observed decay on the eastern face of wall 1. Contour intervals 2 mm. Contours (relative to the patch of original surface): dark green 11–22; green 0–10; yellow −13−−1; orange −29−−14; red −50−−30.

Wholly unexpected, however, was the fact that the majority of the lower sections of the unprotected wall seemed to be protruding from the baseline (as defined by the section under the eave). In particular, the lower section of the wall towards the northern end appeared to be much thicker than the rest. The contours clearly show a bulging wall surface (Figure 14). Gentle impact testing (with the blunt end of a broad marker pen) showed that the surface was 'drummy,' indicating a large-scale separation of the surface layer from the wall substrate. This indicates eventual structural failure and cleaving of the wall surface. The extent of the bulging suggests that the fissure between the core of the wall and the surface layer is considerable.

Macroscopic observations of the surface on the eastern face of wall 1 show five states (Figure 13A), which, at different heights and to different degrees, are manifested on the surfaces of all the other walls (Figures 13 and 15–19):

(i). An original surface with a rougher texture and some loss of detail compared to the surfaces of the control walls that are roofed and protected from the environment.

(ii). Surfaces that show pitting and general loss of finish, resulting in a coarse-textured surface revealing the nature of the aggregate. The top of the wall is eroding and loses definition, exposing the aggregate.

(iii). Below-surface separation of the external skin from the core, resulting in bulging of the exterior and noticeable 'drumminess'.

(iv). Surfaces where the original skin has spalled off, resulting in a very uneven and very coarse textured fabric, exposing the aggregate. The top of the wall has become rounded.

(v). Continued deep erosion.
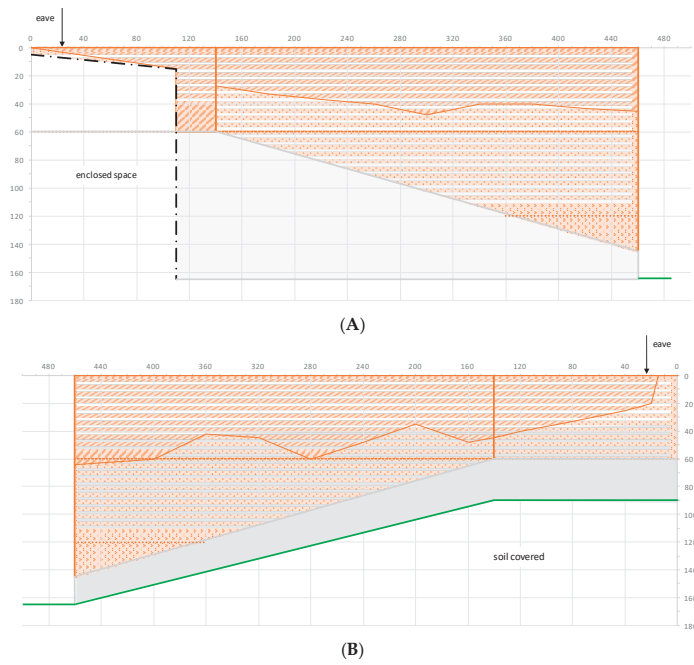
Figure 15. Schematic representation of the observed decay of wall 2: (**A**) eastern face; (**B**) western face. For the legend, see Figure 13.
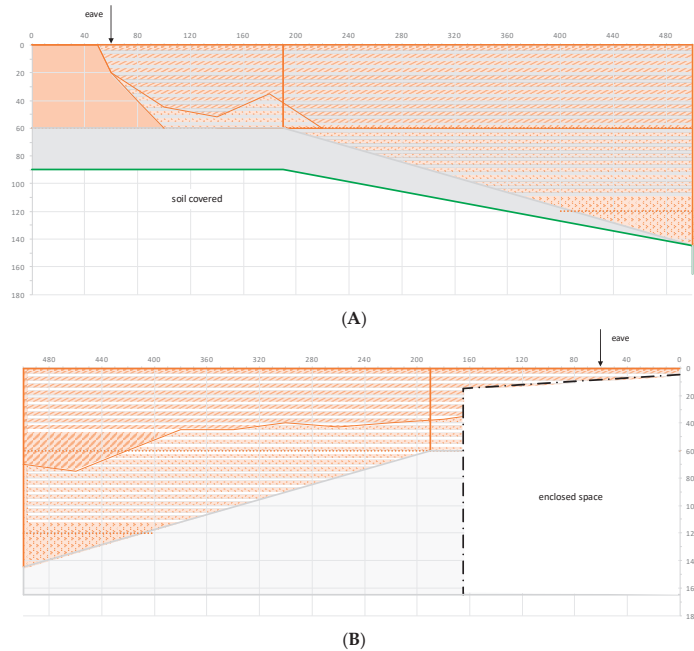
Figure 16. Schematic representation of the observed decay of wall 3: (**A**) eastern face; (**B**) western face. For the legend, see Figure 13.
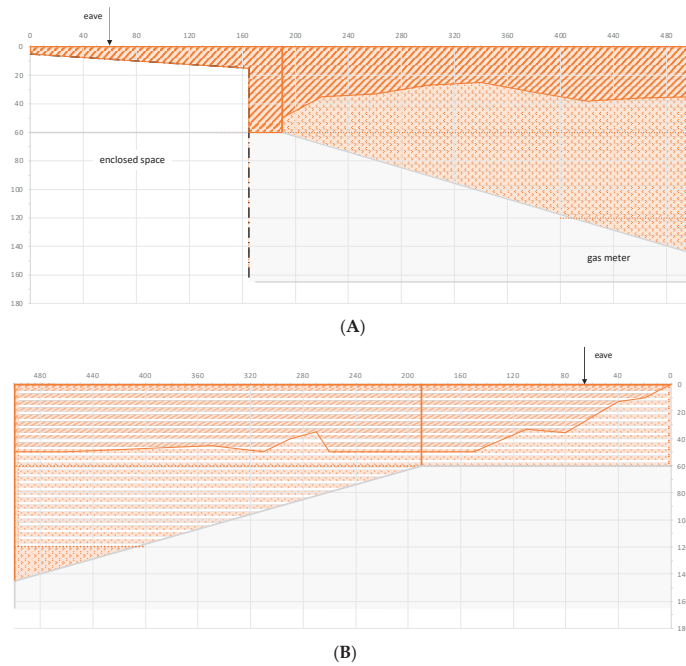
Figure 17. Schematic representation of the observed decay of wall 4: (**A**) eastern face; (**B**) western face. For the legend, see Figure 13.
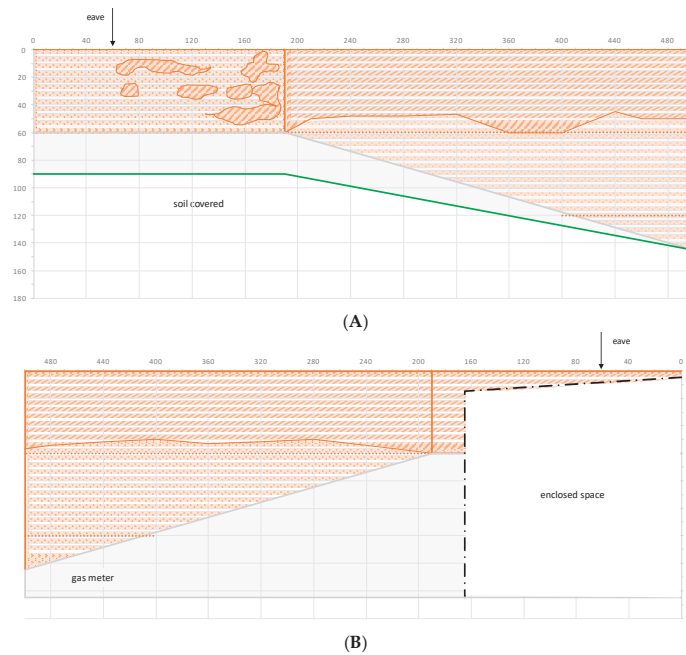
Figure 18. Schematic representation of the observed decay of wall 5: (**A**) eastern face; (**B**) western face. For the legend, see Figure 13.

(A)

(B)
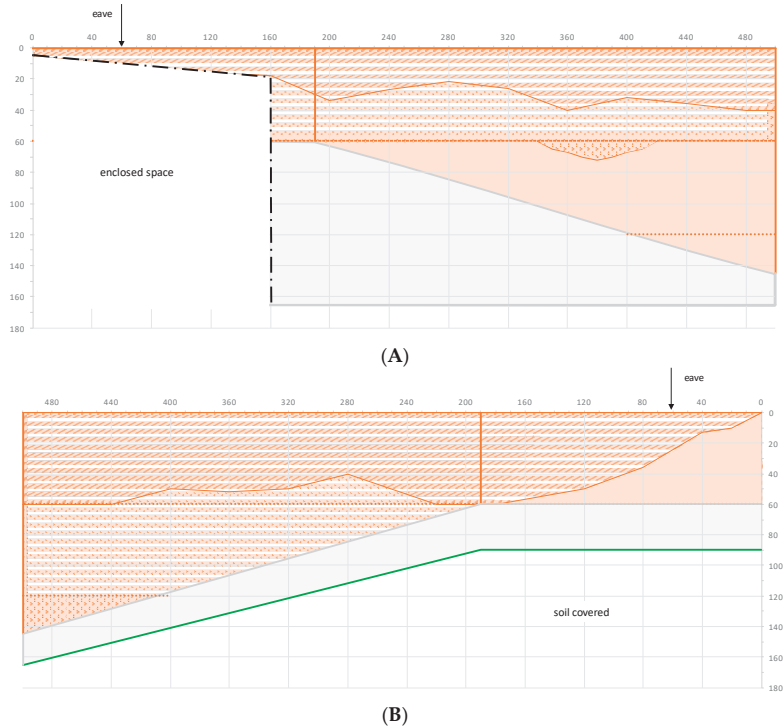
Figure 19. Schematic representation of the observed decay of wall 6: (**A**) eastern face; (**B**) western face. For the legend, see Figure 13.

A variation occurs when the external skin does not spall off as a large chunk, but in horizontal stripes that seem to reflect different levels of compaction during construction.

In the case of the eastern face of wall 1, these four states only partially correlate with the observed contours (Figure 14). The major bulging occurs in the area that shows pitting and general loss of finish, but no spalling. Some of the area returned a hollow sound when knocked, indicating a separation of the external surface from the core. Tapping the surface at the upper margins of that zone led to spalling.

4.4. Ancillary Observations

The bases of all the wing walls are erected on at least one row of 200 mm-high concrete brick, which effectively protects the lower sections of the *pisé* walls from splash impacts. The composting storage area between each set of walls is enclosed by a 0.9 m-high *pisé* wall towards the north and covered with a skillion roof covered with corrugated iron, which prevents falling damp. The eaves of these small structures are generally very narrow (100 mm) and unguttered. Consequently, the surface of the wall shows only very limited loss, mainly in the form of broadscale erosion. As the floor space between the walls is paved (Figure 20), however, rainwater dripping off the unguttered short skillion roof will bounce off the hardened surface and cause splash-effect damage to the lower section of the wall. The effects are variable, with a height of 75–220 mm above the level of the pavers between wing walls 1 and 2, 145–175 mm between wing walls 3 and 4, and 145–220 mm between wing walls 5 and 6.

Figure 20. Paved space between wing walls 3 (left) and 4 (right) of Building 762. Note the decay at the base of the wall of the composting chamber.

The effects of merely capping the walls instead of roofing with an eave can be studied at the entrances to buildings 761 and 762. These show raised parapets as architectural features (Figure 21A). These walls are capped with concrete pavers but have no eaves and only 20 mm-wide protective overhangs. Consequently, the rainfall runs off the flat capping onto the wall and then straight down the front façade (and presumably also the back), causing slight but broadscale erosion of the surface of the *pisé* wall (Figure 21B). The fact that the tops of the walls are flat contributes to the problem, as a similarly capped, but sloping, feature wall of the network facility (Bldg 754) does not show this level of decay. The walls of the single-storey buildings, 760–762, that are protected by overhanging eaves do not exhibit any obvious decay and only exhibit a broadscale micro-erosion. This manifests itself in a loss of the shine on the otherwise smooth surface.
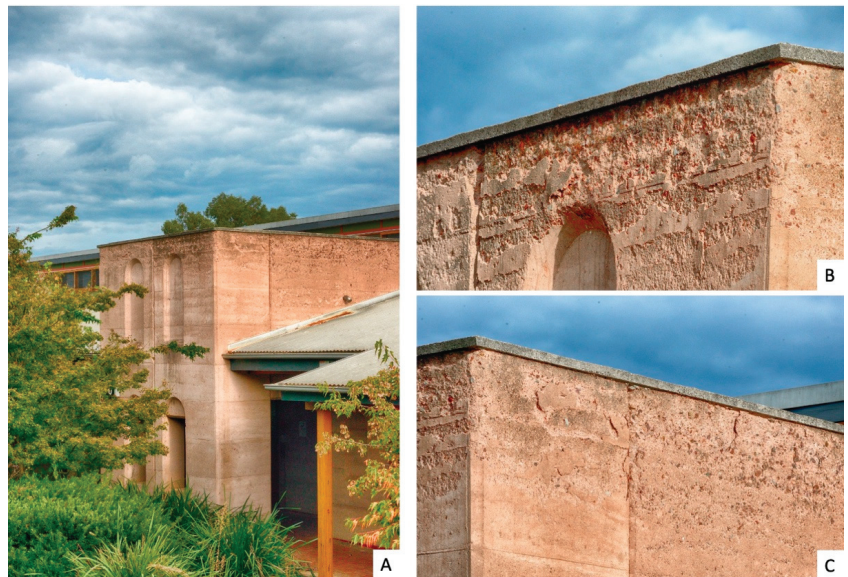
Figure 21. Parapet over the entrance to building 761, seen from southeast: (**A**) the portico; (**B**) decay below the capping, southern façade; (**C**) decay below the capping, eastern façade.

An examination of the walls of building 760 at the ground-floor level showed that eaves even protect the rammed earth walling of two-storey structures. Very limited micro-

erosion occurred, and the walls have retained both the very smooth surface and the small circular protrusions that originate from the recessed bolt sections of the form boards. Any observable micro-erosion that exceeds the loss of the surface shine is limited to a small section at the very bottom that would have been exposed to the splash effects of very heavy rain.

5. Discussion

The buildings at CSU's Thurgoona Campus, erected between 1996 and 2004 (Table 1), were an early adoption of the emerging technology of stabilized rammed earth architecture. The nature of the buildings, which have been exposed to the same environmental conditions, provides examples of the propensity for decay of four different wall types: roofed walls, with and without eaves, capped walls, and uncapped walls. It is very obvious that those walls that are uncapped and otherwise unprotected from the elements, suffer decay much more than the other walls.

From the observations gleaned at all the wall types, the following decay sequence can be inferred:

Phase 1. Moisture ingress into the walling occurs primarily through the top as falling damp. Where the walls are roofed, the falling damp is prevented altogether, whereas the capped walls show a reduced exposure to falling damp. The hygroscopic characteristics of the clay particles lead to a retention of moisture, as well as a swelling of the clay matrix at the top of the wall. This will recede during each drying phase. The cyclic expansion and contraction of the clay particles during the successive wetting and drying phases leads to reduced adhesion to the aggregate. In parallel, extreme diurnal temperature fluctuations, particularly during the summer months, cause a differential expansion and contraction of the binding matrix and the embedded aggregate. This is particularly true for the aggregate components closest to the wall's surface. The resulting micro-fissures set up a capillary action which progressively allows moisture ingress to ever deeper sections of the wall. This leads to an increasing swelling of the clay matrix, which explains why the surface contour map (Figure 14) shows a thickening of the wall. The admixture of the Portland cement (Table 2) seems to have had little effect.

Due to the very smooth nature of the form boards, and the compression used, fresh rammed earth seems to have a higher-density outer skin, akin to, but not as strong as, the fire skin of brick. As long as that skin remains intact, penetrating damp seems to be restricted.

Phase 2. Adhesion failure will progress to such a degree that the surface skin separates from the wall's core, leading to spalling. This large-area cleaving can only be explained by the differential adhesive qualities and stability of the clay matrix between the external skin and the core of the wall. While the compression caused by the form boards plays a major role in establishing a dense skin, it can be posited that the application of deep-penetrating sealants added to this. Even though the sealant, which is designed to repel penetrating damp, is supposed to allow for moisture evaporation, the hygroscopic potential and the sorption of the compressed and impregnated skin are fundamentally different from the less compacted core. Thus, any moisture trapped in the core will expand during increases in daily temperatures and thus set up pressures that will exploit differences in the adhesive potential. This results in structural bonding failure between the matrix and the aggregate and between the core and the skin, opening up ever-expanding and widening fissures that will eventually result in small- to large-scale spalling.

Phase 3. Once this skin has eroded, or spalled off, the surface area increases and the less compacted material with a higher hygroscopic index is exposed. Moisture ingress from both falling and penetrating damp impacts on the clay particles, causing adhesion failure to the gravelly component of the aggregate, which results in a gradual degranulation of the wall. In the case of the walls under discussion, a considerable amount of erosion material had accumulated at the base of the walls.

6. Conclusions

In the past twenty years, rammed earth/*pisé* buildings have seen a resurgence in popularity, primarily in terms of their environmentally friendly, passive energy characteristics, but also because of the aesthetic appeal of the fabric. As with all other earth architecture, *pisé* is susceptible to decay by moisture ingress.

To counteract the ingress of environmental moisture, primarily penetrating damp, both the stabilized and the unstabilized rammed earth walls have been treated with a water-repellent coating, commonly a silane/siloxane sealer with a deep-penetrating, substrate-bonding clear impregnating finish. The effectiveness of these sealants has never been formally assessed in the actual, built environment, let alone as a longitudinal study.

The exposure and decay data available for the Thurgoona buildings span a period of 18–26 years (1996–2004, depending on the building), which is equivalent to between one third and one half of the average life span of an office building (50 years).

The observed patterns of decay show that the stabilized rammed earth at Thurgoona that has been permanently roofed with wide eaves is less likely to show evidence of falling or penetrating damp. The sloping walls that are capped show no falling damp either, while the horizontal walls with capping exhibit falling damp effects in the upper sections below the capping. The capped walls also exhibit broadscale slight surface erosion.

Uncapped walls exhibit both broadscale surface erosion as well as structural failures between the part of the wall that was saturated with the deep-penetrating, substrate-bonding sealer and that part that remained untreated. The sealed skin effectively cleaves off. Based on the available data, the decay of the tops of the capped walls will continue to progress, extending down the walling with deepening erosion at the top.

7. Implications

The future design of both stabilized and unstabilized external rammed earth walls must ensure effective protection from rainfall through well-proportioned overhanging eaves. While the capping of the feature walls may be aesthetically pleasing, and thus architecturally desirable, it does not adequately protect the walling from long-term decay.

References

1. Boltshauser, R.; Veillon, C.; Maillard, N. *Pisé. Stampflehm–Tradition und Potenzial*; Triest: Zürich, Switzerland, 2019.
2. Güntzel, J.G. *Zur Geschichte des Lehmbaus in Deutschland. 1. Massive Lehmbauten: Geschichte, Techniken, Verbreitung*; Ökobuch-Verlag: Rastede, Germany, 1988.
3. Morgan, W.N. *Earth Architecture: From Ancient to Modern*; University Press of Florida: Gainesville, FL, USA, 2008.
4. Maher, J.; Madrigal, J. Earth Architecture in Rural Egypt: Challenges of the context and the material. *A+ Arch Des. Int. J. Archit. Des.* **2021**, *7*, 99–112.
5. Macdonald, K.C.; Morgan, D.W. African earthen structures in colonial Louisiana: Architecture from the Coincoin plantation (1787–1816). *Antiquity* **2012**, *86*, 161–177. [CrossRef]
6. Ruiz, D.; López, C.; Unigarro, S.; Domínguez, M. Seismic rehabilitation of sixteenth-and seventeenth-century rammed earth–built churches in the Andean highlands: Field and laboratory study. *J. Perform. Constr. Facil.* **2015**, *29*, 04014144. [CrossRef]
7. Hallock, G. Pisé construction in early nineteenth-century Virginia. *Perspect. Vernac. Archit.* **2004**, *11*, 40–53.

8. Spennemann, D.H.R. Managing the heritage of German-style mud and pine buildings in Australia. In *Keller, Klöster und Kataster. Festschrift zum 30-Jährigen Bestehen der Bodendenkmalpflege Neuss*; Striewe, K., Ed.; Neusser Schriften zur Archäologie und Bodendenkmalpflege; Stadt Neuss: Neuss, Germany, 2021; Volume 1, pp. 79–88, *in press*.

9. Spennemann, D.H.R. *Diachronic Observations of the Decay of a Pisé Building at Jugiong (NSW)*; Institute for Land, Water and Society, Charles Sturt University: Albury, NSW, Australian, 2015.

10. Spennemann, D.H.R. *Callitris and Mud. An Analysis of the Construction and Decay of a German Farmhouse Complex at Edgehill near Henty (NSW)*; Institute for Land, Water and Society, Charles Sturt University: Albury, NSW, Australian, 2015.

11. Spennemann, D.H.R. *Echoes of the Past. Visions of the Future. The German Colonial Experience in Australia. A Travelling Exhibition*; Retrospect: Albury, NSW, Australian, 2009.

12. Archer, J.; Archer, G. *Dirt Cheap. The Mud Brick Book*; Second Back Row Press, Compendium Pty: Melbourne, Australian, 1976.

13. Sameh, S.H. Promoting earth architecture as a sustainable construction technique in Egypt. *J. Clean. Prod.* **2014**, *65*, 362–373. [CrossRef]

14. Hall, M.R.; Lindsay, R.; Krayenhoff, M. *Modern Earth Buildings: Materials, Engineering, Constructions and Applications*; Elsevier: Amsterdam, The Netherlands, 2012.

15. Dobson, S. Rammed earth in the modern world. In *Rammed Earth Construction Cutting-Edge Research on Traditional and Modern Rammed Earth*; Ciancio, D., Beckett, C., Eds.; CRC Press: London, UK, 2015; pp. 3–10.

16. Guillaud, H. Markers of Earthen Construction Modern Revival. In Proceedings of the Vernacular and Earthen Architecture: Conservation and Sustainability Proceedings of SosTierra 2017, Valencia, Spain, 14–16 September 2017; pp. 3–8.

17. Piani, T.L.; Weerheijm, J.; Koene, L.; Sluys, L. Safe Use of Sustainable Building Materials: A reappraisal of Adobe. In Proceedings of the ICSBM 2019. 2nd International Conference of Sustainable Building Materials, Eindhoven, The Netherlands, 12–15 August 2019; p. 306.

18. Webster-Mannison, M. Integrated systems with rammed earth: Charles sturt university, Thurgoona campus, New South Wales, Australia. In *Alternative Construction: Contemporary Natural Building Methods*; Elizabeth, L., Adams, C., Eds.; John Wiley & Sons: Hoboken, NJ, USA, 2000; pp. 273–282.

19. Webster-Mannison, M. Cooling rural Australia. *EcoLibrium* **2003**, *1*, 22–26.

20. Lindsay, R. Australian modern earth construction. In *Modern Earth Buildings*; Elsevier: Amsterdam, The Netherlands, 2012; pp. 609–649.

21. Illampas, R.; Ioannou, I.; Charmpis, D.C. Overview of the pathology, repair and strengthening of adobe structures. *Int. J. Archit. Herit.* **2013**, *7*, 165–188. [CrossRef]

22. Velosa, A.; Varum, H.; Sáez, M. Characterization of Adobe Blocks from Burgos. In Proceedings of the 9º SIACOT, Seminário Ibero-Americano de Construção e Arquitectura com Terra/6º ATP, Seminário de Arquitectura de Terra em Portugal, Coimbra, Portugal, 20–23 February 2010; pp. 20–23.

23. Dal, M.; Ergin, Ş. Alterations Seen in Adobe Structures. In Proceedings of the Kerpic'19–Earthen Heritage, New Technology, Management 7th International Conference, Köycegiz, Turkey, 5–7 September 2019.

24. Silva, R.A.; Mendes, N.; Oliveira, D.V.; Romanazzi, A.; Domínguez-Martínez, O.; Miranda, T. Evaluating the seismic behaviour of rammed earth buildings from Portugal: From simple tools to advanced approaches. *Eng. Struct.* **2018**, *157*, 144–156. [CrossRef]

25. Liang, R.; Stanislawski, D.; Hota, G. Material characterization and structural response under earthquake loads of hakka rammed earth buildings. *Sustain. Struct.* **2021**, *1*. Available online: https://par.nsf.gov/biblio/10297497 (accessed on 20 March 2022).

26. Zawistowski, K.; Zawistowski, M.; Joffroy, T. Evolving Vernacular: Reinventing Rammed Earth in the Context of Twenty-First Century Seismic Regulation. *Technol. | Archit. +Des.* **2020**, *4*, 158–165. [CrossRef]

27. Holub, M.; Stone, C.; Balintova, M.; Grul, R. Intrinsic Hydrophobicity of Rammed Earth. In Proceedings of the IOP Conference Series: Materials Science and Engineering, Leoben, Austria, 20–24 September 2015; p. 12024.

28. Kebao, R.; Kagi, D. Integral admixtures and surface treatments for modern earth buildings. In *Modern Earth Buildings*; Elsevier: Amsterdam, The Netherlands, 2012; pp. 256–281.

29. Stazi, F.; Nacci, A.; Tittarelli, F.; Pasqualini, E.; Munafò, P. An experimental study on earth plasters for earthen building protection: The effects of different admixtures and surface treatments. *J. Cult. Herit.* **2016**, *17*, 27–41. [CrossRef]

30. Bureau of Meteorology. Climate Statistics for Australian Locations. Monthly Climate Statistics. Albury Airport. Available online: http://www.bom.gov.au/climate/averages/tables/cw_072146_All.shtml (accessed on 12 January 2022).

31. de Teel Tiller, P.; Look, D.W. *Preservation of Adobe Buildings. Preservation Briefs*; Preservation Assistance Division, U.S. National Park Service, U.S. Department of the Interior: Washington, DC, USA, 1978; Volume 5.

32. Guillaud, H. "Pisé": Evolution, innovations, resistances and future directions. In *Rammed Earth Conservation*; Mileto, C., Vegas, F., Cristini, V., Eds.; CRC Press Balkema: London, UK, 2012; pp. 3–9.

33. Hall, M.; Djerbib, Y. Moisture ingress in rammed earth: Part 1—The effect of soil particle-size distribution on the rate of capillary suction. *Constr. Build. Mater.* **2004**, *18*, 269–280. [CrossRef]

34. Hall, M.; Djerbib, Y. Moisture ingress in rammed earth: Part 2—The effect of soil particle size distribution on the absorption of static pressure-driven water. Construction and Building. *Constr. Build. Mater.* **2006**, *20*, 374–383. [CrossRef]

35. Hall, M.; Djerbib, Y. Moisture ingress in rammed earth: Part 3—Sorptivity, surface receptiveness and surface inflow velocity. *Constr. Build. Mater.* **2006**, *20*, 384–395. [CrossRef]

36. Anonymous. Pise, or clay buildings. *The Australian Town & Country Journal (Sydney)*, 12 March 1870; p. 16.

37. Anonymous. Pise or clay buildings. *The Australian Town & Country Journal (Sydney)*, 11 November 1871; p. 621.
38. Anonymous. On building with earth of pise. *The Australian Town & Country Journal (Sydney)*, 10 May 1873; p. 11.
39. Anonymous. Building in pisé. *The Australian Town & Country Journal (Sydney)*, 20 May 1876; p. 817.
40. Anonymous. Pisé Buildings. Their construction and suitability. *Australian Town & Country Journal (Sydney)*, 26 November 1892; p. 30.
41. Anonymous. Pise Buildings. *Albury Banner*, 13 August 1897; p. 13.
42. Anonymous. Pise Walls. *Albury Banner*, 19 November 1897; p. 13.
43. Anonymous. On Building in Pise. *Albury Banner*, 24 January 1902; p. 12.
44. Anonymous. Pisé Buildings. Their construction and suitability. *Australian Town and Country Journal*, 10 February 1904; p. 26.
45. Rirsch, E.; Zhang, Z. Rising damp in masonry walls and the importance of mortar properties. *Constr. Build. Mater.* **2010**, *24*, 1815–1820. [CrossRef]
46. Spennemann, D.H.R. Mitigation of salt damage to the historic built environment. In *PUR$L Productive Use and Rehabilitation of Saline Land. Managing Saltland into the 21st Century: Dollars and Sense from Salt*; Marcar, N.E., Afzal Hossain, A.K.M., Eds.; National Committee for the Productive Use and Rehabilitation of Saline Land: Canberra, Australia, 1999; pp. 13–19.
47. Spennemann, D.H.R.; Marcar, N.E. Urban and heritage landscapes. Under the saline threat. *Nat. Resour. Manag.* **1999**, *2*, 14–17.
48. Spennemann, D.H.R. *Urban Salinity as a Threat to Cultural Heritage Places. A Primer on the Mechanics and Effects of Chloridation*; Johnstone Centre of Parks, Recreation and Heritage, Charles Sturt University: Albury, NSW, Australia, 1997.
49. Allen, D.; Sanchez, G.; Hill, J. The effects of the Loma Prieta earthquake on the seismically retrofitted Santa Cruz Mission Adobe. In *The Seismic Retrofit of Historic Buildings Conference Workbook 1991*; Look, D.W., Ed.; Western Chapter of the Association of Preservation Technology: San Francisco, CA, USA, 1991; pp. 8/1–8/7.
50. Green, M.; Watson, A. Sesimic rehabilitation of the Parra Adobe. In *The Seismic Retrofit of Historic Buildings Conference Workbook 1991*; Look, D.W., Ed.; Western Chapter of the Association of Preservation Technology: San Francisco, CA, USA, 1991; pp. 23/21–23/26.
51. Tolles, E.L.; Webster, F.A.; Thiel, C.C.; Kimbro, E.E.; Ginell, W.S. Recent developments in understanding the seismic performance of historic adobe buildings. In *The Seismic Retrofit of Historic Buildings Conference Workbook 1991*; Look, D.W., Ed.; Western Chapter of the Association of Preservation Technology: San Francisco, CA, USA, 1991; pp. 7/1–7/32.
52. *AS 2121-1979*; The Design of Earthquake Resistant Buildings. Standards Australia: Sydney, Australia, 1979.
53. *AS 1170.4-2007*; Structural Design Actions Part 4: Earthquake Actions in Australia. Standards Australia: Sydney, Australia, 2007.
54. Burbidge, D.R. *The 2012 Australian Earthquake Hazard Map. Record 2012/071*; Geoscience Australia: Canberra, Australia, 2012.
55. Leonard, M.; Burbidge, D.; Edwards, M. *Atlas of Seismic Hazard Maps of Australia. Record 2013/041*; Geoscience Australia: Canberra, Australia, 2013.
56. Spennemann, D.H.R. *The Effects of the 1871–72 Earthquakes on the Southern Riverina. An Overview of Historical and Anecdotal Data*; The Johnstone Centre, Charles Sturt University: Albury, NSW, Australia, 1998.
57. Spennemann, D.H.R. Effects of earthquakes on Wagga Wagga: The 1871 and 1872 events. *Bull. Wagga Wagga Hist. Soc.* **1996**, *300*, 3–6.
58. Webster-Mannison, M. Greening of a University Campus. In Proceedings of the Shaping the Sustainable Millennium-Collaborative Approaches Conference, Brisbane, Australia, 5–7 July 2000.
59. Howard, J.; Mitchell, D.S.; Spennemann, D.H.R.; Webster-Mannison, M. Is today shaping tomorrow for tertiary education in Australia? a comparison of policy and practice. *Int. J. Sustain. High. Educ.* **2000**, *1*, 83–96.
60. Mitchell, D.S.; Croft, I.; Harrison, T.; Webster-Mannison, M. Water Management on the Thurgoona Campus of Charles Sturt University. In Proceedings of the On-Site '01 Conference: Advancing On-Site Wastewater Systems, Armidale, Australia, 25–27 September 2001; pp. 287–294.
61. Mitchell, D.S.; Webster-Mannison, M. *Management of Water Resources: Pilot Project for Integrated Waste Management Systems. Technical Report. Thurgoona Campus, Charles Sturt University*; Charles Sturt University: Albury, NSW, Australia, 1998.
62. Taylor, P.; Fuller, R.; Luther, M. Validated Model and Study of a Rammed Earth Wall building. In Proceedings of the ANZSES 2004: Solar 2004: Life, the Universe and Renewables, Perth, Australia, 30 November–3 December 2004.
63. Taylor, P.A. *Energy and Thermal Comfort in a Rammed Earth Office Building*; Deakin University: Geelong, Australia, 2005.
64. Johnston, L. Deep Green: Charles Sturt University, Thurgoona Campus, NSW. *Archit. Rev. Aust.* **2000**, *73*, 94–99.
65. Spennemann, D.H.R. From Retrospectivity to Strategic Foresight. Towards a paradigm shift in Cultural Heritage Management [Poster]. **2007**. [CrossRef]
66. O'Halloran, C. *City of Albury–City Wide Heritage Study*; Albury City Council: Albury, Australia, 2004.
67. Minister for Planning. *Albury Local Environmental Plan 2010 under the Environmental Planning and Assessment Act 1979 NSW*; Minister for Planning: Sydney, Australia, 2010; Volume 2010/433. Available online: https://legislation.nsw.gov.au/view/whole/html/inforce/current/epi-2010-0433 (accessed on 20 March 2022).
68. Webster-Mannison, M.; McInerney, C. *Charles Sturt University Thurgoona Campus Development Application Report*; Division of University Properties, Charles Sturt University: Bathurst, Australia, 1998.
69. *AS 1141.51—1996*; Methods for Sampling and Testing Aggregates. Method 51: Unconfined Compressive Strength of Compacted Materials. Standards Australia: Sydney, Australia, 1996.
70. *AS 1289.3.1.1—1995*; Methods of Testing Soils for Engineering Purposes. Method 3.1.1: Soil Classification Tests—Determination of the Liquid Limit of a Soil—Four Point Casagrande Method. Standards Australia: Sydney, Australia, 1995.

71. *AS 1289.3.2.1—1995*; Methods of Testing Soils for Engineering Purposes. Method 3.2.1: Soil Classification Tests—Determination of the Plastic Limit of a Soil—Standard Method. Standards Australia: Sydney, Australia, 1995.
72. *AS 1289.3.3.1—1995*; Methods of Testing Soils for Engineering Purposes. Method 3.3.1: Soil Classification Tests—Calculation of the Plasticity Index of a Soil. Standards Australia: Sydney, Australia, 1995.
73. *AS 1289.3.4.1—1995*; Methods of Testing Soils for Engineering Purposes. Method 3.4.1: Soil Classification Tests—Determination of the Linear Shrinkage of a Soil Standard Method. Standards Australia: Sydney, Australia, 1995.
74. *AS 1289.3.6.1—1995*; Methods of Testing Soils for Engineering Purposes. Method 3.6.1: Soil Classification Tests—Determination of the Particle Size Distribution of a Soil—Standard Method of Analysis by Sieving. Standards Australia: Sydney, Australia, 1995.
75. *AS 1289.5.2.1—1995*; Methods of Testing Soils for Engineering Purposes. Method 5.2.1: Soil Compaction and Density Tests—Determination of the Dry Density/Moisture Content Relation of a Soil Using Modified Compactive Effort. Standards Australia: Sydney, Australia, 1995.
76. *AS 3972—1997*; Portland and Blended Cements. Standards Australia: Sydney, Australia, 1997.
77. McInerney, C. *Thurgoona Campus. Specification for Student Association Faciliities, Rammed Earth*; Office of Design, Charles Sturt University: Wagga Wagga, Australia, 2001.
78. McInerney, C. *Thurgoona Campus. Specification for School of Business, 4–Rammed Earth*; Office of Design, Charles Sturt University: Wagga Wagga, Australia, 2003.
79. Middleton, G.F.; Schneider, L.M. *Earth-Wall Construction*; National Building Technology Centre: Chatswood, NSW, Australia, 1987.
80. Tech-Dry Building Protection Systems. Tech-Dry Plasticure RPKR2. 2022. Available online: https://www.techdry.com.au/wp-content/uploads/2018/08/Plasticure-PDS-1.pdf (accessed on 22 January 2022).

Challenges and Future Development Paths of Low Carbon Building Design: A Review

Chang Xi [1] **and Shi-Jie Cao** [1,2,*]

1 School of Architecture, Southeast University, Nanjing 210096, China; chang_xi@seu.edu.cn
2 Global Centre for Clean Air Research, Department of Civil and Environmental Engineering, Faculty of Engineering and Physical Sciences, University of Surrey, Guildford GU2 7XH, UK
* Correspondence: shijie_cao@seu.edu.cn

Abstract: Excessive carbon emissions are causing the problems of global warming and the greenhouse effect, which urgently need to be controlled worldwide. It is crucial to reduce the carbon emissions of the construction industry as it is one of the main sources. Carbon is generated at all phases of the building life cycle, including in material production, building design, and building operation and maintenance. Notably, building design has various extents of influence on carbon emissions at each phase, for which a low carbon method urgently needs to be explored. This paper aims to summarize the current status of building design through literature review considering standard systems, carbon emission calculations, and building design optimization. The challenges of building design are as follows: lack of (1) a comprehensive standard system considering different factors, (2) lack of a carbon emission calculation method for the design phase, and a (3) no real-time optimization model aiming at carbon reduction. The path of "standard−calculation−prediction−optimization" (SCPO) for future building design is proposed to address these challenges. It takes standard system as the framework, the carbon calculation method as the foundation, the prediction model as the theory, and the low carbon building as the objective. This paper can provide theoretical guidance for low carbon building design.

Keywords: low carbon building; building design; standard system; carbon emission calculation; building factor optimization

1. Introduction

Increased fossil fuel combustion and the exploitation of finite resources are causing excessive carbon emissions, further resulting in global warming and the greenhouse effect [1,2]. If the atmospheric CO_2 doubles, the global average temperature will rise by about 3 °C [2]. It is predicted that the increase in global temperature could reach at least 1.5 °C or more by 2030–2052 due to carbon emissions [3]. Countries around the world urgently need to control carbon emissions. In 2015, the Paris Agreement was negotiated. Almost all countries and regions have pronounced low carbon emission policies [4,5]. The European Union has set a goal of achieving carbon neutrality by 2050 [4]. China is the largest carbon emitter in the world, with carbon emissions already reaching 10.251 billion tons in 2020 [6]. In response, the president of China first committed at the 75th UN General Assembly to achieve the goal of carbon peaking by 2030 and carbon neutrality by 2060 [7]. Reducing carbon emissions has become an urgent issue worldwide.

The report from the Intergovernmental Panel on Climate Change (IPCC) stated that industry, buildings, and transportation are the main sources of carbon emissions. Reducing building carbon emissions, which account for almost 40% of the total carbon emissions globally, is the key to achieving carbon peaking and neutrality [8]. The global building stock is on the rise annually. Taking Norway as an example, the building stock is predicted to increase to 448 million m^2 in 2050, which is about 20 % compared to 2020 [9]. China

has about 2 billion m^2 of new construction annually, which accounts for almost 50% of the world's total [10]. It is expected that 800 million m^2 of new urban residential buildings will be built in per year by 2030 [11]. Thus, it is undoubtedly a major challenge to reduce carbon emissions in the building sector in order to achieve the goal of carbon neutrality.

Strategies have been developed in several countries and regions in order to achieve the goal of zero carbon, largely by reducing the carbon emissions from buildings [12]. The main principles are as follows: (1) making full use of renewable energy to reduce the embedded carbon emissions from the production of building materials, to building construction, to the completion phase; (2) using renewable energy and advanced energy-saving technologies to reduce the carbon emissions in the operation phase; and (3) the remaining carbon can be neutralized by means of carbon sinks or compensated carbon, in order to finally achieve the goal of low carbon building [12]. To this end, the carbon emission process of the life cycle of the building should be fully comprehended. As can been seen in Figure 1, there are seven phases in the whole life cycle, including building material production, building transportation, building design, building construction, building operation and maintenance [13], building renewal, and building demolition. Embedded carbon is generated in the phases of building material production, transportation, construction, and demolition [14], while the carbon generated in the phases of operation and maintenance is operational carbon [15,16]. The carbon emissions from building construction and operation can be up to 40% of the global total emissions [17]. Of the phases of the building life cycle, taking office buildings as an example, building operation and maintenance generates about 66% of the operational carbon, with about 27% of embedded carbon generated in the material production, transportation, and construction, and at least 7% of carbon emissions generated in the other phases [18]. This phenomenon means that each phase of the building life cycle has a diverse impact on carbon emissions.
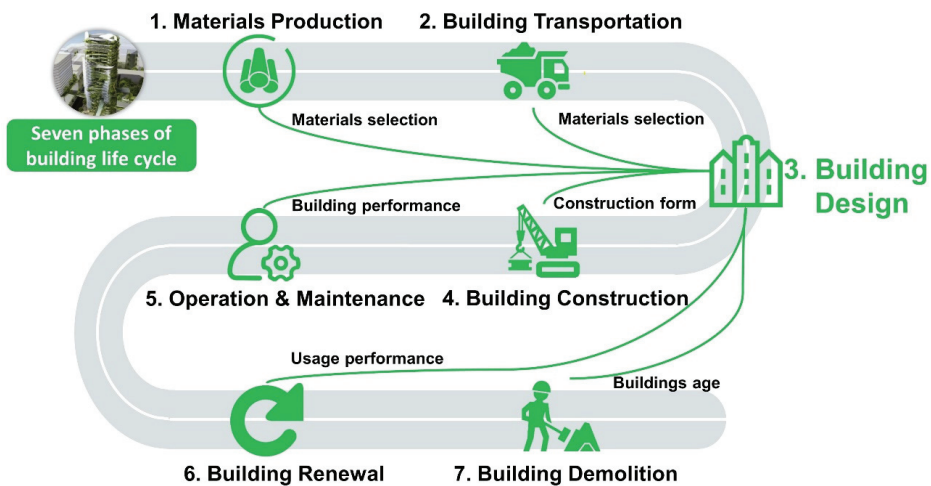
Figure 1. Seven phases of the building life cycle.

It is important to note that building design affects carbon emissions in all phases of the building life cycle to variable extents [19]. Figure 1 clearly depicts that the building design phase can determine the form of the building envelope, material selection, etc., which directly affects the carbon emits in the phases of building material production and building transportation, etc. [20]. The design of air conditioning and ventilation systems in the building operation and maintenance, and building renewal phases are based on the finalized building morphology [21]. More seriously, if the building performance is optimized by active technology or retrofitting, such as adding insulation facilities or retrofitting the original operation system [22,23], the embedded carbon emission of the

building could be increased [24]. Thus, low carbon building design is crucial to reduce carbon emissions throughout the building life cycle.

At present, scholars from all over the world have fully recognized and conducted in-depth research about the impact of building design on carbon emissions [25], such as building design models and tools [26], optimization of the building design factors [27], and passive and active coupling design [28]. There are many challenges for low carbon building design in the actual application because of the complex building environment. This paper aims to summarize the current status of low carbon building design through literature analysis, and to discuss the challenges and possible developments for the future. Section 2 is the methodology of this work. Section 3 is the current status and challenges regarding research on low carbon building design. Section 4 is possible future work of low carbon building design. Section 5 is the main conclusion. This paper aims to have a guiding effect on low carbon building design.

2. Methodology

Literature research is the main method used in this work. Firstly, the keywords of "low carbon, carbon emission, building design, embodied carbon, operation carbon, and energy saving" were searched in academic databases (i.e., ScienceDirect and Web of Science). Secondly, more relevant literature was uncovered by further searching the cited reference of the review articles. Finally, screening the literature was done according to the following three main criteria: (a) The selected publications should cover one or more of the issues related to building design, such as building form, building performance, building energy use, and building optimization. (b) The selected journals focus on the scopes of buildings, cities, building design, built environment, built engineering, etc. (c) The selected publications should be limited to the last ten years, with a focus on the relevant results from the last three to five years.

After literature screening, the traditional building design was introduced, as follows: the current status and future challenges of the possible low carbon building design path were analyzed, mainly including low carbon standards, carbon emission calculation methods, and building optimization design. The proposed low carbon building design path was summarized as well as the implementation methods of traditional building design.

3. The Status and Challenges of Low Carbon Building Design

3.1. The Traditional Building Design Process

Figure 2 illustrates the traditional process of building design, namely conceptual design, preliminary design, development design, and detailed design [29]. Conceptual design is a design concept jointly negotiated by the architect and the project client [21], which can confirm the building type, volume, functions, and main structural systems. The preliminary design details the content of the conceptual design, such as the layout of the building group, building envelope, structural system, acoustical environment, luminous environment, and air conditioning system. Development design, as a phase to supplement the preliminary design content, mainly covers detailed drawings of the building envelope, detailed layouts of the building, selection of building materials, detailed layouts of the air conditioning and ventilation system [30], detailed electrical systems, and fire safety. Detailed design is the last phase, in which the development phase design is optimized in detail using simulation software [29].

The process of building design

Step 1: Conceptual design
A design concept.

Step 2: Preliminary design
Detailing the content of the conceptual design.

Step 3: Development design
Supplement the preliminary design content.

Step 4: Detailed design
Optimized in detail by simulation software.

Building morphology design

Building envelope design

Active management design

Renewable energy utilization

Combination with local meteorological conditions

Carbon Reduction Methods

Figure 2. The process of building design and methods of carbon reduction.

It is necessary to carry out a low carbon design system in the mentioned design process, aimed at low building carbon emissions.

(1) Low carbon design standards are needed to provide constraints in the conceptual design phase, such as renewable energy utilization [31–33] and local meteorological conditions [34,35]. The local climate type, dominant wind direction and speed, solar radiation, and other meteorological conditions should be taken into account, as well as local renewable energy sources such as wind, solar, geothermal, and biomass energy.

(2) In the preliminary and development design phases, carbon emission calculation methods are needed to compare the carbon emissions of different design alternatives. Building carbon emissions are needed to calculate, in real-time, when the design of building morphology (i.e., the block-scale building height, layout, density, green space ratio, building area, and volume and orientation of an individual building [36–39]) and building envelope (i.e., roof, external wall, internal wall, window-to-wall ratio, and shading [40–42]) should be changed.

(3) It is necessary for active regulation of low carbon optimization design in the detailed design phase, such as for air conditioning systems [43], lighting systems [44], etc.

Thus, the standard system, carbon emission calculation, and optimal design should be integrated into the building design process, considering the five carbon reduction methods of building morphology design, building envelope design, renewable energy utilization, combination with local meteorological conditions, and active management design (shown in Figure 2) [26]. The status and challenges of the standard system, carbon calculation, and optimal design are discussed as follows.

3.2. The Status of Low Carbon Building Design

As shown in Figure 3, this paper describes the status of low carbon building design from three aspects, namely (1) the standard system of low carbon building design, (2) the calculation methods of carbon emissions, and (3) the optimal building design.

	Status	Challenges
Standard system	• Low carbon requirements • Local characteristics	• Global standard system
Calculation method	• Life cycle assessment • IO-LCA and process analysis	• Carbon emission factor database • Detailed building inventory
Optimal design	• Univariate optimization • Multivariate optimization • Life cycle carbon emission model	• Drawing-prediction-design

Low carbon building design

Figure 3. The statues and challenges of low carbon building design.

(1) The standard system of low carbon building design: Developed countries in North Europe and North America established related policies at an early stage, and have built numerous low-carbon buildings. Europe formulated the European Energy Technology Strategic Plan in 2008 [45]. The United States developed the Leadership in Energy and Environmental Design (LEED) [46]. These countries have been leading in the field of green and low carbon buildings, and are further exploring new technologies and new routes for "zero energy and zero carbon" buildings. Green buildings with a low energy consumption and high comfort are emerging gradually.

China's Ministry of Housing and Urban−Rural Development released the national standard "General Specification for Building Energy Efficiency and Renewable Energy Utilization" to make the calculation of building carbon emissions aiming at "carbon peaking and carbon neutral" a mandatory demand [47]. "The announcement on the issuance of the implementation plan for the in-depth development of green low-carbon leading action for public institutions to promote carbon peaking" states that the promotion of ultra-low energy buildings and low-carbon buildings should be accelerated and green buildings should be developed. Solar photovoltaic photothermic systems should be vigorously promoted. Photoelectric high-efficiency photovoltaic power generation facilities should be installed, making full use of the suitable site space, such as on building roofs and facades [48].

Several provinces and cities in China have put forward relevant development plans for low-carbon building design successively. In Shanghai, it is suggested that assembled buildings should be developed as ultra-low energy buildings, which advocate for the use of exterior wall insulation, high-performance exterior windows, and related technological innovation [49]. Sichuan Province encourages the establishment of a building energy-saving system in accordance with the local climate, humanities, and natural resources [50,51], while Yunnan Province mentions similar suggestion [52]. The Chongqing government has a standard and management system for ultra-low energy consumption buildings, further providing technical support for projects in the design and construction phases [53].

Currently, there are timely development requirements for low carbon building design in all regions. The building design is a complex issue influenced by climate, humanities, economy, culture, and other factors [54,55]. The standard system of low-carbon building design should be improved.

(2) The calculation methods of carbon emissions: Embedded carbon emissions and operational carbon emissions are generated in the life cycle of a building. In the "Standard for building carbon emission calculation" (GB/T 51366-2019) [56], the operational carbon emission calculation is determined based on the amount of different types of energy consumption and the carbon emission factors. Simulation software, such as Energy Plus, eQuest, and TRNSYS [26,40], are used as tools to calculate energy consumption. For the embedded carbon emission, life cycle assessment (LCA) is an internationally and nationally

acknowledged method [24,57–59]. Based on LCA, the input−output analysis (IO-LCA) method is widely used around the world [60–62]. It can calculate industry-wide carbon emissions by using economic input and output data, without the ability to perform specific calculations and analyses during the detailed building processes. The process analysis method [63] can overcome the limitations of IO-LCA by means of carbon emission factors for each phase, which can calculate the carbon emissions from the material production, transportation, construction, operation, disassembly, and recycling of buildings [58,59]. Specifically, the detailed process inventory for each phase is necessary for the process analysis method.

Carbon emission factors are an essential part of the calculation of embedded and operational carbon. IPCC provides a basic database of carbon emission factors. The database cannot be entirely suitable for all buildings, owing to the complex and diverse building types [64]. To be specific, more building forms and composites are gradually being proposed to meet the growing needs of high-rise buildings, resulting in carbon emission factors needing to be updated [18]. Moreover, the sources of carbon emission factors are not uniform, including the basic databases, literature, and standards [65,66]. This is an urgent issue that needs to be solved for the establishment of a standardized and comprehensive carbon emission factor database for low carbon building design.

A detailed building inventory is also crucial for the calculation, without carbon emission factors. As the building inventory information can be commonly obtained from engineering drawings, less detailed information is available on the conceptual and preliminary design phases of building design [67]. Therefore, the carbon emission calculation method should also consider the life cycle process with less inventory information [68].

(3) The optimal building design: There are three types of the optimization of low carbon building design. The first one is to investigate the impact of different factors in building design on carbon emission or energy saving (univariate optimization). Compared with active means, passive design can effectively reduce energy consumption and carbon emissions. Studies have been carried out on passive design factors for energy saving or low carbon emissions, including green roofs [69,70], window-to-wall ratios [71], and building orientation [72], which can provide sufficient theoretical support for low carbon and low energy consumption building design. However, strong interactions are exited between different design factors, causing limitations in practical applications for the univariate optimization.

The second is the multi-objective optimization of building design factors. Construction cost and energy consumption are the commonly used objective functions [73,74]. Low energy consumption and low carbon building design can be achieved by finding the optimal objective [17,27,75]. However, this refers more to the carbon emissions of operational energy consumption [28], which are not enough to indicate the actual carbon emission reduction [76]. Life cycle carbon emissions should be considered in low carbon building design [77]. Many scholars have conducted research on the life cycle carbon emission calculation model of buildings, which is also the research content of the third type.

Generally, in the research of the carbon emission model of buildings, the carbon emission database for life-cycle should first be established [78]. Secondly, the model can be constructed by machine learning and regression fitting, etc. [79–82]. The current database construction mainly includes research statistics and energy consumption simulation [26,29,57,83]. Research statistics require continuous statistical data over several years or months, for which it takes more time to build a database of carbon emissions. The existing building design optimization is time-consuming and investment heavy. It is necessary to explore a fast and convenient optimization method for low carbon building design.

3.3. The Challenges of Low Carbon Building Design

As shown in Figure 3, based on the analysis of the status of the standard system, the calculation method, and the optimal low carbon building design, several challenges in the development of low carbon building design are present.

The first challenge is the lack of a global perspective design standard system. China's building stock is relatively high, with various climate characteristics [84], population densities, economic levels, and human characteristics [54]. There is an urgent need for low-carbon buildings to consider multiple factors and develop novel design approaches for different characteristics [85], which consider the spatial form of buildings and being low carbon as the common optimization objectives.

The second challenge is the lack of carbon emission calculation methods applicable to the design phase. The existing calculation methods of embedded and operational carbon require a comprehensive database of carbon emission factors and detailed process inventories [56]. The current database of carbon emission factors needs to be improved in order to be applicable to more building types [18]. The information in the detailed process inventory is assumed, which may differ from the actual construction and operation process information, further affecting the accuracy of the calculation of building carbon emissions [68,86]. Hence, in order to reduce the difference between the design and operating phase, exploring a calculation method applicable to the design phase remains a great challenge.

The third challenge is the lack of real-time optimization methods in the design phase aiming at low carbon emissions. Low carbon building design should take into account the building morphology, for example circulation space, open space and aesthetics, floor area, floor layout, floor height, building volume, building orientation, and fenestration, as well as windows, doors, shading and exterior walls, etc. [74]. Each factor affects the carbon emission directly or indirectly [87]. Moreover, there is the problem of the design process being the time-consuming and this needs to be optimized [81]. Low carbon building design needs to use convenient and fast optimization methods, i.e., drawing−prediction−design, which can provide accurate guidance for building design.

4. Possible Future Work

As shown in Figure 4, the design standard system of "spatial regulation" and "performance regulation" for low carbon green buildings that can adapt to various climatic characteristics will be established in future work. The standard system of building design can provide the low carbon constraints for the conceptual design phase, as well as low carbon concepts for climate and renewable energy adaptation. Specifically, this includes building morphology design, envelope design, low carbon material selection, balancing control between light and heat, passive−active coupling design, indoor humidity independent control, etc.
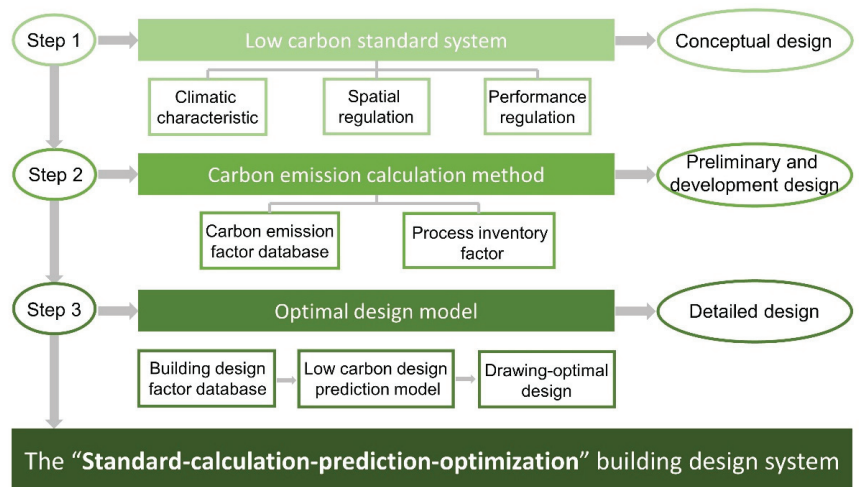
Figure 4. Possible future work for low carbon building design.

Then, based on the low carbon building design standard system, the carbon emission calculation methods applicable to the design phase will be explored in future work. Real-time and rapid calculation of building carbon emissions, important for evaluating design alternatives, will be used for different design alternatives during the preliminary design and development design phases. A comprehensive database of carbon emission factors will be built to meet the needs of different climatic conditions, building types, and building heights, etc. In addition, the carbon emission calculation in the design phase will meet the demand of incomplete content of inventory information in future research. Based on the carbon emission factor and the process inventory database, a convenient and fast carbon emission calculation method should be formed to facilitate the rapid assessment of carbon emissions in the design phase.

In the final step, building design in the future will be optimized through the design model. The design parameters will be accurately quantified to minimize the building carbon emissions. Firstly, different climate zones and building types are used as the first boundary conditions. Site area, floor/area ratio, and building height limits should be used as the second boundary conditions. The building orientation and window-to-wall ratio should be used as the third boundary conditions. The influence of each building design factor on carbon emission should be constructed, further contributing a comprehensive database of design factors. Secondly, a low-carbon design prediction model will be constructed through big data analysis and machine learning methods based on the above boundary conditions. Finally, building design drawing software, including Computer Aided Design (CAD) and Building Information Modeling (BIM), will be coupled with the low carbon design prediction model, forming a design pattern so that buildings can be optimized immediately after drawing.

5. Conclusions

This paper reviews the current status of the building standards system, carbon emission calculation methods, and building design optimization in the traditional building design process. The main challenges are as follows: (1) the lack of a comprehensive standard system for different climate zones, space, and performance requirements in the building design phase; (2) the existing carbon emission calculation methods lack a comprehensive database of carbon emission factors, which are not applicable to the design phase without a detailed process inventory; and (3) not being able to optimize building design factors based on real-time carbon emissions during the drawing process in the design phase.

Possible future work in building design should examine dealing with the above-mentioned challenges. A standard design system integrating spatial building information and low carbon performance needs to be formed, which is a constraint framework for the traditional conceptual design phase. A convenient carbon calculation method based on a comprehensive carbon emission factor database and a process inventory factor database should be explored, which is significant for the preliminary and development design phase. The prediction model will be proposed for detailed design using machine learning methods. Specifically, the spatial-low carbon standard system, carbon calculation method, prediction model of building design, and the optimal design of low carbon will be the framework, the foundation, the theory, and the objective, respectively. The system of "standard−calculation−prediction−optimization (SCPO)" will provide precise guidance for future building design.

Author Contributions: Conceptualization, investigation, and writing—original draft preparation, C.X.; resources, funding acquisition, and writing—review and editing, S.-J.C. All authors have read and agreed to the published version of the manuscript.

Institutional Review Board Statement: Not applicable.

References

1. Martins, T.; Barreto, A.C.; Souza, F.M.S.; Souza, A.M. Fossil fuels consumption and carbon dioxide emissions in G7 countries: Empirical evidence from ARDL bounds testing approach. *Environ. Pollut.* **2021**, *291*, 118093. [CrossRef] [PubMed]
2. Denning, A.S. Combustion to concentration to warming: What do climate targets mean for emissions? climate change and the global carbon cycle. *Encycl. Anthr.* **2018**, *1*, 443–452.
3. Smith, D.M.; Scaife, A.A.; Hawkins, E.; Bilbao, R.; Boer, G.J.; Caian, M.; Caron, L.P.; Danabasoglu, G.; Delworth, T.; Doblas-Reyes, F.J.; et al. Predicted chance that global warming will temporarily exceed 1.5 °C. *Geophys. Res. Lett.* **2018**, *45*, 11895–11903. [CrossRef]
4. EC. Committing to Climate-Neutrality by 2050: Commission Proposes European Climate Law and Consults on the European Climate Pact. Available online: https://ec.europa.eu/commission/presscorner/detail/en/ip_20_335 (accessed on 4 March 2020).
5. Jan, G.; Thomas, B.; Ashok, J.; Jan, S.; Felix, W.; Martin, S. Overview of Member States Information on NZEBs. Available online: https://ec.europa.eu/energy/sites/ener/files/documents/Updated%20progress%20report%20NZEB.pdf (accessed on 8 October 2014).
6. CABEE. *China Building Energy Consumption Annual Report 2020; Building Energy Efficiency, International Energy Charter*; CABEE: Brussels, Belgium, 2021; Volume 49, pp. 1–6.
7. CHINADAILY. Statement by H.E. Xi Jinping President of the People's Republic of China At the General Debate of the 75th Session of The United Nations General Assembly. Available online: http://www.chinadaily.com.cn/a/202009/24/WS5f6c08aca3 1024ad0ba7b776.html (accessed on 22 September 2020).
8. UNEP. Global Status Report for Buildings and Construction. 2019. Available online: https://www.iea.org/reports/global-status-report-for-buildings-and-construction-2019 (accessed on 20 December 2019).
9. Nina, H.S.; Jan, S.N.; Helge, B.; Inger, A.; Arild, G. Large potentials for energy saving and greenhouse gas emission reductions from large-scale deployment of zero emission building technologies in a national building stock. *Energ Policy* **2021**, *152*, 112114.
10. NBS. *China Statistical Yearbook*; National Bureau of Statistics of People's Republic of China: Beijing, China, 2014.
11. IEA. *World Energy Outlook 2007: China and India Insights; Sourceoecd Energy*; IEA/OECD: Paris, France, 2007; Volume 3, pp. 1–672.
12. Council, U.G.B. *Net Zero Carbon Buildings: A framework Definition*; UK Green Building Council: London, UK, 2019.
13. Zhang, S.; Xiang, X.; Ma, Z.; Ma, M.; Zou, C. Carbon neutral roadmap of commercialbuilding operations by mid-century: Lessons from China. *Buildings* **2021**, *11*, 510. [CrossRef]
14. Ibn-Mohammed, T.; Greenough, R.; Taylor, S.; Ozawa-Meida, L.; Acquaye, A. Operational vs. embodied emissions in buildings-A review of current trends. *Energy Build.* **2013**, *66*, 232–245. [CrossRef]
15. Li, L. Integrating climate change impact in new building design process: A review of building life cycle carbon emission assessment methodologies. *Clean. Eng. Technol.* **2021**, *5*, 100286. [CrossRef]
16. Grynning, S.; Gradeci, K.; Gaarder, J.E.; Time, B.; Lohne, J.; Kvande, T. Climate adaptation in maintenance operation and management of buildings. *Buildings* **2020**, *10*, 107. [CrossRef]
17. Xue, Q.W.; Wang, Z.J.; Chen, Q.Y. Multi-objective optimization of building design for life cycle cost and CO_2 emissions: A case study of a low-energy residential building in a severe cold climate. *Build. Simul.-China* **2022**, *15*, 83–98. [CrossRef]
18. Gan, V.J.L.; Cheng, J.C.P.; Lo, I.M.C.; Chan, C.M. Developing a CO_2-e accounting method for quantification and analysis of embodied carbon in high-rise buildings. *J. Clean. Prod.* **2017**, *141*, 825–836. [CrossRef]
19. Basbagill, J.; Flager, F.; Lepech, M.; Fischer, M. Application of life-cycle assessment to early stage building design for reduced embodied environmental impacts. *Build. Environ.* **2013**, *60*, 81–92. [CrossRef]
20. Gustavsson, L.; Joelsson, A.; Sathre, R. Life cycle primary energy use and carbon emission of an eight-storey wood-framed apartment building. *Energy Build.* **2010**, *42*, 230–242. [CrossRef]
21. Braganca, L.; Vieira, S.M.; Andrade, J.B. Early stage design decisions: The way to achieve sustainable buildings at lower costs. *Sci. World J.* **2014**, 365364. [CrossRef] [PubMed]
22. Leinartas, H.A.; Stephens, B. Optimizing whole house deep energy retrofit packages: A case study of existing Chicago-area homes. *Buildings* **2015**, *5*, 323–353. [CrossRef]
23. Far, C.; Far, H. Improving energy efficiency of existing residential buildings using effective thermal retrofit of building envelope. *Indoor Built Environ.* **2019**, *28*, 744–760. [CrossRef]
24. Su, X.; Tian, S.C.; Shao, X.L.; Zhao, X. Embodied and operational energy and carbon emissions of passive building in HSCW zone in China: A case study. *Energy Build.* **2020**, *222*, 110090. [CrossRef]
25. Cao, S.J.; Leng, J.; Qi, D.; Kumar, P.; Chen, T. Sustainable underground spaces: Design, environmental control and energy conservation. *Energy Build.* **2022**, *257*, 111779. [CrossRef]
26. Alwisy, A.; BuHamdan, S.; Gul, M. Evidence-based ranking of green building design factors according to leading energy modelling tools. *Sustain. Cities Soc.* **2019**, *47*, 101491. [CrossRef]

27. Zemero, B.R.; Tastes, M.E.D.; Bezerra, U.H.; Batista, V.D.; Carvalho, C.C.M.M. Methodology for preliminary design of buildings using multi-objective optimization based on performance simulation. *J. Sol. Energy Eng.-Trans. ASME* **2019**, *141*, 040801. [CrossRef] [PubMed]

28. Xia, B.; Li, X. Analysis and comparison on the potential of low-carbon architectural design strategies. *Sustain. Comput.-Inform. Syst.* **2019**, *21*, 204–211. [CrossRef]

29. Gao, H.; Koch, C.; Wu, Y.P. Building information modelling based building energy modelling: A review. *Appl. Energy* **2019**, *238*, 320–343. [CrossRef]

30. Cao, S.J.; Feng, Z.; Wang, J.; Ren, C.; Zhu, H.C.; Chen, G.; Mei, J. Ergonomics-oriented operation, maintenance and control of indoor air environment for public buildings. *Chin. Sci. Bull.* **2022**, *67*. [CrossRef]

31. Ascione, F.; Bianco, N.; De Masi, R.F.; De Stasio, C.; Mauro, G.M.; Vanoli, G.P. Multi-objective optimization of the renewable energy mix for a building. *Appl. Therm. Eng.* **2016**, *101*, 612–621. [CrossRef]

32. Srinivasan, R.S.; Campbell, D.E.; Wang, W. Renewable substitutability index: Maximizing renewable resource use in buildings. *Buildings* **2015**, *5*, 581–596. [CrossRef]

33. Matic, D.; Calzada, J.R.; Todorovic, M.S. Renewable energy sources-integrated refurbishment approach for low-rise residential prefabricated building in Belgrade, Serbia. *Indoor Built Environ.* **2016**, *25*, 1016–1023. [CrossRef]

34. Wang, Q.; Holmberg, S. A methodology to assess energy-demand savings and cost effectiveness of retrofitting in existing Swedish residential buildings. *Sustain. Cities Soc.* **2015**, *14*, 254–266. [CrossRef]

35. Qi, J.; Wei, C.Y. Performance evaluation of climate-adaptive natural ventilation design: A case study of semi-open public cultural building. *Indoor Built Environ.* **2021**, *30*, 1714–1724. [CrossRef]

36. Richman, R.; Simpson, R. Towards quantifying energy saving strategies in big-box retail stores: A case study in Ontario (Canada). *Sustain. Cities Soc.* **2016**, *20*, 61–70. [CrossRef]

37. Chen, X.; Yang, H.X.; Zhang, W.L. Simulation-based approach to optimize passively designed buildings: A case study on a typical architectural form in hot and humid climates. *Renew. Sustain. Energy Rev.* **2018**, *82*, 1712–1725. [CrossRef]

38. Kerdan, I.G.; Galvez, D.M.; Raslan, R.; Ruyssevelt, P. Modelling the energy and exergy utilisation of the Mexican non-domestic sector: A study by climatic regions. *Energy Policy* **2015**, *77*, 191–206. [CrossRef]

39. Xi, C.; Ren, C.; Wang, J.Q.; Feng, Z.B.; Cao, S.J. Impacts of urban-scale building height diversity on urban climates: A case study of Nanjing, China. *Energy Build.* **2021**, *251*, 111350. [CrossRef]

40. Ali-Toudert, F.; Weidhaus, J. Numerical assessment and optimization of a low-energy residential building for Mediterranean and Saharan climates using a pilot project in Algeria. *Renew. Energy* **2017**, *101*, 327–346. [CrossRef]

41. Aksamija, A. Regenerative design and adaptive reuse of existing commercial buildings for net-zero energy use. *Sustain. Cities Soc.* **2016**, *27*, 185–195. [CrossRef]

42. Echenagucia, T.M.; Capozzoli, A.; Cascone, Y.; Sassone, M. The early design stage of a building envelope: Multi-objective search through heating, cooling and lighting energy performance analysis. *Appl. Energy* **2015**, *154*, 577–591. [CrossRef]

43. Wang, J.Q.; Yu, C.W.; Cao, S.J. Technology pathway of efficient and climate-friendly cooling in buildings: Towards carbon neutrality. *Indoor Built Environ.* **2021**, *30*, 1307–1311. [CrossRef]

44. Setiawan, A.F.; Huang, T.L.; Tzeng, C.T.; Lai, C.M. The effects of envelope design alternatives on the energy consumption of residential houses in Indonesia. *Energies* **2015**, *8*, 2788–2802. [CrossRef]

45. Eikeland, P.O.; Skjærseth, J.B. The politics of low-carbon innovation: Implementing the European Union's strategic energy technology plan. *Energy Res. Soc. Sci.* **2021**, *76*, 102043. [CrossRef]

46. Hu, M. 2019 energy benchmarking data for LEED-certified buildings in Washington, D.C.: Simulation and reality. *J. Build. Eng.* **2021**, *42*, 102475. [CrossRef]

47. MOHURD. Announcement on the Release of National Standards of General Specification for Energy Conservation and Renewable Energy Utilization in Buildings. Available online: http://www.mohurd.gov.cn/gongkai/fdzdgknr/zfhcxjsbwj/202110/2021101 3_762460.html (accessed on 8 September 2021).

48. FORESTRY. The Announcement on the Issuance of the Implementation Plan for the In-Depth Development of Green Low-Carbon Leading Action for Public Institutions to Promote Carbon Peaking. Available online: http://www.forestry.gov.cn/zlszz/4262/2 0211123/110547204815318.html (accessed on 19 November 2021).

49. ZJWSH. The 14th Five-Year Plan for Green Buildings in Shanghai. Available online: http://zjw.sh.gov.cn/ghjh/20211109/a3b0 3c1ee247418ebce706bd0b08da10.html (accessed on 9 November 2021).

50. SCJST. "Fourteen Five" Construction Industry Development Plan of Sichuan Province. Available online: http://jst.sc.gov.cn/ scjst/ghxx/2021/9/26/0f6d7763bd2b4f66b2cfeb568dfb66e1.shtml (accessed on 26 September 2021).

51. CDZJ. The Notice on the Issuance of the "14th Five-Year Plan for the Development of the Construction Industry in Chengdu" by Chengdu Housing and Urban-Rural Development Bureau. Available online: http://cdzj.chengdu.gov.cn/cdzj/c131968/2021-11/ 15/content_8516cf63f9cf4195b6894ae4444e59a2.shtml (accessed on 15 November 2021).

52. ZFCXJSTYN. Announcement on the Issuance of the "Fourteenth Five-Year Plan for the Development of Green Assembly Building Industry in Yunnan Province". Available online: https://zfcxjst.yn.gov.cn/zhengfuwenjian8655/284647.html (accessed on 22 November 2021).

53. ZFCXJWCQ. Announcement on the Issuance of the "Green Finance in Chongqing to Support the Green Development of the Construction Industry Pilot Program". Available online: http://zfcxjw.cq.gov.cn/zwxx_166/gsgg/202111/t20211112_9968747.html (accessed on 12 November 2021).
54. Wang, J.G.; Cao, S.J.; Yu, C.W. Development trend and challenges of sustainable urban design in the digital age. *Indoor Built Environ.* **2021**, *30*, 3–6. [CrossRef]
55. Meng, M.R.; Cao, S.J.; Kumar, P.; Tang, X.; Feng, Z. Spatial distribution characteristics of PM2.5 concentration around residential buildings in urban traffic-intensive areas: From the perspectives of health and safety. *Saf. Sci.* **2021**, *141*, 105318. [CrossRef]
56. Standard for building carbon emission calculation. *GB/T 51366-2019*; MOHURD: Beijing, China, 2019.
57. Mao, X.K.; Wang, L.X.; Li, J.W.; Quan, X.L.; Wu, T.Y. Comparison of regression models for estimation of carbon emissions during building's lifecycle using designing factors: A case study of residential buildings in Tianjin, China. *Energy Build.* **2019**, *204*, 109519.
58. Dodoo, A.; Gustavsson, L.; Sathre, R. Lifecycle carbon implications of conventional and low-energy multi-storey timber building systems. *Energy Build.* **2014**, *82*, 194–210. [CrossRef]
59. Hong, J.K.; Shen, G.Q.; Feng, Y.; Lau, W.S.T.; Mao, C. Greenhouse gas emissions during the construction phase of a building: A case study in China. *J. Clean. Prod.* **2015**, *103*, 249–259. [CrossRef]
60. Huang, Y.A.; Weber, C.L.; Matthews, H.S. Categorization of scope 3 emissions for streamlined enterprise carbon footprinting. *Environ. Sci. Technol.* **2009**, *43*, 8509–8515. [CrossRef] [PubMed]
61. Guan, J.; Zhang, Z.H.; Chu, C.L. Quantification of building embodied energy in China using an input-output-based hybrid LCA model. *Energy Build.* **2016**, *110*, 443–452. [CrossRef]
62. Han, M.Y.; Chen, G.Q.; Shao, L.; Li, J.S.; Alsaedi, A.; Ahmad, B.; Guo, S.; Jiang, M.M.; Ji, X. Embodied energy consumption of building construction engineering: Case study in E-town, Beijing. *Energy Build.* **2013**, *64*, 62–72. [CrossRef]
63. Li, Y.L.; Han, M.Y.; Liu, S.Y.; Chen, G.Q. Energy consumption and greenhouse gas emissions by buildings: A multi-scale perspective. *Build. Environ.* **2019**, *151*, 240–250. [CrossRef]
64. Gan, V.J.L.; Chan, C.M.; Tse, K.T.; Lo, I.M.C.; Cheng, J.C.P. A comparative analysis of embodied carbon in high-rise buildings regarding different design parameters. *J. Clean. Prod.* **2017**, *161*, 663–675. [CrossRef]
65. Marinova, S.; Deetman, S.; van der Voet, E.; Daioglou, V. Global construction materials database and stock analysis of residential buildings between 1970–2050. *J. Clean. Prod.* **2020**, *247*, 119146. [CrossRef]
66. Gan, V.J.L.; Cheng, J.C.P.; Lo, I.M.C. A comprehensive approach to mitigation of embodied carbon in reinforced concrete buildings. *J. Clean. Prod.* **2019**, *229*, 582–597. [CrossRef]
67. Kumanayake, R.; Luo, H.B.; Paulusz, N. Assessment of material related embodied carbon of an office building in Sri Lanka. *Energy Build.* **2018**, *166*, 250–257. [CrossRef]
68. Rock, M.; Hollberg, A.; Habert, G.; Passer, A. LCA and BIM: Visualization of environmental potentials in building construction at early design stages. *Build. Environ.* **2018**, *140*, 153–161. [CrossRef]
69. Mahmoud, S.; Ismaeel, W.S.E. Developing sustainable design guidelines for roof design in a hot arid climate. *Archit. Sci. Rev.* **2019**, *62*, 507–519. [CrossRef]
70. Rakotondramiarana, H.T.; Ranaivoarisoa, T.F.; Morau, D. Dynamic simulation of the green roofs impact on building energy performance, case study of Antananarivo, Madagascar. *Buildings* **2015**, *5*, 497–520. [CrossRef]
71. Feehan, A.; Nagpal, H.; Marvuglia, A.; Gallagher, J. Adopting an integrated building energy simulation and life cycle assessment framework for the optimisation of facades and fenestration in building envelopes. *J. Build. Eng.* **2021**, *43*, 103138. [CrossRef]
72. Yu, Z.; Zhang, W.L.; Fang, T.Y. Impact of building orientation and window-wall ratio on the office building energy consumption. *Appl. Mech. Mater.* **2013**, *409-410*, 606–611. [CrossRef]
73. Lartigue, B.; Lasternas, B.; Loftness, V. Multi-objective optimization of building envelope for energy consumption and daylight. *Indoor Built Environ.* **2014**, *23*, 70–80. [CrossRef]
74. Zhu, J.J.; Chew, D.A.S.; Lv, S.; Wu, W.W. Optimization method for building envelope design to minimize carbon emissions of building operational energy consumption using orthogonal experimental design (OED). *Habitat Int.* **2013**, *37*, 148–154. [CrossRef]
75. Longo, S.; Montana, F.; Sanseverino, E.R. A review on optimization and cost-optimal methodologies in low-energy buildings design and environmental considerations. *Sustain. Cities Soc.* **2019**, *45*, 87–104. [CrossRef]
76. Fenner, A.E.; Kibert, C.J.; Li, J.X.; Razkenari, M.A.; Hakim, H.; Lu, X.S.; Kouhirostami, M.; Sam, M. Embodied, operation, and commuting emissions: A case study comparing the carbon hotspots of an educational building. *J. Clean. Prod.* **2020**, *268*, 122081. [CrossRef]
77. O'Neill, R.; Window, A.; Kenway, S.; Dargusch, P. Integrated operational and life-cycle modelling of energy, carbon and cost for building facades. *J. Clean. Prod.* **2021**, *286*, 125370. [CrossRef]
78. Legorburu, G.; Smith, A.D. Incorporating observed data into early design energy models for life cycle cost and carbon emissions analysis of campus buildings. *Energy Build.* **2020**, *224*, 110279. [CrossRef]
79. Cao, S.J.; Ren, C. Ventilation control strategy using low-dimensional linear ventilation models and artificial neural network. *Build. Environ.* **2018**, *144*, 316–333. [CrossRef]
80. Zhu, H.C.; Yu, C.W.; Cao, S.J. Ventilation online monitoring and control system from the perspectives of technology application. *Indoor Built Environ.* **2020**, *29*, 587–602. [CrossRef]
81. Nguyen, A.T.; Reiter, S.; Rigo, P. A review on simulation-based optimization methods applied to building performance analysis. *Appl. Energy* **2014**, *113*, 1043–1058. [CrossRef]

82. Wang, J.Q.; Hou, J.; Chen, J.P.; Fu, Q.M.; Huang, G.S. Data mining approach for improving the optimal control of HVAC systems: An event-driven strategy. *J. Build. Eng.* **2021**, *39*, 102246. [CrossRef]
83. Westermann, P.; Evins, R. Surrogate modelling for sustainable building design—A review. *Energy Build.* **2019**, *198*, 170–186. [CrossRef]
84. Yang, F.; Chou, J.M.; Dong, W.J.; Sun, M.Y.; Zhao, W.X. Adaption to climate change risk in eastern China: Carbon emission characteristics and analysis of reduction path. *Phys. Chem. Earth* **2020**, *115*, 102829. [CrossRef]
85. Han, X.J.; Yu, J.L.; Xia, Y.; Wang, J.J. Spatiotemporal characteristics of carbon emissions in energy-enriched areas and the evolution of regional types. *Energy Rep.* **2021**, *7*, 7224–7237. [CrossRef]
86. Cang, Y.J.; Luo, Z.X.; Yang, L.; Han, B. A new method for calculating the embodied carbon emissions from buildings in schematic design: Taking "building element" as basic unit. *Build. Environ.* **2020**, *185*, 107306. [CrossRef]
87. Pal, S.K.; Takano, A.; Alanne, K.; Siren, K. A life cycle approach to optimizing carbon footprint and costs of a residential building. *Build. Environ.* **2017**, *123*, 146–162. [CrossRef]

MDPI

Article

Innovation in Sustainable Solar-Powered Net-Zero Energy Solar Decathlon Houses: A Review and Showcase

Yeganeh Baghi [1,*], Zhenjun Ma [1], Duane Robinson [2] and Tillmann Boehme [3]

[1] Sustainable Buildings Research Centre, University of Wollongong, Wollongong, NSW 2522, Australia; zhenjun@uow.edu.au

[2] Australian Power Quality & Reliability Centre, University of Wollongong, Wollongong, NSW 2522, Australia; duane@uow.edu.au

[3] Sydney Business School, University of Wollongong, Wollongong, NSW 2522, Australia; tbohme@uow.edu.au

* Correspondence: yb790@uowmail.edu.au; Tel.: +61-2-4221-8111

Abstract: Solar Decathlon is a showcase of cutting-edge residential buildings containing innovative solutions and technologies. This study reviewed, identified, and categorized technological innovations from past Solar Decathlon competitions. The review was based on publicly available data of the top five houses from each U.S. and international Solar Decathlon competition. The most prolific innovations identified were from building services systems and architectural design and construction. It was observed that most innovations within building services systems were in heating, ventilation, and air-conditioning, and home automation, while architectural design and construction innovations focused on building adaptability, façade, structure, and building materials. It was found that although there is no fixed relationship between the numbers of innovations in the houses and their overall competition points, there is a high probability for an innovative house to be placed within the top five houses. This study also provides information about technological innovations within Solar Decathlon houses and offers an innovation classification scheme to guide Solar Decathletes to understand what innovations could be implemented in their future entries.

1. Introduction

1.1. Innovation

Sustainable development is part of the solution to high resource consumption in the building sector [1]. Hence, engineers in the building and construction industry need to think more innovatively to achieve sustainable development. Innovation enables companies to increase competitiveness [2,3], grow market share [4], and avoid lagging behind international perspectives or disappearing [3].

Eurostat and the Organization for Economic Co-operation and Development (OECD) jointly developed the "Oslo Manual" in order to study innovation [5]. Early editions of the manual focused on technological innovation in manufacturing from a product and process point of view, and later in 2005, organizational innovation was added. Based on this manual, the definition of innovation used through this research is "the implementation of a new or significantly improved product, or process, a new marketing method, or a new organizational method in business practices, workplace organization or external relations" [5]. The international Solar Decathlon (SD) competition houses were used as the data source in this study, since SD is a platform for implementation and showcase of technological innovations within the building and construction sector.

1.2. Solar Decathlon

SD is an international competition that challenges students to design, build and operate full-size solar-powered sustainable homes. Students involved in the project ranged

from the undergraduate through to the Ph.D. levels from different disciplines. The SD competition, first held in 2002 by the U.S. Dept. of Energy, has intended to provide communities with information and education about opportunities and advantages of clean energy products for designing and building sustainable and high-energy efficient solar-powered houses and help encourage the implementation of net-zero energy homes. The competition is a showcase of affordability and comfort that combines energy-efficient construction and appliances with the renewable energy systems available today [6].

In SD, each house is judged based on 10 sub-contests (thus the term decathlon). Between 2002 and 2019, 16 competitions were held across nearly all continents. The location and innovation sub-contest detail for each competition are summarized in Table 1.

Table 1. Solar Decathlon competitions' sub-contests related to innovation. The asterisk indicates competitions that were considered for the analysis in this study.

Solar Decathlon Competition	Sub-Contests or Sub-Contest Component (Innovation Related Points/Total Points)
Europe 2019	Innovation & Viability Sub-contest (100/1000)
Middle East 2018 *	Innovation Sub-contest (80/1000)
China 2018	Innovation Sub-contest (100/1000)
U.S. 2017 *	Innovation Sub-contest (100/1000)
Latin America 2015	Viability & Innovation Sub-contest (100/1000)
U.S. 2015 *	No specific innovation contest criteria
China 2013	No specific innovation contest criteria
Europe 2014 *	Innovation Sub-contest (80/1000)
U.S. 2013 *	No specific innovation contest criteria
Europe 2012 *	Innovation Sub-contest (80/1000)
U.S. 2011 *	No specific innovation contest criteria
EUR 2010 *	Innovation Sub-contest (80/1000)
U.S. 2009 *	No specific innovation contest criteria
U.S. 2007 *	No specific innovation contest criteria
U.S. 2005 *	No specific innovation contest criteria
U.S. 2002 *	Presentation & Simulation (15/1100), Comfort zone (30/1100), Refrigeration (30/1100), Hot water (30/1100), Lighting (20/1100)

1.3. Importance of Innovation in the Solar Decathlon Competition

SD is an innovation-based competition with multiple aims: (i) challenge students to develop innovative solutions; (ii) encourage professionals to reduce the environmental impact of their buildings by selecting the best materials and technologies; and (iii) educate the public about renewable energy, energy efficiency, responsible energy use, and available technologies in these areas [7]. SD is also a good way for government agencies to support/seed innovation [8]. In the SD competition, innovation is embedded in all project areas such as engineering, energy production, construction, and architecture [6–12]. Although innovation is important in SD contests, there is a lack of studies that highlight and summarize the innovations arising from SD competitions.

Innovation is increasingly becoming an important factor for the success of a project. While studies such as [13,14] have reviewed specific innovative technologies in buildings, this paper is the first to document and analyse the concept of innovation in the SD competitions and offer a new classification method for technological innovations. It is expected that the findings obtained from this study can be used to facilitate the development and implementation of innovations in future Solar Decathlon competitions and innovations in the built environment.

2. Method for Analysis and Classification of Innovation

The proposed methodology for analysing the data on innovation from past SD contests is a qualitative research method using thematic analysis [15,16]. For this process, as there were approximately from 12 to 22 teams in each competition and there have been 16

competitions since the inaugural event in 2002, the scope was limited to the top five ranked houses (by the competition points). The documents used for undertaking this research were: U.S. Dept. of Energy Solar Decathlon web-page [6], contest codes/rules [17–24], and reviews [8,9,25] available from the various competitions as well as reports and house manuals from individual entrant web-pages, academic papers, and multimedia.

In order to analyse the data, general themes of the innovative technologies were first categorized and then applied to the individual SD house (Top 5). In the last step, the data was analysed by finding the number of innovations in each house and calculating the percentage of each innovation in the two main classifications of "building services" (BS) and "architecture and construction". The detail of the analysis is provided in Figure 1 and discussed in the following sections.
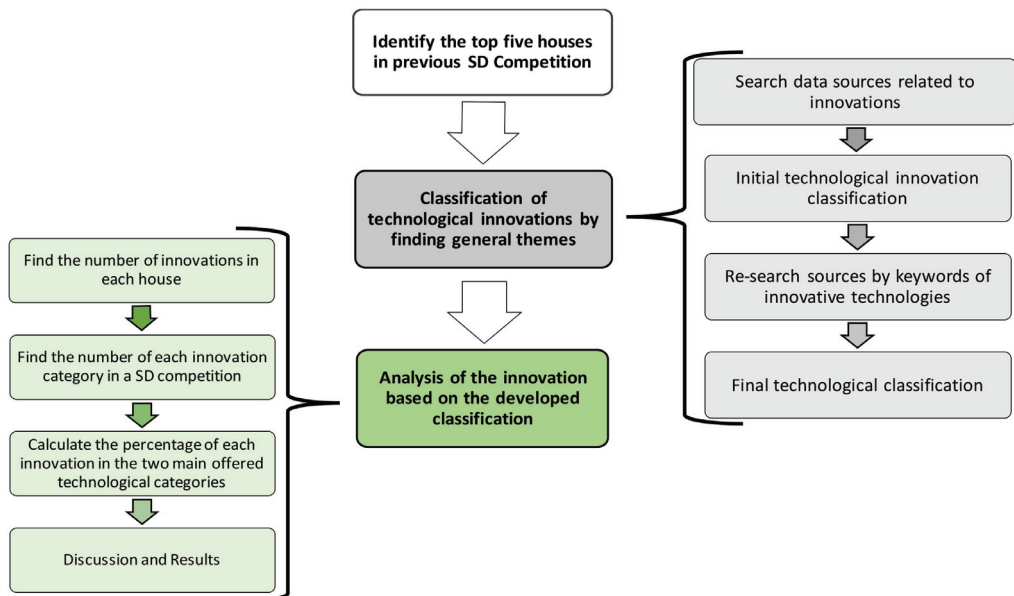
Figure 1. Data analysis methodology used in this study.

3. Analysis of Solar Decathlon Competitions 2002–2019

3.1. Innovation Concept from the Perspective of Time in SD Contests

From the perspective of time, the competition process can be divided into four temporal phases of pre-contest, competition development, contest period, and post-event (refer to Figure 2). The first phase can contain innovations in the conceptual design, name, and marketing of the house. Innovations in this phase determine the qualification to enter the competition. This is followed by the development and implementation phase, which stretches from early development to prototyping. In this phase, almost all elements such as communication, architecture, and building services are involved. This is followed by the period in which contestants build and operate the house at the competition location. The post-event phase mostly involves communications; however, there can be a major innovation in the destination of the house after the competition. Considering all these phases, the most significant opportunity for major technological innovations occurs in the development and implementation phase.
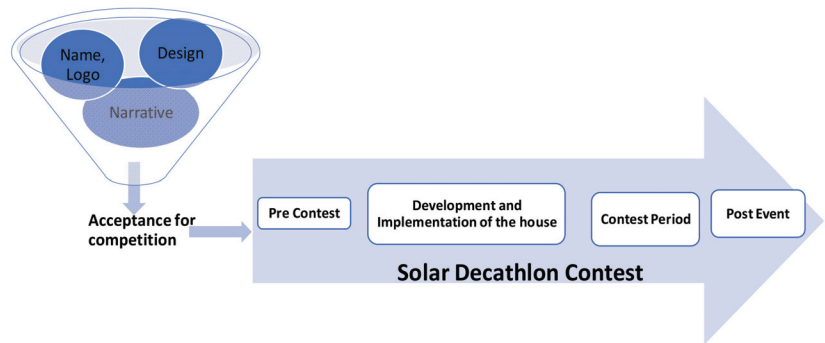
Figure 2. Innovation from the perspective of time during the SD Contest.

3.2. Innovation Concept from the Perspective of Judgement in SD Contests

In all SD competitions, the houses were judged based on 10 sub-contests. These sub-contests vary from one competition to another, and scores or judgment categories also change. Generally, the five sub-contests of architecture, engineering, energy balance (efficiency), thermal comfort, and house functioning have remained in all competitions.

There are various scoring methods for sub-contests: successful completion of tasks (e.g., washing dishes, cooking, and laundry to simulate real-life activities); measuring performance and monitoring (e.g., meeting certain CO_2 levels, humidity, and temperature for thermal comfort); or expert jury perceptions. Jurors assess the house based on their expertise in the specific field in which specific measurements cannot, such as aesthetics, innovation, and design inspiration [9]. There were no fixed or certain identifiers for innovation judgement except for the expertise of the jury members.

Over the history of SD, innovation has been judged in two main ways: a scoring system (as part of a sub-contest or a separate sub-contest by itself); and special award. In the U.S. 2002 competition, "innovation and consumer appeal" was considered as part of the design presentation and simulation, comfort zone, refrigeration, hot water, communication, and lighting sub-contests. Innovation was not part of a U.S. SD competition sub-contest or a separate sub-contest until 2017. For the SD competitions held in other countries, innovation has remained a separate sub-contest, except for China 2013. Table 1 shows how the innovation judgment approach was changed over time from one SD to another. The innovation-related sub-contest has gained more attention and is considered a separate sub-contest in the last five SD competitions.

4. Review of Innovations in Solar Decathlon Competitions

The main innovations within the analysed SD contests, considering the top five houses, can be categorized as per Figure 3. This classification was developed through thematic analysis as explained in Section 2. As innovation into passive design features was previously analysed [26], the classification of technological innovation in the present study (from the subject of passive design) only considers building envelope, façade, and passive use of phase change materials (PCMs).

As shown in Figure 3, the two main categories of innovation are architectural design and construction and building services systems. In Sections 4.1 and 4.2, these classifications are evaluated by being applied to the cohort of the top five SD houses.
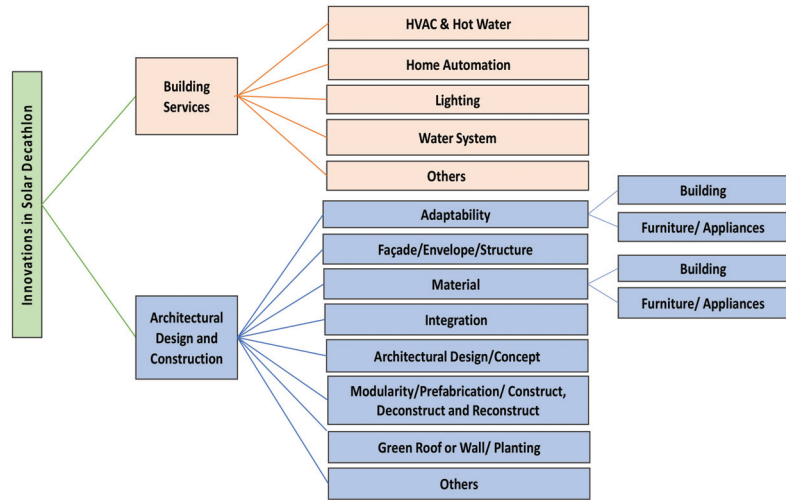
Figure 3. Classification of the technological innovations in SD competitions.

4.1. Innovations in Building Services

The abovementioned classification of innovations was applied to the cohort of the top five houses. Details of each classification are shown in Table 2. The percentage of each classified innovation within building services is shown in Figure 4.
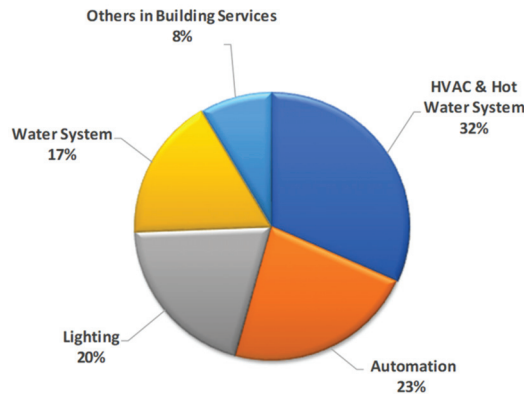
Figure 4. Building services innovations within the top five houses of SD competitions.

The highest percentage of innovations within building services has been in the area of heating, ventilation and air conditioning (HVAC) and hot water systems. This high percentage confirms opportunities for innovation in the HVAC area, and that innovative solutions are needed to maintain thermal comfort conditions while minimizing energy use. As an example, an energy-efficient HVAC system for the harsh desert climate of -Solar Decathlon Middle East (SDME) 2018 was difficult to design as HVAC systems are high energy users and mandatory for thermal comfort conditions. Increasing efficiency can raise the chance of success in innovation sub-contests. As such using a novel HVAC [27] system was key to the University of Wollongong Desert Rose Solar Decathlon house in winning the innovation sub-contest in SD Middle East 2018. The main innovations within the building services are presented in Table 2.

Table 2. Main innovations in building services.

Innovation Category	Main Innovations in Building Services	
HVAC & Hot Water System	• Energy recovery ventilator (ERV) unit, desiccant energy recovery ventilator (DERV) unit, heat recovery ventilator (HRV), [9,27–48] • Geothermal/ground source heat pump [8,9] • Radiant (cooling/heating) floor/ceiling [9,10,27,29,35,37–39,49–53]. • Evacuated tube solar thermal collector [32,33,38,41,54–56]	• Desiccant system: desiccant wheel, waterfall, desiccant cooling [27,30,35,36,57–59] • PCMs [11,27,29,34,36,40,41,45,47,50,51,56,60–67] • Other HVAC Creative Solution [8,39,58,59,68]. • Cooling/ventilation tower, evapotranspiration cooling [49,51,69,70]
Home Automation	• Control system senses conditions and takes inputs lighting, temperature, moisture, and CO_2 inside the house and adjusts mechanical systems accordingly by sending commands to receivers, motors, and valves, Controls shading, lighting, and HVAC systems [9,27,29,31,32,34,38,40,41,43–45,47–49,52,53,57,59,69–82]. • Predictive control strategies [27,41,47].	• Designed/produced gateways as a mediator between two different protocols [27]. • Smartphone/touch-pad applications allow for instant modifications such as energy use, and power up the house, usage of touch-pads [9,10,29,38,47,80].
Lighting	• Ambient natural lighting: skylight/Solatube/optical fiber/sky-wall (made of translucent aerogel allowing daylight into the interior spaces) [8,52,76,78,81,83–85]. • Light emitting diode (LED)/LED strip/LED framed in the plexiglass [8,9,27,36,42,43,47–49,51,57,60,63,69,70,74,78,79,86–88].	• Dimming features [44,52,57,82,89,90] • Lighting design, where switches with Radio Frequency (RF) emitters are used, along with RF adapters placed on the lights [78].
Water System	• Hydroponic wetland/garden [10,35,44,87,91]. • Recovering and harvesting of the rainwater [41,43,45,48,52,53,74,80]. • Aquaponics [49,80]. • Usage of natural domestic purifying plant/photo-ozonolysis/charcoal/bio-microbic recovering system [53,82,85]	• Grey/black water collecting/treatment and re-use: irrigation, flushing, etc. [27,36,39,40,43,45,47,48,52,59,70,74,79,82,85,91–96]. • Joulia shower: shower pan with heat recovery [37,41,52,97]. • Orbital system [47].
Others	• Hydronic dryer cupboard using the hot water generating from the sun for drying clothes [98]. • Zeolites in dishwasher [11,52]. • Hybrid application [30,79,99]. • Home smart sensors including face recognition able to activate operations within the house based on the people detected [70]. • Interactive/Smart mirror [47,48,59]. • Plug and play cable installation [27,100].	• Sun-tracking photovoltaics, which also serves as sunscreen on the rooftop terrace [41]. • Dye-sensitized solar panel [81]. • Innovative combination of the classical residual current device (RCD) and main circuit breaker (MCB) devices in the electrical system of the house, innovative RCD installation [79,100]. • Photoluminescent ceramic tiles [53]. • Luminous solar collector (LSC) [101]

As an HVAC system is a set of different technologies and components, innovation could occur at different levels. For instance, for the dissipation of hot air, a heat recovery unit was located behind the refrigerator by the University of Colorado in the U.S. in 2002. This engineering design was marketable as it used off-the-shelf technologies [8]. Auburn University designed and decorated a room of their house with large water-filled cylinders and used them as thermal mass to moderate the building temperature by staying cooler in the summer and warmer in the winter [8]. The idea of grouping appliances together on a specific wall was implemented by Virginia Tech University to not only use them as serving tools but also consider them as a thermal buffer [8]. Radiant floor heating [9], ground source heat pumps [8,9], and evacuated tubes for hot water systems [9,54] are among the technologies that have been used extensively and could be considered as the innovations at the time. An ERV [102] unit was used to minimize cooling and heating load. A custom manufactured DERV made of a non-toxic silica gel wheel, which exchanged heat and humidity between the intake and exhaust air was used by the Cornell University [28]. The liquid desiccant made up of calcium chloride mixed into the waterfall was an outstanding creative solution for controlling the humidity level in the house [57]. A prototype absorption chiller sized for residential use and designed to be tied up with the solar thermal system was a feature of the Santa Clara University HVAC system [103].

Phase Change Material has been applied in SD buildings in various ways to cool down or heat them up. Phase change gel was used under the floor as thermal mass by Universidad Politécnica de Madrid. The phase change gel helped heat the internal area by realizing the thermal energy on a winter night (Figure 5-left) and cool the house on a summer night (Figure 5-right) [55]. The same technology was applied by the Team Deutschland through microscopic-sized phase change material as Micronal plasterboards in their house. More innovation related to the HVAC innovations can be found in the study conducted by Ma et al. [104].
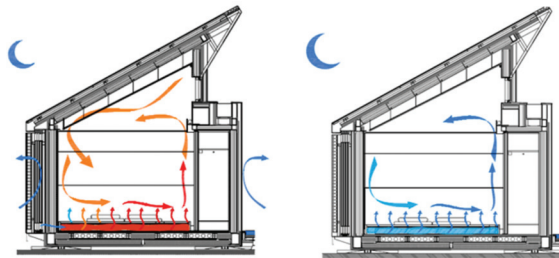
Figure 5. (**Left**): Winter night heating of phase change gel in the floor. (**Right**): Summer night cooling. Adapted from ref. [55].

Over the past SD competitions, innovations in automation systems have changed dramatically from simple controls to developed building management systems (BMS). In the U.S. in 2005, Cornell university used an automatic computerized control system for an ERV and its HVAC system [9]. Recently, the University of Wollongong's automation systems used KNX and digital addressable lighting interface (DALI) lighting protocols systems integrated with the Internet of Things (IoT), implemented in the Solar Decathlon house for the SDME 2018 [27].

Lighting the house is an important feature in any building. The usage of electrochromic windows allowed occupants to block or let the sun's rays pass through. Applying small voltage to the electrochromic glass results in darkening or lightening the house [105]. One of the specifications of Santa Clara University in the U.S. 2007 was applying Solatube, an innovation in daylighting system. As shown in Figure 6, it transferred the captured sunlight from the roof and distributed it throughout the room [83].
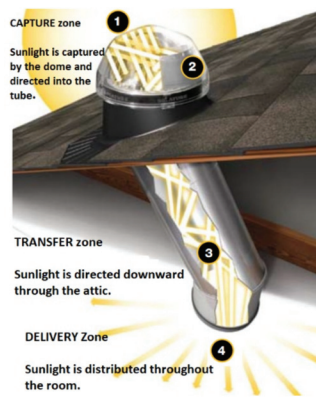
Figure 6. Solatube daylighting system. Adapted from ref. [83].

Auburn University skylight, which was filled with prisms to amplify sunlight for daylighting, was a different technique. Another interesting daylighting system was Skywall used by Virginia Tech. These outer walls were made up of a translucent aerogel material allowing daylight into the interior spaces [8,9]. The University of Virginia used a light-emitting diode wall as a climate control aspect [8]. This wall reflected the building's environmental condition through colour changes, showing whether the house is cool or warm.

Water is a precious and limited resource. Therefore, it is crucial to harvest, treat and reuse water. Many innovative solutions were implemented in the water waste systems and irrigation of the SD houses. As an example, water can be referred to as irrigation of the roof garden through the treated greywater from appliances [106]. More details about technological innovations in the SD houses are provided in Table 2. In conjunction with the innovations from building services, the second most significant collection of technological innovations came from architecture and construction, which will be discussed in the next section.

4.2. Innovations in Architectural Design and Construction

Applying the pre-offered classification shown in Figure 3 in the top five SD houses, the percentage of the categorized innovations in the architecture and construction was found and is presented in Figure 7.
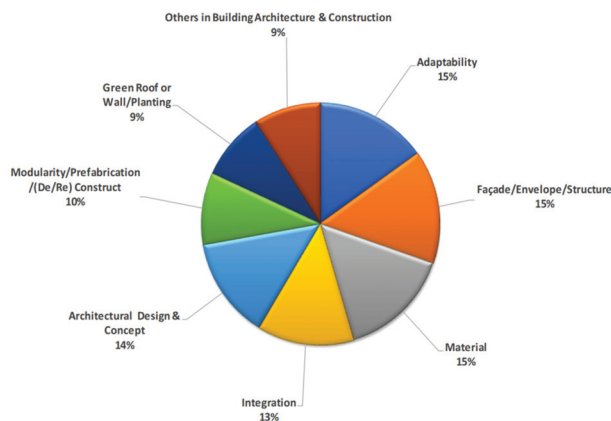
Figure 7. Architecture and construction innovations within the top five houses of SD competitions.

The main innovations for architectural design and construction are listed in Table 3.

Table 3. Main innovations in architectural design and constructions.

Innovation Category	Main Innovations in Architectural Design and Construction	
Adaptability	• Moveable roof/wall [9,27,57,82,107]. • NanaWall and shutters [9,42,45,80,108]. • Sliding/folding door/Photovoltaic panel/Screen [27,37,43,45,52,55,80,87,109]. • Automated awning system/curtain [41,75]. • Folding façade [79].	• Fold down-slide out/adjustable cabinets [10,47]. • Reconfigurable blocks/furniture/spaces such as workstation, bed, toilet, etc. [10,11,30,32,41,48,53,59,74,78,79,85,87,107]. • Two-faced/extended/combined (usage of rolling cart and locking caster) table [30,43,59,107].
Façade/Envelope/Structure	• SIP [9,32,40–45,47,110]. • Trombe wall [102]. • Integrated PV on façade [111,112]. • Large operable shutter [42,81]. • Sand/hemp infilled cavities in the building structure [11,52]. • Oriented strand board (OSB) [73,92]. • Exchangeable façade [41]. • Innovative skin wall [27,49,78]. • Ventilated façade [27,113]. • Bend-proof wooden rigid corner joints [114]. • Mashrabiyah shade screen [47].	• Circular façade of laser-cut holes with folded tabs, laser cut-innovative screen [72,95]. • Façade layer of nanogel filled polycarbonate panels [72]. • Zigzag/jagged façade structure [96]. • Vacuum insulated panel [11]. • Façade made of disused CDs [36]. • Lucido façade system [52]. • Texture façade [37]. • Structural bamboo (I-beams)/Lamboo frame [29,57,115].
Material	• Aerogel material [8,70]. • Bamboo, spruce, hemp, veneer, cork, compressed wheat straw/sawdust, soybean, pine, cellulose wadding, oak wood [9,27,29,39,45,52,62,73,79,85,92,116]. • Durable and water resistance composite materials adapted from the boating industry [42]. • Texsteel (magnetic and conductive) [11]. • Innovative cement [83].	• Milk bottles [57]. • Recycled steel, stone, glass, wood, aluminium [27,49,53,57,69,79,117]. • Harvested timber [36]. • Reclaimed wood, redwood plywood [36,40,49]. • Innovative (crushed, hemp, recycled, foamed) concrete [27,41,57,99]. • Sustainable lyptus flooring [118]. • 3D printing material [47].
Integration	• Integrated solar panel and awning [8,9,47,48,106]. • Building integrated photovoltaic (BIPV) in different elements, such as shutters, façade, roof, etc. [27,29,37,41,42,48,49,56,57,79,81,99,100,119,120].	• Integrated solar shingles [64]. • Bifacial PV in the façade [45]. • Integration of the evacuated solar collectors in the envelope [121].

Table 3. *Cont.*

Innovation Category	Main Innovations in Architectural Design and Construction	
Architectural Design and Concept	• Core concept [9,11,40,45,53,79,99]. • Onion-like design [57]. • Skin system design blended in the green house [78]. • Single-room house [111]. • Butterfly roof [122,123]. • Health-related designs [27,118]. • 'Dry-flood-proofing' approach design [42]. • Design of self-supporting, custom-made ceiling elements used for distribution of conditioned air [81].	• Conceptual landscape design [124]. • Saferoom design [59]. • Loggia with the modern application [53]. • A bent tubular design which controls the light entry [29]. • Home as a place of food production [43]. • A penthouse design as a solution to the city restoration and more living space in the old buildings [79]. • Greencourt [91].
Modularity/Prefabrication/De-Construction/Construction	• House on a chassis so it could be moved to and from the location of competition in one piece/usage of the transportation system, built into house structure [9,56]. • Prefabricated constructions, modular wall, roof [9,27,45,49,52,53,70,79,81,116].	• A container as part of the house [9].
Green roof or wall/planting	• Green roof, wall [9,27,37,48,55,64,70,71,81,82,85,115,125,126]. • Vertical farm [11].	• Greenhouse [43,78]. • Permaculture companion planting [91].
Others	• Composting bin with included worms in the kitchen [9,106]. • Triple/quadruple-glazed, krypton/argon fill, low-e film windows [27,29,49,62,85,89]. • Spider-shaped anchor for the anchoring system of the house [37].	• Heat-trapping planters, canning table [43]. • Composting toilet [81,91]. • Solar dryer [43,81,91]. • Electro-chromic windows [105].

The integration of solar panels in a building was an innovation as it is adding extra value, such as shading and insulation to the building, while providing electricity. As an example, PV awning acted as a shading element (Figure 8) [9]. Also, providing overhangs through PV on the roof shaded the south-facing windows, which let the tenants enjoy better indoor comfort by having winter sun and omitting summer solar gain [106]. One of the most innovative integrations of PV in the building (BIPV) was implemented by team Technische Universität Darmstadt through applying PV into louvered oak shutters around the building, which provided adjustable shading (Figure 9) [71].

Figure 8. California Polytechnic PV awning. Reprinted from ref. [9].
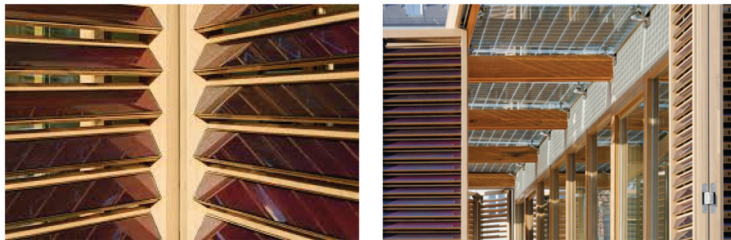
Figure 9. Technische Universität Darmstadt: (**Left**): BIPV in louvered oak shutters. Adapted from ref. [127]. (**Right**): BIPV awning. Adapted from ref. [128].

Moveable elements in the building could be considered innovative ideas. Moveable roof from [49] provided their house with the capability of adjusting openness and daylight entering the house. Moreover, NanaWall (i.e., a folding, rather than sliding glass wall between the living room and patio) provided a thermal seal as well as connected the interior and exterior spaces together [9]. Sliding doors and gliding room dividers [27] were other examples of moveable building elements that provide the building with more flexibility.

Usage of Structurally Insulated Panel (SIP) made up of various materials, as a primary building envelope/insulation, has been repeated [9]. The structure of SIP and materials used for its production can be considered innovative. Agriboard, a structurally insulated panel made of compressed wheat straw between two pieces of the oriented strand board [92], and BioSIP [129], were examples of SIP, as an innovative material for building construction used by the University of Colorado. More building construction system details can be found in the study conducted by Liu et al. [114].

Fast and economical ways to construct, deconstruct and reconstruct a building were another area for innovation. Prefabricated building structure [27] allows components to be built while minimizing the use of fossil fuels and construction logistics. As another solution, the New York Institute of Technology [9] used the transport shipping container to form the primary part of the house and contained the kitchen, bathroom, and mechanical systems. It included all the expensive components in a central core section. This prefabricated core was observed as adding market potential [9].

The selection of building materials played an important role in SD houses. The previously mentioned BioSIP, a patented wall type, was produced using lightweight but strong panels made from recycled materials which were filled with lightweight foam

insulation (produced from soybean oil and waste paper) [9]. Usage of bio-fuel (bio-diesel) for transportation, as well as making furniture and tableware from natural materials such as soy, wheat, corn, and coffee [9] in civil and urban communities and cities can be considered as an innovation. Similarly, other material innovations included engineered wall panels, furniture, and cabinets using fast-growing woods from managed forests [129], and soybean-based insulation sprayed between wall studs, ceiling, and floor joists [92]. Innovative materials considering durability and sustainability included Lyptus [118] and bamboo flooring, and Trespa wall panels built by paper, wood fibre, and resin-based composite used for exterior and interior walls [116]. Homes have also featured a recycled milk bottle wall and structural bamboo I-beams [57]. Newly developed cement containing recycled material [83] is another example of innovation. More details on the skin material of the building have been offered by Zhang et al. [130] through case studies of Solar Decathlon Europe 2010.

Other innovations included: roof garden [9], green wall [49,70], usage of hydrogen fuel cell on the premises [9], composting bin with included worms in the kitchen [129], composting toilet [91], and Trombe wall [102].

The abovementioned innovations were identified and categorized. This classification could be used to develop the technological component of an innovation management framework.

4.3. Innovations at Solar Decathlon Middle East 2018

In November 2018, the Solar Decathlon competition was held for the first time in the Middle East. This competition was different from other Solar Decathlon competitions in terms of its location, where it was in a dry and humid climate of the desert. In the following section, some of the outstanding innovations of this competition are reviewed.

In SDME 2018, Virginia Tech University received first overall rank by presenting FutureHAUS, a prototype smart house built with smart construction techniques. The house was made of prefabricated modular structures that were pre-wired and pre-plumbed. These cartridges were designed in a way to be finished off-site and hooked up on-site using a plug-and-play assembly method [47]. The suites of the cartridges are shown in Figure 10. This assembly method using prefabricated cartridges could provide a construction project with minimal site pollution, fast construction, and accurate scheduling, timeline, and pricing.
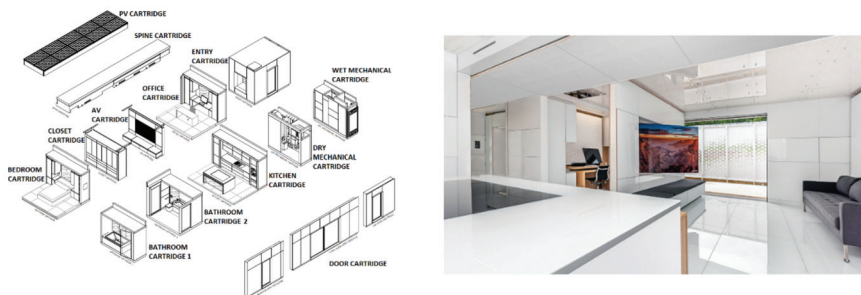
Figure 10. FutureHAUS. (**Left**): Suite of cartridges. Adapted from ref. [47]. (**Right**): Office and living room flex-space with rotating audio-visual (AV) wall, which could be moved mechanically. Reprinted from ref. [47].

The bathroom cartridge contained innovative features such as a smart mirror interface, a one-piece 3-D printed sink and countertop, and the toilet and vanity were height adjustable.

Team Virginia Tech implemented creative spatial flexibility in FutureHAUS called Flex-space. In this space, three program spaces of a home office, a bedroom, and a living room could be created through movable walls. The walls were powered by direct current (DC) through the conductive rail integrated to the house central spine cartridge which contained all home-run communication and electrical lines and all ductwork of the HVAC system. In the flex-space, the rotating AV wall shown in Figure 10 allowed the user to

share the television and audio-visual technology between the living room and home office modes [47].

Team UOW from the University of Wollongong won second place in SDME 2018. Team UOW had a strong aim to change the way the world views homes for the elderly. Their innovative smart solar-powered Desert Rose was designed and developed to provide for occupants with age-related disabilities and diseases including dementia. The Desert Rose house innovative air to water HVAC system making use of on-site thermal storage and desiccant system provided the house with thermal comfort and suitable air conditioning based on the Dubai climate. The building integrated photovoltaic thermal (BIPVT) system of the house was innovative as they not only provided the house with electricity and hot water, they were also the roof structure of the house by themselves. The developed Model Predictive Control (MPC) was the major energy management strategy of the house. This MPC system along with the usage of KNX, DALI protocols, and IoT techniques led to the innovative smart automation system of the house. The digital water taps shown in Figure 11 include features like "tap on and off" functionality and free-spinning tapware. These novel taps could improve the quality of life for people with arthritis and dementia [131].
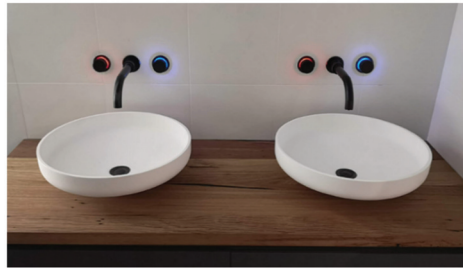
Figure 11. Innovative Desert Rose water tap. Reprinted from ref. [131].

In the Middle Eastern culture, having privacy is important. Considering this cultural aspect as well as reducing the heat gain from the harsh climate, an innovative façade was used. As an illustration, Team UOW Desert Rose house was wrapped by an innovative second skin wall made of a foamed concrete containing recycled crushed glass as a cement replacement. For the construction of this wall, instead of conventional steel reinforcement, carbon-fibre mesh reinforcement was used [27]. BAITYKOOL house, which won third place in the competition, had a similar envelope around it. This façade was made of ultra-high performance fibre-reinforced concrete [49]. The biomimetic solar cells [126] of this house were integrated in two different ways into the building. The first integration was within the façade and the second innovative way was BIPV in a movable roof over the patio. As shown in Figure 12, this movable roof could be closed and acts as a shading element throughout the day.
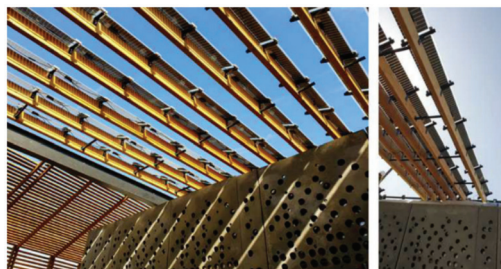
Figure 12. Movable PV integrated roof over BAITYKOOL house. Adapted from ref. [49].

A hybrid innovation was implemented in the water recycling system (Figure 13) of the BAITYKOOL house. The greywater could go through two ecological processes for filtration. The first stage was waste filtration through earthworms called lumbri-filtration, followed by treatment via Ultraviolet (UV) rays from the sun (bio-solar purification) [49]. The recycled water fed the ecosystems of the house, including the aquaponics system of the house for growing vegetables and raising edible fish.
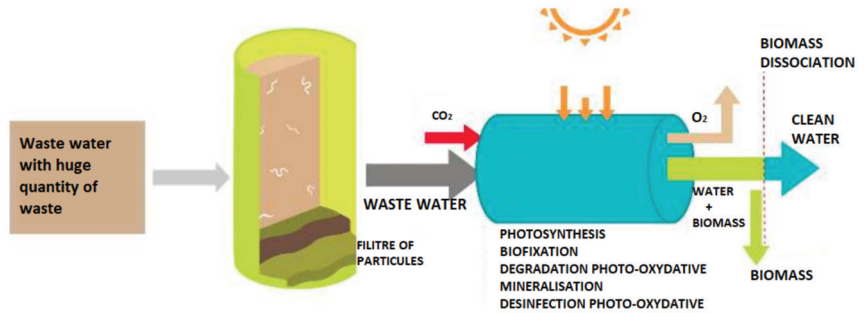
Figure 13. Greywater filtration of BAITYKOOL house. Adapted from ref. [49].

The Efden team won fourth overall rank in SDME 2018. They implemented hybrid innovative home automation based on energy efficiency and user experience. The automation system integrated the entire equipment into a programming logic controller (PLC), which runs the logic behind the automation scenarios. Integration of gateways for converting DALI to KNX and EnOcean to Modbus module made DALI and EnOcean compatible with the controller. A voice support system through which the occupants could use simple voice commands to find out the temperature and humidity of the house, access the lighting control system or operate the doors/windows open/closing mechanisms was created. This voice system was integrated into the automation via message queuing telemetry transport (MQTT)protocol; a Smart Mirror that displayed news, date and time, the weather forecast was developed. However, the most interesting feature about this mirror was the face recognition and understanding of the person's mood [48].

The University of Rome Sapienza implemented the concept of "innovative within tradition" by designing and building their smart solar house blended in with the Arab tradition and heritage. They combined a traditional internal patio with a green wall and a smart wall fountain integrated with the home automation system. Also, innovative augmentation of a wind tower (Figure 14) with an active air conditioning system was used. These combinations of modernity and tradition were implemented through an innovative building construction system with Cross Laminated Timber augmented with post-tensioning technique (Press-Lam), ventilated floor-wall connection technology, and innovative selective windows with advanced aluminium-wood frames enriched with aerogel thermal breaks [70]. The adaptive shading system with automated semitransparent light-reflective blinds and the car shading were other aesthetic innovative features of this house [70]. This electrical car canopy included a demonstrative off-grid PV system based on LSC [101] technology.

The above review showed that innovation has become an essential component in Solar Decathlon competitions to demonstrate how to use and implement innovative solutions and technologies to achieve net-zero energy consumption of solar-powered houses and how innovations assisted student teams in winning the competition.

Figure 14. Sapienza house with semitransparent blinds and the wind tower. Reprinted from ref. [70].

5. Discussion

As part of the innovative solution, flexible designs such as a Murphy bed, moveable roof, and wall have been developed, which provide the building and furniture with more flexibility and adaptability. Another key innovation is to find efficient and fast ways to construct, deconstruct and reconstruct SD houses. For example, prefabricated constructed components, modular designs that fit into a shipping container, usage of the container as part of the building, and number-coded prefabricated construction systems, which allow non-builders to construct a house and/or reduce the construction logistics, are among the methods being considered.

There is no linear or fixed relationship between the technological innovation features of an SD house and its overall ranking in the contest. However, it can be concluded that innovation can assist the house to stay among the top five. As an example, the University of Maryland participated in four SD competitions (2002-4th, 2007-2nd, 2011-1st and 2017-2nd). The innovations of their entries were radical and incremental. The liquid desiccant waterfall (LDW) system was first used in LEAFHouse in 2007; and later in 2011, the improved LDW was employed in the WaterShed house. Although each time their entry had innovative features, the overall rankings did not follow any trend (other than being highly rated) (shown in Figure 15). One reason is that innovative features do not necessarily help houses to function to competition requirements. Another reason is that the innovation concept is quite broad; contests, sub-contests, and judgment, as well as grading approaches, change from one SD to another. In summary, there is a lack of fixed/equal identifiers for innovation judgment.
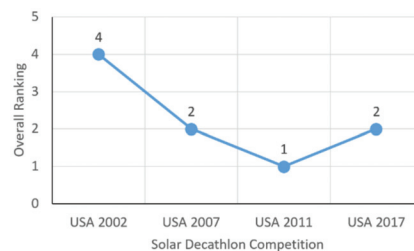
Figure 15. The overall ranking of the University of Maryland in four Solar Decathlons.

In SDME 2018, Desert Rose won first place in the innovation sub-contest and second overall. Figure 16 shows the details of the innovation sub-contest in that competition. Team Virginia Tech won the overall competition and Team UOW and Baitykool were respectively

placed in the second and third overall. Figure 17 also confirms the abovementioned assertion in that there is no direct relationship between the ranking and number of innovations in the top five houses within any of the SD competitions.
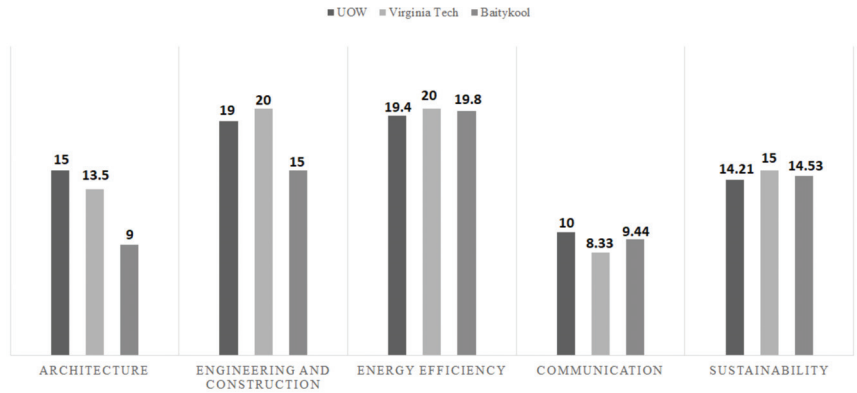
Figure 16. Innovation contest scoring for Team UOW and place getters in SD Middle East 2018.
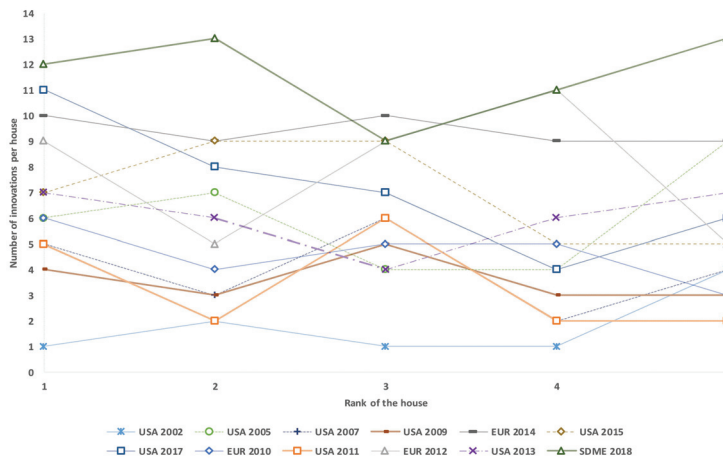
Figure 17. Innovations versus the ranking of the houses in the competition.

In general, it was found that the most innovations were implemented in HVAC, architectural design, adaptability of the building appliances to different lifestyles and climates, building materials, and integration of different features into the body of the building.

Figure 18 illustrates the number of total innovations in the first top-five houses in the SD competitions. Overall, before 2015, the competitions in Europe had more innovations than those held in the U.S. In recent years, the total innovations in the houses ranked 1st to 5th were increased. This could be due to the advances in technology innovations providing teams with easier and economical ways to implement their ideas. As discussed in the previous sections, SD competitions commenced in 2002, and this long history provides teams with more data and information compared to the teams in the early stages of competitions. Therefore, being more familiar with the process and rules of competitions can have an impact on the selection of a successful innovative idea or process of implementation. As an illustration, new teams are able to add values to a previously defined and developed innovative idea from the past SD houses, such as usage of DALI protocol for LED strips which was an innovation from early competitions, or integrating Google Home to the BMS of the house. Figure 18 also shows that most innovations occurred in the 1st-placed houses.
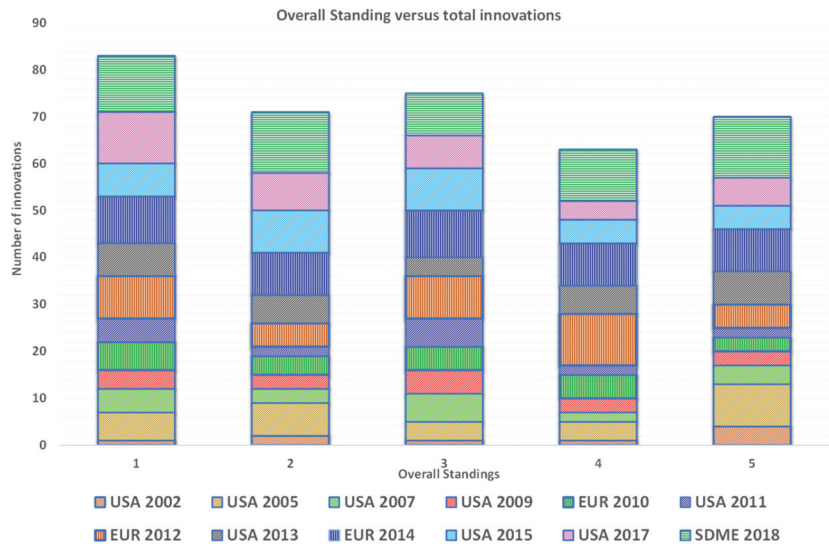
Figure 18. Overall standing versus total innovations in SD competitions.

As shown in Table 4 and mentioned above, more innovations were implemented in building services than those in architecture and construction. The innovation percentages increase as the competition time approaches the year 2017. This table has been compiled by considering only the top five houses in each of the SD competitions.

Table 4. Percentage of innovations in SD competitions between 2002 and 2018.

SD Competition	HVAC & Hot Water System	Automation	Lighting	Water System	Others in Building Services	Adaptability	Façade/Envelope/Structure	Material	Integration	Architectural Design & Concept	Modularity/Prefabrication/ (De/Re) Construct	Green Roof or Wall/Planting	Others in Building Architecture & Construction
USA 2002	80%	0%	60%	0%	0%	0%	0%	10%	10%	0%	0%	0%	0%
USA 2005	100%	10%	40%	10%	0%	40%	80%	80%	40%	10%	80%	10%	60%
USA 2007	80%	60%	60%	0%	40%	10%	40%	0%	10%	10%	0%	40%	10%
USA 2009	100%	40%	0%	0%	0%	0%	40%	40%	60%	40%	0%	10%	10%
EUR 2010	80%	10%	40%	10%	10%	40%	60%	40%	40%	40%	40%	0%	10%
USA 2011	100%	80%	0%	0%	10%	40%	10%	0%	10%	40%	0%	10%	0%
EUR 2012	100%	80%	60%	80%	40%	60%	60%	100%	10%	60%	60%	10%	40%
USA 2013	100%	80%	10%	60%	0%	40%	40%	60%	40%	40%	10%	40%	10%
EUR 2018	100%	100%	100%	80%	80%	100%	80%	60%	80%	80%	40%	40%	10%
USA 2015	100%	80%	100%	80%	0%	80%	60%	40%	40%	60%	10%	10%	10%
USA 2017	10%	80%	80%	100%	40%	80%	10%	10%	40%	80%	40%	60%	60%
SDME 2018	100%	100%	100%	100%	80%	80%	100%	100%	100%	60%	80%	80%	80%

Innovation is a broad topic and its concept can change over time, i.e., a product which is considered as a novel technology this year, may not be an innovation in the next

year. In some cases, adding value to previous innovations can result in a new product or service which will be an incremental innovation. Successful innovations may continue to be included in newly built houses.

It is worthy to mention that innovative technologies in a house are not limited to the building itself. As an example, building an electrical vehicle (EV) [132] charger can provide energy for electric transportation systems. SDME 2018 competition provided the competition teams with testing ground for new ideas in housing as well as urban planning and sustainable transportation. Therefore, the solar-powered houses are required to produce enough energy to cover the demand of the building and the eco-friendly vehicle. The energy consumption for EV chargers should be monitored and controlled through the BMS of the house. For instance, the Desert Rose house BMS is able to control and monitor HVAC systems, EV charger, windows, lighting, smart appliances and the renewable energy systems [27].

SD is a suitable vehicle for showcasing and making innovative prototypes as the scientific and business sectors can come together and make changes by offering prototypes that will be operated and tested during competition and prepared for market.

6. Conclusions

In this study, technological innovations in the top five ranked sustainable net-zero houses in the Solar Decathlon competitions have been analysed. This was completed by applying thematic qualitative analysis. Consequently, the final classification has been derived. The classifications identified the areas where technological innovations have happened the most. It was found that the innovations in HVAC and home automation were the most focused technological innovations within building services, while within architectural design and construction, most innovations were in the adaptability of the building to lifestyles and climates, façade and structure, and building materials.

Based on this study, there is no direct relationship between the technological innovation features of SD houses and their overall ranking in the competition. However, it can be concluded that innovation helped the student teams to be placed among the top five houses in the competition. For example, the Desert Rose house in the Solar Decathlon Middle East 2018 won first place in the innovation sub-contest; however, it received the second overall ranking. Also, it was observed in recent years, specifically after 2017, that the innovation percentages have increased. This can be because of the advances in technology which provide SD teams with economical and improved ways to implement their innovative idea. The greater usage of incremental innovations can be another reason for this increase.

In this review, a technological innovations classification was developed that is a suitable tool for researchers, building and construction sector practitioners, and future Solar Decathletes. The developed classification is a fundamental starting point for establishing standards for an innovative net-zero sustainable house. It can also be used for future solar decathlon judgment criteria (with respect to both identifiers and weightings). Furthermore, the classification is a key component for developing the technological component of a sustainability-oriented innovation management framework for buildings. Moreover, the offered innovation quantification shows where in the building and construction sector, innovative sustainable technologies are more needed and can be applied in order to address sustainable developments needs of this sector.

Abbreviations

AV	Audio-visual
BIPV/T	Building Integrated Photovoltaic Thermal System
BMS	Building Management System
BS	Building Services
DALI	Digital Addressable Lighting Interface
DC	Direct Current
DERV	Desiccant Energy Recovery Ventilator
ERV	Enthalpy Recovery Ventilator
EV	Electrical Vehicle
HVAC	Heating Ventilation and Air Conditioning
HRV	Heat Recovery Ventilator
IoT	Internet of Things
LSC	Luminous Solar Collector
LED	Light-Emitting Diode
LDW	Liquid Desiccant Waterfall
MCB	Main Circuit Breaker
MQTT	Message Queuing Telemetry Transport
OECD	Organization for Economic Co-operation and Development
OSB	Oriented-Strand Board
PV	Photovoltaic
PCM	Phase Change Material
PLC	Programming Logic Controller
RCD	Residual Current Device
RF	Radio Frequency
SD	Solar Decathlon
SDME	Solar Decathlon Middle East
SIP	Structurally Insulated Panel
UV	Ultraviolet

References

1. Pullen, S.; Chiveralls, K.; Zillante, G.; Palmer, J.S. Minimising the impact of resource consumption in the design and construction of buildings. In Proceedings of the ASA2012: 46th Annual Conference of the Architectural Science Association (Formerly ANZAScA)—Building on Knowledge: Theory and Practice, Griffith University, Brisbane, Australia, 14–16 November 2012; pp. 1–8.
2. Drucker, P. *The essential Drucker: The Best of Sixty Years of Peter Drucker's Essential Writings on Management*; Harper Collins: New York, NY, USA, 2001.
3. Porter, M. Competitive advantage of nations. *Compet. Intell. Rev.* **1990**, *1*, 14.
4. Banbury, C.; Mitchell, W. The effect of introducing important incremental innovations on market share and business survival. *Strateg. Manag. J.* **1995**, *16*, 161–182. [CrossRef]
5. Organizations for Economic Co-Operation and Development Statistical Office of the European Communities. Oslo Manual Guidelines for Collecting and Interpreting Innovation. Available online: https://ec.europa.eu/eurostat/documents/3859598/5889925/OSLO-EN.PDF.pdf/60a5a2f5-577a-4091-9e09-9fa9e741dcf1?t=1414781154000 (accessed on 15 April 2021).
6. Solar Decathlon. Solar Decathlon: About Solar Decathlon. Available online: https://www.solardecathlon.gov/about.html (accessed on 20 October 2020).
7. Rules and Building Code—Solar Decathlon Middle East 2018. Available online: https://www.solardecathlonme.com/image/catalog/documents/sdme-rules.pdf (accessed on 20 October 2020).
8. Eastment, M.; Hayter, S.; Nahan, R.; Stafford, B.; Warner, C.; Hancock, E.; Howard, R. Solar Decathlon 2002: The Event in Review. Available online: https://www.nrel.gov/docs/fy04osti/33151.pdf (accessed on 20 October 2020).
9. Moon, S.; Nahan, R.; Warner, C.; Wassmer, M. Solar Decathlon 2005: Event in Review 7–16 October 2005. Available online: https://www.nrel.gov/docs/fy04osti/38264.pdf (accessed on 20 October 2020).
10. Sánchez, S.V.; Murcutt, G.; Ernst, W.; Mumovic, D.; Pich, F.; Baurier, A.; Koleeny, J.; García, P.J.; Wheeler, J.; Dunay, R.; et al. Solar Decathlon Europe 2010 Towards Energy Efficient Building. Available online: https://download.hrz.tu-darmstadt.de/media/FB15/FGee/SOLAR-DECATHLON-EUROPE-2010.pdf (accessed on 23 October 2020).
11. Sánchez, S.V.; Torre, S.; Kolleeny, J.; Todorovic, M.; Urculo, R.; Pilkington, H.; Twill, J.; Unimas, E.R.; Rollet, P.; Bonnevie, J.; et al. *Solar Decathlon Europe 2012—Improving Energy Efficient Buildings*; Imprenta Kadmos: Salamanca, Spain, 2013.

12. Warner, C.; Farrar-Nagy, S.; Wassmer, M.; Stafford, B.; King, R.; Sánchez, S.V.; Ubiñas, E.R.; Cronemberger, J.; María-Tomé, J.S. The 2009 Department of Energy Solar Decathlon and the 2010 European Solar Decathlon—Expanding the global reach of zero energy homes through collegiate competitions. In Proceedings of the 34th IEEE Photovoltaic Specialists Conference (PVSC), Philadelphia, PA, USA, 7–12 June 2009; pp. 002121–002125.

13. Nundy, S.; Mesloub, A.; Alsolami, B.M.; Ghosh, A. Electrically actuated visible and near-infrared regulating switchable smart window for energy positive building: A Review. *J. Clean. Prod.* **2021**, 126854. [CrossRef]

14. Ghosh, A. Potential of building integrated and attached/applied photovoltaic (BIPV/BAPV) for adaptive less energy-hungry building's skin: A comprehensive review. *J. Clean. Prod.* **2020**, *276*, 123343. [CrossRef]

15. Bowen, G. Document analysis as a qualitative research method. *Qual. Res. J.* **2009**, *9*, 27–40. [CrossRef]

16. O'Leary, Z. *The Essential Guide to Doing Research*; Vistaar Publications: New Delhi, India, 2005.

17. U.S. Department of Energy. 2005 Solar Decathlon Rules and Regulations. Available online: https://www.solardecathlon.gov/past/pdfs/05_rulesregs/sd05rr_all.pdf (accessed on 20 October 2020).

18. U.S. Department of Energy. 2007 Solar Decathlon Rules and Regulations. Available online: https://www.solardecathlon.gov/past/pdfs/07_techreport/07_rulesregs.pdf (accessed on 20 October 2020).

19. U.S. Department of Energy. 2009 Solar Decathlon Rules. Available online: https://www.solardecathlon.gov/past/pdfs/09_techreport/09_rules.pdf (accessed on 20 October 2020).

20. U.S. Department of Energy. U.S. Department of Energy Solar Decathlon 2011 Rules. Available online: https://www.solardecathlon.gov/past/2011/pdfs/2011_rules.pdf (accessed on 20 October 2020).

21. U.S. Department of Energy. U.S. Department of Energy Solar Decathlon 2013 Rules. Available online: https://www.solardecathlon.gov/past/2013/pdfs/2013_rules.pdf (accessed on 20 October 2020).

22. U.S. Department of Energy. U.S. Department of Energy Solar Decathlon 2015 Rules. Available online: https://www.solardecathlon.gov/2015/assets/pdfs/2015_rules.pdf (accessed on 21 October 2020).

23. U.S. Department of Energy. U.S. Department of Energy Solar Decathlon 2017 Rules. Available online: https://www.solardecathlon.gov/2017/assets/pdfs/sd2017-rules_final.pdf (accessed on 21 October 2020).

24. Organizing Committee of Solar Decathlon China. Solar Decathlon China Rules. Available online: https://www.scribd.com/document/394982436/SDC2018-Rules-V2-2-pdf (accessed on 21 October 2020).

25. McCarthy, T.J.; Banfield, B.; Baghi, Y.; Faidutti, L.; McDowell, C. Advocating for Net-Zero Energy Sustainable Houses through the International Solar Decathlon Competition. In Proceedings of the 3rd World Congress on Civil, Structural, and Environmental Engineering (CSEE'18), Budapest, Hungary, 8–10 April 2018.

26. Cheng, C.; Rongwen, D.; Hao, Z. The analysis of passive design in Zero-energy buildings: A case study of solar Decathlon. *Adv. Mater. Res.* **2013**, *689*, 119–124. [CrossRef]

27. Team UOW. Desert Rose Project Manual. Available online: https://www.solardecathlonme.com/2018/teams/team-uow (accessed on 21 October 2020).

28. Cornell University. Comprehensive Assessment of Thermal Comfort Report. Available online: https://www.solardecathlon.gov/past/pdfs/05_techreport/cornell_thermal_comfort_report.pdf (accessed on 21 October 2020).

29. National Renewable Energy Laboratory for the U.S. Department of Energy. Solar Decathlon 2009 Highlights of Team Innovations and Cutting-Edge Building Technologies. Available online: https://www.solardecathlon.gov/past/pdfs/09_techreport/innovations.pdf (accessed on 21 October 2020).

30. Team Maryland. As-Built Project Manual. Available online: https://www.solardecathlon.gov/past/2011/pdfs/umd_manual.pdf (accessed on 21 October 2020).

31. Team Purdue. Project Manual As-built Documentation. Available online: https://www.solardecathlon.gov/past/2011/pdfs/pur_manual.pdf (accessed on 22 October 2020).

32. Victoria University of Wellington First Light. Project Manual. Available online: https://www.solardecathlon.gov/past/2011/pdfs/nz_manual.pdf (accessed on 21 October 2020).

33. Team Middlebury. Design Development Project Manual. Available online: https://www.solardecathlon.gov/past/2011/pdfs/midd_manual.pdf (accessed on 22 October 2020).

34. The Ohio State University. Project Manual. 2011. Available online: https://www.solardecathlon.gov/past/2011/pdfs/osu_manual.pdf (accessed on 22 October 2020).

35. Team Med in Italy. Project Manual. 2012. Available online: http://www.sdeurope.org/wp-content/pdf/ROME_PM_7.pdf (accessed on 29 August 2017).

36. Counter Entropy Team. Jury Report. 2012. Available online: https://building-competition.org/file/5909f1952dd2ae34bd8096fe/9f396cf030463e3a45dcfe513be687484635e1ee1c9be17dfeee11109bcca38c (accessed on 23 October 2020).

37. Team Austria. Project Manual. 2011. Available online: https://www.solardecathlon.gov/past/2013/pdfs/vut_manual.pdf (accessed on 21 October 2020).

38. Team Las Vegas. As-Built Phase Project Manual. 2013. Available online: https://www.solardecathlon.gov/past/2013/pdfs/unlv_manual.pdf (accessed on 23 October 2020).

39. Team Czech Republic. Project Manual As-Built Documentation. 2013. Available online: https://www.solardecathlon.gov/past/2013/pdfs/ctu_manual.pdf (accessed on 22 October 2020).

40. Stanford University. As-Built Construction Documentation Project Manual. 2013. Available online: https://www.solardecathlon.gov/past/2013/pdfs/su_manual.pdf (accessed on 21 October 2020).

41. Team Lucerne. Project Manual. 2014. Available online: https://building-competition.org/file/5909f18f2dd2ae33eb8d15cd/6823 f6eaf05d9f23c394adf8ba2b0750cb28a7833c92defc1f777049cad289b7 (accessed on 21 October 2020).

42. Stevens Institute of Technology. Jury Narratives. 2015. Available online: https://www.solardecathlon.gov/2015/assets/pdfs/sd2015_narrative_sit.pdf (accessed on 21 October 2020).

43. University at Buffalo the State University of New York. Jury Narratives. 2015. Available online: https://www.solardecathlon.gov/2015/assets/pdfs/sd2015_narrative_nybuff.pdf (accessed on 21 October 2020).

44. Missouri University of Science and Technology. Jury Narratives. 2015. Available online: https://www.solardecathlon.gov/2015/assets/pdfs/sd2015_narrative_mst.pdf (accessed on 2 October 2020).

45. California Polytechnic State University. Jury Narratives. 2015. Available online: https://www.solardecathlon.gov/2015/assets/pdfs/sd2015_narrative_calpoly.pdf (accessed on 21 October 2020).

46. University of Maryland. Engineering Narrative. 2017. Available online: https://www.solardecathlon.gov/2017/assets/pdfs/sd2017_maryland_narrative_engineering.pdf (accessed on 22 October 2020).

47. Team Virginia Tech. FutureHAUS Project Manual. 2018. Available online: https://www.solardecathlonme.com/2018/teams/team-virginia-tech (accessed on 22 October 2020).

48. Team EFden. EFdeN Signature Project Manual #6. 2018. Available online: https://www.solardecathlonme.com/2018/teams/team-efden (accessed on 22 October 2020).

49. Team Baitykool. Baitykool Project Manual #6. 2018. Available online: https://www.solardecathlonme.com/2018/teams/team-baitykool (accessed on 22 October 2020).

50. Team Ikaros Bavaria. Solar System and Hot Water Brief Report. Available online: https://building-competition.org/file/5909f1 892dd2ae330fc57a0a/43a4003f48051a948123db74f7453cd28f8348c8ab37d94e8c7ad6ab0238abb5 (accessed on 23 October 2020).

51. Team HFT Stuttgart. Project Manual. Available online: https://building-competition.org/file/5909f18b2dd2ae334bec6098/a506 4c88063f4883ce707dd6a00970cd259ccae3f09c22f4b4e47b64a7fc8459 (accessed on 23 October 2020).

52. Ecolar Team. Project Manual. 2012. Available online: http://www.sdeurope.org/wp-content/pdf/HTWG_PM_7.pdf (accessed on 29 August 2017).

53. Universita Degli Studi di Roma TRE. Project Manual. 2014. Available online: http://www.solardecathlon2014.fr/ftp/docs/ROME_PM7.pdf (accessed on 21 October 2020).

54. Cornell University. Comprehensive Assessment of Hot Water System Report. Available online: https://www.solardecathlon.gov/past/pdfs/05_techreport/cornell_hot_water_report.pdf (accessed on 21 October 2020).

55. Universidad Politécnica de Madrid. Casa Solar Construction Specifications. Available online: https://www.solardecathlon.gov/past/download/07_techreport/madrid_tech_specs.zip (accessed on 15 April 2021).

56. Team Ontario/BC. Project Manual. Available online: http://www.solardecathlon.gov/past/download/09_construction_docs/manual_ontario_bc.zip (accessed on 15 April 2021).

57. National Renewable Energy Laboratory for the U.S. Department of Energy. Solar Decathlon 2007 Highlights of Team Innovations and Cutting-Edge Building Technologies. Available online: https://www.solardecathlon.gov/past/pdfs/07_techreport/07_innovations.pdf (accessed on 21 October 2020).

58. University of Minnesota. Project Manual. Available online: http://www.solardecathlon.gov/past/download/09_construction_docs/manual_minnesota.zip (accessed on 15 April 2021).

59. Team Alabama. Innovation Narrative. 2017. Available online: https://www.solardecathlon.gov/2017/assets/pdfs/sd2017_alabama_narrative_innovation.pdf (accessed on 22 October 2020).

60. Technische Universität Darmstadt. TU Darmstadt Solar Decathlon 07 Specification. Available online: https://www.solardecathlon.gov/past/download/07_techreport/darmstadt_specs.zip (accessed on 15 April 2021).

61. Universidad Politécnica de Madrid. Casa Solar Madrid As-Built Drawings. Available online: https://www.solardecathlon.gov/past/download/07_techreport/madrid_as_built_drawings.zip (accessed on 15 April 2021).

62. Team Luuku House. Engineering and Construction Brief Report. Available online: https://building-competition.org/file/5909f1 8c2dd2ae3369033ffb/908ceb0c3152caf5d1a835b57aa274aeddff257558505b14b9d5c02050409060 (accessed on 23 October 2020).

63. Ecolar Team. Jury Report. 2012. Available online: https://building-competition.org/file/5909f1972dd2ae35031cf8b4/7cea0bf887 1b48e22dc30bb9142f00fa428987dfd0c678d57edd1e61dfc3dfc3 (accessed on 23 October 2020).

64. Stevens Institute Team. As-Built Project Manual. 2013. Available online: https://building-competition.org/file/5992e867ecb8f5 5195527287/edab3e409227d4ef928c4e9ba2e465b1bdb00b14519ad9f0df130684cebc69a7 (accessed on 21 October 2020).

65. Team Prê-à-Loger. Project Drawing. 2014. Available online: https://building-competition.org/file/5909f1902dd2ae33ffb78cf8/3 68028d6872eff3b6016b8ea8eb70a67c350bb86a2a61b9cd2cc6fc16e0206b8 (accessed on 21 October 2020).

66. Team Rooftop. Engineering and Construction Report. 2014. Available online: https://building-competition.org/file/5909f190 2dd2ae3409b62ab6/2bc69144e79424b8bf312cb196dbe1fe61820d1dba0f3eae756e0d534d54ed27 (accessed on 21 October 2020).

67. Rodríguez-Ubiñas, E.; Ruíz-Valero, L.; Sánchez, S.V.; González, F.J.N. Latent heat thermal energy storage systems in lightweight construction: Review of PCM applications in Solar Decathlon Houses. *WIT Trans. Ecol. Environ.* **2011**, *150*, 935–946.

68. Powered by the Sun 2007 Solar Decathlon. Available online: https://www.nrel.gov/docs/fy07osti/41540.pdf (accessed on 21 October 2020).

69. Andalucia Team. Project Manual. 2012. Available online: http://www.sdeurope.org/wp-content/pdf/AND_PM_7.pdf (accessed on 29 August 2017).

70. Sapienza Universita Di Roma. Project Manual. 2018. Available online: https://www.solardecathlonme.com/2018/teams/team-sapienza (accessed on 22 October 2020).

71. Wendt, A. German Team Wins Solar Decathlon. Building Green. Available online: https://www.buildinggreen.com/newsbrief/german-team-wins-solar-decathlon (accessed on 21 October 2020).

72. Virginia Tech Team. As-Built Project Manual. Available online: https://building-competition.org/file/5909f18a2dd2ae3337cac5e5/113ecf2a21b69dfb172fffe4d1643612e83becbeecf5b0f721cb86ced3f1f980 (accessed on 23 October 2020).

73. Team Canopea. Jury Brief. Available online: https://building-competition.org/file/5909f1972dd2ae35177746d4/b380e38a7599562e60e25c341583f6ff210aa41056b3729a2a754c8d760f094e (accessed on 22 October 2020).

74. Team Med in Italy. Jury Report. 2012. Available online: https://building-competition.org/file/5909f1962dd2ae34efb63b4c/cd0154492119813b7886d3551290b555f4186e1ff2ae88bd7cac1bc5f1bd9c40 (accessed on 23 October 2020).

75. Visitors Guide Solar Decathlon 2013. 2013. Available online: https://www.solardecathlon.gov/past/2013/pdfs/2013_visitors_guide.pdf (accessed on 21 October 2020).

76. Universita Degli Studi di Roma TRE. Project Drawing. 2014. Available online: http://www.solardecathlon2014.fr/ftp/docs/ROME_PD7.pdf (accessed on 21 October 2020).

77. Atlantic Challenge Team. Project Manual. 2014. Available online: http://www.solardecathlon2014.fr/ftp/docs/ATC_PM7.pdf (accessed on 21 October 2017).

78. Team Prê-à-Loger. Project Manual #7. 2014. Available online: https://building-competition.org/file/5909f1902dd2ae33ffb78cf8/2f8c45fd02e7616363ff63e9ac1e1da8c77e1aeaee785074178a1f9e04ca6872 (accessed on 3 November 2014).

79. Team Rooftop. Project Manual. 2014. Available online: https://building-competition.org/file/5909f1902dd2ae3409b62ab6/80c85a0fa31c10da582349c89f2d673b717ac77211c61278450d72419a385fdc (accessed on 21 October 2020).

80. University of Texas at Austin; Technische Universitaet Muenchen. Jury Narratives. 2015. Available online: https://www.solardecathlon.gov/2015/assets/pdfs/sd2015_narrative_tex.pdf (accessed on 22 October 2020).

81. Swiss Living Challenge Team. Innovation. 2017. Available online: https://www.solardecathlon.gov/2017/assets/pdfs/sd2017_swissteam_narrative_innovation.pdf (accessed on 21 October 2020).

82. Missouri University of Science and Technology. Innovation Narrative. 2017. Available online: https://www.solardecathlon.gov/2017/assets/pdfs/sd2017_missouri_narrative_innovation.pdf (accessed on 21 October 2020).

83. Fonts, A. Santa Clara University Specifications. Available online: https://www.solardecathlon.gov/past/download/07_techreport/santa_clara_specs.zip (accessed on 15 April 2021).

84. University of Maryland. Construction Drawings. 2017. Available online: https://www.solardecathlon.gov/2017/assets/pdfs/maryland-drawings.pdf (accessed on 22 October 2020).

85. UC Berkley; University of Denver. Innovation Narrative Submission. 2017. Available online: https://www.solardecathlon.gov/2017/assets/pdfs/sd2017_berkeleydenver_narrative_innovation.pdf (accessed on 21 October 2020).

86. Team Ikaros Bavaria. Sustainability Brief Report. Available online: https://building-competition.org/file/5909f1892dd2ae330fc57a0a/35d40a6429c44cb414ff2832be2e143ba62f2b4bfe309cf7b7502c80cba9dbe5 (accessed on 23 October 2020).

87. Swiss Living Challenge. Construction Specifications. 2017. Available online: https://www.solardecathlon.gov/2017/assets/pdfs/swiss-specs.pdf (accessed on 24 October 2020).

88. Frascarolo, M.; Martorelli, S.; Vitale, V. An innovative lighting system for residential application that optimizes visual comfort and conserves energy for different user needs. *Energy Build.* **2014**, *83*, 217–224. [CrossRef]

89. Cornell University. Electric Lighting Quality. Available online: https://www.solardecathlon.gov/past/pdfs/05_techreport/cornell_electric_lighting_report.pdf (accessed on 21 October 2020).

90. Virginia Polytechnic Institute; State University. Lighting. Available online: https://www.solardecathlon.gov/past/pdfs/05_techreport/va_tech_electric_lighting_report.pdf (accessed on 21 October 2020).

91. University of Maryland. Innovation Narrative. 2017. Available online: https://www.solardecathlon.gov/2017/assets/pdfs/sd2017_maryland_narrative_innovation.pdf (accessed on 21 October 2020).

92. New York Institute of Technology. NYIT Brief Contest Report: Dwelling. Available online: https://www.solardecathlon.gov/past/pdfs/05_techreport/nyit_dwelling_report.pdf (accessed on 11 April 2021).

93. Andalucia Team. Jury Report. 2012. Available online: http://www.sdeurope.org/wp-content/pdf/AND_JuryBriefReports.pdf (accessed on 29 August 2017).

94. Liedl, P.; Pyrek, A.; Garrison, M.; Upshaw, C.; Lang, W. The Nexushaus: Get connected in central Austin. *J. Green Build.* **2015**, *10*, 44–54. [CrossRef]

95. Weber, E. Creating the UNLV Solar Decathlon House: Processes and lessons. *Int. J. Architecton. Spat. Environ. Des.* **2014**, *8*, 17–31. [CrossRef]

96. Yang, X.Q.; Yang, W.; Gao, H. The life cycle oriented concepts of zero energy solar house: A review of SDE2010 projects. *Appl. Mech. Mater.* **2013**, *361*, 281–285. [CrossRef]

97. Stieldorf, K. Building physics, design, and the collaborative build: Sustainability and resilience in architectural education. *Archit. Des.* **2018**, *88*, 102–109. [CrossRef]

98. DOE Solar Decathlon. New Zealand Virtual Tour-Solar Decathlon 2011. Available online: https://www.youtube.com/watch?v=OJnoextCURc (accessed on 23 October 2020).

99. Team Armadillo Box. Project Manual. Available online: https://building-competition.org/file/5909f18d2dd2ae33a54b21c4/25fc54de48b49f43e1206677a250fac5e38f1b16c0f7407bd3ff1aa217393df7 (accessed on 23 October 2020).

100. Team Prê-à-Loger. Engineering & Construction. 2014. Available online: https://building-competition.org/file/5909f1902dd2ae33ffb78cf8/0d430d1c783ac7d6525499caf0e4e236eda60409fd491095660703ac86690aa8 (accessed on 21 October 2020).

101. Casini, M. A positive energy building for the Middle East climate: ReStart4Smart solar house at solar decathlon Middle East 2018. *Renew. Energy* **2020**, *159*, 1269–1296. [CrossRef]

102. Solar Calpoly Team. Thermal Comfort Comprehensive Assessment Report. Available online: https://www.solardecathlon.gov/past/pdfs/05_techreport/calpoly_thermal_comfort_report.pdf (accessed on 21 October 2020).

103. Team California. Project Manual. 2009. Available online: http://www.solardecathlon.gov/past/download/09_construction_docs/manual_california.zip (accessed on 15 April 2021).

104. Ma, Z.; Ren, H.; Lin, W. A review of heating, ventilation and air conditioning technologies and innovations used in solar-powered net zero energy Solar Decathlon houses. *J. Clean. Prod.* **2019**, *240*, 118158. [CrossRef]

105. Solar Decathlon 2009. 2009. Available online: https://www.nrel.gov/docs/fy09osti/45753.pdf (accessed on 21 October 2020).

106. New York Institute of Technology. NYIT Brief Contest Report: Architecture. 2005. Available online: https://www.solardecathlon.gov/past/pdfs/05_techreport/nyit_architecture_report.pdf (accessed on 21 October 2020).

107. Team Ikaros Bavaria. Architectural Brief Report. 2010. Available online: https://building-competition.org/file/5909f1892dd2ae330fc57a0a/753604629be4cbcdfd70029998ecdb2becafeee923bbc4d6dfc210ce0fd6352f (accessed on 23 October 2020).

108. Snell, C. Practical resilience: Low-tech plug-and-play innovation in the SU + RE house. *Archit. Des.* **2018**, *88*, 56–63. [CrossRef]

109. Battista, G.; Carnielo, E.; Evangelisti, L.; Frascarolo, M.; Vollaro, R. Energy performance and thermal comfort of a high efficiency house: RhOME for denCity, winner of solar decathlon Europe 2014. *Sustainability* **2015**, *7*, 9681–9695. [CrossRef]

110. Garrison, M. The 2005 Solar D house. *WIT Trans. Built Environ.* **2006**, *86*, 155–162.

111. Technische Universität Darmstadt. Project Manual. 2009. Available online: http://www.solardecathlon.gov/past/download/09_construction_docs/manual_germany.zip (accessed on 15 April 2021).

112. Team HFT Stuttgart. Architectural Brief Report. 2010. Available online: https://building-competition.org/file/5909f18b2dd2ae334bec6098/e0ece1f33ea9ca9d641bac99d3d9a33c06b16c7e63c276f6062d5b2848e51980 (accessed on 23 October 2020).

113. Pujadas-Gispert, E.; Alsailani, M.; van Dijk, K.C.A.; Rozema, A.D.K.; ten Hoope, J.P.; Korevaar, C.C.; Moonen, S.P.G. Design, construction, and thermal performance evaluation of an innovative bio-based ventilated façade. *Front. Archit. Res.* **2020**, *9*, 681–696. [CrossRef]

114. Liu, H.; Gao, H.; Wan, D. Research on building construction system of SDE2010. *Adv. Mater. Res.* **2011**, *368*, 3638–3642. [CrossRef]

115. University of Illinois at Urbana-Champaign. Construction Drawing. 2009. Available online: http://www.solardecathlon.gov/past/download/09_construction_docs/cd_illinois.zip (accessed on 15 April 2021).

116. Team Solar CalPoly. Architecture Report. 2005. Available online: https://www.solardecathlon.gov/past/pdfs/05_techreport/calpoly_architecture_report.pdf (accessed on 21 October 2020).

117. Luna-Tintos, J.; Cobreros, C.; López-Escamilla, Á.; Herrera-Limones, R.; Torres-García, M. Methodology to Evaluate the Embodied Primary Energy and CO_2 Production at Each Stage of the Life Cycle of Prefabricated Structural Systems: The Case of the Solar Decathlon Competition. *Energies* **2020**, *13*, 4311. [CrossRef]

118. Virginia Polytechnic Institute; State University. Dwelling. 2005. Available online: https://www.solardecathlon.gov/past/pdfs/05_techreport/va_tech_dwelling_report.pdf (accessed on 21 October 2020).

119. Cronemberger, J.; Corpas, M.; Cerón, I.; Caamaño-Martín, E.; Sánchez, S. BIPV technology application: Highlighting advances, tendencies and solutions through solar decathlon Europe houses. *Energy Build.* **2014**, *83*, 44–56. [CrossRef]

120. Zanelli, A.; Spinelli, L.; Monticelli, C.; Pedrali, P. *Lightweight Landscape*; Springer International Publishing: Cham, Switzerland, 2016.

121. DOE Solar Decathlon. Maryland's Solar Decathlon 2011 Architecture Audio-Visual Presentation. 2011. Available online: https://www.youtube.com/watch?v=IAzO-wdKUxg (accessed on 23 October 2020).

122. Team Maryland. Construction Drawing. 2011. Available online: https://www.solardecathlon.gov/past/2011/pdfs/umd_cd.pdf (accessed on 21 October 2020).

123. University of Nevada Las Vegas. Construction Drawing. 2013. Available online: https://www.solardecathlon.gov/past/2013/pdfs/unlv_cd.pdf (accessed on 21 October 2020).

124. Firstlight, N.Z. First Light NZ—Solar Decathlon—Walkthrough. 2011. Available online: https://www.youtube.com/watch?v=J55Ad-95rCA (accessed on 23 October 2020).

125. DOE Solar Decathlon. Middlebury College's Solar Decathlon 2011 Video Walkthrough. 2011. Available online: https://www.youtube.com/watch?v=YxrXCbgCsoY (accessed on 23 October 2020).

126. Samuel, A.K.; Mohanan, V.; Sempey, A.; Garcia, Y.F.; Lagiere, P.; Bruneau, D.; Mahanta, N. Sustainable approach for a climate responsive house in United Arab Emirates: Case study of SDME 2018 BAITYKOOL project. In Proceedings of the 2019 International Conference on Computational Intelligence and Knowledge Economy (ICCIKE), Dubai, United Arab Emirates, 11–12 December 2019.

127. SolarHaus TU Darmstadt. Solar Decathlon 2007. 2020. Available online: http://eud.leneurbanity.com/6-most-sustainable-and-energy-efficient-designs-for-the-future-of-urban-housing/peh_bmvbs_2/ (accessed on 21 October 2020).
128. SolarHaus TU Darmstadt. Solar Decathlon 2007. 2020. Available online: http://eud.leneurbanity.com/6-most-sustainable-and-energy-efficient-designs-for-the-future-of-urban-housing/peh_bmvbs_1/ (accessed on 21 October 2020).
129. University of Colorado. Dwelling in the cu "BIO-S$^{(H)}$IP". 2005. Available online: https://www.solardecathlon.gov/past/pdfs/05_techreport/co_dwelling_report.pdf (accessed on 21 October 2020).
130. Zhang, S.; Liu, H.; Wang, Y. New trends of green building's skin material: Take the solar decathlon Europe 2010 for example. *Adv. Mater. Res.* **2013**, *671*, 1905–1908. [CrossRef]
131. Enware. Enware and UOW Create Dementia-Friendly House of the Future. 2020. Available online: https://www.enware.com.au/news/enware-and-uow-create-dementia-friendly-house-of-the-future (accessed on 22 October 2020).
132. Ghosh, A. Possibilities and challenges for the inclusion of the electric vehicle (EV) to reduce the carbon footprint in the transport sector: A review. *Energies* **2020**, *13*, 2602. [CrossRef]

![buildings logo]

Review

Implementation of Passive Radiative Cooling Technology in Buildings: A Review

Suhendri, Mingke Hu *, Yuehong Su *, Jo Darkwa and Saffa Riffat

Department of Architecture and Built Environment, University of Nottingham, Nottingham NG7 2RD, UK; suhendri.suhendri@nottingham.ac.uk (S.); j.darkwa@nottingham.ac.uk (J.D.); saffa.riffat@nottingham.ac.uk (S.R.)
* Correspondence: mingke.hu@nottingham.ac.uk (M.H.); yuehong.su@nottingham.ac.uk (Y.S.)

Abstract: Radiative cooling (RC) is attracting more interest from building engineers and architects. Using the sky as the heat sink, a radiative cooling material can be passively cooled by emitting heat to the sky. As a result of the development of material technology, RC research has been revived, with the aim of increasing the materials' cooling power as well as finding reliable ways to utilize it in cooling for buildings. This review identifies some issues in the current implementation of RC technologies in buildings from an architectural point of view. Besides the technical performance of the RC technologies, some architectural aspects, such as integration with architectural features, aesthetic requirements, as well as fully passive implementations of RC, also need to be considered for building application. In addition, performance evaluation of a building-integrated RC system should begin to account for its benefit to the occupant's health and comfort alongside the technical performance. In conclusion, this review on RC implementation in buildings provides a meaningful discussion in regard to the direction of the research.

Keywords: radiative cooling; architectural application; combination; passive design architecture

---

1. Introduction

Global warming forces buildings to consume more energy for cooling. For buildings in urban areas, they also experience the so-called urban heat island (UHI), and this increases the cooling demand even more in the warm and hot climate region [1]. Some locations that used to maintain their thermal comfort via passive cooling also now need mechanical assistance. The International Energy Agency (IEA) reported that energy consumption for cooling has tripled during the last three decades [2]. Reliance of the energy generation on fossil fuel makes the cooling demand somewhat paradoxical, i.e., by cooling down our buildings, we made the earth even warmer [3]. Thus, passive cooling in buildings plays a crucial role in the environment [4].

Various passive cooling techniques have been developed by researchers and engineers. The general mechanism of passive cooling is actually by dissipating heat from buildings to the environmental heat sink [5]. The most commonly utilized mechanism is convection and evaporation. These two heat transfer mechanisms mainly deal with ambient air or ground as the heat sinks. Nowadays, there is an emerging field of study in which thermal radiation is used as a means of cooling with the sky as the heat sink [6]. This mechanism is not new in nature, e.g., plants experienced this with the effect of dew and frost formation on their leaves [7]. In buildings, radiative cooling (RC) can be applied to building envelopes, especially those that acquire the highest sky view factor (SVF).

Despite their potential, RC techniques have not been widely used in buildings. Challenges of RC application are well defined by researchers. The two most frequently mentioned challenges are technical and cost problems. Technical problems are related to low cooling power, sophisticated material

technology to produce the radiator, complicated systems in implementations, durability, and maintenance issues [8]. Cost problems consist of high production cost and high installation cost [9,10].

There is also a problem regarding geographical constraints. Generally, the RC panel is highly dependent on climate and geographical conditions. Factors such as sky condition, wind speed, atmospheric particle, etc. strongly affect the performance of RC panels [5,7,11–13]. RC performs badly in humid conditions. Moreover, a problem also occurs in the form of a mismatch between the cooling demand and the supply. The highest cooling power of an RC panel occurs at night, while building occupants require cooling in the daytime [5,14]. From an architectural point of view, options for design are more crucial. RC panels should be placed on the side that is fully exposed to the sky, which already limits the design option of the building roof, or other smaller sky-facing building components [15]. Moreover, the roof-to-floor area ratio is significantly low for multi-story buildings. This again constraints the design option for architects [9]. Furthermore, structural considerations could also limit the design options [15].

In short, implementing passive RC in buildings does not appear to be beneficial for utility and architectural demand. RC power is not enough for a larger building. Moreover, the technology needs to be more building-integrated [5,7,16]. Many proposals for the implementation of RC in buildings are still in the stage of research and development, and they are mainly about the emitter material or the use of RC to assist active cooling technology [17]. These challenges remain further research topics in the RC field.

Although there are several reviews on RC technologies, and some of their conclusions are cited above, to the authors' best knowledge, only two reviews focused on the applications of RC in buildings. The first paper by Lu et al. [7] elaborates on the cooling power of RC materials, which back in 2016 seemed to be the main barrier for the adoption of RC in buildings. A recent review on a similar topic by Chen et al. [18] in 2020 updated the conditions on RC material explorations, which have been improved since 2016 but still require a real building application, not to mention a large-scale one. Chen et al. [18] suggested that the potential for real RC application in buildings might lie in RC combination with a heating, ventilation, and air conditioning (HVAC) system. Moreover, the two reviews also mentioned that there is a need for study on the economic aspect of many prototype RC systems.

However, one stakeholder that is also important for the application of RC in buildings, i.e., the architects, was excluded in the reviews. Architects should be taken into consideration as they implement RC concepts in their designs [19]. Thus, this review offers to fill in the gap by analyzing the current development of RC technology in buildings from an architectural point of view and proposes some possible research direction of passive RC application in buildings. This review does not only include works that directly implement RC in building, but also looks at some relevant papers on the technological development of RC. The review is arranged in six sections with the main content, besides the introduction and conclusions, describing RC principles, its state-of-the-art application in buildings, the architectural features that are involved in current applications, and an outlook for architectural application of passive RC.

2. Radiative Cooling Principles

All solid surfaces radiate heat in the form of electromagnetic radiation, whose power is proportional to temperature and emissivity, and is distributed across the frequency spectrum. Thus, the term total emissive power is differentiated from spectral emissive power, where the former refers to energy emitted over the entire spectrum, while the latter suggests energy emitted at a specific wavelength interval. The spectral emissive power of an ideal blackbody is governed by Planck's law as stated by Equation (1).

$$E_{\mathrm{B}\lambda}(T, \lambda) = \frac{2\pi h c_0^2}{n^2 \lambda^5 [e^{hc_0/n\lambda kT} - 1]} \tag{1}$$

$E_{\mathrm{B}\lambda}(T, \lambda)$ is the spectral emissive power of a blackbody at a certain temperature T for a particular wavelength λ, h is Planck's constant (6.626×10^{-34} J·s), c_0 is light speed in vacuum (2.998×10^8 m/s), n is

the refractive index of the medium (1 for vacuum), and *k* is Boltzmann's constant (1.3807×10^{-23} J·K^{-1}). Figure 1 plots the distribution of blackbody emissive power for some temperatures against the wavelength. It indicates that emissions from different blackbody temperatures peaked at different wavelengths. The maximum wavelength λ_{max}, the wavelength in which a blackbody at a certain temperature *T* emits the maximum power of radiation, can be calculated from Equation (2), which is obtained from Equation (1). When applied to terrestrial bodies with a temperature around 300 K, Equation (2) gives λ_{max} of 9.6 μm [20].

$$\lambda_{max} = \frac{2898}{T} \tag{2}$$
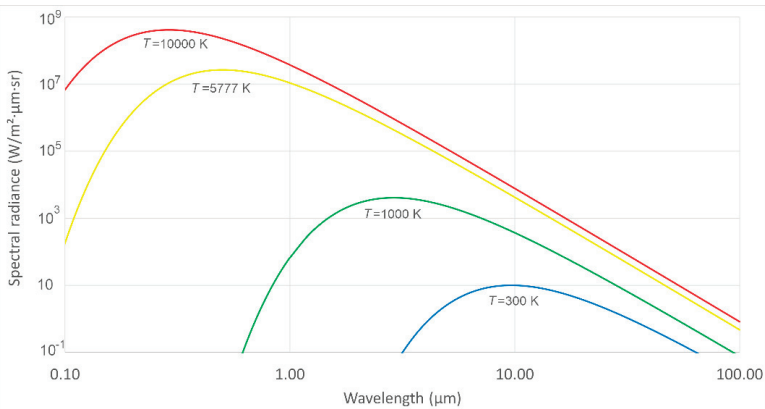
Figure 1. Distribution of spectral emissive power of a blackbody for different temperatures, replotted from SpectralCal [21].

The earth's thermal radiation, which peaks at 9.6 μm, is radiated to outer space through the atmosphere. Fortunately, the earth's atmosphere is relatively transparent for thermal radiation at 8–13 μm, the wavelength in which the λ_{max} of terrestrial radiation peaks. This band is called the atmospheric window. This atmospheric window makes possible the cooling of the earth's surface via radiation in the direction of the sky. Figure 2 superimposes the thermal radiation of a terrestrial body with 300 K temperature on the value of atmospheric transmittance.
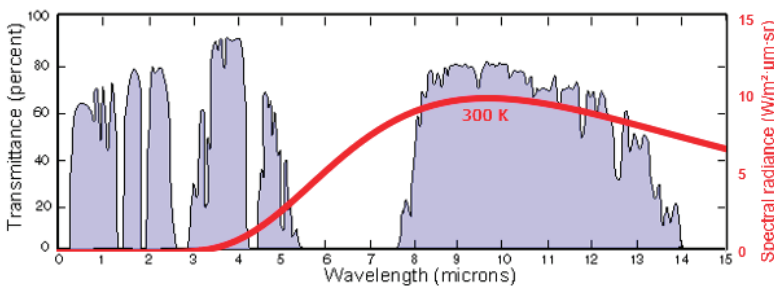
Figure 2. Thermal radiation of average terrestrial temperature (*T* = 300 K) lies within the atmospheric window band of 8–13 μm [22].

Passive RC techniques utilize this phenomenon. A typical RC panel places the emitter inside a fully insulated frame and protects it from convective heat loss by a transparent cover, usually a polyethylene film, as illustrated by Figure 3. The cooling power (Q_{net}) of a radiative surface is defined as net heat transfer from the surface. A surface exposed to the sky absorbs radiation from the sun (Q_{sun})

and the atmosphere (Q_{atm}) and emits its radiation (Q_{rad}). In addition to the radiative heat emitted or received by the surface, it also gains and loses heat from conduction and convection ($Q_{cond+conv}$). Thus, the energy balance equation of a radiative surface can be written as Equation (3).

$$Q_{net} = Q_{rad}(T, \lambda) - Q_{atm}(T_{amb}) - Q_{sun} \pm Q_{conv+cond} \qquad (3)$$
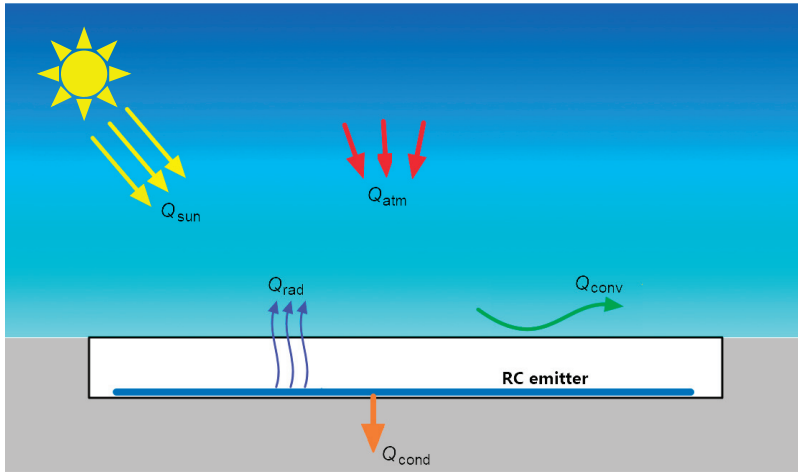
Figure 3. Illustration of typical radiative cooling (RC) panel design and heat transfer on the panel.

Detailed equations for each component of the above equation are summarized by Raman et al. [12]. Q_{rad} is the emissive power of an RC surface with area A at temperature T for the wavelength λ, as shown in Equation (4). The absorbed heat due to incident atmospheric thermal radiation (Q_{atm}) at ambient temperature T_{amb} is given by Equation (5).

$$Q_{rad}(T, \lambda) = A \int d\Omega cos\,\theta \int_0^\infty d\lambda E_{B\lambda}(T, \lambda)\, \epsilon(\lambda, \theta) \qquad (4)$$

$$Q_{atm}(T_{amb}) = A \int d\Omega cos\,\theta \int_0^\infty d\lambda E_{B\lambda}(T, \lambda)\, \epsilon(\lambda, \theta)\, \epsilon_{atm}(\lambda, \theta) \qquad (5)$$

where,

$$\int d\Omega = 2\pi \int_0^{\frac{\pi}{2}} d\theta sin\theta \qquad (6)$$

In Equations (4) and (5), A represents the area of the emitter, and $\int d\Omega$ denotes angular integral over a hemisphere as shown in Equation (6). Moreover, $E_{B\lambda}(T, \lambda)$ represents the spectral emissive power of blackbody at the emitter's temperature T for the wavelength λ as formulated by Equation (1), whereas $\epsilon(\lambda, \theta)$ is the angle-dependent emissivity of the emitter. For Equation (5), there is an additional emissivity, $\epsilon_{atm}(\lambda, \theta)$, which is the angle-dependent emissivity of the atmosphere.

Further, the absorbed solar radiation is formulated using Kirchoff's radiation law as shown by Equation (7), where $\epsilon(\lambda, \theta_{sun})$ is the emissivity of the emitter at the angle of the sun's position (θ_{sun}). In Equation (7), $I_{AM\,1.5}$ is solar intensity using AM 1.5 spectra. Conduction and convection heat transfer $Q_{cond+conv}(T, T_{amb})$ between the absorber/emitter with the surroundings are also considered

in Equation (8), where h_c is heat transfer coefficient, T_{amb} is ambient temperature, and $T_{emitter}$ is the surface temperature of the RC emitter.

$$Q_{sun} = A \int_0^\infty d\lambda \epsilon(\lambda, \theta_{sun}) \, I_{AM \, 1.5}(\lambda) \tag{7}$$

$$Q_{cond+conv}(T, T_{amb}) = A \, h_c (T_{amb} - T_{emitter}) \tag{8}$$

From the mathematical model of a typical RC emitter as shown above, factors for a successful RC emitter can be derived. Firstly, the RC emitter needs to be properly insulated from conduction and protected from unwanted convective loss. Secondly, the emitter must have high emissive power in the atmospheric window band. This also means the convection cover needs to be transparent in the same band to transmit the thermal radiation from the emitter. Thirdly, the emitter needs to reflect as much as possible the incident solar radiation to work in the daytime. Another important factor is the atmospheric or sky condition, i.e., a humid atmosphere limits the transparency of the atmospheric window. In other words, a clear sky is more beneficial to the RC emitter than an overcast sky.

3. Research on the Application of Radiative Cooling in Buildings

Attempts to utilize RC in buildings can be traced back to the 1970s when Bartoli et al. [23] and Harrison and Walton [24] conducted experiments using two similar RC emitter designs with different materials, namely TEDLAR (a polyvinyl fluoride film) and TiO_2 white paint as the emitter, respectively. In the same period, Givoni [25] proposed another design of a passive RC system that can provide heating and cooling for buildings. The field started to attract more attention from researchers during the 1990s. During the decade, besides explorations that focused on the cooling power of emitter materials [26–30], some proposed RC systems involving working fluid to extract the cooling and other elements such as thermal storage [31–33] and desiccant [34] to improve the system's performance. Since then, the number of explorations of the application of RC in buildings has grown significantly.

There are different classifications of RC technologies applied in buildings. Erell and Santamouris [15] classified RC technologies into two categories based on how the RC system is utilized, namely movable insulation and heat exchangers. In an RC system with movable insulation, the emitter, which was actually a solar thermal collector, was protected from solar radiation at daytime and exposed to the sky at nighttime by turning the insulation off from the emitter [31,35]. In contrast, in an RC system with a heat exchanger, a working fluid, either water or air, was used as a medium to "carry the coldness" of the emitter to the building interior [16,36]. On the other hand, Zeyghami et al. [16] classified the RC technologies into two categories based on working time, namely nocturnal and diurnal. Nocturnal cooling consists of two general designs, i.e., a gray emitter which emits in the whole range of the wavelength, and a selective emitter which was designed to have emissivity higher or lower at a certain wavelength. Meanwhile, diurnal RC prefers to be equipped with selective emitter material and assisted with a cover shield.

The classifications of RC technology that have been performed by researchers mark a historical or rather a sequential development of RC technology. In this review, we classify RC technologies based on the type of improvement carried out by researchers in order to obtain technology applicable to buildings. The first category is "material improvement", which includes studies that focus on new materials or that enhance the current materials for emitters. The second category is "design improvement", i.e., researchers tried to modify the panel configuration, design, or supporting element to improve the emitter performance. The last category is "combination with other technologies", which includes applications of RC "to assist" or "with the assistance of" other technologies. Table 1 summarizes the classifications of improvement strategies and the reported performance.

Table 1. Improvement strategies for RC technology application in buildings.

Researcher	Category	Time	Improvement Strategy	Maximum Cooling Power/Minimum Temperature
[37]	Emitter material improvement	Nocturnal	Film-based emitter	energy saving for cooling up to 26–49%
[38]			Film-based emitter	43 W/m^2
[39]			Photonic emitter	5 °C below ambient
[40]			Photonic emitter	5.2 °C below ambient
[41]		Diurnal	Film-based emitter	120 W/m^2
[42]			Film-based emitter	not available (N/A)
[43]			Film-based emitter	2.5 °C below ambient
[8]			Film-based emitter	4.2 °C below ambient
[44]			Film-based emitter	95.1 W/m^2
[45]			Photonic emitter	110 W/m^2
[46]			Nanoparticle-based emitter	25.5 °C below ambient
[47]			Nanoparticle-based emitter	35 °C below ambient
[48]			Photonic emitter	N/A
[49]			Photonic emitter	14.3 W/m^2
[50]			Photonic emitter	7.7 ± 0.2 °C below ambient
[51]	Cover material improvement	Nocturnal	Film-based cover	23 W/m^2
[52]			Film-based cover	175 W/m^2
[53]			Film-based cover	N/A
[54]			Film-based cover	N/A
[55]		Diurnal	Photonic cover	50 W/m^2
[56]	Design improvement	Nocturnal	Design aspect: water contact with the emitter, insulation	97.8 W/m^2
[11]			Design aspect: construction material	2.5 °C below ambient
[57]			Design aspect: water contact with the emitter	52 W/m^2
[58]			Design aspect: air duct	90 W/m^2
[59]			Design aspect: insulation, air duct	2.5–4 °C below ambient
[60]			Design aspect: insulation	38 W/m^2
[61]			Design aspect: insulation	N/A
[62]			Design aspect: cover, air duct	1–6 °C below ambient
[63]		Diurnal	Design aspect: insulation	37 °C below ambient through a 24 h cycle
[64]			Design aspect: glazing and convection scheme	100 W/m^2
[65]			Design aspect: orientation	7.4 °C below ambient
[66]			Design aspect: appearance	3.9 °C below ambient

Table 1. *Cont.*

Researcher	Category	Time	Improvement Strategy	Maximum Cooling Power/Minimum Temperature
[67]			Trombe wall	energy saving for cooling up to 53%
[30]			Wall material	55.8 W/m^2
[68]			Wall material and insulation, cold water storage	87 W/m^2
[69]			Solar Collector, phase change material (PCM)	N/A
[70]			Photovoltaics (PV)	128.5 W/m^2
[71]			Solar Collector	50.3 W/m^2
[72]			Cold storage	N/A
[73]			Solar Collector	27.3 W/m^2
[74]			PV, heating, ventilation, and air conditioning (HVAC) system	123.9 W/m^2
[75]			PV	41.7 W/m^2
[76]			HVAC	N/A
[77]			Solar Collector and PV, cold water storage	75 W/m^2
[78]			PCM	energy saving potential can reach 77% for low-rise buildings
[79]			Desiccant	5.5–7 °C below ambient
[34]	Combination	Nocturnal	Solar Collector, desiccant	energy saving up to 7400 kWh per year
[80]			PV, solar collector, HVAC	N/A
[81]			HVAC	energy saving for cooling up to 46% for
[82]			Radiant cooling, air handling unit (AHU)	18.1 W/m^2
[83]			Fan or HVAC	5–10W/m^2
[84]			Ground coupled heat pump	energy saving 10.22% compared to conventional ground heat pump
[85]			PV, solar collector	72 W/m^2
[86]			HVAC	N/A
[87]			Thermosyphon and cold water storage	energy saving for cooling up to 8%
[88]			Solar Collector	36.61 W/m^2
[32]			Heat pipe	14.5 W/m^2
[17]			Photovoltaic thermal (PV/T)	65 W/m^2
[89]			Thermosyphon and cold water storage	N/A
[25]			Solar Collector	4–5 °C below ambient
[90]			Solar Collector	55.1 W/m^2
[91]			Solar Collector	40 W/m2
[33]			Thermosyphon and cold water storage	15 °C below ambient
[31]			Thermal mass	77.2 W/m^2

Table 1. *Cont.*

Researcher	Category	Time	Improvement Strategy	Maximum Cooling Power/Minimum Temperature
[92]			PV	72.94 W/m^2
[93]			Solar Collector, HVAC	4.7 °C below ambient
[94]			Water tank	8.4 °C temperature reduction
[95]			HVAC	16 W/m^2
[96]			HVAC	more than 200 W/m^2
[97]		Diurnal	Thermoelectric, cold water storage tank	daytime and nighttime cooling of the radiative sky cooling subsystem contribute to 55.0% and 45.0% of annual cold generation, respectively
[98]			Attic insulation	energy saving for cooling up to 3.7–11.8 kWh/m^2
[99]			Cold water storage, radiant cooling in the room	12.5 W/m^2
[100]			PCM, thermosyphon	energy saving for cooling up to 25%
[101]			PCM, wall material	energy saving for cooling up to 47.9%
[102]			PCM, cold water storage	energy saving for cooling up to 10%
[103]			Wall material and insulation	50 W/m^2 on the wall, and 120 W/m^2 on the roof
[104]			Shading device	reduces solar gain by up to 40%
[105]			Glazing	energy saving for cooling between 40.9–63.4%

3.1. Material Improvement

The development of nanomaterial technology has helped to increase the cooling power of RC materials. The material improvement involves two parts, namely emitter material and convection cover material. Detailed reviews of the emitter materials have been carried out by Zhao et al. [14] and Family and Menguc [106]. In the work of Zhao et al. [14], they categorize the material technologies for passive RC into four categories, i.e., a natural emitter, film-based emitter, nanoparticle-based emitter, and photonic emitter. Examples of these different emitters are shown in Figure 4. In this review, only some material examinations that are relevant to the application of RC in buildings are included.

There are at least three goals in the RC emitter material field of study, namely, improving cooling power in daytime [12], improving performance in humid conditions [44], and making a cost-efficient material [25,58]. Efforts on daytime RC were conducted using different approaches by material researchers, i.e., film-based emitters [8,41–44], nanoparticle-based emitters [46,47], and photonic emitters [45,48–50]. The engineered material must reflect most of the solar and atmospheric radiation and at the same time be able to produce thermal radiation in the specific atmospheric window band. The film-based emitter could produce all-day cooling between 2–9 °C for buildings on a typical sunny day in northern US latitudes [41]. The photonic emitter recorded a 110 W/m^2 cooling power under direct sunlight [45]. Further, nanoparticle-based emitters in the works of Liu et al. [46] and Kim and Lenert [47] were also recorded at sub-ambient temperature at daytime, with 25.5 °C and 35 °C below ambient, respectively.
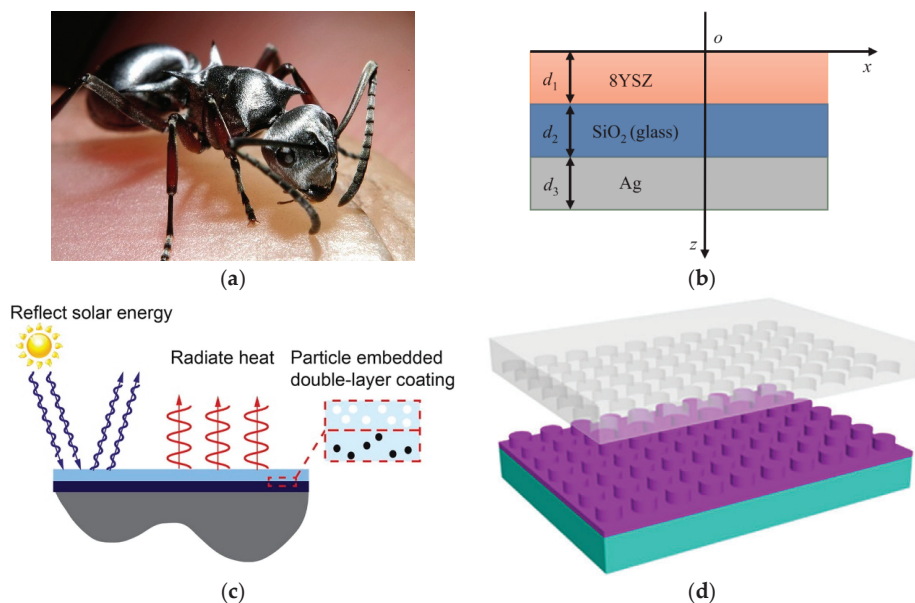
Figure 4. Different mechanism used in four categories of passive RC materials: (**a**) natural emitter, a mechanism found in Saharan silver ants [107] (reprinted from Solar Energy Materials and Solar Cells, 206, Jeong et al., Daytime passive radiative cooling by ultra-emissive bio-inspired polymeric surface, 110296, Copyright (2020), with permission from Elsevier); (**b**) film-based emitter design by Fan et al. [44] (reprinted from Applied Thermal Engineering, 165, Fan et al., Yttria-stabilized zirconia coating for passive daytime radiative cooling in humid environment, 114585, Copyright (2020), with permission from Elsevier); (**c**) nanoparticle-based emitter design by Huang and Ruan [108] (reprinted from International Journal of Heat and Mass Transfer, 104, Huang and Ruan, Nanoparticle embedded double-layer coating for daytime radiative cooling, 890–896, Copyright (2017), with permission from Elsevier); (**d**) photonic emitter design by Gao et al. [50] (reprinted Solar Energy Materials and Solar Cells, 200, Gao et al., Approach to fabricating high-performance cooler with near-ideal emissive spectrum for above-ambient air temperature radiative cooling, 110013, Copyright (2019), with permission from Elsevier).

In the subtropical climate, daytime RC emitters in the work of Jeong et al. [49] give a remarkable result, which is 7.2 °C below ambient at daytime. However, in the region of tropical climate with higher humidity, daytime RC is hardly achieved [39,40,44]. The best results in experimenting with RC materials for humid climate came from an enhanced specular reflector (ESR) material by 3M [109] that could be at sub-ambient temperature on a very humid and cloudy night [39,40].

Despite many scientists pursuing higher RC power both in the daytime and humid conditions, only a few have focused on the affordability of the materials. For instance, Givoni [25] and Erell and Etzion [58] proposed cheaper RC emitter options, but their examination resulted in a very low cooling power of RC compared to the other materials. Current high-performance RC materials are still expensive to produce and have limited durability [8].

In terms of convection cover materials, the spectral properties and durability are key issues. Benlattar et al. [53,54] are among the first to modify the spectral properties of convection cover. Using a chemical solution deposition method, they create a cadmium sulfide (CdS) thin film that is transparent for infrared radiation in the 8–13 μm band. They estimated a temperature reduction of 65 K between the uncovered nocturnal emitter and the covered one [54]. In another study, Naghshine and Saboonchi [52] compared different thin film multilayer structures for RC convection cover. Among the 30 possible

multilayers structures from a combination of 16 thin film materials, structures that involved cubic ZnS in their layers are better at protecting the RC emitter from parasitic heat loss during the day and night. Their schematic thin film multilayer structure is shown in Figure 5. Moreover, investigations for durable alternatives of convection cover were conducted by Bathgate and Bosi [51]. They found that zinc sulfide (ZnS) was the most promising material for the RC emitter cover, as shown in Figure 6.
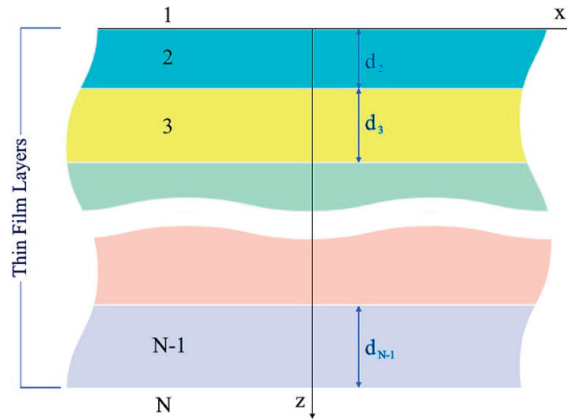
Figure 5. Multilayer structure thin film scheme of Naghshine and Saboonchi [52] (reprinted from Optics Communications, 410, Naghshine and Saboonchi, Optimized thin film coatings for passive radiative cooling applications, 416–423, Copyright (2018), with permission from Elsevier). They investigated 30 combinations of layers.
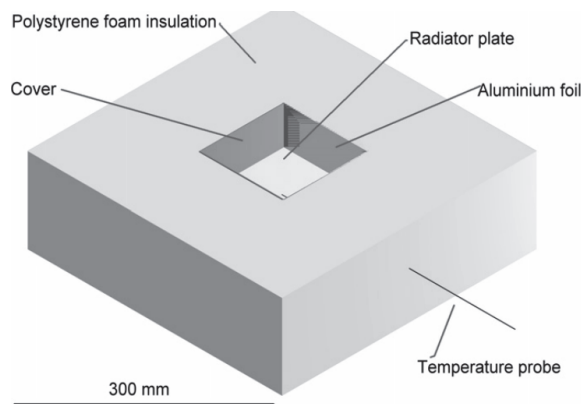
Figure 6. Typical RC panel design with insulation and convection cover [51] (reprinted from Solar Energy Materials and Solar Cells, 95/10, Bathgate and Bosi, A robust convection cover material for selective radiative cooling applications, 2778–2785, Copyright (2011), with permission from Elsevier).

3.2. Design Improvement

Besides enhancements in RC materials, improvements in the design of RC systems have also been proposed. Most researchers focused on two main aspects of RC system design, namely emitter insulation, and emitter contact to the working fluid. The emitter's insulation is one of the crucial elements in the roof-integrated RC systems designed by Dimoudi and Androutsopoulos [56] and Khedari et al. [62]. Craig et al. [110] went further by suggesting that improving the RC emitter's insulation on the roof not only increases its performance, but by modifying the configuration of

the roof's insulation, a conventional roof material could even be an RC emitter. Figure 7 shows the roof-integrated RC system and how the roof insulation was structured [56].
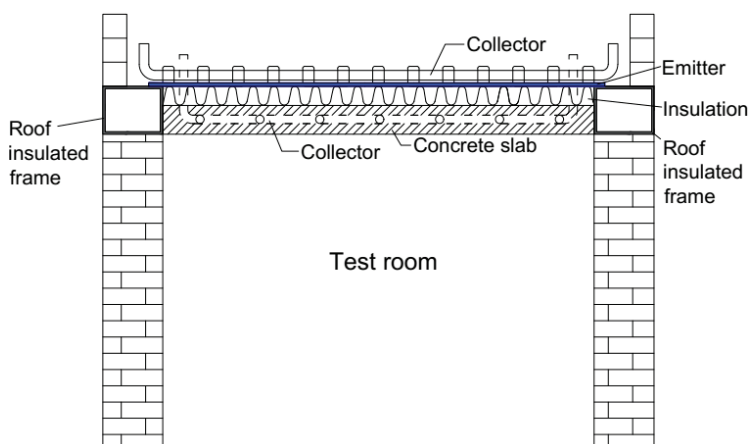
Figure 7. Proposed configurations of insulation for roof—integrated solar collector—RC emitters by Dimoudi and Androutsopoulos [56] (Adapted from Solar Energy, 80/8, Dimoudi and Androutsopoulos, The cooling performance of a radiator based roof component, 1039–1047, Copyright (2006), with permission from Elsevier).

Regarding the insulation from convection between the emitter material and the cover shield, some researchers proposed the use of vacuum to minimize parasitic thermal load to the emitter [60,63]. Chen et al. [63] are the first to experiment with a vacuum-enhanced RC emitter. Their design intends to achieve daytime RC and succeeds in obtaining a maximum of 42 °C below ambient under intense solar radiation. Tso et al. [60], however, did not achieve a daytime RC effect but could deliver nocturnal RC in a more humid climate in Hong Kong. Their design, shown in Figure 8, could provide a cooling power of 38 W/m^2 at night.

A different approach was used in the cover design by Falt et al. [61,64]. They proposed a triple-glazing skylight which features high absorptivity. The gas blocks the infrared part of solar radiation, and, thus, reduces heat gain to the building's interior and at night releases heat via radiation to the sky. The novelty of their design lies in the middle that could tilt, allowing the formation of a gap between the glass and the skylight's edge. This gap, in turn, enables the gas to move between the upper and lower part of the skylight, thus, when the upper gas is cooled by nocturnal radiation, it is replaced by the warmer lower gas. See Figure 9 for the illustration of the design.

Moreover, to utilize cooling from an RC emitter in the building, the most feasible way is by using a working fluid, which can either be a water-based or an air-based system. Furthermore, the water-based system is divided into an open system and a closed system. In the water-based open system, the cold storage water directly contacts the RC emitter, without any circulation of any working fluid. In the closed system, however, circulated water is used as a working fluid to deliver coldness either to storage or to a heat exchanger. The conceptual drawing of the typical water-based and air-based RC system is shown in Figure 10. The advantages and disadvantages of the water and air-based system are already summarized by Lu et al. [7] and Zhang et al. [81]. The lower installation cost and the simplicity of the system are among the advantages of the air-based system, while the water-based system is better in terms of cooling performance because water has a higher heat capacity than air. It is important to note that the effectiveness of the heat transfer between the emitter and the fluid has also been the focus of investigations for both the water- and air-based RC [11,57–59]. The investigations prescribed the optimum mass flow rate of the fluid to obtain the maximum cooling effect, as Hosseinzadeh and

Taherian [57] indicated that the mass flow rate of the fluid is critical in achieving the best cooling performance of an RC emitter.
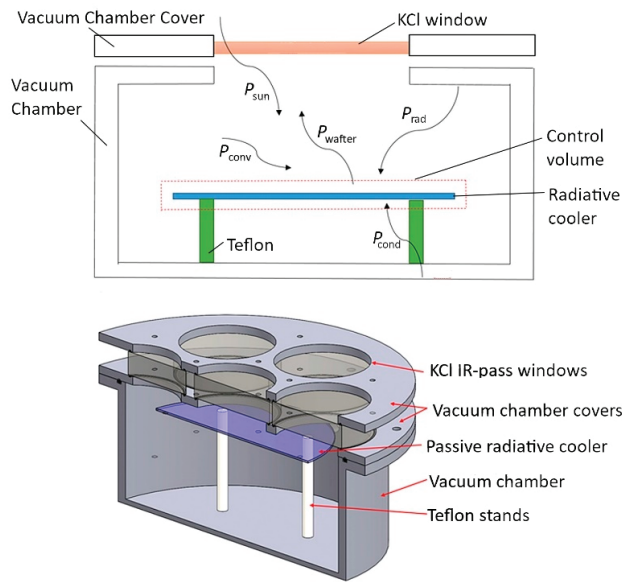
Figure 8. Design of vacuum chamber as insulation and part of the convective cover for the RC emitter [60] (reprinted from Renewable Energy, 106, Tso et al., A field investigation of passive radiative cooling under Hong Kong's climate, 52–61, Copyright (2017), with permission from Elsevier).
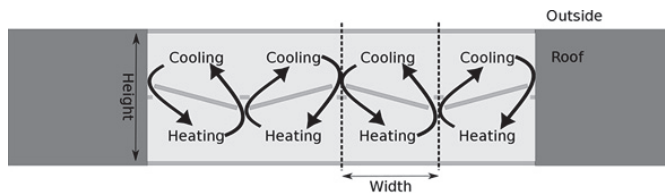
Figure 9. Design of a triple-glazing skylight that can operate as an RC emitter by incorporating a high-absorptivity gas. RC occurs for the upper gas, while the lower gas obtains heat from the building's interior. The middle glass then switches the cool and warm air in the upper and lower part of the glazing, enabling the cycle to continue [61] (reprinted from Building and Environment, 126, Falt et al., Modified predator-prey algorithm approach to designing a cooling or insulating skylight, 331–338, Copyright (2017), with permission from Elsevier).

Other small design considerations were also studied, such as the aesthetic appearance of the emitter. The appearance of the RC emitter is obviously interesting for architects and might accelerate the implementation of RC in building design. Lee et al. [66] and Son et al. [111] employed different techniques to create colored emitters. By adding a photonic nanolayer in the order of metal–insulator–metal (MIM) below the emitter, Lee et al. [66] could decorate their RC emitter. The MIM layers consisted of Ag-SiO_2-Ag, and a variation of the colors was achieved by varying the thickness of the SiO_2 layer. On the other hand, Son et al. [111] coated the emitter with silica-embedded perovskite to color it. Figure 11 displays the colored RC emitter by Son et al. [111]. Both colored RC emitters could achieve sub-ambient temperature during the daytime.
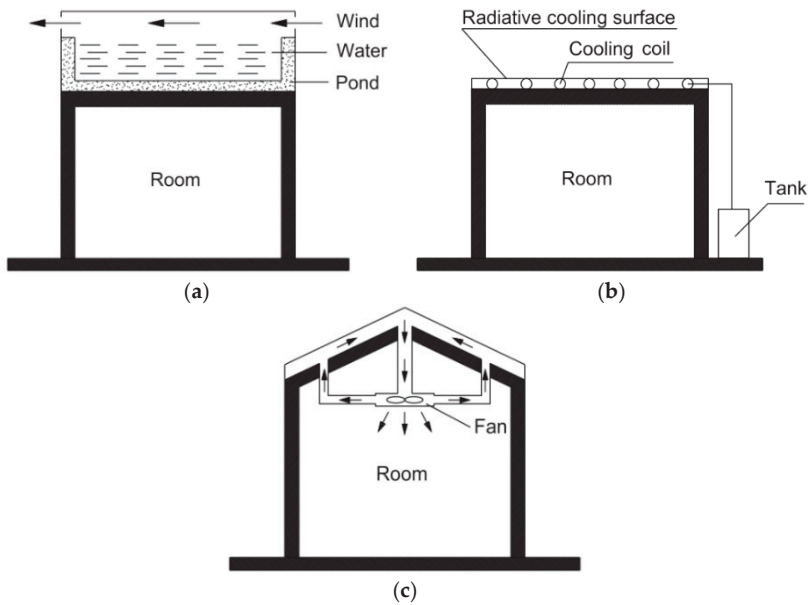
Figure 10. Configuration of different ways to utilize cooling from the RC emitter: (**a**) water-based open system; (**b**) water-based closed system (**c**) air-based system [81] (reprinted from Applied Energy, 224, Zhang et al., Energy saving and economic analysis of a new hybrid radiative cooling system for single-family houses in the USA, 271–281, Copyright (2018), with permission from Elsevier).
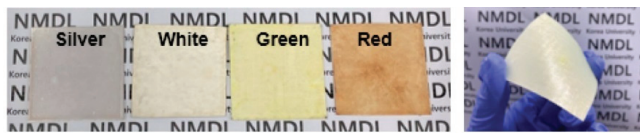
Figure 11. Samples of colored daytime RC emitter researched by Son et al. [111] (reprinted from Nano Energy, Son et al., Colored emitters with silica-embedded perovskite nanocrystals for efficient daytime radiative cooling, 105461, Copyright (2020), with permission from Elsevier).

3.3. Combination with Other Technologies

Application of RC in buildings often appears in combinations with other cooling technologies. These combinations can be categorized as active systems and passive systems. Many of the water-based RC systems are active systems, i.e., assisted by a pump to circulate the water. The passive water-based system is found where a thermosyphon mechanism drives the flow of the fluid. Air-based systems, on the other hand, are more often found as a passive system. Some strategies involve a fan as the active part of an air-based RC to maintain the airflow to the RC panel. A detailed comparison for the precedent of RC combinations is shown in Table 2.

Table 2. Comparison of different means of architectural implementation of RC.

Researcher	Architectural Feature	Means of Implementation		Combination
[25]			Air-based	Solar Collector
[31]		Passive system	Air-based	Thermal mass
[30]			Air-based	Thermal mass
[98]			Air-based	Attic Insulation
[94]			Water-based open system	Water tank
[93]			Air-based	Solar Collector, HVAC
[83]			Air-based	Fan or HVAC
[79]			Air-based	Desiccant
[34]			Air-based	Solar Collector, Desiccant
[80]			Air-based	PV, Solar Collector, HVAC
[74]			Air-based	PV, HVAC
[75]			N/A	PV
[76]			Water-based closed system	HVAC
[77]			Water-based closed system	Solar Collector and PV, cold water storage
[78]			Water-based closed system	PCM
[81]	Roof		Water-based closed system	HVAC
[82]			Water-based closed system	Radiant cooling, HVAC
[84]		Active system	Water-based closed system	Ground coupled heat pump
[85]			Water-based closed system	PV, Solar Collector
[86]			Water-based closed system	HVAC
[87]			Water-based closed system	Thermosyphon and cold water storage
[32]			Water-based closed system	Heat pipe
[17]			Water-based closed system	PV, Solar Collector
[89]			Water-based closed system	Thermosyphon and cold water storage
[90]			Water-based closed system	Solar Collector
[33]			Water-based closed system	Thermosyphon and cold water storage
[95]			Water-based closed system	HVAC
[96]			Water-based closed system	HVAC
[99]			Water-based closed system	Cold water storage
[102]			Water-based closed system	PCM, Cold Water Storage
[88]		N/A	Air-based	Solar Collector
[92]			N/A	PV
[103]	Roof and Wall	Passive system	Air-based	Wall material and insulation
[112]		Passive or active	Air or water-based	Temperature-regulating module
[113]		Passive system	Air-based	Trombe wall
[67]		Passive system	Air-based	Trombe wall
[100]	Wall	Passive system	Water-based closed system	PCM wall
[101]		Passive system	Water-based closed system	PCM wall
[68]		Active system	Water-based closed system	Wall material and insulation, cold water storage
[105]	Window or skylight	Passive system	Air-based	Glazing material
[114]		Passive system	Air-based	Glazing material

3.3.1. Active System

Specifically, the solar collector [25,34,77,90], photovoltaics (PV) [17,76,77,85], air conditioning (AC) [81,83,86,95,96], and cold water storage [33,89,99,102] are among the frequently studied combinations for the active systems. Givoni [25] is among the first to utilize a solar collector panel as an RC panel. The strategy is to utilize the absorber of the solar collector during the day as an emitter at night. This so-called dual-functional collector is further developed using more advanced techniques and materials [17,88,90]. Spectral-selective coating on the solar thermal absorber was used, as well as a low-density polyethylene (LDPE) film as the cover, replacing the glass cover in the conventional solar thermal collector. The latest results by Hu et al. [90] produce 55.1 W/m^2 cooling power at night. Their design is illustrated in Figure 12.
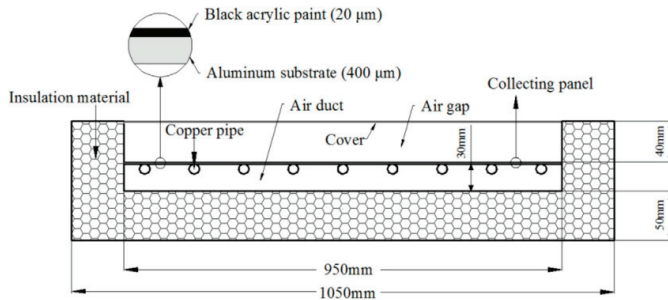
Figure 12. Cross-section schematic drawing of photo-thermal and RC (PTRC) design by Hu et al. [90] (reprinted from Renewable Energy, 139, Hu et al., Experimental study on a hybrid photo-thermal and radiative cooling collector using black acrylic paint as the panel coating, 1217–1226, Copyright (2019), with permission from Elsevier).

Combining PV with RC was initially visualized in the design of Harbeman House by Saitoh and Fujino [77], a so-called sustainable house proposal that attempted to integrate various sustainable technologies in the house. A more persistent study on the possible application of the PV-RC combination is conducted by Zhao et al. [70,75,92,115]. Using photonic material, they develop several strategies in PV-RC ranging from nocturnal to diurnal cooling. In terms of building energy consumption, PV-RC can be more beneficial because the combined electricity and cooling energy resulting from the system is more than the output energy from PV alone [74,75]. Both RC combinations with solar thermal and PV can be divided into two types when installed on the roof, i.e., similar orientation or opposite orientation. With similar orientation, the researchers placed the RC panel on the same side of the roof as the solar collector or PV, normally the sun-facing side [17,70,88,90]. In contrast, the opposite orientation used the opposite side of the roof to reduce solar heat gain to the emitter [75,77,85].

Furthermore, RC is also commonly used to assist HVAC systems. Usually, the emitter is used to provide chilled water for the cooling coil of AC, enabling the system to be more energy efficient [95,96]. The design by Jeong et al. [95], for instance, used two types of cooling coils, conventional cooling coils and RC-supplied cooling coils, thus, RC acted as a supplementary cooling supplier. The system was claimed to be able to reduce cooling energy consumption by 35%. Another variant of the RC-HVAC system came from Zhang et al. [81], who added a cold water storage to stock cooling energy from RC. Figure 13 displays the schematic diagram of an RC-assisted HVAC system.
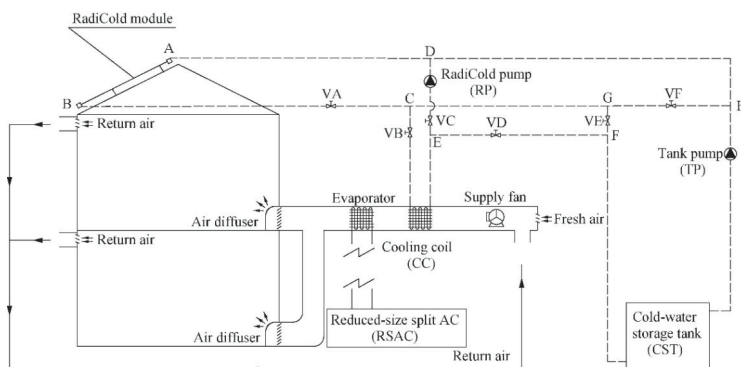
Figure 13. Schematic of a typical RC-assisted HVAC system [81] (reprinted from Applied Energy, 224, Zhang et al., Energy saving and economic analysis of a new hybrid radiative cooling system for single-family houses in the USA, 271–281, Copyright (2018), with permission from Elsevier).

3.3.2. Passive System

In terms of the passive system, RC has been combined with more diverse techniques such as wall-mounted RC [68,98,103], phase change material (PCM) [100,101], thermal mass [30,31], and the Trombe wall [67,113]. Oliveti et al. [103] attempted to include thermal radiation from the wall to the sky to the overall heat exchange model of a wall. Yong et al. [68] went further than developing a mathematical model by proposing an RC system mounted on the wall. Their system is a dual-functional solar collector that can provide heating in winter and cooling in summer, as shown in Figure 14. However, the system is an active system, involving pumps to circulate water to be stored in the cold and hot water storage. The fully passive implementations of a wall-mounted RC were performed by Shen et al. [100] and He et al. [101]. Their designs are quite similar in principle, using the thermosyphon method to extract cooling from the wall and storing the heat in a PCM (see Figure 15). In terms of cooling performance, the wall-mounted dual-functional heating–cooling emitter was predicted to be able to reduce building energy consumption by 47.9% [68].
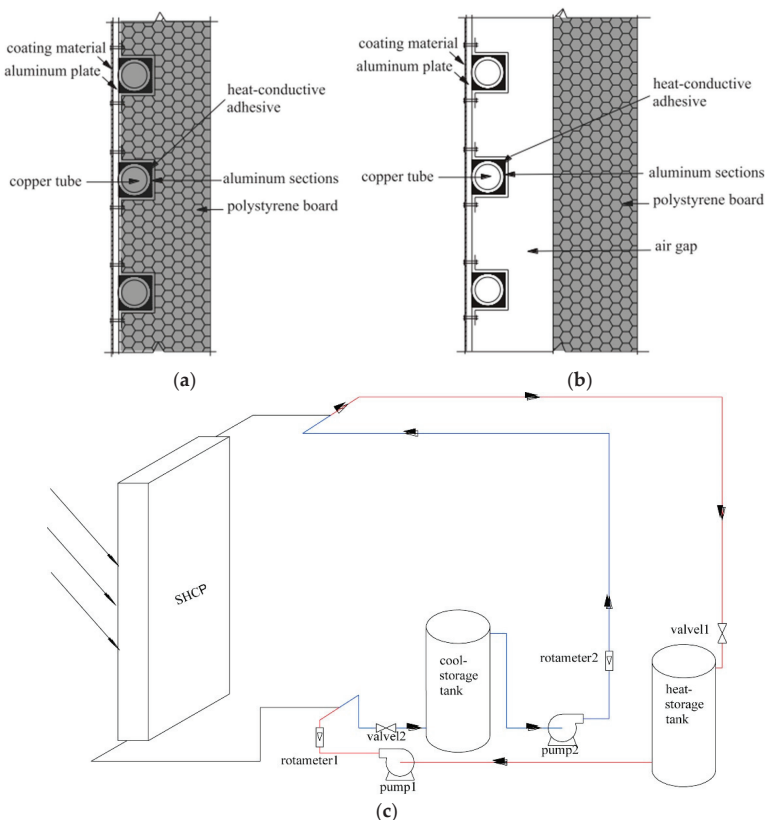
Figure 14. Structure of solar absorber that serves, i.e., two functions for heating and cooling as designed by Yong et al. [68]: (**a**) design without an air gap for insulation purposes; (**b**) design with an air gap for an area with nighttime ambient temperature that is low enough to be used as cooling, nocturnal cooling thus provided by both the sky and the surroundings; (**c**) schematic diagram showing the mechanism in which the dual-functional system works—red line for heating, blue line for cooling (reprinted from Renewable Energy, 74, Yong et al., Performance analysis on a building-integrated solar heating and cooling panel, 627–632, Copyright (2015), with permission from Elsevier).
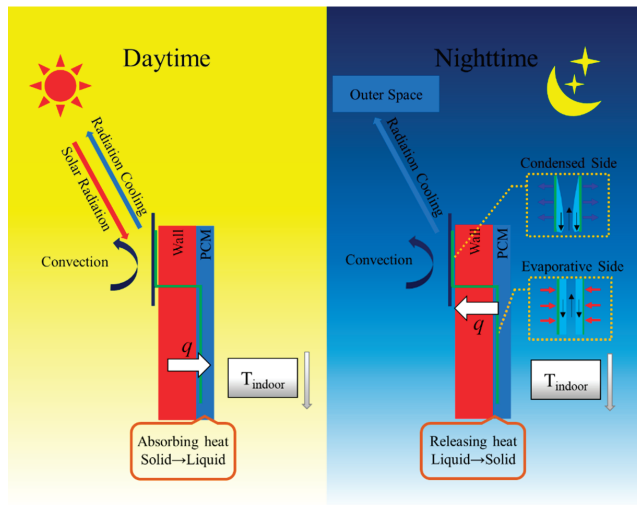
Figure 15. Dual-functional RC-PCM wall design by He et al. [101]. During the daytime, the absorbed heat is stored by PCM and is later released at night via RC, thus, the temperature of the room can be kept comfortable, and the PCM can "recharge" (reproduced from Energy and Buildings, 199, He et al., Experimental study on the performance of a novel RC-PCM-wall, 297–310, Copyright (2019), with permission from Elsevier).

Whereas the aforementioned researchers used PCM to regulate the heat gain and loss in the wall or building enclosure, some researchers have attempted to use insulation and thermal mass to regulate heat transfer from an RC emitter to the building. Etzion and Erell [31] mentioned at least two functions of thermal mass or other types of thermal storage strategies when combined with nocturnal RC for a building. Firstly, thermal mass can absorb the excessive heat received by the RC emitter during the daytime. Secondly, it maintains the cooling rate of the RC emitter to a desired rate, thus, heat does not dissipate rapidly from the building, and the RC emitter becomes steady. Thus, Etzion and Erell [31] examined the best location for placing thermal mass. They found that thermal mass should be placed on the roof or, in more general terms, should be closely coupled with the radiative emitter [31].

Furthermore, Liu et al. [112] also developed a temperature-regulating module (TRM) for solar heating and RC. The TRM consists of polyethylene film as the convection cover, a porous RC material, an aluminum sheet, and a solar absorber (Figure 16). The layer order was reversed for heating mode. The TRM maintained a maximum indoor temperature of 27.5 °C in the hottest days of summer and 25 °C for some hours on winter days. The heating and cooling provided by the TRM correspond to 42.4% saving in the electricity bill.

Figure 16. *Cont.*

(**c**)
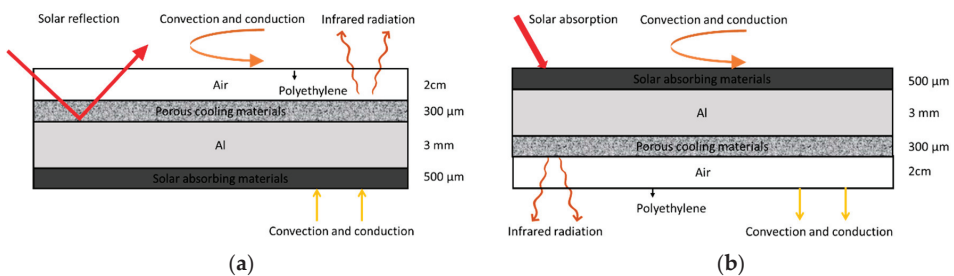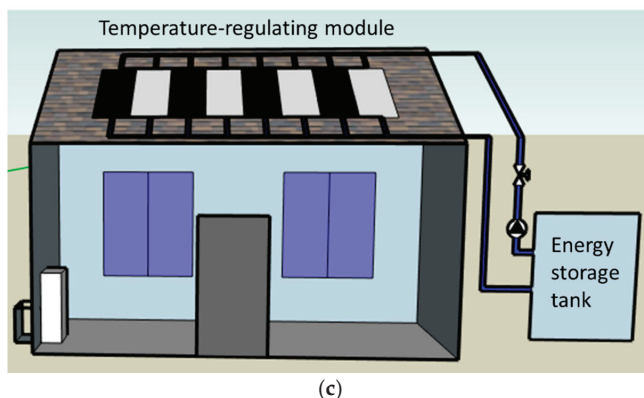
Figure 16. Temperature-regulating module by Liu et al. [112]: (**a**) cooling mode; (**b**) heating mode; (**c**) when applied on the roof (reproduced from Energy Conversion and Management, 205, Liu et al., Research on the performance of radiative cooling and solar heating coupling module to direct control indoor temperature, 112395, Copyright (2020), with permission from Elsevier).

4. Architectural Features of Current Radiative Cooling Systems

As the previous section summarizes, RC for buildings has been prototyped in very diverse ways. Design alternatives are even numerous when RC is combined with other cooling technologies. Nevertheless, analysis of the RC systems from an architectural point of view should be conducted before it is widely accepted by the architectural community as one of the promising passive design strategies for sustainable buildings [19]. One way of doing so is by analyzing the precedents of architectural features involved in the proposals of passive applications of RC. As compiled in Table 2, some building components or architectural features that have been involved in passive RC systems are revealed. Theoretically, the roof is the best location to place an RC emitter compared to other building envelopes. However, architects might want more flexibility in their design, and few researchers have applied RC in the wall and façade. These researches, although very few in number, offer alternatives in architectural implementation.

4.1. Roof

Installing the RC emitter on the roof is the simplest and most promising way. Besides its highest sky view factor compared to the wall or other building components, the roof is also a common place for building service installations. Available roof-integrated passive RC systems consist of both air- and water-based systems. The roof water-based RC is an open system which is quite similar to a roof pond design [94,116] (Figure 17). Disadvantages of the roof water-based RC are more or less the same as the roof pond, such as difficulty in waterproofing the roof, additional load to the roof structure, and maintenance of the cleanliness of the water. It can also only be installed on top of flat roofs and affects the accessibility of the roof for other uses [117].

Moreover, the roof air-based system offers more techniques. The most straightforward use of an RC emitter was firstly proposed by Etzion [31], where the RC emitter is attached to a concrete roof slab. By this design, the cooling effect of the RC emitter is absorbed by the thermal mass of the roof slab and in turn transmitted to the room. Another air-based roof system uses an air channel to extract the cooling from the RC emitter [25,98]. By using an air channel attached to an RC emitter, cooling is provided by means of cool airflow from the air channel instead of convection of the interior air with the building envelops. This is arguably better for the distribution of the cool and fresh air. Figure 18 shows one example of how the air channel was used to extract cooling from the RC emitter [98]. In the design, the air was used for heat removal in the attic, although it can be further explored for the room's heat removal as well.
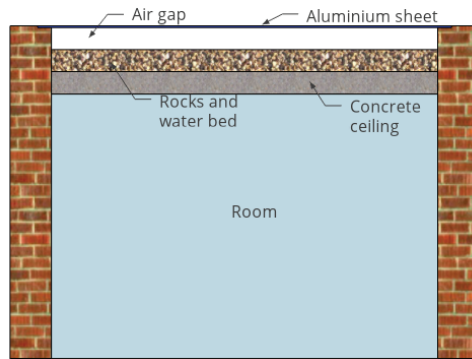
Figure 17. Water-based open system RC on the roof of a building [116] (reproduced from Renewable Energy, 29/11, Cheikh and Bouchair, Passive cooling by evapo-reflective roof for hot dry climates, 1877–1886, Copyright (2004), with permission from Elsevier).
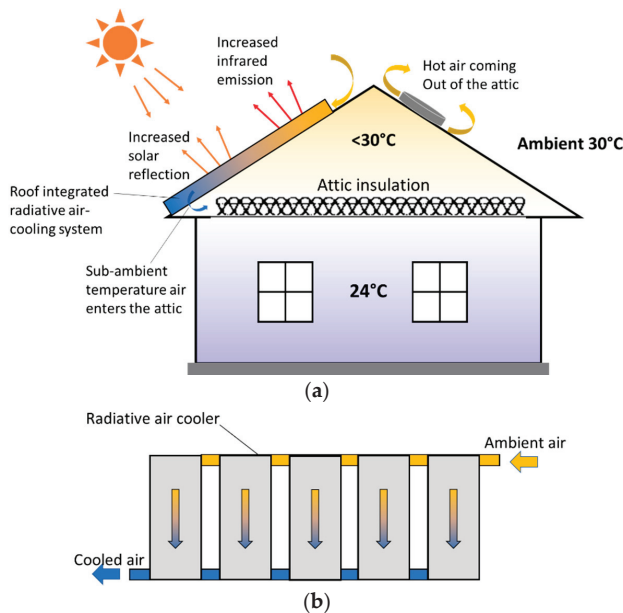
Figure 18. Air-based RC system on the roof using an air channel to utilize the cooling [98]: (**a**) illustration of how the system works to remove heat from the attic; (**b**) schematic of the air channel and the RC panel (reproduced from Energy and Buildings, 203, D. Zhao et al., Roof-integrated radiative air-cooling system to achieve cooler attic for building energy saving, 109453, Copyright (2019), with permission from Elsevier).

4.2. Wall

The second most appropriate architectural feature to place the RC emitter on is the wall. The wall has the advantage of providing a large surface when compared to the roof or other building envelopes. As with the roof RC, the wall RC also appeared in two systems, air-based and water-based systems. It is worth noting that most of the existing proposals on passive RC systems mounted on the wall are dual-functional (heating–cooling) modules. For instance, the air-based wall RC system is a combination with Trombe wall, which was developed by Sameti and Kasaeian [67] and consists of a glass cover and

a thermal mass located directly behind the glass. The thermal mass function is to collect the sunlight entering the façade during heating mode and dissipate the heat to the night sky during cooling time. The glass cover is open during the heating days to protect it from solar radiation and closed during the heating nights to prevent radiative heat loss. The reverse is applied for cooling days. Nevertheless, it is important to note that an RC-Trombe wall system has some features that can affect its performance such as external glazing material, vents geometry and position, thermal storage, and Trombe wall area [118,119].

For the water-based RC wall, the system is accompanied by PCM to store the coldness and uses thermosyphon phenomena to extract it from the emitter, as described in Section 3 (see Figure 15) [101]. A similar design to that of He et al. [101] was also tested by Shen et al. [100]. Compared to the testing room with a brick wall, the cooling load in the RC-PCM wall room was 42% and 25% lower at ideal and moderate conditions. Furthermore, there are concerning factors that affect the performance of an RC-PCM wall system, i.e., the parasitic heat loss due to outdoor wind. Their system was not equipped with a convection cover, thus, the effect of wind speed was significant. The implementation of the RC-PCM wall in the testing room can be seen in Figure 19.
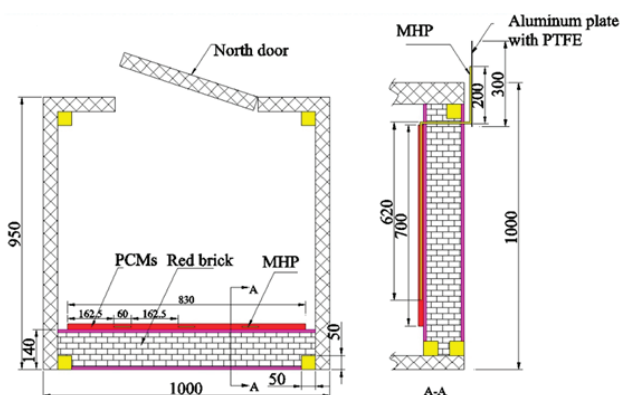
Figure 19. The drawing of an experimental room for an RC-PCM wall by Shen et al. [100]. The RC-PCM wall was mounted on the south wall. The measurement data from this room were compared with a conventional brick wall room (reprinted from Applied Thermal Engineering, 176, Shen et al., Investigation on the thermal performance of the novel phase change materials wall with radiative cooling, 115479, Copyright (2020), with permission from Elsevier).

4.3. Other Building Components

4.3.1. Glazing Material

Openings on the building envelope are the source of solar fenestration into the building's interior. Various glazing materials have been developed to reduce their transmissivity in the solar and infrared bands. Furthermore, researchers intended to also maximize thermal radiation of the glazing material in the atmospheric window band. With this strategy, the glazing materials not only reduce heat gain but also produce cooling for the building. Two prototypes, namely transparent film and coating to be added on top of glazing materials, have recently been developed [105,114,120]. Currently, the transparent RC materials are only studied for skylight application, as shown in Figure 20. Future development for transparent RC film or coating might be evaluated for window application.
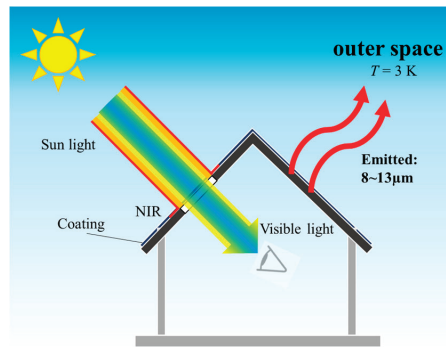
Figure 20. A transparent RC emitter used on a skylight to provide daylighting as well as passive cooling for buildings [114] (reproduced from Solar Energy Materials and Solar Cells, 213, Ziming et al., Low-cost radiative cooling blade coating with ultrahigh visible light transmittance and emission within an "atmospheric window", 110563, Copyright (2020), with permission from Elsevier).

4.3.2. Paints

Recently, paint was proposed as a means to act as a scalable RC emitter. It is well known by researchers of passive RC that the currently available technologies are not yet scalable and feasible for building use. Considering paint as a mature technology and always certainly used in buildings (either for roof, walls, or other parts of a building), for Mandal et al. [121], an RC paint might be the answer to the problem of scalability of RC technologies. For them, the material technologies have the capability to develop a scalable and effective RC paint. The current development of cool roof coating is an example of the success of material technologies to enhance paint performance. However, they also highlighted some general challenges for the development of RC paint besides the technical difficulties. The challenges are the assessment of geographical conditions in which RC paint benefits the most, as well as the examination of the effect of pollution, dirt, and dust on the durability and performance of the paint.

Furthermore, RC paint can also be seen in the perspective of the aesthetic appearance of RC surfaces. Currently, research on this aspect is scarce. The study conducted by Lee et al. [66] is one example of the attempt to answer the aesthetic appearance of an RC emitter (see Figure 21). Research on RC paint might promote the progress on aesthetic studies of RC surfaces.
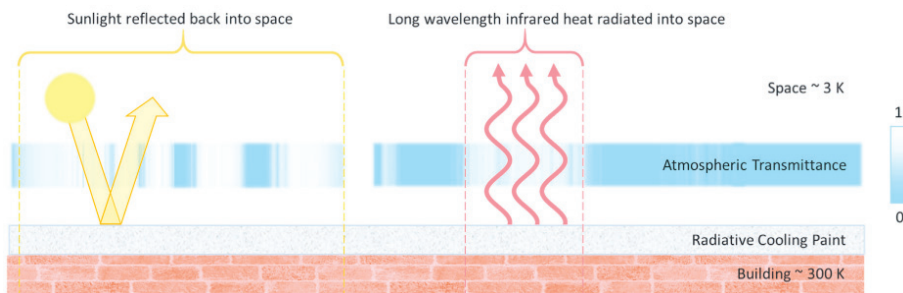
Figure 21. Schematic diagram showing the potential role of RC paints for buildings [121] (reprinted from Joule, 4/7, Mandal et al., Paints as a scalable and Effective Radiative Cooling Technology for Buildings, 1350–1356, Copyright (2020), with permission from Elsevier).

5. Outlook for Architectural Application of Passive Radiative Cooling

The previous sections have discussed the development of RC technologies and how they have been applied to reduce the cooling energy of buildings. From an architectural perspective, some issues regarding the implementation of passive RC in buildings arise from the discussions.

- In the range of the current RC power and the challenge to overcome the mismatch in cooling supply and demand, studies on the application of RC in buildings can search for an efficient RC system or effective storage mechanism. Additionally, exploration of the combination of RC with other passive or active cooling techniques should be continued and even extended, because in this way, the disadvantages of RC technologies can be compensated by the advantages of other cooling techniques. Moreover, in terms of exploration of potential RC combinations, there might be other passive design strategies in architecture, outside the cooling techniques, that have not yet been taken into consideration by RC researchers, such as natural ventilation and daylighting strategies. Therefore, a review on the type of strategies of passive design architecture that are suitable for combination with RC is still outstanding.

- Regarding architectural aspects, there are many considerations neglected by current RC studies. The roof may have an advantage in regard to the sky view factor, but another building element, such as the wall, may offer advantages in surface area as well as design flexibility. Additional façade elements on the wall, such as a shading device, secondary skin, cladding, and window, are potential locations for the RC emitter. In addition, the aesthetic aspect is also important. Thus, research on transparent and colored RC materials or even RC paints would encourage more flexibility in the architectural application.

- Following the notions on architectural aspects, another important point arises, that is, the lack of research on the integration of RC systems in building design. Observations of the implementation of the RC system into real buildings should be introduced. The design process of such an observation and the observation itself might reveal some influential details that have not yet been considered.

- Most of, if not all, the investigations of RC in buildings have focused on reducing cooling energy. Besides, the benefit of the RC system, if working ideally, may lead to healthy and comfortable buildings. This area of study, namely the contribution of passive RC in creating thermal comfort for building occupants as well as its further effect on health (and productivity in the working space), will eventually arise.

- Lastly, two general factors should not be forgotten, namely, the durability of the radiative material and the cost of the material. Since there are many studies still in the lab scale, these factors have not been calculated by many researchers. Nevertheless, these two aspects can be determinant in terms of real application. Architects and building owners usually prefer to directly know the cost of installation, saving potential, and payback period of the implemented RC systems. Full life-cycle analysis of the system can also be an object of study by researchers in the field.

6. Conclusions

The RC research field was revived by the development of new materials. There have been many high-performance RC materials that resulted from the experimentations. The present challenge in this field is to provide scalable and durable RC materials. Besides these two purposes, research on colored and transparent RC materials could also widen the application of RC in buildings. Likewise, pursuing RC paints might be an alternative way to create scalable and colorful emitters, and thus could attract more attention from the architectural community. Furthermore, the available RC materials have been implemented in various RC module designs, as their utilization to reduce cooling energy demand for buildings has also been conducted. Such efforts can continue to be pursued with emphasis on the combination of RC with other passive design strategies. The combination is not limited only to other passive cooling techniques but could also be carried out with natural ventilation, heat storage,

daylighting, etc. In addition to this, the designs of building-integrated RC should begin to look at building components other than the roof to be the place for installation. Only a handful of building features have been involved in the current explorations such as walls and skylights.

Another research direction for the application of RC in buildings is the evaluation of the RC performance in terms of the occupant's health and comfort. The two indicators could be supplementary to the current performance evaluation, i.e., cooling power or energy saving. This is especially relevant when the RC is combined with other passive design strategies, which may require multi-perspective performance evaluation. At the latter stage, a life-cycle analysis of a building-integrated RC system could also be included. Nevertheless, the efforts to apply RC in buildings need to be more integrated into the architectural design. One way of achieving this is by implementation of the currently available RC materials or panels to a real building, which can be an existing building or a newly constructed building. This type of case study using real building would necessitate a design integration and could uncover some unanticipated aspects of building-integrated RC. Moreover, the uncovered aspects will be further examined in future studies in the field.

Author Contributions: Conceptualization, S. and M.H.; writing—original draft preparation, S.; writing—review and editing, S., M.H., Y.S., J.D. and S.R.; visualization, S. All authors have read and agreed to the published version of the manuscript.

Conflicts of Interest: The authors declare no conflict of interest.

Nomenclature

RC	radiative cooling
PCM	phase change material
PV	photovoltaics
PV/T	photovoltaics thermal
AC	air conditioning
HVAC	heating, ventilation, and air conditioning
TRM	temperature-regulating module
LDPE	low-density polyethylene
MIM	metal-insulator-metal
ESR	enhanced specular reflector
$E_{B\lambda}$	spectral emissive power (W·m^{-2}·μm^{-1})
T	temperature (K)
T_{amb}	ambient temperature (K)
$T_{emitter}$	emitter temperature(K)
A	emitter's area (m^2)
λ	wavelength λ (μm)
λ_{max}	the wavelength in which a blackbody emits maximum radiation (μm)
h	Planck's constant (6.626×10^{-34} J·s)
c_0	speed of light in vacuum (2.998×10^8 m· s^{-1})
n	refractive index (1 for vacuum)
k	Boltzmann's constant (1.3807×10^{-23} J·K^{-1})
Q_{net}	cooling power of the RC emitter (W)
Q_{sun}	radiation from the sun (W)
Q_{atm}	atmospheric radiation (W)
$Q_{cond+conv}$	parasitic heat loss from the RC emitter due to conduction and convection (W)
h_c	heat transfer coefficient (W · m^{-2}· K^{-1})
ϵ	emissivity of the emitter
ϵ_{atm}	emissivity of the sky

References

1. Santamouris, M. *Advances in Passive Cooling*; Earthscan: London, UK, 2012; ISBN 9781844072637.
2. Delmastro, C.; Dulac, J.; Abergel, T. Cooling. Available online: http://iea.org (accessed on 22 December 2019).
3. Parsloe, C.; Race, G.L.; Gay, L.; Butcher, K. *Sustainable Low Energy Cooling: An Overview*; Chartered Institution of Building Services Engineers: London, UK, 2005; ISBN 1903287626.
4. Cheshire, D.; Menezes, A.C. *Evaluating Operational Energy Performance of Buildings at the Design Stage*; Chartered Institution of Building Services Engineers: London, UK, 2013; ISBN 9781906846381.
5. Ahmad, M.I.; Jarimi, H.; Riffat, S. *Nocturnal Cooling Technology for Building Applications*; Springer: Singapore, 2019.
6. Hossain, M.M.; Gu, M. Radiative cooling: Principles, progress, and potentials. *Adv. Sci.* **2016**, *3*, 1500360. [CrossRef] [PubMed]
7. Lu, X.; Xu, P.; Wang, H.; Yang, T.; Hou, J. Cooling potential and applications prospects of passive radiative cooling in buildings: The current state-of-the-art. *Renew. Sustain. Energy Rev.* **2016**, *65*, 1079–1097. [CrossRef]
8. Li, N.; Wang, J.; Liu, D.; Huang, X.; Xu, Z.; Zhang, C.; Zhang, Z.; Zhong, M. Selective spectral optical properties and structure of aluminum phosphate for daytime passive radiative cooling application. *Sol. Energy Mater. Sol. Cells* **2019**, *194*, 103–110. [CrossRef]
9. Santamouris, M.; Feng, J. Recent progress in daytime radiative cooling: Is it the air conditioner of the future? *Buildings* **2018**, *8*, 168. [CrossRef]
10. Argiriou, A. Radiative Cooling. In *Passive Cooling of Buildings*; Matheos Santamouris, D.A., Ed.; Earthscan: New York, NY, USA, 2013; pp. 424–454.
11. Okoronkwo, C.A.; Nwigwe, K.N.; Ogueke, N.V.; Anyanwu, E.E.; Onyejekwe, D.C.; Ugwuoke, P.E. An experimental investigation of the passive cooling of a building using nighttime radiant cooling. *Int. J. Green Energy* **2014**, *11*, 1072–1083. [CrossRef]
12. Raman, A.P.; Anoma, M.A.; Zhu, L.; Rephaeli, E.; Fan, S. Passive radiative cooling below ambient air temperature under direct sunlight. *Nature* **2014**, *515*, 540–544. [CrossRef] [PubMed]
13. García, M.P.; De Luis, F.J. Influence of site dependent effects on the assessment of the radiative cooling potential. *Int. J. Sol. Energy* **2002**, *22*, 33–45. [CrossRef]
14. Zhao, B.; Hu, M.; Ao, X.; Chen, N.; Pei, G. Radiative cooling: A review of fundamentals, materials, applications, and prospects. *Appl. Energy* **2019**, *236*, 489–513. [CrossRef]
15. Erell, E. Radiative Cooling. In *Advances in Passive Cooling*; Santamouris, M., Ed.; Earthscan: Sterling, VA, USA, 2012; pp. 262–296, ISBN 9781844072637.
16. Zeyghami, M.; Goswami, D.Y.; Stefanakos, E. A review of clear sky radiative cooling developments and applications in renewable power systems and passive building cooling. *Sol. Energy Mater. Sol. Cells* **2018**, *178*, 115–128. [CrossRef]
17. Eicker, U.; Dalibard, A. Photovoltaic-thermal collectors for night radiative cooling of buildings. *Sol. Energy* **2011**, *85*, 1322–1335. [CrossRef]
18. Chen, L.; Zhang, K.; Ma, M.; Tang, S.; Li, F.; Niu, X. Sub-ambient radiative cooling and its application in buildings. *Build. Simul.* **2020**, *13*, 1165–1189. [CrossRef]
19. Prieto, A.; Knaack, U.; Klein, T.; Auer, T. 25 Years of cooling research in office buildings: Review for the integration of cooling strategies into the building façade (1990–2014). *Renew. Sustain. Energy Rev.* **2017**, *71*, 89–102. [CrossRef]
20. Modest, M.F. *Radiative Heat Transfer*; Academic Press: Oxford, UK, 2013; ISBN 9780123869449.
21. SpectralCal.com. Blackbody calculator. Available online: www.spectralcalc.com (accessed on 21 October 2020).
22. Commons, W. Atmosfaerisk Spredning. Available online: Commons.wikimedia.org (accessed on 26 October 2020).
23. Bartoli, B.; Catalanotti, S.; Coluzzi, B.; Cuomo, V.; Silvestrini, V.; Troise, G. Nocturnal and diurnal performances of selective radiators. *Appl. Energy* **1977**, *3*, 267–286. [CrossRef]
24. Harrison, A.W.; Walton, M.R. Radiative cooling of TiO2 white paint. *Sol. Energy* **1978**, *20*, 185–188. [CrossRef]
25. Givoni, B. Solar Heating and Night Radiation Cooling by a Roof Radiation Trap. *Energy Build.* **1977**, *1*, 141–145. [CrossRef]
26. Argiriou, A.; Santamouris, M.; Balaras, C.; Jeter, S. Potential Of Radiative Cooling In Southern Europe. *Int. J. Sol. Energy* **1992**, *13*, 189–203. [CrossRef]

27. Orel, B.; Gunde, M.K.; Krainer, A. Radiative cooling efficiency of white pigmented paints. *Sol. Energy* **1993**, *50*, 477–482. [CrossRef]

28. Argiriou, A.; Santamouris, M.; Assimakopoulos, D.N. Assessment of the Radiative Cooling Potential of a Collector Using Hourly Weather Data. *Energy* **1994**, *19*, 879–888. [CrossRef]

29. Diatezua, D.M.; Thiry, P.A.; Dereux, A.; Caudano, R. Silicon oxynitride multilayers as spectrally selective material for passive radiative cooling applications. *Sol. Energy Mater. Sol. Cells* **1996**, *40*, 253–259. [CrossRef]

30. Mihalakakou, G.; Ferrante, A.; Lewis, J.O. The cooling potential of a metallic nocturnal radiator. *Energy Build.* **1998**, *28*, 251–256. [CrossRef]

31. Etzion, Y.; Erell, E. Thermal Storage Mass in Radiative Cooling Systems. *Build. Environ.* **1991**, *26*, 389–394. [CrossRef]

32. Ezekwe, C.I. Performance of a Heat Pipe Assisted Night Sky Radiative Cooler. *Energy Convers. Manag.* **1990**, *30*, 403–408. [CrossRef]

33. Al-Nimr, M.A.; Kodah, Z.; Nassar, B. A Theoretical and Experimental Investigation of A Radiative Cooling System. *Sol. Energy* **1998**, *63*, 367–373. [CrossRef]

34. Lu, S.-M.; Yan, W.-J. Development and experimental validation of a full-scale solar desiccant enhanced radiative cooling system. *Renew. Energy* **1995**, *6*, 821–827. [CrossRef]

35. Hay, H.R.; Yellott, J.I. International aspects of air conditioning with movable insulation. *Sol. Energy* **1969**, *12*, 427–438. [CrossRef]

36. Zhao, D.; Aili, A.; Zhai, Y.; Lu, J.; Kidd, D.; Tan, G.; Yin, X.; Yang, R. Subambient Cooling of Water: Toward Real-World Applications of Daytime Radiative Cooling. *Joule* **2019**, *3*, 111–123. [CrossRef]

37. Muselli, M. Passive cooling for air-conditioning energy savings with new radiative low-cost coatings. *Energy Build.* **2010**, *42*, 945–954. [CrossRef]

38. Cunha, N.F.; AL-Rjoub, A.; Rebouta, L.; Vieira, L.G.; Lanceros-Mendez, S. Multilayer passive radiative selective cooling coating based on Al/SiO$_2$/SiN$_x$/SiO$_2$/TiO$_2$/SiO$_2$ prepared by dc magnetron sputtering. *Thin Solid Films* **2020**, *694*, 137736. [CrossRef]

39. Han, D.; Ng, B.F.; Wan, M.P. Preliminary study of passive radiative cooling under Singapore's tropical climate. *Sol. Energy Mater. Sol. Cells* **2020**, *206*, 110270. [CrossRef]

40. Dong, M.; Chen, N.; Zhao, X.; Fan, S.; Chen, Z. Nighttime radiative cooling in hot and humid climates. *Opt. Express* **2019**, *27*, 31587. [CrossRef]

41. Zhou, L.; Song, H.; Liang, J.; Singer, M.; Zhou, M.; Stegenburgs, E.; Zhang, N.; Xu, C.; Ng, T.; Yu, Z.; et al. A polydimethylsiloxane-coated metal structure for all-day radiative cooling. *Nat. Sustain.* **2019**, *2*, 718–724. [CrossRef]

42. Gentle, A.R.; Smith, G.B. A Subambient Open Roof Surface under the Mid-Summer Sun. *Adv. Sci.* **2015**, *2*, 1500119. [CrossRef] [PubMed]

43. Ao, X.; Hu, M.; Zhao, B.; Chen, N.; Pei, G.; Zou, C. Preliminary experimental study of a specular and a diffuse surface for daytime radiative cooling. *Sol. Energy Mater. Sol. Cells* **2019**, *191*, 290–296. [CrossRef]

44. Fan, J.; Fu, C.; Fu, T. Yttria-stabilized zirconia coating for passive daytime radiative cooling in humid environment. *Appl. Eng.* **2020**, *165*, 114585. [CrossRef]

45. Torgerson, E.; Hellhake, J. Polymer solar filter for enabling direct daytime radiative cooling. *Sol. Energy Mater. Sol. Cells* **2019**, *206*, 110319. [CrossRef]

46. Liu, Y.; Bai, A.; Fang, Z.; Ni, Y.; Lu, C.; Xu, Z. A pragmatic bilayer selective emitter for efficient radiative cooling under direct sunlight. *Materials* **2019**, *12*, 1208. [CrossRef]

47. Kim, H.; Lenert, A. Optical and thermal filtering nanoporous materials for sub-ambient radiative cooling. *J. Opt.* **2018**, *20*, 084002. [CrossRef]

48. Huang, Y.; Pu, M.; Zhao, Z.; Li, X.; Ma, X.; Luo, X. Broadband metamaterial as an "invisible" radiative cooling coat. *Opt. Commun.* **2018**, *407*, 204–207. [CrossRef]

49. Jeong, S.Y.; Tso, C.Y.; Ha, J.; Wong, Y.M.; Chao, C.Y.H.; Huang, B.; Qiu, H. Field investigation of a photonic multi-layered TiO$_2$ passive radiative cooler in sub-tropical climate. *Renew. Energy* **2020**, *146*, 44–55. [CrossRef]

50. Gao, M.; Han, X.; Chen, F.; Zhou, W.; Liu, P.; Shan, Y.; Chen, Y.; Li, J.; Zhang, R.; Wang, S.; et al. Approach to fabricating high-performance cooler with near-ideal emissive spectrum for above-ambient air temperature radiative cooling. *Sol. Energy Mater. Sol. Cells* **2019**, *200*, 110013. [CrossRef]

51. Bathgate, S.N.; Bosi, S.G. A robust convection cover material for selective radiative cooling applications. *Sol. Energy Mater. Sol. Cells* **2011**, *95*, 2778–2785. [CrossRef]

52. Naghshine, B.B.; Saboonchi, A. Optimized thin film coatings for passive radiative cooling applications. *Opt. Commun.* **2018**, *410*, 416–423. [CrossRef]

53. Benlattar, M.; Oualim, E.M.; Harmouchi, M.; Mouhsen, A.; Belafhal, A. Radiative properties of cadmium telluride thin film as radiative cooling materials. *Opt. Commun.* **2005**, *256*, 10–15. [CrossRef]

54. Benlattar, M.; Oualim, E.M.; Mouhib, T.; Harmouchi, M.; Mouhsen, A.; Belafhal, A. Thin cadmium sulphide film for radiative cooling application. *Opt. Commun.* **2006**, *267*, 65–68. [CrossRef]

55. Wong, R.Y.M.; Tso, C.Y.; Chao, C.Y.H.; Huang, B.; Wan, M.P. Ultra-broadband asymmetric transmission metallic gratings for subtropical passive daytime radiative cooling. *Sol. Energy Mater. Sol. Cells* **2018**, *186*, 330–339. [CrossRef]

56. Dimoudi, A.; Androutsopoulos, A. The cooling performance of a radiator based roof component. *Sol. Energy* **2006**, *80*, 1039–1047. [CrossRef]

57. Hosseinzadeh, E.; Taherian, H. An experimental and analytical study of a radiative cooling system with unglazed flat plate collectors. *Int. J. Green Energy* **2012**, *9*, 766–779. [CrossRef]

58. Erell, E.; Etzion, Y. Analysis and Experimental Verification of an Improved Cooling Radiatior. *Renew. Energy* **1999**, *16*, 700–703. [CrossRef]

59. Bagiorgas, H.S.; Mihalakakou, G. Experimental and theoretical investigation of a nocturnal radiator for space cooling. *Renew. Energy* **2008**, *33*, 1220–1227. [CrossRef]

60. Tso, C.Y.; Chan, K.C.; Chao, C.Y.H. A field investigation of passive radiative cooling under Hong Kong's climate. *Renew. Energy* **2017**, *106*, 52–61. [CrossRef]

61. Fält, M.; Pettersson, F.; Zevenhoven, R. Modified predator-prey algorithm approach to designing a cooling or insulating skylight. *Build. Environ.* **2017**, *126*, 331–338. [CrossRef]

62. Khedari, J.; Waewsak, J.; Thepa, S.; Hirunlabh, J. Field investigation of night radiation cooling under tropical climate. *Renew. Energy* **2000**, *20*, 183–193. [CrossRef]

63. Chen, Z.; Zhu, L.; Raman, A.; Fan, S. Radiative cooling to deep sub-freezing temperatures through a 24-h day-night cycle. *Nat. Commun.* **2016**, *7*, 1–5. [CrossRef] [PubMed]

64. Fält, M.; Zevenhoven, R. Combining the Radiative, Conductive and Convective Heat Flows in and Around a Skylight. In Proceedings of the World Renewable Energy Congress-Sweden, Linköping, Sweden, 8–13 May 2011; Volume 57.

65. Zhao, B.; Ao, X.; Chen, N.; Xuan, Q.; Hu, M.; Pei, G. General strategy of passive sub-ambient daytime radiative cooling. *Sol. Energy Mater. Sol. Cells* **2019**, *199*, 108–113. [CrossRef]

66. Lee, G.J.; Kim, Y.J.; Kim, H.M.; Yoo, Y.J.; Song, Y.M. Colored, Daytime Radiative Coolers with Thin-Film Resonators for Aesthetic Purposes. *Adv. Opt. Mater.* **2018**, *6*, 1–8. [CrossRef]

67. Sameti, M.; Kasaeian, A. Numerical simulation of combined solar passive heating and radiative cooling for a building. *Build. Simul.* **2015**, *8*, 239–253. [CrossRef]

68. Yong, C.; Yiping, W.; Li, Z. Performance analysis on a building-integrated solar heating and cooling panel. *Renew. Energy* **2015**, *74*, 627–632. [CrossRef]

69. Amarloo, A.; Shafii, M.B. Enhanced solar still condensation by using a radiative cooling system and phase change material. *Desalination* **2019**, *467*, 43–50. [CrossRef]

70. Zhao, B.; Hu, M.; Ao, X.; Xuan, Q.; Pei, G. Comprehensive photonic approach for diurnal photovoltaic and nocturnal radiative cooling. *Sol. Energy Mater. Sol. Cells* **2018**, *178*, 266–272. [CrossRef]

71. Hu, M.; Pei, G.; Wang, Q.; Li, J.; Wang, Y.; Ji, J. Field test and preliminary analysis of a combined diurnal solar heating and nocturnal radiative cooling system. *Appl. Energy* **2016**, *179*, 899–908. [CrossRef]

72. Al-Nimr, M.; Tahat, M.; Al-Rashdan, M. A night cold storage system enhanced by radiative coolingÐa modi®ed Australian cooling system. *Appl. Therm. Eng.* **1999**, *19*, 1013–1026. [CrossRef]

73. Hu, M.; Zhao, B.; Ao, X.; Su, Y.; Pei, G. Numerical study and experimental validation of a combined diurnal solar heating and nocturnal radiative cooling collector. *Appl. Eng.* **2018**, *145*, 1–13. [CrossRef]

74. Sohel, M.I.; Ma, Z.; Cooper, P.; Adams, J.; Niccol, L.; Gschwander, S. A feasibility study of night radiative cooling of BIPVT in climatic conditions of major Australian cities. In Proceedings of the Asia-Pacific Solar Research Conference, Kensington, Australia, 8–10 December 2014.

75. Zhao, B.; Hu, M.; Ao, X.; Chen, N.; Xuan, Q.; Su, Y.; Pei, G. A novel strategy for a building-integrated diurnal photovoltaic and all-day radiative cooling system. *Energy* **2019**, *183*, 892–900. [CrossRef]

76. Farmahini Farahani, M.; Heidarinejad, G.; Delfani, S. A two-stage system of nocturnal radiative and indirect evaporative cooling for conditions in Tehran. *Energy Build.* **2010**, *42*, 2131–2138. [CrossRef]

77. Saitoh, T.S.; Fujino, T. Advanced Energy-Efficient House (Harbeman House) With Solar Thermal, Photovoltaic, And Sky Radiation Energies (Experimental Results). *Sol. Energy* **2001**, *70*, 63–77. [CrossRef]

78. Zhang, S.; Niu, J. Cooling performance of nocturnal radiative cooling combined with microencapsulated phase change material (MPCM) slurry storage. *Energy Build.* **2012**, *54*, 122–130. [CrossRef]

79. Ali, A.H.H. Desiccant enhanced nocturnal radiative cooling-solar collector system for air comfort application in hot arid areas. *Sustain. Energy Technol. Assess.* **2013**, *1*, 54–62. [CrossRef]

80. Fiorentini, M.; Cooper, P.; Ma, Z. Development and optimization of an innovative HVAC system with integrated PVT and PCM thermal storage for a net-zero energy retrofitted house. *Energy Build.* **2015**, *94*, 21–32. [CrossRef]

81. Zhang, K.; Zhao, D.; Yin, X.; Yang, R.; Tan, G. Energy saving and economic analysis of a new hybrid radiative cooling system for single-family houses in the USA. *Appl. Energy* **2018**, *224*, 371–381. [CrossRef]

82. Fernandez, N.; Wang, W.; Alvine, K.; Katipamula, S. *Energy Savings Potential of Radiative Cooling Technologies*; National Technical Information Service, U.S. Department of Commerce: Springfield, VA, USA, 2015.

83. Parker, D.S.; Sherwin, J.R. *Evaluation of the NightCool Nocturnal Radiation Cooling Concept: Annual Performance Assessment in Scale Test Buildings Stage Gate 1B*; Florida Solar Energy Center: Cocoa, FL, USA, 2008.

84. Man, Y.; Yang, H.; Spitler, J.D.; Fang, Z. Feasibility study on novel hybrid ground coupled heat pump system with nocturnal cooling radiator for cooling load dominated buildings. *Appl. Energy* **2011**, *88*, 4160–4171. [CrossRef]

85. Hu, M.; Zhao, B.; Ao, X.; Zhao, P.; Su, Y.; Pei, G. Field investigation of a hybrid photovoltaic-photothermic-radiative cooling system. *Appl. Energy* **2018**, *231*, 288–300. [CrossRef]

86. Heidarinejad, G.; Farmahini Farahani, M.; Delfani, S. Investigation of a hybrid system of nocturnal radiative cooling and direct evaporative cooling. *Build. Environ.* **2010**, *45*, 1521–1528. [CrossRef]

87. Chotivisarut, N.; Kiatsiriroat, T. Cooling load reduction of building by seasonal nocturnal cooling water from thermosyphon heat pipe radiator. *Int. J. Energy Res.* **2009**, *33*, 1089–1098. [CrossRef]

88. Hu, M.; Zhao, B.; Ao, X.; Su, Y.; Pei, G. Parametric analysis and annual performance evaluation of an air-based integrated solar heating and radiative cooling collector. *Energy* **2018**, *165*, 811–824. [CrossRef]

89. Chotivisarut, N.; Nuntaphan, A.; Kiatsiriroat, T. Seasonal cooling load reduction of building by thermosyphon heat pipe radiator in different climate areas. *Renew. Energy* **2012**, *38*, 188–194. [CrossRef]

90. Hu, M.; Zhao, B.; Ao, X.; Feng, J.; Cao, J.; Su, Y.; Pei, G. Experimental study on a hybrid photo-thermal and radiative cooling collector using black acrylic paint as the panel coating. *Renew. Energy* **2019**, *139*, 1217–1226. [CrossRef]

91. Vall, S.; Johannes, K.; David, D.; Castell, A. A new flat-plate radiative cooling and solar collector numerical model: Evaluation and metamodeling. *Energy* **2020**, *202*, 117750. [CrossRef]

92. Zhao, B.; Hu, M.; Ao, X.; Chen, N.; Xuan, Q.; Jiao, D.; Pei, G. Performance analysis of a hybrid system combining photovoltaic and nighttime radiative cooling. *Appl. Energy* **2019**, *252*, 113432. [CrossRef]

93. Hollick, J. Nocturnal radiation cooling tests. *Energy Procedia* **2012**, *30*, 930–936.

94. Ali, A.H.H. Passive cooling of water at night in uninsulated open tank in hot arid areas. *Energy Convers. Manag.* **2007**, *48*, 93–100. [CrossRef]

95. Jeong, S.Y.; Tso, C.Y.; Zouagui, M.; Wong, Y.M.; Chao, C.Y.H. A numerical study of daytime passive radiative coolers for space cooling in buildings. *Build. Simul.* **2018**, *11*, 1011–1028. [CrossRef]

96. Bergman, T.L. Active daytime radiative cooling using spectrally selective surfaces for air conditioning and refrigeration systems. *Sol. Energy* **2018**, *174*, 16–23. [CrossRef]

97. Zhao, D.; Yin, X.; Xu, J.; Tan, G.; Yang, R. Radiative sky cooling-assisted thermoelectric cooling system for building applications. *Energy* **2019**, *190*, 116322. [CrossRef]

98. Zhao, D.; Aili, A.; Yin, X.; Tan, G.; Yang, R. Roof-integrated radiative air-cooling system to achieve cooler attic for building energy saving. *Energy Build.* **2019**, *203*, 109453. [CrossRef]

99. Wang, W.; Fernandez, N.; Katipamula, S.; Alvine, K. Performance assessment of a photonic radiative cooling system for office buildings. *Renew. Energy* **2018**, *118*, 265–277. [CrossRef]

100. Shen, D.; Yu, C.; Wang, W. Investigation on the thermal performance of the novel phase change materials wall with radiative cooling. *Appl. Eng.* **2020**, *176*, 115479. [CrossRef]

101. He, W.; Yu, C.; Yang, J.; Yu, B.; Hu, Z.; Shen, D.; Liu, X.; Qin, M.; Chen, H. Experimental study on the performance of a novel RC-PCM-wall. *Energy Build.* **2019**, *199*, 297–310. [CrossRef]

102. Katramiz, E.; Ghaddar, N.; Ghali, K. Daytime radiative cooling: To what extent it enhances office cooling system performance in comparison to night cooling in semi-arid climate? *J. Build. Eng.* **2020**, *28*, 101020. [CrossRef]

103. Oliveti, G.; Arcuri, N.; De Simone, M.; Bruno, R. Experimental evaluations of the building shell radiant exchange in clear sky conditions. *Sol. Energy* **2012**, *86*, 1785–1795. [CrossRef]

104. Domínguez-Torres, C.A.; León-Rodríguez, A.L.; Suárez, R.; Domínguez-Delgado, A. Numerical and experimental validation of the solar radiation transfer for an egg-crate shading device under Mediterranean climate conditions. *Sol. Energy* **2019**, *183*, 755–767. [CrossRef]

105. Yi, Z.; Lv, Y.; Xu, D.; Xu, J.; Qian, H.; Zhao, D.; Yang, R. A Transparent Radiative Cooling Film for Building Energy Saving. *Energy Built Environ.* **2020**, in press. [CrossRef]

106. Family, R.; Mengüç, M.P. Materials for Radiative Cooling: A Review. *Procedia Environ. Sci.* **2017**, *38*, 752–759. [CrossRef]

107. Jeong, S.Y.; Tso, C.Y.; Wong, Y.M.; Chao, C.Y.H.; Huang, B. Daytime passive radiative cooling by ultra emissive bio-inspired polymeric surface. *Sol. Energy Mater. Sol. Cells* **2020**, *206*, 110296. [CrossRef]

108. Huang, Z.; Ruan, X. Nanoparticle embedded double-layer coating for daytime radiative cooling. *Int. J. Heat Mass Transf.* **2017**, *104*, 890–896. [CrossRef]

109. 3M. *3M^{TM} Enhanced Specular Reflector (ESR)*; 3M: Saint Paul, MN, USA, 2018.

110. Craig, S.; Harrison, D.; Cripps, A.; Knott, D. BioTRIZ Suggests Radiative Cooling of Buildings Can Be Done Passively by Changing the Structure of Roof Insulation to Let Longwave Infrared Pass. *J. Bionic Eng.* **2008**, *5*, 55–66. [CrossRef]

111. Son, S.; Jeon, S.; Chae, D.; Yeop Lee, S.; Liu, Y.; Lim, H.; Ju Oh, S.; Lee, H. Colored emitters with silica-embedded perovskite nanocrystals for efficient daytime radiative cooling. *Nano Energy* **2020**, *79*, 105461. [CrossRef]

112. Liu, J.; Zhou, Z.; Zhang, D.; Jiao, S.; Zhang, J.; Gao, F.; Ling, J.; Feng, W.; Zuo, J. Research on the performance of radiative cooling and solar heating coupling module to direct control indoor temperature. *Energy Convers. Manag.* **2020**, *205*, 112395. [CrossRef]

113. Hu, Z.; He, W.; Hong, X.; Ji, J.; Shen, Z. Numerical analysis on the cooling performance of a ventilated Trombe wall combined with venetian blinds in an office building. *Energy Build.* **2016**, *126*, 14–27. [CrossRef]

114. Ziming, C.; Fuqiang, W.; Dayang, G.; Huaxu, L.; Yong, S. Low-cost radiative cooling blade coating with ultrahigh visible light transmittance and emission within an "atmospheric window". *Sol. Energy Mater. Sol. Cells* **2020**, *213*, 110563. [CrossRef]

115. Zhao, B.; Hu, M.; Ao, X.; Pei, G. Conceptual development of a building-integrated photovoltaic–radiative cooling system and preliminary performance analysis in Eastern China. *Appl. Energy* **2017**, *205*, 626–634. [CrossRef]

116. Ben Cheikh, H.; Bouchair, A. Passive cooling by evapo-reflective roof for hot dry climates. *Renew. Energy* **2004**, *29*, 1877–1886. [CrossRef]

117. Sharifi, A.; Yamagata, Y. Roof ponds as passive heating and cooling systems: A systematic review. *Appl. Energy* **2015**, *160*, 336–357. [CrossRef]

118. Bevilacqua, P.; Benevento, F.; Bruno, R.; Arcuri, N. Are Trombe walls suitable passive systems for the reduction of the yearly building energy requirements? *Energy* **2019**, *185*, 554–566. [CrossRef]

119. Hu, Z.; He, W.; Ji, J.; Zhang, S. A review on the application of Trombe wall system in buildings. *Renew. Sustain. Energy Rev.* **2017**, *70*, 976–987. [CrossRef]

120. Cheng, Z.; Wang, F.; Wang, H.; Liang, H.; Ma, L. Effect of embedded polydisperse glass microspheres on radiative cooling of a coating. *Int. J. Sci.* **2019**, *140*, 358–367. [CrossRef]

121. Mandal, J.; Yang, Y.; Yu, N.; Raman, A.P. Paints as a Scalable and Effective Radiative Cooling Technology for Buildings. *Joule* **2020**, *4*, 1350–1356. [CrossRef]

Analysis of the Air-Reversed Brayton Heat Pump with Different Layouts of Turbochargers for Space Heating

Shugang Wang [1], Shuangshuang Li [2,*], Shuang Jiang [3] and Xiaozhou Wu [1]

[1] Faculty of Infrastructure Engineering, Dalian University of Technology, Dalian 116024, China; sgwang@dlut.edu.cn (S.W.); fonen519@dlut.edu.cn (X.W.)

[2] College of Civil Engineering and Architecture, Dalian University, Dalian 116622, China

[3] College of Civil Engineering, Dalian Minzu University, Dalian 116600, China; shjiang@dlnu.edu.cn

[*] Correspondence: lishuangshuang@dlu.edu.cn; Tel.: +86-155-4268-6558

Abstract: The air-reversed Brayton cycle produces charming, environmentally friendly effects by using air as its refrigerant and has potential energy efficiency in applications related to space heating and building heating. However, there exist several types of cycle that need to be discussed. In this paper, six types of air-reversed Brayton heat pump with a turbocharger, applicable under different heating conditions, are developed. The expressions of the heating coefficient of performance (COP) and the corresponding turbine pressure ratio are derived based on thermodynamic analysis. By using these expressions, the effects of turbine pressure ratio on the COP under different working conditions are theoretically analyzed, and the optimal COPs of different cycles under specific working conditions are determined. It is observed that Cycles A and C have the highest heating COPs, and there is an optimal pressure ratio for each cycle. The corresponding pressure ratio of the optimal COP is different, concentrated in the range of 1.5–1.9. When the pressure ratio reaches the optimal value, increasing the pressure ratio does not significantly improve the heating COP. Take Cycle F as an example: the maximum error between the calculated results and experimental observation is lower than 5.6%. These results will enable further study of the air-reversed Brayton heat pump with a turbocharger from a different perspective.

Keywords: air-reversed Brayton heat pump; turbocharger; system layout; pressure ratio; COP

1. Introduction

The use of heat pumps for space heating and drying is one of the solutions for providing a stable and affordable energy supply which contributes to environmental protection and sustainable energy development. Although the theoretical coefficient of performance (COP) value is relatively low, air-source devices may have great potential for development. A reversed Brayton cycle using air as the green working fluid is a potential alternative to conventional vapor compression systems of heating and drying [1–3]. Recent exploitation of the unification of expansion/compression into a single operation (compander) promotes the productization of air-reversed Brayton heat pump (air cycle heat pump) products [4,5].

Air as the working fluid in the reversed Brayton cycle is a potential substitute for the conventional vapor compression cycles. However, compared with conventional vapor compression heat pumps, the energy efficiency of a basic air cycle heat pump (air-reversed Brayton heat pump) is lower under normal temperature conditions. Thus, a regenerated air cycle was utilized for improving the overall system performance. The performance of an air cycle heat pump can be remarkably enhanced by adding a regenerator [1,6,7]. Based on finite-time thermodynamics, an analytical solution was derived that demonstrated the effects of pressure ratio, heat exchanger effectiveness, and the ratio between the inlet temperature of the cooling fluid and that of the heating fluid of the heat reservoir on key performance indices [8–12].

The reversed Brayton cycle, which uses air as a refrigerant, has more typical operation characteristics compared with the traditional ones. Most notably, the regenerated air-reversed Brayton heat pump is more suitable for application in cold and frigid regions. It can not only break through the limits of the ambient temperature of air-source heat pumps but can also remove the heat exchange of the low-temperature side when using a semi-open form, which means that the air can directly enter the compressor and avoid various problems caused by evaporator frosting. A thermodynamic model of an air cycle heat pump with a compressor and an expander was proposed by Zhang et al.; heating capacity in line with heating load was found [13]. This thermodynamic model was further developed by Yuan and Zhang, who added a regenerator so that the regenerated air cycle heat pump could not only ensure heating capacity that was in line with the heating load but could also achieve a higher COP compared with trans-critical CO_2 heat pumps under a large temperature difference [14]. A simulation model of an air cycle heat pump water heater was developed by Yang et al., and it was found that this system could save the heating-up period, especially when operating at low ambient temperature conditions [15]. As the expansion device in the market is too large for domestic and vehicle heating usage, the existing experimental studies were primarily limited to improving the structure of individual components such as the compressor and the expander [16–18].

A turbocharger was used in air cycle systems to substitute the compressor and the expander. It miniaturized the air cycle system and also simplified the system design without considering the matching and connection problems between the compressor and the expander. A comprehensive report on an air cycle with a turbocharger was released by TNO [19], in which it was mentioned that a pilot plant processed air in open and recuperated cycles for freezing applications. Spence et al. [20,21] designed and established a prototype for existing trailer refrigeration units for road transport, where the overall COP was about 0.3 at the cryogenic temperature of $-20\ °C$. Catalano et al. [22,23] designed an air cycle using a turbocharger and roots blowers for refrigeration. A COP higher than 0.6 was reported for the turbine exit temperature of $-42\ °C$. Li et al. [24–26] theoretically and experimentally studied the air-reversed Brayton heat pump system with an automotive turbocharger. A thermodynamic model for this system was presented, and the relationships between the system performance and the operating parameters were illustrated. Moreover, a test bench of a regenerated air cycle heat pump with a turbocharger was presented, and the measurement results illustrated that the heating capacity of the air cycle heat pump could match the heating load well.

However, the form of the air-reversed Brayton cycle with a turbocharger in the current research is single, and the application scope is narrow. As the functions and application conditions of the single-cycle form are limited, it is necessary to derive a variety of cycle processes to improve this type of heat pump cycle form, and the difference in cycle form can also lead to changes in heating characteristics. This paper develops a different thermodynamic process for the air-reversed Brayton cycle with a turbocharger. The relations between the heating COPs and the turbine pressure ratio are established based on reasonable assumptions and the thermodynamic diagram. Therefore, an in-depth look into the variation of performance parameters with pressure ratio parameters in different cycles is achieved.

2. Theoretical Analysis of Different Types of Air Heat Pump with a Turbocharger

Compared with a traditional air-source heat pump system, the air-reversed Brayton heat pump system with a turbocharger has great potential in low-temperature heating, energy saving, and emission reduction. As the turbocharger is used to replace the compressor and expander, and the blower is added as the power source, it is possible to use the air-reversed Brayton heat pump system in civil building winter heating and domestic hot water supplies and other projects. By designing various thermodynamic processes of the air-reversed Brayton heat pump system with a turbocharger driven by a blower, the service

conditions and application scope of this kind of heat pump can be widened, which endows this system with greater diversity.

2.1. Description of Different Cycle Structures and Characteristics

Considering the limitations of heating objective conditions and the diversity of user needs, a single form of air-reversed Brayton heat pump with a turbocharger cannot meet all the application conditions. Furthermore, a variety of cycle forms have their own heating characteristics and structural advantages. Therefore, it is necessary to design more structural forms by designing combined modes of blowers and turbochargers, the number of blowers and their setting positions, the number of heat exchangers in the system, and their settings in the system position, etc. These forms can be extended from the six kinds of new heat pump cycle with a turbocharger to different heat demands and conditions, named Cycle A–Cycle F and shown in Figure 1. These six forms can not only provide different terminal heat-carrying fluids, such as water or air for heating and domestic hot water, but can also discharge cooler air from the system that can be used for refrigeration. In this section, heating is used as an example. Although these six kinds of cycle have certain representativeness, the structure is not limited to these six forms. Its application range can be further expanded by deriving other structures not covered in this paper.
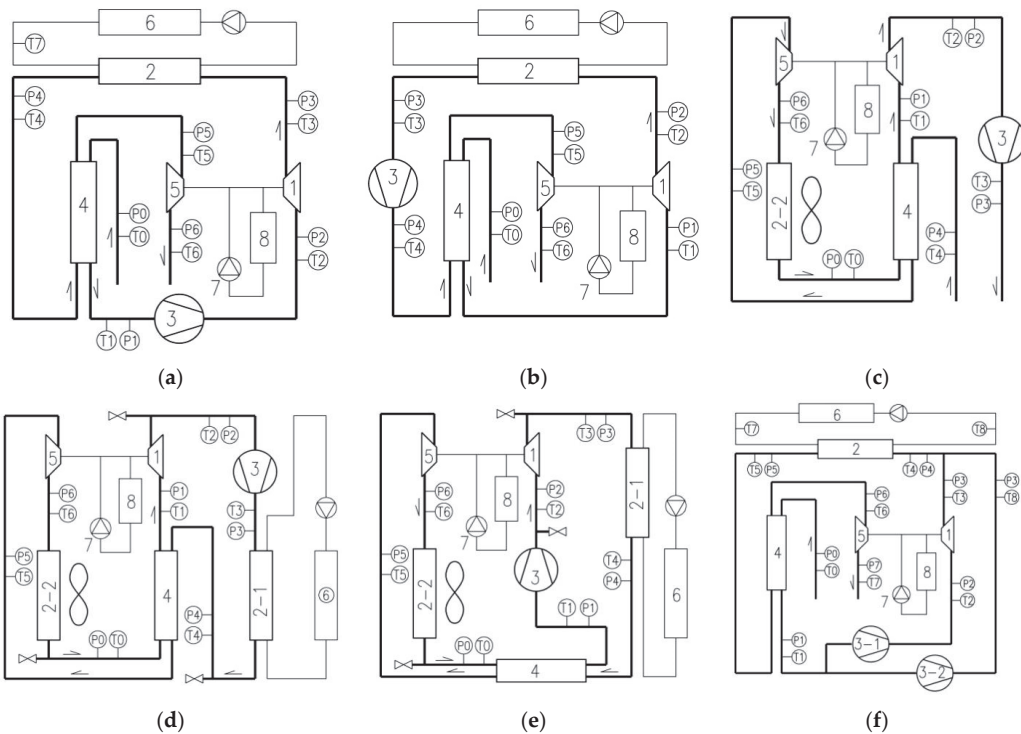
Figure 1. Different cycles of the air-reversed Brayton heat pump system with a turbocharger. 1: compressor, 2: heat exchanger, 3: blower, 4: preheater (regenerative), 5: turbine, 6: fan coil, 7: oil pump, 8: oil tank (P/T pressure sensor/temperature sensor). (**a**) Cycle A; (**b**) Cycle B; (**c**) Cycle C; (**d**) Cycle D; (**e**) Cycle E; (**f**) Cycle F.

Except for Cycle F, which was set as having two blowers, all other cycles adopt one blower as the power-driving equipment, i.e., a single-fan system. In Cycle A, the blower is set before the compressor of the turbocharger, and the cold air in the environment is initially preheated through preheater 4. This equipment can significantly improve the

heating performance of the system. Subsequently, the air first passes through the blower 3 and then enters the turbocharger compressor 1 to be heated up and boosted. The setting of oil pump 7 and oil tank 8 ensures the normal, high-speed operation of the turbocharger. High-temperature air through heat exchanger 2 is mainly used for the heat exchanger. The fan coil unit 6 and similar equipment can be used for the heating end equipment. The exothermic air still has some residual heat that is used as a heat source for preheater 4 to preheat the air from the environment. Finally, the air is expanded through the turbocharge turbine 5 and then diverted outside. In another semi-open cycle, Cycle B, the blower is placed in front of the turbine as shown in Figure 1b. The starting resistance is smaller than in Cycle A. These two forms are the most basic modifications of the traditional air-reversed Brayton heat pump cycle.

Cycle C is also a series combination of a single fan and a compressor. The indoor air first enters preheater 4 and then expands and cools through turbocharger turbine 5. Subsequently, it absorbs heat from the outdoor air heat source through heat exchanger 2. After heating up through preheater 4, it enters turbocharger compressor 1 and blower 3 and is finally sent into the room directly. The simple system structure can improve the temperature of the air entering the compressor and reduce the temperature of the air entering the turbine, which improves the heating efficiency of the system. Considering the practical application, blower 3 is set after the turbocharger compressor 1. This configuration can lower the exhaust pressure and temperature of the compressor, which is convenient for the recovery of lubricating oil at the outlet of the compressor. The hot air is directly fed into the room to reduce the heat loss caused by the end equipment. At the same time, system requirements are reduced as the system operates under a low vacuum.

Cycles D and E are closed circulation cycles which are not affected by the ambient air quality. However, due to the use of two heat exchangers, the overall efficiency of the whole machine is reduced, and the cost is higher than that of Cycles A and B. The above cycles have the same flow rates of the compressor and the turbine. By adding another blower, the system can be transformed into a dual-blower system, which is closer to the actual operating condition of the vehicle turbocharger. The circulation form of the dual-blower system, shown by Cycle F in Figure 1, is slightly more complicated than that of the single-blower system. One blower is connected in series with the compressor, which is subsequently in parallel with another blower. The air flows through the two parallel pipelines and is mixed together and then sent to gas-water heat exchanger 2 for heat transfer. Subsequently, the air is used to preheat the ambient air temperature and is finally discharged outdoors.

The heat-carrying fluid in the end equipment of the other cycles is water, except for in Cycle C. The equipment is not only limited to the fan coil, but can also use the floor radiant coil, radiator, etc., and is designed for a domestic hot water system. However, the temperature of the hot water is affected to a certain extent. To ensure the optimal pressure ratio of Cycle C, the air temperature as the circulating refrigerant is lower because the closed heat exchanger must be used on the heat-source side.

2.2. Analytical Expression of Heating COP

2.2.1. T-s Diagram

At present, only a limited amount of research exists on the air-reversed Brayton heat pump system with a turbocharger and a blower. Theoretical analysis is mostly carried out for the conventional, regenerated air-reversed Brayton heat pump system. However, this cannot truly reflect the heating characteristics of this system driven by a blower with a turbocharger and the relationship between the related parameters and the heating COP. Therefore, this section derives the expressions reflecting the analytical relation between the COP and the pressure ratio based on the temperature entropy diagram (*T-s* diagram) of different heat pump forms and relevant assumptions.

Figure 2 depicts the *T-s* diagram of each cycle shown in Figure 1, where the numbers correspond to the position of the temperature/pressure sensor (T/P) in Figure 1. Curve 1–2 in Cycle A represents the compression process of the blower; curves 2–3 and 5–6 represent

the compression and expansion processes in the turbocharger, respectively. Curve 3–4 represents the heat release process of the heat exchanger; curves 4–5 and 0–1 represent the heat release and heat absorption of the preheater, respectively.

Curves 1–2 and 5–6 in Cycle B represent the compression and expansion processes in the turbocharger, respectively. Curve 2–3 represents the heat release process of the heat exchanger; curve 3–4 indicates the compression process of the blower; curves 4–5 and 0–1 represent the heat release and heat absorption of the preheater, respectively. Curve 0–2 in Cycle C represents the compression process of the blower, and the hot air is directly sent to the end users; curves 1–2 and 4–5 represent the compression and expansion processes in the turbocharger, respectively. Curve 5–6 represents the heat release process of the heat exchanger; curves 3–4 and 6–1 represent the heat release and heat absorption processes of the regenerator, respectively.

Cycles D and E are closed cycles. Taking Cycle E as an example, curves 2–3 and 5–6 represent the compression and expansion processes in the turbocharger, respectively. Curve 1–2 represents the compression process of the blower; curves 4–5 and 0–1 represent the heat release and heat absorption process of the regenerator, respectively. Curve 6–0 represents the heat absorption process of the cold-end heat exchanger, the purpose of which is to obtain heat from the heat source. Such a system form is suitable as the system cannot use the open type, which is conducive to ensuring that the heat pump cycle working medium is kept clean and has low water content.

Cycle F is a semi-open cycle with two blowers. Curve 1–2 represents the compression process of the blower; curve 2–3 is the turbocharger compressor compression process; curve 1–8 represents the compression process of the parallel fan. Subsequently, point 8 is mixed with points 3–4; curve 4–5 represents the heat release process of the heat exchanger; curves 5–6 and 0–1 represent the heat release and heat absorption process of the preheater, respectively; curve 6–7 represents the expansion of the turbine in the turbocharger. The *T-s* diagram based on these different forms of air-reversed Brayton heat pump with a turbocharger describes the air state and thermodynamic process more intuitively and vividly.
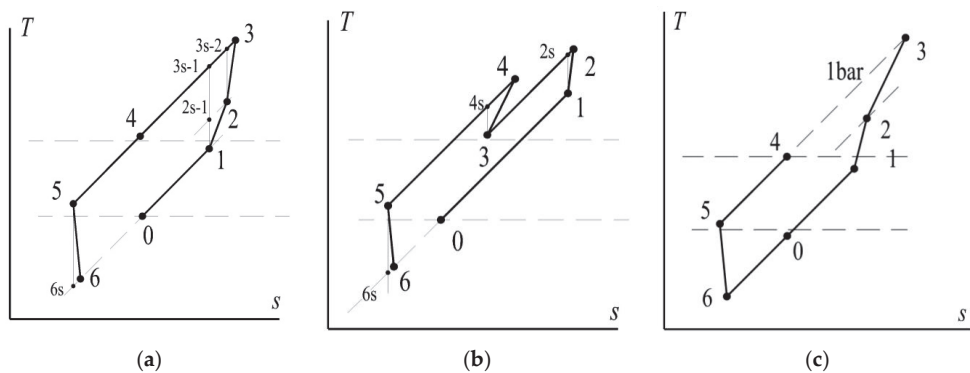
Figure 2. *Cont.*
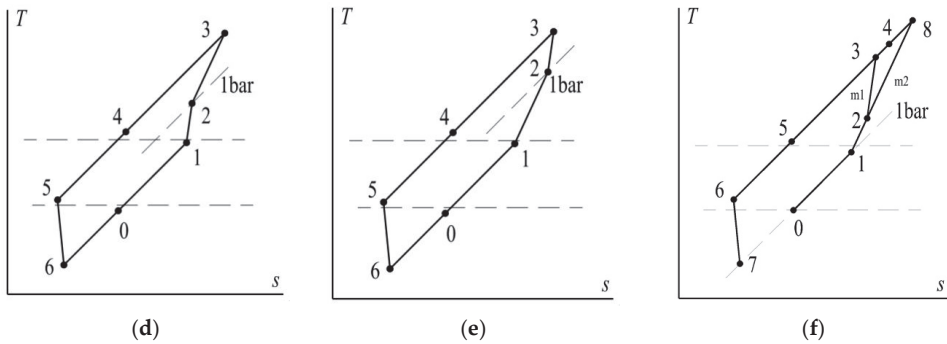
Figure 2. *T-s* diagram of different air-reversed Brayton heat pump systems with a turbocharger. (**a**) Cycle A; (**b**) Cycle B; (**c**) Cycle C; (**d**) Cycle D; (**e**) Cycle E; (**f**) Cycle F.

2.2.2. Mathematical Modeling

The mathematical model of Cycle A can be found in study [24]. It can be gathered from the system structure that the heating performance of Cycle B is slightly worse than that of other cycles. Its mathematical model is not described in this paper. The mathematical models of the other cycles are discussed where each cycle's hypothesis refers to Li et al. [24,25]. The mathematical model of Cycle C can be established by referring to the above thermodynamic model and *T-s* diagram.

The heating capacity of Cycle C is defined as:

$$Q_H = m_1(h_3 - h_4) = m_1 c_p(T_3 - T_4) \tag{1}$$

while the blower energy consumption and heating COP are given as follows:

$$W_f = m_1 c_p(T_3 - T_2) \tag{2}$$

$$COP_H = \frac{Q_H}{W_f} = \frac{T_3 - T_4}{T_3 - T_2} \tag{3}$$

The ideal gas equation is as follows:

$$pv = RT \tag{4}$$

The adiabatic process of the blower from 2–3 is described by the following expressions:

$$T_{3s} = T_2 \left(\frac{p_3}{p_2}\right)^{\frac{k-1}{k}} = T_2 \gamma_{2-3} \tag{5}$$

$$T_3 - T_2 = \frac{T_{3s} - T_2}{\eta_f} \tag{6}$$

The turbine polytropic process can be written as:

$$T_5 = T_{6s} \left(\frac{p_5}{p_6}\right)^{\frac{k-1}{k}} = T_{6s} \gamma_{5-6} \tag{7}$$

The compressor variable process is:

$$T_{2s} = T_1 \left(\frac{p_2}{p_1}\right)^{\frac{k-1}{k}} = T_1 \gamma_{1-2} \tag{8}$$

$$T_2 - T_1 = \frac{T_{2s} - T_1}{\eta_c} \tag{9}$$

The following expression gives the turbine efficiency equation:

$$T_5 - T_6 = (T_5 - T_{6s})\eta_e \tag{10}$$

For a better representation, the following one dimensionless parameter is defined:

$$\theta = \frac{T_4}{T_0} \tag{11}$$

According to the balance equation of the turbocharger, the following hold:

$$T_5 - T_6 = T_2 - T_1 \tag{12}$$

$$T_5\left(1 - \frac{1}{\gamma_{1-3}}\right)\eta = T_1(\gamma_{1-2} - 1) \tag{13}$$

$$\gamma_{1-2} = \frac{b\left(1 - \frac{1}{\gamma_{1-3}}\right)\eta}{a} + 1 \tag{14}$$

$$\gamma_{2-3} = \frac{\gamma_{1-3}}{\gamma_{1-2}} \tag{15}$$

where $a = 1 - \varepsilon_r + \varepsilon_r\theta$; $b = \theta - \varepsilon_r\theta + \varepsilon_r$; $\eta = \eta_c\eta_e$.

The balance equation of the regenerator is given as:

$$T_4 - T_5 = T_1 - T_0 = \varepsilon_r(T_4 - T_0) \tag{16}$$

$$T_1 = aT_0 \tag{17}$$

$$T_5 = bT_0 \tag{18}$$

and the heating COP as:

$$\text{COP}_H = \frac{Q_H}{W_f} = \frac{T_3 - T_4}{T_3 - T_2} = \frac{T_2\left(1 + \frac{\gamma_{2-3} - 1}{\eta_f}\right) - T_4}{T_2\left(1 + \frac{\gamma_{2-3} - 1}{\eta_f}\right) - T_2} = \frac{\left(1 + \frac{\gamma_{2-3} - 1}{\eta_f}\right) - \frac{T_4}{T_2}}{\left(1 + \frac{\gamma_{2-3} - 1}{\eta_f}\right) - 1}$$
$$= \frac{\left(1 + \frac{\gamma_{2-3} - 1}{\eta_f}\right) - \frac{\theta}{a\left(1 + \frac{\gamma_{1-2} - 1}{\eta_c}\right)}}{\frac{\gamma_{2-3} - 1}{\eta_f}} \tag{19}$$

The variable γ_{2-3} is a function of γ_{1-3}. Therefore, COP_H can be described as a function of the pressure ratio.

Cycle E is a closed system, which is conducive to the stability of the lubricating oil system and is not affected by environmental conditions. It is easy to exchange the cooling and heating functions, and it also has cooling and heating functions. Therefore, the cooling coefficient energy efficiency ratio (EER) + 1 is used to obtain the analytical expression of COP in the calculations, and the heat transfer temperature difference is used to correct the heat source temperature and heat sink temperature.

The cooling capacity can be written as:

$$Q_C = m(h_0 - h_6) = c_p m(T_0 - T_6) \tag{20}$$

The blower energy consumption and cooling *EER* are described by the following expressions:

$$W_f = mc_p(T_2 - T_1) \tag{21}$$

$$EER = \frac{Q_C}{W_f} = \frac{T_0 - T_6}{T_2 - T_1} \tag{22}$$

The compressor and blower isentropic compression processes are described by the following equation:

$$T_{3s-1} = T_1 \gamma_{5-6} \tag{23}$$

while the turbine expansion process is:

$$T_5 = T_{6s}\left(\frac{p_5}{p_6}\right)^{\frac{k-1}{k}} = T_{6s}\gamma_{5-6} \tag{24}$$

The balance equation of turbocharger can be written as follows:

$$T_5 - T_6 = T_3 - T_2 \tag{25}$$

$$(T_5 - T_{6s})\eta = T_{3s-2} - T_2 \tag{26}$$

According to the approximate parallel hypothesis, we obtain:

$$T_{3s-2} - T_2 = T_{3s-1} - T_{2s-1} \tag{27}$$

$$(T_5 - T_{6s})\eta = T_{3s-1} - T_{2s-1} \tag{28}$$

$$\gamma_{1-2} = \gamma_{5-6} - \frac{b}{a}\eta\left(1 - \frac{1}{\gamma_{5-6}}\right) \tag{29}$$

The heat transfer process of the recovery heat exchanger can be written as follows:

$$T_1 - T_0 = T_4 - T_5 = \varepsilon_r(T_4 - T_0) \tag{30}$$

We define the following dimensionless parameter:

$$\theta = \frac{T_4}{T_0} \tag{31}$$

where

$$T_2 = T_1 + \frac{1}{\eta_f}(T_{2s-1} - T_1) \tag{32}$$

$$T_3 = T_2 + \frac{1}{\eta_c}(T_{3s-2} - T_2) \tag{33}$$

The *EER* can be written as only related to the turbine pressure and γ_{5-6} as follows:

$$EER = \frac{T_0 - T_6}{T_2 - T_1} = \frac{1 - b\left[1 - \left(1 - \frac{1}{\gamma_{5-6}}\right)\eta_e\right]}{\frac{1}{\eta_f}a(\gamma_{1-2} - 1)} \tag{34}$$

$$COP = EER + 1 \tag{35}$$

The flow ratio of two blowers should be introduced as another variable for Cycle F with two parallel blowers. However, the mass flow rate is only related to the performance of the blowers; therefore, it is treated as a constant in the derivation of the expressions. The absolute performance of the system is lower than that of the other single-blower cycles; however, it is found through measurements that this cycle can ensure the efficient operation of the turbocharger, which is more in line with the actual operating conditions of the turbocharger and obtains a better practical, operational effect [26]. The specific calculation process is as follows.

The heating capacity is calculated as follows:

$$Q_H = (m_2 + m_1)(h_4 - h_5) = c_p(m_2 + m_1)(T_4 - T_5) \tag{36}$$

where m_1 and m_2 are parallel mass flows in Figure 2f, and the blower energy consumption is:

$$W_f= m_2 c_p (T_8 - T_1) + m_1 c_p (T_2 - T_1) \tag{37}$$

Assuming that the flow ratio G is a known quantity, i.e.,

$$G = \frac{m_1}{m_2} \tag{38}$$

we can describe the heating COP as follows:

$$\text{COP}_H = \frac{Q_H}{W_f} = \frac{(m_2 + m_1) c_p (T_4 - T_5)}{m_2 c_p (T_8 - T_1) + m_1 c_p (T_2 - T_1)} \tag{39}$$

The variable process of two parallel blowers can be written as:

$$T_{2s}= T_1 \left(\frac{p_2}{p_1}\right)^{\frac{k-1}{k}} = T_1 \gamma_{1\text{-}2} \tag{40}$$

$$T_2 - T_1 = \frac{T_{2s} - T_1}{\eta_f} \tag{41}$$

$$T_{8s}= T_1 \left(\frac{p_8}{p_1}\right)^{\frac{k-1}{k}} = T_1 \gamma_{6\text{-}7} \tag{42}$$

$$\begin{aligned} T_8 &= T_1 + \frac{T_1 \gamma_{6\text{-}7} - T_1}{\eta_f} = T_1 \left(1 + \frac{\gamma_{6\text{-}7} - 1}{\eta_f}\right) \\ &= T_0 (\theta \varepsilon_r - \varepsilon_r + 1)(1 + \frac{\gamma_{6\text{-}7} - 1}{\eta_f}) \end{aligned} \tag{43}$$

and the heat transfer process of the recovery heat exchanger is described as follows:

$$T_5 - T_6= T_1 - T_0= \varepsilon_r (T_5 - T_0) \tag{44}$$

$$T_6= T_0 (\theta - \theta \varepsilon_r + \varepsilon_r)= b T_0 \tag{45}$$

$$T_1= T_0 (\theta \varepsilon_r - \varepsilon_r + 1) = a T_0 \tag{46}$$

The compressor variable process can be written as:

$$T_{3s}= T_2 \left(\frac{p_3}{p_2}\right)^{\frac{k-1}{k}} = T_2 \gamma_{2\text{-}3} \tag{47}$$

$$T_6= T_{7s} \gamma_{6\text{-}7} \tag{48}$$

while the parallel blowers mixing process is:

$$T_4 = \frac{m_1 T_3 + m_2 T_8}{m_1 + m_2} = \frac{G T_3 + T_8}{G + 1} \tag{49}$$

We define the following one dimensionless parameter:

$$T_5= \theta T_0 \tag{50}$$

The balance equation of turbocharger is given as follows:

$$(m_1 + m_2)(T_6 - T_7)= m_1 (T_3 - T_2) \tag{51}$$

$$(m_1 + m_2)(T_6 - T_{7s}) \eta_e= m_1 \frac{T_{3s} - T_2}{\eta_c} \tag{52}$$

$$(G+1)(T_6 - T_{7s})\eta_e = G\frac{T_{3s} - T_2}{\eta_c} \tag{53}$$

$$b(G+1)(1 - \frac{1}{\gamma_{6-7}})\eta = aG(1+\frac{\gamma_{1-2}-1}{\eta_f})(\gamma_{2-3}-1) \tag{54}$$

Based on these assumptions, the following equations can be derived:

$$T_1\gamma_{6-7} - T_1\gamma_{1-2} = T_2\gamma_{2-3} - T_2 \tag{55}$$

$$(G+1)(T_6 - T_{7s})\eta = G(T_1\gamma_{6-7} - T_1\gamma_{1-2}) \tag{56}$$

$$\gamma_{6-7} = \gamma_{1-2}\gamma_{2-3} \tag{57}$$

$$\frac{b}{a}\left(\frac{G+1}{G}\right)\left(1 - \frac{1}{\gamma_{6-7}}\right)\eta = \gamma_{6-7} - \gamma_{1-2} \tag{58}$$

$$\gamma_{1-2} = \gamma_{6-7} - \frac{b}{a}\left(\frac{G+1}{G}\right)\left(1 - \frac{1}{\gamma_{6-7}}\right)\eta \tag{59}$$

$$\gamma_{2-3} = \frac{\gamma_{6-7}}{\gamma_{1-2}} \tag{60}$$

Based on the above expression, the calculation method of COP_H related to γ_{6-7} can be derived as follows:

$$\begin{aligned} COP_H &= \frac{Q_H}{W_f} = \frac{(m_2+m_1)c_p(T_4-T_5)}{m_2c_p(T_8-T_1)+m_1c_p(T_2-T_1)} = \frac{(1+G)c_p(T_4-T_5)}{c_p(T_8-T_1)+Gc_p(T_2-T_1)} \\ &= \frac{(1+G)\left(\frac{Ga(1+\frac{\gamma_{1-2}-1}{\eta_f})\gamma_{2-3}+a(1+\frac{\gamma_{6-7}-1}{\eta_f})}{G+1} - \theta\right)}{a\frac{\gamma_{6-7}-1}{\eta_f}+aG\frac{\gamma_{1-2}-1}{\eta_f}} \end{aligned} \tag{61}$$

3. Results and Analysis

3.1. Theoretical Calculation Results

Using the above mathematical models to calculate the heating COP, the following results were obtained according to the calculation results shown in Figures 3 and 4. It can be noted that the heating performance of Cycle C and that of Cycle A were similar. They were both the highest, followed by Cycles E, B, and F under all working conditions.

There was an optimal pressure ratio for all cycles under certain working conditions. As the pressure ratio gradually reached the optimal value, the heating performance also reached a peak value (the optimal COP). Afterwards, the heating COP could not increase with an increase in the pressure ratio. When the ambient temperature was fixed at −15 °C at the heating water temperature of 45 °C, the optimal pressure ratio was about 1.5–1.7 for each single-blower cycle. The optimal pressure ratio of the double-blower cycle was close to 1.8–1.9, and the optimal COP ranged from 1.22 to 1.27. When the water supply temperature dropped to 35 °C, the optimal pressure ratio of all cycles remained almost unchanged, with the optimal COP in the range of 1.24–1.29. Therefore, the heating was not influenced by the water temperature at a fixed ambient temperature. When the water supply temperature was fixed, the optimal pressure ratio of each cycle showed a minor decrease as the ambient temperature rose from −15 °C to 5 °C. It should be noted that the optimal pressure ratio was not sensitive to the ambient temperature. Therefore, for the air-reversed Brayton heat pump systems with a turbocharger driven by blowers, the ambient temperature and the water supply temperature were not the main factors that affected the optimal pressure ratio.

Figures 3 and 4 show that once the pressure ratio between the turbine inlet pressure and the outlet pressure reaches a certain value, the COP of heating did not increase with an increase in the pressure ratio. Therefore, for the reversed Brayton heat pump with a single blower, this heat pump maintained a high heating efficiency when the turbine pressure ratio

was greater than 1.5. For Cycle C, when the water supply temperature varied from 45 °C to 35 °C, the optimal COP increased by about 0.04 under the same ambient temperature. The ambient temperature varied from −15 °C to 5 °C, and the optimal COP rose by about 0.09 at the same water temperature. Therefore, the COP in the optimal heating system was insensitive to the ambient temperature and the temperature of hot water, which is also a significant advantage.

The calculation results also showed that the highest COP of the single-fan heat pump system under different working conditions was maintained in the range of 1.2–1.4. Taking the example of Cycle A, it can be observed that the COP increased by at least 27% while the turbocharger compressor efficiency and the turbine efficiency increased to 0.85 and 0.9, respectively [27]. Apparently, the heating performance of the system is significantly improved as the efficiency of the turbocharger is improved. Therefore, it requires more attention. In addition, the variation range of air refrigerant pressure was not large under the operating conditions, which reduced the requirements of equipment airtightness. Consequently, it reduced the processing difficulty.

3.2. Experimental Results

The above theoretical results pointed to the way to establish the test bench and provide support for the late promotion. The relevant experimental rigs are shown in Figure 5, which integrate the traditional, regenerated air-reversed Brayton heat pump cycle and the cycles with a turbocharger and blowers, as described in Section 2.1. Based on a reconstruction of this test bench, more cycles under different working conditions were realized. The experimental conditions and specific results were provided in the literature by Li et al. [26].

The representative Cycle F, which was simple to implement in the existing experimental bench, was selected as the typical one for comparison in this paper. Figure 6 shows the theoretical and measured results of Cycle F under the same initial conditions. Here, the calculated results were in good agreement with the experimental observation, and the maximum error was lower than 5.6%. Because of the assumption that the pressure lines are approximately parallel within a certain range of entropy in-crease in the derivation of the formula [24], but the measured system energy consumption is close to a fixed value, due to the use of a constant-frequency blower as the power equipment in actual measurement it was different from the power calculated by the enthalpy difference in the calculation. So, there were some deviations between the calculated and experimental results. Moreover, the computation procedure neglected a few factors, such as heat transfer from the heat pump system to the outside, friction resistance in the pipe, and so on. In general, the expressions can be used to predict the ranges of turbine pressure value and COP, which can simplify the calculation process, optimize the system form, and achieve the optimal pressure ratio quickly when designing experiments or products.
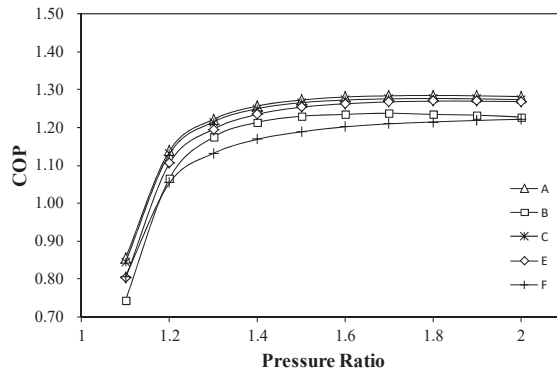
(**a**)
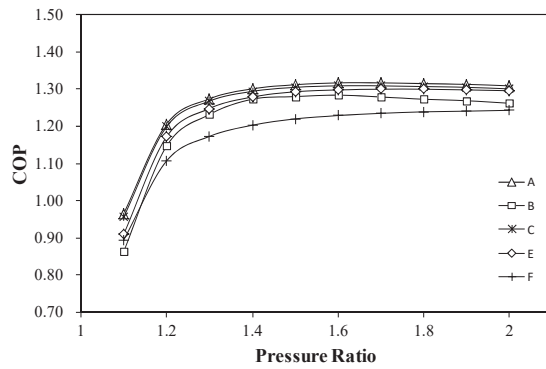
(**b**)
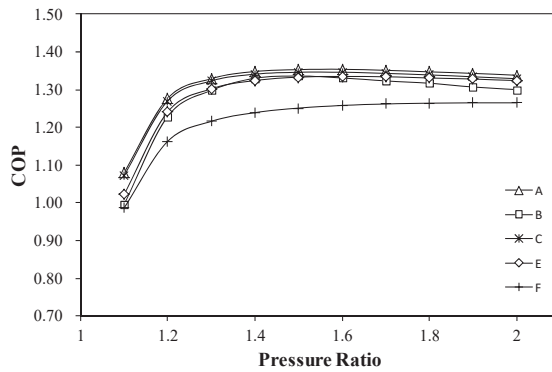
(**c**)

Figure 3. Variation of COP versus pressure ratio at 45 °C hot water temperature. (**a**) Ambient temperature of −15 °C. (**b**) Ambient temperature of −5 °C. (**c**) Ambient temperature of 5 °C.
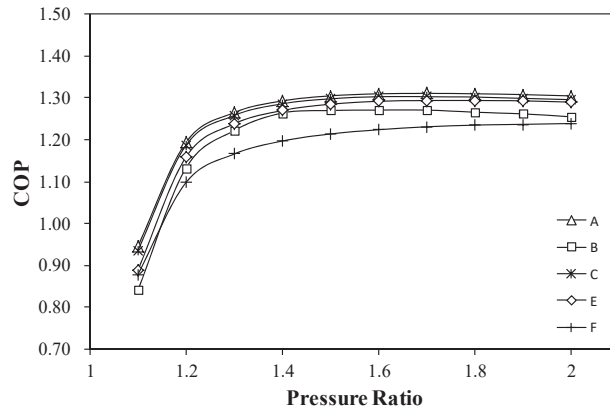
(**a**)
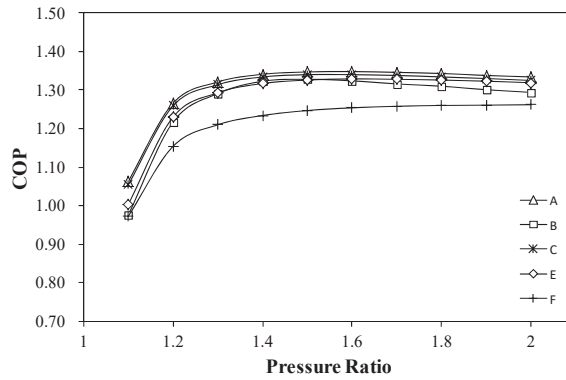
(**b**)
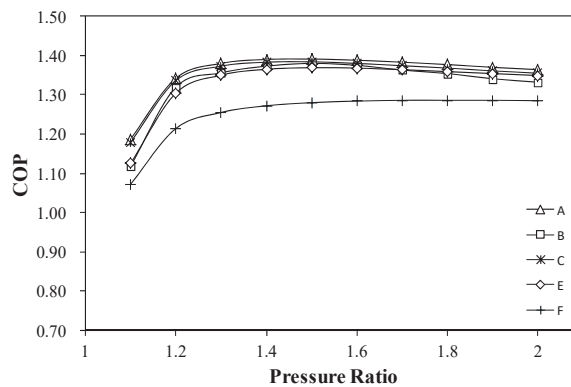
(**c**)

Figure 4. Variation of COP versus pressure ratio at 35 °C hot water temperature. (**a**) Ambient temperature of −15 °C. (**b**) Ambient temperature of −5 °C. (**c**) Ambient temperature of 5 °C.
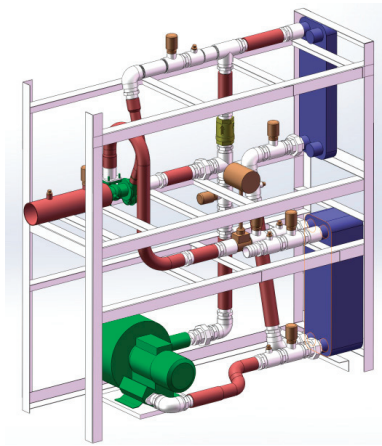
(**a**)
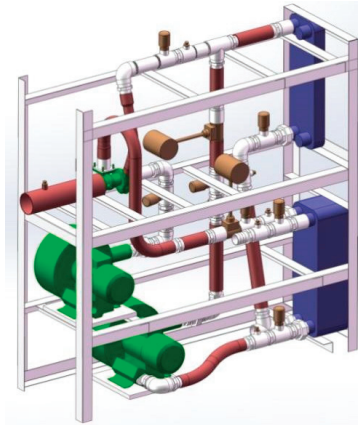
(**b**)

(**c**)

Figure 5. Diagrams of the test bench of the air-reversed Brayton heat pump with a turbocharger. (**a**) One-blower system. (**b**) Two-blower system. (**c**) Photograph of the air cycle heat pump system.
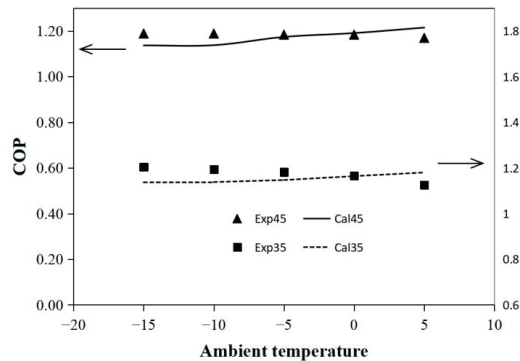
Figure 6. Comparison of calculation and experimental results under different conditions (45 °C/35 °C hot water temperature).

4. Conclusions

Six types of air-reversed Brayton heat pump system with turbochargers driven by blowers were proposed according to the location of the system in contact with the environment and the number and position of the blowers. The thermodynamic expressions of the heating COP and the corresponding turbine pressure ratio were derived and analyzed, respectively. The main conclusions were drawn as follows:

There is an optimal pressure ratio for each cycle. The optimal pressure ratio of the single-blower system is about 1.5–1.7, while that of the dual-blower system is about 1.8–1.9.

Cycle A (with a single blower before the compressor, open to the heat source side) and Cycle C (with a single blower after the compressor, open to the heat sink side) have the highest heating COPs and are worthy of more attention.

The theoretical results of Cycle F were in agreement with the experimental observations, with a maximum error of less than 5.6%.

5. Prospects

In this paper, the air-reversed Brayton heat pump was mainly used for a heating system. However, it can be applied under circumstances with a large temperature difference between the heat source and the sink, such as high-temperature water supply or cryogenic refrigeration, high-temperature drying, and combined heating with other heat pumps which meet the demands of different heating conditions and building functions. All these issues need to be further studied. In addition, it is necessary to consider the dynamic coupling characteristics between the building thermal environment and the air-reversed Brayton heat pump system, as well as the association between the energy consumption of the system and the building and climatic conditions throughout a whole year.

Author Contributions: Conceptualization, S.W.; methodology, S.W. and S.L.; investigation, S.L. and S.W.; writing—original draft preparation, S.L. and S.J.; writing—review and editing, S.W., S.L., S.J. and X.W. All authors have read and agreed to the published version of the manuscript.

Institutional Review Board Statement: Not applicable.

Informed Consent Statement: Not applicable.

Data Availability Statement: The data presented in this study are available on request from the corresponding author.

Conflicts of Interest: The authors declare no conflict of interest.

Nomenclature

Nomenclature

c_{P}	specific heat at constant pressure (J/kgK)	COP/EER	coefficient of performance
h	enthalpy (J/kg)	Q_{H}	heating capacity (W)
m	mass flow rate (kg/s)	Q_{C}	cooling capacity (W)
p	pressure (Pa)	T	temperature (°C/K)
R	gas constant (J/Kmol)	v	specific volume (m^3/kg)
W_{f}	blower energy consumption(W)		
Greek symbols		Subscripts	
η	effectiveness	c	compressor
θ	temperature ratio defined in Equation (11)	f	blower
ε_{r}	effectiveness of regenerator	e	expander; turbine
γ	a function of pressure ratio	s	isentropic

References

1. White, A.J. Thermodynamic analysis of the reversed Joule-Brayton cycle heat pump for domestic heating. *Appl. Energy* **2009**, *86*, 2443–2450. [CrossRef]
2. Braun, J.; Bansal, P.; Groll, E. Energy efficiency analysis of air cycle heat pump dryers. *Int. J. Refrig.* **2002**, *25*, 954–965. [CrossRef]
3. Park, S.K.; Ahn, J.H.; Kim, T.S. Off-design operating characteristics of an open-cycle air refrigeration system. *Int. J. Refrig.* **2012**, *35*, 2311–2320. [CrossRef]
4. Elland, H.X. Air Cycle Feasibility Using a Novel, Single Rotor Compander for Refrigeration and Heating. In Proceedings of the IIR International Rankine 2020 Conference-Heating, Cooling and Power Generation, Glasgow, UK, 27–31 July 2020.
5. Mundhra, R.; Mukhopadhyay, A. Thermodynamic analysis of irreversible reversed brayton cycle heat pump with finite capacity finite conductance heat reservoirs. In *Advances in Mechanical Engineering. Lecture Notes in Mechanical Engineering*; Biswal, B., Sarkar, B., Mahanta, P., Eds.; Springer: Singapore, 2020; pp. 763–775.
6. ASHRAE. *Cogeneration Systems and Engine and Turbine Drives*; ASHRAE: Atlanta, GA, USA, 2000.
7. Wang, S.G. Air Cycle Heat Pumps. In *Handbook of Energy Systems in Green Buildings*; Springer: Berlin/Heidelberg, Germany, 2018.
8. Bi, Y.H.; Chen, L.G.; Sun, F.R. Exergy-based ecological optimization for an endoreversible variable-temperature heat reservoir air heat pump cycle. *Rev. Mex. Fis.* **2009**, *55*, 112–119.
9. Bi, Y.H.; Chen, L.G.; Sun, F.R. Heating load, heating load density and COP optimisations for an endoreversible variable temperature heat reservoir air heat pump. *J. Energy Inst.* **2009**, *82*, 43–47. [CrossRef]
10. Bi, Y.H.; Chen, L.G.; Sun, F.R. Exergetic efficiency optimization for an irreversible heat pump working on reversed Brayton cycle. *Pramana* **2010**, *74*, 351–363. [CrossRef]
11. Bi, Y.H.; Chen, L.G.; Sun, F.R. Heating load density optimization of an irreversible simple Brayton cycle heat pump coupled to counter-flow heat exchangers. *Appl. Math. Model.* **2012**, *36*, 1854–1863. [CrossRef]
12. Chen, L.G.; Ni, N.; Sun, F.; Wu, C. Performance of real regenerated air heat pumps. *Int. J. Power Energy Syst.* **1999**, *19*, 231–238.
13. Zhang, C.L.; Yuan, H. An important feature of air heat pump cycle: Heating capacity in line with heating load. *Energy* **2014**, *72*, 405–413. [CrossRef]
14. Yuan, H.; Zhang, C.L. Regenerated air cycle potentials in heat pump applications. *Int. J. Refrig.* **2015**, *51*, 1–11. [CrossRef]
15. Yang, Y.; Yuan, H.; Peng, J.W.; Zhang, C.L. Performance modeling of air cycle heat pump water heater in cold Climate. *Renew. Energy* **2015**, *87*, 1067–1075. [CrossRef]
16. Dieckmann, J.; Erickson, A.; Harvey, A.; Toscano, W. *Research and Development of an Air-Cycle Heat-Pump Water Heater*; Foster-Miller Associates, Inc.: Waltham, MA, USA, 1979; pp. 1–341.
17. Edwards, T.C.; McDonald, A.T. *ROVACS: A New Rotary-Vane-Cycle Air-Conditioning and Refrigeration System*; 720079; S.A.E.: Warrendale, PA, USA, 1972.
18. Edwards, T.C. *The Rovac Automotive Air Conditioning System*; 750403; S.A.E.: Warrendale, PA, USA, 1975.
19. TNO. *Cooling, Freezing and Heating with the Air Cycle, Documentation Sheet*; TNO Environment. Energy and Process Innovation, Department of Refrigeration and Heat Pump Technology: Apeldoorn, The Netherlands, 2003.
20. Spence, S.W.T.; Doran, W.J.; Artt, D.W. Design, construction and testing of an air-cycle refrigeration system for road transport. *Int. J. Refrig.* **2004**, *27*, 503–510. [CrossRef]
21. Spence, S.W.T.; Doran, W.J.; Artt, D.W.; McCullough, G. Performance analysis of a feasible air-cycle refrigeration system for road transport. *Int. J. Refrig.* **2005**, *28*, 381–388. [CrossRef]
22. Catalano, L.A.; Bellis, F.D.; Amirante, R. Improved inverse Joule Brayton air cycle using turbocharger units. In Proceedings of the Conference on Thermal and Environmental Issues in Energy Systems, Sorrento, Italy, 6–19 May 2010; pp. 16–19.
23. Catalano, L.A.; Bellis, F.D.; Amirante, R. Development and testing of sustainable refrigeration plants. In Proceedings of the ASME Turbo Expo, Vancouver, BC, Canada, 6–10 June 2011; pp. 1–8.
24. Li, S.S.; Wang, S.G.; Ma, Z.J. Using an air cycle heat pump system with a turbocharger to supply heating for full electric vehicles. *Int. J. Refrig.* **2017**, *77*, 11–19. [CrossRef]

25. Li, S.S.; Wang, S.G.; Ma, Z.J. Performance analysis of an air cycle heat pump system with a turbocharger driven by a blower. *Procedia Eng.* **2017**, *205*, 2720–2727.
26. Li, S.S.; Wang, S.G.; Ma, Z.J.; Zhang, C.L. Experimental investigation of a regenerated air cycle heat pump heating system with a turbocharger. *Int. J. Refrig.* **2019**, *100*, 48–54. [CrossRef]
27. Zhang, C.L.; Yuan, H.; Cao, X. New insight into regenerated air heat pump cycle. *Energy* **2015**, *91*, 226–234. [CrossRef]

The Impact of Building Orientation and Window-to-Wall Ratio on the Performance of Electrochromic Glazing in Hot Arid Climates: A Parametric Assessment

Imene Lahmar [1], Alessandro Cannavale [2,3,*], Francesco Martellotta [2] and Noureddine Zemmouri [1]

[1] Laboratoire LACOMOFA, University of Mohamed Khider, Biskra 07000, Algeria; i.lahmar@univ-biskra.dz (I.L.); pr.zemmouri@gmail.com (N.Z.)
[2] DICAr—Politecnico di Bari, Via Orabona 4, 70125 Bari, Italy; francesco.martellotta@poliba.it
[3] National Research Council, Institute of Nanotechnology (CNR-NANOTEC), Via Monteroni, 73100 Lecce, Italy
* Correspondence: alessandro.cannavale@poliba.it

Abstract: The significant increase in construction industry demand with its negative effects on energy consumption is particularly evident in areas with severe climatic factors. Here, the designers aim at providing comfort with the least amount of energy, and consequently have resorted to using different software tools to choose the optimal solution in the early phase of design to avoid time and cost losses. The use of smart innovative technologies such as electrochromic (EC) glazing may provide an important contribution in reducing consumptions while providing good thermal and visual comfort conditions. Nonetheless, as shown in the literature, such glazing should be used and managed carefully to avoid any adverse effects or low performance. Thus, a parametric simulation was carried out using Rhinoceros and Grasshopper to assess the advantages in terms of energy use resulting from use of EC glazing in residential buildings as a function of façade orientation and window-to-wall ratio (WWR) with reference to the city of Biskra, located in the northeastern region of Algeria. Eight main orientations and ten WWR scenarios were investigated in order to evaluate the benefit of using this technology in the selected climatic region. The research results proved the benefit of using EC glazing in all orientations, with energy savings ranging from 35.88% in the northern façade to 60.47% in the southwestern façade.

Keywords: parametric simulation; orientation; energy performance; hot and arid climate; solar irradiation; window–wall ratio; electrochromic glazing

1. Introduction

Two compelling challenges of current times are the timely fight against climate changes and fossil fuels dependency. Since the construction sector is responsible for 35% of worldwide CO_2 emissions [1], and residential buildings in Algeria consume approximately 33.6% of total electricity demand [2], an adequate choice of building materials envelope can play a major role in minimizing the negative impacts of unsustainable energy resources on the environment. The largest effects in terms of reduction of energy consumption of buildings can be obtained by improving the weakest link in the building envelope: the windows. In hot climates, the window-to-wall ratio was determined to be the most important indicator of total load, particularly for cooling loads, whereas it was negligible for heating loads [3].

Among the diverse solutions that can be used to control window behavior, one of the most promising is represented by dynamic smart windows based on EC glazing (Figure 1). An EC glazing is a device resembling an electrical battery, generally including five superimposed layers, between two glass or plastic substrates, covered with transparent conductive oxides (e.g., indium tin oxide or fluorine-doped tin oxide): the middle layer is a transparent electrolyte (containing small cations, such as lithium or hydrogen ions). This layer is in direct contact with at least one EC material and an ion accumulation layer, or a

further EC layer [4,5]. The most widely investigated EC materials are inorganic transition metal oxides, such as tungsten trioxide (WO_3) or nickel oxide (NiO).
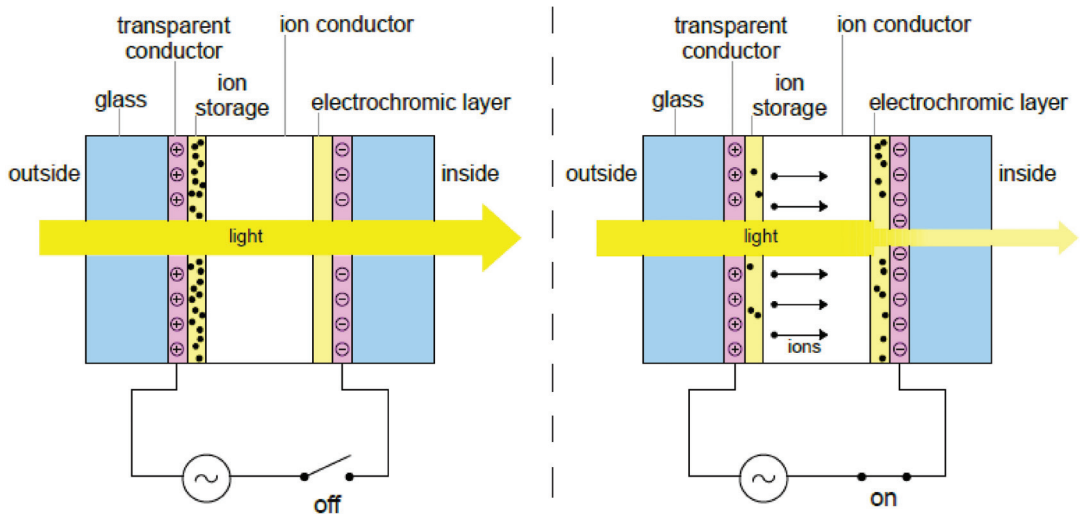

Figure 1. Electrochromic glazing schematic diagram.

The former is a cathodic EC material, because it reversibly colors upon electron insertion and ion intercalation, by applying a small bias, in a redox reaction. Anodic EC materials, such as NiO, show a "complementary" behavior, because they color upon charge extraction and ion deintercalation. Moreover, they effectively work as ion storage layers when devices are bleached. Due to their behavior, upon ion intercalation/deintercalation, these two materials have been often used jointly to enhance visual contrast of EC devices [6,7].

Several organic EC materials are also reported in literature, such as polyaniline, viologens, poly (3, 4- ethylenedioxythiophene)-poly (styrenesulfonate) (PEDOT: PSS) [8].

Different manufacturing processes have been used in the fabrication of EC devices (Table 1), where the main aspects are the EC materials and the deposition of the ion accumulation material onto a transparent electrode. These depositions can be made either in liquid, vapor, or solid phase [9].

According to Jud Einstein et al., the sol–gel process was firstly used in the fabrication of EC devices in 1988. It is a chemical solution process that is one of the simplest techniques, compatible with spraying, spin-coating, and dip-coating deposition [10].

In comparison to sol–gel, other techniques that are widely used, but have more advantageous characteristics (Table 1), are the physical and chemical vapor depositions, that take place under vacuum conditions [11].

Physical vapor deposition is a vaporization coating method in which a solid material is heated to produce vapors that cover the surface of the substrate [12]. In chemical vapor deposition, the precursor heated is in gaseous form and reacts chemically [13].

Table 1. Advantages and disadvantages of fabrication processes for electrochromic devices.

Processes	Advantages	Disadvantages	References
Electrode position	- Economical and versatile process - Can be performed under atmospheric pressure - Large deposition areas are possible	Material preparation and post-processes (drying, annealing) require: - Toxic chemicals - Relatively high temperatures - Long process times	[14–16]
Sol–gel	- Easy control of the microstructure and composition at relatively low temperatures - Simple and low-cost equipment - Can be performed under atmospheric pressure	- Weak bonding - Difficulty in controlling porosity - Mismatch of cracks from thermal expansion with the substrate	[10,17–19]
Spray pyrolysis	- Cost-effective - Large area - Thin films - Can be performed under atmospheric pressure	- Slow deposition rate - Wastage of solution	[20–22]
Chemical vapor deposition (CVD)	- High-purity films - High deposition rate	- Requires volatile precursors - Maximum process temperature can reach over 1000 °C	[11,13,23,24],
Physical vapor deposition (PVD)	- Thin film - Low contamination - Controlling film deposition rates	- Expensive	[11,12,25–27]
Sputtering	- Widely used - Deposition at room temperature - Magnetron and pulsed magnetron sputtering processes were developed to improve the deposition rate	- Some processes require high vacuum and temperature	[28–30]
Nanoparticle deposition system (NPDS)	- Under dry conditions - Uses room temperature - Under low vacuum conditions - Relatively simple and low-cost process	- Performance and durability have not yet been verified sufficiently by other researchers in this area	[31–34]

Several research activities state the importance of window orientation, type of glazing, and window-to-wall ratio (WWR) for the energy efficiency of buildings. A study conducted by Mehaoued and Lartigue [35] in Algeria showed that in hot regions, augmenting the WWR led to a rise in the cooling demand caused by an increase in the temperature of the air surrounding the building due to multiple reflections of the heat flux. In the same context, Leskovar et al. [36] found that the impact of increasing WWR is less critical in the north than in the south orientation.

Hassouneh et al. [37] studied the impact of eight types of window glazing on thermal behavior of an apartment located at latitude 32 °N in Amman. The results indicated that a larger window with clear glass facing east, west, and south reduces heating load.

According to Friess et al. [38], in hot climates, the building orientation is the first factor that must be taken into account in passive design.

Yang et al. [39] studied the impact of WWR on the heating and cooling energy consumption of residential buildings in the hot summer and cold winter zone in China. They reported that the most important parameters for determining the optimum WWR are air conditioning system, window orientation, and glazing types.

Qiong et al. [40] tested twenty types of glazing, in three different Chinese climates, using Design Builder software. It was found that 6 mm double-glazed units (equipped with tinted glass panes) embodying 13 mm air interspace showed advantages in a climate characterized by hot summer and cold or warm winter, compared to single glazing and double-glazed units filled with argon, which was more expensive, while the same glazing (without tinting) was more suitable in cold climate.

Sibilio et al. [41] concluded—in their review paper dealing with smart windows for residential applications—that when using EC glazing, the energy saving may range from

39% to 59% compared to conventional static glazing, depending on the building orientation, climatic conditions, and control strategy.

Piccolo et al. [42] used an experimental and theoretical model to investigate the behavior of EC glazing based on WO_3 in a cooling-dominated climate. The results showed that the performance of EC glazing in dynamic mode was comparable to that of low-emissivity double glazing (about 31% savings) in comparison with clear glass.

Another study [43], based on EnergyPlus dynamic simulation software, was conducted in an office building located in Milan, with the goal of determining the best option among three different types of glazing (EC glazing, common glass, and one equipped with an external venetian blind system), as compared to standard glazing. EC glazing decreased energy consumption by 39.5% and by 26.2% when using an external venetian blind device.

Using the same software as Ref. [43], Cannavale et al. [44] compared the efficiency of innovative solid-state EC devices with transparent glazing in commercial buildings in three different locations (Rome, London, and Aswan): the best scenario was discovered in Rome, using innovative EC devices, with energy savings ranging from 20.7% to 28.7%.

A study using the eQuest building simulation tool [45] analyzed three different United States climate zones; the model was a commercial office building with 60% WWR, according to a comparison of static and EC glazing efficiency: energy savings of up to 45% were observed in various climate zones.

Aldawoud [46] also analyzed the effect of EC glazing on building energy consumption in a hot and dry climate, using Design Builder software to compare EC glazing to various glazing types. The reduction in solar heat gains varied from 53% to 59%.

According to Piccolo et al. [47], the performance of EC glazing in residential buildings has been investigated in a few simulation studies, one of which was conducted in a cooling dominated climate, using Grasshopper software. The results show that larger EC window openness area on the exterior can be used without affecting the energy [48].

Tavares et al. [49] used the ESP-r software to estimate the energy savings for heating and cooling in the case of using a commercial EC glazing in a Mediterranean climate. The case study was an old building in Portugal, which was simulated in various window orientations with different WWR and different control strategies (outdoor and indoor air temperature, solar irradiance); the results indicated that the energy savings ranged from 20.28 to 36.94 kWh/m^2 year (per square meter of glazed area), and the best saving was obtained in the west orientation.

According to previous studies, we observed that several interactive parameters affect the energy performance of buildings, and this point confirms the importance of using a parametric approach to simulate the building behavior. On the other hand, the lack of research on the impact of using EC glazing in Northern Africa, as well as the absence of building energy regulations in Algeria, complicate the choice of designers, hence the importance of highlighting the performance of such new technology in this country.

2. Materials and Methods

2.1. Climatic Condition

The case study of this work was located in the northeast part of the Algerian desert, at latitude 34.80 °N, longitude 5.73 °E, and an altitude of 82 m above sea level, classified as a hot and dry climate according to Köppen–Geiger classification [50].

Climatic data were taken from the international weather for energy calculations database for the location of Biskra [51], where the climate is influenced by solar radiation, given in Figure 2b, that represents a summary of the different monthly average solar irradiation values for different exposures.
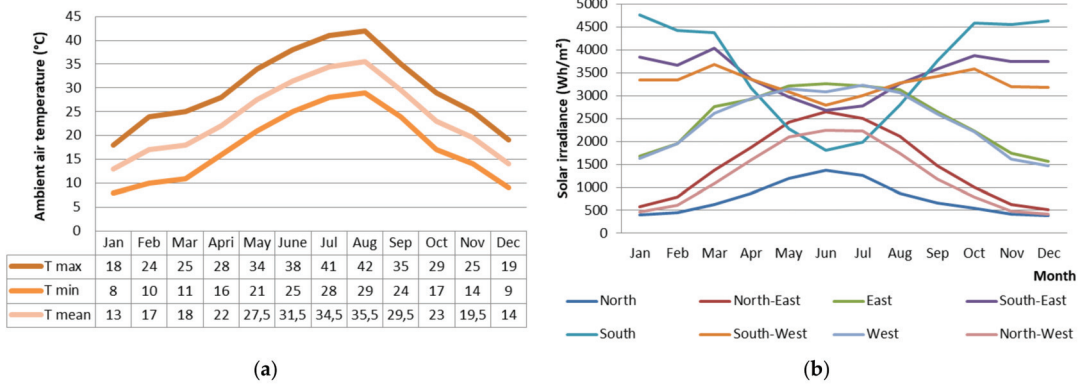
Figure 2. (**a**) Ambient air temperature (°C). (**b**) Incident global irradiation on a vertical plane.

According to the ambient air temperature of the city of Biskra shown in Figure 2a, the period from June to September represents the hot season with average maximum temperature of 35.5 °C and minimum of 29.5 °C, respectively; the hottest month is August, with an average maximum temperature of 42 °C and minimum temperature of 29 °C. While the cool season extends from the second half of November to the first week of March, with an average maximum of 19.5 °C and minimum of 13 °C, the coldest month is January, with an average maximum of 18 °C and minimum of 8 °C.

2.2. Building Description

In the present study, the building context was a typical residential project located in the city of Biskra consisting of four floors, each one hosting two apartments, composed of two bedrooms, kitchen, bathroom, hall, and a living room; based on the Algerian national office of statistics [52], it represents a typical apartment in collective housing model in Algeria.

The case study deals with a southwest-oriented living room with 8.5% Window-to-Wall Ratio (WWR) and a surface area of 19.09 m², representing about a quarter of the apartment total area (80 m²), located on the ground floor (Figure 3).
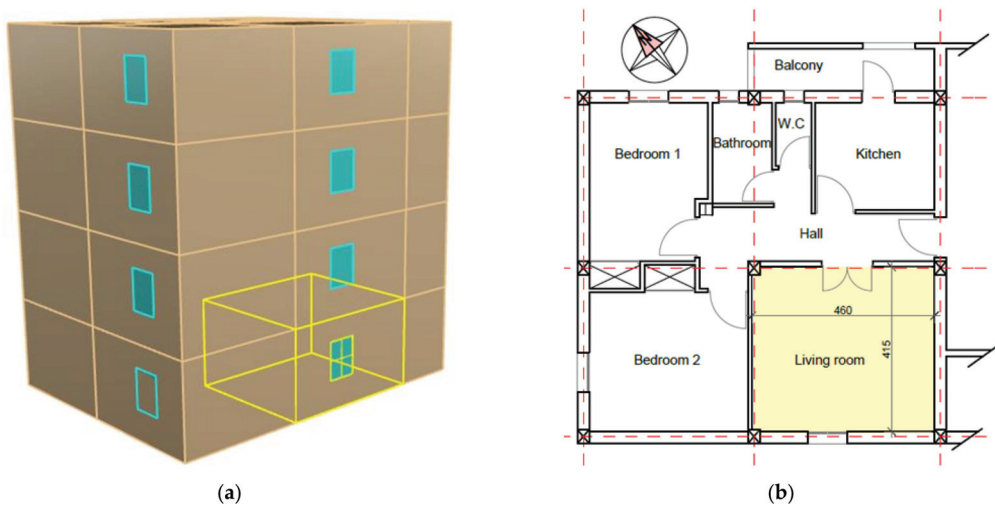
Figure 3. Case study (**a**) 3D and (**b**) plan.

Based on typical characteristics of similar buildings, the material specifications of the boundaries of the space to be analyzed were defined and are listed in Table 2. As said above, there is no building regulation in Algeria that gives reference values for U-values. The opaque building envelope data and characteristic have been fixed for all the case studies to appreciate the effect of glazing.

Table 2. Thermal characteristics of the building envelope.

	Materials Thickness	Thermal Properties U-Value (W/(m^2·K))	Front Mass (kg/m^2)
Exterior Wall	0.02 m cement plaster	1.14	329
	0.15 m hollow brick		
	0.05 m air barrier		
	0.1 m hollow brick		
	0.01 m coated plaster		
Interior Wall	0.01 m coated plaster	2.49	188
	0.1 m hollow brick		
	0.01 m coated plaster		
Roof	0.02 m flooring	2.42	537
	0.04 m mortar		
	0.16 m concrete blocks hollow		
	0.04 m concrete slab		
	0.01 m coated plaster		
Floor	0.15 m clay	2.25	809
	0.15 m stones of valley		
	0.04 m concrete slab		
	0.04 m mortar		
	0.02 m flooring		
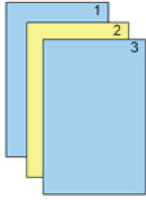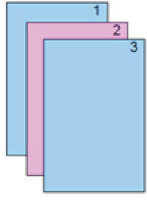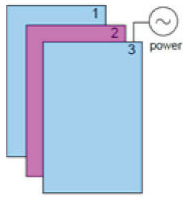
With reference to transparent elements (listed in Table 3), three different options were evaluated, assuming a laminated glazing based on the characteristics of the base case, and then it was compared to EC glazing to estimate the amount of energy saved when used in the real-life building.

Due to the significant differences in the properties of both glazing, an intermediate case (double vacuum glazing) was considered, taking into account the similarities between the double vacuum and the EC glazing in terms of thermal characteristics, cost, layer number, and pane glass thickness, with one exception: the thickness and materials of the space between panes.

As the EC glazing is significantly more expensive than the standard static glazing used, the vacuum glazing was chosen based on the comparable price range of 300 to 500 €/m^2 according to the market information in 2021 [53,54]. The high cost of both glazing is due to their manufacture processes, which both need high vacuum conditions.

For the EC glazing, it was assumed based on its commercial availability by the manufacturer Sage Glass [55], even though it is less efficient than other types of EC glazing. Moreover, all glazing properties were calculated using LBNL Window 7.5 [56].

Table 3. Thermal and optical characteristics of windows.

Windows		Laminated Glazing	Double Vacuum Glazing	EC Glazing
Structure diagram				
Materials thickness	Layer 1	3.1 mm clear glass	5.7 mm clear glass	5.7 mm clear glass
	Layer 2	1.05 mm PVB color film	0.1 mm vacuum	12 mm air space
	Layer 3	3.1 mm clear glass	5.7 mm clear glass	7 mm sage glass
Thermal and optical properties U-value (W/(m²·K))	U-value	5.64	2.2	1.9
	SHGC	0.65	0.70	0.44 (0.10)
	Tvis	0.68	0.78	0.64 (0.01)

2.3. Simulation Data

The main aim of the research is to assess the efficiency of EC glazing in reducing solar heat gain and providing new design alternatives without increasing energy consumption, in order to address the problem of limited building openness and orientation flexibility in hot climates.

There are two basic simulation tools for evaluating building energy performance: static, which uses a simple mathematical procedure, and dynamic, which uses circumstances that vary over time [57]. Recently, software based on parametric simulation has been developed, giving designers the ability to work out possible combinations between the different parameters, resulting in more variables. Another advantage of these tools is the possibility to use many plugins adding on the same platform; for example, Grasshopper links to Rhinoceros, Honeybee, EnergyPlus, Open studio, Ladybug, and Radiance [58].

In the present work, once the building and site specifications were defined, the model was implemented in Rhinoceros; afterwards, it was exported to Grasshopper.

In order to specify the zone properties, another plugin, named Ladybug, was used to identify the envelope materials used in the existing building and listed in Table 2, as well as to create the windows with the assigned ratio variation, with glazing properties (Table 3), calculated using LBNL Window 7.5 and then exported as an input data file.

In this step, all parameters were kept as in the reference building (Table 4) except the orientation, which was changed in eight different directions, with an increment of 45 degrees, with 0° corresponding to north, 90° to east, etc.

Because of the specific environmental conditions of the case study and in reference to literature review [59], the boundary conditions have been set as follows:

- 18 °C setpoint temperature for heating.
- 26 °C setpoint temperature for cooling.
- 300 lux limit for lighting (illuminance level).

Table 4. Boundary conditions for the base case.

Characteristics	Description of the Base Case
location	Biskra, Algeria 34.80° N/ 5.73° E/82 m
building azimuth	225° (southwest)
plan shape	rectangular 4.6 × 4.15 m
setpoint temperature for heating	18 °C
setpoint temperature for cooling	26 °C
limit for lighting	300 lux
occupied period	12 p.m.–12 a.m.
infiltration	0.0003 m^3/(s·m^2)
internal heat gain	1 Tv, 4 people, 2 LED lights
equipment load	5 W/m^2
lighting density	5 W/m^2
occupancy density	4 persons
weather file	EnergyPlus weather file
COP	2.7

The occupation period of the space has been defined as 12:00 to 24:00, according to the authors' own observations and to previous investigation [60]. Indeed, the living room as a main space in the apartment is used mostly in the afternoon after work or school for family gathering and for recreative and pleasure activities in the night, such as watching television, playing, reading studying, etc.

For the building infiltration, an average building was considered, with an infiltration rate of 0.0003 m^3/(s·m^2), the equipment load per area was supposed to be 5 W/m^2, and 5 W/m^2 for lighting density [61].

Ventilation was calculated according to the windows opening, assumed to be two hours a day from 9 a.m. to 11 a.m. in order to simulate a realistic window-opening behavior of occupants that are supposed to be four individuals.

Using Honeybee plugin, the city's weather data were imported as an EPW file from the international weather for energy calculations database [51].

The component "EP output" was used to control the type of calculation and results, analyzed in terms of cooling and heating, that were calculated assuming an "ideal loads air system" converted to equivalent electric energy by a COP of 2.7 [62], as well as in terms of electrical lighting and overall consumption.

Through a parametric simulation, the WWR was varied from 8.5% to 10% and then, with 10% steps, to 90%, thus including 10 alternatives, with three different types of glazing (Table 3), where the laminated glass was replaced by a double vacuum glazing and commercial EC glazing, controlled by the "interior illuminance" strategy that ensures a 300 lux target over a virtual sensor, located at the center of the zone, 2.8 m above the floor. The living room window was also rotated in eight different orientations, obtaining 240 scenarios, summarized in Figure 4.

The consumption of the base case was then compared to the other variants, which were normalized with reference to floor surface area to allow for greater generalization of results.

Figure 4. Energy consumption as a function of WWR, glazing window, and orientation for Cooling. Heating. Lighting. Overall consumption.

3. Results and Discussion

The electric energy consumption of the reference case with laminated glazing as a function of orientation and WWR (Figure 5) illustrates that minimizing the WWR decreases the energy consumption and the disparity between the different orientations.

Furthermore, when the WWR is less than 10%, the difference between the eight orientations is insignificant, due to the decrease in sun radiation entering the building, and the heat transfer from outside to inside, while in the case of WWR 90%, the difference between the north and southwest facades reaches 39.31 kWh/(m^2.y).

Due to the long hot season, the overall consumption is largely influenced by the cooling needs, with the maximum values corresponding to the SW exposure and minimum to the north exposure.
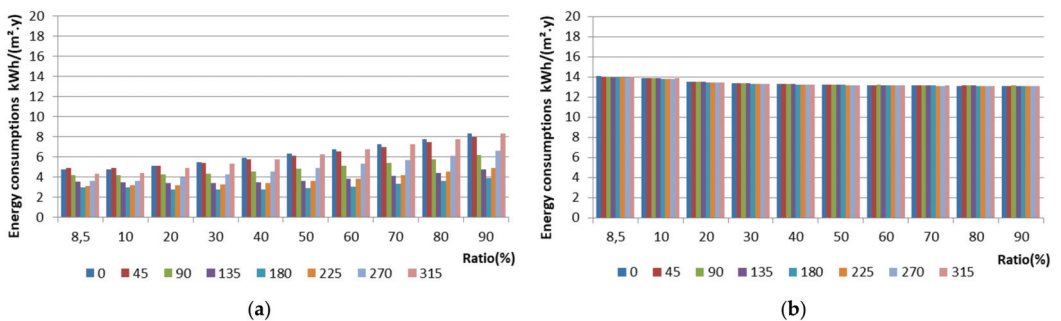
Figure 5. *Cont.*
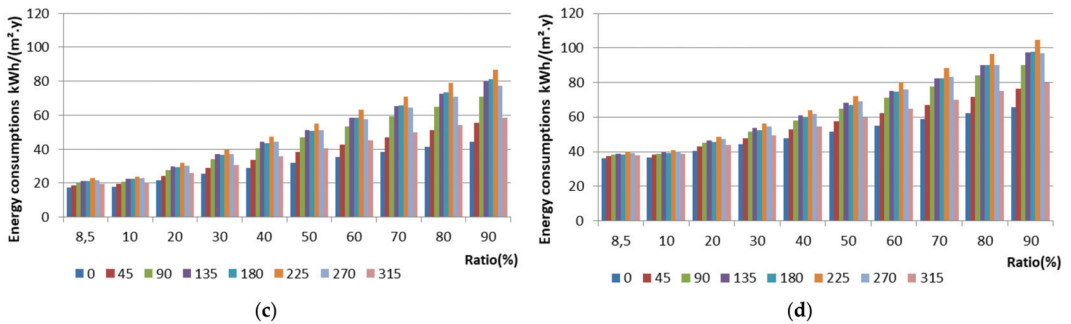
Figure 5. Electric energy consumptions for laminated glazing as a function of different orientations and WWR kWh/(m²·y). (**a**) Heating. (**b**) Lighting. (**c**) Cooling. (**d**) Overall consumptions.

It is clear from the results that the energy consumptions were affected by the solar irradiation (Figure 2b). The highest heating needs were found in the case of north orientation, which receives the least amount of irradiation for the whole year. On the other hand, the southwest façade receives convergent irradiation during the different seasons (maximum in spring, 3678.33 Wh/m², and autumn, 3579.66 Wh/m²), which increases the cooling needs periods.

In all the orientations, increasing the WWR decreases the lighting demand, while in the case of north orientation, the lighting needs are slightly higher because of the relatively minimum amount of irradiation. Moreover, all the other orientations have approximately the same lighting consumptions due to the type of building, where the majority of consumption occurs at night, therefore the natural lighting has a negligible effect compared to artificial lighting.

Figure 4 summarizes results from the investigated scenarios, showing that the highest energy consumption was found in the base case (laminated glazing), and for both alternative glazing, the results show a positive correlation between the WWR and the energy consumption. However, the increment is small compared to laminated glazing, due to a decrease in the amount of radiation entering the building.

Moreover, in the case of EC glazing, the disparity of cooling needs between different orientations is less than 3 kWh/(m²·y). This results from the combination of both reduced solar heat gain coefficient (SHGC) and visible light transmittance (T_{vis}) that characterize the EC glazing in its colored state, which greatly reduce the amount of thermal radiation entering the building. In fact, during the cooling season, increased daylight illuminance contributes to set the EC glazing in tinted status in most of the time.

On the other hand, it was found that using double vacuum glazing reduces heating needs (to nearly zero from WWR 70% up, in the south orientation). This is because the high SHGC combined with low thermal transmittance decreases heat loss. Consequently, an increase in cooling needs can be observed.

In terms of energy expenditures for artificial lighting, EC glazing increased the consumption, compared to the reference glazing. This increase was inversely related to the WWR, due to the decreasing sunlight entering the space, while the consumption decreases when using double vacuum glazing, because the T_{vis} of laminated glass is greater than T_{vis} of the former. This slight difference is a result of the material used in laminated glazing between the two glasses (this type of glass is widely used in residential buildings in Algeria). In addition, the use of lighting during night hours results in a slight difference of consumption between the different types of glazing.

Figures 6 and 7 report the amount of energy saved after using the EC glazing compared to the double vacuum glazing and the reference window, respectively.
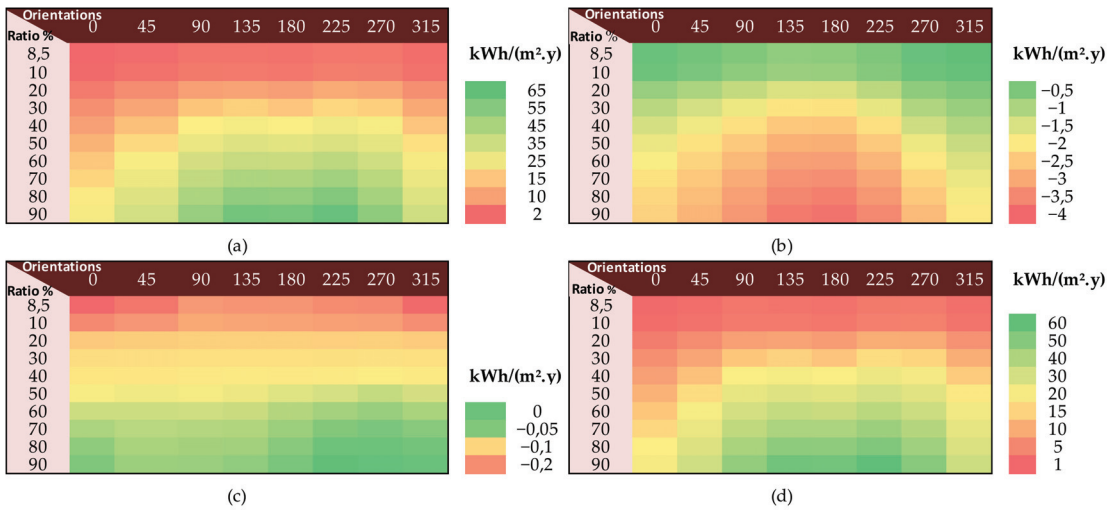
Figure 6. Variation in energy demand resulting from use of EC glazing instead of double glazing window, as a function of WWR and orientations for (**a**) cooling. (**b**) Heating. (**c**) Lighting. (**d**) Overall consumption. per unit area kWh/(m^2.y).
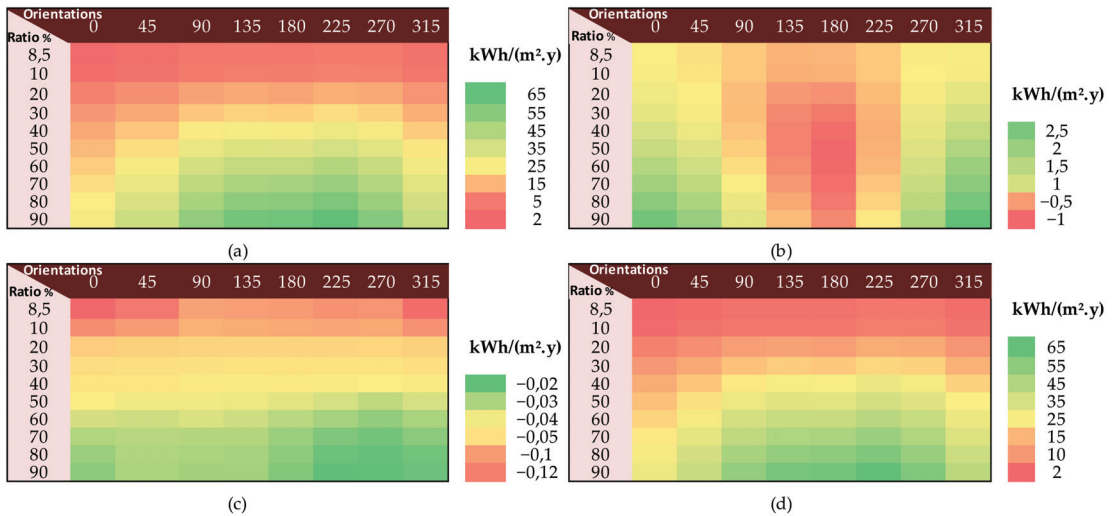

Figure 7. Variation in energy demand resulting from use of EC glazing instead of reference window, as a function of WWR and orientations for (**a**) Cooling. (**b**) Heating. (**c**) Lighting. (**d**) Overall energy consumption per unit area kWh/(m^2.y).

Either way, the improvement was higher in terms of cooling consumption (a), due to the long cooling season, which is why the EC glazing outperforms vacuum glazing in terms of overall consumption reduction (d), even though the vacuum glazing is more efficient in reducing the heating needs because of the high SHGC value.

In Figure 7b, which represents the variation in energy required for heating, a small increase was found in the south orientation, which receives the highest irradiation in December (4635 Wh/m^2), after using EC glazing as a result of reduced solar radiation

entering the space. Conversely, in the north orientation a slight decrease was found, thanks to the improved U-value of the EC glazing compared to simple laminated glazing.

Moreover, the best saving observed for overall consumption was about 62.87% compared to laminated glazing and about 60.47% compared to double vacuum glazing, which is consistent with previous research that found improvements up to 59% [41], while the findings are higher than the energy saving reported in [42] (31%), in [43] (39.5%), and in [44] (28.7%).

4. Conclusions

This research activity focuses on the energy savings that can be obtained using EC windows in residential buildings located in a hot arid climate. The chosen glazing has already been commercialized by a well-known manufacturer and we are strongly confident that using EC glazing with improved characteristics may yield even better results.

As a consequence of the yearly long period of overheating, the cooling is more important, and heating shows minimum loads.

Furthermore, the results led to some design recommendations; since the space function impacts the choice of orientation, it is recommended, in the case of laminated glazing, to orient the living room toward north with WWR up to 90 as it is a space that needs a panoramic view. This orientation also prevents the interference of intense luminance with the television; however, it may be oriented toward the south to ensure a warmer ambient in winter plus more of the natural light, without exceed WWR 50%, which has a similar overall consumption with WWR 90 north-facing.

Meanwhile, it is preferred to orient the bedroom toward the east so it obtains the advantage of facing the sunrise plus keeping it cool at the end of the day.

In the kitchen, the internal heat gains are high due to cooking, so north orientation is an adequate choice; however, the zone may be dimly lit; therefore, a double orientation northeast to southeast will increase the benefit of the natural light in the morning.

As the bathroom and garage do not require an outside view, a double northwest or southwest orientation choice will be sufficient.

The best advantage resulting from the use of EC glazing was found for the orientations with high solar radiation, where it allowed obtaining significant savings compared to laminate and double vacuum glazing.

The best improvement, compared to double vacuum glazing, was obtained in the case of WWR 90% for southwest facing windows, with 60.47% savings for overall yearly energy consumption, followed by south orientation with 59.85%, southeast orientation with 59.83%, west orientation with 55.81%, east orientation with 55.71%, northwest orientation with 45.89%, northeast orientation with 45.65%, and north orientation with 35.88%.

The results show that, starting from WWR 40%, in the case of laminated or vacuum glazing, the influence of orientation is greater than the influence of WWR. While in the case of EC glazing, the influence of WWR and orientations is negligible, due to the significant reduction in solar heat gain, thus solves the problem of limited WWR and orientation choices.

However, because of the relatively high cost of EC glazing, it is recommended that it be used when savings greater than a quarter of initial overall consumption are achieved, such as in the southwest orientation from WWR 20%, from 30% in southeast and south, from 50% in the northwest or east, or from 70% in the north or northeast.

The major limitation that obstructs large-scale market introduction of the EC glazing is the high cost of the production process that can be developed in the future to be less expensive, such as the (NPDS) process mentioned in the introduction. Even with the high cost, it is considered as a useful technology to reduce energy consumptions and, therefore, the environmental consequences obtained through CO_2 emission to the atmosphere.

At this stage, visual and thermal comfort parameters were not included in the analysis, although other studies show that EC may significantly contribute to improve it. However, it will be interesting for future research work on this subject to concentrate on parametric

optimization, in order to find a suitable balance between daylighting, thermal comfort, and energy consumption.

Nomenclature

EC	Electrochromic
CVD	Chemical vapor deposition
PVD	Physical vapor deposition
NPDS	Nanoparticle deposition system
WWR	Window-to-wall ratio
Low-e	Low emissivity
WO3	Tungsten trioxide
NiO	Nickel oxide
SHGC	Solar heat coefficient
Tvis	Visible light transmittance
U-values	Thermal transmittance
PVB	Polyvinyl butyral
EPW file	EnergyPlus weather file
IDF	Input data file
COP	Coefficient of performance

References

1. Gyamfi, S.; Krumdieck, S.; Urmee, T. Residential peak electricity demand response—Highlights of some behavioural issues. *Renew. Sustain. Energy Rev.* **2013**, *25*, 71–77. [CrossRef]
2. Van, L.P.; Malyavina, E.G.; Malikova, O.Y. Impact of Glass Window to Heat Load in Office Building in Different Climates. In *IOP Conference Series: Materials Science and Engineering*; IOP Publishing: Bristol, UK, 2021; Volume 1079, p. 042084. [CrossRef]
3. Chiffres Clés du Bilan Energetique de L'année 2017. Available online: https://www.energy.gov.dz/?article=bilan-energetique-national-du-secteur (accessed on 1 May 2022).
4. Granqvist, C.G. Recent progress in thermochromics and electrochromics: A brief survey. *Thin Solid Film.* **2016**, *614*, 90–96. [CrossRef]
5. Granqvist, C.G. Electrochromics for smart windows: Oxide-based thin films and devices. *Thin Solid Film.* **2014**, *564*, 1–38. [CrossRef]
6. Casini, M. Active dynamic windows for buildings: A review. *Renew. Energy* **2018**, *119*, 923–934. [CrossRef]
7. Piccolo, A.; Simone, F. Performance requirements for electrochromic smart window. *J. Build. Eng.* **2015**, *3*, 94–103. [CrossRef]
8. Monk, P.; Mortimer, R.; Rosseinsky, D. *Electrochromism and Electrochromic Devices*; Cambridge University Press: Cambridge, UK, 2007; Volume 1, pp. 1–24. [CrossRef]
9. Park, S.-I.; Quan, Y.-J.; Kim, S.-H.; Kim, H.; Kim, S.; Chun, D.-M.; Lee, C.S.; Taya, M.; Chu, W.-S.; Ahn, S.-H. A review on fabrication processes for electrochromic devices. *Int. J. Precis. Eng. Manuf.-Green Technol.* **2016**, *3*, 397–421. [CrossRef]
10. Pierre, A.C. *Introduction to Sol-Gel Processing*; Springer Science & Business Media: Cham, Switzerland, 2013; Volume 1.
11. Ilangovan, R.; Subha, V.; Ravindran, R.E.; Kirubanandan, S.; Renganathan, S. Nanomaterials: Synthesis, physicochemical characterization, and biopharmaceutical applications. In *Nanoscale Processing*; Elsevier: Amsterdam, The Netherlands, 2021; pp. 33–70.
12. Devasia, R.; Painuly, A.; Devapal, D.; Sreejith, K.J. Continuous fiber reinforced ceramic matrix composites. In *Fiber Reinforced Composites*; Woodhead Publishing: Sawston, UK, 2021; pp. 669–751.
13. Creighton, J.R.; Ho, P. Introduction to chemical vapor deposition (CVD). *Chem. Vap. Depos.* **2001**, *2*, 1–22.

14. Yuan, Y.F.; Xia, X.H.; Wu, J.B.; Chen, Y.B.; Yang, J.L.; Guo, S.Y. Enhanced electrochromic properties of ordered porous nickel oxide thin film prepared by self-assembled colloidal crystal template-assisted electrodeposition. *Electrochim. Acta* **2011**, *56*, 1208–1212. [CrossRef]

15. Sonavane, A.C.; Inamdar, A.I.; Shinde, P.S.; Deshmukh, H.P.; Patil, R.S.; Patil, P.S. Efficient electrochromic nickel oxide thin films by electrodeposition. *J. Alloy. Compounds* **2010**, *489*, 667–673. [CrossRef]

16. Zhang, J.; Tu, J.P.; Cai, G.F.; Du, G.H.; Wang, X.L.; Liu, P.C. Enhanced electrochromic performance of highly ordered, macroporous WO₃ arrays electrodeposited using polystyrene colloidal crystals as template. *Electrochim. Acta* **2013**, *99*, 1–8. [CrossRef]

17. Zarzycki, J. Past and present of sol-gel science and technology. *J. Sol-Gel Sci. Technol.* **1997**, *8*, 17–22. [CrossRef]

18. Scherer, G.W. Sintering of sol-gel films. *J. Sol-Gel Sci. Technol.* **1997**, *8*, 353–363. [CrossRef]

19. Dimitriev, Y.; Ivanova, Y.; Iordanova, R. History of sol-gel science and technology. *J. Univ. Chem. Technol. Metall.* **2008**, *43*, 181–192. [CrossRef]

20. Mukherjee, R.; Sahay, P.P. Improved electrochromic performance in sprayed WO₃ thin films upon Sb doping. *J. Alloy. Compd.* **2016**, *660*, 336–341. [CrossRef]

21. Mousavi, M.; Kompany, A.; Shahtahmasebi, N.; Bagheri-Mohagheghi, M.M. The effect of solution concentration on the physical and electrochemical properties of vanadium oxide films deposited by spray pyrolysis. *J. Semicond.* **2013**, *34*, 103001. [CrossRef]

22. Bertus, L.M.; Enesca, A.; Duta, A. Influence of spray pyrolysis deposition parameters on the optoelectronic properties of WO₃ thin films. *Thin Solid Film.* **2012**, *520*, 4282–4290. [CrossRef]

23. Obraztsov, A.N.; Obraztsova, E.A.; Tyurnina, A.V.; Zolotukhin, A.A. Chemical vapor deposition of thin graphite films of nanometer thickness. *Carbon* **2007**, *45*, 2017–2021. [CrossRef]

24. Chandrakala, M.; Bharath, S.R.; Maiyalagan, T.; Arockiasamy, S. Synthesis, crystal structure and vapour pressure studies of novel nickel complex as precursor for NiO coating by metalorganic chemical vapour deposition technique. *Mater. Chem. Phys.* **2017**, *201*, 344–353. [CrossRef]

25. Chiu, P.K.; Chiang, D.; Lee, C.T.; Hsiao, C.N.; Yang, J.R.; Cho, W.H.; Huang, C.L. Investigation of the Microstructure, Porosity, Adhesion, and Optical Properties of a WO₃ Film Fabricated Using an E-Beam System with Ion Beam-Assisted Deposition. *IEEE Trans. Magn.* **2014**, *50*, 3500204. [CrossRef]

26. Selvakumar, N.; Barshilia, H.C. Review of physical vapor deposited (PVD) spectrally selective coatings for mid-and high-temperature solar thermal applications. *Sol. Energy Mater. Sol. Cells* **2012**, *98*, 1–23. [CrossRef]

27. Tajima, K.; Yamada, Y.; Okada, M.; Yoshimura, K. Fabrication study of proton injection layer suitable for electrochromic switchable mirror glass. *Thin Solid Film.* **2010**, *519*, 934–937. [CrossRef]

28. Kubo, T.; Nishikitani, Y.; Sawai, Y.; Iwanaga, H.; Sato, Y.; Shigesato, Y. Electrochromic properties of Li x Ni y O films deposited by RF magnetron sputtering. *J. Electrochem. Soc.* **2009**, *156*, 629. [CrossRef]

29. Chu, C.H.; Wu, H.W.; Huang, J.L. Novel WO₃-Based Electrochromic Device for High Optical Modulation and Infrared Suppression. *IEEE Electron Device Lett.* **2015**, *36*, 256–258. [CrossRef]

30. Tajima, K.; Yamada, Y.; Okada, M.; Yoshimura, K. Accelerated degradation studies on electrochromic switchable mirror glass based on magnesium–nickel thin film in simulated environment. *Sol. Energy Mater. Sol. Cells* **2010**, *94*, 1716–1722. [CrossRef]

31. Kim, H.; Park, Y.; Choi, D.; Ahn, S.H.; Lee, C.S. Novel fabrication of an electrochromic antimony-doped tin oxide film using a nanoparticle deposition system. *Appl. Surf. Sci.* **2016**, *377*, 370–375. [CrossRef]

32. Kim, M.S.; Chun, D.M.; Choi, J.O.; Lee, J.C.; Kim, Y.H.; Kim, K.S.; Ann, S.H. Dry-spray deposition of TiO2 for a flexible dye-sensitized solar cell (DSSC) using a nanoparticle deposition system (NPDS). *J. Nanosci. Nanotechnol.* **2012**, *12*, 3384–3388. [CrossRef]

33. Chun, D.M.; Kim, C.S.; Choi, J.O.; Lee, G.Y.; Lee, C.S.; Ahn, S.H. Multilayer deposition of ceramic and metal at room temperature using nanoparticle deposition system (NPDS) and planarization process. *Int. J. Adv. Manuf. Technol.* **2014**, *72*, 41–46. [CrossRef]

34. Kim, H.; Yang, S.; Ahn, S.H.; Lee, C.S. Effect of particle size on various substrates for deposition of NiO film via nanoparticle deposition system. *Thin Solid Film.* **2016**, *600*, 109–118. [CrossRef]

35. Mehaoued, K.; Lartigue, B. Influence of a reflective glass façade on surrounding microclimate and building cooling load: Case of an office building in Algiers. *Sustain. Cities Soc.* **2019**, *46*, 101443. [CrossRef]

36. Leskovar, V.Ž.; Premrov, M. An approach in architectural design of energy-efficient timber buildings with a focus on the optimal glazing size in the south-oriented façade. *Energy Build.* **2011**, *43*, 3410–3418. [CrossRef]

37. Hassouneh, K.; Alshboul, A.; Al-Salaymeh, A. Influence of windows on the energy balance of apartment buildings in Amman. *Energy Convers. Manag.* **2010**, *51*, 1583–1591. [CrossRef]

38. Friess, W.A.; Rakhshan, K. A review of passive envelope measures for improved building energy efficiency in the UAE. *Renew. Sustain. Energy Rev.* **2017**, *72*, 485–496. [CrossRef]

39. Yang, Q.; Liu, M.; Shu, C.; Mmereki, D.; Hossain, U.; Zhan, X. Impact analysis of window-wall ratio on heating and cooling energy consumption of residential buildings in hot summer and cold winter zone in China. *J. Eng.* **2015**, *2015*, 538254. [CrossRef]

40. He, Q.; Ng, S.T.; Hossain, M.; Skitmore, M. Energy-efficient window retrofit for high-rise residential buildings in different climatic zones of China. *Sustainability* **2019**, *11*, 6473. [CrossRef]

41. Sibilio, S.; Rosato, A.; Scorpio, M.; Iuliano, G.; Ciampi, G.; Vanoli, G.P.; de Rossi, F. A review of electrochromic windows for residential applications. *Int. J. Heat Technol.* **2016**, *34*, S481–S488. [CrossRef]

42. Piccolo, A. Thermal performance of an electrochromic smart window tested in an environmental test cell. *Energy Build.* **2010**, *42*, 1409–1417. [CrossRef]
43. Aste, N.; Compostella, J.; Mazzon, M. Comparative energy and economic performance analysis of an electrochromic window and automated external venetian blind. *Energy Procedia* **2012**, *30*, 404–413. [CrossRef]
44. Cannavale, A.; Martellotta, F.; Cossari, P.; Gigli, G.; Ayr, U. Energy savings due to building integration of innovative solid-state electrochromic devices. *Appl. Energy* **2018**, *225*, 975–985. [CrossRef]
45. Sbar, N.L.; Podbelski, L.; Yang, H.M.; Pease, B. Electrochromic dynamic windows for office buildings. *Int. J. Sustain. Built Environ.* **2012**, *1*, 125–139. [CrossRef]
46. Aldawoud, A. Conventional fixed shading devices in comparison to an electrochromic glazing system in hot, dry climate. *Energy Build.* **2013**, *59*, 104–110. [CrossRef]
47. Piccolo, A.; Marino, C.; Nucara, A.; Pietrafesa, M. Energy performance of an electrochromic switchable glazing: Experimental and computational assessments. *Energy Build.* **2018**, *165*, 390–398. [CrossRef]
48. Lahmar, I.; Zemmouri, N.; Cannavale, A.; Martellotta, F. Investigating the impact of electrochromic glazing on energy performance in hot arid climate using parametric design. In *IOP Conference Series: Materials Science and Engineering*; IOP Publishing: Bristol, UK, 2019; Volume 609, p. 062027. [CrossRef]
49. Tavares, P.F.; Gaspar, A.R.; Martins, A.G.; Frontini, F. Evaluation of electrochromic windows impact in the energy performance of buildings in Mediterranean climates. *Energy Policy* **2014**, *67*, 68–81. [CrossRef]
50. Kottek, M.; Grieser, J.; Beck, C.; Rudolf, B.; Rubel, F. World map of the Köppen-Geiger climate classification updated. *Meteorol. Z.* **2006**, *15*, 259–263. [CrossRef]
51. EPW File. Available online: https://climate.onebuilding.org/WMO_Region_1_Africa/DZA_Algeria/index.html (accessed on 1 May 2022).
52. Hadjij, C. Famille, logement, propriété à Alger. *Insaniyat. Rev. Algérienne D'anthropologie Et De Sci. Soc.* **1998**, *4*, 99–107. [CrossRef]
53. Vacuum Glazing. Available online: https://www.vacuum-glass.com/vacuum-insulating-glass-price-costs/ (accessed on 14 May 2022).
54. Will Smart Glass come to windows and doors? Available online: https://www.aluminiumtradesupply.co.uk/12549/will-smart-glass-come-windows-doors/ (accessed on 14 May 2022).
55. SageGlass. Available online: https://www.sageglass.com/en/products/sageglass (accessed on 14 May 2022).
56. LBNL Window 7.5. Available online: https://windows.lbl.gov/tools/window/software-download (accessed on 14 May 2022).
57. Lomas, K.J. Empirical validation of building energy simulation programs. *Fuel Energy* **1997**, *26*, 253–275. [CrossRef]
58. Toutou, A.; Fikry, M.; Mohamed, W. The parametric based optimization framework daylighting and energy performance in residential buildings in hot arid zone. *Alex. Eng. J.* **2018**, *57*, 3595–3608. [CrossRef]
59. Silvero, F.; Rodrigues, F.; Montelpare, S. A parametric study and performance evaluation of energy retrofit solutions for buildings located in the hot-humid climate of Paraguay—sensitivity analysis. *Energies* **2019**, *12*, 427. [CrossRef]
60. Bre, F.; Silva, A.S.; Ghisi, E.; Fachinotti, V.D. Residential building design optimisation using sensitivity analysis and genetic algorithm. *Energy Build.* **2016**, *133*, 853–866. [CrossRef]
61. Handbook, A.F. *Chapter 31: Energy Estimating and Modeling Methods*; American Society of Heating, Refrigerating, and Air-Conditioning Engineers: Atlanta, GA, USA, 2001.
62. Al-Saadi, S.N.; Al-Hajri, J.; Sayari, M.A. Energy-efficient retrofitting strategies for residential buildings in hot climate of Oman. *Energy Procedia* **2017**, *142*, 2009–2014. [CrossRef]

An Innovative Modelling Approach Based on Building Physics and Machine Learning for the Prediction of Indoor Thermal Comfort in an Office Building

Giovanni Tardioli [1],*, Ricardo Filho [1], Pierre Bernaud [2] and Dimitrios Ntimos [1]

[1] Integrated Environmental Solutions R&D, D01 Dublin, Ireland; ricardo.filho@iesve.com (R.F.); dimitrios.ntimos@iesve.com (D.N.)

[2] Laboratoire d'Innovation pour les Technologies des Energies Nouvelles et les Nanomatériaux (CEA-LITEN), Department of Solar Energy, 73370 Le Bourget-du-Lac, France; pierre.bernaud@cea.fr

* Correspondence: giovanni.tardioli@iesve.com; Tel.: +353-861075116

Abstract: The estimation of indoor thermal comfort and the associated occupant feedback in office buildings is important to provide satisfactory and safe working environments, enhance the productivity of personnel, and to reduce complaints. The assessment of thermal comfort is a difficult task due to many environmental, physiological, and cultural variables that influence occupants' thermal perception and the way they judge their working environment. Traditional physics-based methods for evaluating thermal comfort have shown shortcomings when compared to actual responses from the occupants due to the incapacity of these methods to incorporate information of various natures. In this paper, a hybrid approach based on machine learning and building dynamic simulation is presented for the prediction of indoor thermal comfort feedback in an office building in Le Bour-get-du-Lac, Chambéry, France. The office was equipped with Internet of Things (IoT) environmental sensors. Occupant feedback on thermal comfort was collected during an experimental campaign. A calibrated building energy model was created for the building. Various machine learning models were trained using information from the occupants, environmental data, and data extracted from the calibrated dynamic simulation model for the prediction of thermal comfort votes. When compared to traditional predictive approaches, the proposed method shows an increase in accuracy of about 25%.

Keywords: building physics model; machine learning; thermal comfort; hybrid modelling; data-driven; occupant feedback

1. Introduction

The prediction of indoor environmental quality (IEQ) levels in office buildings is important for providing satisfactory and safe work environments, to enhance the productivity of personnel, and to reduce complaints [1]. Recent research studies in health, wellbeing, and productivity in buildings show that satisfaction is affected by many different environmental, physical, and psychological factors [2]. For example, a strong connection between daylight and student performance was found in [3], and correlations between productivity levels and indoor thermal conditions for office buildings were found in [4,5]. Studies show that the overall costs associated to people for companies can be divided following the 1-9-90 estimation [6]: one percent of the operative cost is associated to energy, nine percent is associated to building rental costs, and ninety percent is associated to the cost of personnel. This explains why, in recent years, occupant health, comfort, wellbeing, and productivity have been considered among influential factors for performance evaluations from a facility management perspective. Maintaining satisfactory work conditions during the operation of a building can be difficult, as building control strategies should be able to account for different factors affecting thermal and visual comfort and air quality as well as noise, odours, and nuisance. The achievement of holistic control over IEQ is challenging,

as it requires advanced evaluation capabilities of the current and future conditions for the occupants and how they interact with the environment [7]. In this context, in order to optimise IEQ, building control approaches need to take into account direct feedback from the occupants as well as a variety of additional decision variables of different natures, which may increase the complexity of the control problem [8].

Thermal comfort is affected by many factors related to the indoor environments and their occupants, such as the physical properties of a space (e.g., air temperature, humidity, solar radiation, surface temperatures, and air speed) [9], ambient and human body parameters, psychological characteristics of the occupants [9,10], gender [11], background, and ethnicity [12]. Reliable thermal comfort models should be able to consider a wide range of inputs and subjective preferences. In recent years, many different techniques have been proposed for the prediction of thermal comfort, such as: mathematical modelling of the heat transfer between the human body and the environment [9]; the coupling of human thermal comfort models with computational fluid dynamics (CFD) analyses [10,13–16]; Fanger's physics-based method for the evaluation of the predicted mean vote (PMV) and the predicted percentage of dissatisfied (PPD) [2]; adaptive models that refer to the behavioural, psychological, and physiological adaptation of the humans in an indoor environment over time [17,18]; data-driven applications based on artificial neural networks (ANN) [17]; methods based on fuzzy logic [18]; Bayesian approaches [19]; and methods based on other machine learning (ML) techniques [20]. Overall, thermal comfort models can be classified as physics-based or data-driven approaches. These studies show the difficulties in achieving a holistic approach to thermal comfort and focus on particular areas of interests. Recently, with the proliferation of light, portable, and easy to access and use IoT devices, a large amount of data have been collected from the built environment. Data proliferation from buildings provided the basis for the development of innovative machine learning models. ML models showed the ability of learning complex interactions among the available data, surpassing in accuracy the current comfort calculation methods [21,22]. Given the learning nature of these approaches, they can consider complex phenomena, such as biased decision, as well as personalised preferences, such as direct feedback, making them flexible in terms of targeting large audiences [23]. Among the different ML methods tested in the literature, the random forest (RF) algorithm seems to reach the best performances [24]. Advanced ensemble machine learning (EML) methods have been successfully adopted for thermal perception prediction [25] as well as more recent studies related to the use of deep learning techniques [26]. The use of artificial neural network models has been suggested for thermal comfort and sensation vote prediction in naturally ventilated buildings [27]. Other ML-based methods have been investigated to detect outliers in subjective thermal comfort campaigns by the means of anomaly detection techniques and by quantifying the dissimilarity of the occupants' votes from their peers under similar thermal conditions [28]. From these studies emerged that one of the main limitations of data-driven models is their dependency on historical data and the challenges in predicting conditions that largely differ from their training environment. The thermal comfort problem has been addressed not only with innovative techniques but also with a focus on testing alternative inputs for the models [29]. As such, a combination of readings of skin temperatures and settings of the personalized heating system as input parameters in personal thermal comfort models have been suggested, with a substantial prediction accuracy improvement compared to the more traditional approaches [30,31]. Nearable and wearable solutions have been implemented to provide additional inputs to personalized predicted models [32] by extending the range of measurements that is possible to collect from users and, therefore, facilitating the investigation and development of personalised scenarios [33]. Individual thermal comfort levels have been suggested, as opposed to average votes, by leveraging more granular and precise data that are able to describe environmental and human factors as inputs [20]. Nevertheless, innovative data collection techniques may be expensive as well as intrusive and require full participation of the occupants.

The prediction of thermal comfort feedback from occupants of a building is a complex problem. Recently, several studies underlined the main limitation of traditional methods to predict thermal comfort, such as the limited accuracy achieved when compared to actual votes from the occupants (41.68–65.5% [2]); the need for dedicated expensive equipment for capturing specific environmental variables; the inability to consider non-physics-related variables (e.g., real feedback, preferences, and behavioural patterns); and the need for time-consuming, costly, and difficult setups, as in the case of CFD analyses. One explanation for the identified validation discrepancies is that traditional methods only leverage a limited set of variables for the calculations. Considering this, several research studies started to address the thermal comfort satisfaction as a holistic concept that encompasses behavioural, physiological, and psychological aspects. From a technical point of view, this translates to the adoption of unconventional methods based on real data, data analysis, and, more recently, machine-learning techniques. Nevertheless, data-driven approaches rely on the available data, which, if it is scarce, may affect the prediction capability of the model. They require expensive equipment and the setup of dedicated data collection campaigns. Hybrid modelling, intended as the combination of data-driven methods and physics-based approaches, is rarely adopted, although it could overcome many shortcomings of the most traditional methods. In recent years, with the rapid diffusion of IoT devices, a large amount of high-resolution data became available from the built environment [20], facilitating the creation of accurate digital twins of buildings, defined here as accurate and calibrated building energy models. When calibrated, digital twin models can be considered as an additional source of information and a virtual asset to assess the environmental quality of a building [34] and to generate scenarios. This is performed by extracting virtual sensor variables from simulations for which the equivalent real variables would be difficult and expensive to measure by sensors (e.g., operative temperature, mean radiant temperature, surface temperature, heat fluxes, etc.) [29]. This approach has not been fully leveraged in the literature. Therefore, the current work contributes to the current literature by focusing on three main objectives:

- Test the capabilities of ML models when used for predicting the thermal comfort votes of occupants.
- Combine the use of ML models with physics-based dynamic simulation to leverage virtual sensor variables and to generate dynamic predictions of relevant thermal comfort metrics.
- Establish a comparison with traditional normative methods for the evaluation of thermal comfort.

2. Materials and Methods

The research methodology presented in this work is based on the combination of data-driven methods and building dynamics simulation techniques for the creation of an accurate predictive model. First, relevant data are collected by organising an occupant comfort experiment in a building case study and by installing a network of IoT sensors to gather relevant environmental information. Then, an accurate calibrated building energy model is generated. The calibrated model is used to satisfy two objectives: (i) to use simulation variables (virtual sensors) to extend the set of predictors of the ML model and (ii) as a client of a co-simulation framework for data exchange between the dynamic energy model and an ML algorithm that is used for dynamic prediction of thermal comfort values. As a result, the scenario evaluation capabilities of the physics-based simulation model can be used to generate data for operational scenarios of the building and can be processed by the ML model trained for this purpose.

2.1. Methodology Overview and Workflow

Figure 1 shows the different parts of the methodology presented in the current paper. Three major workflows can be identified: (i) a data-driven part related to the training and deployment of a machine learning model starting from the occupant feedback; (ii) a

building energy modelling framework based on a physics-based model and the workflow relative to its calibration; and (iii) a co-simulation framework that allows for a robust data exchange between the dynamic simulation model and the ML model. The following sections describe in detail the different parts of the methodology.
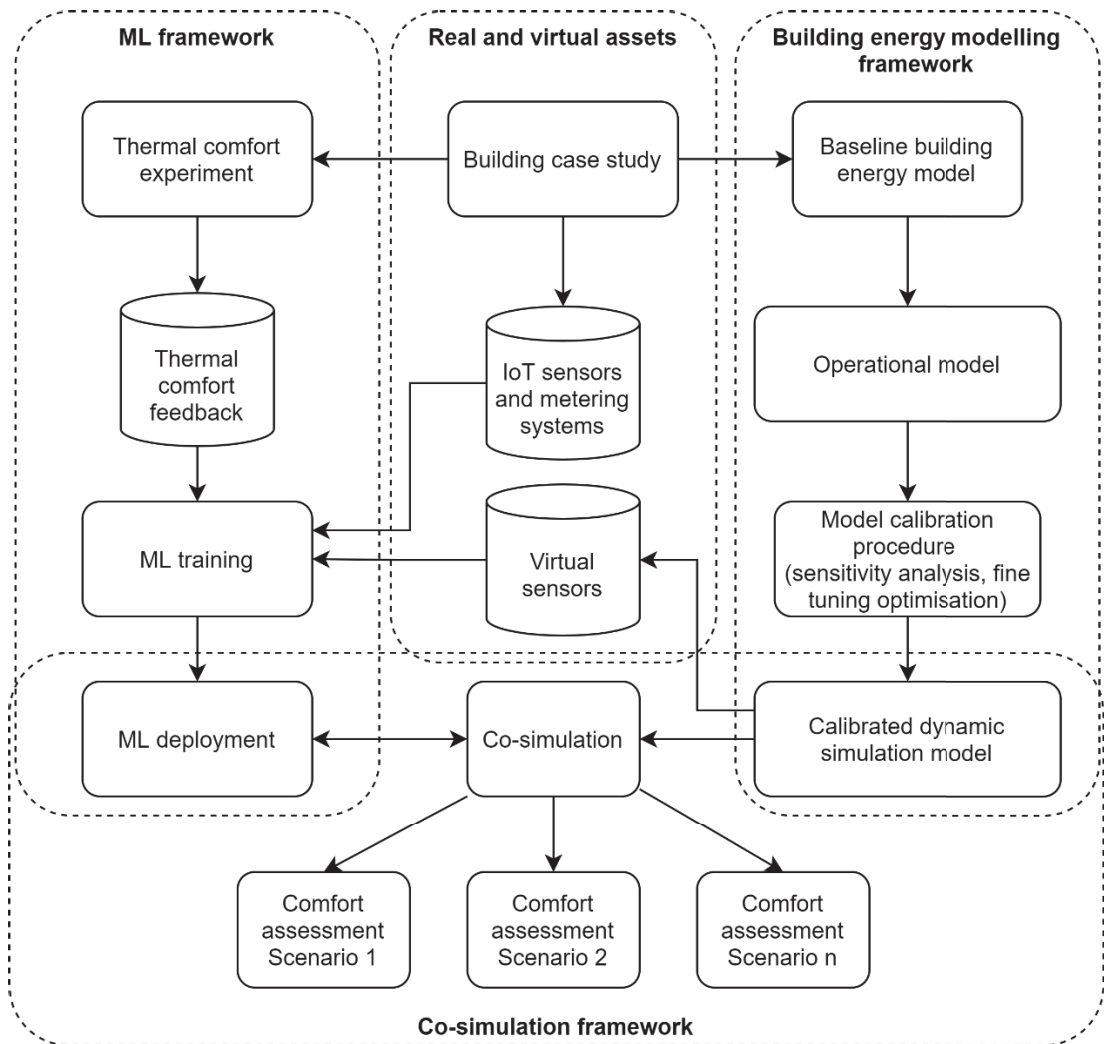

Figure 1. Methodology diagram.

2.2. ML Framework: Thermal Comfort Experiment and Data-Driven Modelling

An innovative data-driven predictive approach for thermal comfort estimation is deployed with the following objectives: (i) investigate a novel method to predict actual thermal comfort votes using ML approaches; (ii) evaluate the accuracy of the models and validate the results; (iii) compare the results of different predictive methods; (iv) identify the most suitable model for the case study; and (v) enable a data exchange mechanism between a dynamic simulation software and the ML model.

The first step to address the research objectives is the setup of a thermal comfort experiment. For this purpose, a data-gathering procedure is required to collect the required

inputs for the training of the ML model and for the calibration of the dynamic simulation model. IoT sensors measuring temperature, CO_2, and humidity levels as well as data coming from BMS systems and local weather stations are employed in this phase for both the calibration of the energy model and the training of the predictive algorithms. The target variable of the ML model is the comfort vote; therefore, a data collection campaign is required to ensure that comfort feedback votes are collected in different parts of the buildings and during an extensive period. Several thermal comfort devices (tablets) are installed in different rooms of the building to let the users submit their feedback. Once the relevant data are collected, each dataset is pre-processed to remove missing values, to convert/translate different labels, perform imputation, if required, and restructure the dataset in the desired format. Following this, a data merging procedure, summarized in Figure 2, is used to combine the IoT sensor data and the thermal comfort votes as well as the information from the dynamic simulation model. This is achieved by relating the closest date-time stamp of the IoT sensor measurements with the closest feedback vote and simulation result; a tolerance of 30 min is used to map and merge the data. Therefore, for a room, the IoT sensor data, feedback votes, and virtual sensor results coming from the dynamic simulation model are combined in a unique dataset.
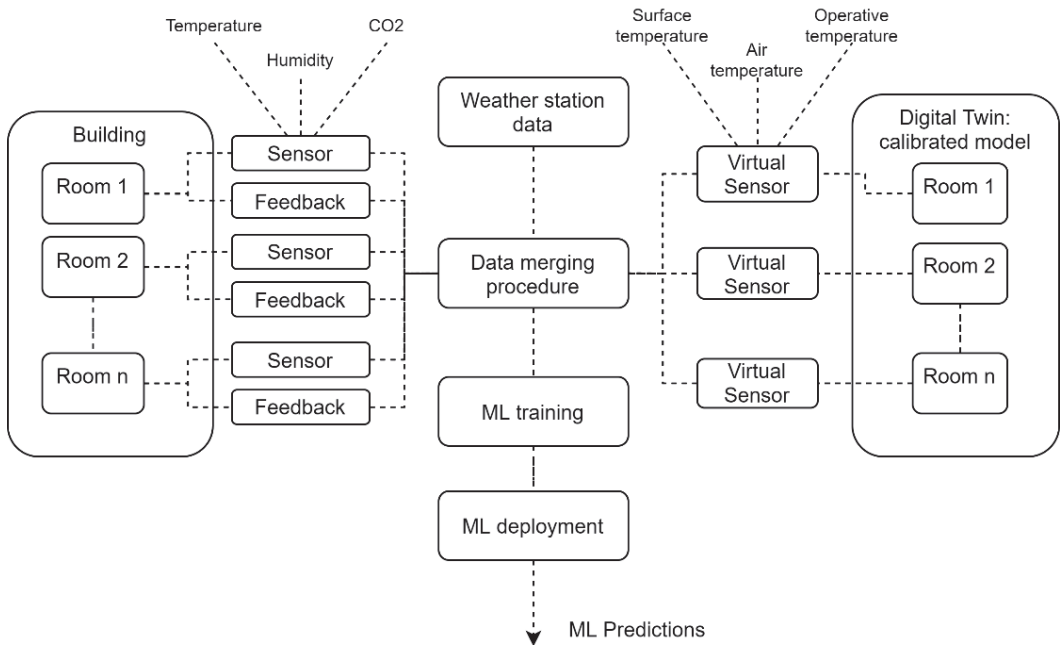
Figure 2. Data merging procedure.

Next, feature engineering procedures are implemented to generate the set of predictors for the ML models. The timestamps of the sensor readings are further processed to extract the hour, the day, the day of the week, and the month as numerical values. The thermal comfort votes are classified and divided in a seven or three value scale as recommended by the ASHRAE guidelines for thermal comfort. The thermal comfort scales are reported in Figure 3. The objective of the ML models is to classify the thermal comfort vote on a fixed scale; therefore, the problem falls under the multi-output classification methods. Two different tests are conducted using either seven- or three-value scales to test the accuracy of the different ML methods, with the objective to identify the best-performing approach.
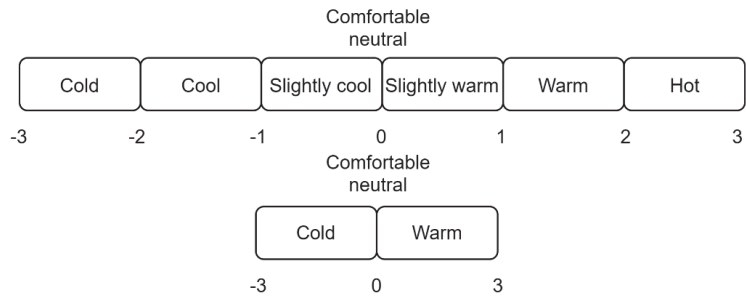
Figure 3. Seven- and three-value thermal comfort scales.

The training of the ML model is performed by splitting the total dataset into training and testing parts. This approach is required to use a part of the historical data for tuning the parameters of the ML models in order to achieve the best predictive results and to have a set of unseen values to validate the model. A 70/30% ratio is used to split the dataset into the training and testing parts. The selection of the best ML model is performed by testing several ML techniques that are commonly used in the literature. The k-neighbours, decision tree, random forest, logistic regression, gradient boosting methods are tested, and their accuracy is recorded for comparison. In order to achieve a more granular evaluation of thermal comfort and to provide continuous results rather than a categorical scale, a regression approach is employed. The method is based on Bayesian modelling and enables the evaluation of the votes of the occupants in a non-deterministic way. This approach is considered more appropriate to reflect the subjective uncertainties related to thermal comfort inputs, the actual comfort model, and the subjective votes of the occupants. To this end, a multi-linear regression method was selected as the right candidate for the problem formulation. A description of the method is reported below, where v indicates the predicted vote, a is the intercept, W (b, c, d, e) are the weights in the equation, and X (x_1, x_2, x_3, x_4) are the predictors.

$$v = a + bx_1 + cx_2 + dx_3 + ex_4 + \dots \tag{1}$$

$$v = XW + \varepsilon \tag{2}$$

$$v \sim N\left(XW, \sigma^2\right) \tag{3}$$

$$P(W|v, X) = \frac{P(v|W, X) \times P(W, X)}{\int P(v, X|W_i) dW_i} \tag{4}$$

Equation (4) describes the Bayesian formulation that was adopted. The method involves the use of a resampling approach based on the Markov chain Monte Carlo technique with the "no-u-turn" algorithm [35]. The training part of the Bayesian method uses the available historical data to generate the most probable distribution for the weights of the predictors. In this way, by resampling each distribution and providing input parameters, it will be possible to obtain a prediction of the vote. To reflect the non-deterministic philosophy of the method, multiple samplings are used to generate a distribution of the output. This also reflects the idea that it is likely to obtain a distribution of values from multiple people, rather than a single vote. Further analyses of the results allow for the estimation of expected maximum and minimum values of the thermal feedback in those particular conditions.

One of the underlining objectives of the analysis was to simplify the number of predictors for the model. Therefore, five predictors were used: (i) the dry bulb external temperature, (ii) the internal air temperature, (iii) the mean radiant temperature, (iv) the hour of the day, and (v) the month. The mean radiant temperature is a parameter that considers heat transfer by radiation and can be measured with a sensor called a black-globe or globe-thermometer. To adequately calculate the thermal comfort, the mean radiant

temperature would ideally be measured considering all the surfaces in the room; however, such an exercise would be complex and costly if carried out continuously in every room of the building. In order to alleviate this issue, the mean radiant temperature is evaluated with the use of the calibrated building energy model. For this purpose, the calibration of environmental variables, such as air temperature, is considered fundamental to obtaining reliable results of other derived measurements for a room. To provide this input to the ML model, the sensor data are combined with the simulation results for that particular room and time. The deployment of the model is facilitated in a co-simulation infrastructure where the dynamic simulation software sends data to the ML model for predictions at each time step as described in Section 2.4. The comparison with the normative methods is achieved by calculating the more traditional thermal comfort metrics, such as the PMV index. This is achieved by leveraging the Python module 'Pythermalcomfort'. The module is linked to the dynamic simulation software to extract, at each simulation time-step, metrics related to the PMV-PPD method. The 'true vote' of the occupants is reconstructed for an entire year. This is achieved by associating the closer value of the vote to the environmental conditions recorded for the building in the case of data gaps. To this end, outdoor temperature, indoor temperature, CO_2 concentration, and relative humidity have been used to identify the closest vote to the environmental conditions and remove the data gap.

2.3. Physics-Based Simulation

One of the first steps in the methodology requires the creation of a baseline building energy model. This can be developed using a dynamic simulation software. An extensive data gathering campaign is organised to collect all the relevant data for the generation of the building energy model. This data are leveraged to create a baseline model of the building. The baseline model undergoes a process of calibration that will deliver a representative digital twin of the building. The calibration process is carried out in three major phases: the generation of a baseline model, the development of an operational model, and improvement toward a calibrated and optimized model. In detail, the overall calibration process can be described in several sub-steps. First, an extensive data collection campaign is carried out to gather as much information as possible on the building, with the intent of collecting all the important parameters for the dynamic simulation software. Examples of data collected in this first step are geometry, construction properties, thermal representative templates of the building, schedules of operations, internal gains, occupancy patterns, system information, ventilation and infiltration rates or estimates, detailed heating ventilation and air conditioning (HVAC) network layouts and characteristics, hot/cold water loop components, air side systems, controls, etc ... When data are not available, educated guesses and normative values are used in place of default values of the simulation software. The output of the first phase is a baseline model, the results of which are compared to the actual building data for accuracy assessment procedures. Following this, another data collection campaign is performed, this time to define the operation of the building by gathering operational data from building management systems (BMS), IoT, automated metering systems, or smart meters. This additional set of data provides information regarding the dynamic profiles and schedules of systems and occupants. Actual schedules of operations are included in the baseline model in the form of time series data to generate an accurate model of the building. A continuous data stream from sensors and metering systems generates sets of updated schedules and profiles that represent the most recent operational patterns of the building that can be included in the building energy model. This generates the operational model of the building. Accuracy assessments are repeated to establish new accuracy measures for the energy model and to check if they comply with standards such as ASHRAE Guideline 14 [36]. If a higher level of accuracy is required, an additional phase of calibration is carried out with advanced optimisation methods. This is implemented using an optimisation tool that is able to find the best values for a set of uncertain parameters that are identified through sensitivity analysis. The method searches values of uncertain parameters in a large parameter space by minimizing objective

functions that are defined using calibration metrics. The objective function considers the error between the metered and simulated data. Equations (5)–(9) describe the list of calibration metrics used by the optimisation tool where the RNRMSE indicates the range-normalised root-mean-square error, which is the main calibration metric considered; the CVRMSE is the coefficient of variation of the root-mean-square error; the NMBE indicates the normalised mean-biased error; and the MAE is the mean absolute error. In the equation, Y and Ŷ indicate the measured and simulated output variables; μ indicates the mean value, and *n* indicates the total number of points. The user defines variables that are considered of primary importance, such as energy, or secondary importance, such as air temperature and CO_2. In this way, the optimisation method is able to account for the importance of different sets of variables that will be optimised at once by minimising the relative objective functions. The use of the RNRMSE variable to perform optimisation provides the possibility to consider variables characterised by different numerical scales in the same optimisation problem. The procedure of fine-tuning by optimisation leads to the creation of a high-fidelity calibrated model that, at this stage, is a reliable emulator of the actual thermal behaviour of the building and its IEQ characteristics and can be used as predictive tool for scenario evaluation.

$$\text{RNRMSE}(\%) = \frac{\text{RMSE}}{\text{range}(Y)} * 100 = \frac{\sqrt{\frac{\sum_{k=1}^{n}\left(Y_k - \hat{Y}_k\right)^2}{n}}}{\max(Y) - \min(Y)} * 100 \tag{5}$$

$$\text{CVRMSE}(\%) = \frac{\text{RMSE}}{\mu} * 100 = \frac{\sqrt{\frac{\sum_{k=1}^{n}\left(Y_k - \hat{Y}_k\right)^2}{n-p-1}}}{\mu} * 100 \tag{6}$$

$$\text{NMBE}(\%) = \frac{\sum_{k=1}^{n}\left(Y_k - \hat{Y}_k\right)}{(n-p)*\mu} * 100 \tag{7}$$

$$\text{MAE}(\%) = \frac{\sum_{k=1}^{n}|Y_i - x_i|}{n} \tag{8}$$

$$\text{RMSE} = \sqrt{\frac{\sum_{k=1}^{n}\left(Y_k - \hat{Y}_k\right)^2}{n-p-1}} \tag{9}$$

2.4. The Co-Simulation Framework

The presented machine learning models described in Section 2.2 are developed for the calculation of comfort metrics. In order to leverage the scenario evaluation capabilities of the dynamic simulation software, a data exchange mechanism is deployed. To enable this, a co-simulation framework is developed to incorporate the ML models with the dynamic simulation software to generate a hybrid physics–ML method. In order to include each model in the co-simulation infrastructure, a four step process is implemented: (1) each room considered should be first calibrated on indoor environmental variables, such as CO_2 or air temperature; (2) an ML model is trained on a mixture of synthetic and real data; (3) the ML model is deployed as a stand-alone entity and Python object to be called as a black box model for predictions; and (4) the deployed model is included in the co-simulation environment and fed by the dynamic simulation software, which provides, at each iteration, the required sets of inputs. By using the presented hybrid model, it is possible to fully leverage the dynamic simulation software for the creation of control scenarios for the enhancement of the operation of the building.

3. Results

The following section describes the results of the presented methodology. First, the case study building is described by providing information on the thermal comfort experiment conducted to gather relevant feedback from the occupants. Then, the steps and the results

for the creation of the calibrated energy model are described, with particular attention to the validation and comparison with the real data gathered from the metering systems and IoT devices in the building. Next, the results of the training/tuning and validation of the machine learning models are presented.

3.1. The Building Case Study: The Helios Building

The Helios building is located at the southern end of the Savoie Technolac science and technology park in the city of Chambéry, France. The building is the headquarters of the National Solar Energy Institute (INES). Delivered in December 2013, the building houses the institute's laboratories and the directors' offices as well as the administrative services and training departments, covering an area of 7500 sq.m. Figure 4 shows the building layout. Each room in the building case study is equipped with one or more CO_2/T/S Trend series sensors. The CO_2/T/S series sensors monitor the carbon dioxide concentration, temperature, and humidity of the air. The space sensors operate with the following technical specifications: a range from 0 to 2000 ppm for the CO_2 concentration measurement with an accuracy of ±50 ppm +2% of the measured value; a range of 0 °C to +40 °C with an accuracy of ±3 °C for the temperature values; and a range of 0 to 95 %RH with ±3 % RH accuracy. Each sensor is connected to a Trend IQ3 Controller and to the BMS of the building. The IoT sensors were used for monitoring the openings in each room (windows and doors) as well as to monitor the electric consumption of fans. The z-wave power socket series (Fibaro) was used for electric fan operations.
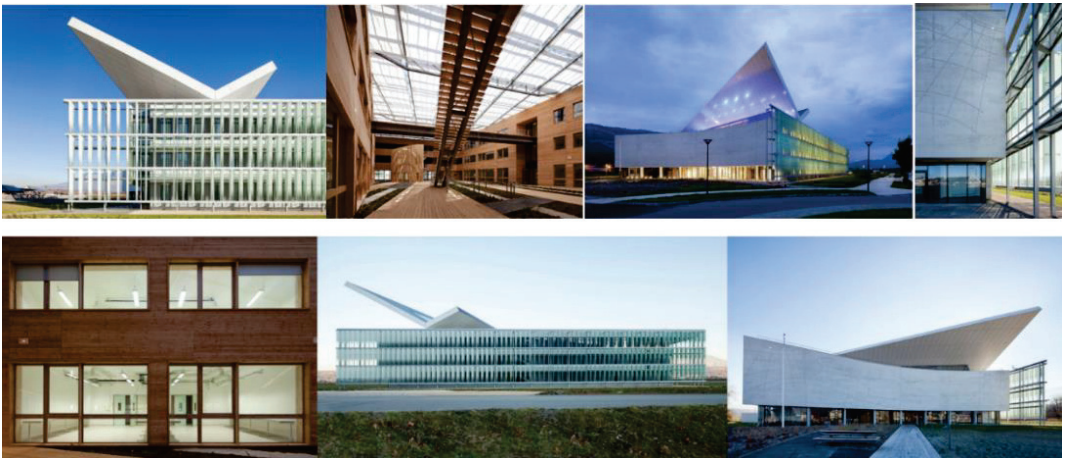
Figure 4. The Helios building.

3.2. The Thermal Comfort Experiment

A data collection campaign spanning from July 2018 to June 2019 was conducted to gather thermal comfort votes from the occupants of the building. A thermal comfort feedback device was installed in ten different rooms and was used to collect votes from the occupants. A total of 7430 votes were collected during the duration of the experiment. Figure 5 shows the distribution of the collected votes during the period of analysis. With reference to the ASHRAE seven-value scale for thermal comfort, from an analysis of the collected data, it is possible to summarise that between 1–2% of the total votes were within the range [−3, −2], about 16% of the total were in the range (−2, −1], a majority of 65% were within the range (−1, 0], 13% were in the range (0, 1], about 3% were in the range (1, 2], and less than 1% were in the range (2, 3]. The overall distribution is presented in Figure 5.
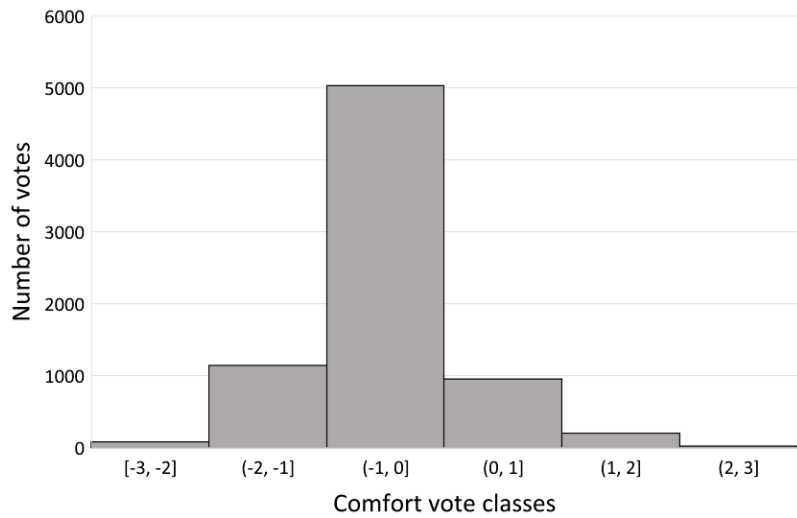
Figure 5. Distribution of the comfort votes collected in the Helios building during the period from July 2018 to June 2019.

Figures 6 and 7 show the scatterplot of the thermal comfort votes and the relative temperature ranges for the indoor and outdoor air temperatures. From the graph, it is possible to evaluate the means and standard deviations of the range of temperatures for each perceived comfort vote for the indoor air temperature. This is reported in Table 1. As expected, there is a positive trend between the mean of the indoor and outdoor air temperature and the comfort vote, while the standard deviation values seem to be larger for the central classes, underlining that what the occupants think to be a neutral and comfortable temperature is more subjective than the extreme votes. A quadratic equation was used to interpolate the data and extract a relationship between the votes and the indoor and outdoor temperatures. The equations are reported in Figures 6 and 7.

$$y = 0.23x^2 + 1.56x + 24.73$$
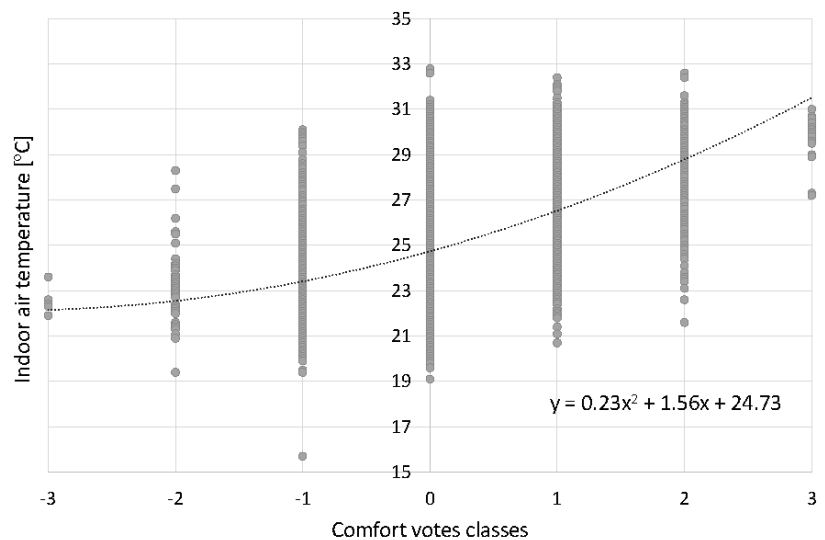
Figure 6. Indoor air temperature and thermal comfort votes scatter plot.

(**a**)

(**b**)
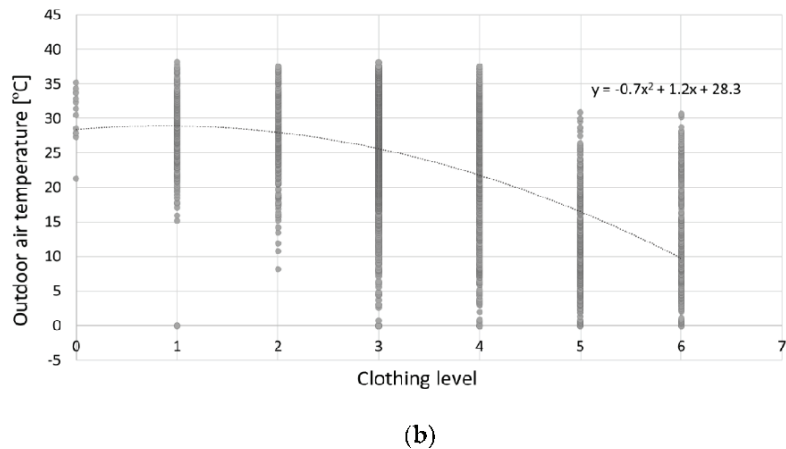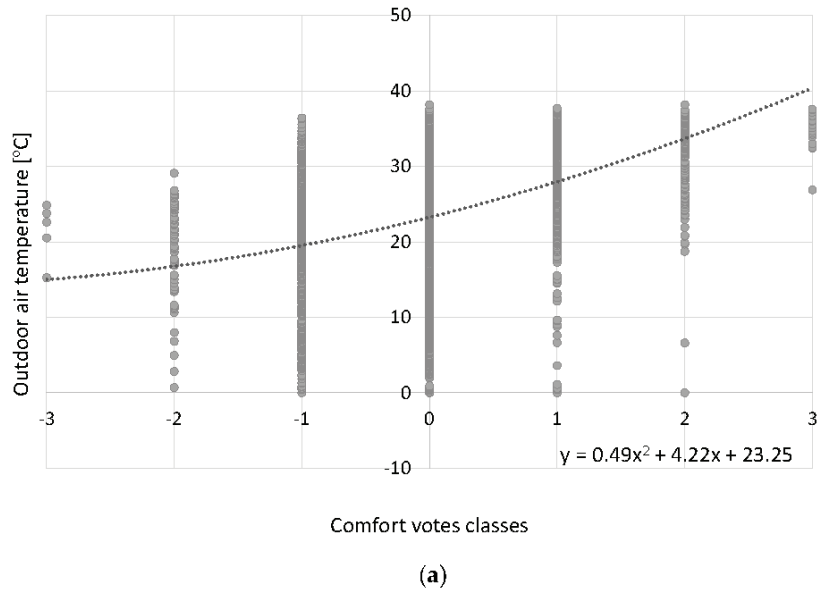
Figure 7. (**a**) Outdoor air temperature and thermal comfort votes scatter plot; (**b**) Clothing level and outdoor air temperature.

Table 1. Means and standard deviations of temperatures for each thermal comfort vote range.

Vote Range	−3	−2	−1	0	1	2	3
Mean	22.56	23.07	23.50	24.63	27.1	28.21	29.7
Standard deviation	0.56	1.35	1.68	2.04	2.21	2.08	0.93

From the two quadratic equations, it is possible to extract the comfort temperature for which feedback are equal to value zero. If this is repeated for indoor and outdoor temperatures, the following temperature can be evaluated: 24.73 °C for indoor temperature and 23.25 °C for outdoor temperature. Figure 8 shows the layout of the comfort vote device used by the occupants to submit feedback during the duration of the experiment. The additional following variables were collected from information submitted by the occupants:

The thermal comfort vote, perceived air flux, and current outfit. Figure 7b shows the trend of the thermal insulation (clothing) of the occupants related to the outdoor air temperature. From the graph, it is evident that, as the outdoor air temperature increases, insulation levels decrease, indicating that the occupants wear less heavy clothing. The clothing level is the sum of the upper body first and eventual second layer, lower body layer, and feet layer. The clothing level was submitted by each occupant using the feedback app, along with the thermal comfort vote. A second order polynomial equation was extracted from the data and can be used to estimate the expected average temperature once the clothing level has been defined.

Figure 8. UI of the thermal comfort vote device.

3.3. Building Energy Modelling: The Baseline Model

The building energy model was created with the Integrated Environmental Solution's software Virtual Environment. Building geometry data, such as layout of elevations, floor plans, and sections, were used to accurately reconstruct the geometry of the building as a first step in the modelling procedure. The result of this operation is shown in Figure 9. Weather data were collected from the service Athenium Analytics, which is able to communicate with IES's iSCAN platform for data storage and analysis. According to the service, the weather station is located 59 km from the building. A variety of additional data were collected to recreate a high-fidelity digital representation of the building, such as the thermal properties of the construction materials, occupancy patterns, lighting fixtures, and equipment usage. The year considered for the simulation was 2018. Air temperature, window opening, door opening, louvre opening, carbon dioxide concentrations, and additional weather variables were gathered from IoT sensors and were used for the creation of the model.
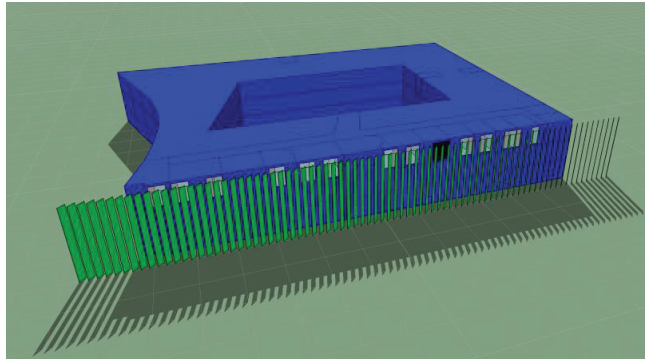
Figure 9. IESVE model of the building.

All the relevant internal gains in the building were modelled with accuracy, as it is likely they have a high impact on the resulting air temperature and, therefore, the perceived thermal comfort of the occupants. Therefore, occupancy, equipment, and lighting gains were modelled, starting from the information of each room or data analysis of the IoT sensors, to derive possible schedules of operation. The number of people and their schedules were gathered from the building documentation provided and by interviews. Most of the offices had traditional hours of operation (8:30 -> 17:30) for an office building, with lunch breaks between 12:00 and 13:00 for 50% of occupants and 12:30–13:30 for the other 50%. For all the offices, the sensible and latent heat gains were based on normative values for the relative activity conducted in the room: 70 W/person for sensible heat and 45 W/person for latent heat (as recommended in CIBSE [37], Guide A—Table 6.3—for seated, very light work). It was assumed that lights and equipment have the same schedules, they are on all the time while the space is occupied. For internal gains related to equipment, values of 15 W/m^2 were used, while an average value of 9 W/m^2 was adopted for the lights, which are values similar to the recommended threshold set in the normative values. After this, the HVAC system was modelled using a wood pellet boiler in combination with a solar heating system to match the current system in the building. The heating-related profiles and setpoints were applied to the model after an accurate analysis of the metered data available for the building. Building openings were modelled, with particular care to reproduce the right amount of fresh air for the naturally ventilated building. For this, the data collected on window and door operations was integrated directly into the model to represent occupant behaviour by the means of time series profiles. Finally, window shadings were modelled for each room in the model. In order to accurately mimic the use of the blinds, opening and closing data were included in the model. The operation of the blinds influences the solar radiation values, and it is likely to have a large impact on the perceived thermal comfort of the occupants.

3.4. Model Calibration Results

The calibration of the Helios building was conducted by targeting the building's environmental variables, and it was validated by comparing the measured data with the simulated data at an hourly timestep resolution. The procedure was conducted as described in Section 2.3. The mean absolute error (MAE) and the root-mean-square error (RMSE) were used as the main metrics for the environmental variables, while the range-normalised root-mean-square error was employed to drive the process of automated parameter tuning via optimisation. As the calibration was completed for the environmental variables, the traditional metrics for calibration, such as the coefficient of variation of the root-mean-square error (CVRMSE) and the normalised mean bias error (NMBE) were not suitable metrics, as they are intended mostly for energy studies. When calibration is driven by IEQ problems, it is recommended that the MAE and RMSE are used in the normative TM63 [37].

TM63 states that most studies indicate sufficient calibration if metrics are less than ~2 °C for air temperature, while there are no other direct indications for CO_2 concentrations. One of the main final uses of the model is to simulate different operational control options for the building; therefore, it is essential that the model is as accurate as possible. An optimisation technique based on evolutionary algorithms (NSGA2) was used to automatically fine-tune some of the driving parameters identified by the sensitivity analysis of the model. An example of the results of the calibration by optimisation procedures is shown in Figure 10 below. The triangles indicate the value of the metrics for a given room at the beginning of the calibration procedure. From the figure, it is evident that the minimisation of the calibration error progressively reduces the RMSE (°C) and the MAE (°C) for all the rooms considered.
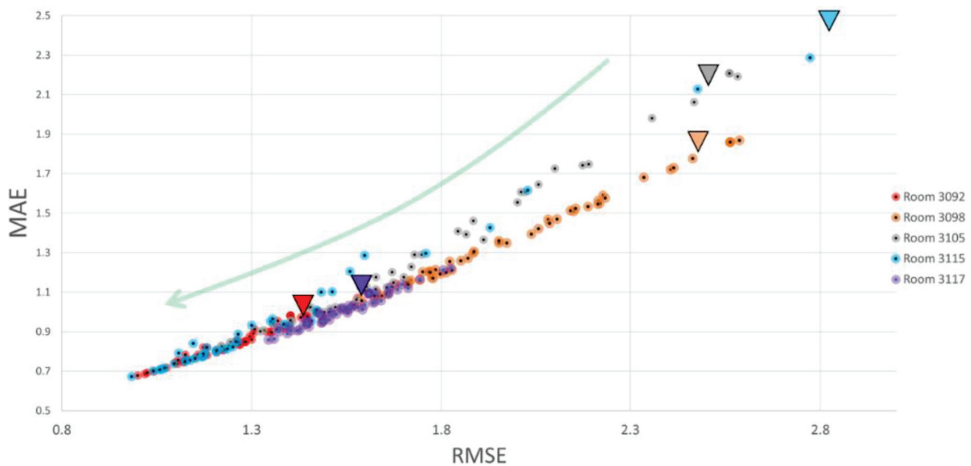
Figure 10. Results of the optimisation procedures and progressive improvements of the calibration metrics for 5 rooms in the Helios building. The triangles represent the values of the calibration metrics at the beginning of the optimisation procedure.

Table 2 shows the initial values of the calibration metrics at the end of the manual calibration procedure. For the results in rooms of the Helios building, at the end of this procedure, the majority of the values for the metrics MAE and RMSE were below the threshold recommended by TM63. Table 3 summarizes the results of the fine-tuning technique for the four rooms considered for the analysis. Comparing the results from Tables 2 and 3, it is evident that the fine-tuning procedure is able to further improve the calibration of the model. A visual comparison of the results is provided in Figures 11–14.

Table 2. Calibration results for three rooms of the Helios building for the period January–March 2018.

Room	Variable	MAE (°C, PPM)	RMSE (°C, PPM)
3072	Air temperature (°C)	4.12	2.41
3072	CO_2 (PPM)	126.13	83.01
3071	Air temperature (°C)	3.61	1.16
3071	CO_2 (PPM)	186.12	169.93
3033	Air temperature (°C)	1.33	0.725
3033	CO_2 (PPM)	219.2	140.7
3092	Air temperature (°C)	1.38	0.425
3092	CO_2 (PPM)	105.15	20.98

Table 3. Calibration metrics after fine-tuning with optimisation for various rooms of the Helios building for the period January–March 2018.

Room	Variable	MAE (°C, PPM)	RMSE (°C, PPM)
3072	Air temperature (°C)	2.45	2.12
3072	CO_2 (PPM)	67.20	53.78
3071	Air temperature (°C)	0.65	0.51
3071	CO_2 (PPM)	129.45	122.13
3033	Air temperature (°C)	0.74	0.59
3033	CO_2 (PPM)	67.01	53.19
3092	Air temperature (°C)	1.17	0.33
3092	CO_2 (PPM)	156.84	34.17
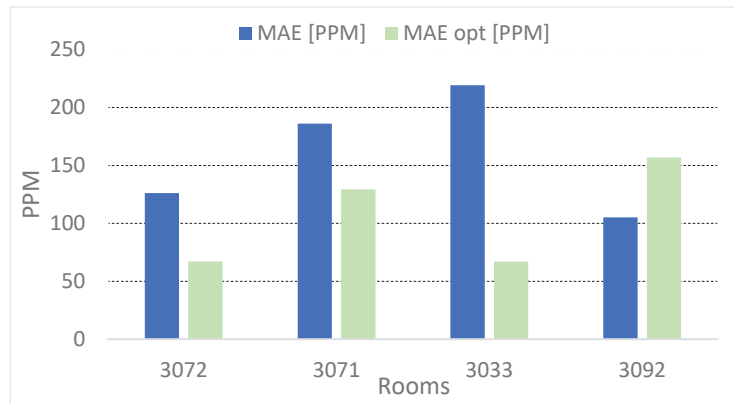
Figure 11. Mean absolute error for the CO_2 concentration: comparison calibrated model vs. optimized model.
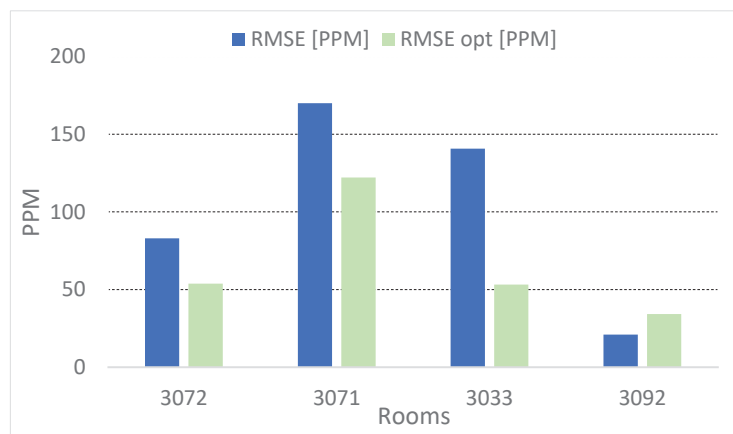
Figure 12. Root-mean-square error of the CO_2 concentration: comparison calibrated model vs. optimized model.
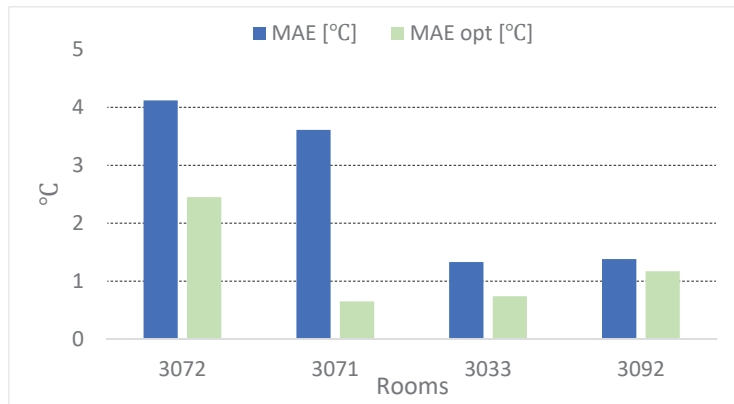
Figure 13. Mean absolute error for the air temperature: comparison calibrated model vs. optimized model.
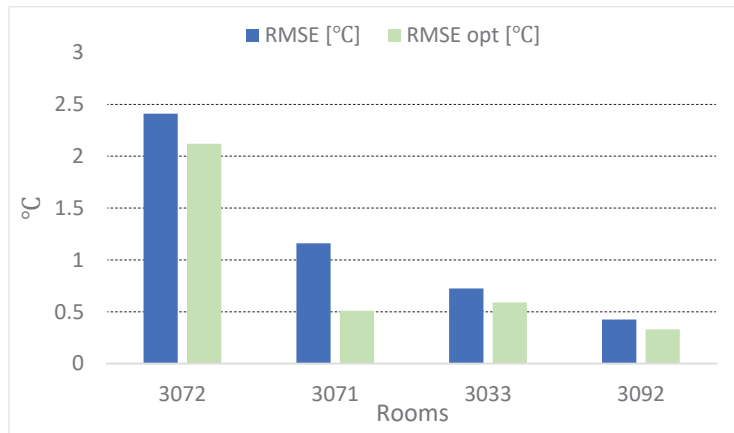

Figure 14. Root-mean-square error for the air temperature: comparison calibrated model vs. optimized model.

Figure 15 shows the time series comparison between the internal air temperature and CO_2 levels for a single room in the building after the completion of the fine-tuning procedure. Overall, the model is able to accurately predict the two metered variables, especially during the occupied hours that are more relevant to conducting an IEQ-related analysis. Improvements could be achieved by gathering more detailed information for un-occupied hours and the relative schedules and settings of operation of the heating systems as well as the active equipment and real time occupancy values.
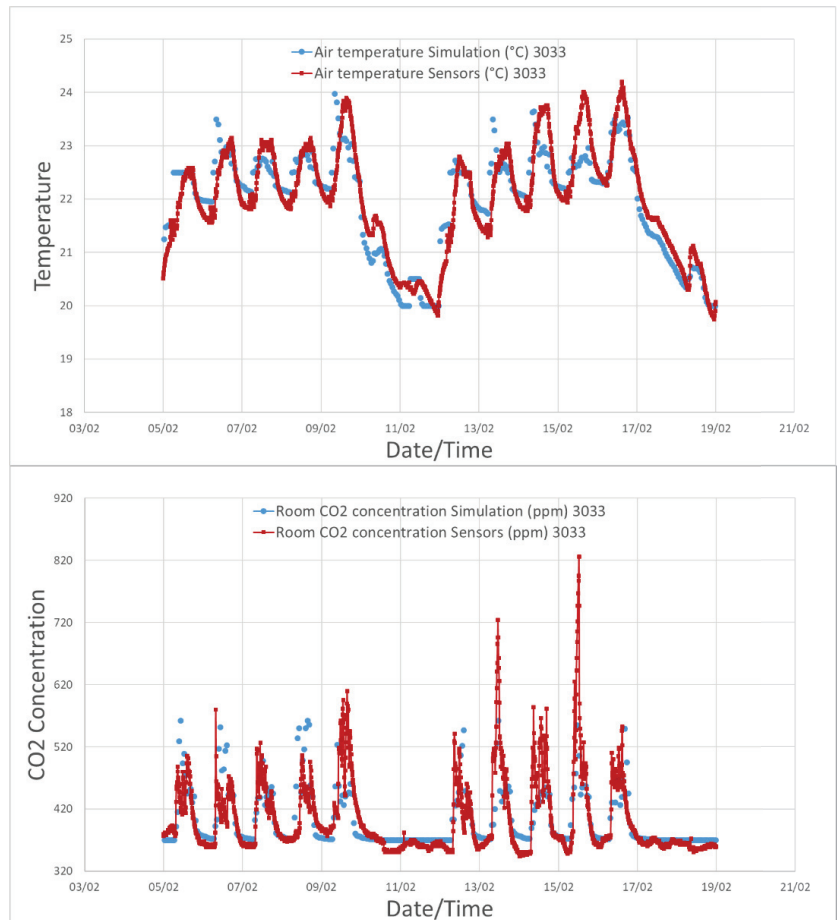
Figure 15. Comparison between the air temperature measurements in one room of the Helios building and the output of the simulation across 2 weeks in winter.

3.5. The Thermal Comfort Models: Training and Results

The training and testing of the machine learning models was performed using available methods of the scikit python package [29]. In particular, the available data were split in a 30/70 ratio, where 70% of the total data were used for training, while the remaining 30% were used for testing. A fine-tuning approach and best algorithm searching method was performed for each algorithm using a 10-fold cross validation technique on the training dataset. The grid search method was used for testing many different combinations of the tuning parameters of each algorithm. The best predictors for each method were selected and compared to each other to evaluate their performance.

Table 4 summarises the validation results achieved with different ML techniques on the seven-value scale for the prediction of the thermal comfort votes in the Helios building. From the accuracy results, it is evident that the random forest approach and the gradient boosting classifier achieved the best results. The accuracy value was calculated as the average value across the different classes. A more granular analysis of the results shows that predictive models in classes with a larger amount of feedback achieved better results, as there were more historical values for the training. On the other hand, classes with fewer values, such as the extreme of the scale, were difficult to predict, as there were not enough

instances to accurately train the model. To address this problem, class balancing approaches are recommended to unify the prediction accuracy of the model.

Table 4. Accuracy results achieved by different ML techniques.

ML Classifier	Accuracy
K-Neighbours Classifier	62%
Decision Tree Classifier	56%
Random Forest Classifier	69%
Logistic Regression	62%
Gradient Boosting Classifier	66%

The results of the ML models evaluated on a three-value scale are reported in Table 5. The random forest approach and the gradient boosting method achieved higher performances in this case as well. Overall, the accuracy of the model was higher across the classes of the scale, as a less granular classification was required.

Table 5. Accuracy of various ML models in a three-value thermal comfort scale.

ML Classifier	Accuracy
K-Neighbors Classifier	78%
Decision Tree Classifier	79%
Random Forest Classifier	84%
Logistic Regression	77%
Gradient Boosting Classifier	81%

Figure 16 shows the results of predictive Bayesian model when compared with the actual comfort values submitted by the occupants. The predictions are for a continuous value scale, which constitutes a more challenging task compared to class prediction as analysed in the examples before. The image shows the expected accuracy of the model for an acceptable maximum error. The graph can be interpreted considering the following example: if an error of ± 0.4 with respect to the actual vote is accepted on the thermal comfort scale, the model is able to generate a distribution that can include the actual vote with 76% accuracy. In this example, an acceptable error of ± 0.4 on the ASHRAE scale for thermal comfort $(-3, +3)$ indicates that the true vote of the occupant lies within a range of size ± 0.4 from the predicted value of the ML model.
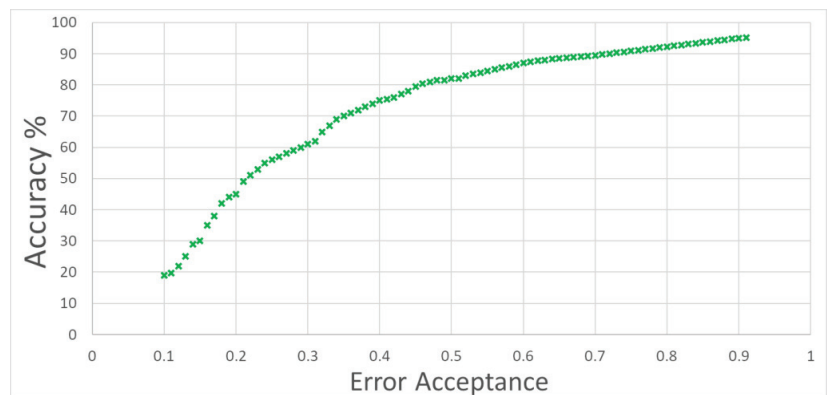

Figure 16. Prediction accuracy of the Bayesian multi-linear regression model under various error acceptance thresholds.

3.6. Accuracy and Comparison

Figure 17 shows the results of the comparison between the reconstructed true vote of the occupants (as explained in Section 2), the PMV calculations, and the ML prediction for the thermal comfort for an entire year (2019). The PMV calculations and the ML predictions were calculated using the co-simulation technique for the year of analysis. An analysis of the results shows that the PMV–PPD model significantly overestimates the comfort votes starting in spring and for the entire summer months and underestimates the severity of the votes in the winter months. It is clear from these results that the PMV–PPD model would be insufficient for informing control algorithms compared to the developed ML prediction algorithm. The ML vote predictions effectively follow the true vote trend for the entire year. In particular, the model is able to predict values on the warm part of the scale as well on the cold part for each day of the year for the occupied hours. It is also important to note that the ML model seems to be less accurate at predicting thermal comfort votes on the extreme hot or cold end of the scale. This is because few training instances were available for extreme votes from the occupants to accurately train the model. For this reason, the adoption of balancing techniques may be required to further improve the results. Figure 18 shows the comparison of the predictions of the PMV method and the machine learning method when compared to the true vote over five working days. In the image, it is possible to identify the minimum and maximum derived from the distributions generated by the machine learning model. A comparison of the results shows the overpredictions of the PMV model for the considered days in April.
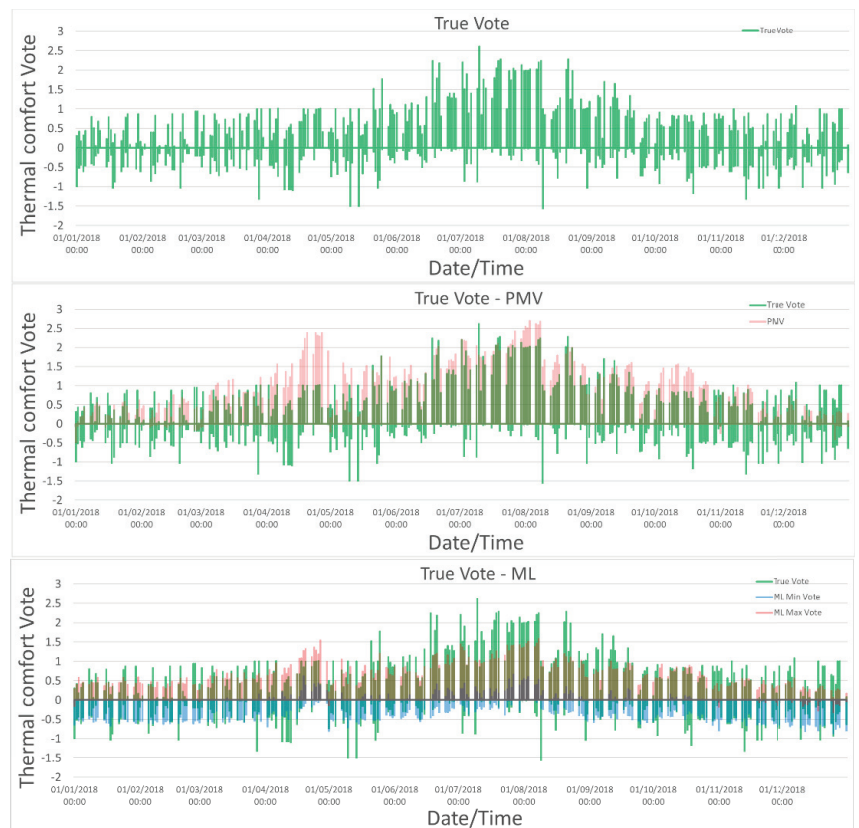

Figure 17. Comparison between the true comfort vote, the PMV evaluation, and the ML model results.
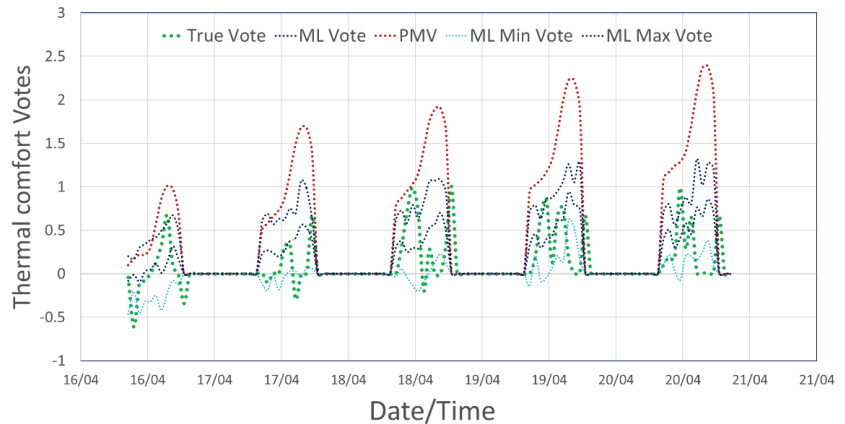
Figure 18. Comparison of the votes from the occupants with the ML model predictions and the normative PMV approach.

The Bayesian ML model produces ranges of predictions that are comparable to the actual vote from the occupants. Generally, the maximum and minimum values of the ML prediction always include the true vote from the occupants for the period of analysis. This information can be used to predict the expected thermal comfort range and to inform optimum building controls. In the context of optimizing thermal comfort, setpoints and heating/cooling operation may be controlled in order to maintain predicted thermal comfort within the predicted ranges.

4. Discussion

The results of model calibration show the reliability of the proposed methodology to facilitate the creation of digital representations of the real office building. In particular, the multi-step calibration methodology and the continuous data gathering and integration into the simulation model allow for the evolution of the baseline model over time to an operational and finally to an optimized model that accurately represents the actual physical behaviour of the building. The use of data analysis for the creation of actual schedules of operations at the building and system levels enables a more accurate representation of the building. The automatic optimization procedure based on the automatic fine-tuning of the modelling parameters further shortens the gap between the real building and the simulated one. The comparison between Tables 2 and 3 reveals the improvements in terms of the metrics achieved with the final fine-tuning procedure. The final outcome of the procedure shows that values of the me trics are mostly within the suggested ranges, and, therefore, the model can be considered calibrated for the variables under analysis. From a visual perspective, Figure 5 shows the quality of the results when compared to the actual metered data. The final model is very capable of reproducing the behaviour of the real building for the considered IEQ variables and, therefore, is suitable to be used as an additional source of training data for the machine learning approaches.

The validation of the different machine learning models deployed for this study underlines the capacity of these techniques to produce more reliable results compared to traditional thermal comfort studies. In this regard, classification models trained on a seven-value scale show a top accuracy of about 69%, which constitutes an improvement of about 20–25% with respect to the traditional PMV method (45–50% accuracy). When the model is trained on a smaller scale (three-value) the top accuracy is about 85%. In both cases, the random forest approach seems to be the most accurate method of prediction. A linear Bayesian implementation of the predictive approach allowed the model to consider a continuous scale rather than a categorical scale, increasing the granularity of the response of the prediction to the entire spectrum of possible continuous values (−3, +3). In this case,

the accuracy of the model is dependent on the acceptable range of error. For example with an error acceptance of ± 0.4, the model shows an accuracy of about 76%. In addition, the Bayesian approach of generating a distribution of possible values intrinsically takes into account the uncertainties related to the measurements, the model, and subjective decision of the occupants, providing a much more realistic figure of the thermal sensation of the room. Moreover, by generating maximum and minimum boundaries, it is suitable to be integrated into control methods that act on air temperature set points.

The connection between the calibrated energy simulation model and the machine learning predictive approach allows for generating data in different scenarios. This approach takes the most useful features of the two methods and combines them together. On one side, it uses the scenario evaluation approach of the physics-based simulation, and, on the other, it uses the predictive capabilities of the ML model that was directly trained on occupant feedback. The result is the possibility to generate realistic thermal comfort feedback by simulating different scenarios in the energy model. This is very useful for a control mechanism, as it provides the possibility of changing settings in the model before performing any change in the operation of the real building. By using this approach, it was possible to generate thermal comfort data for an entire year of simulation.

5. Conclusions

The prediction of thermal comfort feedback in office buildings is a difficult task that generally is approached using physics-based calculations derived from a number of environmental variables. Thermal comfort was found to be related to a number of subjective and personal judgements of the occupants of the building. Machine learning models that are trained on actual data inherit personal judgments, skewed preferences, and personalised feedback as well as historical trends. Therefore, underlining the information captured in the actual data can be learnt and used for future predictions. In this work, the capabilities of the ML models when used for predicting thermal comfort votes from occupants were tested. The results show that different configurations of the ML models are able to capture personal preferences of the occupant, overcoming the main limitations of traditional methods. When compared to normative approaches, such as the PMV method, the ML algorithms reduced the prediction error by at least 25%, reaching a top accuracy of almost 70% on a seven-value scale and about 85% on a three-value scale. The use of Bayesian modelling allowed for a more realistic response in terms of the possible ranges of thermal comfort, with minimum and maximum limits of acceptability, and enabled the possibility of predicting thermal comfort on a continuous value scale rather than being discretized in three or seven values. When physics-based simulation and ML data-driven model are combined, the new modelling technique constitutes a useful predictive tool for testing different control strategies and operations of the building before applying them in the real one. In addition, by merging the two modelling techniques, it was possible to extract additional information for the training of the ML algorithms from the calibrated building energy model, such as the mean radiant temperature. The use of ML techniques is important for taking into account many occupant-related variables for thermal comfort. Nevertheless, some limitations should be taken into account. ML model accuracy and precision is directly related to the available data. Missing data limits the quality of the predictive models. For this reason, for extreme vote classes it is important either to gather a sufficient number of training samples or to use advanced balancing techniques that are able to generate synthetic data from the available ones. In future work, several pre-processing techniques could be tested on the training dataset for balancing purposes as well as the extraction of additional variables from the calibrated building energy model as additional predictors. In conclusion, the union of building physics modelling and machine learning techniques generates a hybrid modelling approach that showed several advantages. This can be leveraged to create tailored predictive models for testing building control routines as well as optimised operational scenarios as testing options before being applied on the actual building.

References

1. Mallawaarachchi, H.; De Silva, L.; Rameezdeen, R. Modelling the relationship between green built environment and occupants' productivity. *Facilities* **2017**, *35*, 170–187. [CrossRef]
2. Van Hoof, J.; Mazej, M.; Hensen, J.L.M. Thermal comfort: Research and practice. *Front. Biosci.* **2010**, *15*, 765–788. [CrossRef] [PubMed]
3. Yacine, S.M.; Noureddine, Z.; Piga, B.E.A.; Morello, E.; Safa, D. Towards a new model of light quality assessment based on occupant satisfaction and lighting glare indices. *Energy Procedia* **2017**, *122*, 805–810. [CrossRef]
4. Lan, L.; Wargocki, P.; Lian, Z. Quantitative measurement of productivity loss due to thermal discomfort. *Energy Build.* **2011**, *43*, 1057–1062. [CrossRef]
5. Lan, L.; Lian, Z.; Pan, L. The effects of air temperature on office workers' well-being, workload and productivity-evaluated with subjective ratings. *Appl. Ergon.* **2010**, *42*, 29–36. [CrossRef]
6. Parkinson, T.; Parkinson, A.; de Dear, R. Continuous IEQ monitoring system: Context and development. *Build. Environ.* **2019**, *149*, 15–25. [CrossRef]
7. Larsen, T.S.; Rohde, L.; Jønsson, K.T.; Rasmussen, B.; Jensen, R.L.; Knudsen, H.N.; Witterseh, T.; Bekö, G. IEQ-Compass—A tool for holistic evaluation of potential indoor environmental quality. *Build. Environ.* **2020**, *172*, 106707. [CrossRef]
8. Gao, G.; Li, J.; Wen, Y. DeepComfort: Energy-Efficient Thermal Comfort Control in Buildings Via Reinforcement Learning. *IEEE Internet Things J.* **2020**, *7*, 8472–8484. [CrossRef]
9. Djongyang, N.; Tchinda, R.; Njomo, D. Thermal comfort: A review paper. *Renew. Sustain. Energy Rev.* **2010**, *14*, 2626–2640. [CrossRef]
10. Cheng, Y.; Niu, J.; Gao, N. Thermal comfort models: A review and numerical investigation. *Build. Environ.* **2012**, *47*, 13–22. [CrossRef]
11. Karjalainen, S. Thermal comfort and gender: A literature review. *Indoor Air* **2012**, *22*, 96–109. [CrossRef] [PubMed]
12. Rupp, R.F.; Vásquez, N.G.; Lamberts, R. A review of human thermal comfort in the built environment. *Energy Build.* **2015**, *105*, 178–205. [CrossRef]
13. Alizadeh, M.; Sadrameli, S.M. Numerical modeling and optimization of thermal comfort in building: Central composite design and CFD simulation. *Energy Build.* **2018**, *164*, 187–202. [CrossRef]
14. Croitoru, C.; Nastase, I.; Bode, F.; Meslem, A.; Dogeanu, A. Thermal comfort models for indoor spaces and vehicles—Current capabilities and future perspectives. *Renew. Sustain. Energy Rev.* **2015**, *44*, 304–318. [CrossRef]
15. Halawa, E.; Van Hoof, J. The adaptive approach to thermal comfort: A critical overview. *Energy Build.* **2012**, *51*, 101–110. [CrossRef]
16. Ioannou, A.; Itard, L.; Agarwal, T. In-situ real time measurements of thermal comfort and comparison with the adaptive comfort theory in Dutch residential dwellings. *Energy Build.* **2018**, *170*, 229–241. [CrossRef]
17. Palladino, D.; Nardi, I.; Buratti, C. Artificial neural network for the thermal comfort index prediction: Development of a new simplified algorithm. *Energies* **2020**, *13*, 4500. [CrossRef]
18. Menyhárt, J.; Kalmár, F. Investigation of thermal comfort responses with fuzzy logic. *Energies* **2019**, *12*, 1792. [CrossRef]
19. Mui, K.W.; Tsang, T.W.; Wong, L.T. Bayesian updates for indoor thermal comfort models. *J. Build. Eng.* **2020**, *29*, 101117. [CrossRef]
20. Salamone, F.; Belussi, L.; Currò, C.; Danza, L.; Ghellere, M.; Guazzi, G.; Lenzi, B.; Megale, V.; Meroni, I. Integrated method for personal thermal comfort assessment and optimization through users' feedback, IoT and machine learning: A case study. *Sensors* **2018**, *18*, 1602. [CrossRef]
21. Wang, Z.; Wang, J.; He, Y.; Liu, Y.; Lin, B.; Hong, T. Dimension analysis of subjective thermal comfort metrics based on ASHRAE Global Thermal Comfort Database using machine learning. *J. Build. Eng.* **2020**, *29*, 101120. [CrossRef]
22. Farhan, A.A.; Pattipati, K.; Wang, B.; Luh, P. Predicting individual thermal comfort using machine learning algorithms. In Proceedings of the 2015 IEEE International Conference on Automation Science and Engineering (CASE), Gothenburg, Sweden, 24–28 August 2015; pp. 708–713.

23. Pritoni, M.; Salmon, K.; Sanguinetti, A.; Morejohn, J.; Modera, M. Occupant thermal feedback for improved efficiency in university buildings. *Energy Build.* **2017**, *144*, 241–250. [CrossRef]
24. Luo, M.; Xie, J.; Yan, Y.; Ke, Z.; Yu, P.; Wang, Z.; Zhang, J. Comparing machine learning algorithms in predicting thermal sensation using ASHRAE Comfort Database II. *Energy Build.* **2020**, *210*, 109776. [CrossRef]
25. Wu, Z.; Li, N.; Peng, J.; Cui, H.; Liu, P.; Li, H.; Li, X. Using an ensemble machine learning methodology-Bagging to predict occupants' thermal comfort in buildings. *Energy Build.* **2018**, *173*, 117–127. [CrossRef]
26. Zhang, W.; Hu, W.; Wen, Y. Thermal comfort modeling for smart buildings: A fine-grained deep learning approach. *IEEE Internet Things J.* **2019**, *6*, 2540–2549. [CrossRef]
27. Kim, J.; Zhou, Y.; Schiavon, S.; Raftery, P.; Brager, G. Personal comfort models: Predicting individuals' thermal preference using occupant heating and cooling behavior and machine learning. *Build. Environ.* **2018**, *129*, 96–106. [CrossRef]
28. Tang, S.; Shelden, D.R.; Eastman, C.M.; Pishdad-bozorgi, P.; Gao, X. Automation in Construction A review of building information modeling (BIM) and the internet of things (IoT) devices integration: Present status and future trends. *Autom. Constr.* **2019**, *101*, 127–139. [CrossRef]
29. Aivaliotis, P.; Georgoulias, K.; Arkouli, Z.; Makris, S. Methodology for enabling digital twin using advanced physics-based modelling in predictive maintenance. *Procedia CIRP* **2019**, *81*, 417–422. [CrossRef]
30. Park, J.Y.; Nagy, Z. Comprehensive analysis of the relationship between thermal comfort and building control research—A data-driven literature review. *Renew. Sustain. Energy Rev.* **2018**, *82*, 2664–2679. [CrossRef]
31. Drgoňa, J.; Picard, D.; Kvasnica, M.; Helsen, L. Approximate model predictive building control via machine learning. *Appl. Energy* **2018**, *218*, 199–216. [CrossRef]
32. Chaudhuri, T.; Soh, Y.C.; Li, H.; Xie, L. Machine learning based prediction of thermal comfort in buildings of equatorial Singapore. In Proceedings of the 2017 IEEE International Conference on Smart Grid and Smart Cities (ICSGSC), Singapore, 23–26 July 2017; pp. 72–77.
33. Liu, S.; Schiavon, S.; Das, H.P.; Jin, M.; Spanos, C.J. Personal thermal comfort models with wearable sensors. *Build. Environ.* **2019**, *162*, 106281. [CrossRef]
34. Shahinmoghadam, M.; Natephra, W.; Motamedi, A. BIM- and IoT-based virtual reality tool for real-time thermal comfort assessment in building enclosures. *Build. Environ.* **2021**, *199*, 107905. [CrossRef]
35. Chong, A.; Poh Lam, K. A Comparison of MCMC Algorithms for the Bayesian Calibration of Building Energy Models. In Proceedings of the 15th International Conference of IBPSA—Building Simulation 2017, San Francisco, CA, USA, 7–9 August 2017; pp. 494–503.
36. *ASHRAE Guideline 14-2014 Measurement of Energy, Demand, and Water Savings*; ASHRAE: Atlanta, GA, USA, 2014; Volume 4, pp. 1–150.
37. Jain, N.; Burman, E.; Mumovic, D.; Davies, M. *Operational Performance: Building Performance Modelling and Calibration for Evaluation of Energy in-Use*; CIBSE TM63: London, UK, 2020.

Optimization of Useful Daylight Illuminance for Vertical Shading Fins Covered by Photovoltaic Panels for a Case Study of an Office Room in the City of Wroclaw, Poland

Marcin Brzezicki [1],*, Paweł Regucki [2] and Jacek Kasperski [2]

[1] Faculty of Architecture, Wroclaw University of Science and Technology, Prusa 53/55, 50-317 Wrocław, Poland

[2] Faculty of Mechanical and Power Engineering, Wrocław University of Science and Technology, Wybrzeże Wyspiańskiego 27, 50-370 Wrocław, Poland; pawel.regucki@pwr.edu.pl (P.R.); jacek.kasperski@pwr.edu.pl (J.K.)

* Correspondence: marcin.brzezicki@pwr.edu.pl

Abstract: A building's facade is its main interface with the external environment, as it controls almost all energy flows in the building—losses and gains. In this context, the most recent invention of adaptive façades allows for the introduction of an optimized system for both daylight management and electrical energy production. The authors of the presented paper propose a novel adaptive façade system that is equipped with vertical shading fins of 1×4 m that are covered with PV panels. The fins are kinetic and rotate around a vertical axis in order to optimize solar irradiation for producing electricity. The presented adaptive façade is analyzed in two stages. Firstly, the number of vertical shading fins is optimized in the context of useful daylight illuminance (UDI) and daylight glare probability (DGP) using Radiance-cored software. Next, two scenarios of PV installation are verified for fixed and the Sun-tracking solution. The results show that the Sun-tracking system is more efficient than the fixed one, but electricity production is only increased by 3.21%. The reason for this is the fact that—while following the Sun's azimuth position—fins shade each other and reduce the effective area of the adjacent PV panels. Based on this, the authors conclude that the Sun-tracking system might be justified due to its protective or decorative function and not because of its improved effectiveness in generating electrical energy.

Keywords: adaptive facade; kinetic facade; glass facade; photovoltaic installation; renewable energy

1. Introduction

Buildings account for 40% of the total energy consumption in the European Union, and even more in other countries in which energy-saving policies are not so up-to-date [1]. In December 2019, the European Council set a target of carbon neutrality by 2050 [2,3]. The construction industry is booming worldwide, which may substantially increase the energy demand. In order to help bring about a carbon-neutral future, it is necessary to reduce the consumption of energy from non-renewable sources, as well as to decrease the energy demand through energy-saving environmentally-friendly technologies. The increase in energy gain from renewable sources would simultaneously cut down greenhouse gas emissions.

In fact, more energy is required to cool buildings than to heat them [4]. Therefore—in light of the ongoing climate change and global warming, technologies designed to reduce energy consumption in the warm seasons of the year are receiving particular attention [5]. Any technology that prevents heat build-up in a building translates into energy savings and the reduction of CO_2 emissions. This includes shading integration, which "leads to comfortable thermal conditions indoors and also may lead to significant energy savings when compared to a building without shading devices" [6].

A building's facade is its main interface with the external environment, and it controls almost all energy flows in the building—losses and gains. Given the high expectations

for the continuous reduction of CO_2 emissions, it has become evident that the current building envelope systems will not be able to satisfy new EU requirements. The invention of the adaptive facade transforms a passive and static facade into a unique system that resembles a living organism, the elements of which react to the changes in the internal and external environment [7]. The hereby proposed adaptive facade is a "complex system that in terms of spatial configurations and the behavior of its external skin" [8] improves the indoor visual comfort in a test room and generates electricity as a building integrated photovoltaic (BIPV) system. On the one hand, this revolutionizes how a building works and how the user's comfort is achieved, but on the other hand, it also tests the viability of vertical, rotating adaptive shading elements that simultaneously generate electricity. Shading systems are particularly important in this respect because they have a significant influence on the users' visual comfort.

Identification of the Problem

All-glass facades are used in buildings worldwide, regardless of their orientation and location. All-glass facades originated as an act of protest against low dwelling standards in 19th-century tenement houses and became a part of the so-called "international style", especially with regards to high-rise office blocks. However, fully glazed facades cause specific problems, especially concerning the microclimate in the room located behind such a facade; these problems include overheating and glare. To prevent problems, systems are being developed that regulate direct solar gain and reduce glare. At the beginning of the 20th century, a solution was to use thin layers of metal on glass, which in turn reflected a large part of the direct insolation. This solution, although effective to a limited extent, was widely criticized, which was mainly due to the broken contact between the inside and outside of the building, as well as the far-reaching unacceptable formal consequences in architecture. At the end of the 20th century, other daylight regulation systems were developed, among which the most popular and energy-efficient systems are those that block insolation before rays of light enter the room and cause the greenhouse effect. Such solutions include systems of external blinds, louvres, curtains, and fins [9].

The emergence of affordable photovoltaic (PV) systems has enabled the evolution of systems with dual functionality, which feature both shading and energy-generating elements. Such a system, in the form of fins that rotate around their vertical axis, is the subject of analysis in the presented article. Firstly, the number of vertical shading fins is optimized in the context of the useful daylight illuminance (UDI) metric. Next, the fins' surface is considered as a surface covered by photovoltaic panels, which, while gaining solar irradiation, produce electricity. This idea allows the fins to be perceived as multifunctional elements that not only improve the daylight and thermal comfort of office rooms but also constitute an integral element of the building's energy system.

2. State of the Art

The authors of the paper have provided a systematic literature review concerning the subject of daylight management and electrical energy gain. The data for the literature review were acquired from international scientific databases (WoS and Scopus—last search 20 September 2021). The authors have examined the words in the titles and abstracts of similar studies to specify candidate search terms ("keywords"). Search strategy for all databases included the papers with keywords: "daylight"; "PV facade"; "PV electricity production". The scientific method applied in the paper includes the simulation of shading elements, therefore, the references from this were also included. Study selection was a multi-stage process. Screening of titles and abstracts allowed for the identification of potential studies for inclusion. It became evident that "daylight" and "PV electricity production" were a subject of many studies in the span of the last 20 years in the discipline of building engineering. In the discipline of daylight simulation, a single researcher (M.B.) reviewed the titles in approx. 970 published papers in the years 2017–2021. In the discipline of PV energy production, two researchers (P.R. and J.K.) reviewed titles in approx. 480 published

papers in the years 2017–2021. After the removal of duplicates, the same team of researchers double screened the abstract from the years 2017–2021. Subsequently, 160 records were screened, from which 34 full-text documents were reviewed, and finally 24 (each cited) papers are included in the literature review: the authors have selected for their detailed studies 17 papers regarding daylight regulation using external blinds and PV blinds, and 7 papers referring to electricity production by PV systems.

The main scientific method for the literature study used was a desk study (a PC with an internet connection); no automation tools were used.

2.1. Literature Review: Standard Blinds and PV Blinds in Different Scenarios

Daylight assessment methodology has been thoroughly discussed in many scientific papers, and the issue of the UDI metric and glare, along with more details regarding the simulation procedure, are discussed in detail in Section 4.2.

Standard blinds in different orientations and PV blinds in different scenarios are a field of vibrant scientific discussion. In 2007, Gratia and De Herde [10] studied the most efficient position of shading devices in a double-skin facade; in 2010, Palmero-Marrero and Oliveira [6] showed the effect of louvre shading devices on the energy requirements of a building; in 2014, Manzan [11] employed a genetic algorithm for the analysis of the most efficient position of shading devices; in 2017, Azmi et al. [12] studied a west-facing window in the context of a green office building; in 2018, Atzeri et al. [13] conducted a performance analysis of different glazing systems coupled with three shading control strategies; in 2021, Brzezicki and Regucki presented a paper including the optimization of the number of shading fins according to two variables: daylight distribution and the drag force induced on the elements of the shading system [14].

PV systems are opaque, and therefore the idea of coupling the PV element with a shading system is a subject of many research papers and continues to be a matter of scientific debate. The most systematic theoretical background for the subject was provided in the Ph.D. dissertation of Alzoubi in 2005 [15]. In 2013, Bahr [16] investigated the performance of an external shading device with integrated photovoltaic panels, which was followed by a comprehensive assessment methodology of the building's integrated photovoltaic blind system by the same author a year later [17]. In 2014, Kim et al. [18] published a paper concerning BIPV systems integrated with the power system of a building. In 2017, Hong et al. [19] developed a new control method for the slats of bi-directional blinds. Starting from the year 2018, two leading teams, Luo et at. and Kang et al., addressed the issue of PV blinds. The first team addressed multilayer glazing facades using shading blinds, and validated simulated results with experimental data [20–22]. The other team worked similarly (comparing simulation and experimental data) on sun-tracking methods for intelligent photovoltaic blinds [23]. The results of the study of Kang et al. in 2019 demonstrated that the technical performance of PV blinds could be improved by up to 24.8% by using the optimal solar tracking method [24,25]. Both teams worked on models and prototypes that featured horizontal louvres. None of the analyzed studies addressed the issues of shading elements in the vertical orientation.

2.2. Selection of Shading Elements

The selection of the type of shading elements was made according to the procedure described in the most recent paper published by the authors [14]. This analysis showed that various types of blinds and shutters are used, which have different angles and orientations. Vertical and horizontal shading devices for southern exposure facades in a dry climate were analyzed by Alzoubi and Al-Zoubi [15], with the conclusion that horizontal shading louvres "can simultaneously provide good daylighting and minimum heat gain in spaces". Although these types of blinds are effective in terms of illumination uniformity, they also significantly reduce the visual contact between the interior and exterior of the room, in turn preventing the users of the room from observing what is happening outside. Therefore, it is likely that the European Standard EN17037 criteria for the horizontal view angle (required

minimum angle of between 14° and 28°) are not met (for the view). In response to this, the presented paper concentrates on the optimization of rotating vertical shading fins that are located along the facade and which track the azimuthal position of the Sun. Moreover, the reasons for the choice of vertical fins are strictly utilitarian ones: (i) there is no accumulation of snow or dust on the vertical fins; (ii) fins in vertical orientation are optimal in terms of mechanical design because the vertical orientation is less susceptible to the forces generated by wind or gravity which lowers the material use and—in the result—the maintenance costs; (iii) fins in vertical orientation provide much better conditions for the outside view according to European Standard EN17037 because they block a smaller portion of the view; (iv) previous research proved that vertical fins can regulate the level of daylight inside a room successfully while significantly reducing the drag force, see [14]. However, it has to be noted that in areas without shading, patches of very high brightness occur, which disturbs the outside view in large offices, as addressed by Katunský et al. [26].

2.3. Photovoltaic Installations as a Part of a Building's Energy System

Photovoltaic cells are a renewable energy source that is considered as an alternative to electricity production from fossil fuels. The three most popular types of photovoltaic cells can be distinguished: monocrystalline, polycrystalline, and amorphous silicon panels. They are widely used in numerous industrial and urban installations [27]. Reducing the weight of the PV cells, while also increasing the efficiency of solar energy conversion and the ease of installation has made photovoltaic panels an attractive architectural solution. The standard approach to the problem of a building-integrated PV installation is presented, e.g., by Bahr [28], who investigated a home building case study and considered different aspects, such as energy demand, energy price, and solar intensity. Particular attention when considering the utilization of PV installations is focused on public buildings, which usually have a high demand for electricity and heat all year round. Radomski et al. [29] presented a case study of a multicriteria decision for the selection of a PV installation that provides electrical energy to a public utility building. They identified the technical, economical, energy, and environmental aspects that need to be considered as the main criteria when making decisions concerning the planning and development of energy supply systems. A similar approach to the optimization model for a building envelope retrofit with a roof-top PV installation is presented by Fan and Xia in [30]. They considered the retrofitting of old buildings with a roof-top PV installation as an effective method for improving their energy efficiency. The idea of installing PV cells on the facades and roof-tops of newly erected and existing buildings in order to improve their long-term sustainability of energy was also studied in [31]. Atmaja [32] analyzed building-integrated photovoltaic (BIPV) systems for optimizing electricity production from a building envelope. He noticed that facades and roof-tops could be treated as a part of an external building's envelope to be used for the PV installation. Vulkan et al. in [33] estimated the electricity generation by building-integrated PV systems in typical residential buildings in dense urban locations, accounting for shading by adjacent structures. They developed a 3D model of the shadows cast by adjacent objects with regards to different types of buildings., which was tested on a case-study neighborhood in Rishon LeZion, Israel.

In light of the above literature review, the vertical or horizontal fins initially installed on facades to shade the interior of office buildings can be seen as an attractive place for PV installations. Thus, the analysis of the BIPV system presented in this paper is part of a mainstream study concerning self-sufficient, intelligent building management systems. The estimation of electricity gain is conducted for both a fixed system and the Sun-tracking system of fins in order to evaluate the possible energy yields of an office room located in Wroclaw, Poland.

3. Objectives

The main goal of the presented study was to evaluate the effectiveness of the adaptive shading scenario of the south exposed facade of an office room (with an area of 72 m^2)

based on the results of computer simulations. Calculations were conducted for the case study of an office room located in the city of Wroclaw (Poland, 51 North latitude).

This effectiveness was the subject of a two-stage assessment with regards to the following criteria:

- the appropriate level of daylight illumination based on useful daylight illuminance ($UDI_{300-3000}$). The EN17037 standard states that at least 50% of an area should be illuminated for at least 50% of the time, and therefore the aim was to simultaneously maximize the time and the area;

- the evaluation of the amount of electricity generated by PV panels covering shading fins in both the fixed and tracking scenario.

According to the presented methodology, the assumption is made that it is possible to determine the optimal number of vertical shading fins according to daylight requirements and assess the effectiveness (or not) of their kinetic scenario regarding the production of electricity from the BIPV system.

4. Method

4.1. Optimization Procedure

The optimization procedure was performed in two stages. In the first stage, the authors focused on defining the optimum number n of vertical fins while taking into account useful daylight illuminance (UDI) and DGP. The optimum solution should provide the maximum number of hours with the illumination in the range of 300–3000 lx for the maximum possible area in the room during the office hours 09:00–17:00. Fixed (static) fins located parallel to the surface of the facade were used in the first stage of the research. A clear facade (no fins, $n = 0$) was assumed as the reference. In the preparatory stage of the research, it became clear that the optimal number of fins n_{opt} must be between 1 and 12. This is because the gradual increase of the number of fins leads to a situation of the total blockage of light for $n = 12$. Therefore, the first stage aimed to determine the proper number of fins n_{opt} for the optimal illumination of the office room. In this solution, avoiding the over-illumination, glare, and potential overheating of the room (which might result from the excessive solar gain) should also be considered. The results, given in the $UDI_{300-3000}$ metric, describe the percentage of the floor area that meets the range of 300–3000 lx for the number of hours according to the false color scale.

Daylight simulations were made using De Luminae software (DL-Light platform, ver. 11.0.9, DL-Instant, ver. 6.1.4). The core of the De Luminae engine uses a tool of established prestige—Radiance, which was previously validated by other researchers. Reinhart and Walkenhorst prove that Radiance based simulation methods "are able to efficiently and accurately model complicated daylighting elements" [34]. The validation studies, which were carried by Ng et al. [35] in Singapore, "showed that Radiance can be used to predict the internal illuminance with a high degree of accuracy". Also, as Yoon et al. [36] state: "Radiance, which is validated computational software and is well known to provide reliable prediction results under various sky conditions". Additionally, De Luminae is commercial software, which was also validated by the producer De Luminae SARL.

In the next stage, after the optimal number of fins was determined in daylight simulation, the authors verify which type of PV panel installation (either fixed or Sun-tracking) generates more electricity. The rationale is that if fixed fins provide adequate daylighting comfort, then presumably tracking fins will also provide at least the same comfort, as was the case in the fixed scenario.

4.2. The Choice of Daylight Metric

In the presented paper, two metrics were used to evaluate visual comfort: (i) useful daylight illuminance ($UDI_{300-3000}$) and (ii) daylight glare probability (DGP).

- $UDI_{300-3000}$ metric specifies the percentage of the floor area that meets the illuminance range between 300–3000 lx for a given number of daylight hours (for detailed results, see Section 5). This metric was chosen as a result of the ongoing scientific discussion

that was concluded in the paper titled "A comparison of four daylighting metrics in assessing the daylighting performance of three shading systems" by Boubekri and Lee [37]. UDI was proposed by Nabil and Mardaljevic in 2005 in the paper titled "Useful daylight illuminance: a new paradigm for assessing daylight in buildings" [38]. UDI, unlike the obsolete daylight metrics, e.g., the daylight factor, is constructed so that the real weather data are taken into account. Therefore "UDI represents the annual occurrence of daylight illuminances falling within the given range" [37]. In the literature, authors consider different intervals of illuminance values, but the value of 3000 lx is commonly used as the maximum threshold. Therefore, based on the scientific literature, this maximum value was also applied in the presented calculations. Suk et al. [39] published a review of different glare discomfort thresholds, the summary of which is presented in Table 1.

- Daylight glare probability (DGP, expressed in %) was defined for the first time by Jan Wienold at the Fraunhofer Institute for Solar Energy Systems [40]. DGP is higher when the luminance increases, with some influence on the direction of the view. As Wienold and Christoffersen claim that DGP above 35% the glare is rated as "perceptible" while with DGP above 45% the glare is "intolerable". DGP in the presented paper was calculated automatically using the below-presented Formula (1):

$$\text{DGP} = 5.87 \cdot 10^{-5} \cdot E_v + 9.18 \cdot 10^{-2} \cdot \log\left(1 + \sum_i \frac{L_{s,\,i}^2 \cdot \omega_{s,i}}{E_v^{1.87} \cdot P_i^2}\right) \tag{1}$$

where E_v is the vertical eye illuminance (lx); L_s is the luminance of the source (cd/m^2); ω_s is the solid angle of the source, and P is the position index (see Reference [40]).

Table 1. Different glare discomfort thresholds by different authors.

Ref. No.	Authors	Year	Thresholds	Remarks
[41]	Sutter et al.	2006	>3200 lx	
[42]	Linney	2008	>2740 lx	
[43]	Van Der Wymelenberg and Inanici	2016	>4000 lx	
[44]	Mardaljevic et al.	2012	>3200 lx	
[40]	Wienold and Christoffersen	2006	<2000 lx	Perceptible
			>6000 lx	Intolerable

4.3. Experimental Setup for Simulating UDI, DGP/DGI, and Electricity Production

This paper aims to analyze the influence of different spacings between shading elements on the visual comfort measured using the $UDI_{300\text{-}3000}$ metric and DGP/DGI. The room that is the subject of the analysis is a 12×6 m office room (72 m^2 area, 6 m depth) with a height/clearance of 4.0 m. The long side of the room faces directly south, and the south facade is entirely clad in glass. In the simulation, the glass with the daylight transmittance of 0.52 is used, which is analogous to the Insulating Glass Unit made of Pilkington Suncool™ OW 50/25, as given by Pilkington in [45], which would be conventionally used at the surface of the south-exposed facade. The vertical fins were located at a distance of 0.6 m from the surface of the facade in a parallel position in relation to the surface of the facade. They have a rectangle shape and dimensions of 1 m (width) × 4 m (height). For the first stage of the simulation (daylight), the fins are in a fixed (static) position, parallel to the surface of the facade. For the second stage of the simulation (energy generation), the fins track the Sun position by rotating around their vertical axis of symmetry. The PV-covered surface of the fin is always perpendicular to the direction of the sunlight in the horizontal plane. Each fin has a surface of 4.0 m^2, and the side of the fin, which is always oriented towards the Sun, is covered by PV cells. This PV system generates electricity

as a sustainable and renewable source of energy to be used for the internal needs of the building. A schematic diagram of the method is given in Figure 1.
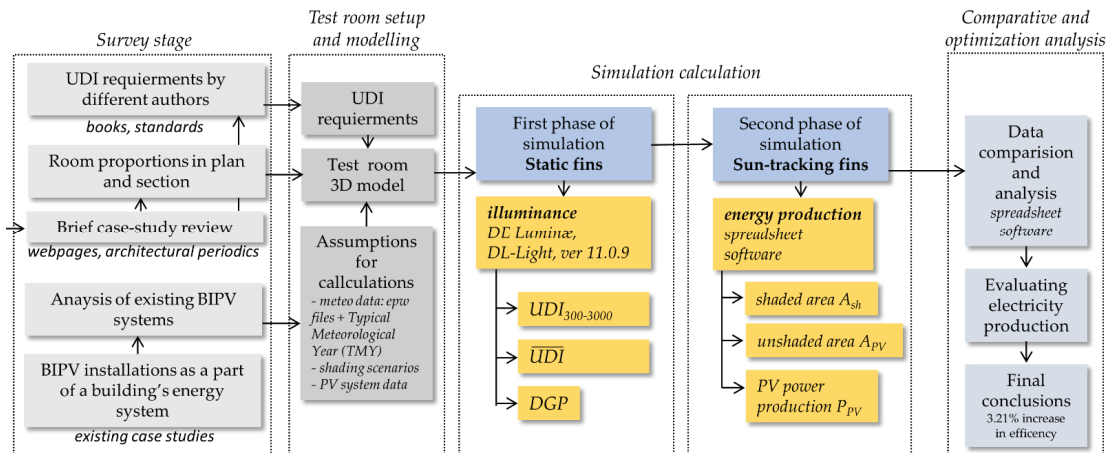

Figure 1. The schematic diagram of the adopted methodology and sequence of simulation.

4.4. Assumptions for Daylight Analysis

The $UDI_{300-3000}$ and DGP/DGI calculations were carried out for the city of Wroclaw, which is located in Poland (in Central Europe) on the 51 North latitude. The real weather data files, recorded by the Institute of Meteorology and Water Management of the National Research Institute in 2017, were used to simulate the insolation. The data was retrieved in *.epw format from the site of Energy Plus+ software [46]. The geometrical model of the office room was made using SketchUp (3D-modeling software), and the daylight simulations were made using De Luminae software (DL-Light platform, ver 11.0.9, DL-Instant, ver. 6.1.4). Figure 2 shows the simulation setup. The values of illuminance were calculated by virtual sensors placed at the grid of 0.5 × 0.5 m in the office room, as shown in Figure 3.

The $UDI_{300-3000}$ calculations were performed for the worst-case scenario from the point of view of visual comfort in the room, for the days with the longest daylight duration in the year. This circumstance occurs in Wroclaw for the period of 31 days, from 9 June to 9 July. The simulation was carried out for every hour in the above defined period, however, the results were presented only for 168 working hours, taking into account the occupant schedule in the range of 09:00–17:00 h. Calculations were performed in incremental steps for the number of fins from 4 to 11. This range of fins was selected because the previous research conducted by the authors in [14] showed that: (i) less than 4 fins do not effectively change the daylight distribution in the room (half of the work plane is exposed to the values of 3000 lx and more); (ii) 12 fins block the daylight completely. In the numerical calculations, the 31-day period was selected in order to average the weather data and exclude the influence of single overcast days on the final results (if the shorter interval would be selected).

DGP/DGI was calculated automatically using the DL-Instant, ver. 6.1.4. The calculation of DGP/DGI and the estimation of glare were performed on 4 July (in the middle of the assumed test period), at 12:30 for a person of average height (1.8 m) standing inside the room looking west. This particular day and the time of the day was chosen because of the high Sun altitude in the sky. Bright patches of light were one of the most significant factors contributing to the glare sensation. The radiance materials (used both for $UDI_{300-3000}$ and DGP/DGI) and the relative parameter values of the surfaces, glazing, and solar shading screens are shown in Table 2.
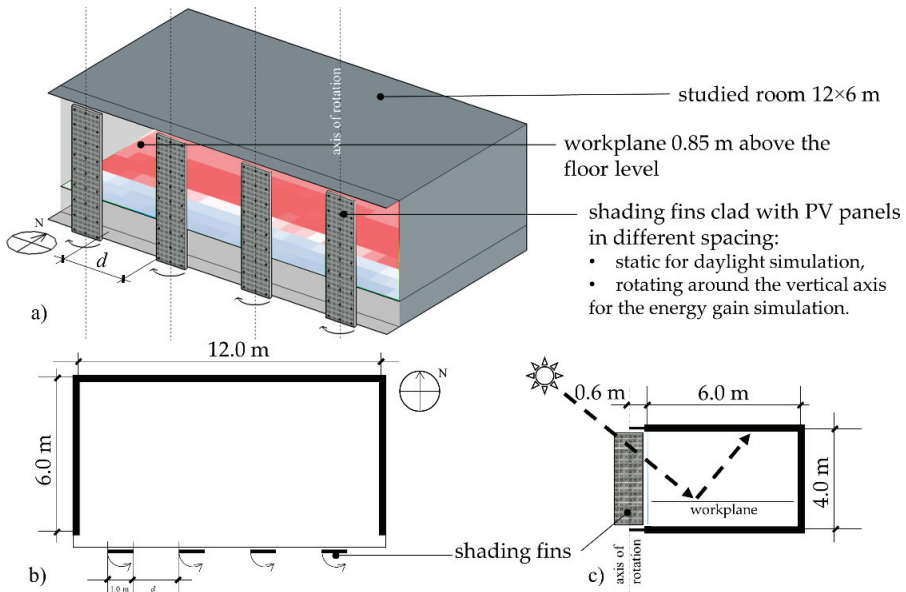
Figure 2. Simulation setup: (**a**) an axonometric view showing the test room, below: (**b**) the schematic plan showing the location of the shading fins; (**c**) the schematic section showing the location of the shading fins.
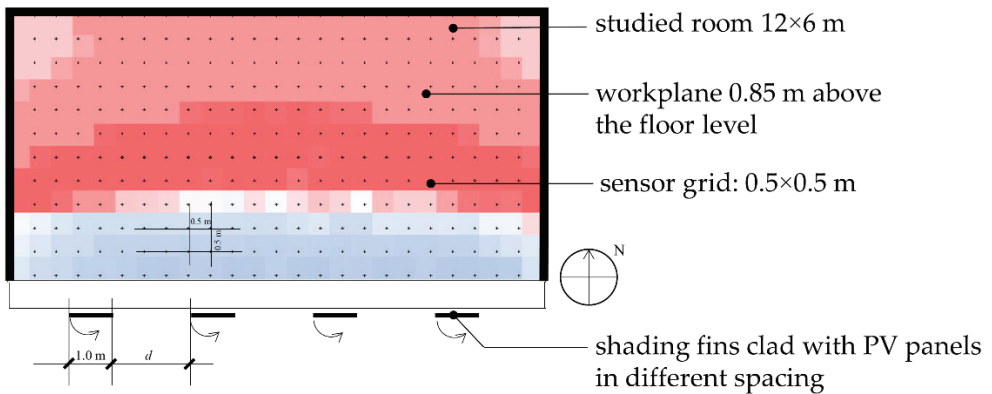

Figure 3. Test room plan: the dimension of the working plane and the location of measuring sensors.

Table 2. Materials and radiance parameters of the room surfaces and shading fins.

	Vertical Surfaces of the Test Room	Work Plane	Ceiling	Standard Window	Shading Fin Shaded-Side
Material	Grey concrete	Dark gray (RAL 7000)	Grey concrete	Transparent glass	White metal
Reflectance	0.42	0.23	0.42	0	0.28
Transmittance	0	0	0	0.52 [1]	0

[1] Insulating Glass Unit made of Pilkington Suncool™ OW 50/25.

4.5. Electricity Generation Assumptions for the Calculations

Types of photovoltaic technologies and systems are well described in academic textbooks [47,48]. In the presented case study, the authors analyzed the possibility of producing electricity by a PV installation consisting of monocrystalline panels. This type of panel is popular in domestic and industrial systems due to its relatively low price, easy installation, and low operating costs. The product warranty given by the producer is 12 years, and the power warranty is 90% and 80% of the nominal output power after 10 and 25 years, respectively.

Solar radiation and ambient temperature have an important influence on the power production of a photovoltaic panel. The PV power production P_{PV} is described by Equation [47–49]:

$$P_{PV} = P_{max}\frac{GI}{G_{STC}}\left(1 - \frac{\gamma}{100}(T_{NOCT} - T_{cell})\right) \cdot \eta_{inv} \cdot \eta_{wire} \cdot N \tag{2}$$

where:

P_{max}—the rated maximum power, W/panel;

GI—current global irradiance, W/m^2;

G_{STC}—solar radiation in standard test conditions (STC), W/m^2;

γ—the temperature coefficient of P_{max}, %/°C;

T_{cell}—current cell temperature, °C;

T_{NOCT}—normal operating cell temperature (NOCT), °C;

η_{inv} and η_{wire}—the efficiency of the inverter and wire, respectively;

N—the total number of PV panels.

For the considered panel, the standard test conditions are: G_{STC} = 1000 W/m^2, cell temperature T_{STC} = 25 °C and AM1.5G. The cell temperature is T_{NOCT} = 45 °C under normal operating conditions: G_{NOCT} = 800 W/m^2, ambient temperature $T_{a,NOCT}$ = 20 °C, wind speed of 1 m/s and AM1.5G. The current cell temperature T_{cell} is described by the Equation:

$$T_{cell} = T_{a,DBT} + \frac{GI}{G_{NOCT}}(T_{NOCT} - T_{a,NOCT}) \tag{3}$$

where $T_{a,DBT}$ is the current ambient temperature of the dry-bulb thermometer. During the day, the cell temperature T_{cell} changes with solar radiation GI. Therefore, the calculations of electricity production were done within 1-h time intervals applying the meteorological data collected in the Typical Meteorological Year (TMY) database for Wrocław city, Poland [50].

5. Results and Discussion

5.1. UDI Metric

Daylight analysis was carried out for fixed fins located parallel to the facade. The numerical calculations were conducted for the number of fins ranging from 4 to 11 evenly spaced along the length of the entire facade. The distance between adjacent fins was described as spacing d. The results of the daylight calculations are presented in the form of the false-color-scale diagrams in Figure 4 and the form of the data in Table 3.

In Figure 4, the colors refer to the number of hours that meet the illuminance conditions in the range of 300–3000 lx at the level of the work plane. Two metrics were used to assess the optimal number of fins: (i) percentage of the work plane area that falls in the range of 300–3000 lx for a specified number of hours and (ii) mean $\overline{UDI}$ (see Figure 4 and Supplementary Materials for the results).
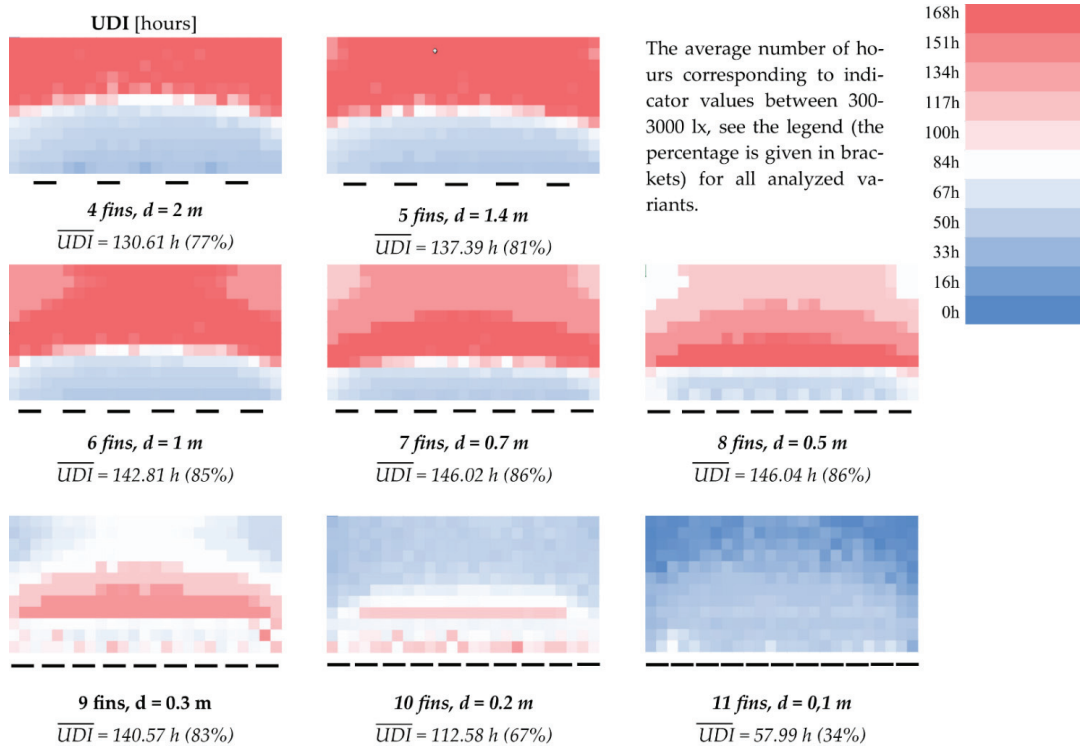
Figure 4. Results of the first phase of the simulation: test room plan and spatial distribution of $UDI_{300\text{-}3000}$ over the test period from 9 June to 9 July for the specified number of hours. Exact values are given in the data file in the Supplementary Materials.

Table 3. Work plane area (in m^2) for which the $UDI_{300\text{-}3000}$ metric is satisfied for a given number of fins. The results for fins 7 and 8 are given in bold type because those values would be the subject of further consideration.

Interval, h		(0–16)	(16–33)	(33–50)	(50–67)	(67–84)	(84–100)	(100–117)	(117–134)	(134–151)	(151–168)
	4	0.00	0.00	0.00	0.71	9.31	13.63	6.77	3.22	3.81	34.55
	5	0.00	0.00	0.00	0.00	6.03	11.61	7.49	3.14	4.15	39.58
number of fins, *n*	6	0.00	0.00	0.00	0.00	3.40	9.91	6.01	2.88	3.37	46.43
	7	**0.00**	**0.00**	**0.00**	**0.00**	**1.07**	**7.52**	**5.88**	**2.18**	**3.48**	**51.87**
	8	**0.00**	**0.00**	**0.00**	**0.00**	**0.00**	**5.06**	**3.96**	**5.93**	**6.65**	**50.41**
	9	0.00	0.00	0.00	0.00	0.00	1.01	4.26	11.04	32.02	23.67
	10	0.00	0.00	0.00	0.12	5.23	27.90	5.91	9.96	17.01	5.87
	11	8.01	9.37	8.12	10.61	20.74	13.39	1.33	0.26	0.17	0.00

All the $UDI_{300\text{-}3000}$ results in Table 3 are calculated for 168 office hours in the 31-day period (from 9 June to 9 July). Generally, the results show that a large part of the work plane area was correctly daylit throughout the whole simulation period. This especially applied to the part which was located deeper into the office room (larger distance from the glazed facade). In turn, a part of the work plane area located closer to the glazed facade was overexposed, especially if a small number of fins was used for shading. For example, the simulation for four fins shows that more than half of the work plane area was overexposed for more than half of the simulation time (84 h out of 168 in total). However, for the specified model setup, the $UDI_{300\text{-}3000}$ had an interesting tendency. From the data

presented in Table 3, it can clearly be seen that the increase in the number of fins to seven caused a gradual increase in the work plane area for which the UDI criteria were satisfied for a longer period of time. From nine fins onward, the tendency was reversed, and the UDI values gradually decreased. This behavior is explained by the obvious fact that less daylight is admitted to the office room when there are more fins. Initially, the visual comfort is improved with the increasing number of fins (fewer hours and less area illuminated above 3000 lx), but the further addition of fins resulted in a worse penetration of daylight (more hours and more area illuminated below 300 lx). As was mentioned above, according to EN 17,037, at the first stage of simulation, the number of fins was optimized simultaneously towards two parameters: (i) the longest period of time (expressed in the number of office working hours) and (ii) the maximum area for which the illuminance satisfied the desired range of 300–3000 lx. When studying the data from Table 3, it is easy to notice that this percentage exceeded 70% of the work plane area for n = 7 and 8 fins. Simple observation showed that for n = 7, the largest part of the work plane area was occupied for the longest time interval (151–168 h), but it was not a decisive argument. The data presented in Table 3 must be analyzed using statistical tools. For each value of n, information about the work plane area is presented in the form of the surface distribution of grouped data arranged into 10 class intervals (from (0–16) up to (151–168)). Figure 5 presents the histograms of the surface distribution of the grouped data for n = 7 and 8.
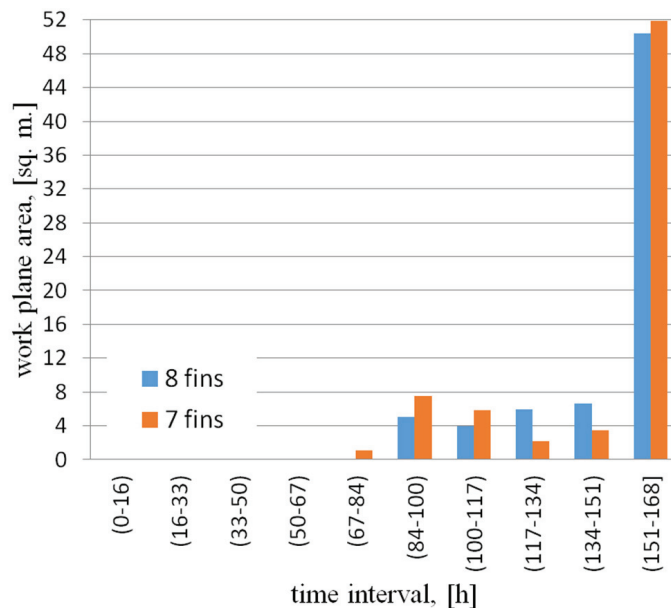

Figure 5. Histograms of the surface distribution of the grouped data for n = 7 and 8.

When analyzing the histograms, it can clearly be seen that for n = 8, the largest work plane area was occupied for the longest time. Therefore, for the time period of 100–168 h, the $UDI_{300\text{-}3000}$ metric was fulfilled on 66.94 m^2 for n = 8 when only on 63.41 m^2 for n = 7.

To decide which value of n is optimal (7 or 8), the mean value of office hours $\overline{m}$ (for which the UDI metric is satisfied) was calculated using the formula:

$$\overline{m} = \frac{1}{A_{tot}} \sum_{i=1}^{10} \overline{m}_i \cdot A_i \tag{4}$$

where: A_{tot}—total work plane area equal to 72 m^2, $\overline{m}_i$—middle of the i hour interval; A_i—work plane area for the i hour interval. The i variable numerates the hour intervals ($i = 1, \ldots, 10$).

Using (4), the mean value $\overline{m}$ is equal to 145.2 h and 147.6 h for $n = 7$ and 8, respectively. Based on this, the authors established that the optimum number of fins n_{opt} is 8. The results of mean $\overline{UDI}$ and DGP (see below) also support this choice (146.02 h for 7 fins and 146.04 h for 8 fins, respectively).

5.2. DGP Metric

DGP/DGI analysis was carried out for fixed fins located parallel to the facade. The results of DGP calculations are presented in the form of the false-color-scale diagrams in Figure 6.
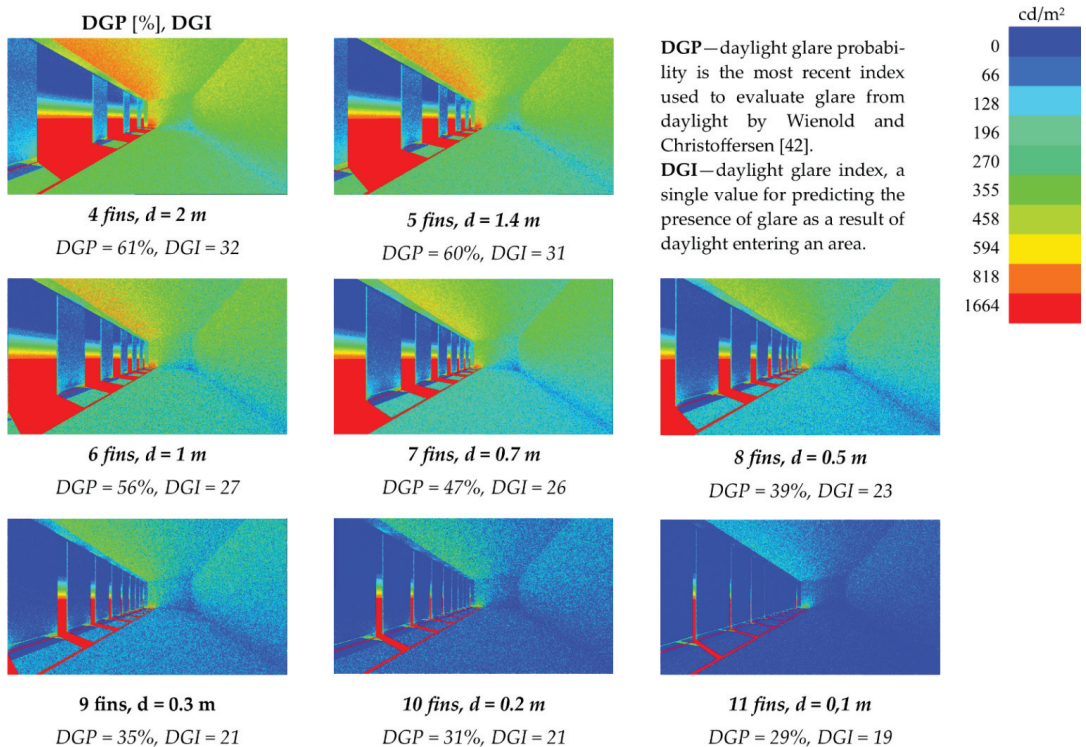

DGP [%], DGI

4 fins, d = 2 m
DGP = 61%, DGI = 32

5 fins, d = 1.4 m
DGP = 60%, DGI = 31

DGP—daylight glare probability is the most recent index used to evaluate glare from daylight by Wienold and Christoffersen [42].
DGI—daylight glare index, a single value for predicting the presence of glare as a result of daylight entering an area.

cd/m²
0
66
128
196
270
355
458
594
818
1664

6 fins, d = 1 m
DGP = 56%, DGI = 27

7 fins, d = 0.7 m
DGP = 47%, DGI = 26

8 fins, d = 0.5 m
DGP = 39%, DGI = 23

9 fins, d = 0.3 m
DGP = 35%, DGI = 21

10 fins, d = 0.2 m
DGP = 31%, DGI = 21

11 fins, d = 0,1 m
DGP = 29%, DGI = 19

Figure 6. Results of the first phase of the simulation: test room plan and spatial distribution of $UDI_{300\text{-}3000}$ over the test period from 9 June to 9 July for the specified number of hours. Exact values are given in the data file in the Supplementary Materials.

In general, the results of the glare analysis DGP/DGI confirm the results that were obtained using $UDI_{300\text{-}3000}$. The variants with fins from 4 to 7 were characterized by very high or high values of DGP (61, 60, 56, 47%, respectively) or DGI (32, 31, 27, 26, respectively). With 8 fins, the value of DGP dropped below 39%, which generally signifies perceptible glare (35% $\leq$ DGP < 40%), but not disturbing (40% $\leq$ DGP < 45%), while the value of DGI is 23, which was in the range of acceptable values (22 $\leq$ DGI < 24). For variants with fewer fins, the glare was obviously lower, down to the level of imperceptible glare (DGP < 35%), but as could be concluded from the analysis of UDI, the illuminance dropped below the accepted levels, therefore, those variants were rejected. See the false-color diagrams presented in Figure 6.

5.3. Electricity Produced by the PV System

In the considered case study, the authors compared two variants of the PV panels:

- fixed vertical panels that are always oriented towards the south and which are parallel to the facade;
- vertical panels equipped with a tracking system that always orients their surface perpendicularly to the solar beams.

Each shading fin was constructed from two monocrystalline panels with standard geometrical dimensions (H/W/D) of 1960 × 991 × 40 mm. The maximum power of a single PV panel was P_{max} = 350 Wp. Thus, for n_{opt} = 8 shading fins, the total number of PV panels was N = 16. The total electrical power of the considered BIPV system was 5.6 kW. For the considered PV panels, the temperature coefficient of P_{max} is equal to γ = −0.38%/°C, and the panel's efficiency under STC was 18%. The inverter and wire efficiencies were η_{inv} = 0.97 and η_{wire} = 0.99, respectively [48,49]. The details of the analyzed PV installation are presented in Table 4.

Table 4. The details of the analyzed PV installation.

The maximum power of a single PV panel, Wp	350
The total number of PV panels	16
The total electrical power of the BIPV system, kW	5.6
The temperature coefficient of P_{max} γ, %/°C	−0.38
The panel's efficiency under STC conditions, %	18
The geometrical dimensions of a single PV panel (H/W/D), mm	1960/991/40
The inverter's efficiency	0.97
The wire's efficiency	0.99

Based on the Typical Meteorological Year (TMY) database for Wroclaw, Poland [50], the electricity production calculations were conducted for a 31-day period (9 June to 9 July) between the hours of 09:00–17:00. The meteorological data was stored at one-hour intervals, and therefore in the calculations, the authors used global irradiance *GI* and ambient temperature $T_{a,\text{DBT}}$ as the fixed values during the one-hour intervals. In this approach, the unit of solar irradiance (W/m^2) is identical to the unit of energy (Wh/m^2).

5.3.1. Fixed Variant

In the first variant, the PV panels were oriented to the South and had a fixed distance from the facade. In this case, they did not shade each other. Based on the TMY database, Equations (2) and (3) allow the total electricity production in the period from 9 June to 9 July between the hours of 09:00–17:00 (8 h) to be calculated.

During these 31 days, the total global irradiance for the 8-h period was 106.2 kWh/m^2, and for the 24-h period (whole day) it was 107.5 kWh/m^2. This means that the PV panels were exposed to almost 98.8% of the daily solar irradiance during the designated office hours (09:00–17:00). This justifies the fact that the authors only calculate electricity production for the aforementioned office hours.

Based on (2), the production of electricity by 16 PV panels for the 8 h period is 420.7 kWh. It is worth mentioning that the overall energy conversion efficiency was at the level of 12.6% for the considered BIVP system. This is the result of the losses of energy in the inverter and wires, as well as the higher cell temperature T_{cell} when compared to the standard temperature T_{NOCT}.

5.3.2. Tracking Variant

The tracking position (expressed by angle α) was calculated individually for every single hour from 09:00 to 17:00 for the city of Wroclaw. The TMY database [50] allowed to

calculate the values of global irradiance *GI* for tracking angles α based on *GI* values for N, NE, E, SE, S, SW, and W azimuth direction. To find a *GI* value for a particular angle α, the interpolation polynomial of second-order was fitted using the Lagrange method [51].

It is worth mentioning that the rotation of panels could cause the partial shading of the fins by adjacent elements, as illustrated in Figure 7. It is easy to notice that for $\alpha = 0°$, only the first PV panel was exposed to direct solar radiation. All the other panels were partially in the shadow of the first one. Thus, the shaded part of a panel was affected only by diffuse radiation. On the contrary, for the fixed variant $\alpha = 90°$ and all panels are exposed to direct solar radiation. The criterion that allows us to judge whether partial shading occurred can be formulated in the form of inequality:

$$z > 2x + d \tag{5}$$

where *d* is the distance between adjacent fins and *x*, *z* are the lengths that are marked in Figure 7.
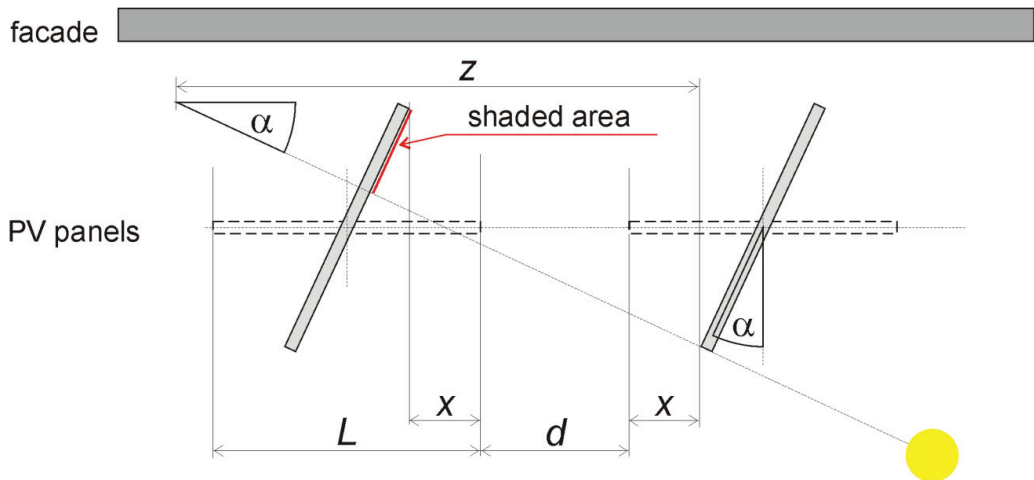

Figure 7. Example of the positioning of the adjacent PV panels' shaded area and mathematical notation provided.

Based on the geometric and trigonometric relationships, one can derive the formulas for *z* and *x*:

$$z = L\frac{\cos^2(\alpha)}{\sin(\alpha)}; \quad x = 0.5L(1 - \sin(\alpha)) \tag{6}$$

Formulas (5) and (6) allow the interval of tracking angles α for which shading does not occur to be found. The shading does not occur when ($z \leq 2x + d$). For length $L = 1$ m and spatial distance $d = 0.571$ m (for $n_{opt} = 8$ fins), the shading phenomenon does not occur if $\alpha \in (39.5°, 140.5°)$. If condition (5) is satisfied, the shaded area A_{sh} is calculated from the formula:

$$A_{sh} = H \cdot (z - (2x + d)) \sin(\alpha) \tag{7}$$

where *H* is the height of the fin, which is equal to 4 m. The resultant unshaded area of PV system A_{PV}, which consists of *n* fins, is defined as:

$$A_{PV} = n \cdot H \cdot L - (n - 1) \cdot A_{sh} \tag{8}$$

It is worth mentioning that the term $(n - 1)$ in (8) refers to the number of fins that are partially shaded. Table 5 presents the tracking angles α for each office hour and the resultant unshaded area A_{PV} of the PV system. When analysing these data, it can clearly be seen that partial shading occurs during the morning (09:00–10:00) and afternoon (14:00–17:00)

hours. The resultant unshaded area A_{PV} has the maximum value between the hours of 10:00 and 14:00.

Table 5. The tracking angles α for each office hour and the resultant unshaded area A_{PV} of the PV system consisting of 8 fins.

Office Hours	09:00–10:00	10:00–11:00	11:00–12:00	12:00–13:00	13:00–14:00	14:00–15:00	15:00–16:00	16:00–17:00
Tracking angle α, deg	23	41	64	93	121	143	160	176
A_{PV}, m^2	21.19	32.00	32.00	32.00	32.00	30.48	19.05	7.07

The shading phenomenon limits the production of electricity because the direct solar radiation does not have access to the whole surface of the PV panels. In this case, only diffuse radiation affects the shaded area. Taking into account partial shading, the electricity production from the tracking PV system for the considered period (9 June to 9 July, 09:00–17:00) is equal to 434.2 kWh. In comparison to the fixed variant, the tracking solution gives an improvement in electricity production of only about 3.21%. This low improvement is mainly due to the partial shading of the panels during the morning and afternoon hours. The shadow that is cast reduces the area exposed to direct sunlight, and therefore the electricity production is reduced.

It is worth noting that the obtained result depends on many parameters, including orientation of the facade towards the side of the world, latitude, climatic zone (related to TMY), method of shading fins assembly (vertical or horizontal) and the period of time for which the calculations are made.

6. Conclusions

The conducted research and calculations allow the following conclusions to be formulated:

- In the daylight analysis, the comparison of the quantitative parameter $UDI_{300\text{-}3000}$ showed an interesting tendency. When the distance between fins is too large (e.g., $d = 2$ m), the room is overlit; however, when the fins are too close to each other, the illumination in the room is reduced and the office room is under-exposed (e.g., $d = 0.1$ m).
- The maximum area in which the $UDI_{300\text{-}3000}$ is met for the longest period is reached for the variant with 8 fins. The presented study confirms the publicly available recommendation that the window opening area should not exceed 25% of the room's floor area (here 16 m^2 of opening out of 72 m^2 of clear floor space—22%).
- For the variant with 8 fins, the electricity production for 16 PV panels in the considered period is 420.7 and 434.2 kWh for the fixed and the Sun-tracking variant, respectively. This shows that the tracking system is only 3.21% more efficient than the static system.
- The study highlighted that the self-shading had a very high negative impact on the vertical kinetic PV systems for the South exposed facade. The authors conclude that the additional cost of the installation would not be justified by the increased production of electricity.
- The obtained improvement of efficiency is very low, especially in the context of the values achieved by other researchers analyzing horizontal shading elements. This result provides important insight into the limitations associated with kinetic shading systems.

The main innovations of the study are:

- a two-stage evaluation and assessment process based on computer simulations according to two criteria: visual comfort and electricity production,
- the introduction of a vertical Sun-tracking shading system covered with PV panels,
- the recognition of the relationship between the size of the window opening area and visual comfort in an office room,
- insights regarding the efficiency of the electricity production of the proposed shading system.

6.1. Limitation of the Study

However, the presented study has some limitations, which should be explicitly stated. First, due to the climatic considerations in Wroclaw (high probability of snow coverage in the winter), only vertical shading fins have been analyzed. The authors are aware that in hot climates, the horizontal orientation of fins is more effective, as shown by Mesloub et al. [52] and Mesloub et al. [53], resulting in higher electricity production, but this solution would entail much higher material and maintenance costs (deicing and snow removal). In addition and intentionally, analysis was conducted for a limited period, for 31 days between 9 June and 9 July, taking into account that in this period, potentially the most unfavorable sunlight conditions occur (high angle of incidence). Moreover, in daylight analysis, the static fins have been used. This decision is supported by the fact that mechanized fins would only improve the penetration of the daylight deep into the room. Therefore—in the perspective of the visual comfort—the use of the static fin is the worst-case scenario and can be used as a benchmark value for the conducted analysis. The readers should also be aware that external vertical fins with PV panels installed are at risk of being destroyed by violent weather phenomena. This issue was a subject of the previous papers by the authors of the presented research [14].

6.2. Future Research

Future studies for different climate zones should aim to analyze more variants with different possible geometries of PV panels, e.g., the horizontal ones. Furthermore, a fully retractable system of fins might be analyzed, allowing more light to penetrate the office room in the days with full cloud coverage. Visual comfort throughout the entire year should also be investigated with particular attention to the period of the equinox when the Sun altitudes are lower. Potential improvement of the credibility of results is associated with experimental research that might deliver data based on measurements, as previously discussed by Bodart and Cauwerts, in a room with a different geometry [54].

In further research, the authors plan to provide similar analyses for facades with horizontal shading elements (including facades with different orientations) and different kinetic scenarios. It might also be promising to check pantograph-based systems instead of simple vertical axis rotation systems. It is also necessary to state that vertical, kinetic PV systems for East or West exposed facades require additional research since the azimuth angles are different.

Nomenclature

$UDI_{300\text{-}3000}$	useful daylight illuminance,
$\overline{UDI}$	mean UDI,
A	area, m^2
d	distance between adjacent shading fins, m
E_v	vertical eye illuminance
G_{STC}	solar radiation in standard test conditions (STC), W/m^2
GI	global solar irradiance, W/m^2
H	height of shading fin, m
i	integer number,
L	length of shading fin, m
L_s	luminance of the source, cd/m^2
m	office hours, h
n	number of fins,
N	number of panels in PV system,
P	power, W
P_i	position index (see Reference [36]).
t	time, h
T	temperature, °C
x, z	length, m

Greek letter

α	tracking angle, deg
γ	temperature coefficient of the panel, %/°C
η	efficiency,
ω_s	solid angle of the source

Subscripts

a	ambient,
$cell$	cell,
DBT	dry-bulb temperature,
inv	inverter,
max	maximum,
$NOCT$	normal operating cell temperature,
opt	optimal,
tot	total,
PV	photovoltaic,
sh	shaded,
STC	standard test condition,
$wire$	wire,

References

1. Thewes, A.; Maas, S.; Scholzen, F.; Waldmann, D.; Zürbes, A. Field study on the energy consumption of school buildings in Luxembourg. *Energy Build.* **2014**, *68*, 460–470. [CrossRef]
2. European Council Meeting Conclusions. 2019. Available online: https://www.consilium.europa.eu/media/41768/12-euco-final-conclusions-en.pdf (accessed on 13 September 2021).
3. Going Climate-Neutral by 2050, A Strategic Long-Term Vision for a Prosperous, Modern, Competitive and Climate-Neutral EU Economy. Available online: https://op.europa.eu/en/publication-detail/-/publication/92f6d5bc-76bc-11e9-9f05-01aa75ed71a1 (accessed on 13 September 2021).
4. Kolokotroni, M.; Ren, X.; Davies, M.; Mavrogianni, A. London's urban heat island: Impact on current and future energy consumption in office buildings. *Energy Build.* **2012**, *47*, 302–311. [CrossRef]
5. Datta, G. Effect of fixed horizontal louver shading devices on thermal perfomance of building by Trnsys simulation. *Renew. Energy* **2001**, *23*, 497–507. [CrossRef]
6. Palmero-Marrero, A.I.; Oliveira, A.C. Effects of louver shading devices on building energy requirements. *Appl. Energy* **2010**, *87*, 2040–2049. [CrossRef]
7. Brzezicki, M. A typology of adaptive façades. An empirical study based on the morphology of glazed facades. *Cogent Arts Humanit.* **2021**, *8*, 1960699. [CrossRef]
8. Romano, R.; Aelenei, L.; Aelenei, D.; Mazzucchelli, S. What is an Adaptive Façade? Analysis of Recent Terms and Definitions from an International Perspective. *J. Facade Des. Eng.* **2018**, *6*, 65–76. [CrossRef]

9. O'Brien, W.; Kapsis, K.; Athienitis, A.K. Manually-operated window shade patterns in office buildings: A critical review. *Build. Environ.* **2013**, *60*, 319–338. [CrossRef]
10. Gratia, E.; De Herde, A. The most efficient position of shading devices in a double-skin façade. *Energy Build.* **2006**, *39*, 364–373. [CrossRef]
11. Manzan, M. Genetic optimization of external fixed shading devices. *Energy Build.* **2014**, *72*, 431–440. [CrossRef]
12. Azmi, N.A.; Kandar, M.; Toe, D. Daylight Optimization for Green Office Building: A Study of West Facing Window Design and Configuration. *Adv. Sci. Lett.* **2017**, *23*, 9177–9182. [CrossRef]
13. Atzeri, A.M.; Gasparella, A.; Cappelletti, F.; Tzempelikos, A. Comfort and energy performance analysis of different glazing systems coupled with three shading control strategies. *Sci. Technol. Built Environ.* **2018**, *24*, 545–558. [CrossRef]
14. Brzezicki, M.; Regucki, P. Optimization of useful daylight illuminance vs. drag force for vertical shading fins/panels. *Sci. Technol. Built Environ.* **2021**, *27*, 367–376. [CrossRef]
15. Alzoubi, H.H.; Al-Zoubi, A.H. Assessment of building façade performance in terms of daylighting and the associated energy consumption in architectural spaces: Vertical and horizontal shading devices for southern exposure facades. *Energy Convers. Manag.* **2010**, *51*, 1592–1599. [CrossRef]
16. Bahr, W. Optimal Design Parameters Of The Blinds Integrated Photovoltaic Modules Based On Energy Efficiency And Visual Comfort Assessments. In Proceedings of the Central Europe towards Sustainable Building 2013, CESB13 Prague, Prague, Czech Republic, 26–28 June 2013.
17. Bahr, W. A comprehensive assessment methodology of the building integrated photovoltaic blind system. *Energy Build.* **2014**, *82*, 703–708. [CrossRef]
18. Kim, S.-H.; Kim, I.-T.; Choi, A.-S.; Sung, M. Evaluation of optimized pv power generation and electrical lighting energy savings from the PV blind-integrated daylight responsive dimming system using led lighting. *Sol. Energy* **2014**, *107*, 746–757. [CrossRef]
19. Hong, S.; Choi, A.-S.; Sung, M. Development and verification of a slat control method for a bi-directional PV blind. *Appl. Energy* **2017**, *206*, 1321–1333. [CrossRef]
20. Luo, Y.; Zhang, L.; Wu, J.; Wang, X.; Liu, Z.; Wu, Z. Modeling of solar transmission through multilayer glazing facade using shading blinds with arbitrary geometrical and surface optical properties. *Energy* **2017**, *128*, 163–182. [CrossRef]
21. Luo, Y.; Zhang, L.; Liu, Z.; Xie, L.; Wang, X.; Wu, J. Experimental study and performance evaluation of a PV-blind embedded double skin façade in winter season. *Energy Part B* **2018**, *165*, 326–342. [CrossRef]
22. Luo, Y.; Zhang, L.; Su, X.; Liu, Z.; Lian, J.; Luo, Y. Improved thermal-electrical-optical model and performance assessment of a pv-blind embedded glazing façade system with complex shading effects. *Appl. Energy* **2019**, *255*, 113896. [CrossRef]
23. Kang, H.; Hong, T.; Jung, S.; Lee, M. Techno-economic performance analysis of the smart solar photovoltaic blinds considering the photovoltaic panel type and the solar tracking method. *Energy Build.* **2019**, *193*, 1–14. [CrossRef]
24. Kang, H.; Hong, T.; Lee, M. Technical performance analysis of the smart solar photovoltaic blinds based on the solar tracking methods considering the climate factors. *Energy Build.* **2019**, *190*, 34–48. [CrossRef]
25. Kang, H.; Hong, T.; Lee, M. A new approach for developing a hybrid sun-tracking method of the intelligent photovoltaic blinds considering the weather condition using data mining technique. *Energy Build.* **2020**, *209*, 1–11. [CrossRef]
26. Katunský, D.; Dolníková, E.; Dolník, B. Daytime Lighting Assessment in Textile Factories Using Connected Windows in Slovakia: A Case Study. *Sustainability* **2018**, *10*, 655. [CrossRef]
27. O'Shaughnessy, E. Trends in the market structure of US residential solar PV installation, 2000 to 2016: An evolving industry. *Prog. Photovolt. Res. Appl.* **2018**, *26*, 901–910. [CrossRef]
28. Bahr, W. A PV installation framework concerning electricity variable rates. *Int. J. Ambient Energy* **2018**, *39*, 802–812. [CrossRef]
29. Radomski, B.; Ćwiek, B.; Mróz, T.M. The choice of primary energy source including PV installation for providing electric energy to a public utility building—A case study. In *E3S Web of Conferences*; EDP Sciences: Ulis, France, 2017; Volume 22, p. 00141. [CrossRef]
30. Fan, Y.; Xia, X. A multi-objective optimization model for energy-efficiency building envelope retrofitting plan with rooftop PV system installation and maintenance. *Appl. Energy* **2017**, *189*, 327–335. [CrossRef]
31. Kotak, Y.; Gago, E.J.; Mohanty, P.; Muneer, T. Installation of roof-top solar PV modules and their impact on building cooling load. *Build. Serv. Eng. Res. Technol.* **2014**, *35*, 613–633. [CrossRef]
32. Atmaja, T.D. Façade and rooftop PV installation strategy for building integrated photo voltaic application. *Energy Procedia* **2013**, *32*, 105–114. [CrossRef]
33. Vulkan, A.; Kloog, I.; Dorman, M.; Erell, E. Modeling the potential for PV installation in residential buildings in dense urban areas. *Energy Build.* **2018**, *169*, 97–109. [CrossRef]
34. Reinhart, C.F.; Walkenhorst, O. Validation of dynamic radiance-based daylight simulations for a test office with external blinds. *Energy Build.* **2001**, *33*, 683–697. [CrossRef]
35. Ng, E.Y.-Y.; Poh, L.K.; Wei, W.; Nagakura, T. Advanced lighting simulation in architectural design in the tropics. *Autom. Constr.* **2001**, *10*, 365–379. [CrossRef]
36. Yoon, Y.; Moon, J.W.; Kim, S. Development of annual daylight simulation algorithms for prediction of indoor daylight illuminance. *Energy Build.* **2016**, *118*, 1–17. [CrossRef]
37. Boubekri, M.; Lee, J. A comparison of four daylighting metrics in assessing the daylighting performance of three shading systems. *J. Green Build.* **2017**, *12*, 39–53. [CrossRef]

38. Nabil, A.; Mardaljevic, J. Useful daylight illuminance: A new paradigm for assessing daylight in buildings. *Lighting Res. Technol.* **2005**, *37*, 41–59. [CrossRef]
39. Suk, J.Y. Luminance and vertical eye illuminance thresholds for occupants' visual comfort in daylit office environments. *Build. Environ.* **2019**, *148*, 107–115. [CrossRef]
40. Wienold, J.; Christoffersen, J. Evaluation methods and development of a new glare prediction model for daylight environments with the use of CCD cameras. *Energy Build.* **2006**, *38*, 743–757. [CrossRef]
41. Sutter, Y.; Dumortier, D.; Fontoynont, M. The use of shading systems in vdu task offices: A pilot study. *Energy Build.* **2006**, *38*, 780–789. [CrossRef]
42. Linney, A. Maximum Luminances and Luminance Ratios and Their Impact on Users' Discomfort Glare Perception and Productivity in Daylight Offices. Master's Thesis, Victoria University of Wellington, Wellington, New Zealand, 2008.
43. Wymelenberg, K.V.D.; Inanici, M. Evaluating a New Suite of Luminance-Based Design Metrics for Predicting Human Visual Comfort in Offices with Daylight. *Leukos* **2016**, *12*, 113–138. [CrossRef]
44. Mardaljevic, J.; Andersen, M.; Roy, N.; Christoffersen, J. Daylighting metrics: Is there a relation between useful daylight illuminance and daylight glare probability? In Proceedings of the First Building Simulation and Optimization Conference Loughborough 2012, Leicester, UK, 10–11 September 2012.
45. Pilkington. Glass Handbook. 2014. Available online: https:www.pilkington.com/-/media/pilkington/site-content/poland/trade/downloads/handbook_2014_eng.pdf (accessed on 13 September 2021).
46. Energy Plus Weather Web Page. Available online: https://energyplus.net/weather (accessed on 14 October 2021).
47. Kalogirou, S.A. Photovoltaic systems. In *Solar Energy Engineering: Processes and Systems*; Elsevier Inc.: London, UK, 2014.
48. Duffie, J.A.; Beckman, W.A. Design of photovoltaic systems. In *Solar Engineering of Thermal Processes*; John Wiley & Sons, Inc.: Hoboken, NJ, USA, 2013.
49. Ameur, A.; Berrada, A.; Loudiyi, K.; Aggour, M. Forecast modeling and performance assessment of solar PV systems. *J. Clean. Prod.* **2020**, *267*, 122167. [CrossRef]
50. Data for Energy Calculation of Buildings in Poland. Available online: https://archiwum.miir.gov.pl/strony/zadania/budownictwo/charakterystyka-energetyczna-budynkow/dane-do-obliczen-energetycznych-budynkow-1/ (accessed on 13 September 2021). (In Polish)
51. Mathews, J.H.; Fink, K.D. *Numerical Methods Using MATLAB*, 4th ed.; Pearson Prentice Hall: Upper Saddle River, NJ, USA, 2004.
52. Mesloub, A.; Ghosh, A.; Touahmia, M.; Albaqawy, G.A.; Noaime, E.; Alsolami, B.M. Performance Analysis of Photovoltaic Integrated Shading Devices (PVSDs) and Semi-Transparent Photovoltaic (STPV) Devices Retrofitted to a Prototype Office Building in a Hot Desert Climate. *Sustainability* **2020**, *12*, 10145. [CrossRef]
53. Mesloub, A.; Albaqawy, G.A.; Kandar, M.Z. The Optimum Performance of Building Integrated Photovoltaic (BIPV) Windows Under a Semi-Arid Climate in Algerian Office Buildings. *Sustainability* **2020**, *12*, 1654. [CrossRef]
54. Bodart, M.; Cauwerts, C. Assessing daylight luminance values and daylight glare probability in scale models. *Build. Environ.* **2017**, *113*, 210–219. [CrossRef]

MDPI